OPTIMISATION OF A SOLAR PHOTOVOLTAIC-DRIVEN, ROOF SLATE-BASED VENTILATION PREHEATING SYSTEM

NASER A. ODEH

A thesis submitted in partial fulfilment of the requirements of Napier University for the degree of Doctor of Philosophy

July 2005

DECLARATION

I hereby declare that the work presented in this thesis was solely carried out by myself at Napier University, Edinburgh, except where due acknowledgement is made, and that it has not been submitted for any other award.

Naser Odeh

Date

ABSTRACT

Condensation related dampness and the subsequent mould formation, resulting from the lack of ventilation, in airtight buildings lead to significant health problems inside dwellings. Delivering sufficient ventilation rates for energy efficient modern buildings is a necessity. In cold climates, in order to avoid energy losses, this ventilation air must be preheated before being admitted to the house. Due to the continuous depletion of oil resources and the escalating impact of the greenhouse effects on global climate it is necessary to economise energy consumption. Solar energy offers itself as a means for preheating ventilation air. Solar ventilation preheating is an emerging technology not only in countries with cold climates but also in warm climates where it is used for drying crops.

The newly developed roof-slate based solar ventilation preheater makes use of the existing roof slates as a solar collector. A photovoltaic-driven fan draws warm air through the spaces between the slates and delivers it via a flexible duct into the house underneath for ventilation. The photovoltaic module acts as a quick response sensor, which allows the fan to operate only when the slates are warm. A model for predicting the flow rate of air in the system as a function of irradiance, ambient temperature and wind speed in addition to the photovoltaic, fan and duct specifications was developed. The model predicts the fan's speed and the system's flow rate with an accuracy of 92% and 88% respectively.

The model was employed for system optimisation with respect to the maximum volume of air delivered. The optimum system comprises a 24 V DC, 9.5 W fan with a free flow capacity of 69 l/s. This system delivers $9.6 \times 10^4 m^3$ of warm air (a constant 9.2 l/s on a continuous basis which meets the ASHRAE recommendations for a 100-m^3 room with one occupant). The optimum system can also potentially deliver 161 kWh energy with a solar fraction of 11% during the heating season. The optimum system was found to be optimum in several respects including maximising volume, efficiency, solar savings, and minimising payback period (13 years). This system can contribute to CO_2 savings by as much as 100 kg annually.

Recommendations to further maximise the utilisation of the maximum power of the PV module included using an optimum motor constant so that the fan operates in the maximum power vicinity for most of the year. A new method for obtaining the photovoltaic current-voltage characteristic was developed. This method predicts the maximum power of the photovoltaic module with 92% accuracy. The optimum motor constant was expressed directly as a function of irradiance and module temperature. The yearly output of the PV module employing the optimum system is 10.4 kWh. Using a fan with the optimum motor constant would increase the energy utilised by 14 %. Furthermore, an optimum length of duct (8 m) would maximise pneumatic output and deliver higher overall flow efficiencies.

Upon comparative testing, it was found that a cooling effect was associated with an early start of the optimum system. This can be overcome by delaying the start of the fan until the slates are warm enough or by enhancing the properties of the slates (using dark paint or anti-reflective coating) so that they warm up synchronously with the fan starting time.

ACKNOWLEDGEMENTS

I would like first to thank my supervisory team, Thomas Grassie, Douglas Henderson, and Tariq Muneer for their great support and helpful discussions. I am most grateful to the confidence they had in me and in my work.

I would also like to thank my family for their help and support. I am most grateful to my parents for their encouragement and support throughout my years of education. To my wife, Sondos, and my children Yazan and Tala, I thank you for making this the greatest experience of my life. I will treasure the memories for years to come.

Special thanks to Meg Beresford and everybody at Wiston Lodge for their hospitality. I will always remember the friendly environment and wonderful discussions.

I would like also to thank the technical staff, Ian Campbell, Kevin McCann, Pete Bruce, Derek Cogle, Alan Barber, Jim Gordon and all the others. Your help throughout my work is deeply appreciated.

Finally, I would like to thank my office colleagues, Asif, Feng, Wissrutta, Serge, Saima, Andy, and Haroon. I wish you all the best in your present studies and future careers.

CONTENTS

LIST OF FIGURES

LIST OF TABLES

LIST OF TEXTBOXES

NOMENCLATURE

a	Effective area of PV module, m^2
a_s	Area of slates from which air is drawn, m^2
A	Curve fitting parameter, V
AM	Air mass
C_S	Initial investment, £
D	Diameter of duct, m
dr	Diffuse ratio
e	Band gap energy, eV
E	Heat delivered, J
E'	Rate of heat, W
E_x	Extraterrestrial irradiance, W/m^2
Ext	Extension of flexible duct, %
f	friction factor
F	Exponential term ($e^{\frac{V + I \cdot R_S}{A}} - 1$)
FF	Filling factor
F_{IR}	Clearness function
G	irradiance falling on PV module, W/m^2
G_{sc}	Solar constant, W/m^2
h	Inverse of iteration step
I	Irradiance on horizontal surface, W/m^2
I_0	reverse saturation current, A
I_b	Horizontal beam irradiance, W/m^2
I_D	Diode current, A
I_d	Horizontal diffuse irradiance, W/m^2
I_G	Thermally generated current, A
I_m	Current at maximum power of PV module, A
Is	Start-up current, A
I_{SC}	Short circuit current of PV module, A
I_{Sh}	Current through shunt resistance, A
I_{Tc}	Threshold irradiance, W/m^2
I_{fan}	Fan current, A
I_{PV}	Photovoltaic current, A

I_{tilt}	Global irradiance on tilted surface, W/m^2
$I_{b,\,tilt}$	Beam irradiance on tilted surface, W/m^2
$I_{d,\,tilt}$	Diffuse irradiance on tilted surface, W/m^2
k	Roughness coefficient, mm
K_B	Boltzmann constant, J/K
k_T	Clearness index
K_f	Motor – fan Coupling constant, $Kg.m^2/rad^2$
K_m	Motor constant, V.s/rad
L	Length of duct, m
L_A	Auxiliary energy purchased, J
L_o	Load required by house, J
L_s	Solar energy delivered, J
L_{eff}	Effective duct length, m
N_p	Payback period, years
N_{Re}	Reynolds number
P_{el}	Electrical power of the fan, W
P_m	Maximum power of PV module, W
P_v or ΔP_{Vel}	Velocity pressure, Pa
P_w	Pneumatic power, W
P_{atm}	Barometric pressure, Pa
q	Electron charge, Coulomb
Q	Flow rate, l/s
r	Ratio of volume delivered to radiation received by PV module, m^3/J
R	Ratio of global irradiance on tilted surface to horizontal irradiance
R_a	Armature resistance, Ω
R_b	Ratio of beam irradiance on tilted surface to horizontal irradiance
R_d	Ratio of diffuse irradiance on tilted surface to horizontal irradiance
R_S	Series resistance of PV cell, Ω
R_{Sh}	Shunt resistance of PV cell, Ω
sf	Solar fraction
TF	Surface tilt factor
T_L	Load torque, N.m
T_m	Motor torque, N.m
T_{air}	Temperature of air in the duct, C

T_{amb}	Ambient temperature, C
T_{Box}	Temperature of air in the fan box, C
T_{mod}	PV module temperature, C
T_{outlet}	Temperature of air at the outlet or delivered temperature, C
T_{Slate}	Slate temperature, C
U	Loss coefficient, W/C
V_e	Voltage dissipated in electronic components of brushless DC motor, V
V_{OC}	Open circuit voltage of PV module, V
V_m	Voltage at maximum power, V
Vs	Start-up voltage, V
V_{fan}	Fan voltage, V
V_{PV}	Photovoltaic voltage, V
ws	wind speed, m/s

Symbols

α	Slope of surface
δ	Declination
δI	Change in current, A
$\delta\eta$	Change in efficiency
ΔP_f	Pressure across fan, Pa
ΔP_s	System pressure, Pa
ΔP_{St}	Static pressure, Pa
ΔP_{Tot}	Total pressure, Pa
ΔP_{Vel} or P_v	Velocity pressure, Pa
ε	Effectiveness
ϕ	Latitude
ϕ_h	Utilisability
$\eta_{PV\text{-}Fan}$ or η_c	Efficiency of PV-fan system $= \frac{V \cdot I}{G \cdot a}$
$\eta_{Fan\text{-}Duct}$	Efficiency of fan-duct system $= \frac{\Delta P \cdot Q}{I \cdot V}$
$\eta_{Overall}$	Overall flow efficiency $= \eta_{Fan-Duct} = \frac{\Delta P \cdot Q}{G \cdot a}$
μ	Viscosity, kg/m.s

μ_{ISC}	Temperature coefficient of short circuit current, A/C
μ_{Pm}	Temperature coefficient of maximum power, W/C
μ_{VOC}	Temperature coefficient of open circuit voltage, V/C
v	Air velocity in duct, m/s
$\bar{v}$	Average air velocity in duct, m/s
v_{max}	Maximum air velocity in duct, m/s
θ	Incidence angle of irradiance
ρ	Density, kg/m^3
$\tau\alpha$	transmittance-absorptance product
ω	Rotational speed, rad/s
ω_s	Sun hour angle
ω_{max}	maximum rotational speed, rad/s

SUBSCRIPTS

ref	Reference conditions
PV	PV module
Fan	fan

LIST OF ABBREVIATIONS

AC	Alternating current
BIPV	Building integrated PV module
DC	Direct current
DOE	Department of Energy
DTI	Department of Trade and Industry
EPA	Environmental Protection Agency
EST	Energy Saving Trust
ESRU	Energy Systems Research Unit
IV	Current-voltage fan characteristic
MPT	Maximum power tracking
NOCT	Nominal Operating Cell Temperature, C
NLR	Nonlinear regression
NPMV	Negative pressure mechanical ventilation
Q-G	Flow vs. irradiance curve
PDCF	Pressure drop correction factor
PM	Permanent magnet
PPMV	Positive pressure mechanical ventilation
PV	Photovoltaic
RSB	Roof slate-based
SAH	Solar air heating
SEDC	Separately Excited DC
SSEG	Scottish Solar Energy Group
STC	Standard Test Conditions
TSC	Transpired Solar Collector
VBA	Visual Basic for Applications
WF	Wound field
ΔP_f-Q	Fan head-flow characteristic
ΔP_s-Q	System head-flow characteristic
η-G	Efficiency vs. irradiance curve
ωV	speed-voltage fan characteristic
ωG	Speed vs. irradiance curve
ωT	Speed vs. torque characteristic

LIST OF PUBLICATIONS

1 ESTIMATING THE PERFROMANCE OF A PV-DRIVEN FAN IN A SOLAR AIR HEATING SYSTEM
Pub. Eurosun 2004, Freiberg, Germany, May 2004.

2 SLOPE IRRADIANCE MODELLING FOR SCOTLAND
Pub. Eurosun 2004, Freiberg, Germany, May 2004.

3 COMPARATIVE TESTING OF PV-DRIVEN ROOF SLATE-BASED SOLAR VENTILATION PREHEATING SYSTEMS
Pub. Northsun 2005, Vilnius, Lithuania, May 2005

4 A NEW METHOD FOR ESTIMATING THE OPTIMUM MOTOR CONSTANT FOR PV-DRIVEN SYSTEMS
Pub. Northsun 2005, Vilnius, Lithuania, May 2005

5 MODELLING OF FLOW RATE IN A PHOTOVOLTAIC-DRIVEN ROOF SLATE-BASED SOLAR VENTILATION PREHEATING SYSTEM
Accepted by Energy Conversion And Management, June 10, 205. IN PRESS.

ARTICLES COMMUNICATED

OPTIMISATION OF A PHOTOVOLTAIC-DRIVEN ROOF SLATE-BASED SOLAR VENTILATION PREHEATING SYSTEM
Communicated. Energy Conversion and Management, June, 2005.

1. INTRODUCTION

1.1 INDOOR COMFORT AND HEALTH IN SCOTLAND

In modern, western societies, people spend more than 90% of their time indoors and so it is necessary to provide both a comfortable and healthy internal living environment. The ASHRAE comfort standard 55 (ASHRAE, 1981) defines an acceptable level of comfort as that provided by an environment in which 80 % of all occupants are, by their own definition, comfortable. Building designers and engineers should be familiar with both thermal and air quality requirements necessary to achieve an acceptable level of comfort for the majority of occupants. This necessitates an awareness of the factors affecting comfort inside the house. These include temperature, humidity, air movement, and air quality. It is very important to keep room temperature, humidity, and air movement constant for comfort inside the house to be achieved. These three parameters are well recognised as the direct indices for describing the environment inside a house, (Awbi, 1991). Controlling ventilation rates inside the house contributes to maintaining these factors at a comfortable level. In addition to these environmental factors, the quality of indoor air with regard to odor, dust, and bacteria also influences human comfort. Until recently, the control of indoor air quality came about naturally by infiltration through the building structure. The indoor air quality question has become rather important as a result of the energy crisis in the early 1970s when construction of airtight energy-efficient buildings became a pattern (Awbi, 1991).

The sources of indoor pollutants can be external or internal. Outdoor air is considered a source of pollution because it contains pollutants from automotive exhausts and other industrial sources. Recently, problems have arisen from contaminants generated by the building and its contents. It is reported that air pollution in the average American home, as measured by the Environmental Protection Agency (EPA), is usually 2 to 5 times worse than outdoors (U.S. Environmental Protection Agency, 1995). Examples of indoor pollutants include argon, asbestos, tobacco smoke, and dust mites. Poor indoor air quality causes 50% of all illnesses and can lead to a host of health problems for people of all ages.

In addition to the aforementioned indoor contaminants, water vapor is also considered a pollutant (NuAire Group, 2004). Water vapor is produced by day-to-day

activities such as bathing, cooking and washing and it soon dissolves in air and travels throughout the house. When moist air comes into contact with a cold surface, such as windows and internal walls, condensation occurs if the surface temperature is equal to, or below, the dew point. The relation between air temperature, relative humidity, and percentage saturation of the water vapor–air mixture is usually presented graphically by the Psychrometric chart. For a given level of humidity, the dew point is readily determined from this chart.

Increased humidity and condensation dampness can cause discomfort and, in the long term, create and maintain an environment, which can support the growth of harmful species. High humidity can cause thermal discomfort through reducing the rate of sweat evaporation through the skin. Furthermore, dust mites, who are very harmful to the respiratory system, breed best in humid environments. It is clinically proven that more than 80 % of asthmatics are allergic to the faeces of dust mites (Johnston, 2002). Condensation can also cause degradation of the wall and furniture fabric. It is estimated that the cost of repairing the damage caused by timber decay in the UK housing stock is presently £ 400 M per annum (Singh, 1995 as reported by Strathclyde Energy Systems Research Unit, 2004). Moreover, increased humidity can cause stuffiness and smell and, if prolonged, can result in fungal growth.

Dampness and mould growth, resulting from condensation, are recognised as major problems affecting about 2.5 million houses in the UK (0.25 million in Scotland) (Scottish Homes, 1993). Data from the 1991 Scottish housing condition survey reveal that about 12 % of all houses are affected. In 1996, similar studies showed that 25 % of houses in Scotland (534,000) are affected. Given suitable humidity conditions and nourishment, spores of mould and fungi can germinate and grow on surfaces over a wide range of temperatures and certainly between 0 and 20° C. Some mould spores can germinate at 80 – 85 % relative humidity and can spread if the humidity is over 70 % for long periods (Wilkinson, 1999).

Well-established research in the field of environmental health shows that there is a strong relationship between both dampness and mould and ill health inside the house. Many moulds in damp houses are allergenic and provide a food supply for dust mites. At some stages of their life cycle, some fungi become toxic. A 1984 World Health Organisation Committee report suggested that up to 30 % of new and remodelled

buildings worldwide suffer from poor air quality. A Scottish study in Edinburgh and Glasgow (Martin et al, 1987, as reported by Wilkinson, 1999) concluded that mould allergy is a cause of ill health for both children and adults. Symptoms of illness included vomiting, blocked nose, breathlessness, backache, fainting and bad nerves. Another study in Glasgow (Williamson et al, 1997) demonstrated links between dampness and asthma. The above study found that people living in damp houses were two to three times more likely to have asthma.

Poor heating is also a problem for housing in Britain. While, in Britain, high humidity, and consequently dampness and mould growth is commonly associated with cold temperatures, a body of research has focused on the effects of air temperature on health. Studies showed that for each degree Celsius by which the winter is colder than the average, there are an excess of 8000 deaths (Wilkinson, 1999). From January to March, there are typically 20,000 more deaths in the UK than the average rate for the year. A report on health in the Lothians estimated that the number of excess winter deaths in Scotland is 4,000 to 7,500 (a greater proportion per capita) (Zealey, 1991 as reported by Wilkinson, 1999)

1.1.1 Summary

In consideration of the situation when internal surfaces may be at, or below the dew point, the preceding discussion detailed the potential health risks posed by both poor heating and condensation dampness as a result of water vapor accumulation inside the house. It is concluded that, in order to achieve comfort in houses, it is important to prevent condensation dampness. The build-up of moisture indoors can be reduced by ventilation because outdoor air normally has lower moisture content particularly in the winter (Strathclyde Energy Systems Research Unit, 2004).

1.2 VENTILATION

Ventilation of a building performs two functions: provision of fresh air and dilution or extraction of contaminants. Ventilation can be performed either mechanically or using natural ventilation. The amount of outdoor air required for ventilation is dependent on the rate of contaminant generation and the maximum acceptable contaminant level. ASHRAE standard 62 (ASHRAE, 1988) defines acceptable air quality as ambient air in which there are no known contaminants at harmful concentrations and with which substantial majority of occupants do not express dissatisfaction. When the outdoor air contaminant levels exceed the values provided by ASHRAE, the air must be treated of offending contaminants. Indoor air quality is considered acceptable when the recommended ventilation rates of acceptable outdoor air are provided. According to ASHRAE standards, for residential spaces, the recommended outdoor air requirement for ventilation is 0.35 air changes per hour (ACH) but not less than 7.5 l/s per person (ASHRAE, 2001). Misunderstanding of the factors affecting required ventilation rates can lead to delivering excessive quantities of outdoor air and thus loss of energy.

1.2.1 Natural ventilation

The most common form of natural ventilation is using openable windows. The driving force for natural ventilation is either wind or thermally (stack) generated pressure difference between indoors and outdoors (Liddament, 1996). In the former type, wind causes a positive pressure on the windward side and a negative pressure on the leeward side of buildings as shown in Fig. 1.1. To equalize pressure, fresh air will enter any windward opening and be exhausted from any leeward opening. In summer, wind is used to supply as much fresh air as possible while in winter, ventilation is normally reduced to levels sufficient to remove excess moisture and pollutants.

In the case of "stack pressure," a pressure difference will exist due to the density gradient caused by temperature difference. If the inside air temperature is higher than the outside air temperature, ventilation air enters through openings at the bottom and escapes through openings at a higher level.

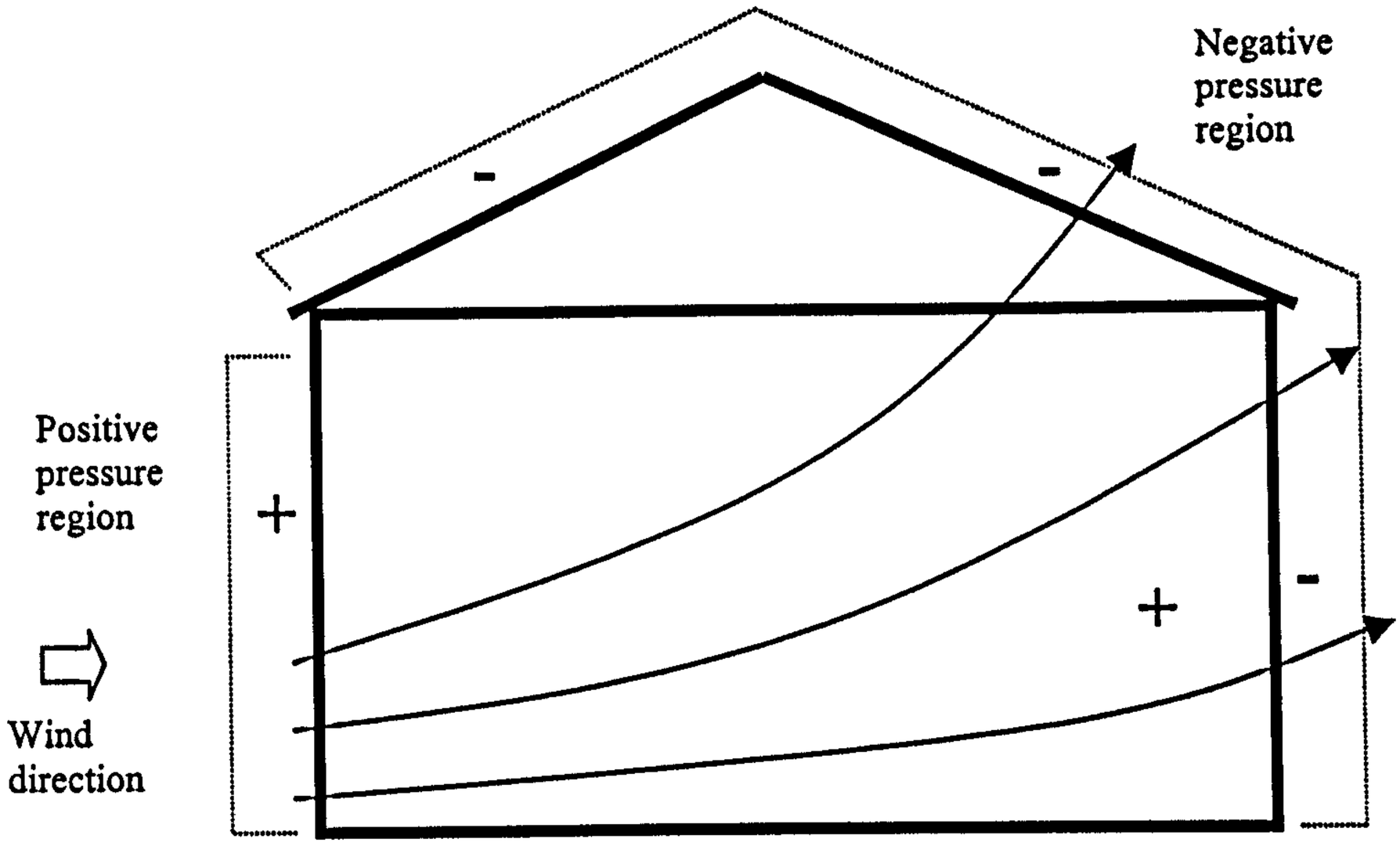

Fig. 1.1: Natural ventilation with wind as the driving force.

In recent years, the concept of a solar chimney for enhancing natural ventilation has been introduced. A solar chimney can be either south facing or it can be the roof of a building. South-facing chimneys are constructed of concrete or masonry walls. The outer south-facing wall is replaced with glazing and the interior of the other walls is blackened and the exterior insulated. After being warmed by solar energy, air rises through the chimney and leaves at the upper opening thus inducing fresh air to enter the house as shown in Fig. 1.2. Several researchers showed that natural ventilation rate increased with chimney wall temperature (Bouchair, 1994). Khedari et al (1997) added a photovoltaic-driven DC fan in the structure of a roof solar collector to enhance the rate of natural ventilation. Ventilation rates were 2-4 times higher than those obtained when no fan was used.

Natural ventilation is most suited to buildings in climates with mild to moderate outdoors average temperatures. For climates with severe weather conditions, such as in Northern Europe and Canada, outside air temperatures are usually too cold and average wind speeds too high for natural ventilation to be energy efficient. Natural ventilation is also suitable to buildings away from inner city locations where outdoors air is more polluted. So, even though it is inexpensive, when compared to mechanical ventilation, natural ventilation can cause indoor air quality problems and excessive heat loss. Furthermore, cleaning and filtration of incoming air in not usually practicable when natural ventilation is used.

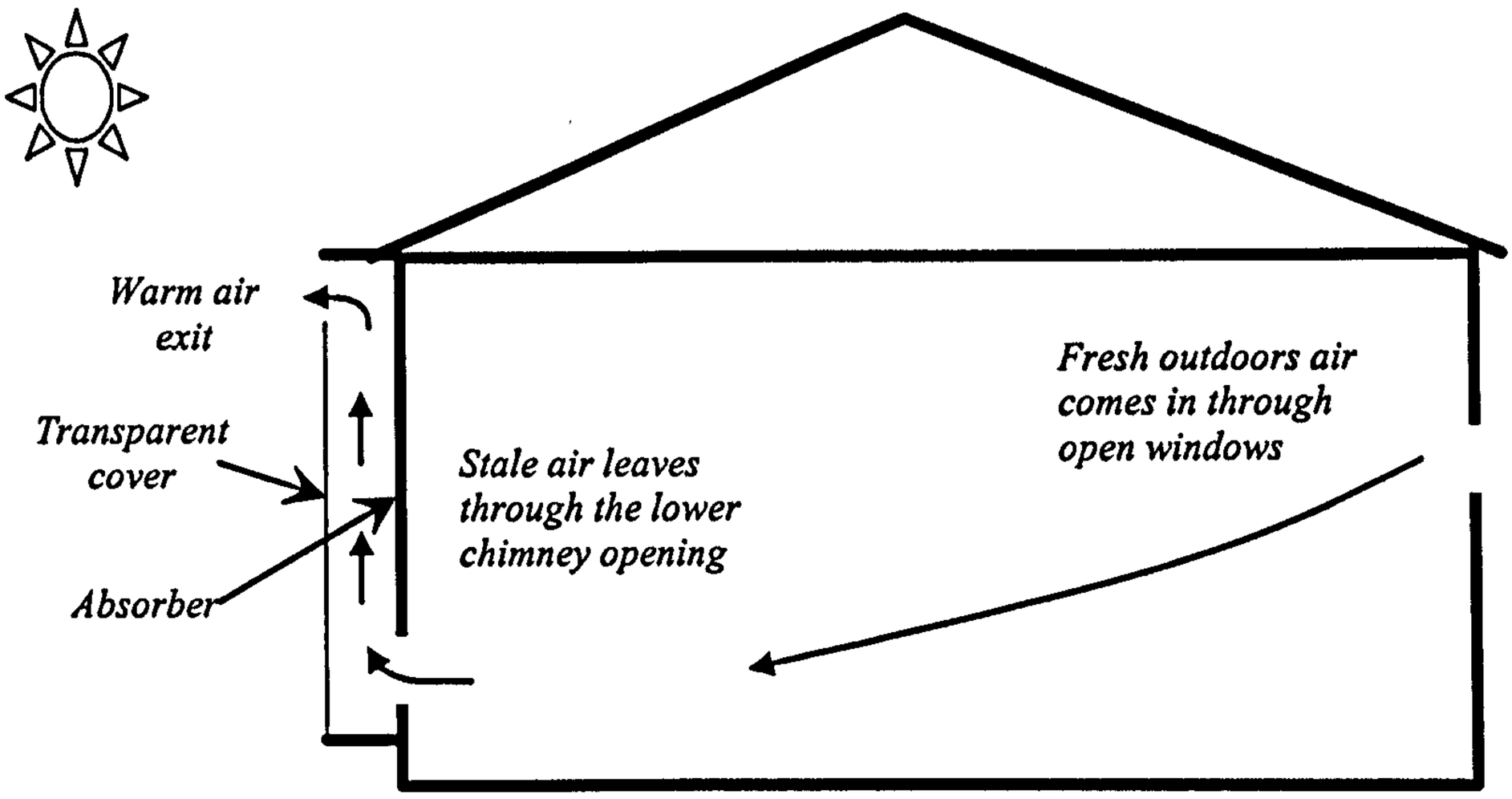

Fig. 1. 2: A solar chimney for enhancing natural ventilation.

1.2.2 Mechanical ventilation

A mechanical ventilation system comprises various components including fans, ducts, and grills. They are appropriate for providing controlled ventilation to a house and they are most appropriate for severe climatic regions. Mechanical ventilation systems can either operate in an extract mode (negative-pressure) or supply mode (positive pressure) as discussed later in this section.

Unlike natural ventilation systems, mechanical ventilation systems allow the control of ventilation rates. Moreover, through the use of filters and dehumidifiers, they reduce the risk of pollutant ingress into occupied spaces and the risk of moisture entering walls. Furthermore, they allow heat recovery from the exhaust air stream. These systems, however, are more expensive and require higher operational and maintenance costs. In airtight buildings with a ventilation system, 50 % of energy used is by fans and so mechanical ventilation can considerably add to the energy cost. Liddament (1996) states that good mechanical ventilation systems require electrical power at 1 W or less for each litre/s of airflow.

1.2.2.1 Negative-pressure mechanical ventilation

In a negative-pressure mechanical ventilation (NPMV) system, a fan is used to mechanically remove air from a space. This process induces a "suction" thus promoting outdoors air to flow into the living space through provided air inlets. Optimum operational efficiency is achieved by designing the NPMV system so that it always operates at slightly higher pressures than those induced by weather (i.e. natural ventilation).

1.2.2.2 Positive-pressure mechanical ventilation

In positive-pressure mechanical ventilation (PPMV) systems, the air is mechanically introduced into the system where it either mixes with or completely replaces air in the living space. This process induces a positive pressure forcing stale air to leave the living space through provided infiltration openings as shown in Fig. 1.3. If the system is well designed and the building is airtight, a PPMV system inhibits the ingress of infiltrating air and thus allows inlet air to be pre-cleaned and thermally conditioned.

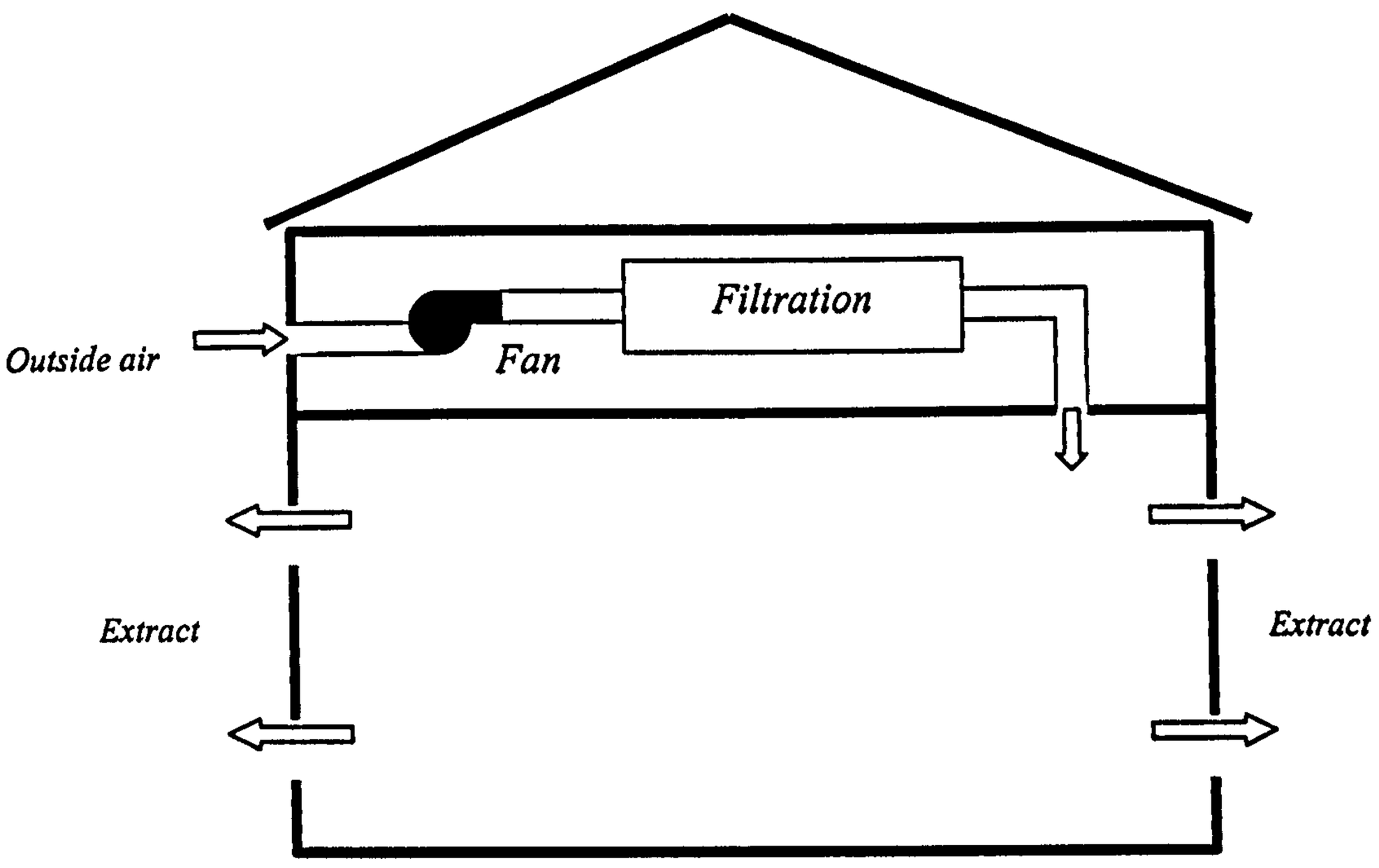

Fig. 1.3: Positive pressure mechanical ventilation system.

Since the incoming air can be pre-cleaned by filtration, PPMV systems are extremely useful in areas with highly polluted outdoor air. Furthermore, these systems can also be used in residences where allergy control is required. In this case, care is needed to prevent moisture, generated in the dwelling, from penetrating and condensing in the building fabric. This can be achieved by placing the grilles and extractors in these areas.

PPMV systems have several advantages over NPMV systems. In the former type, the risk of flue back-draughting is reduced and entry of outside pollutants and soil gases such as Radon is inhibited. Moreover, in PPMV systems, good air control is possible and outdoor air can be cleaned and conditioned. However, in PPMV systems, heat recovery is not possible as is the case with NPMV systems.

1.2.3 Summary

The previous discussion shows that a mechanical ventilation system is most appropriate for Scotland where adverse weather conditions usually exist. Furthermore, PPMV is advantageous because it allows for elimination of outside contaminants. For adverse weather conditions, however, if ventilation rates are increased then heating bills also rise, as extra heat must be supplied to warm up the cooler incoming air. The use of fan in mechanical ventilation systems can also add to the energy cost. This extra cost can be minimised if solar energy is used as a thermal energy source to preheat ventilation air, and also, through the use of photovoltaic (PV) modules as a source of electrical energy to run the fan. The following section discusses the potential for solar energy utilisation at higher latitudes.

1.3 SOLAR ENERGY AT HIGHER LATITUDES

The utilization of solar energy for domestic and industrial use has become one of the fastest growing areas of research. This accelerated interest in solar energy is attributed to the increase in oil prices, depletion of oil resources, and growing environmental pollution consciousness. Figure 1.4 indicates future predictions for depletion in oil and gas resources. While these sources are depleting, it is predicted that by the year 2020 the energy demand worldwide will increase by 50 % (International Energy Outlook, 2004). This necessitates searching for other sources of energy.

The sun is an inexhaustible and clean source of energy. It can be calculated that as much solar energy falls on the surface of Earth in one hour as the world's nations consume as fuel in the course of a whole year. Even in cloudy northern countries there is more than enough solar energy to meet the demand. The total falling on the UK over a year, for example, exceeds over twenty fold the countries current annual requirement for energy. If widely adopted, solar technology can dramatically decrease CO_2 emissions from oil, gas and electricity production by displacing a significant proportion of these fuels.

Figure 1.5 (for the UK) indicates that a very large portion of the heat requirement goes into the domestic sector. Thus, it is very important to make use of solar energy for purposes such as domestic water heating and space heating. However, the amount of solar energy available at higher latitudes is less than that generally available at locations closer to the equator. It is reported by Page and Lebens (1986) that, for the UK, the average annual irradiation falling on a south-facing surface tilted at 45° is approximately 1000 kWhr/m^2. Moreover, Strathcylde's Energy Systems Research Unit (ESRU) has calculated that each south facing roof in Scotland receives between 700-1100 kWh/m^2 each year. For locations closer to the equator this can reach up to 2500 kWh/m^2. However, as temperatures to the north (i.e. Northern Europe) are generally lower and, consequently, the heating season is longer, solar generated heat may be better utilised at higher latitudes. For example, the use of solar water heating systems as the primary heat source for heating both domestic hot water and under floor heating systems is becoming very common in Northern Europe (Renewable Energy World, 2002).

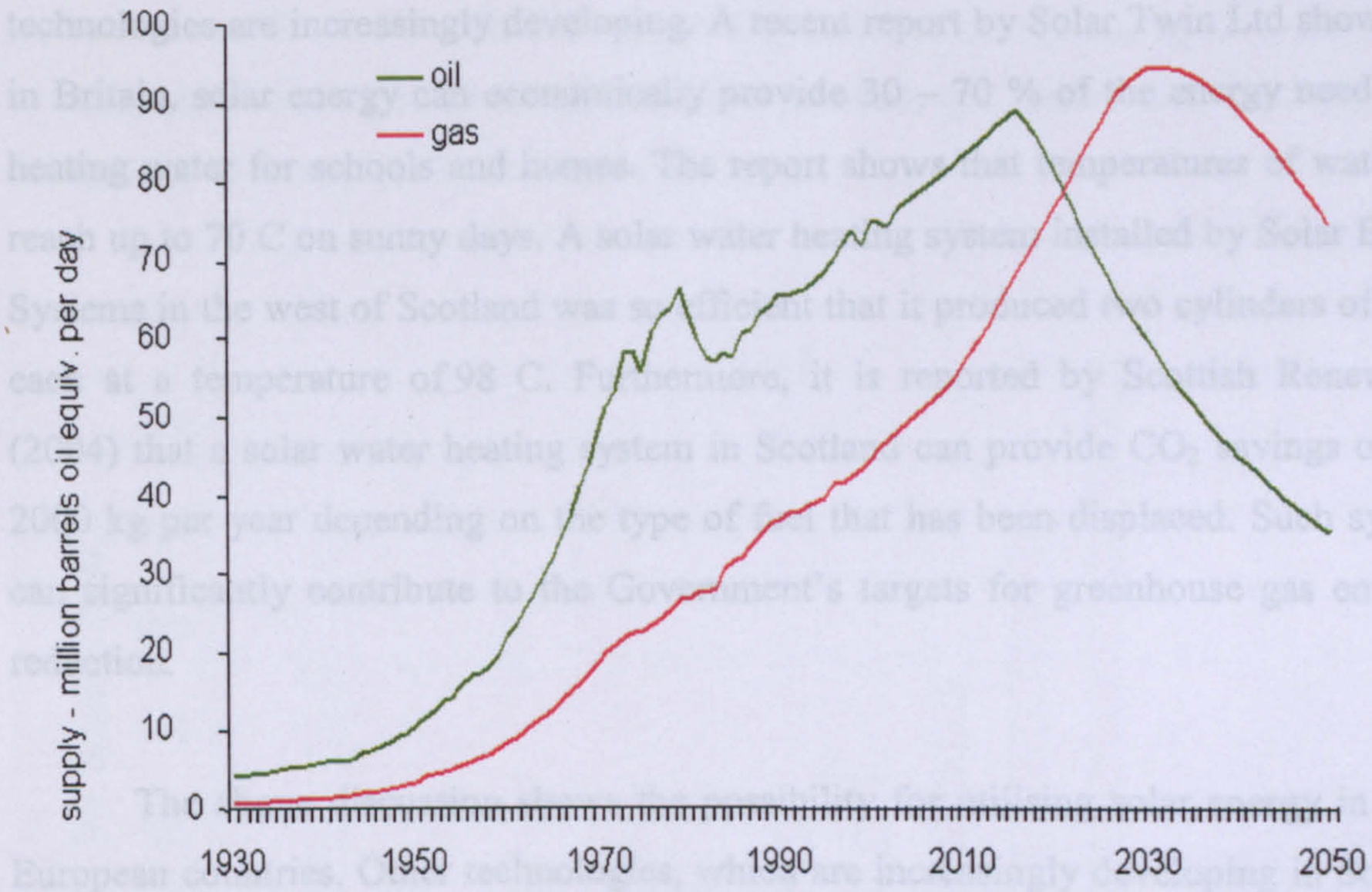

Fig. 1.4: Future prediction for oil and gas supply (European Commission).

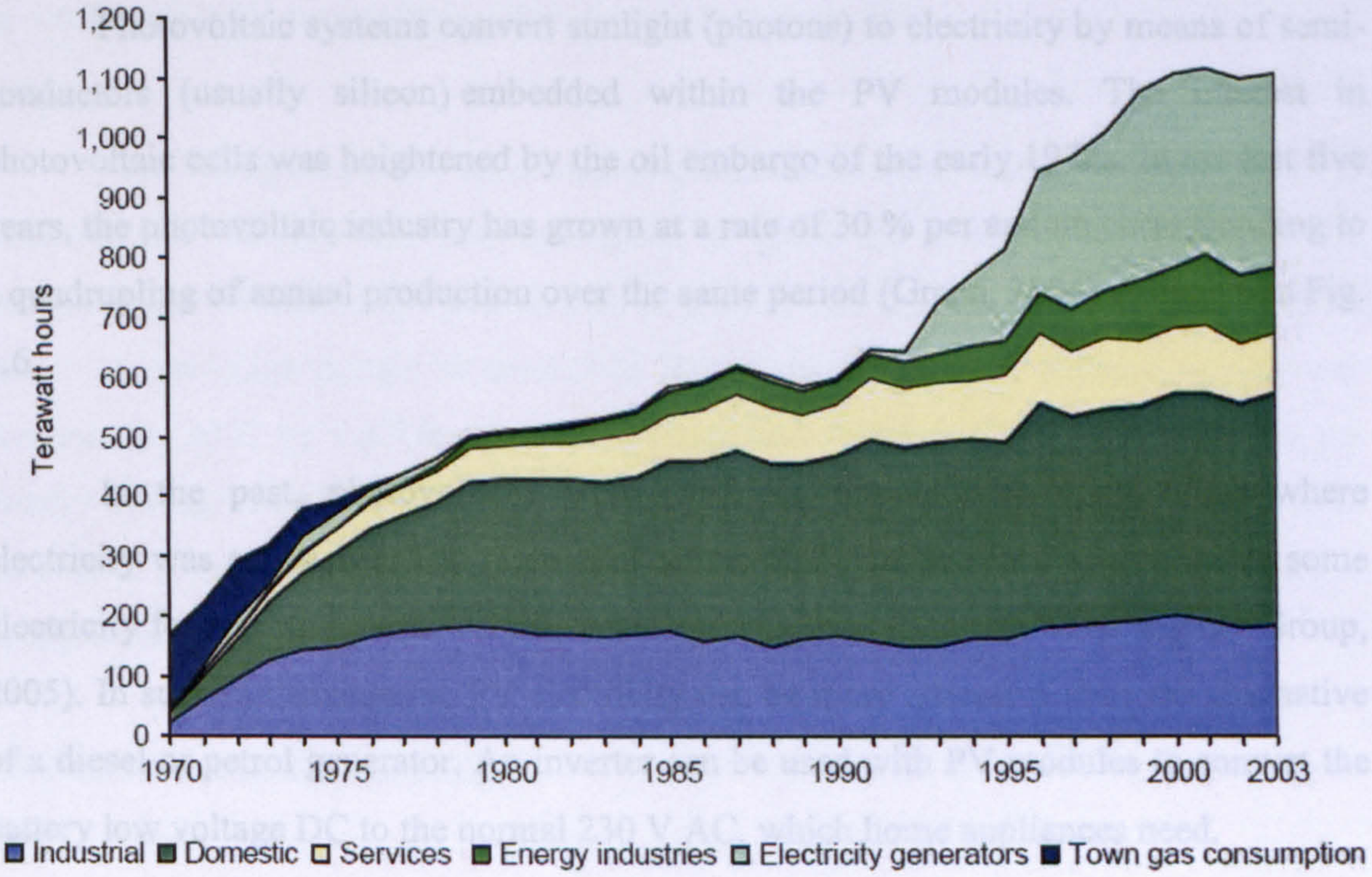

Fig. 1.5: Consumption of town gas and natural gas in the UK, 1970 to 2003.

In Scotland, as well as in other North-European countries, solar water heating technologies are increasingly developing. A recent report by Solar Twin Ltd shows that in Britain, solar energy can economically provide 30 – 70 % of the energy needed for heating water for schools and homes. The report shows that temperatures of water can reach up to 70 C on sunny days. A solar water heating system installed by Solar Energy Systems in the west of Scotland was so efficient that it produced two cylinders of water each at a temperature of 98 C. Furthermore, it is reported by Scottish Renewables (2004) that a solar water heating system in Scotland can provide CO_2 savings of over 2000 kg per year depending on the type of fuel that has been displaced. Such systems can significantly contribute to the Government's targets for greenhouse gas emission reduction.

The above discussion shows the possibility for utilising solar energy in North European countries. Other technologies, which are increasingly developing in Scotland and worldwide, are photovoltaic (PV) technology and solar ventilation preheating technology.

1.3.1 Photovoltaic technology

Photovoltaic systems convert sunlight (photons) to electricity by means of semi-conductors (usually silicon) embedded within the PV modules. The interest in photovoltaic cells was heightened by the oil embargo of the early 1970s. In the last five years, the photovoltaic industry has grown at a rate of 30 % per annum corresponding to a quadrupling of annual production over the same period (Green, 2004) as shown in Fig. 1.6.

In the past, photovoltaics were used for remote area applications where electricity was expensive. The main application of PV in Scotland is to provide some electricity for remote houses, cabins, boats and caravans (Scottish Solar Energy Group, 2005). In such circumstances, PV electricity can be more attractive than the alternative of a diesel or petrol generator. An inverter can be used with PV modules to convert the battery low voltage DC to the normal 230 V AC, which home appliances need.

It is also possible to have a PV system on dwellings which have a mains power supply. In that case, no battery is needed and the direct current (DC) supplied by the PV

can be changed to the alternating current (AC) of the mains, so the two systems can be interconnected. If the PV module is generating more electricity than needed, the surplus is transported to the grid/mains. If the electrical needs are greater than the PV supply, the difference is supplied by the mains as normal.

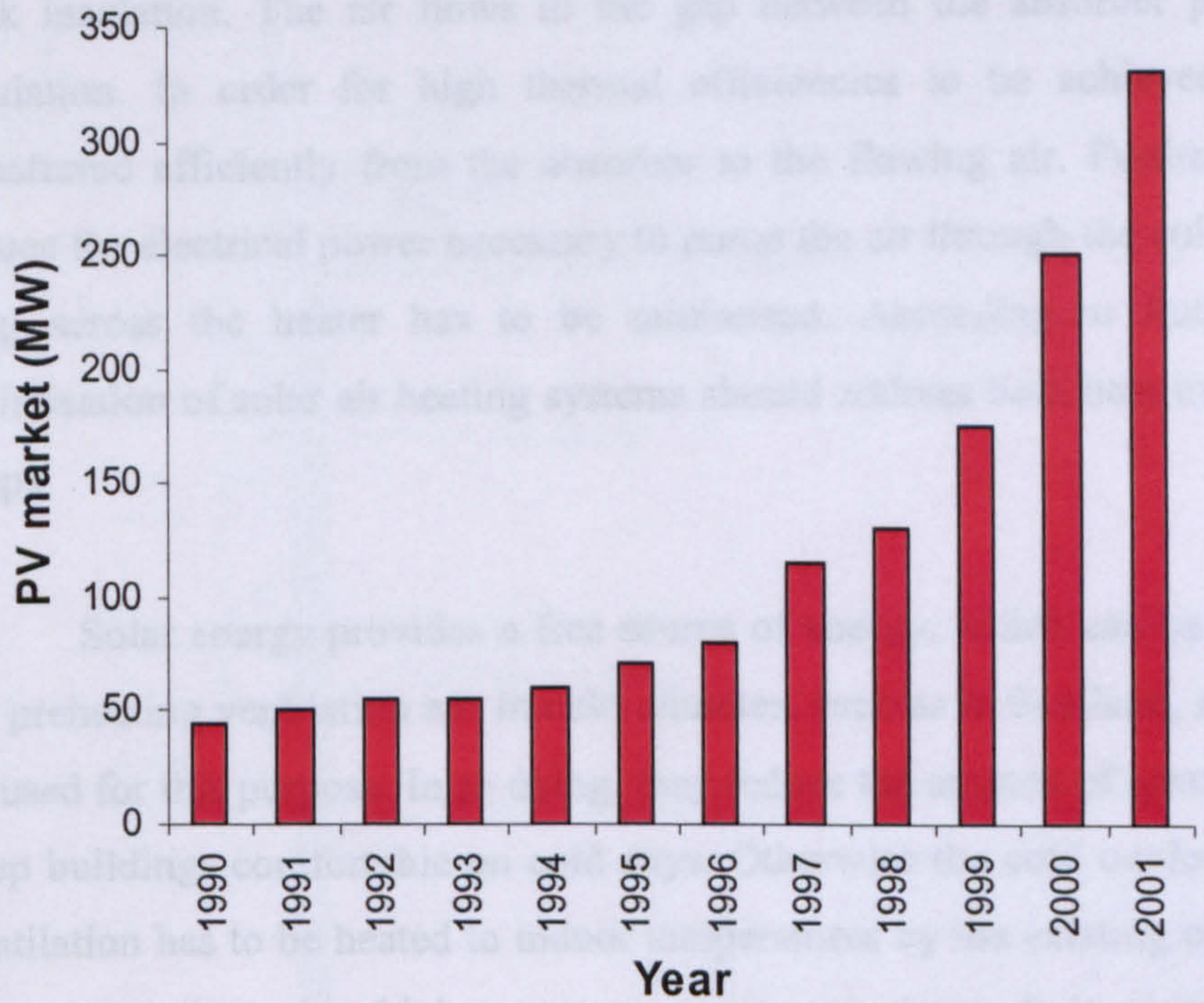

Fig. 1.6: Growth in PV market (1990 – 2001). Adapted from Green, 2004.

Even though there are no subsidies available for solar water heating systems in Scotland, the Government has introduced a grant aid scheme to encourage the installation of PV panels for households. A total of £20 million will be available in an effort to encourage people to switch to Renewable energy. A scheme, which was launched in 2002 by the Department of Trade and Industry (DTI) and is run by the Energy Saving Trust (EST), gives home owners the opportunity to save up to 50% of the cost of solar electric systems between 0.5 and 5 kW_p in size. Up to date, about 82 % of applications were approved with £3.4M granted and 820 kW_p installed.

1.3.2 Solar ventilation preheating

Solar air heaters (SAHs) offer some advantages over solar water heaters. In SAHs, freezing or boiling of the fluid does not occur and they run at small fluid pressure. In addition, even though leaks decrease the thermal performance, they do not

disable the system as a whole. However, solar air heaters are limited in their thermal performance due to low density, small volumetric heat capacity and small heat conductivity of air (Pottler et al., 2000).

Generally, a solar air heater consists of an absorber plate, a front cover and a back insulation. The air flows in the gap between the absorber plate and the back insulation. In order for high thermal efficiencies to be achieved, heat has to be transferred efficiently from the absorber to the flowing air. Furthermore, in order to reduce the electrical power necessary to pump the air through the collector, the pressure drop across the heater has to be minimised. According to Pottler et al. (2000), optimisation of solar air heating systems should address both heat transfer and pressure drops.

Solar energy provides a free source of energy, which can be effectively utilised for preheating ventilation air. In cold climates, such as in Scotland, solar air heaters can be used for this purpose. In so doing, they reduce the amount of space heating needed to keep buildings comfortable on cold days. Otherwise the cold outdoor air necessary for ventilation has to be heated to indoor temperatures by the existing conventional heating system thus incurring higher cost as mentioned above. It is estimated that 30 % of energy in OECD countries, most of which are located in cold climates, is consumed in buildings and that 42 % of this energy is dissipated through ventilation (International Energy Agency, 2001). It is suggested that the energy loss through ventilation can be reduced to 4 % by ensuring that the need for ventilation within dwellings is met with the minimum of energy consumption (AIVC, 2002). However, attempts to minimise ventilation energy loss can result in poor indoor air quality and comfort problems.

1.3.2.1 Transpired solar collectors

Solar ventilation air preheating technology existed since the early 1990s as a result of research supported by the U.S. Department of Energy (DOE). The commercially available transpired solar collectors (TSC) exemplified by Fig. 1.7 is widely used in the U.S. and Canada for both residential and commercial buildings. These collectors consist of a dark, perforated metal plates installed over a building's south-facing wall or on the roof. An air space is created between the old wall (or roof) and the new façade. A fan or blower draws ventilation air through the tiny holes in the

collector and up through the space between the building wall (or roof) and the collector before delivering it into the house. The solar energy absorbed by the collectors warms the incoming air by as much as 30 C. A summer bypass damper is included to allow outdoor air to enter the building directly and avoid overheating the ventilation air on warm days.

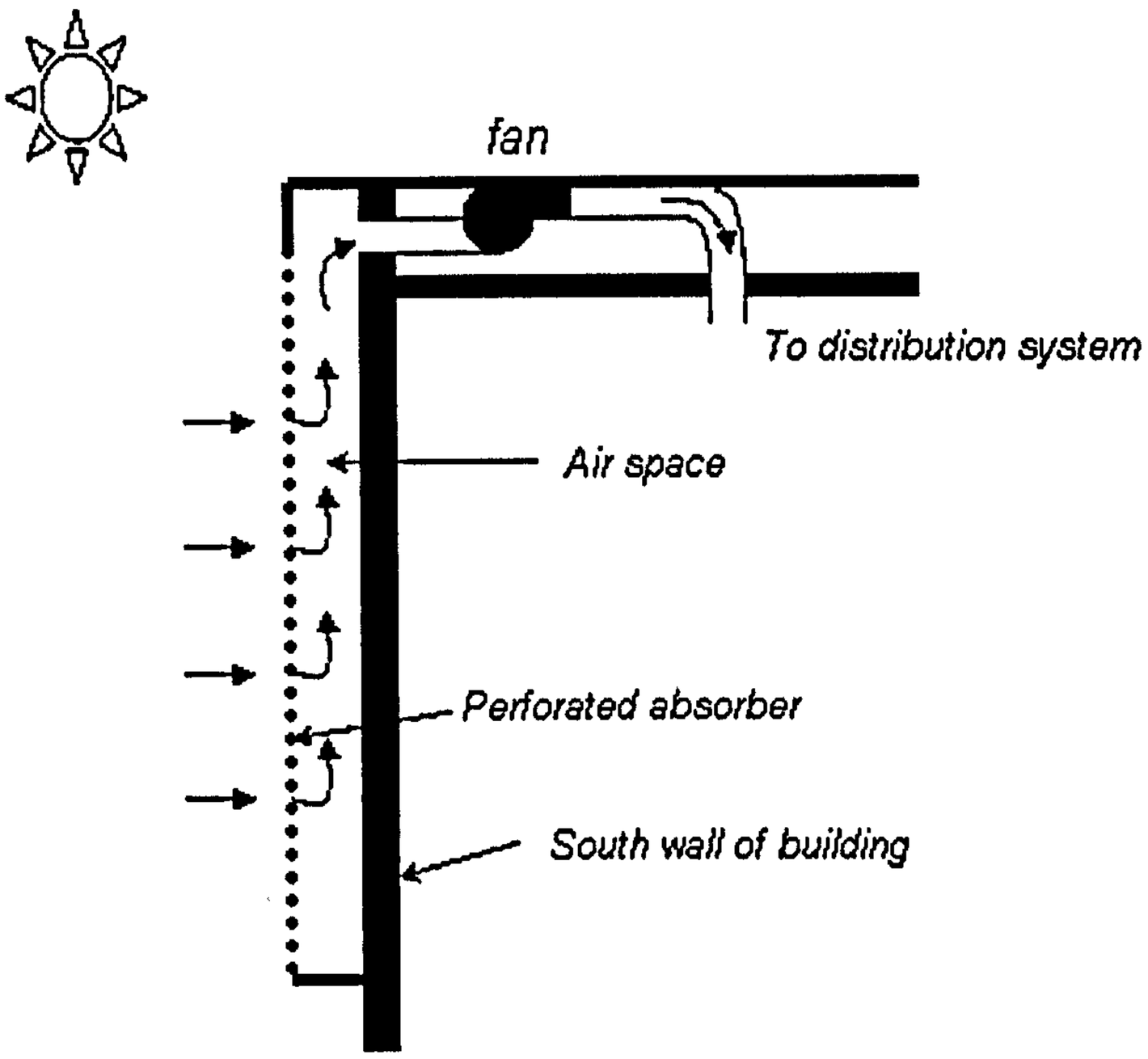

Fig. 1.7: A transpired (perforated) solar collector for preheating ventilation air.

Such systems can only be used to preheat incoming fresh ventilation air and they cannot be used to warm recirculated indoor air as can be done with other solar heating systems. It is reported by (U.S. Department of Energy, 1998), that, due to the elimination of glass covers, the TSC collects 80 % of solar radiation and has an efficiency of over 70 %. It costs about £63/m^2 of collector area and has a payback period of 3 – 12 depending on the climate and the type of fuel displaced. The system has no moving parts (except the fan) and so requires no maintenance. In 1995, the system was recognised by R&D Magazine as one of the 100 most important technology innovations.

This system can also play an important role in warm climates for drying indoor crops such as tea, coffee, fruit, beans, rice, spices, rubber, cocoa, and timber (Conserval Engineering Inc., 2005).

The cost, performance, and economics of transpired solar collectors and SAHs in general can be assessed using the RETScreen software (Carpenter and Meloche, 2002). Software, SWIFT (Solar Wall International Feasibility Tool), can also be used for job quotations and system design of applications for nearly all air-based solar collectors. Using weather data inputted from a specified file, or using built in files containing average weather data, the software predicts the amount of heat gathered from solar energy, the resulting air temperature inside the building, and the amount of energy used by conventional heating systems that has been avoided as a result of using the TSC. The next section introduces a newly developed concept for preheating ventilation air.

1.3.2.2 Roof slate based collectors

The simplest way to use solar energy for heating ventilation air is to use the existing roof surface (e.g. south facing slates or tiles) as a solar collector as shown in Fig.1.8 Such a system does not need any solar panels, as with TSCs because the existing roof serves as a solar collector and so the extra cost of buying a solar collector is eliminated.

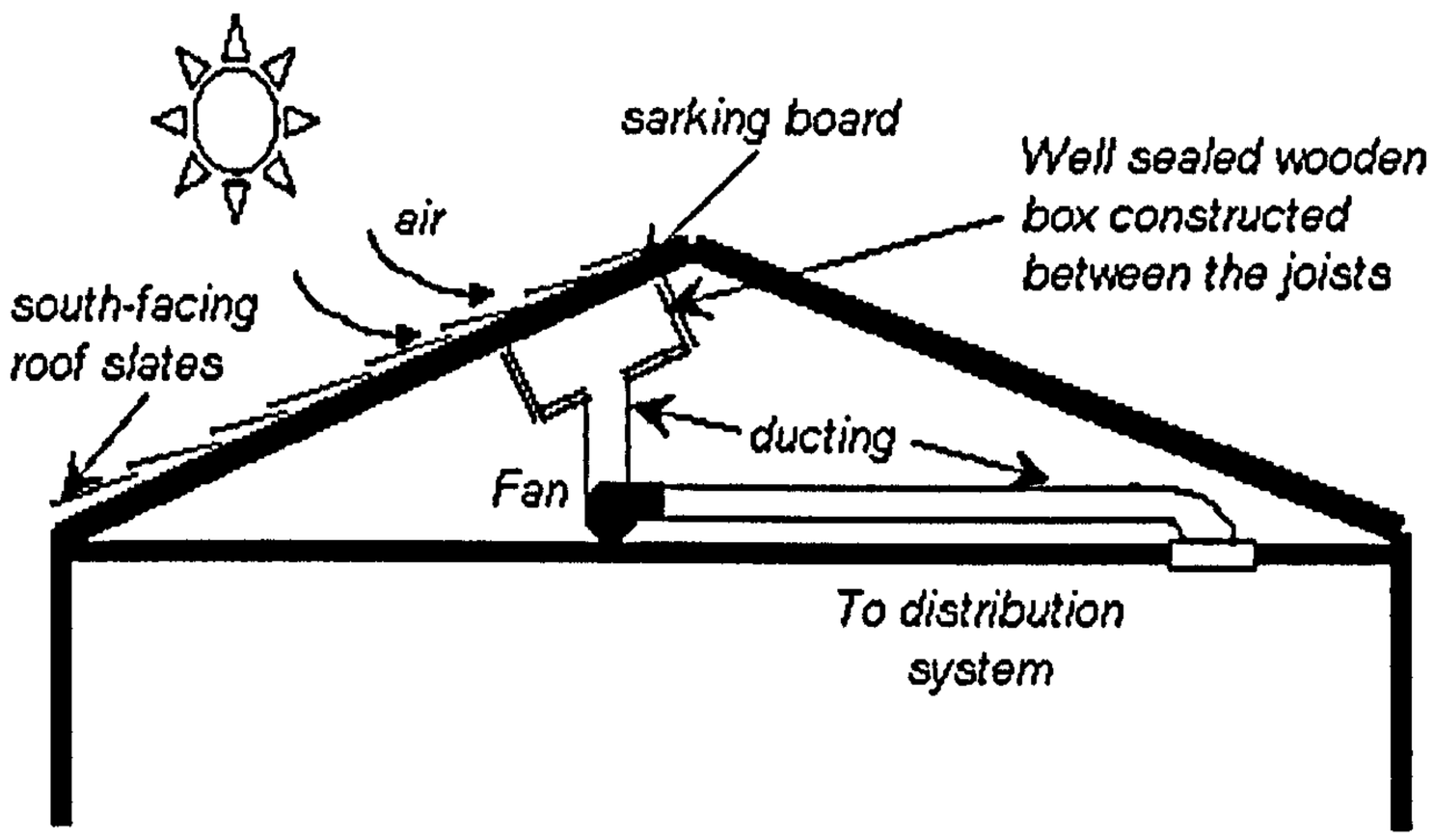

Fig. 1.8: A roof slate-based (RSB) solar ventilation preheating system.

Research shows that dark color commercial tiles have absorptivity values over 0.8 and reflectance less than 0.25. Red brick interlocking tiles, for example have an absorptivity of 0.88 and a reflectance of 0.12 (HK-OTTV, 1995). Thus, the temperature of the roof tiles can be many degrees higher than the surrounding ambient temperature

due to the solar energy falling on them. In bright sunshine, dark coloured slates can be up to 40 C warmer than the outdoor air and can heat the incoming air by up to 30 C (Scottish Solar Energy Group, 2004). In Scotland, slate temperatures can exceed 50 C depending on the time of the day, the time of the year, the wind speed and the type of slates. The energy absorbed by the slates can be either transferred to the attic or it can be lost to the surrounding atmosphere by convection and radiation. A mechanical ventilation system can be designed to utilise the energy of the slates to preheat outdoor air and deliver it into the house for ventilation. The benefits should include a warmer house, lower heating bills, a reduction in dampness and condensation, and an improvement in air quality.

The idea to utilise roof slates as solar ventilation preheaters has been introduced at Napier University in Edinburgh in 1996 and deployed by Berwickshire Housing Association. Several of these systems have been constructed in Edinburgh. Ten houses with dampness were identified and studied. The houses were divided into three groups (no ventilation, solar ventilation, ventilation from attic) and were monitored for a year. The results showed that all seven houses with ventilation enjoyed reduced levels of dampness. The four houses with solar ventilation enjoyed warmer temperatures with two of them reporting a reduction in respiratory problems such as asthma and other health improvements.

The current thesis is concerned with studying the potential of these roof-slate based (RSB) systems as solar ventilation preheaters. Chapters 6, 7 and 8 then give conclusions about these systems regarding ventilation rates, heating potential, anticipated monetary and environmental (CO_2) savings, solar fractions and payback period . The following section gives a detailed description of the PV-driven RSB mechanical ventilation system under investigation. Next the specific objectives of this thesis with regard to these systems are outlined.

1.4 PRESENT WORK

1.4.1 System description

The procedure for constructing an RSB system is described in chapters 4 and 7. A summary is given here. The space between the joists is used to build a well-sealed box. 10-cm holes are drilled in the sarking board and felt underneath the slates. A fan, situated on a board and driven by a photovoltaic module on the roof, constitutes the front cover of the box. A flexible duct is extended across the attic from the fan box to the room ceiling underneath.

The fan draws air through the spaces between the slates and through the holes in the sarking board before delivering it into the duct. As air is drawn past the warm slates, it absorbs the energy stored before being delivered through the flexible duct into the house. The system utilises solar energy in two ways: both to generate heat and electrically. Solar energy is used to both warm the slates which serve as a solar collector and also to run the fan via the PV module and so, generally, air is only delivered when the slates are warm.

The effectiveness of these ventilation preheating systems is judged by their potential as solar air preheaters. An optimum system is that which maximises the amount of heat delivered in a given period of time. The instantaneous heat delivered by the system, on the other hand, depends on both the temperature difference (delivered – ambient) and the flow rate of air delivered to the house. The RSB mechanical system described above can be considered as two interacting subsystems. A thermal system, comprising the roof slates (heat gain) and the duct, in addition to the attic and the house underneath (heat loss). The slate temperature directly influences the temperature of air delivered. For a given flow rate of air, modelling of this subsystem can lead to the estimation of the outlet air temperature. The other subsystem is a flow system, which consists of the PV module, the motor/fan combination, and the duct. The modelling of this subsystem leads to the prediction of flow rate at the outlet of the duct as a function of the environmental factors in addition to PV module, motor/fan and duct specifications.

1.4.2 Factors affecting the performance of the system

A brief account of the effect of the different factors on air outlet temperature and flow rate is given below. These are summarised in Fig. 1.9.

1.4.2.1 Environmental factors

These include irradiance, ambient temperature, spectral variation, and wind speed over the roof where the system is installed. Environmental factors directly affect both the slate temperature (which is directly related to the air outlet temperature) and PV module electrical output. The latter influences the outlet flow rate. This is discussed in detail in chapter 3. A brief account of these effects is given below.

i. Irradiance (G, W/m^2)

Irradiance has a direct effect on the PV module output. An increase in irradiance, increases the PV output and so higher flow rates are produced. Irradiance also affects the slate and PV module temperatures, which are both directly proportional to irradiance. While higher slate temperatures necessitate higher delivered temperatures, increasing the PV module temperature reduces the operational voltage of the fan and so less flow rates are produced. This is discussed in detail in chapter 2 and 3.

ii. Ambient temperature (T_{amb}, C)

Both the slate temperature and PV module temperature are also directly proportional to ambient temperature. As discussed in (i), the module temperature affects its output. This will be discussed in detail in chapter 3.

iii. Wind speed (ws, m/s)

Wind speed also influences the slate and PV module temperature. In cold weather, as wind speed increases, both the slate temperature and the PV module temperature decrease. Furthermore, high wind speeds may disturb the region over the roof thus affecting the performance of the system.

iv. Spectral variation

The spectral variation, from one season to another, has an effect on the PV module performance as will be discussed in section 2.2.4.

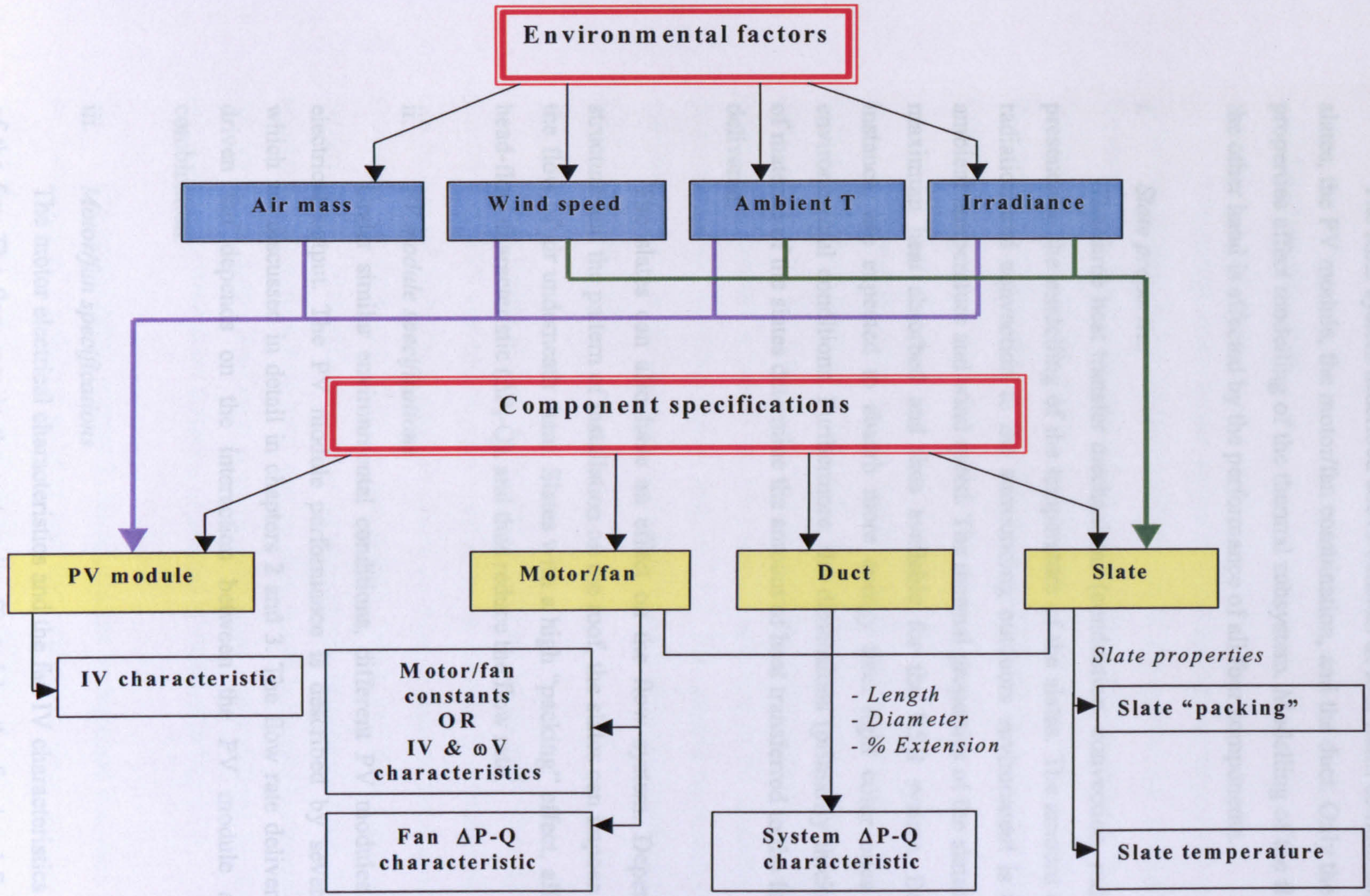

Fig. 1.9: Factors affecting the performance of the RSB system under study.

1.4.2.2 Component specifications

The RSB system described above consists of four main components, namely: the slates, the PV module, the motor/fan combination, and the duct. Only the slate and duct properties affect modelling of the thermal subsystem. Modelling of the flow system, on the other hand is affected by the performance of all four components.

i. Slate properties

The three heat transfer mechanisms (conduction, convection, radiation) show a presence in the modelling of the temperature of the slates. The amount of heat lost by radiation and convection to the surrounding outdoors environment is determined by ambient temperature and wind speed. The thermal properties of the slates determine the maximum heat absorbed and thus available for the RSB system. Dark slates, for instance, are expected to absorb more energy than light color ones under similar environmental conditions. Furthermore, the dimensions (primarily thickness) and type of material of the slates determine the amount of heat transferred to the fan box and that delivered.

The slates can also have an effect on the flow system. Depending on their structure and the pattern of installation on the roof, the slates can impose a resistance to the flow of air underneath them. Slates with a high "packing" effect, affect the system head-flow characteristic (ΔP_s-Q), and thus reduce the flow rate.

ii. *PV module specifications*

Under similar environmental conditions, different PV modules give different electrical output. The PV module performance is described by several parameters, which are discussed in detail in chapters 2 and 3. The flow rate delivered by the PV-driven fan depends on the interaction between the PV module and motor/fan combination.

iii. *Motor/fan specifications*

The motor electrical characteristics and the fan IV characteristics affect the speed of the fan. The flow rate in the system is affected by the fan head-flow characteristic (ΔP_f-Q), which is a function of the fan speed. This will be discussed in detail in chapters 2 and 3.

iv. The duct properties

The duct properties (length, diameter and roughness) affect (ΔP_s-Q) and, consequently, the flow rate of air in the system. This will be discussed in chapter 3.

1.4.3 Research objectives

The current work focuses on the flow subsystem mentioned above. So the effect of factors relating to the thermal performance of the system (i.e. thermal properties of the slates, heat loss to the outdoors or to the attic) are not accounted for. However, the heating potential of the system is investigated using measured slate and air outlet temperatures, which, when used with the modelled flow rates, the heat delivered, can be estimated.

Even though more than a hundred RSB solar ventilation preheating systems have already been installed in Scotland, no optimisation studies have been done yet. The main purpose of the current work is to optimise these systems for Edinburgh. The optimisation process is carried out for a limited selection of PV modules, fans and duct diameters as will be discussed in section 3.3.7. The ground on which the component selection is made is discussed in terms of previous findings in chapter 2 (sections 2.2.1, 2.3.2, 2.3.3 and 2.4.3)

The optimum system is then comparatively tested with other systems and the potential of RSB systems as solar ventilation preheaters is investigated. However, as can be inferred from the discussion above, in order to achieve these goals, a model for predicting the flow rate of air in the system, which can then serve as a means for predicting the heat delivered, is to be developed. Moreover, since the optimisation process must based on long-term weather data, which is usually horizontal data, a model for predicting slope irradiance is to be introduced and validated for Edinburgh. The relationship between these different objectives is clarified in Fig. 1.10.

The next chapter (chapter 2) introduces the background literature review related to modelling of PV-driven systems and that related to slope irradiance modelling. Literature review related to optimisation of PV systems is included in chapter 6 while that related to testing of solar systems is included in chapter 7.

Chapter 3 introduces the mathematical model of the system. The modelling methodology and experimental strategy are introduced in detail. The model for each of the individual components is given and validated experimentally. Chapter 4 introduces the programming strategy and describes the computer algorithms used for determining the flow rate of air in the system. In this chapter, the flow rate model as a whole is also validated by comparing measured flow rates (and fan voltages) to predicted values. Furthermore, model-based simulations of flow rate and efficiency vs. irradiance are also given at the end of chapter 4. These simulations are useful tools for both predicting and explaining the optimisation results.

Chapter 5 introduces the datasets considered for optimisation. Two datasets, a log-term hourly dataset and a one-year 5-min data, are considered for comparison purposes. A north-European anisotropic model for slope irradiance is first checked against the isotropic model and then validated with measurements taken at a tested house at Wiston, Scotland.

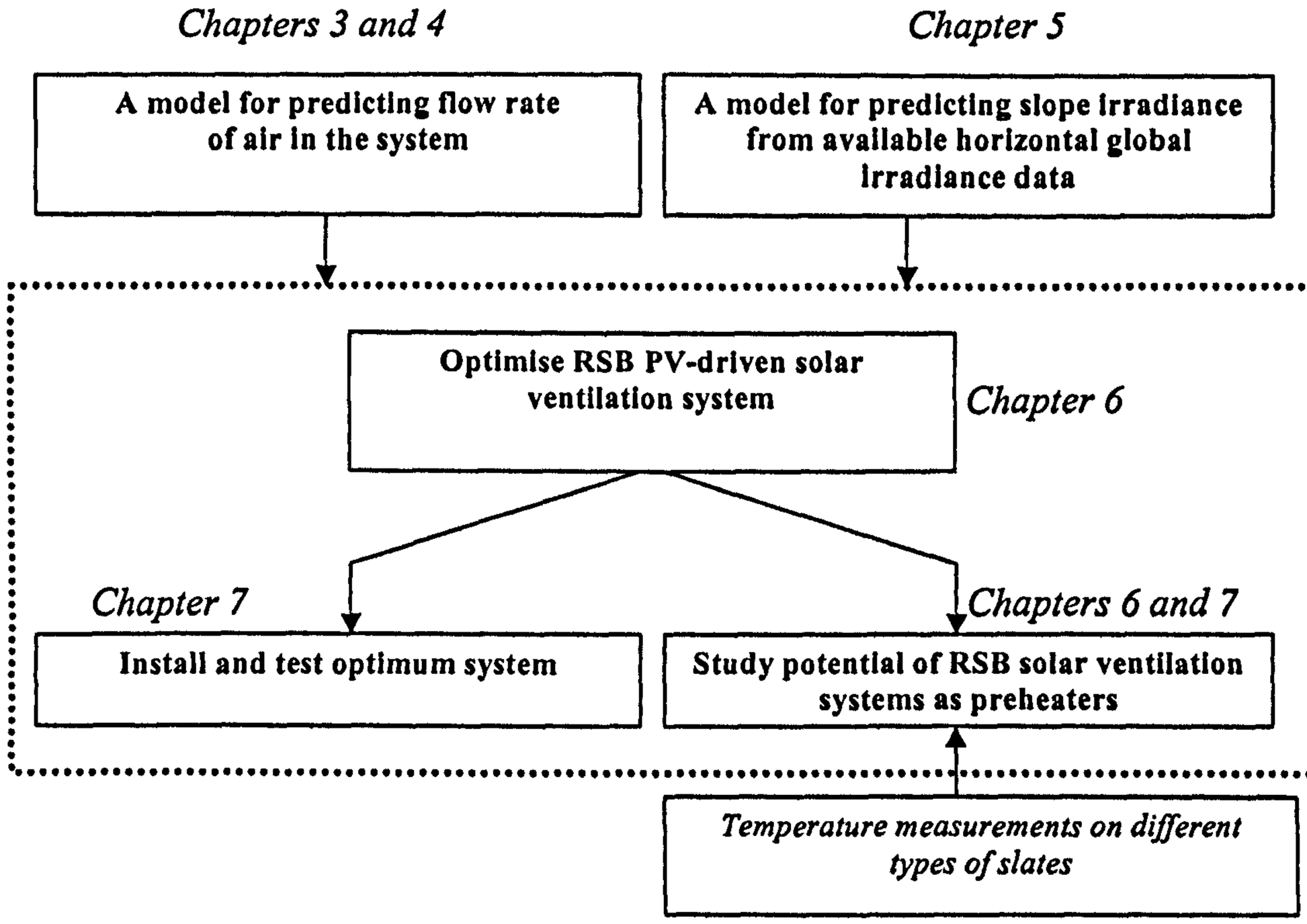

Fig. 1.10: Relating the different objectives of the thesis.

Chapter 6 makes use of the two models developed in chapters 3, 4 and 5 for system optimisation. The optimisation strategy is described in detail and the optimisation results are then reported and explained in terms of utilisability and the model-based simulations described in chapter 4. Next, the optimum system is studied in detail and conclusions are made with respect to the ventilation, heating and economic potential of this system.

Chapter 7 introduces a few case studies. The optimum system is installed and comparatively tested with another RSB system. The methodology for testing the system is given and the results are reported in terms of volume and heat delivered, solar fraction, and effectiveness. In addition, the optimum system is compared in different roof sections with different types of slates. Finally, the RSB system is then compared to the transpired solar collector.

REFERENCES

Air Infiltration and Ventilation Centre (AIVC), (2001), Air Information Review, Evaluation and Demonstration of Domestic Ventilation Systems, Volume 22, No 3, http://www.aivc.org/frameset/frameset.html

American College of Allergy, Asthma and Immunology, ACAAI Online, http://www.acaai.org/public/advice/dust.htm

ASHRAE Standard 55-1981 (1981) Thermal Environmental Conditions for Human Occupancy, American Society of Heating Refrigerating and Air Conditioning Engineers, Atlanta.

ASHRAE (1988), Handbook of Equipment, Chapter 10: Air cleaners for particulate contaminants, American Society of Heating Refrigerating and Air Conditioning Engineers, Atlanta.

ASHRAE, (2001), Handbook of Fundamentals, American Society of Heating Refrigerating and Air Conditioning Engineers, Atlanta.

Awbi, H.B., (1991), Ventilation of Buildings, Clays Ltd, Suffolk, UK.

Bouchair, A., (1994), Solar Chimney for Promoting Cooling Ventilation in Southern Algeria, Building Services Engineering Research and Technology 15 (2), 81-93.

Concannon P., Air Infiltration and Ventilation Centre (AIVC), (2002), AIVC Technical Note 57, pp70, Code TN 57

Environmental Protection Agency, (2005), Indoor Air Quality Home Page, 2005, http://www.epa.gov/iaq.

Green, M.A., (2004), Recent developments in photovoltaics, Solar energy, 76, pp3-8.

HK-OTTV Standard, (1995), Overall Thermal Transfer Value in buildings, Hong Kong, http://www.arch.hku.hk/research/BEER/hkottv/hkottv.htm#Table%204

International Energy Outlook, (2004), World Energy and Economic Outlook http://www.eia.doe.gov/oiaf/ieo/world.html

Johnston, M., (2002), We're far too clean for our children's comfort, New Zealand Herald,http://www.malaghan.org.nz/aboutus/news/2002/06.05.werefartooclean.htm

Khedari, J., Ingkawanich, S., Waewsak, J. and Hirunlabh, J., (2002), A PV System Enhanced the Performance of Roof Solar Collectors, Building and Environment, 37, pp 1317-1320.

Liddament M.W., (1996), A Guide to Energy Efficient Ventilation, Air Infiltration and Ventilation Centre, Coventry, UK.

Martin, C., Platt, S., Hunt, C., (1987), Damp Housing, Mould Growth and Symptomatic Health State, BMJ, 298.

Nuaire Group, (2004), Home ventilation, Drimaster, Caerphilly, United Kingdom, www.nuaire.co.uk

Page, J. and Lebens, R., (1986), Climate in the United Kingdom, HMSO Pubs., Department of Energy, 1986.

Pottler, K., Sippel, C.M., Beck, A. and Fricke, J., (2002), Optimised finned absorber geometries for solar air heating collectors, Solar energy, 67(1-3), pp 35-52.

Scottish Homes, (1993), Scottish Housing Condition Survey 1991 (Edinburgh: Scottish Homes).

The Scottish Office, Central Research Unit, (1999), Poor Housing and Ill Health: A Summary of Research Evidence, http://www.scotland.gov.uk/cru/documents/poor-housing-05.htm

Scottish Solar Energy Group. (2001), Solar ventilation, examples: Burdiehouse, Edinburgh, Edinburgh, United Kingdom, http://www.sseg.org.uk/

Scottish Solar Energy Group, (2001), Solar ventilation, examples: Burdiehouse, Edinburgh, Edinburgh, United Kingdom, http://www.sseg.org.uk/

Sick, F., (1996), The Solar Resource. In Photovoltaics in Buildings: A design Handbook for Architechts and Engineers, Sick F. and Erge T. (eds), pp. 9-12.

Singh, J., (1995), The Built Environment and the Developing Fungi, Building Mycology, 21.

Stephen, R., (1999), Low energy positive input ventilation in dwellings, BRE.

Strathclyde Energy Systems Research Unit, (2004), http://www.esru.strath.ac.uk/Courseware/Class-16458/notes1a.pdf

Thermsaver Heating Solutions, (2005), Heat Recovery Ventilation, Some Frequently Asked Questions, http://www.thermsaver.co.uk/hrv/faq.html#5a

Unison Scotland, (2000), Seminar Report: Keeping Scotland warm, www.unison-scotland.org.uk/energy/nrg.

Wilkinson, D, (1999), The Scottish Office Central Research Unit. Poor Housing and ill health: A summary of research evidence.

Williamson, I.J., Martin, C.J., McGill, G., Monie R.D., and Fennerty, A.G, (1997), Damp Housing and Asthma: A Control Case Study, Thorax, 52, pp 229-234.

2. REVIEW OF PREVIOUS WORK

2.1 INTRODUCTION

As discussed in chapter 1, in order to simulate, and hence define optimum system performance, two submodels are required. The first, necessarily predicts system flow rate as a function of environmental parameters in addition to PV module, motor/fan and duct specifications. The second requires predicting slope irradiance as a function of time of day and day of year, in addition to orientation and tilt. Chapter 2 presents a review of the literature related to modelling of flow rate in PV-driven systems and that related to slope irradiance modelling. In addition, a brief background on optimisation of PV-driven systems is also given. More detailed discussion of previous work related to optimisation is given in chapters 6.

In PV-driven systems, the different components: the PV module, the motor and the mechanical load are modelled separately. Section 2.2 discusses previous work related to measuring the performance and modelling of photovoltaic modules. Section 2.3 then considers the coupling of motors to PV modules. A review of the different types of motors and their associated motor equations is presented. In this manner, a rationale for selecting the best PV module-motor combination is considered.

Section 2.4 describes the previous work on modelling of flow rate of water in PV pumping systems. In section 2.5, a review of slope irradiance modelling is presented. Section 2.6 starts a discussion of strategies for optimisation of PV-driven systems. This discussion is then continued in chapter 6 after the current strategy for optimisation is introduced. The background related to testing of ventilation preheating systems is given in section 7.2. In the current chapter, section 2.7 summarises the conclusions drawn from previous work and states the importance and uniqueness of the current work.

2.2 MODELLING OF PHOTOVOLTAIC OUTPUT

2.2.1 Introduction

Early handmade photovoltaic cells in the 1950s were less than 5 % efficient and had outputs of a few milliwatts. In 1990, laboratory produced cells were reported as having efficiencies of over 30 %. In addition, the cells produced in the world in that year had an aggregate peak generating capacity of about 50 MW (Green, 2004). Nowadays, solar cells can be used in a range of applications from powering calculators to charging batteries for communication systems.

The most common PV cells are made of silicon, as it is a semi-conducting element. Silicon PV cells are usually connected in series to form a PV module. Furthermore, PV modules can be connected in series or in parallel to form an array. Silicon PV cells are either monocrystalline, polycrystalline or amorphous. According to Markvart (2000), most commercially available PV modules are manufactured from polycrystalline silicon wafers. While their efficiency is lower than their monocrystalline counterparts, their reduced cost makes them more common.

2.2.2 The PV IV characteristic

An assessment of the operation of solar cells and the design of power systems based on solar cells must be based on their electrical output. The electrical output of PV modules is given by their current-voltage (IV) characteristic. A precise IV characteristic of PV modules is necessary to accurately estimate their performance, select appropriate components, and improve the efficiency of PV systems. The equivalent circuit, defining the electrical characteristic of a PV cell, as presented by Green (1982), is given in Fig. 2.1. Using Kirchhoff's law, the current produced by this cell is calculated as follows:

$$I = I_G - I_D - I_{Sh} \tag{2.1}$$

where I_G is the light-generated current (A), I_D is the diode current (A) and I_{Sh} is the current through the shunt resistance branch (A).

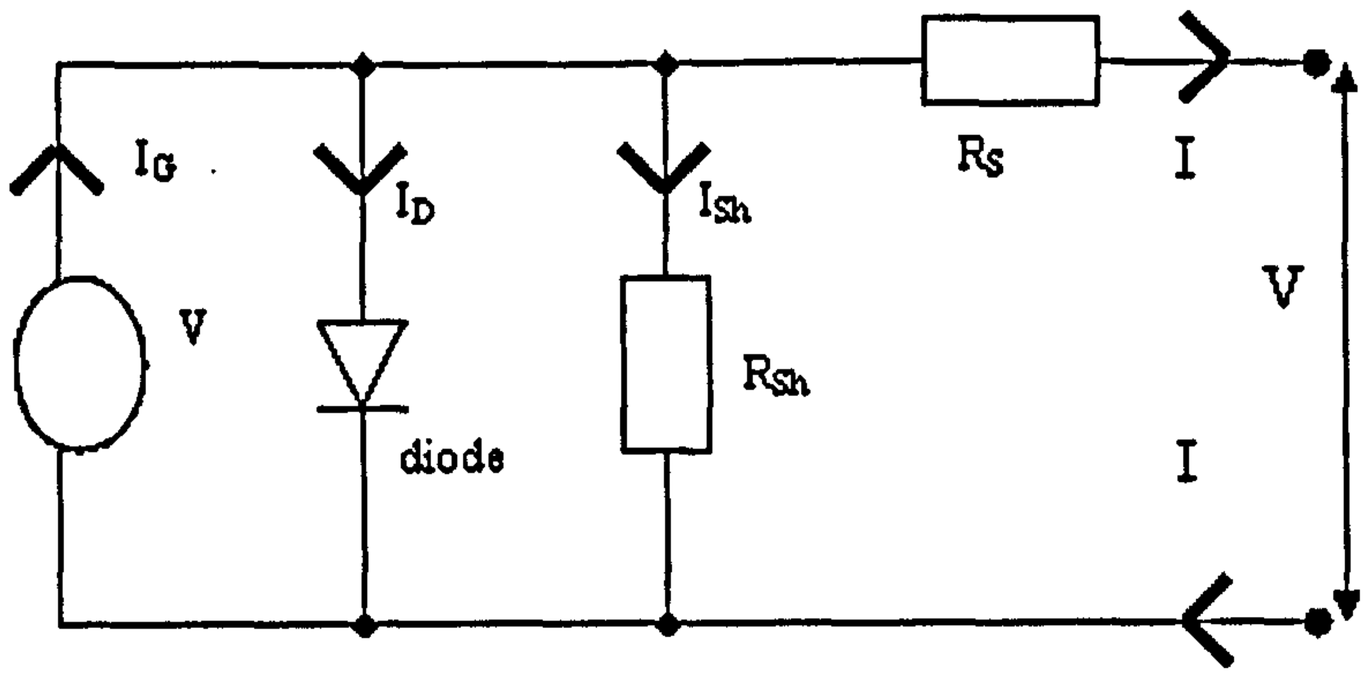

Figure 2.1: An equivalent circuit of a PV cell.

In mathematical terms, the diode current, I_D, is approximated by the following equation as shown by Markvart (2000)

$$I_D = I_0 \left(e^{\frac{V + I \cdot R_S}{A}} - 1 \right) \tag{2.2}$$

where I_0 is the reverse saturation current (A), R_S is the series resistance (Ω) of the PV cell and A is a curve fitting parameter (V). Substituting Eq. 2.2 into 2.1, the current from the solar cell can be calculated from Eq. 2.3

$$I = I_G - I_0 \left(e^{\frac{V + I R_S}{A}} - 1 \right) - \left(\frac{V + I R_S}{R_{Sh}} \right) \tag{2.3}$$

The last term in Eq. 2.3 is often neglected as R_{Sh}, for most modern cells, is very large, (Rauschenbach, 1980). Thus Eq. 2.3 reduces to the following

$$I = I_G - I_0 \left(e^{\frac{V + I R_S}{A}} - 1 \right) \tag{2.4}$$

A typical IV curve as derived from Eq. 2.4 is shown in Fig. 2.2. The short circuit current, I_{SC} (A), the open circuit voltage, V_{OC} (V), the maximum power point, P_m (W) and the filling factor, FF, are the main features of a PV IV curve.

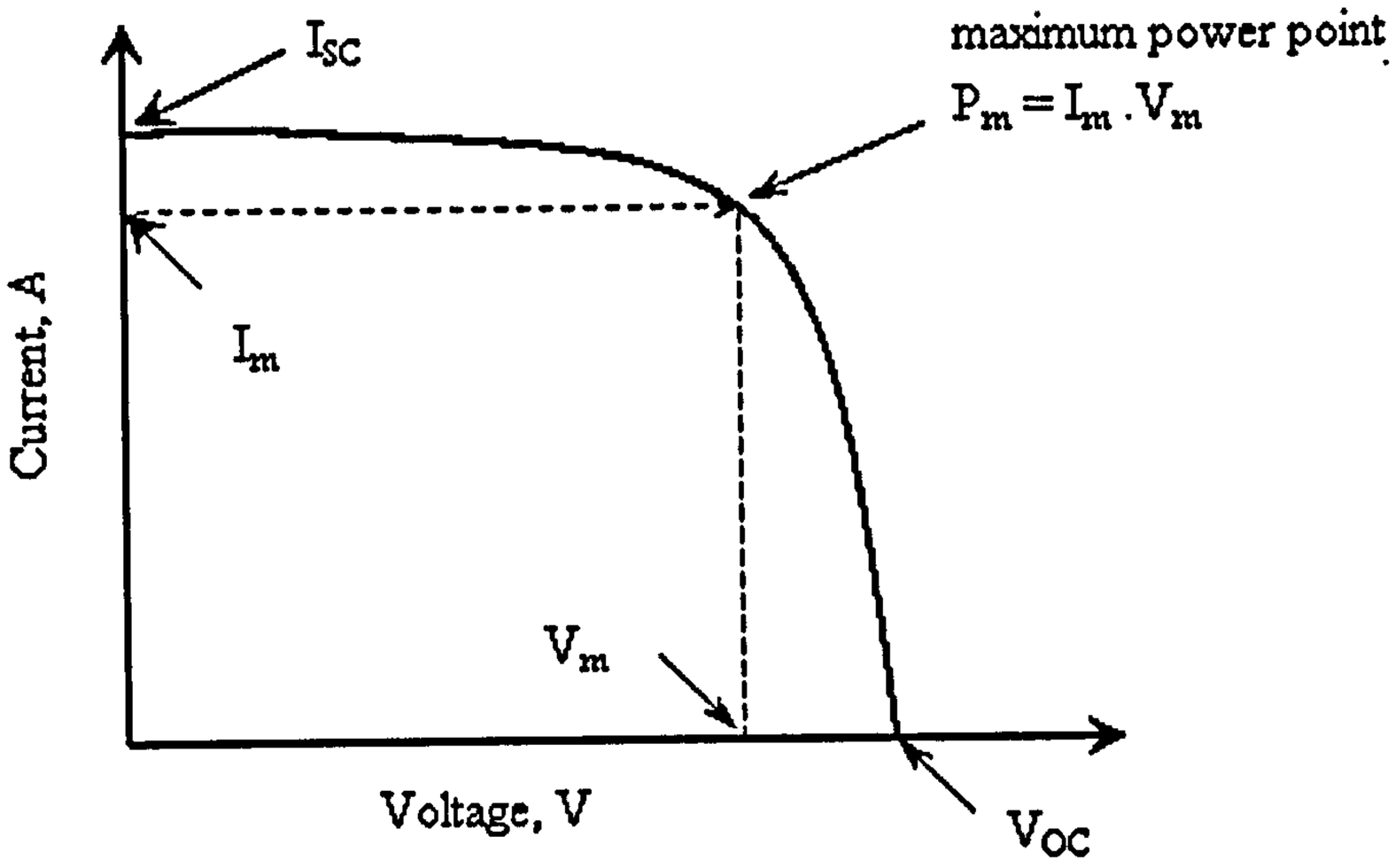

Figure 2.2: IV characteristic of a PV cell.

A PV IV curve can be experimentally constructed by measuring a series of voltage/current values. I_{SC} represents the current at zero voltage while V_{OC} is the voltage at zero current. P_m is the power when the product *(I·V)* is a maximum (i.e. $P_m = I_m \cdot V_m$) where I_m and V_m are respectively the current and voltage at maximum power. The maximum power can only be evaluated after the IV curve has been determined. The filling factor is a measure of how rectangular the IV curve is and can be defined by the equation

$$FF = \frac{P_m}{I_{sc} \; V_{oc}} \tag{2.5}$$

The higher the value of FF, the closer to a rectangle the shape of the IV curve becomes (Green, 1982). A higher FF value indicates a more ideal PV cell or PV module since the series resistance, R_S, in Eq. 2.4 becomes closer to 0. This is considered in more detail in section 2.2.5.4.

The simplest equivalent circuit of a photovoltaic cell consists of a diode and a current source in parallel. In this case, $R_S = 0$ and so the electrical characteristic is an explicit function of I in V. This simplified circuit, however, does not give an optimal representation of the electrical process in a photovoltaic cell. Even though the equivalent circuit depicted in Fig. 2.1 introduces a better account of the electrical process encountered in PV cells, it is more complex since I is an implicit function of V. Therefore, a numeric method such as the Newton-Raphson has to be applied to obtain the IV curve.

2.2.3 Alternative models for describing the PV IV characteristic

Several attempts have been made to simplify the IV characteristic given by Eq. 2.4. Jacobson et al (2000) fitted measured (IV) curves to fourth, fifth, seventh and ninth degree polynomials. The maximum power output was then estimated from these best-fit curves. However, even though, these polynomial fits give reasonably accurate approximations of the maximum power vicinity and the lower section of the IV characteristic, they oscillate considerably at lower voltages and thus do not give accurate predictions of I_{SC}.

Akbaba and Alattawi (1995), on the other hand, introduced a new model, which has an advantage over the traditional model in Eq. 2.4 in that it related the module current explicitly to voltage so that the IV characteristic can be evaluated in a single step. The Akbaba model compared favourably with the traditional model in Eq. 2.4 and provided a simple closed form solution for P_m, I_m and V_m. This original version of the model, however, was based on parameters, which were only irradiance dependent, and so the effect of PV module temperature on its IV characteristic was not accounted for.

Dyk and Meyer (2004) introduced a new equivalent PV cell model consisting of two diodes. Equation 2.1 was therefore rewritten as ($I = I_G - I_{D1} - I_{D2} - I_{Sh}$) with both I_{D1} and I_{D2} calculated from Eq. 2.2 using different I_o values. This new model, however, adds to the complexity of defining the PV IV characteristic especially when solved simultaneously with other equations.

2.2.4 Factors affecting PV characteristic

The present section gives a summary of the literature related to the effect of each of the environmental factors (section 1.4.2.1) on PV performance. The IV characteristic shown in Fig. 2.2 is a function of both irradiance and module temperature as depicted in Fig. 2.3. As irradiance increases, I_{SC} increases linearly while V_{OC} increases logarithmically, Buresch (1983) and Mallick et al (2004). An increase in PV module temperature, on the other hand, results in a slight linear increase in I_{SC} coupled with a significant linear decrease in V_{OC}. Although there is an increase in current with temperature, the overall effect of increased temperature is a decrease in power due to

the larger decrease in voltage. In addition to open circuit voltage, P_m, V_m and FF are also inversely and linearly proportional to temperature.

Due to the fact that the effect of temperature on current and that of irradiance on voltage are small, several researchers simplified their work by ignoring both or one of these effects. Jacobson et al (2000), for example, simplified their work by ignoring the effect of temperature on I_{SC} and that of irradiance on V_{OC}. Chamberlin et al (1995), on the other hand, ignored the effect of temperature on current but included a linear rather than logarithmic term for the effect of irradiance on V_{OC}. The effect of temperature on PV module performance is, however, significant, and subsequent studies have shown that, if a high degree of accuracy is required, it cannot be ignored.

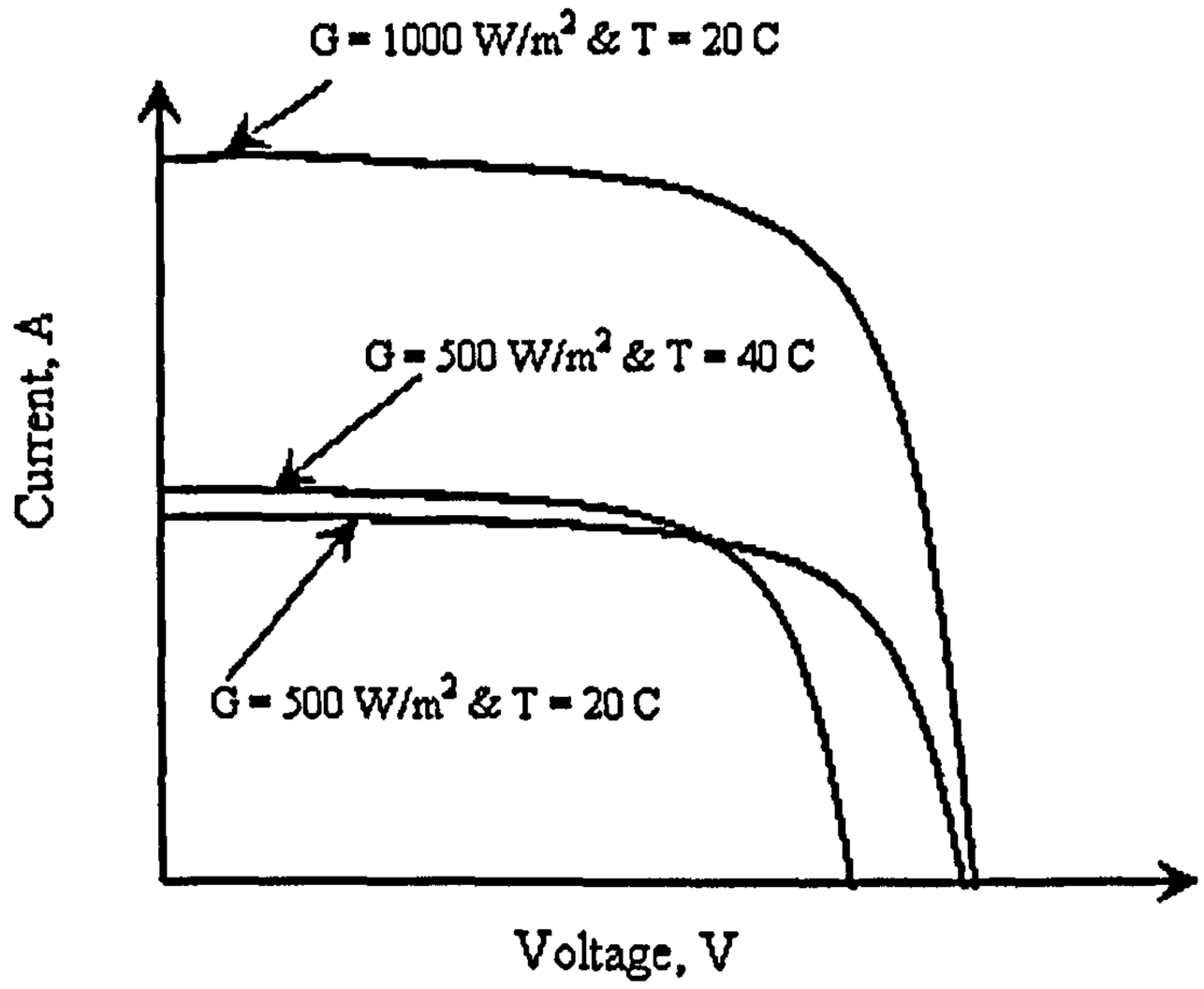

Figure 2.3: The effect of irradiance and module temperature on PV IV characteristic.

Parretta et al (1998) reported that 7 % of all energetic losses are due to the temperature effect. In addition, Dyk et al (2000) considered the aforementioned temperature effect on module performance. They reported that at ambient temperatures of 25 C, PV modules will be operating at temperatures well above ambient and can lose up to 14 % of their potential energy production. Furthermore, in order to estimate the annual output of the system in actual operating environment, Nishioka et al (2003) analysed the dependence of PV output on PV efficiency temperature coefficient. They found that the annual output energy of their PV system increased by about 1 % for an improvement of 0.1 % in efficiency temperature coefficient. In conclusion, they stated

that it is very important to consider the temperature characteristics in solar cell development.

The PV module temperature is dependent on irradiance, ambient temperature, and wind speed. This will be discussed in detail in section 2.2.5.1. In addition to irradiance and the effect of module temperature, the PV output is also a function of the solar spectrum. Hirata et al (1995) found that the ratio of available spectral solar radiation to global spectral solar radiation changes from season to season by 5% for crystalline silicon and 14% for amorphous silicon. Also, they found that the accumulated output of PV modules changes seasonally in the same way. For crystalline Si, the output ratio was 4% while that for amorphous Si was 20 %. They concluded that spectral solar radiation should be taken into account for optimum photovoltaic systems. Berman et al (1999) also demonstrated that the variation in long-term performance of PV modules is caused by seasonal spectral changes in the received sunlight.

Corrections for spectral variations can be applied through correction for air mass (AM). Durisch et al. (2000) developed a formula for correcting the PV efficiency for irradiance, module temperature, and air mass ($AM = \frac{1}{\cos\theta}$ where θ is the incidence angle) from Standard Test Conditions (G = 1000 W/m^2, T_{mod} = 25 C, AM = 1.5 global spectrum). They stated that the maximum efficiency was obtained at AM = 1.5 which occurs relatively rarely in actual operation. The authors stated, however, that knowledge of the spectral composition of the solar radiation (for the whole air mass range) in typical climatic areas is necessary for optimising PV systems.

In measuring the PV IV characteristic, the irradiance, PV module temperature, and (V, I) data points must be defined. However, for modelling purposes, the IV characteristic must be represented mathematically, as in Eq. 2.4. Thus, the four cell parameters in Eq. 2.4 (i.e. I_G, I_0, R_S and A) must be evaluated by non-linear regression (NLR) using measurements of (V, I) data points, Chamberlin et al (1995) and Ikegami et al (2000). Hsiao and Blevins (1984) and Hadi et al (2003) explained that these parameters can also be determined by curve fitting to an experimentally measured curve for a given irradiance and module temperature.

Using a single IV curve, the parameters A, I_0, I_G and R_S are calculated so that Eq. 2.4 can now be used for modelling. The following section introduces the experimental

techniques associated with measurement of the PV IV characteristic and those necessary for estimating the module temperature, the temperature coefficients, and the series resistance. Section 2.2.6 then discusses the methods available for adapting Eq. 2.4 to different environmental conditions of irradiance and module temperature for modelling purposes.

2.2.5 Measurement of PV module performance

When purchased, PV modules are usually accompanied by a manufacturer's data sheet typically specifying I_{SC}, V_{OC}, P_m, V_m, I_m and FF at some reference conditions of temperature, irradiance and air mass. These reference conditions, usually known as Standard Test Conditions (STC) as given above, are simulated indoor conditions. Parretta et al (1998) and Durisch et al (2000) stated that the operating efficiency of an installed PV module is not predicted by its manufacturer's data sheet related to STC. According to the authors, these reference conditions are hardly attainable in the field as they combine the irradiance of a clear sky summer day, with the module temperature of a clear winter day and the spectrum of a clear spring day. In order to accurately describe the performance of PV modules, measurements must be taken under realistic weather conditions. The following subsections introduce the experimental data required to completely describe the performance of PV modules.

2.2.5.1 PV module temperature

Under normal operating conditions, PV module temperature is primarily dependent on irradiance ambient temperature, and wind speed. It is necessary to estimate the PV module temperature as a function of these parameters in order to predict performance. According to Hsiao and Blevins (1984), PV module temperature can be estimated from the empirical equation

$$T_{mod} = T_{amb} + 0.02\ G + \alpha\ (ws) \qquad (2.6)$$

where α (ws) is the larger number of (ws, 0.03 ×(10-ws)).

Alternatively, the manufacturer's datasheet can sometimes include the nominal operating cell temperature (NOCT, C). Duffie and Beckman (1991) define NOCT as the

temperature of the PV module when ambient temperature is 20 C, irradiance is 800 W/m^2, wind speed is 1 m/s and no load is connected. Dyk et al (2002) reported that, usually, for the above conditions, the NOCT is in excess of 40 C. According to Eq. 2.6, a value of 37 C for NOCT is obtained which suggests that Eq. 2.6 is specific to the configuration and circumstances it was obtained under.

Davis et al (2001) reported that the NOCT is based on the assumption that the overall heat transfer coefficient is constant. The heat transfer characteristics of a rack-mounted PV module can be quite different from building integrated PV modules. They presented a new technique for evaluating NOCT for building integrated PV (BIPV) modules using a one-dimensional transient heat transfer model. Menicucci (1986) described an experimental method for the determination of NOCT. By subjecting a single module of the type to be used in the PV array to the conditions described above (i.e. G = 800 W/m^2, T_{amb} = 20 C, ws = 1 m/s) and measuring the steady state cell temperature, the NOCT can be determined. The author also stated that, since the heat exchange parameters vary for different module designs, the NOCTs also vary and so he used a model, which predicted NOCT as a function of irradiance, ambient temperature, wind speed, and mounting configuration.

With NOCT known, for a given irradiance and ambient temperature, T_{mod} can be estimated from Eq. 2.7 as follows

$$T_{mod} = T_{amb} + \frac{G}{800}(NOCT - 20) \qquad (2.7)$$

2.2.5.2 Temperature coefficients

The classic term of a temperature coefficient of a parameter relates to the change in that parameter when only temperature is varied and all other parameters held constant. King (1997) explained that temperature coefficients of I_{SC}, V_{OC}, P_m, V_m, I_m, FF and efficiency can be experimentally determined. Duffie and Beckman (1991), on the other hand, presented an alternative method whereby the temperature coefficients of V_m, I_m, FF, P_m and efficiency (η) can be given in terms of those for I_{SC} and V_{OC}. Moreover, Green (1982), reported that the temperature coefficients of I_{SC} (μ_{ISC}), V_{OC} (μ_{VOC}), and P_m (μ_{Pm}) can be roughly estimated as fixed percentages of, respectively, I_{SC}, V_{OC} or P_m. According to Green (1982), for example, P_m decreases at a rate of 0.4 % per

°C (i.e. μ_{Pm} = -0.4 % of P_m). King (1997), on the other hand, reports that P_m decreases at –0.25 % per °C for amorphous Si and -0.5% per °C for crystalline Si. As reported by Berman et al (1999), in order to measure a temperature coefficient, the module is shaded to reach a temperature near ambient, then it is quickly uncovered and current-voltage measurements are recorded as the module warms to operating temperature.

2.2.5.3 IV curves

In order to measure the IV characteristic of a PV module, it is connected in parallel to a variable resistor. An ammeter is connected in series with the PV module while a voltmeter is connected across both the resistor and the PV module. As the resistance changes, readings of current and voltage are taken and the IV curve is constructed. Chamberlin et al (1995) measured the IV curves using a 0.1 F capacitive load and a data acquisition system sampling at 100 Hz. Sequential measurements of less than 10 mA apart were removed to eliminate redundant observations. Irradiance was measured using an Eppely Precision Pyranometer while temperature was measured using a thermocouple at the center of the back of the PV module. Observed temperatures ranged from 35 to 56 C. Cromer (1983), on the other hand, used two HP digital multimeters and a variable resistance load box built at Florida Solar Energy Center for PV IV determination.

2.2.5.4 Series resistance

As the series resistance increases, the slope of the IV curve to the right of P_m is expected to be steeper (such that the shape of the curve becomes more rectangular). If the shunt resistance term was included in Eq 2.4, then the part of the IV characteristic to the left of P_m is expected to be at a slope rather than levelled off (this implies that I_{SC} will be larger for smaller R_{Sh}), Dyk et al, 2002. Using measured data, and based on minimising the sum of squared residuals, R_S and R_{Sh} can be easily determined, Eckstein et al, 1990 and Chamberlin et al, 1995). Dyk et al (2002) stated that these can be determined from the slope of the parts of the PV IV curve at low voltage (close to I_{SC}) and at high voltage.

Townsend (1989) proposed a method for the determination of R_S from manufacturer's data. If both μ_{ISC} and μ_{VOC} are known, then Townsend showed that R_S

can be determined by equating the manufacturer's value of μ_{VOC} with the value determined from the analytical expression for the derivative, $\frac{dV_{oc}}{dT}$,

$$\mu_{Voc} = \frac{A_{ref}}{T_{mod,\ ref}}\left[\frac{T_{mod}\ \mu_{ISC}}{I_{SC}} + \ln\frac{I_{SC}}{I_O} - \frac{e.q}{K_B.T_{mod}} - 3\right] \tag{2.8}$$

where e is the band gap energy for Silicon (1.1 eV), q is the electron charge constant (1.6×10^{-19} Coulombs) and K_B is the Boltzmann's constant (1.38×10^{-23} J/K). The series resistance does not appear explicitly in Eq. 2.8 but the values of I_o and A depend on R_S as will be shown in section 3.2.1 (Eqs. 3.2 – 3.4). So a value of R_S is assumed and values of I_{SC}, I_o and A are calculated and substituted in Eq. 2.8 to determine μ_{VOC}. This calculated value is then compared to the manufacturer's value or to a measured value. The acceptable value of R_S is that which minimises the error between the measured and calculated μ_{VOC}. Eckstein (1990) stated that R_S is independent of temperature and the value determined by Eq. 2.8 at some given values, can be assumed constant.

2.2.6 Adapting PV IV characteristic to different levels of irradiance and temperature

Considering Fig. 2.3, it is seen that the IV curve is a function of G and T_{mod}. This means that the four cell parameters in Eq. 2.4 (i.e. I_G, I_0, R_S and A) are functions of irradiance and PV module temperature. To provide a versatile and more broadly applicable model, researchers are not only interested in evaluating these four cell parameters at a specific set of environmental conditions (G and T_{mod}), but are also interested in predicting the IV curve at any other conditions. Many models are available in the literature for correcting the PV characteristic. Two of these models, the SANDSTROM model, and the Townsend model are considered for discussion here.

In the SANDSTROM model, by Buresch (1983), an IV curve is generated from a reference curve by correcting every single (V, I) data point for temperature and irradiance. It can be described by the following equations:

$$V = V_{ref} + \mu_{VOC}\left(T_{mod} - T_{mod,\ ref}\right) - R_S\,\Delta I \tag{2.9a}$$

$$I = I_{ref} + \Delta I \tag{2.9b}$$

where

$$\Delta I = \mu_{ISC}\left(\frac{G}{G_{ref}}\right)\left(T_{\text{mod}} - T_{\text{mod, ref}}\right) + \left(\frac{G - G_{ref}}{G_{ref}}\right) I_{sc} \qquad (2.9c)$$

where V (V) and I (A) are respectively the voltage and its corresponding current on the IV curve at the desired values of G and T_{mod}, the subscript "*ref*" represents measurements at reference conditions (i.e. G_{ref} and $T_{mod,\ ref}$) and μ_{VOC} (V/C) and μ_{ISC} (A/C) are respectively the open-circuit voltage and short-circuit current temperature coefficients. The series resistance, R_S, is assumed constant. The equations above also assume that the voltage and current temperature coefficient are constant and equal to μ_{VOC} and μ_{ISC} respectively.

The SANDSTROM model for generating IV data from reference conditions provides highly accurate predictions when compared to measurements. However, since extrapolated points correspond directly to measured values, any irregularities in the measured reference data will be carried on to the new curve. Hsiao and Blevins (1984) and, later, Chamberlin et al (1995) also considered this approach of correcting for single points rather than for the key cell parameters presented in Eq. 2.4.

Eckstein et al. (1990), through considering the earlier work of Townsend (1989) introduced equations of I_G as a function of both irradiance and temperature, and of I_0 and A as functions of temperature only.

$$I_G = \frac{G}{G_{ref}}\left[I_{G,ref} + \mu_{Ics}\left(T_{\text{mod}} - T_{\text{mod},ref}\right)\right] \qquad (2.10a)$$

$$I_o = I_{o,ref}\left(\frac{T_{\text{mod}}}{T_{\text{mod},ref}}\right)^3 \exp\left[\frac{\varepsilon q}{k}\left(\frac{1}{T_{\text{mod},ref}} - \frac{1}{T_{\text{mod}}}\right)\right] \qquad (2.10b)$$

$$A = A_{ref}\frac{T_{\text{mod}}}{T_{\text{mod},ref}} \qquad (2.10c)$$

Lawrence and Wichert (1994) also used the equations developed by Townsend (1989) to describe IV characteristics at any set of conditions.

The SANDSTROM and Townsend methods described by Eqs. 2.9 and 2.10 are based on the traditional IV characteristic described by Eq. 2.4. The common feature

among these two methods, and all other methods in the literature, is that the determination of P_m can be carried out only after the IV characteristic is generated. This is done by searching for the point where the *(I·V)* product is a maximum.

2.2.7 Summary

Accurate estimation of the PV IV characteristic as a function of environmental factors such as irradiance and ambient temperature is an integral part in modelling of PV-driven systems. In the literature, authors usually start by presenting the model they are using for describing this characteristic. The vast majority of models are based on the equivalent circuit, shown in Fig. 2.1. In most cases, researchers use Eq. 2.4, which is a simplified version of Eq. 2.3. The critical task here is to adapt the manufacturer's IV characteristic at STC conditions to different levels of irradiance and different ambient temperatures. This renders it necessary to predict the PV module temperature as a function of ambient temperature and irradiance. Moreover, knowledge of the PV module series resistance and temperature coefficients of the measured parameters is required for this task to be carried out. In section 3.2.2 a new method for adapting the PV IV characteristics to levels different from the reference conditions is introduced and validated by comparison to measurements and to the SANDSTROM and Townsend models. The advantages of the new method are also outlined.

As will be discussed in section 2.3, in coupling PV-motor systems, it is necessary to estimate the maximum power point of the PV module. The closeness of the operational point of a motor to the maximum power point is of interest to many researchers. In the literature, most researchers tend to first estimate the PV IV curve from which P_m can then be determined. However, an analytical expression of P_m in terms of irradiance and PV module temperature can be very useful. Khouzam et al (1991), Zaki and Eskandar (1996) and Akbaba et al (1995) found the derivative of power with respect to voltage and equated it with zero to find P_m in terms of cell parameters. In section 3.2.2, an empirical relationship of P_m as a function of G and T_{mod} is introduced.

2.3 PHOTOVOLTAIC-MOTOR COUPLING

2.3.1 Characteristics of permanent magnet motors

The two major parts of motors (DC and AC) are described in Textbox 2.1. "Brush" DC motors have several drawbacks including relatively high manufacturing cost and short life expectancy if not maintained. However, Newborough and Probert (1990) reported that, when compared with AC motors, traditional DC "brush" motors offer several advantages including higher efficiency, larger starting torque and a simpler means for regulating rotational speed. As reported by Singh et al (1998), in spite of their limitations, DC motors are used extensively in PV pumping systems because they can be coupled directly to the PV module giving a simple and inexpensive system.

Depending on the way the armature is connected to the field, DC motors can either be separately excited, series or shunt motors. In the latter two, as the name implies, the armature is either in series or in parallel with the field. In separately excited DC (SEDC) motors, on the other hand, the field and armature are supplied from independent voltage sources so they are not connected to each other (Fig. 2.4). This configuration offers the advantage of better speed regulation. Another advantage of SEDC motors is that the wound field can be replaced by a permanent magnet (PM).

According to Edwards (1991), PMDC motors are advantageous because less maintenance is required, and, also, they have higher efficiency as no energy is lost in the field windings. During the last 30 years, several improved magnetic materials which are usually made from rare Earth element alloys were developed for high performance PM motors.

The performance of DC motors is described by their speed-torque (ωT) characteristic. A typical (ωT) curve for PM motors is shown in Fig. 2.5. This curve is linear in the case of permanent magnets because, for this type of motors, the magnetic flux is constant. In the case of series or shunt DC motors, on the other hand, the speed-torque relationship is nonlinear (Say, 1980).

The operation of a PMDC motor under steady state conditions is governed by the following equations (Anis and Metwally, 1994):

Textbox 2.1: Types of motors

The two major parts of a motor are a stationary part (called a stator) and a rotating part (called a rotor). The driving torque of motors results from the interaction of magnetic fields in the stator and rotor.

There are two major categories of electric motors: alternating current (AC) and direct current (DC) motors as shown in the figure below. In AC motors, the current source is AC current, which is supplied to the stator in either single phase or three-phase power. The two major types of AC motors are the synchronous motor and the induction motor. In the synchronous motor, the rotor can either be a wound field (WF) or a permanent magnet. The WF rotor is supplied with direct current and so its polarity is fixed. In AC induction motors, on the other hand, the rotor is always WF and the current is induced by the magnetic fields of the stator magnets.

Classical DC motors are "brush" motors which consist of a WF stator and a WF rotor where the supply voltage for both is a DC source. Another type of DC motors is the brushless DC motor where the brushes are eliminated and the WF stator is electronically controlled (section 2.3.2).

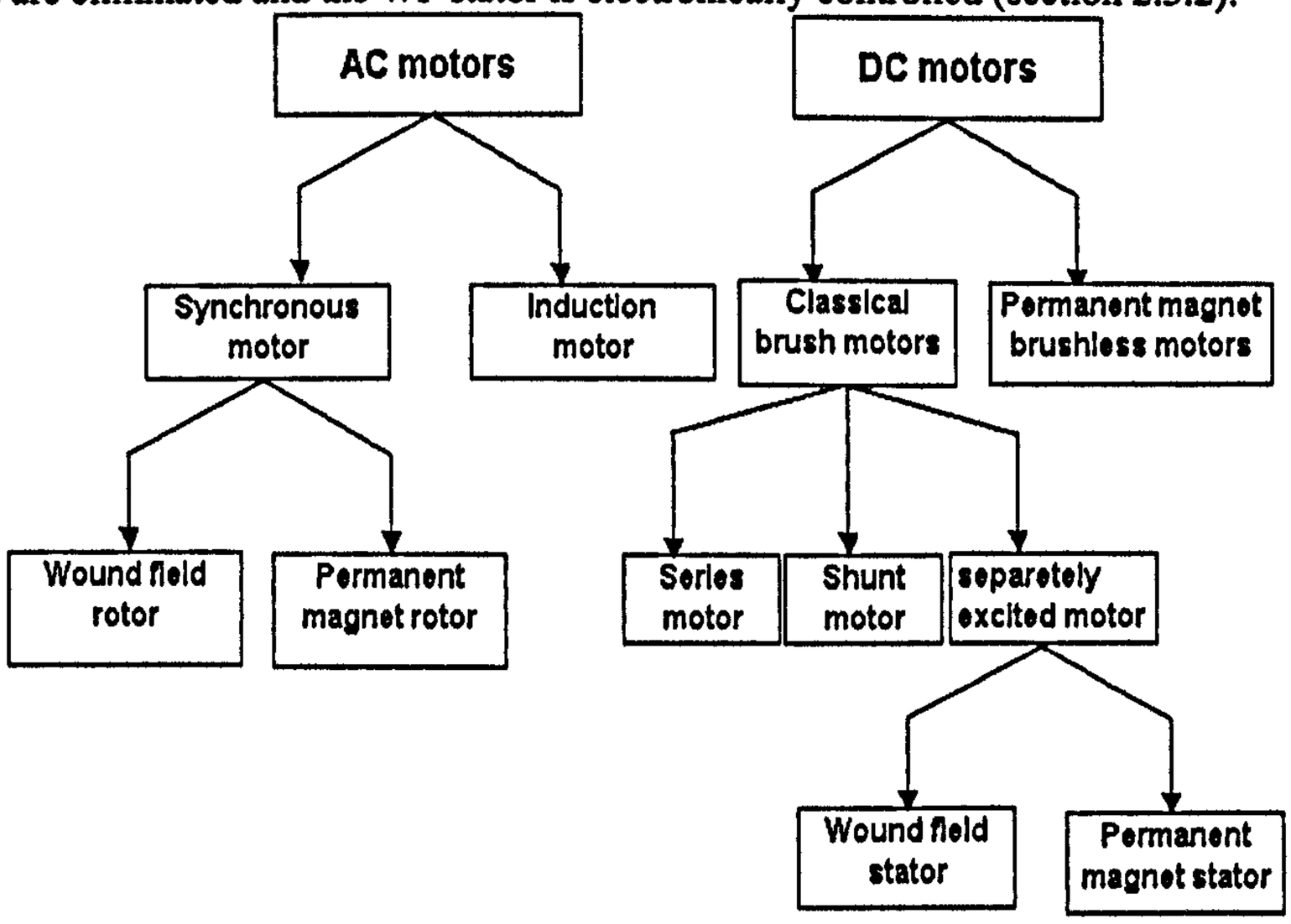

$$E_m = K_m \omega \tag{2.11}$$

$$V = E_m + R_a I \tag{2.12}$$

$$T_m = K_m I \tag{2.13}$$

where ω is the speed of the motor (r/min or rad/s), I is the current through the armature, T_m is the motor torque (Nm) and K_m is the motor constant (Vs^{-1}).

a)

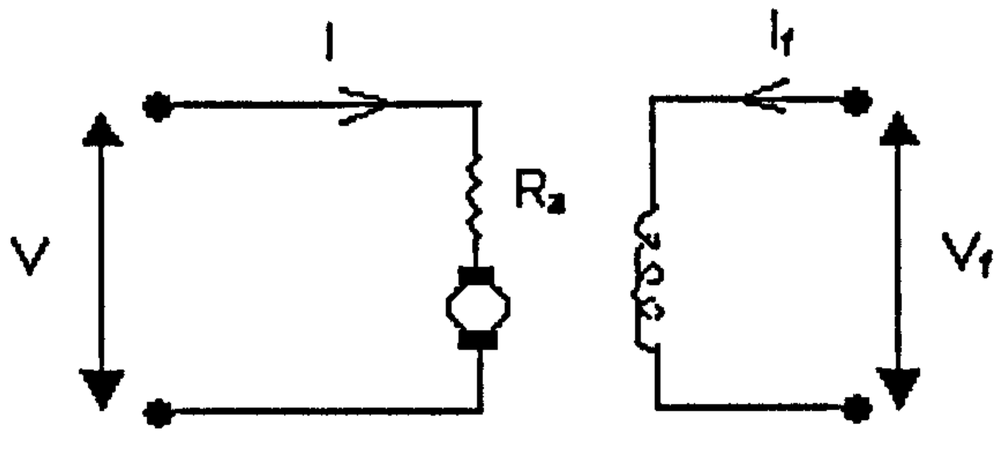

b)

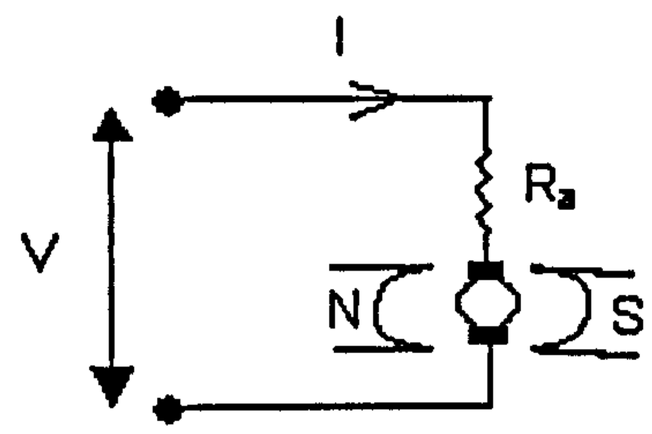

Figure 2.4: Circuit diagrams of two separately excited DC motors where (a) the field is wound (b) the field is a permanent magnet.

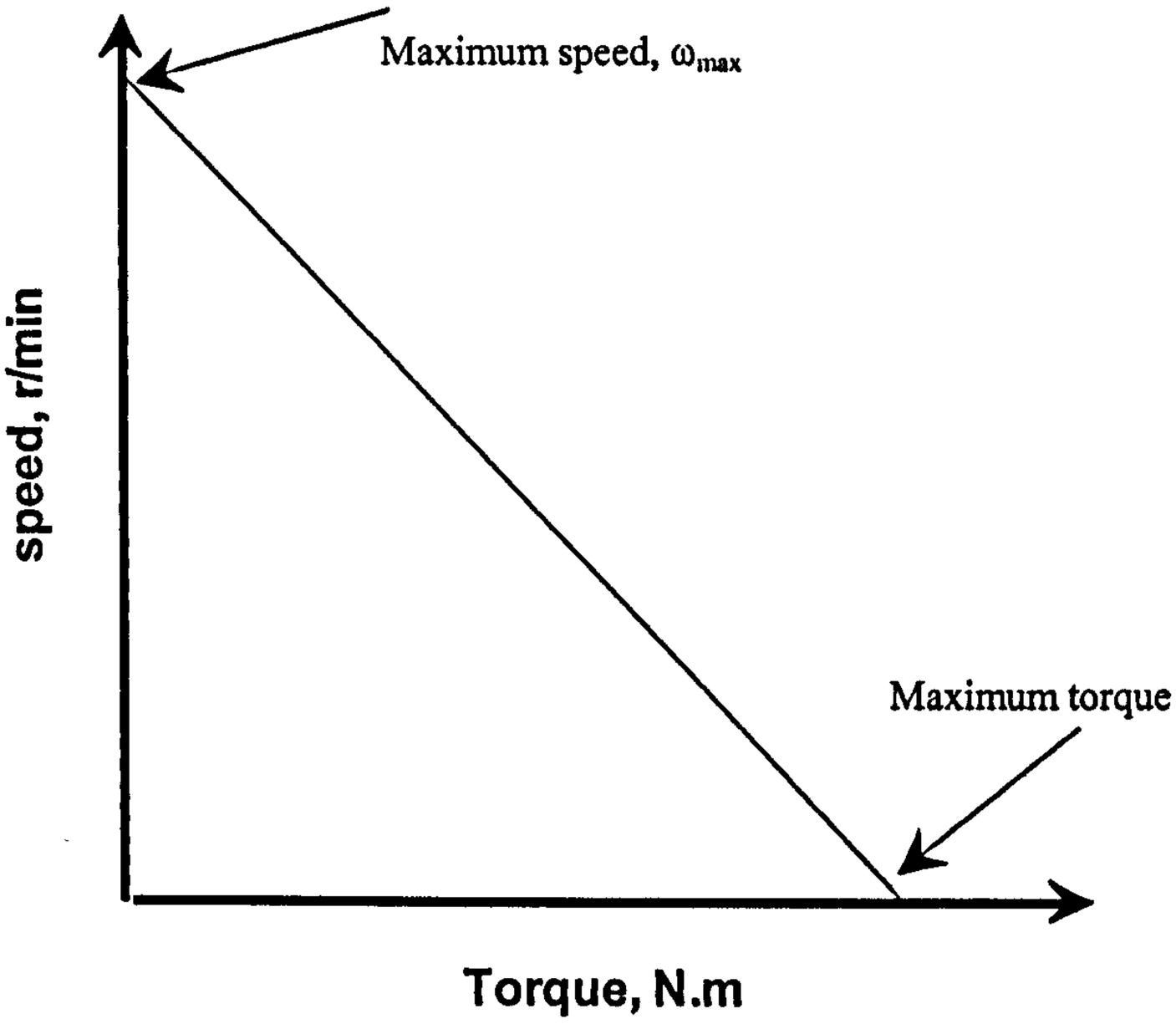

Figure 2.5: Speed-torque characteristic of a permanent magnet DC motor.

2.3.2 Permanent-magnet brushless DC motors

A recent development of PMDC motors is the permanent magnet brushless (PMBL) DC motor. In such a motor, the brushes are eliminated and the WF stator is electronically commutated. While in "brush" DC motors, the direction of the current is switched manually via the motion of the rotor itself, in PMBLDC motors; the commutation is achieved electronically using a rotor position detector. Unlike in conventional "brush" PM DC motors, the rotor in PMBLDC motors is the permanent magnet.

Until recently the major barrier discouraging the employment of a PMBLDC was the cost of its electronic components and magnetic rotor (Singh et al, 1998). PMBLDC motors consist of a wound field stator, a PM rotor, and a control circuit. With this physical arrangement of their components, PMBLDC motors have several advantages of conventional DC motors. Singh et al (1998) stated that the high operating efficiency, the brushless construction, and the maintenance-free operation has given a scope to the demand of PMBLDC motors in water pumping applications operated by PV-array, particularly in remote villages. Furthermore, Langridge et al (1996) reported that, due to their high torque to weight ratio (and hence relatively low volume), PMBLDC motors are most suitable for solar applications. According to Langridge et al (1996), efficiencies (electrical to mechanical) of this type of motors can reach 80 – 90 %. The authors stated that, in PV pumping systems, there is a significant starting torque due to the static friction of the pump. The suitability and advantages of PMBLDC motors for PV pumping systems was also recognised by several other authors, (Swamy et al, 1995 and Benlarbi et al, 2004).

2.3.3 PV-motor coupling

The PV-motor system operation point is determined by the intersection of the electrical characteristics of both the PV module and the motor (Fig. 2.6, point e). The figure also shows the hysteresis effect encountered in starting/stopping the motor.

Under stalled conditions, the motor does not produce a back EMF and thus it will draw stalled rotor current until sufficient armature current is present to overcome the starting torque. The irradiance level at point (b) is just enough to produce this

current and the operating point then jumps to point (d). As the irradiance increases, the operating point moves towards point (e). Between points (d) and (e), even though the PV IV characteristic varies with irradiance and ambient temperature, as discussed in section 2.2, the motor characteristic is not affected. When irradiance decreases, the motor performance follows the motor characteristic to point (c) after which it stalls and the operating point jumps to point (a).

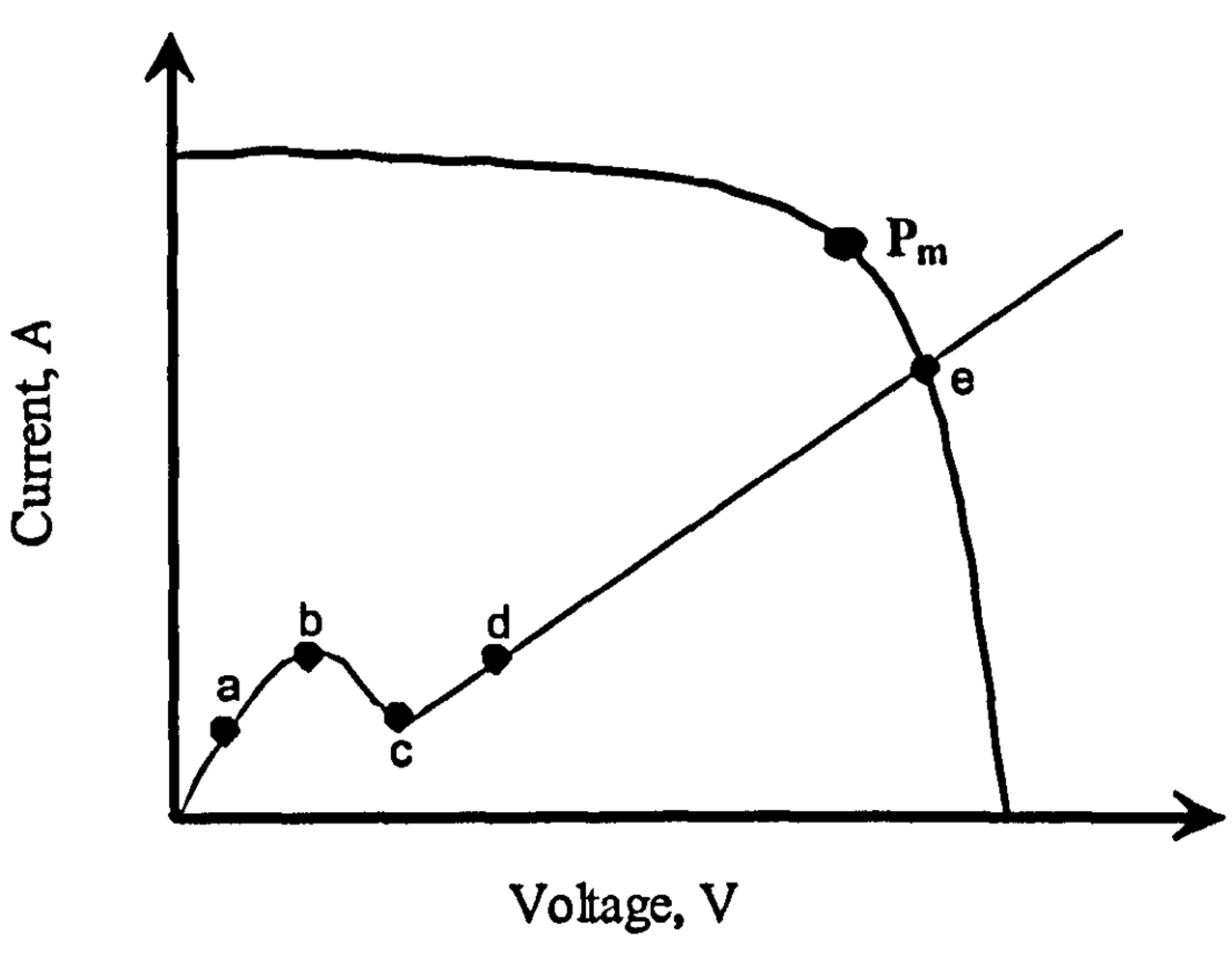

Figure 2.6: IV characteristic of a PV-driven load.

In order to obtain as much energy as possible from the PV module, it is desirable to operate the fan at the module's maximum power point so that most of the PV output is utilised. Figure 2.7 shows the power vs. voltage curves for a PV module at different irradiance levels. It is seen that there is one point on the PV IV curve at which the PV module produces maximum power. The maximum power trajectory is also shown. The ideal load is that which operates in the vicinity of the maximum power trajectory.

A more detailed discussion of the methods for PV module-motor matching is given in section 2.6.2. Presently, a general overview of early studies considering the coupling of different types of motors (DC and AC motors) to PV modules is given.

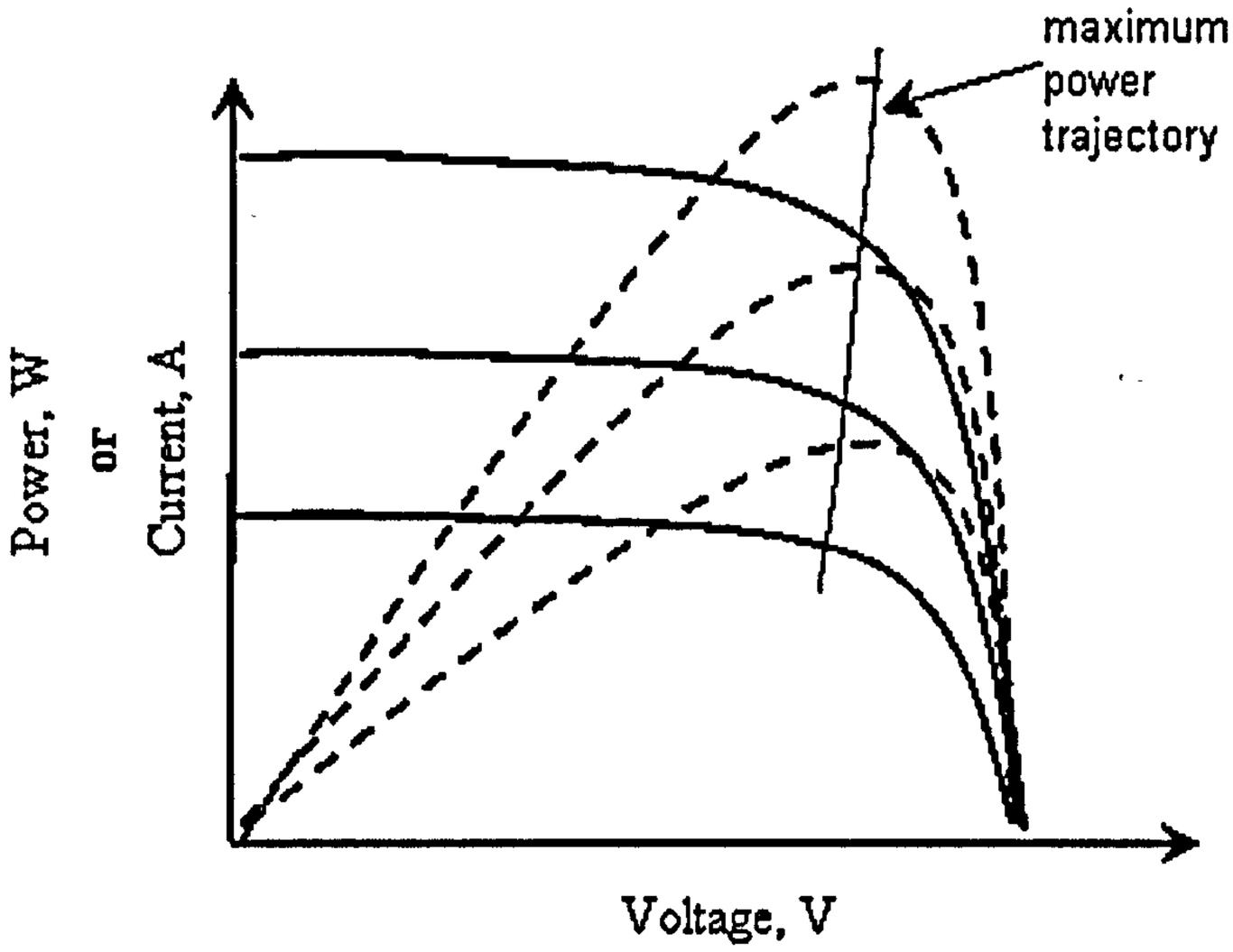

Figure 2.7: PV power vs. voltage curves and PV maximum power trajectory.

2.3.3.1 Optimum motor selection

Many researchers have investigated the design and performance of directly coupled PV systems. Most of this research has focused on the matching between DC motors and PV modules for maximising efficiency. Roger (1979) studied the direct coupling between PV modules and series, shunt and separately excited PM motors. The torque for each motor type was expressed as a function of motor current. Results showed that, as the PM motor presented the highest starting torque it therefore gave the best match when coupled to PV modules. The author further reported that direct coupling is interesting for fans, especially when forced ventilation is needed. In the cases of PV-fan systems, the starting process is completely autonomous and does not necessitate a special procedure as in the case of a constant voltage source or mains driven applications.

Appelbaum and Bany (1978) and Appelbaum (1981) discussed the coupling of separately excited (including PM), series and shunt motor coupling with PV modules in three planes: the motor (ω, T) and (ω, I) planes and the PV converter's (I, V) plane. The points of operation were transformed from one plane to another. The efficiency of the system was determined by the closeness of the system's operating line to the maximum power line. Their results showed that the utilisation efficiency varied throughout the day and reached its peak (100 %) twice: in the morning and in the afternoon. The array

output was well utilised for more than 75 % of the day (more than 12 hours). Speed variation, on the other hand, was found to be rather small and stayed within limits (±300 r/min). Moreover, it was also reported that the ventilator type load (in their case a centrifugal pump with a quadratic IV characteristic) fits very well the PV converter (i.e. operates in the vicinity of P_m) in contrast to a constant load (a horizontal IV characteristic).

Other researches studied the relationship between the PV maximum power point and the point of maximum mechanical power. Zinger and Braunstein (1981) concluded that the maximum power point of the PV module is different from that point for maximum mechanical power. They stated that the maximum mechanical power point ($P_{mechanical} = \omega.T$) is affected by the speed-torque relationship in addition to the motor type and parameters.

Alghuwainem (1992) calculated the maximum mechanical output for two types of DC motors: the separately excited and series motors. It was found that the separately excited motor delivers a greater output mechanical power than the series motor and that the difference is more significant at radiation levels below 30 % and above 70 % of full sun.

Zaki and Eskandar (1996) compared the gross mechanical power produced in PV pumping systems. One system comprised a SEDC motor and the second, an AC induction motor. It was found that the separately excited motor provided better utilisation of the PV module's maximum power. It was also concluded that the DC motor was more advantageous because it was directly coupled to the PV module, while in the case of the induction motor an inverter was required. The output of the PV system with the SEDC motor was controlled by controlling the field excitation while that with the i8nduction motor was controlled by controlling the inverter frequency. Eskandar and Zaki (1997) further investigated matching induction motors to PV modules by controlling the water discharge flow rate.

2.3.3.2 Start up characteristics of PV-coupled motors

Singer and Appelbaum (1986) studied the starting characteristics of different types of motors. It was reported that the starting time of the PV-coupled motor depends

on the inductance of the armature. The shortest starting time was found for separately excited motors.

The start-up characteristics can drastically affect the volume of air delivered by a PV-driven system in a given period of time. This will be discussed in detail in section 6.2.1.

2.3.4 Summary

The discussion above reveals the following facts:

1. The PM motor has the highest starting torque among the different motor types
2. The separately excited motor provides better utilisation of P_m.
3. The PV module utilisation is strongly dependent on the load type. Motors with variable IV characteristics (as opposed to those with constant load) provide a better match for PV modules meaning that they operate closer to P_m at different irradiance levels.
4. The PV maximum power point is different from the point of maximum mechanical power.

In summary it can be stated that PM separately excited DC motors are most suitable for coupling with PV modules. Furthermore, PMBLDC motors are also reported to be most appropriate for solar applications. This type of motors, although more expensive than other types of motors, requires less maintenance and operates at higher efficiencies.

As will be discussed in the next section, the motor equations described by Eq. 2.11 to 2.13 are necessary for the determination of the motor operational point. For these equations to be applicable, the motor constant and armature resistance must be known. Laboratory measurements can be used to determine these constants as described in Textbox 2.2.

Textbox 2.2: Evaluation of motor parameters.

The motor constant (K_m, V.s/rad) and armature resistance (Ω) are usually supplied by manufacturers. In cases where they are not given, they can be determined from experimental measurements or from other manufacturer's data. This is explained below.

Rewriting Eq. 2.13 for I and substituting it with Eq. 2.11 into Eq. 2.12 and rearranging we arrive at the equation

$$\omega = \frac{V}{K_m} - \frac{R_a}{K_m^2} T$$

which, for a fixed voltage, defines the ωT characteristic of the motor as shown by Fig. 2.5 for a PM motor. The slope of the characteristic is $(-\frac{R_a}{K_m^2})$ and the intercept is $(\frac{V}{K_m})$. If the manufacturer supplies this characteristic at a given voltage, then it is possible to obtain the parameters R_a and K_m. If the ωT characteristic is unavailable; these two parameters can be obtained from special cases of the equation above.

R_a can be obtained from stall conditions. In this case, the speed of the motor is zero and there is no back emf, so Eq. 2.12 reduces to

$$V = R_a I$$

Measurements of voltage and current from a locked-rotor test are sufficient for the determination of R_a.

At maximum speed, ω_{max}, the torque is zero as shown by Fig. 2.5 for a PM motor. The above equation reduces to

$$\omega_{max} = \frac{V_{max}}{K_m}$$

The manufacturer usually supplies the maximum speed of a motor at the rated voltage. From this information, it is possible to determine K_m.

2.4 MODELLING OF FLOW RATE IN PV-DRIVEN SYSTEMS

2.4.1 Introduction

Modelling of flow rate in PV-driven systems requires knowledge of the PV IV characteristic as a function of environmental factors. The literature review for this has been discussed in section 2.2. Section 2.3 introduced PV-motor coupling in addition to the relevant motor equations required for modelling. The current section discusses the literature review related to flow rate modelling in PV pumping system.

Most available literature on flow rate modelling of PV-driven systems is on water pumping applications. Water pumping is an important factor in the development of rural and remote areas in developing countries. Firatoglu et al (2004) stated that since solar energy is usually high in arid and dry locations where water is most needed, PV energy is much more suitable for pumping water. Moreover, Jafar (2000) stated that using PV modules for pumping water is specifically advantageous because no storage batteries are required.

The first stage in modelling PV-driven systems is the determination of the operational voltage, current and speed of the motor. The literature review related to this subject with regard to water pumping systems is discussed in section 2.4.2. The modelling of pressure-flow characteristics of fluid moving machines (i.e. pumps and fans) is discussed in section 2.4.3. Section 2.4.4 discusses the modelling of system pressure-flow characteristics. Finally, section 2.4.5 gives a general review of flow rate modelling in PV-driven systems.

2.4.2 Motor voltage and rotational speed

In order to solve for the voltage and the speed of the fan, the PV parameters shown in Eq. 2.4 and the motor parameters (K_m and R_a) shown in Eqs. 2.11-2.12 must be known. Section 2.2.5 outlines both the experimental and analytical methods for determining the PV parameters. Textbox 2.2 above explains how the motor parameters can be experimentally determined.

In PV pumping systems, different methods were used in the literature in order to solve for the pump voltage and rotational speed. The intersection of the PV and load IV characteristics, as shown in Fig. 2.6, is the operational point.

Hsiao and Blevins (1984) reduced the motor equation to a single one relating voltage to current in terms of armature resistance, motor constant and torque and angular speed at some reference conditions. This equation was solved with the PV IV characteristic simultaneously using the Newton's iteration method.

Anis and Metwally (1994) studied the steady state behaviour of PV coupled systems. The torque of the load (a centrifugal pump), T_L, was expressed as a function of the speed of the motor, ω, according to the relationship,

$$T_L = K_f \omega^2 \qquad (2.14)$$

where K_f ($Kg.m^2/rad^2$) for a given load (pump or fan) is a constant which can be determined from reference values of speed and torque. Neglecting the motor-load coupling losses, they equated both motor and load torques so that

$$K_f \omega^2 = K_m I \qquad (2.15)$$

With irradiance as a parameter, the authors then used the Newton-Raphson method to solve the PV IV curve with Eqs. 2.11, 2.12, and 2.15 for the operational voltage, current and speed of the pump. The authors stated that the use of the Newton-Raphson method, which is usually used for solving non-linear simultaneous equations, was found to be satisfactory where no convergence problems have been observed. The computation time was short and in most cases the solution was reached in 30 iterations. The accuracy of the solution could be improved at the expense of increasing the computation time.

In their analysis, Anis and Metwally (1994) used extreme days of the year where for each day, the period between sunrise and sunset was divided into 6-min intervals so that the irradiance does not change significantly during this period and hence G can be considered constant. The steady state parameters of current, voltage and rotational speed where computed for each of these intervals.

Most researchers used the motor equations for the determination of the operational point. A few others, however, treated the motor/load as a single unit and used measured IV characteristics to solve for the operational voltage and current of the fan. This reduces the number of iterative equations to be solved in order to determine the motor's rotational speed and thus simplifies the model. Cromer (1983) and Hadj Arab et al (2004) used measured pump IV characteristics to describe the motor/pump electrical behaviour. These characteristics were then solved simultaneously with the PV module IV characteristic to solve for operational voltage of the pump. Hadj Arab (2004), however, reported that the IV characteristic of the pump changes with pressure across the pump and so it must be expressed in terms of the pump-piping characteristics. This will be discussed in more detail in section 3.7.

2.4.3 Head-flow performance characteristics

In addition to the motor modelling equations given in section 2.3.1 above, the head-flow characteristic (ΔP-Q) of the fluid-moving device (whether a pump or a fan) is also of interest in modelling of PV pumping systems. Figure 2.8 shows a typical head-flow (ΔP-Q) characteristic of a centrifugal pump. It is important to note that at any fixed speed, the pump will operate along this curve and at no other points. For a given pump, in addition to speed, the fluid temperature also affects the ΔP-Q characteristic.

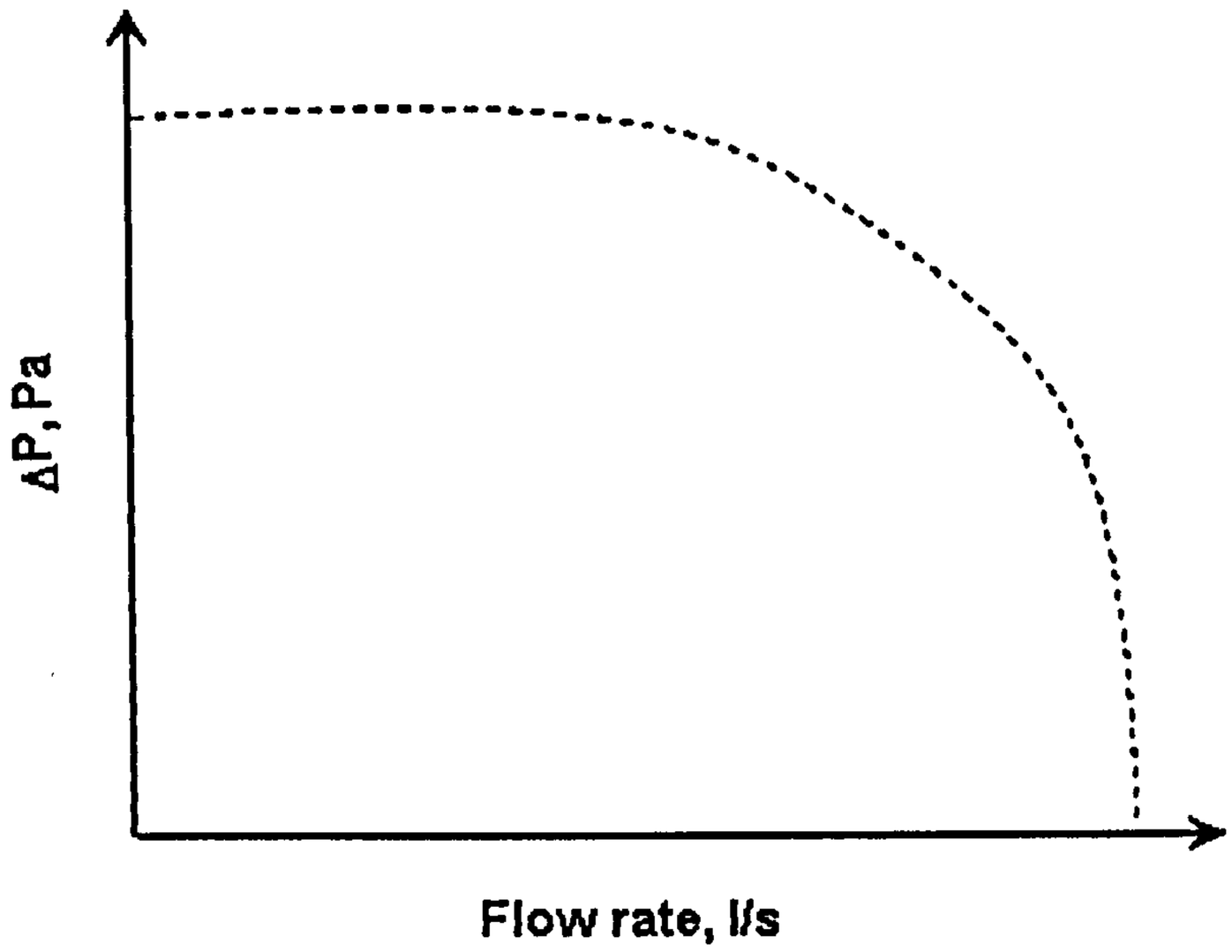

Figure 2.8: Head-flow characteristic of a centrifugal pump or fan.

A single ΔP-Q curve is usually supplied by manufacturers for specific operating conditions of speed and fluid temperature. The performance at other operating conditions is usually obtained through the affinity laws as shown in the equations below:

$$Q_2 = Q_1 \frac{\omega_2}{\omega_1} \tag{2.16}$$

$$\Delta P_2 = \Delta P_1 \left(\frac{\omega_2}{\omega_1}\right)^2 \left(\frac{\rho_2}{\rho_1}\right) \tag{2.17}$$

$$P_{w2} = P_{w1} \left(\frac{\omega_2}{\omega_1}\right)^3 \left(\frac{\rho_2}{\rho_1}\right) \tag{2.18}$$

Where ρ is the fluid density (kg/m^3), P_w is power (W) and other symbols are as defined above.

In PV-driven systems, the PV output and consequently the speed of the motor vary continuously. For modelling purposes, it is important to be able to predict the pump's or fan's ΔP-Q characteristic for any given PV module output. The use of affinity laws is only useful if a reference ΔP-Q curve is known at some reference operational conditions. Several researchers considered different ways of describing this reference curve.

Eckstein et al (1990) approximated the centrifugal pump head at a given speed as a function of flow rate by a quadratic equation. Using this kind of relationship and using affinity laws, the authors generated the pump ΔP-Q characteristic at 3500 r/min from that at 3000. Errors of 2 % were obtained.

Other researchers corrected the ΔP-Q curve by expressing the pressure across the pump as a function of both flow rate and speed. Moussi et al (1985) and Benlarbi et al (2004), however expressed the pressure across a centrifugal pump by a quadratic equation in speed and flow rate as shown below

$$\Delta P = C_1 \omega^2 - C_2 \omega Q - C_3 Q^2 \tag{2.19}$$

2.4.3.1 Axial flow fans

Osborne (1977) stated that axial flow fans are most suitable for high flow rate low pressure systems. They are commonly used for removing heat from computers as reported by Lin and Chou (2004). Another common use of such fans is in air-cooled heat exchangers (Meyer and Kroger, 1997).

It was mentioned above that PMBLDC motors are most suitable for coupling with PV modules. Furthermore, Newborough and Probert (1990) reported that single-phase PMBLDC motors are commonly employed for driving axial fans and that they can achieve efficiencies exceeding 40 %. So it can be concluded that a PMBLDC axial flow fan is appropriate for PV applications where high flow rates are required.

The ΔP-Q characteristic for an axial flow pump (or fan) is different for that for a centrifugal pump (or fan). A typical ΔP-Q characteristic of an axial flow fan is shown in Fig 2.9. In axial flow fans, the flow of air is parallel to the axis of the impeller. An axial flow fan's ΔP-Q characteristic is characterised by a discontinuity region (Fig. 2.9) corresponding to the stalling conditions on the blade aerofoils. Osborne (1977) stated that it is preferable not to operate the fan in this region or at lower flow rate. The affinity laws described by Eqs 2.16 to 2.18 are also applicable for axial flow fans.

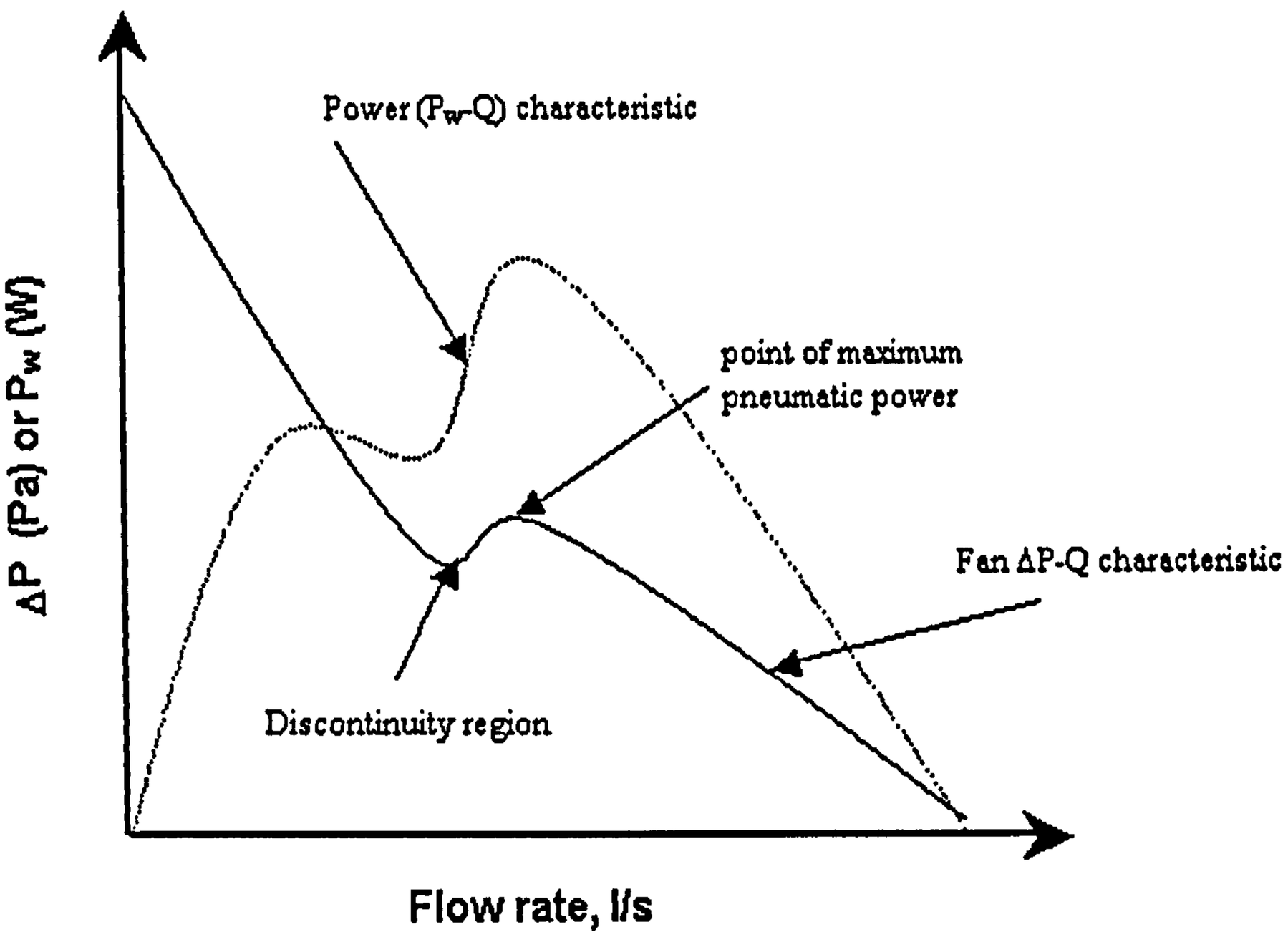

Figure 2.9: ΔP-Q and P_w-Q characteristics of an axial flow fan.

The pneumatic power curve (P_w-Q) is also shown in Fig 2.9. The amount of useful work that a fan performs is the product of flow rate through it and the total pressure differential measured before and after the fan. The first of these quantities is usually referred to as the capacity while the second is commonly known as the head. The capacity, usually provided by the manufacturer as (m^3/hr) or (l/s), is a measure of the maximum flow rate of air that can be delivered by a fan under certain conditions. The fan head can be either total head or static.

2.4.4 System characteristics

The system ΔP-Q curve is a quadratic function of ΔP in Q as shown by the following equation:

$$\Delta P = K Q^2 \tag{2.20}$$

where the coefficient K is a function of duct properties and density of air as shown in Darcy's equation

$$K = \frac{8 f \rho L}{\pi^2 D^5} \tag{2.21}$$

where the friction factor, f, is a function of Reynolds number ($\frac{4\rho Q}{\pi \mu D}$) and roughness of the duct (k, mm) and can be obtained by Colebrook equation (Perry and Green, 1997)

$$\frac{1}{\sqrt{f}} = -4\log\left[\frac{k/D}{3.7} + \frac{1.256}{N_{Re}\sqrt{f}}\right], \mathrm{N_{Re}} > 4000 \tag{2.22}$$

The Colebrook Eq. is implicit in f and so the solution of Eq. 23 requires an iterative method such as the Newton-Raphson method. This will be discussed in more detail in section 3.2.5.

Eckstein et al (1990) stated that the system head profile can be obtained either by measurement or analytically by knowledge of the piping system components.

Knowing the roughness (k, mm), the diameter (mm) and the length of duct in addition to the fluid density and viscosity, Eqs. 2.20 – 2.22 can be used to determine ΔP as an analytical function of Q. Alternatively, a single measurement of ΔP and Q for a given system can be used to generate the full ΔP -Q curve using the affinity laws. Eckstein et al (1990) stated that the affinity laws are applicable for moderate changes in speed but even for large changes in speed, the error is acceptably low.

In analysing and designing pumping or fan-duct systems, it is useful to impose the system characteristic on the pump or fan characteristic as shown in Fig 2.10. The operating point (Q, ΔP) is the intersection of the system and the pump or fan curves.

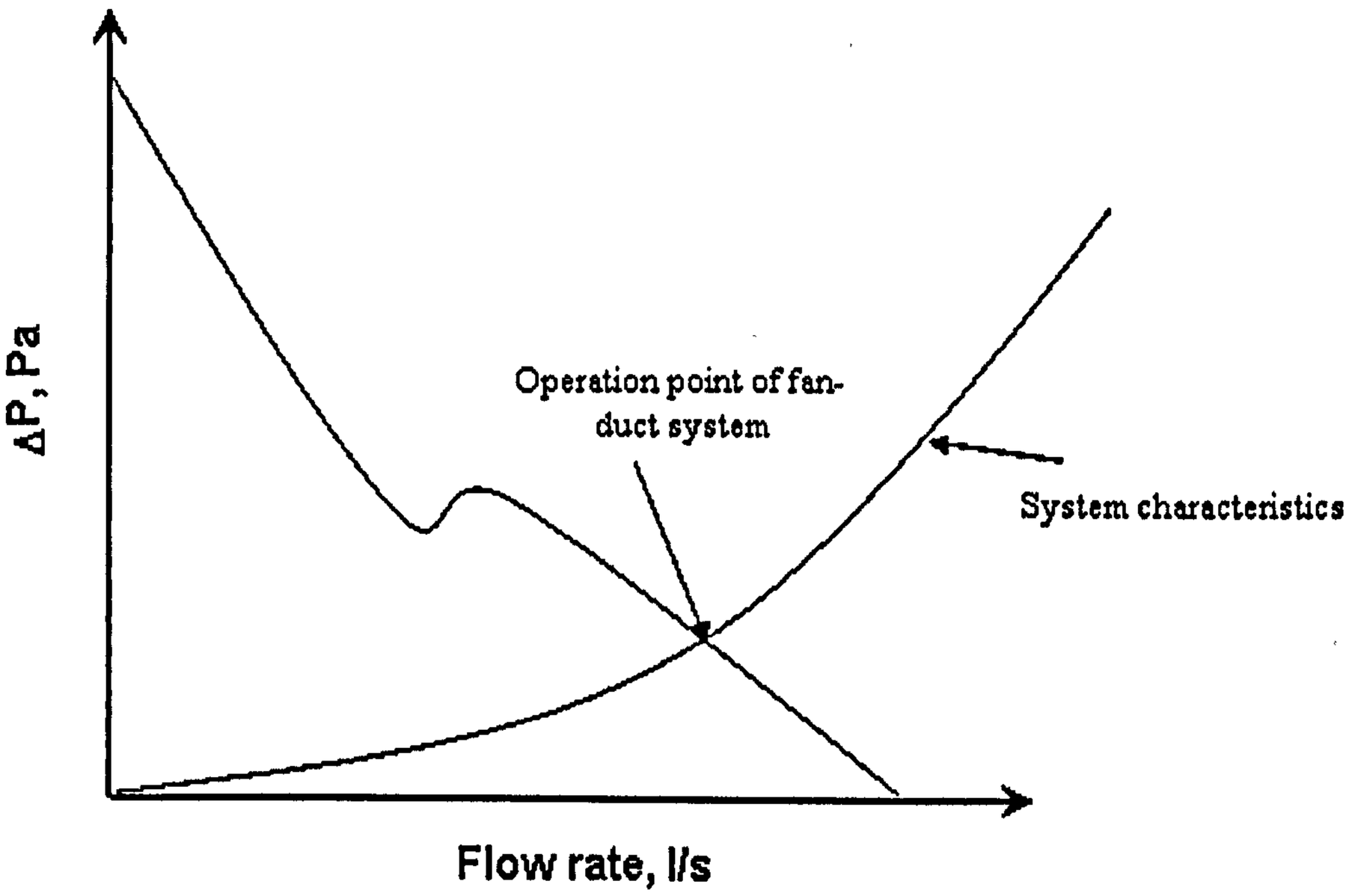

Figure 2.10: Fan and system ΔP-Q characteristics.

2.4.5 Flow rate modelling

Jafar (2000) stated that it is impractical for a manufacturer to supply system output data for infinite combinations of a PV pumping system components and so it is necessary to develop a model for a particular system that can predict the output for any combination of head and irradiance. Empirical relationships of flow rate as a function of irradiance at different pumping heads were developed and the coefficients of these quadratic relationships were further expressed as functions of head. Bione et al (2004) also showed a quadratic relationship between flow rate and irradiance in a PV-driven water-pumping system. Hadj Arab et al. (2004) expressed the flow rate of water as a

quadratic function of the pump voltage. The parameters of this quadratic relationship were obtained by an iterative Newton technique based on measurements of flow rate and voltage. Hadj Arab et al. (2004) stated that the motor-pump IV characteristic is solved simultaneously with the PV module IV characteristic. The operational voltage obtained is then used in the flow rate – voltage relationship to solve for flow rate of water at any irradiance and temperature. The approaches above, as they do not account for the different variables associated with the piping system, are specific, thus limiting their range of application. Other researchers, on the other hand, through considering the properties of the piping system in their models, have broadened their range of applications. Eckstein et al (1990) and Moussi et al. (1999) described the pump pressure as a function of flow rate and fan rotational speed, which is, in turn, a function of irradiance. The system pressure was expressed as the sum of static head and friction head.

Eckstein et al (1990) described the system by two equations relating flow rate and pump rotational speed at a given torque. The first equation represented the difference between the pump head and system head as a function of speed and flow rate, which was equated to zero. The second equation represented the pump efficiency, defined as the ratio of hydraulic power to mechanical power. Efficiency was expressed as cubic function of (flow rate / speed). The two equations were solved simultaneously for flow rate and speed and so head and efficiency were calculated.

2.4.6 Summary

The literature review above reveals that most researchers, in modelling of flow rate in PV-driven systems, consider the system as three components: the PV module, the motor and the load. Determination of the flow rate in the system then requires solving the equations for all the components simultaneously using a computer program. In addition, many researchers solved for the intermediate values of the voltage of the fan but not the rotational speed. A few researchers, however, directly expressed the flow rate as a function of irradiance falling on the PV module. This approach is general because it does not allow for the inclusion of other factors affecting the system such as temperature. Furthermore, simulations of flow rate vs. irradiance (when all other factors are held constant) can be obtained from a computer program, which considers all these factors.

The head-flow characteristics of fans are similar to those for pumps. For a given fan, these characteristics are influenced by the rotational speed of the fan and the temperature of the fluid. Manufacturers usually supply a ΔP-Q characteristic at some given conditions of fan speed and fluid temperature. Most researchers use affinity laws to transform the ΔP-Q characteristic to a new level of speed and temperature. Others, however, ignore the effect of temperature and use equations, which directly relate head to flow rate and speed.

Most researchers base their modelling on manufacturer's data. However, modelling can also be made using measured performance of the different components. In this case, the errors associated with the model will depend significantly on the instruments and techniques used. Nevertheless, using measured parameters in the model rather than manufacturer's data makes it more representative of the actual performance of the system. Furthermore, for modelling purposes, it is necessary to express the ΔP-Q characteristic of the fan at a given speed and temperature, as an analytical function of ΔP in Q.

2.5 SLOPE IRRADIANCE MODELLING

2.5.1 Introduction

In order to predict the performance of solar processes in the future, past measurements of solar radiation at the location in question or from a nearby similar location are used. This section describes the methods available in the literature for estimating solar radiation on a sloped surface from widely available data. Procedures for calculating extraterrestrial radiation and estimating horizontal beam and diffuse irradiation from horizontal global data are first presented. Slope irradiance is calculated from these beam and diffuse values. In addition, section 2.5.3 gives a brief summary of the instruments used for solar measurements.

Solar radiation data is available in different forms. The word irradiance refers to the instantaneous measurement of radiation while the word irradiation refers to those values integrated over some period of time (an hour or a day). Most available solar data are global horizontal data (beam plus diffuse). Two types of data are widely available. The first is monthly average daily total radiation on a horizontal surface. The second is hourly total radiation on a horizontal surface for each hour for extended periods of time such as one or two years.

2.5.2 Extraterrestrial radiation

As a result of the way the earth orbits around the sun, the distance between the two varies by 1.7 %. However, the radiation emitted by the sun and its spatial relationship to the earth result in a nearly fixed intensity of solar radiation outside the earth's atmosphere. The solar constant is defined as the solar energy per unit time received on a unit area of surface perpendicular to the direction of the radiation, at mean sun distance, outside of the atmosphere.

Several types of radiation calculations are done using normalised radiation levels, that is the ratio between the available solar radiation to the theoretically possible radiation if there were no atmosphere. For these calculations, a method for estimating extraterrestrial radiation is required. The extraterrestrial radiation incident on a horizontal surface is given by the Eq.

$$E_x = G_{sc}\left(1 + 0.033 \cos \frac{360\ n}{365}\right)(\cos \phi \cos \delta \cos \omega_s + \sin \phi \sin \delta) \qquad (2.23)$$

where G_{sc} is the solar constant (1367 W/m^2), n is the day number, ϕ is the latitude of the location of interest, δ is the declination and ω_s is the sun hour angle.

2.5.3 Measurement of solar radiation

2.5.3.1 Pyranometers

Measurements of solar radiation on a horizontal surface are usually undertaken by a specialised agency such as the national meteorological office. Most of the available data on solar radiation are measured using pyranometers. These are instruments used for measuring total (beam and diffuse) solar radiation. The detectors for pyranometers are thermal detectors covered with one or two hemispherical glass covers to protect them from extraneous effects.

Several factors must be considered in designing pyranometers. First the detectors must be independent of the wavelength of radiation over the solar energy spectrum. In addition these detectors must have a response independent of the angle of incidence of the solar radiation. Furthermore, the covers should be uniform in thickness so as not to cause uneven distribution of radiation on the detectors. The double glass construction minimises temperature fluctuations and reduces thermal radiation losses to the atmosphere. Weekly cleaning is recommended because the glass covers can collect debris. Furthermore, silica gel crystals in the body of the pyranometer can prevent moisture.

The CM22 is regarded as the standard reference pyranometer due to its accuracy and stability. In these instruments, a black disk absorbs the radiation falling on the pyranometer. The heat generated flows through a thermal resistance and the resulting temperature difference across this resistance is converted to voltage, which can be read by a data logger or a computer.

Diffuse irradiance is measured by placing a shadow band over a pyranometer as shown by Fig. 2.11. The adjustment of this shadow band is required periodically. An account of these adjustments and the associated errors are discussed by Coulson (1975).

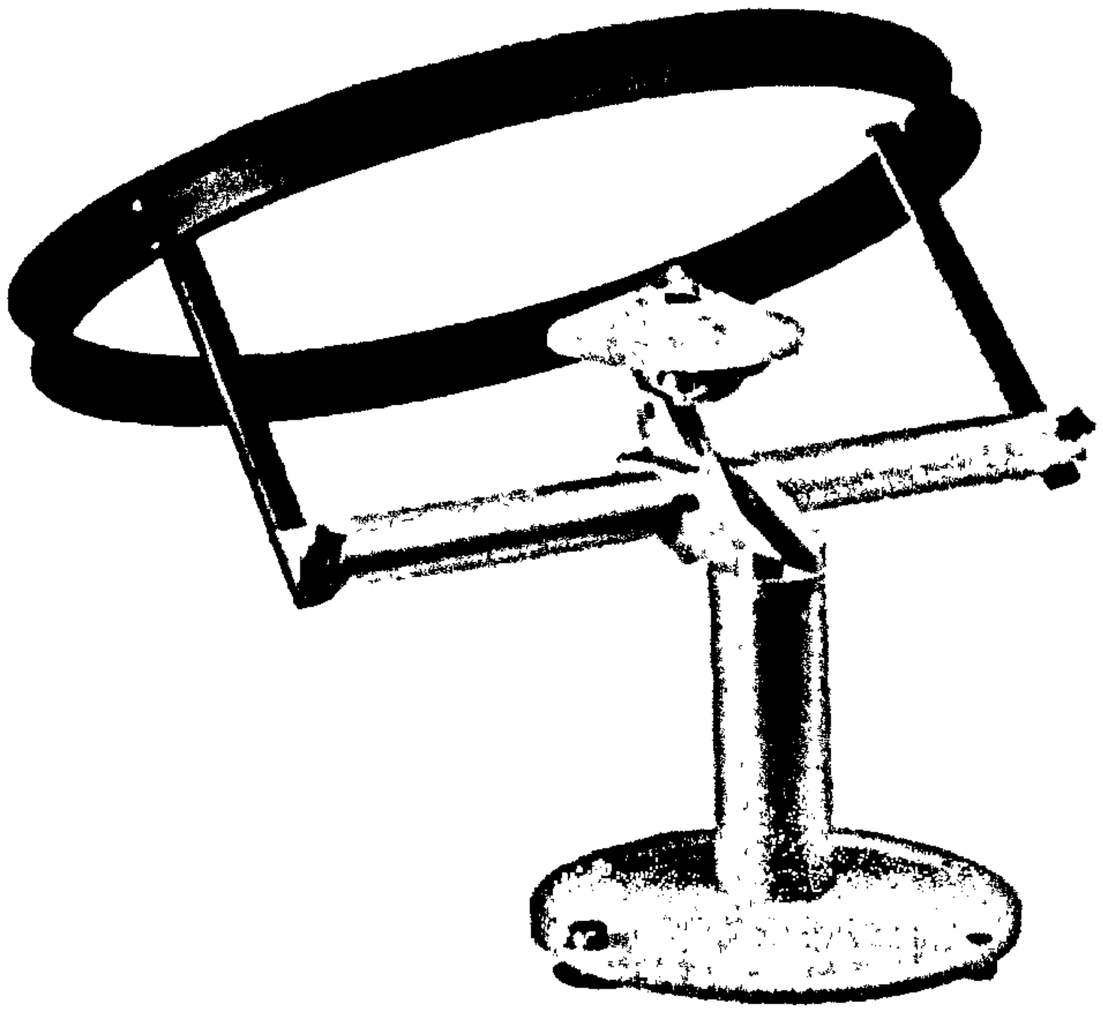

Figure 2.11: Using a shade ring for measuring diffuse irradiance.

2.5.3.2 Errors associated with pyranometers

The most significant errors associated with pyranometers are shown in Fig. 2.12. Instrumental errors arise from the sensors and their construction. The cosine effect is the most common and well-recognised error of pyranometers. This is the sensor's response to the angle at which radiation strikes the sensing area. This error will be greatest at sunrise and sunset when the angle of the sun is very acute. This can be dealt with by excluding data at sunrise and sunset (altitude angles below 6°).

The azimuth and temperature errors are inherent manufacturer errors. The azimuth error results from imperfections in the glass domes. Temperature errors arise from temperature fluctuations of the instrument and they can be reduced by adequately ventilating the instrument. The spectral selectivity is dependent on the spectral absorptance of the black paint and the spectral transmission of the glass. Finally, the deterioration of the cells results a 1 % change in the full-scale measurement per year.

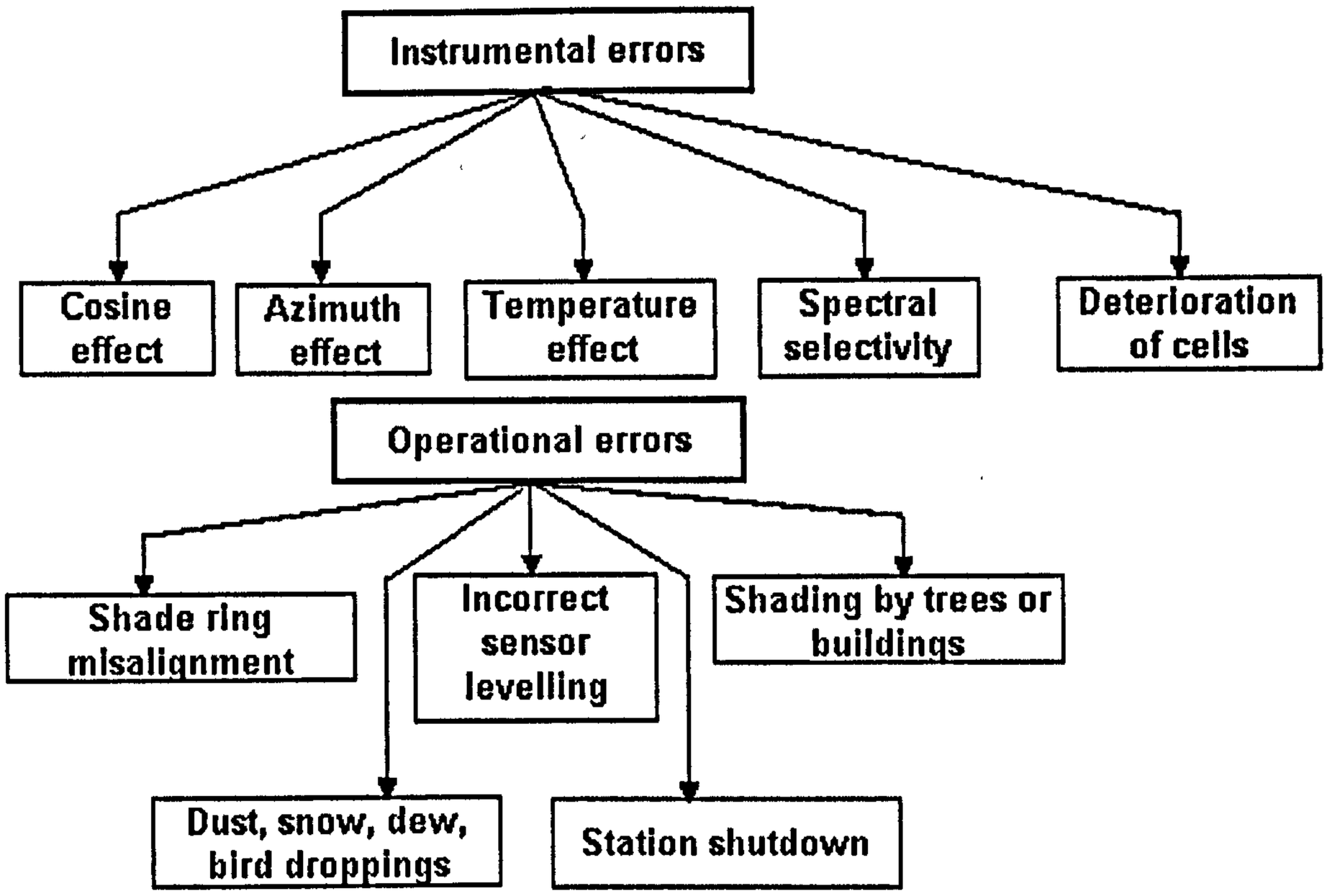

Figure 2.12: The most significant errors associated with pyranometers

Another set of errors associated with measurement of solar radiation are operational errors as shown in Fig. 2.12. These are errors and problems related to the operation of the instrument. The shade-ring misalignment is the most significant of these errors.

2.5.3.3 Delta-T sunshine sensors

The common approach for measuring global and diffuse radiation has been to use two sensors. The shade ring (Fig. 2.11), which can be adjusted to match the track of the sun across the sky for a certain day, is usually used with one of the sensors, to measure the whole sky apart from the sun.

Figure 2.13 shows a newly developed Delta-T BF3 sensor, which allows for the simultaneous measurement of both horizontal global and diffuse irradiation. The BF3 sensor consists of a system of photodiodes and a shading pattern. The shading pattern is such that it allows at least one photodiode to be always exposed to full solar beam and another to be always completely shaded. Furthermore, all photodiodes receive an equal amount of diffuse light from the sky hemisphere. The shading pattern was designed with the help of a computer program.

Figure 2.13: Delta-T BF3 sensor for measuring both global and diffuse radiation.

2.5.4 Estimation of horizontal beam and diffuse components from global irradiance

The performance of this sensor was evaluated by Woods et al (2003) at the school of Engineering at Napier University. Horizontal global and diffuse measurements were collected by the BF3 sensor. Two Kipp and zonen CM11 sensors, one with a shade ring, were set up beside the BF3 sensor on the same roof to allow for cross checking. The global irradiance measured by the BF3 showed values 4.7 % higher with a standard error of 16.5 W/m^2. Diffuse values were 1.4 % higher with a standard error of 13.4 %.

In this section, a method for estimating the fractions of the total horizontal radiation that are diffuse and beam is presented. The split of global radiation into its beam and diffuse components is important because methods for calculating total radiation on sloped surfaces from data on horizontal surfaces require separate treatments of these two components.

The usual and most common approach is to correlate I_d/I, the fraction of the hourly radiation that is diffuse, with k_T, the clearness index. The clearness index is defined as the ratio of global radiation on a horizontal surface to extraterrestrial radiation. In mathematical terms, the clearness index can be written as

$$k_T = \frac{I}{E_x} \tag{2.24}$$

where I is the global radiation (W/m^2) and E_x is the extraterrestrial radiation (W/m^2). A typical plot of diffuse ratio vs. k_T is shown in Fig. 2.14. In order to obtain I_d/I vs. k_T correlations, measurements of diffuse and global radiation in addition to time, date and location must be taken. The three latter parameters are used to calculate extraterrestrial radiation as shown by Eq. 2.23 and a plot similar to that in Fig 2.14 is obtained. Early work in this area by Orgill and Hollands (1977) which was based on data from Canadian stations, Erbs et al (1982) which was based on data from U.S. stations and Reindl et al (1990) which used data from both U.S. and European stations all showed nearly identical correlations of diffuse ratio as a function of clearness index. However, Muneer et al (1983) through developing a correlation for New Delhi and comparing it to other locations reported that these correlations are location dependent.

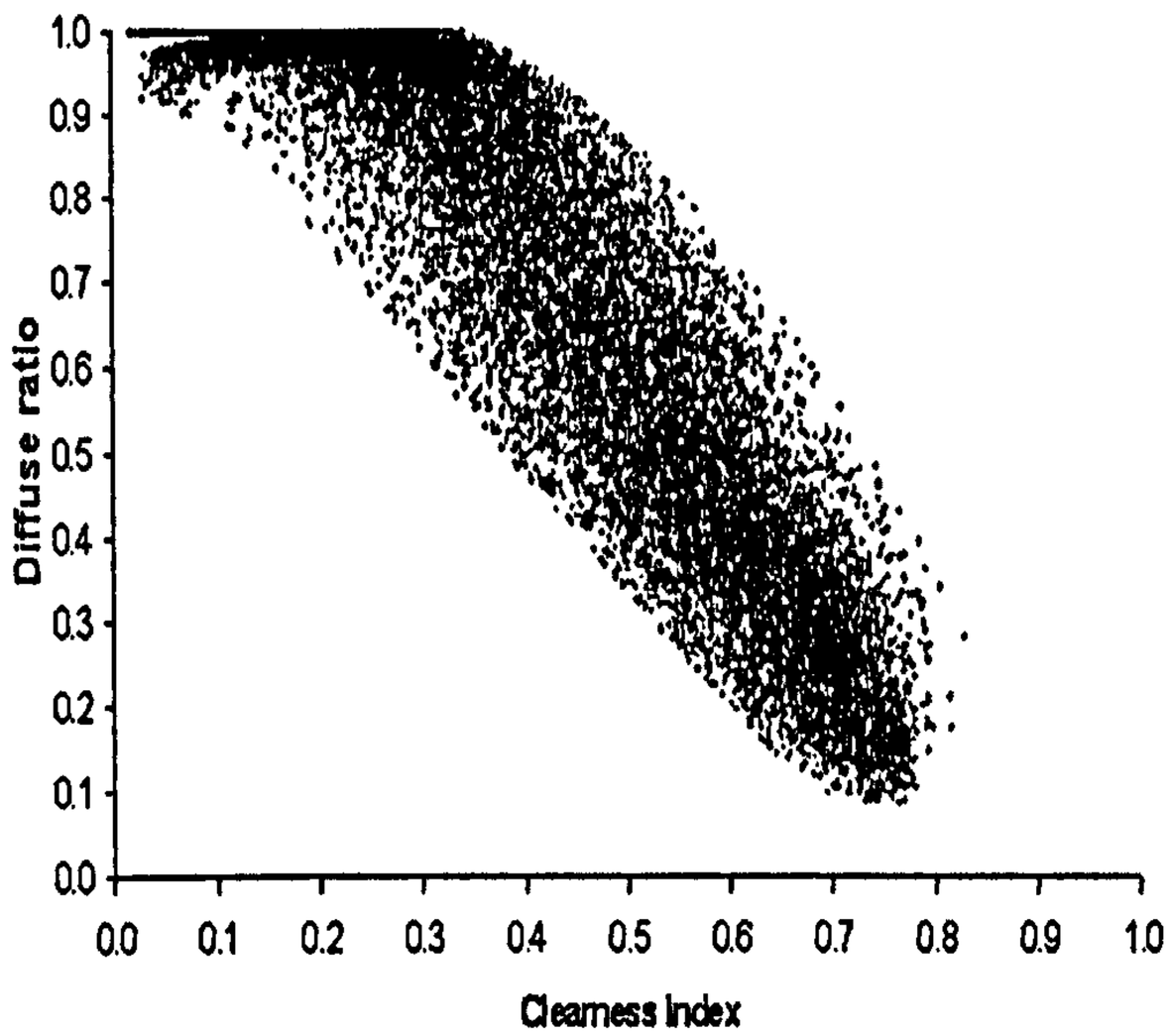

Figure 2.14: A dr vs. k_T envelope for Bracknell, UK.

2.5.5 Estimation of slope irradiance

As mentioned above hourly horizontal global and diffuse irradiation data can be used to estimate slope irradiance provided R, the ratio of global irradiation on a slope surface to that on a horizontal surface is known. The ratio, R can be mathematically expressed as

$$R = \frac{I_{tilt}}{I} \tag{2.25}$$

where I_{tilt} is the total irradiation on the tilted surface and can, for an ideally non-reflecting foreground, be expressed as

$$I_{tilt} = R_b I_b + R_d I_d \tag{2.26}$$

where I_b and I_d are horizontal beam and diffuse irradiation respectively, R_b is ratio of beam irradiance on the sloped surface to that on a horizontal surface and it can be calculated as explained in section 2.5.5.1, R_d is the ratio of diffuse irradiance on the sloped surface to that on the horizontal surface and it can be calculated as shown in section 2.5.5.2.

2.5.5.1 Estimating beam irradiance on a tilted surface

The calculation of beam irradiation on a tilted surface from horizontal beam is a geometric problem (Muneer et al, 2000). It depends on the latitude of the location (ϕ), the slope of the surface (α) in addition to the declination (δ) and hour angle (ω_s). The beam component of irradiation on the sloped surface is simply ($R_b \cdot I_b$). For sloped surfaces, Liu and Jordan (1963) have shown that R_b can be calculated from the following equation:

$$R_b = \frac{\cos(\phi - \alpha)\cos(\delta)\cos(\omega_s) + \sin(\phi - \alpha)\sin(\delta)}{\cos(\phi)\cos(\delta)\cos(\omega_s) + \sin(\phi)\sin(\delta)} \tag{2.27}$$

The beam irradiance on the tilted surface is then calculated from

$$I_{b,tilt} = R_b I \tag{2.28}$$

2.5.5.2 Estimating diffuse irradiance on a tilted surface

Diffuse radiation on a sloped surface consists of three parts. The first is an isotropic part, received uniformly from the entire sky dome. The second is a circumsolar

diffuse, resulting from forward scattering and concentrated in the sky around the sun. The third is horizon brightening that is concentrated near the horizon and is most pronounced in clear skies. If only isotropic diffuse is considered, the calculation of diffuse irradiation on a tilted surface from horizontal diffuse is a simple task and can be calculated as follows:

$$R_d = \frac{1+\cos(\alpha)}{2} \tag{2.29}$$

However, the isotropic model described by Eq. 2.29, tends to underestimate I_{tilt} as explained by Duffie and Beckman (1991). Improved models have been developed which take into account the two other components of diffuse radiation. Hay and Davies (1980) considered the part of diffuse which is circumsolar but ignored horizon brightening. Reindl et al (1990) added a term for horizon brightening to the Hay and Davies model.

2.5.6 Summary

In order to estimate the long-term performance of PV-driven systems, irradiance data is required. This data is usually available as horizontal global data for many locations all over the world. Horizontal diffuse can be easily obtained from global data using the common approach of relating diffuse ratio to clearness index. Several researchers use generalised equations of dr vs. k_T. These relationships are, however, location dependent and must be determined for the location of interest.

Slope irradiance can be determined from horizontal diffuse and beam values. The isotropic model does not fully account for diffuse irradiance and so it tends to under predict irradiance on a sloped surface. Several anisotropic models for predicting slope irradiance were developed as will be discussed in section 5.3. These models, however, are also general and can be location dependent.

2.6 OPTIMISATION OF PHOTOVOLTAIC-DRIVEN SYSTEMS

2.6.1 Introduction

Different optimisation strategies can be considered in order to improve the overall efficiency of a PV-driven system. A number of studies have been done on the optimum matching analysis of directly coupled PV systems. Most of these studies have focused on the ratio between the input electrical energy of the motor and the available maximum power of the PV module. Other authors have extended this matching analysis to the generated mechanical power of the motor with respect to the maximum available power of the PV module. Koner (1995) stated that, since the ultimate goal of PV pumping systems is to pump water, it is necessary to extend this matching analysis to the hydraulic power with respect to the maximum available power of the PV module. Other optimisation techniques are concerned with optimising the configuration of PV modules or maximising the volume of water delivered in a PV pumping system.

2.6.2 PV-motor matching

The importance of operating PV-driven systems near the maximum power point of the PV module has already been discussed in section 2.3.3. Maximum power operation, however, is a challenging task, since it requires that the motor be capable of using all power available at all times. This means that the motor must adjust itself rather quickly on the appearance and disappearance of a cloud cover. This requires that the IV characteristic of the ideal motor intersects the locus of maximum power points on the PV IV characteristics for varying irradiation levels. For this purpose, an electronic maximum power tracker (MPT) can be used between the PV module and the motor. Langridge et al (1996), for example, used an MPT strategy, which operates the PV array at a fixed percentage of the open circuit voltage. However, the inclusion of a matching device can be expensive.

Directly connecting the PV module to the motor and choosing an optimum motor constant so that, for most of the year, the motor is utilising most of the available energy leads to a simple and inexpensive system. Saied (1982) and Kolhe et al (2000) stated that the important parameter of PMDC motors is the magnetic field constant. A method for determination of optimum magnetic field constant of a PMDC motor, when

powered by PV, has been developed. The optimum magnetic field constant was obtained as a function of current at the maximum power point of the PV module. It was found that the maximum output is available at output-energy-weighted average value of magnetic field constant.

Khouzam et al (1991) suggested that MPT can be eliminated if optimum matching is achieved. They defined a matching factor as the ratio of the load energy to the maximum available energy of the PV module. The matching factor depends on the load parameters since the maximum available PV module energy is fixed for a given irradiance and temperature profiles. Optimum matching was achieved by determination of optimal PV module parameters with respect to load parameters using direct-search techniques. They found that the theoretical optimum matching factor for ohmic loads is 94.34 % and that for an electrolyte load is 99.83 %.

Akbaba et al (1998) studied matching between separately excited DC motors and PV modules. They developed an expression of the motor current as a function of the PV module's maximum power point current and voltage. It was shown that by adjusting the field current according to the developed expression, the motor was forced to follow the maximum power locus of the PV module. At any available irradiance level, the input power of the motor was always equal to the maximum output power of the PV module. However, for that study the effect of temperature was neglected.

Another optimisation method for directly coupled PV water pumping systems is the reconfiguration of PV modules under different solar irradiation levels. Saied and Jabori (1989) examined the maximum values of annual output of mechanical energy under several possible combinations of PV modules and motor constants. Salameh and Liang (1990) used a multistage electric array reconfiguration where the optimum switching point was based on the simulated performance of each component. Furthermore, Faldella (1989) studied the electrical coupling efficiencies of a pump load by changing the configuration of PV modules using a switching controller. Koner et al (1991) determined the switching points (cut-off irradiances) for the reconfiguration of PV modules for any centrifugal pump-series DC motor combination using an analytical solution of the PV-motor-pump system.

Koner (1995) studied three different optimisation techniques for a PV driven centrifugal pump-series dc motor system. The three optimisation techniques studied are (i) optimised motor constant (ii) reconfiguration of PV modules and (iii) changing the water head. The calculation procedure for the optimum motor constant, the "cut-off" solar irradiance for the different configurations of PV modules and the "cut-off solar irradiance" for changing the water head have been studied for several systems. It is concluded that all optimisation techniques are not viable for all existing pump sets.

2.6.3 Maximising volume delivered

Another strategy for optimisation of PV-driven systems is maximising the volume delivered. The literature review with respect to this will be given in section 6.2 where the optimisation criteria for the present study are discussed.

2.7 GENERAL CONCLUSIONS

The main purpose of chapter 2 has been to review the literature available on modelling of flow rate in PV-driven systems. All of the literature discussed in this chapter is related to PV-driven water pumping applications since this practise is well established particularly in developing countries. In chapter 1, it was stated that the present study is the first quantitative study on RSB solar ventilation preheating systems. In chapter 2, another aspect of the uniqueness of the present study has been shown. The importance of the present study lies with the fact that it is the first study on modelling of PV-driven fan systems. The principles for modelling both PV-driven pumping and PV-driven fan systems are the same and so the literature review in this chapter is relevant.

The discussion in this chapter clarified that in modelling of PV-driven systems the models for the different components are treated separately. In the case of the PV module, it is not only important to be able to obtain all parameters necessary to describe the IV characteristic at a given irradiance and PV module temperature, but also to be able to adapt this characteristic to different levels. Two models for adapting the PV IV characteristic were discussed. In chapter 3, a new method will be introduced and validated and its advantages in comparison with other methods will be outlined. The procedures for measuring the IV characteristic of a PV module and those for measuring the temperature coefficients were introduced. The methods for estimating the cell

parameters in Eq. 2.4 were also reviewed. Chapter 3 introduces a new procedure for estimating the series resistance of a PV module.

Two methods for describing the motor/fan characteristics are given in the literature. In the first, the motor equations are used while in the other measured current-voltage and speed-voltage characteristics of the motor/fan as a single unit are used. The next chapter will also present two methods for describing the fan's head-flow characteristic. In the next chapter, where more than one method exists, only one will be selected for modelling. The equations for describing the system's head-flow characteristic where also presented. In the literature, the flow rate of a PV-driven system was expressed as a function of irradiance. This approach, however, is specific and does not account for the PV module temperature or the duct properties effectively.

A review of modelling of slope irradiance from horizontal data was also given. In order to obtain slope irradiance, both horizontal global and diffuse data are required. The method for estimating diffuse irradiance from global irradiance was also reviewed. In the current chapter, the isotropic model for predicting slope irradiance was presented. However, in chapter 5 a more general anisotropic model will be considered and results from both models will be compared.

Finally, an overview of optimisation strategies for PV-driven systems was given. For PV pumping systems, the strategy has been to optimise by either maximising efficiency or volume of water delivered. In the former case, the optimisation can be achieved by utilising the maximum power of the PV module, the mechanical power of the load, or the hydraulic power of the pumping system. More literature review on optimisation related to maximising volume delivered is given in chapter 6.

REFERENCES

Akbaba, M., and Alattawi, M.A.A., (1995), A new model for I-V characteristic of solar cell generators and its applications, Solar Energy Materials and Solar Cells, 37, pp123-132.

Akbaba, A., Qamber, I., and Kamal, A., (1998), Matching of separately excited DC motors to photovoltaic generators for maximum power output, Solar Energy, 63, pp375-385.

Akbaba, M., (2003), Matching three-phase AC loads to PVG for maximum power transfer using an enhanced version of the Akbaba model and double step-up converter, Solar Energy, 75, pp17-25.

Alghuwainem, S.M., (1992), Steady state operation of DC motors supplied from photovoltaic generators with step up converters, IEEE Trans Energy Conv, 7(2), pp267–271.

Anis, W.R., and Metwally, H.M.B., (1994), Dynamic performance of a directly coupled PV pumping system, Solar Energy, 53, pp369-377.

Appelbaum, J., and Bany, J., (1978), Performance analysis of D.C.-motor photovoltaic conversion system-I, Solar Energy, 22:439-445.

Appelbaum, J., (1981), Performance Analysis of DC motors-Photovoltaic Converter System-II, Series and shunt excited motors, Solar Energy, 27, pp421-431.

Berman, D., Biryukov, S., and Faiman, D., (1995), EVA laminate browning after 5 years in a grid-connected, mirror-assisted, photovoltaic system in the Negev desert: effect on module efficiency, Solar Energy Materials and Solar Cells, 36, pp421-432.

Berman, D., Faiman, D., and Farhi, B., (1999), Sinusoidal spectral correction for high precision outdoor module characterization, Solar Energy Materials and Solar Cells, 58, pp253-264.

Benlarbi, K., Mokrani, L, and Nait-Said, MS., (2004), A fuzzy global efficiency optimisation of a photovoltaic water pumping system, Solar Energy, 77, pp203-216.

Betka, A., and Moussi, A., (2004), Performance optimization of a photovoltaic induction motor pumping system, Renewable Energy, 29(14), pp2167-2181

Bione, J., Vilela, O.C., and Fraidenraich, N., (2004), Comparison of the performance of PV water pumping systems driven by fixed, tracking and V-trough generators, Solar Energy, 76, pp703-711.

Buresch, M., (1983), Photovoltaic Energy Systems, Design and Installation, New York, McGraw-Hill Book Company.

Chamberlin, C.E., Lehman, P., Zoellick, J., and Pauletto, G., (1995), Effects of mismatch losses in photovoltaic arrays, Solar Energy, 54, pp165-171.

Coulson, K.L., (1975), Solar and Terrestrial Radiation: Methods and Measurements, New York, Academic Press.

Cromer, C., (1983), Sizing and matching a photovoltaic circulation system with a solar domestic hot water system, FSEC-PF-29-83, Florida Solar Energy Center, Cocoa, Florida.

Davis, M.W., Fanney, A.H., and Dougherty, B.P., (2001), Prediction of building integrated photovoltaic cell temperatures, Journal of Solar Energy Engineering, 123(3), pp200-210.

Duffie, J.A., and Beckman, W.A., (1991), Solar Engineering of Thermal Processes, 2nd edn, New York, Wiley Interscience.

Durisch, W., Tille, D., Worz, A., and Plapp, W., (2000), Characterisation of photovoltaic generators, Applied Energy, 65, pp273-284.

Dyk, E.E., and Meyer, E.L., (2004), Analysis of the Effect of Parasitic resistances on the performance of Photovoltaic Modules, Renewable Energy, 29, pp333-344.

Dyk, E.E., Meyer, E.L., Vorster, F.J., and Leitch, A.W.R., (2002), long-term monitoring of photovoltaic devices, Renewable Energy, 25, pp183-197.

Eckstein, J., Townsend, T., Beckman, W.A., and Duffie, J.A., (1990), Photovoltaic powered energy systems, Proceedings of the American Solar Energy Society, Austin, Texas, USA.

Edwards, J.D., (1991), Electrical Machines and Drives : An Introduction to Principles and Characteristics, Basingstoke , Macmillan, 1991.

Erbs, D.G., Klein, A., and Duffie, J.A., (1982), Estimation of the diffuse radiation fraction for hourly, daily and monthly-average global radiation, Solar Energy, 28, p293.

Eskandar, M.N., and Zaki, A.M., (1997), A maximum efficiency photovoltaic-induction motor pump system, Renewable Energy, 10(1), pp53–60.

Faldella, E., (1989), Matching and Control techniques for optimising automatic management of photovoltaic pumping system, Workshop on materials science and Physics of Non-conventional Energy Sources, Italy.

Green, M,A., (1982), Solar Cells, Operating Principles, Technology and System Applications, New Jersey, Prentice Hall.

Gxasheka, A.R., Dyk E.E., and Meyer E.L., (2005), Evaluation of performance parameters of PV modules deployed outdoors, Renewable Energy, 30, pp611-620.

Hadi, H., Tokuda, S., and Rahardjo, S., (2003), Evaluation of performance of photovoltaic system with maximum power point (MPP), Solar Energy Materials and Solar Celsl, 75, pp673-678.

Hadj Arab, A., Chenlo, F., and Benghanem, B., (2004), Loss-f-load probability of photovoltaic water pumping systems, Solar Energy, 76, pp713-723.

Hirata, Y., and Tani, T., (1995), Output variation of photovoltaic modules with environmental factors-I The effect of spectral solar radiation on photovoltaic module output, Solar Energy, 55, pp463-468.

Hsiao R. and Blevins B., (1984), Direct coupling of photovoltaic power source to water pumping system, Solar Energy, 32, pp489-498.

Ikegami, T., Maezono, T., Nakanishi, F., Yamagata, Y., and Edihara, K., (2001), Estimation of equivalent circuit parameters of PV module and its application to optimal operation of PV system, Solar Energy Materials and Solar Cells, 67(1-4), pp389-395.

Jacobson, A., Kammen, D.M., Duke, R., and Hankins, M., (2000), Field performance measurements of amorphous silicon photovoltaic modules in Kenya. Conference Proceedings, American Solar Energy Society (ASES), Madison, Wisconsin, USA, June 16-21, 2000.

Jafar, M., (2000), A model for small-scale photovoltaic solar water pumping, Renewable Energy, 19, pp85-90.

King, D.L, and Kratochvil, J.A., (1997), temperature coefficients for PV modules and arrays: measurement methods, difficulties and results, 26th IEEE Photovoltaic Specialists Conference, September 29-October 3, 1997, Anaheim, California.

Kolhe, M., Kolhe, S., and Joshi, J., (2000), Determination of magnetic field constant of DC permanent magnet motor powered by photovoltaic for maximum mechanical energy output, Renewable energy, 21, pp563-571.

Koner, P.K., Joshi, J.C., and Chopra, K.L., (1991), Optimisation study of a pumping load by different configurations of photovoltaic modules, ISES Solar World Congress 1991, Denver, CO.

Koner, P.K., (1995), Optimisation techniques for a photovoltaic water pumping system, Renewable Energy, 6, pp53-62.

Langridge, D., Lawrance, W., and Wichert, B., (1996), Development of a Photovoltaic Pumping System Using a Brushless D.C. Motor and a Helical Rotor Pump, Solar Energy, 56(2), pp151-160.

Lawrence, W.B., Wichert, B., (1994), A versatile PV module simulation model based on PSI/e, Solar Energy, 52, pp93-109.

Mallick, T.K., Eames, P.C., Hyde, T.J., and Norton, B., (2004), The design and experimental characterisation of an asymmetric compound parabolic photovoltaic concentrator for building façade integration in the UK, Solar Energy, 77, pp319-327.

Markvart, T., (2000), Solar Electricity, 2nd edn, New York, John Wiley & Sons LTD.

Menicucci, D., (1986), Photovoltaic array performance simulation models, Solar Energy material and Solar Cells 1986, 18, pp383-392.

Meyer, C.J., and Kroger, D.G., (1998), Plenum chamber flow losses in forced draught air-cooled heat exchangers, Applied Thermal Engineering, 18, pp875-93.

Moussi, A., Betka, A., and Azoui, B., (1985), Optimised photovoltaic pumping system, Proceedings of the IEEE photovoltaic specialists conference, 1985, Kanematsu, pp1626-1631.

Moussi, A., Betka, A., and Azoui, B., (1999), Optimum design of photovoltaic pumping systems, In: Proceedings of the 34th Universities Power Engineering Conference, September 14-16, Leicester, UK, 1999.

Muneer, T., Hawas, M.M., and Sahili, K., (1984), Correlation between hourly diffuse and global radiation for New Delhi, Energy Conversion and Management, 24, pp265-267.

Muneer, T., Abodahab, N., Weir, G., and Kubie, J., (2000), Windows in Buildings, Architectural Press, Oxford.

Muneer, T., and Fairooz, F., (2002), Quality control of solar radiation and sunshime measurements-lessons learnt from processing worldwide databases, Building Services Engineering Research & Technology, 23, 151-166.

Muneer, T., Zhang, X., and Wood, J., (2002), Evaluation of an innovative sensor for measuring global and diffuse irradiance, and sunshine duration, Int. J. of Solar Energy, 22, pp115-122.

Muneer, T., (2004), Solar radiation and Daylight models, Elsevier, Oxford.

Newborough, L., (1990), Electronically commutated direct-current motor for driving tube-axial fans: A cost effective design, Applied Energy, 36, pp167-190.

Nishioka, K., Hatayama, T., Uraoka, Y., Fuyuki, T., Hagihara, R., and Watanabe, M., (2003), Field Test Analysis of PV System Output Characteristics Focusing on Module Temperature, Solar Energy Materials and Solar Cells, 75(3-4), pp665-671.

Orgill, J.F., and Hollands, K.G.T., (1977), Correlation equation for hourly diffuse radiation on a horizontal surface, Solar Energy, 19, p357.

Osborne, W.C., (1977), Fans, 2nd edition, Oxford, Pergamon.

Parretta, A., Sarno, A., and Vicari, L., (1998), Effects of solar radiation conditions on the outdoor performance of photovoltaic modules, Optics Communications, 153, pp153-163.

Perry, R.H., and Green D.W., (1997), Perry's Chemical Engineers' Handbook, 7th ed., New York, McGraw-Hill.

Rauschenbach, H.S., (1980), Solar Cell Array Design Handbook, New York: Van Nostrand Reinhold Company.

Reindl, D.T., Beckman, W.A., and Duffie, J.A., (1990), Diffuse fraction correlations, Solar Energy, 45, p1.

Roger, J.A., (1979), Theory of the direct coupling between D.C motors and photovoltaic solar arrays, Solar Energy, 23, pp193-198.

Saied, M.M., (1988), Matching of DC motors to photovoltaic generator for maximum gross mechanical energy, IEEE Trans. On Energy Conversion, EC-3(3), pp.465-472.

Saied, M.M., and Jabori, M.G., (1989), Optimal solar array configuration and DC motor field parameters for maximum annual output mechanical energy, IEEE Trans. Energy Convers. 4, 449-465.

Salameh, Z., and Liang, C., (1990), Optimum switching points for array reconfiguration controller, 21st IEEE Photovoltaic Conference, Kissimmee, FL, 1990.

Say, M.G., and Taylor, E.O., (1980), Direct Current Machines. London: Pitman Publishing Limited.

Singer, S., and Applebaum, J., (1993), Starting characteristics of direct current motors powered by solar cells. IEEE Transactions on Energy Conversion, 8, pp47-52.

Singh, B., Swamy, C.L.P., and Singh, B.P., (1998), Analysis and development of a low-cost permanent magnet brushless DC motor drive for PV-array fed water pumping system, Solar Energy Materials and Solar Cells, 51, pp55-67.

Swamy, C.L.P., Singh, B., and Singh, B.P., (1995), Dynamic performance of a permanent magnet brushless DC motor powered by a PV array for water pumping, Solar Energy Materials and Solar Cells, 36, pp 187:200.

Townsend, T.U., (1989), A method for estimating the long-term performance of direct-coupled photovoltaic systems, M.S. Thesis, University of Wisconsin-Madison.

Wood, J., Muneer, T., and Kubie, J., (2003), Evaluation of a new photodiode sensor for measuring global and diffuse irradiance, and sunshine duration, Journal of Solar Energy Engineering, 125, pp1-6.

Zaki, A.M., and Eskandar, M.N., (1996), Matching of photovoltaic motor-pump systems for maximum efficiency operation, Renewable Energy, 7(3), pp279-288.

Zinger, Z., and Braunstein, A., (1981), Optimum operation of a combined system of a solar cell array and a DC motor, IEEE Trans. On Power Apparatus and Systems, PAS-100(3), pp1193-1197.

3. SYSTEM SIMULATION

3.1 INTRODUCTION

As discussed in chapter 1, the optimisation of the PV-driven RSB system requires developing a model for predicting the flow rate of air. It was concluded in chapter 1 that the current research is unique because it is the first quantitative study on the newly developed PV-driven RSB solar ventilation preheating system. Chapter 2 presented a review of relevant previous work in respect of modelling and optimisation of PV systems. The present optimisation study is intended to improve the performance of PV-driven RSB systems and study their value as solar air heaters. More importantly, however, the current research is unique because, as can be seen from the literature review in chapter 2, all research on modelling of flow rate and optimisation of PV systems is related to water pumping applications. Here, a model for a system that consists of a PV module and a fan-duct system is to be developed. The present chapter, which goes in parallel with chapter 2, focuses on developing the mathematical model for the system and on the experimental methodology undertaken for building this model. Chapter 4 presents the computer algorithms associated with predicting the fan operational point and the flow rate in the system. The model is then experimentally validated by comparing computer simulations to flow rate measurements in a roof section constructed at Napier University.

Chapter 2 introduced the equations governing the performance of each of the components comprising the system. As was mentioned in section 2.4, in order to estimate the flow rate in the system, these equations must be solved simultaneously. These equations, however, contain parameters that are component specific and thus they must be obtained either from manufacturer's data or experimentally. The main objective of the current chapter is to present and evaluate the parameters necessary for estimating the performance of each of the components. The equations in chapter 2 are extended and manipulated and the mathematical model for the system is presented. In cases where several methods for describing the performance of each of the components are available, the selection of one of these methods is justified.

A new method for modelling the PV characteristic is introduced and validated. Two methods for describing the motor/fan performance were presented in chapter 2. In

the present chapter, the method based on dealing with the motor/fan as a single unit (i.e. using fan IV and ωV characteristics) is considered for modelling. A general discussion of the quantities measured and the instruments used is given in section 3.3. Since the development of the model is based on measurement of performance of each of the components, the predicted flow rates will be associated with error. This error is a result of operational and instrumental errors. The error analysis methodology undertaken for this work is discussed in section 3.3.

Sections 3.4 through 3.6 outline the experimental measurements undertaken to estimate the key parameters for each of the components. In these sections, the analysis of data and the validation of the individual models for each of the components are also presented and discussed.

3.2 MATHEMATICAL MODEL

The key feature of the present mathematical model is that it is based on three sets of reference measurements from which the component characteristics at any set of conditions are derived. The reference data include the following

1. data from which the PV IV characteristic at any sets of conditions can be derived,
2. data from which the fan ΔP-Q characteristic at any conditions of speed and air temperature can be derived.
3. and data from which the system's ΔP-Q characteristic for any duct specifications (i.e. length, diameter and roughness) can be derived.

This approach is very effective because it generalises the model, broadens its application, and minimises the experimental effort required to build the model. The problem of modelling flow rate in the system is reduced to the task of evaluating several component parameters.

In the case of the PV model, a new procedure for correcting the reference parameters is presented in this section and validated in section 3.4. A new method for estimating the series resistance from reference measurements is also given. For modelling the electrical characteristics of the motor/fan combination, the method

considered here is based on measured IV and ωV characteristics of the motor/fan combination. This approach is considered because it reduces the number of equations to be solved simultaneously. Furthermore, the current section presents methods for expressing ΔP_f as an analytical function of Q at reference conditions. The procedure for updating this function for different fan speeds and air densities is also discussed. Finally, the present section outlines three methods for obtaining the fan/duct system ΔP-Q characteristic from reference conditions. Each of these methods requires the estimation of certain parameters. These methods are compared in section 3.6.

3.2.1 A reference PV IV characteristic

As discussed in section 1.4, the environmental factors of irradiance, ambient temperature and wind speed affect the performance of the PV module. The output of the PV module is described by Eq. 2.4, which can be rewritten in an explicit form as follows;

$$V = A \ln\left(\frac{I_G - I + I_0}{I_0}\right) - I R_s \qquad (3.1)$$

At any irradiance and PV module temperature, the parameters A, I_G, I_0 and R_s can be determined by NLR as discussed in section 2.2.4. Alternatively, equations of I_G, A and I_0 in terms of the measurable quantities I_{SC}, V_{OC}, V_m and I_m in addition to R_S can be easily obtained as shown below.

It is usually assumed that the light generated current, I_G, is equal to the short circuit current I_{SC}, as explained by Green (1982) and Akbaba and Alattawi (1995)

$$I_G = I_{SC} \qquad (3.2)$$

At open-circuit conditions, V = V_{OC} and I = 0, and since I_0 is very small compared to $(I_G - I)$, the following equation can be derived from Eq. 3.1 (Eckstein et al 1990)

$$I_0 = I_{SC}\, e^{-\frac{V_{OC}}{A}} \qquad (3.3)$$

where I_{SC} has been substituted for I_G (Eq. 3.2).

The measured pair at maximum power (V_m, I_m) can be substituted in Eq. 3.1 along with I_0 from Eq. 3.3 and I_G from Eq. 3.2. Again, since I_0 is very small compared to $(I_G - I)$, the following equation of A, the curve fitting parameter, as a function of measurable quantities, is obtained (Duffie and Beckman, 1991)

$$A = \frac{V_m - V_{OC} + I_m R_s}{\ln\left(1 - \frac{I_m}{I_{SC}}\right)} \tag{3.4}$$

If R_S is known, Eq. 3.2 to 3.4 can be used to calculate I_G, A and I_0 based on a measured IV curve. Consequently, Eq. 3.1 can now be used to construct the IV curve for the measured (V, I) data at reference conditions (i.e. G_{ref} and $T_{mod, ref}$).

A single set of (V, I) measurements at known reference conditions (not necessarily manufacturer's data) is satisfactory to fully describe the performance of the PV module. This measured characteristic can be used to determine R_S (amongst other parameters) using NLR and most importantly it serves as a reference from which any other IV curve for the same PV module is derived as will be discussed in section 3.2.2.

3.2.2 A new method for adapting the PV IV characteristic

As discussed in section 2.2.6, in order to adapt the IV characteristic to different levels of irradiance and PV module temperature, researchers usually express the parameters in Eq. 2.4 in terms of irradiance and module temperature. In the SANDSTROM model, (Buresch, 1983), (V, I) data points are corrected for individually. In the method by Townsend (1989), the corrections are carried out for the cell parameters in Eq. 2.4 as shown in Eq. 2.10. The disadvantages associated with each of the two methods are discussed in section 2.2.7. The current work considers a new approach for correcting the PV IV characteristic. The most important feature of this method is that it provides a simple and direct means for estimating P_m from irradiance and module temperature.

The new method can be summarised as follows. At any values of G and T_{mod}, the measured parameters of I_{SC}, V_{OC}, P_m, V_m and I_m are corrected from reference measurements. The parameters A, I_G, and I_0 are then determined in terms of the corrected values at the new conditions (of G and T_{mod}) using Eqs 3.2 to 3.4. Consequently, the IV characteristic at new conditions is constructed. The series resistance can be determined at reference conditions and assumed constant as discussed in section 2.2.5.4.

The new method introduces equations for correcting the main features of the IV characteristic (Eq. 3.5). This approach can be useful, especially when P_m, V_m and V_{OC} are to be directly determined. The dependence of P_m on irradiance and temperature is similar to the I_{SC} dependence reported by Townsend (1989). In addition, the dependence of V_{OC} and V_m on irradiance is accounted for by the addition of a logarithmic term $C_V \ln\left(\frac{G}{G_{ref}}\right)$ where C_V can be either C_{Voc} or C_{Vm}.

$$I_{SC} = \frac{G}{G_{ref}}\left[I_{SC,ref} + \mu_{Isc}\left(T_{mod} - T_{mod,\,ref}\right)\right]$$

$$P_m = \frac{G}{G_{ref}}\left[P_{m,ref} + \mu_m\left(T_{mod} - T_{mod,\,ref}\right)\right]$$

$$V_{OC} = V_{OC,ref} + \mu_{Voc}\left(T_{mod} - T_{mod,\,ref}\right) + C_{Voc}\ln\left(\frac{G}{G_{ref}}\right)$$

$$V_m = V_{m,ref} + \mu_{Vm}\left(T_{mod} - T_{mod,\,ref}\right) + C_{Vm}\ln\left(\frac{G}{G_{ref}}\right)$$

$$I_m = \frac{P_m}{V_m} \qquad (3.5)$$

All temperature-dependent coefficients (μ) are assumed constant and are evaluated at reference conditions. μ_{Voc} and μ_{Vm} are assumed equal, Duffie and Beckman, 1991. The maximum power temperature coefficient, μ_m, can be estimated from the following expression, which is based on the assumption that, the filling factor, FF is independent of temperature.

$$\mu_m = \frac{P_{m,ref}}{I_{SC,ref} V_{OC,ref}} . \left(I_{SC,ref}\ \mu_{Voc}\ + V_{OC,ref}\ \mu_{Isc} \right) \tag{3.6}$$

where the term $\frac{P_{m,ref}}{I_{SC,ref} V_{OC,ref}}$ is the filling factor at reference conditions. The constants C_{Voc} and C_{Vm} are module-specific and can be determined from plots generated at constant temperatures for different irradiances.

As can be seen from the equations above, this new method provides a useful way for predicting P_m without having to generate the whole IV curve. This is especially useful in PV-motor matching where an optimum motor constant (K_m) is to be expressed as a function of PV module parameters. This will be discussed in detail in chapter 6 (section 6.5.4).

3.2.3 PV module temperature

For modelling purposes, the available data is usually irradiance and ambient temperature. The PV module temperature must be experimentally expressed as a function of these two parameters in order to be able to use Eq. 3.5. Considering that NOCT is known, the PV module temperature can be calculated from Eq. 2.7. For purposes of the current research, the NOCT values for the PV modules studied are not supplied by the manufacturer. A relationship between T_{mod}, T_{amb} and G, which takes account of the mounting configuration, has to be developed. The following approach is considered.

The solar energy absorbed by the PV module is converted into both thermal energy and electrical energy. The electrical energy (P_{el}) is calculated from the operational point of the load (i.e. $P_{el} = I \cdot V$). The thermal energy is dissipated by a combination of heat transfer mechanisms, which can be represented by a heat transfer coefficient U (W/C). An energy balance on the PV module can be written as;

$$\tau\alpha \cdot G' = P_{el} + U\ (T_{mod} - T_{amb}) \tag{3.7}$$

where G′ (W) is the irradiance falling on the area of the PV module (i.e. G′ = G.a), τ is the transmittance of the glass cover of the PV module, α is the fraction of solar radiation incident on the surface of the PV module that is absorbed, and η_c is the light-electricity conversion efficiency of the PV module. The term $\tau\alpha$ in Eq. 3.7 is not generally known but according to Duffie and Beckman (1991) an estimate of 0.9 can be used for a single cover collector. Using measurements of T_{mod}, T_{amb}, G and load current and voltage, a plot of $\left(\tau\alpha \cdot G' - P_{el}\right)$ vs. $(T_{mod} - T_{amb})$ should give a straight line with the coefficient, U, as the slope.

The loss coefficient U includes losses by the different mechanisms from top and bottom of the module to the ambient. For a given configuration and wind speed and assuming a constant value of U, the PV module temperature can be calculated from Eq. 3.8, which can be obtained by rearranging Eq. 3.7

$$T_{mod} = T_{amb} + \frac{\tau\alpha}{U} \cdot G' \cdot \left(1 - \frac{\eta_c}{\tau\alpha}\right) \qquad (3.8)$$

The value of U is a function of ws and so Eq. 3.8 is valid for the wind speed at which U was determined. In order to use Eq. 3.8 at a different value of (ws), the loss coefficient must be corrected as discussed in chapter 6 (section 6.3.1.1). Alternatively, an average value of U can be determined if the collected measurements are obtained for a range of wind speeds.

3.2.4 Fan characteristics

As discussed in section 2.4.1, the first stage in modelling a PV system is to solve for the operational voltage and speed of the PV-coupled motor. This necessitates solving Eq. 2.11, 2.12 and 2.15 given in section 2.3.1 and 2.4.2 simultaneously with Eq. 3.1. By treating the motor/fan as a single unit (i.e. black box), the input is taken as the voltage supplied by the PV module and the output is the speed of the fan. This is achieved by making use of the measured IV and ωV characteristics of the fan as discussed in the next section. By determining the speed of the fan, the ΔP_f-Q characteristic can be determined.

3.2.4.1 Fan IV and ωV characteristics

The motor/fan's IV and ωV characteristics are both linear as shown by the equations below

$$I = A_v V + B_v \tag{3.9}$$

$$\omega = A_\omega V + B_\omega \tag{3.10}$$

If measurements of V, ω, and I are available, then constants A_v, B_v, A_ω, and B_ω can be evaluated from the slopes and Y-intercepts of the IV and ωV characteristics respectively. This approach of describing the motor/load characteristics simplifies the problem and reduces the number of equations to be solved simultaneously with the PV IV characteristic.

3.2.4.2 Fan ΔP-Q characteristic

As discussed in section 2.4.3, the fan ΔP_f-Q characteristic is significantly dependent on the fan's rotational speed and to a lesser extent on the air temperature. While the relationship between ΔP_f and Q for a centrifugal fluid moving device is quadratic, as shown by Fig. 2.8, that for an axial flow fan is not, specially because of the dip in the curve, as shown in Fig. 2.9. Manufacturer's data on axial flow fans is usually in the form of ΔP_f-Q curves. For modelling purposes, ΔP_f must be expressed analytically as a function of Q. Two different approaches were considered for describing the ΔP_f-Q performance characteristic of the axial flow fans under investigation.

In order to simplify the ΔP_f-Q relationship of an axial flow fan, the curve can be segmented into three straight lines as shown in Fig. 3.1. The slope and intercept of each of these line segments, as well as the limiting flow rates Q_1 and Q_2, are functions of speed. The head can be expressed as a function of speed and flow rate by the following equation:

$$\Delta P_f = S_{1,j}\,\omega^2 + S_{2,j}\,\omega\, Q + S_{3,j}\,\omega + S_{4,j}\,Q \qquad j = 1,2,3 \tag{3.11}$$

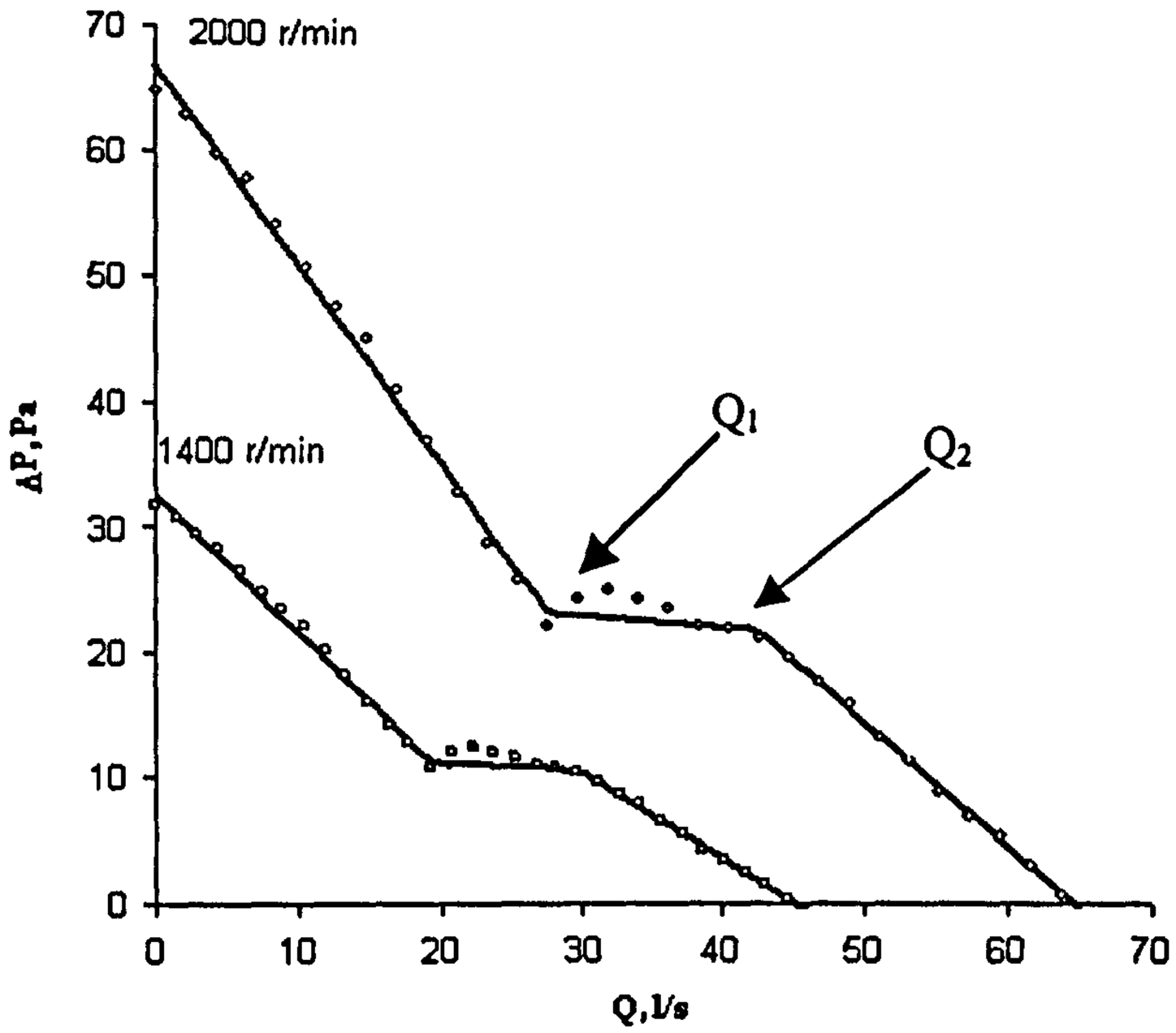

Fig. 3.1: Linear segmentation of the ΔP_f-Q characteristic.

where the S terms are constants and the "j" subscript corresponds to one of the three segments. Thus, for the lower section of the ΔP_f-Q curve, j = 3 and the constants $S_{i,3}$ (for i = 1 to 4) are used only if the flow rate Q is larger than Q_2. These constants are fan-specific and can be determined using the affinity laws by generating several curves at different motor speeds from a single curve which can be either a measured curve or a manufacturer's curve. For a single fan, the number of parameters that need to be evaluated here is 14.

An alternative approach is to express ΔP_f as a function of Q. Measurements show that this function is of the third degree as shown by the equation

$$\Delta P_f = wQ_{ref}^3 + xQ_{ref}^2 + yQ_{ref} + z \tag{3.12}$$

where the constant w, x, y and z are fan-specific and can be determined from the reference curve. The constants w, x, y and z can be determined as functions of speed as described above for the constants $S_{i,j}$ in Eq. 3.11. Alternatively, corrections for speed can be carried out on Q_{ref} and ΔP_f using the following equations

$$Q = C_1 \left[\frac{\omega P_{bar}}{T_{air} + 273.15} \right] Q_{ref} \tag{3.13}$$

$$\Delta P_f = C_2 \left[\frac{\omega^2 P_{atm}^2}{(T_{air} + 273.15)^2} \right] \cdot \left[w Q_{ref}^3 + x Q_{ref}^2 + y Q_{ref} + z \right] \tag{3.14}$$

Determination of the constants C_1, C_2, w, x, y and z is sufficient to generate the ΔP_f-Q fan characteristic at any speed, air temperature and atmospheric pressure.

For the current thesis, this second approach is used for modeling. The advantage of this approach in comparison to the one described by Eq. 3.11 is two-fold. First, the number of parameters needed to fully describe the characteristic is reduced from 14 to 6. In addition, the effect of temperature, even though negligible, can be easily incorporated.

3.2.5 System ΔP-Q characteristic

The system characteristic, ΔP_S–Q, is solved simultaneously with the fan ΔP_f -Q characteristic to obtain the flow rate in the system as shown in Fig. 2.10. The equations necessary for defining the system ΔP-Q characteristic are given in section 2.4.4. For a given flow rate, N_{Re} is calculated and the value of "f" is iteratively determined from the Colebrook equation. With length, diameter, and density known, ΔP_s can be calculated for different flow rates. The iterative determination of "f" requires a lot of computational effort especially if the calculation is to be carried out for a large set of data. In order to save computational time, an explicit form of Eq. 2.22 is required. Muneer et al (2003) stated that the following equation produces "f" values with an accuracy of 98 % when compared to values obtained from the Colebrook equation

$$f = \frac{1.325}{\left(\ln \left(\frac{k/D}{3.7} \right) + \frac{5.74}{N_{Re}^{0.9}} \right)^2} \tag{3.15}$$

For the RSB system described in section 1.4, and due to the limited space in the attic, it is convenient to use a flexible duct for delivering air. Using a flexible duct will

add to the complexity of obtaining the system characteristic. For a flexible duct, the roughness (k) is a function of extension (or compression). Thus, the ΔP_s-Q curve depends on how extended or compressed the duct is in addition to its diameter and length.

Abushakra et al. (2002) introduced a pressure drop correction factor (PDCF) for flexible ducts as a linear function of compression ratio. This factor is defined as the ratio between two pressure drops for two different extensions of the same length of duct. This method, however, is only useful for pressure loss determination and not for generating the ΔP_s-Q at a given extension.

If reference data of ΔP_s and Q are measured at some reference duct and air properties, several methods can be used to determine the ΔP_s-Q curve at different properties as shown in Fig. 3.2. These methods require that the new curve be derived from the reference ΔP_s-Q at the same duct extension. In method 1A, a relationship between the friction factor and Reynolds number can be developed based on measured (Q, ΔP_s) data points for a given extension as shown by Eq. 3.16

$$f = V_1 e^{-V_2 N_{Re}} \tag{3.16}$$

where the parameters V_1 and V_2 are different for different extensions. Using Eqs 3.16 and the expression for N_{Re} in Eqs. 2.21 and 2.22, the following equation can be derived

$$\Delta P_s = \frac{8 V_1 \rho L}{\pi^2 D^5} e^{-\frac{4 V_2 \rho}{\pi \mu D} Q} Q^2 \tag{3.17}$$

Looking up the values of V_1 and V_2 corresponding to the required extension and using Eq. 3.17, the ΔP_s-Q can be determined at any length and diameter of duct and density of air.

Method 1B is basically that described in section 2.4.4 except that Eq. 3.15 is used instead of Eq. 2.23. The reference data is used to determine an average value of k, the roughness coefficient, corresponding to a fixed extension. With this predetermined value, the ΔP_s-Q can be derived at any other duct length and diameter. Different curves

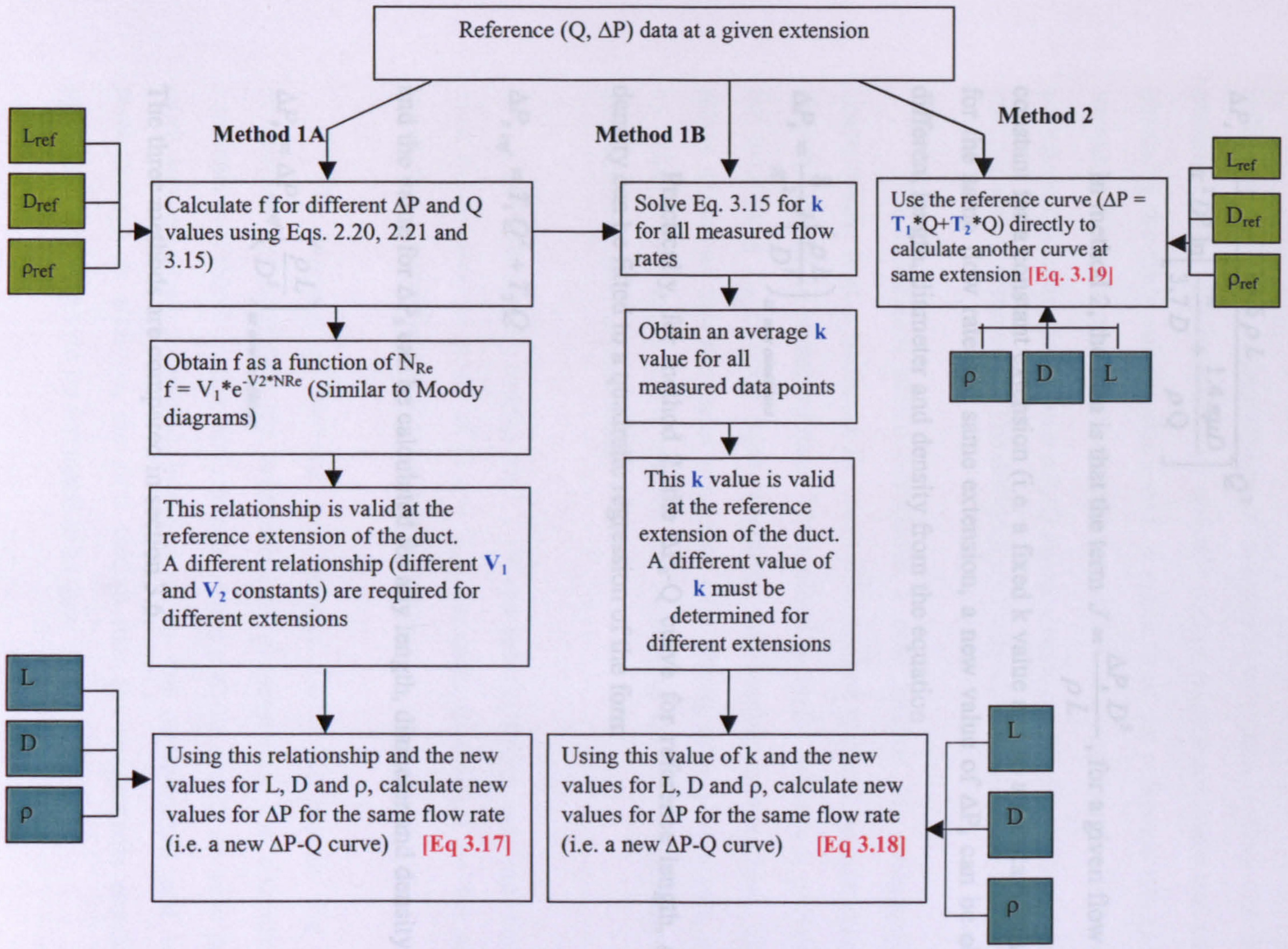

Fig. 3.2: Methods for predicting ΔP_s-Q characteristic from reference data.

can be measured and so different values of k can be determined for different duct extensions. Equation 3.15 can be used with Eqs. 2.21 and 2.22 to obtain the following equation;

$$\Delta P_s = \frac{10.6\,\rho L}{\pi^2 D^5 \ln\left[\frac{k}{3.7D} + \frac{1.4\,\pi\mu D}{\rho Q}\right]} Q^2 \tag{3.18}$$

In method 2, the idea is that the term $J = \frac{\Delta P_s D^5}{\rho L}$, for a given flow rate, remains constant for a constant extension (i.e. a fixed k value and so a constant value of f). Thus for the same flow rate and same extension, a new value of ΔP_s can be obtained for a different length, diameter and density from the equation

$$\Delta P_s = \frac{8}{\pi^2} J \left(\frac{\rho L}{D^5}\right)_{\textit{at new conditions}} \tag{3.19}$$

Practically, for method 2, the ΔP_s-Q curve for reference length, diameter and density can be fitted to a quadratic regression of the form

$$\Delta P_{s\,ref} = T_1 Q^2 + T_2 Q \tag{3.20}$$

and the value for ΔP_s can be calculated for any length, diameter and density from

$$\Delta P_s = \Delta P_{s,ref} \left(\frac{\rho L}{D^5}\right)_{\textit{at new conditions}} \tag{3.21}$$

The three methods are compared in section 3.6.

3.2.6 Summary of mathematical model

The model developed above is based on reference data. It consists of several parameters that are component specific as shown in Table 3.1. These constants can be either derived from manipulations of manufacturer's data or they can be determined experimentally. The motor/fan IV and ωV characteristics are linear and can be used for obtaining the fan's voltage and speed. A cubic fit of the reference ΔP_f-Q characteristic accounts for both speed and temperature effect and requires the determination of 6 parameters. Finally, the system ΔP_s-Q characteristic can be determined from a reference curve in one of three ways. The different methods will be compared in section 3.6.

The discussion above introduced a new method for evaluating the PV IV characteristic from a reference IV curve. The method is based on corrections, which are directly applied to measured data. The method is useful because it provides the means for evaluating P_m directly from irradiance and module temperature. The discussion above explained that the series resistance can, among other parameters, be determined by NLR. In section 3.4.2, a method for estimating the series resistance, R_S, from a measured IV curve is introduced.

In order to fully predict the PV IV characteristic from reference conditions, T_{mod} must be obtained in terms of G and T_{amb}. In order to account for the effect of wind speed, the loss coefficient, U must be evaluated.

The purpose of sections 3.4 through 3.6 is to outline the experimental procedures for measuring the reference data necessary for the determination of the constants in Table 3.1. The analysis procedures and the results are also presented. The next section gives a general introduction to the experimental and error analysis methodology. In addition, the next section lists the components considered for the optimisation process (to be discussed in chapter 6).

Table 3.1: Parameters required for the mathematical model.

Parameter	Units	Data required for determination
PV module		
U	W / C	Irradiance, temperature, current and voltage
R_s	Ω	Reference PV IV curve
μ_{Isc}	mA/C	I_{SC} and temperature
μ_{Voc}	V/C	V_{OC} and temperature
$I_{SC,ref}$	mA/C	Reference PV IV curve
$V_{OC,ref}$	V/C	Reference PV IV curve
$P_{m,ref}$	W	Reference PV IV curve
$V_{m,ref}$	V/C	Reference PV IV curve
C_{Voc}	V	Reference PV IV curve
C_{Vm}	V	Reference PV IV curve
Motor/fan		
A_v	Ω^{-1}	Post start-up IV data
B_v	A	Post start-up IV data
A_ω	rad / V.s	Post start-up ωV data
B_ω	rad / s	Post start-up ωV data
C_1	C. Pa^{-1}. $(rad/s)^{-1}$	Reference speed and temperature for ΔP-Q curve
C_2	C^2. Pa^{-2}. $(rad/s)^{-2}$	Reference speed and temperature for ΔP-Q curve
w	Pa. $(l/s)^{-3}$	Reference ΔP-Q curve
x	Pa. $(l/s)^{-2}$	Reference ΔP-Q curve
y	Pa. $(l/s)^{-1}$	Reference ΔP-Q curve
z	Pa	Reference ΔP-Q curve
Duct (Parameters necessary for all three methods of determining ΔP_s-Q. Only one method is required)		
V_1	-	ΔP and Q data at a given extension of duct
V_2	-	ΔP and Q data at a given extension of duct
k	mm	ΔP and Q data at a given extension of duct
T_1	Pa.$(l/s)^{-2}$	ΔP and Q data at a given extension of duct
T_2	Pa.$(l/s)^{-1}$	ΔP and Q data at a given extension of duct

3.3 EXPERIMENTAL METHODOLOGY

This section introduces the measurements and the instruments required in order to determine the parameters listed in Table 3.1. The instruments used and the errors associated with them are listed in Table 3.2. Determination of the constants in Table 3.1 is based on reference measurements. The reference measurements required for estimating the PV module performance are irradiance, voltage, current, and temperature. For the motor/fan combination, measurements of voltage, current, rotational speed, temperature, pressure and flow rate are required. In order to determine the parameters associated with the fan/duct system characteristic, measurements of temperature, pressure and flow rate are required. The instruments used for measuring each of these quantities and the errors associated with them are also shown in Table 3.2. Appendix A lists the description and serial numbers of the instruments used for the current work. The following discussion briefly describes each of these instruments.

3.3.1 Irradiance

As discussed in section 2.5.3, pyranometers are the typical instrument for measuring global irradiance. Unless associated with a value of irradiance, a PV IV curve is meaningless. Furthermore, as discussed above, adapting the PV IV characteristic to different levels of irradiance requires knowledge of the reference irradiance.

The errors associated with pyranometers were discussed in section 2.5.3.2. For purposes of measuring the PV performance, a Kipp and Zonen pyranometer (Fig. 3.3) with a calibration factor of 5.17×10^{-6} V m^2/ W is used. The instrument is sent back to the manufacturer for calibration on a yearly basis. As given by the manufacturer, this instrument has an accuracy of 3 %.

When measuring a PV IV curve, irradiance is measured at regular intervals to ascertain its stability. For a single IV curve, irradiance is averaged and a standard deviation is determined. Measurements are obtained in millivolts (mV) by connecting the pyranometer to a data logger. The tolerance in the voltage measurement of the data logger (± 0.05 mV) causes a ± 9.7 W/m^2 error in irradiance measurement.

Table 3.2: Quantities to be measured, instruments to be used, and instrumental errors.

	Symbol	Unit	Instrument	Error*
PV measurements				
Global irradiance	G	W/m^2	Kipp & Zonen Pyranometer	± 9.7 W/m^2
Temperature	T	C	k-type thermocouples	± 0.1 C
Voltage	V	V	Multimeter	± 0.01 V
Current	I	A	Multimeter	± 1 mA
Fan characteristics				
Voltage	V	V	Multimeter	± 0.01 V
Current	I	A	Multimeter	± 1 mA
Rotational speed	ω	rad /s	Handheld tachometer	± 1 %
Temperature	T	C	k-type thermocouples	± 0.1 C
Pressure	ΔP	Pa	Airflow development inclined manometer	± 0.86
Flow rate	Q	l/s	Manometer or ultrasonic anemometer	± 2.7 l/s
System characteristics				
Temperature	T	C	k-type thermocouples	± 0.1 C
Pressure	ΔP	Pa	Airflow development inclined manometer	± 0.86
Flow rate	Q	l/s	Manometer or ultrasonic anemometer	± 2.7 l/s

* The errors reported here are those caused by tolerance of the instruments used

3.3.2 Temperature

Temperature measurements are taken using k-type thermocouples with a tolerance of ±0.1 C. For the PV module, ambient and PV module temperature measurements are required. For modelling the ΔP_f-Q and ΔP_s-Q characteristics, however, the temperature of air in the duct is measured.

Fig. 3.3: Kipp and Zonen pyranometer used throughout the present research.

3.3.3 Voltage and current

In measuring the PV IV characteristic, measurements of voltage and current are taken using the two multimeters listed in Appendix A. The voltage measurement is ±0.01 V accurate while that of current is ± 1 mA accurate. Errors in the measured values of voltage and current, when combined with errors in G_{ref} and $T_{mod,\,ref}$, will cause errors in the estimated parameters in Eq. 3.5. This will then translate into errors in estimating the curve fitting parameter, A, and the diode saturation current, I_0. Thus, the measured reference IV characteristic will have an upper and a lower limit of error, and, consequently, the ΔP_f-Q characteristic will be predicted with error.

3.3.4 Rotational speed

The speed of the fan is measured using a handheld optical tachometer (Fig. 3.4) with an accuracy of 1 %. Without an associated value of rotational speed, the fan's ΔP_f-Q characteristic is meaningless. So, whenever, this characteristic is measured, the speed of the fan in addition to the temperature of the air in the duct and the atmospheric pressure must also be measured. During the measurement of the characteristic, the speed

might change so it must be measured at regular intervals and a correction must be applied according to the fan affinity laws.

Fig. 3.4: Handheld optical tachometer for measuring fan rotational speed (r/min)

3.3.5 Pressure

In order to measure the fan ΔP-Q curve, measurements of static pressure and velocity pressure (or flow rate) are required. The total pressure is equal to the sum of these two pressures. The three pressures can be measured using an inclined manometer with Pitot static tubes. The configurations for measuring each of these pressures are shown in Fig. 3.5.

The static pressure describes the difference between the inside and outside disregarding any motion in the system. It is equal to the pressure on a surface which moves with the fluid. So the pressure on a surface parallel to the direction of flow must be measured and thus the opening of the Pitot static tube (Fig. 3.5 (b) is on the side of the tube rather than at the tip (see the small openings in the tube in Fig. 3.5(b)). It is preferable to measure the static pressure as shown in Fig. 3.5 (a). However, the configuration in Fig 3.5 (b) is also acceptable, (Perry and Green, 1997). The total pressure is measured with the opening facing the flow as in Fig. 3.5(c). The velocity pressure at a location is the difference between the total and static pressure at that location as seen from Fig. 3.5(d).

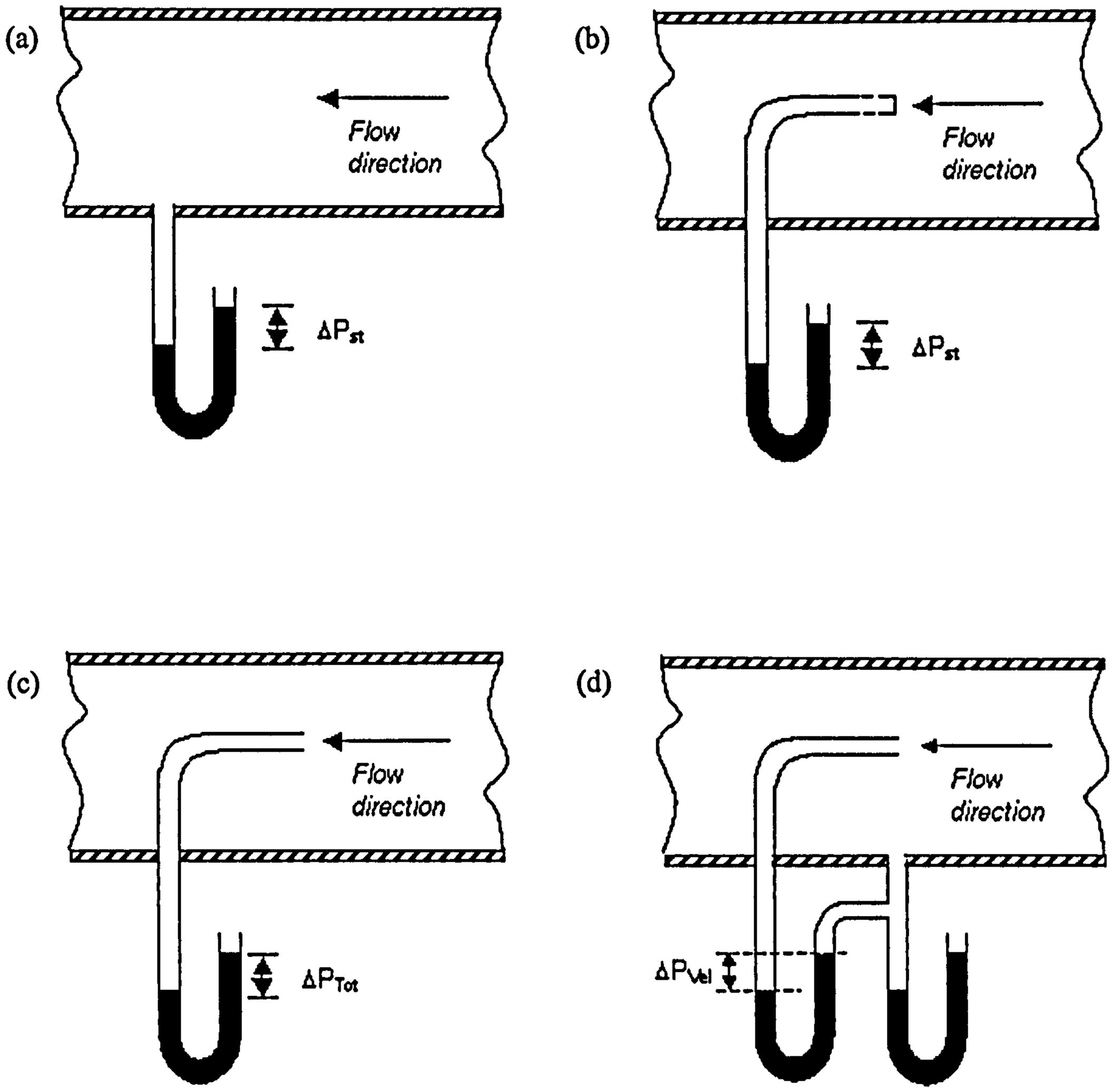

Fig. 3.5: Pitot static tube locations for measuring (a) and (b) static pressure, (c) total pressure and (d) velocity pressure.

In the current study, pressures were measured using an inclined manometer (Fig. 3.6) with a liquid which has a density of 880 kg/m^3. The manometer must be levelled off and set to zero using the knobs at the bottom. In the figure, each cm corresponds to 8.62 Pa and so the reading in the figure below is 36.20 Pa. The uncertainty in taking a pressure reading is 1mm, which corresponds to 0.86 Pa.

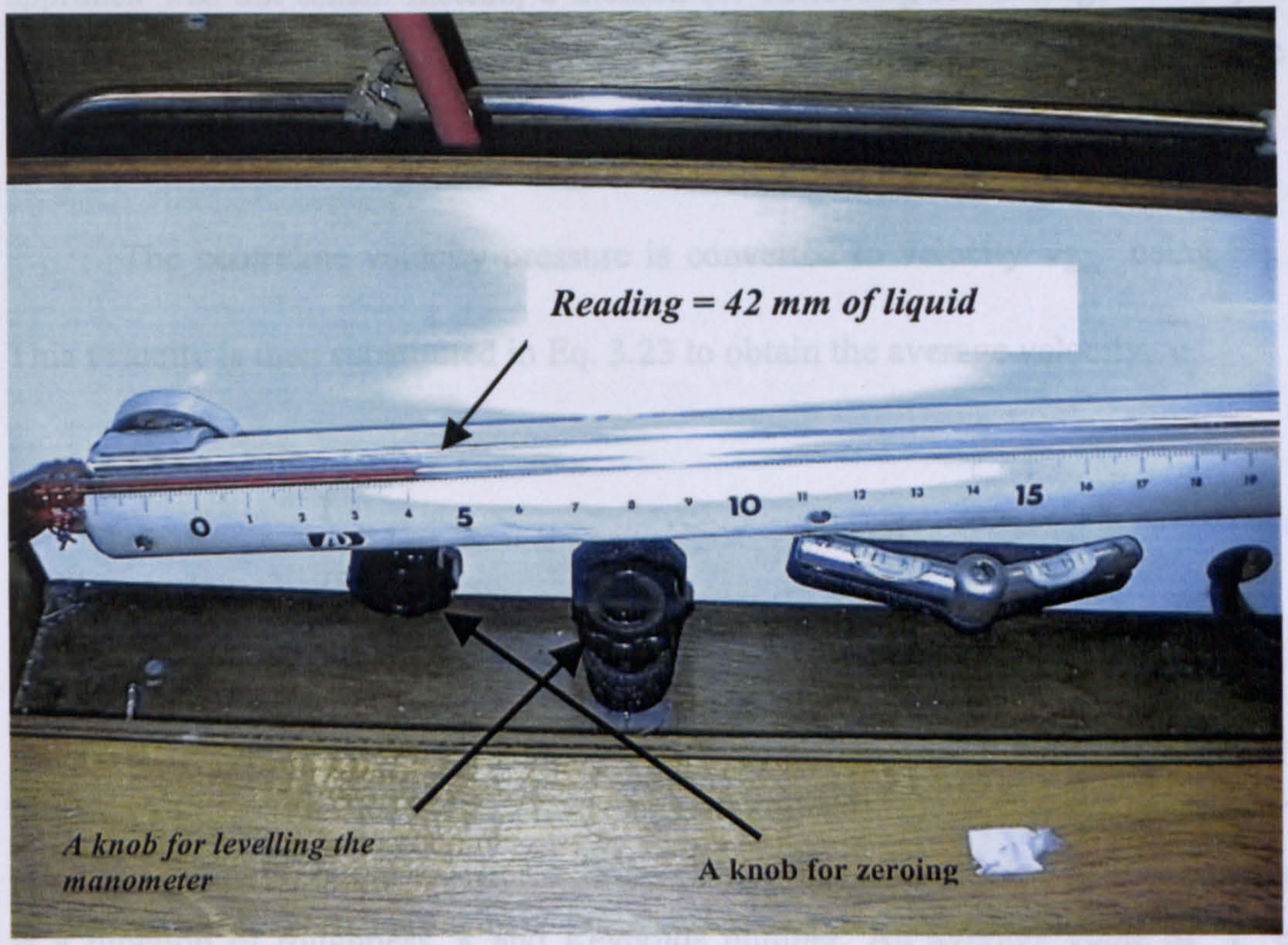

Fig. 3.6: Airflow development inclined manometer used in the present research for measuring pressure.

3.3.6 Flow rate

The velocity pressure (P_v) as measured by Fig. 3.5(d) can be translated into velocity (m/s) using the equation

$$v = \sqrt{\frac{2P_v}{\rho}} \tag{3.22}$$

where ρ is the density of air (kg/m^3).

This measurement, however, represents the local velocity at the exact location where the pressure was measured. If an average velocity is required, it is necessary to perform a Pitot traverse of the duct. This involves taking measurements at various positions across the duct at least 10 duct diameters downstream from the fan. So for each flow rate measurement, a set of at least 12 measurements at different distances

from the centreline is required. An average velocity can be determined by finding the weighted average of these measurements. In the current study, this cumbersome approach was not taken. Instead, a method for correcting for average velocity from a single measurement of maximum velocity at the centreline was adopted (McCabe et al, 1985) as discussed below.

The centreline velocity pressure is converted to velocity v_{max} using Eq. 3.22. This velocity is then substituted in Eq. 3.23 to obtain the average velocity, $\bar{v}$

$$\frac{\bar{v}}{v_{max}} = \frac{1}{1 + 3.75\sqrt{\frac{f}{2}}} \tag{3.23}$$

Equation 3.23 is valid for turbulent flow. Furthermore, it does not take account of the low velocities of the fluid layers near the wall and so it gives average velocities which are 2 % higher the actual values (McCabe et al, 1985). The friction factor, f, in Eq. 3.23 is a function of roughness, k and Reynolds number. An average value of "f" can be determined for the range of the Reynolds numbers experienced in the duct used for measurement. This will be discussed in detail in section 3.5.4.

3.3.7 Component selection

As mentioned in chapter 1, the system is to be optimised with respect to selected components. For the purposes of this research, two PV modules, three fans, and two different duct diameters were selected. The components selected are shown in Table 3.3. Combinations of PV modules and fans in parallel and in series are also considered as discussed in chapter 6 (section 6.1.3).

As explained in chapter 2, polycrystalline silicon PV modules are expected to have higher efficiencies than amorphous silicon modules. However, they are less efficient but are also less expensive than monocrystalline silicon modules. The modules used consist of 36 polycrystalline silicon cells. The modules were of small peak power (i.e. 4.5 W_p and 10 W_p) in comparison to modules used in water pumping applications since, for fan applications the energy required for moving air is much less than that required for moving water.

The fans used are BLDC motor axial flow fans, which are, as mentioned in chapter 2, most suitable for high flow rate low-pressure applications. In addition, in the present study, since the ultimate objective is ventilating the house, then it is desired to deliver air at high flow rates and so the axial flow type of fans is most suitable. Furthermore, this type of fan can be easily mounted into the ducting system and so they are well suited to the RSB solar ventilation preheating system described in chapter 1. The fans were selected based on their rated power and voltage. For example, it was initially estimated that Fan2 (see Table 3.3 for PV module and fan nomenclature) would utilise most of the energy made available by PV2 at high irradiances while Fan1 would utilise the maximum energy at low irradiances. Fan0 was chosen for comparison purposes.

The duct chosen for delivering air was Thermaflex Aliflex flexible ducting with a multiple layer aluminium/polyester laminate. In addition to having the advantage of being cheaper, flexible ducting can be easily controlled in the tight space of an attic.

The parameters in Table 3.1 are to be measured for each of the components. The optimisation of the system in Chapter 6 is based on the configurations that can arise from the different combinations. The optimisation process also considers PV modules and fans connected in parallel or series. This will be discussed in detail in chapter 6.

Table 3.3: Components considered for system optimisation (manufacturer's data).

Component	Specification
PV1	*At STC:* P_m = 4.5 W, I_{SC} = 290 mA, V_{OC} = 20.5 V, V_m = 16.5 V
PV2	*At STC:* P_m = 10 W, I_{SC} = 600 mA, V_{OC} = 21.1 V, V_m = 17.1 V
Fan0	Rating: 12 VDC/ 9.5 W with a free flow capacity of 69 l/s*
Fan1	Rating: 24 VDC/ 9.5 W with a free flow capacity of 69 l/s*
Fan2	Rating: 24 VDC/ 20.3 W with a free flow capacity of 111 l/s*
Duct1	Diameter = 102 mm, different lengths and degrees of extension
Duct2	Diameter = 152 mm, different lengths and degrees of extension

* Manufacturer's data

3.3.8 Error analysis methodology

In Table 3.2, the errors caused in each of the readings due to instrument tolerance are given. These values are used to calculate errors in the predicted values

through propagation of error. This type of calculation is difficult since some equations have to be solved iteratively. The approach taken here is to run the computer programs developed, not only for the measured values but also for their lower and upper limits. For example, for a measured irradiance of 400 W/m^2, the program is run for 391.3, 400 and 409.7 W/m^2) and the three predicted values for, say fan speed, are used to calculate error in fan speed. This requires understanding of whether a given parameter will increase or decrease the predicted values.

Throughout this thesis, whenever predicted values are compared to measurements, the calculated errors are simply a representation of how far the calculated value is from measurements. So errors are calculated as the difference divided by the measured value (see section 4.2.2 for example).

3.4 PHOTOVOLTAIC MODEL

The performance of a PV module is predicted from three sets of measurements. First, a single reference IV curve can be used to evaluate R_S and can also be a source for obtaining the reference values required in Eq. 3.5. Secondly, measurements of G, fan voltage and current and ambient and module temperatures are used to determine an average U value which can then be used to evaluate T_{mod} for any environmental conditions. Thirdly, in order to be able to use Eq. 3.5, temperature coefficients (namely μ_{Isc} and μ_{Voc}) must be determined. The coefficient μ_m can be determined from these two using Eq. 3.6.

3.4.1 Reference IV characteristic

A reference IV characteristic was measured for each of the two modules shown in Table 3.3. The two modules were placed side-by-side at 45° tilt and facing 15° East of South on the roof of Napier University in Edinburgh (Latitude 55.95 ° and longitude 3.3 °). Measurements were taken during the months of February and March of 2003.

For periods of constant irradiance, measurements of module voltage and current were recorded for different selected resistive loads. The resistance was varied manually using a high power rheostat. Two multimeters were used for current and voltage measurements. Irradiance measurements were obtained using the aforementioned Kipp and Zonen pyranometer directly connected to a data logger. Two k-type thermocouples placed in the middle at the back of each of the PV modules, as described by Berman et al (1995) were used for temperature measurements. The thermocouples were connected to the data logger from which temperature readings were obtained at the beginning and at the end of (V, I) measurement trials to ascertain the stability of the temperature throughout the measurement period.

The measured reference curves and the corresponding power-voltage curves are shown in Fig 3.7 and summarised in Table 3.4. The reference conditions for each of the modules were chosen arbitrarily. The uncertainty associated with each of the reference measurements is also shown.

(a)

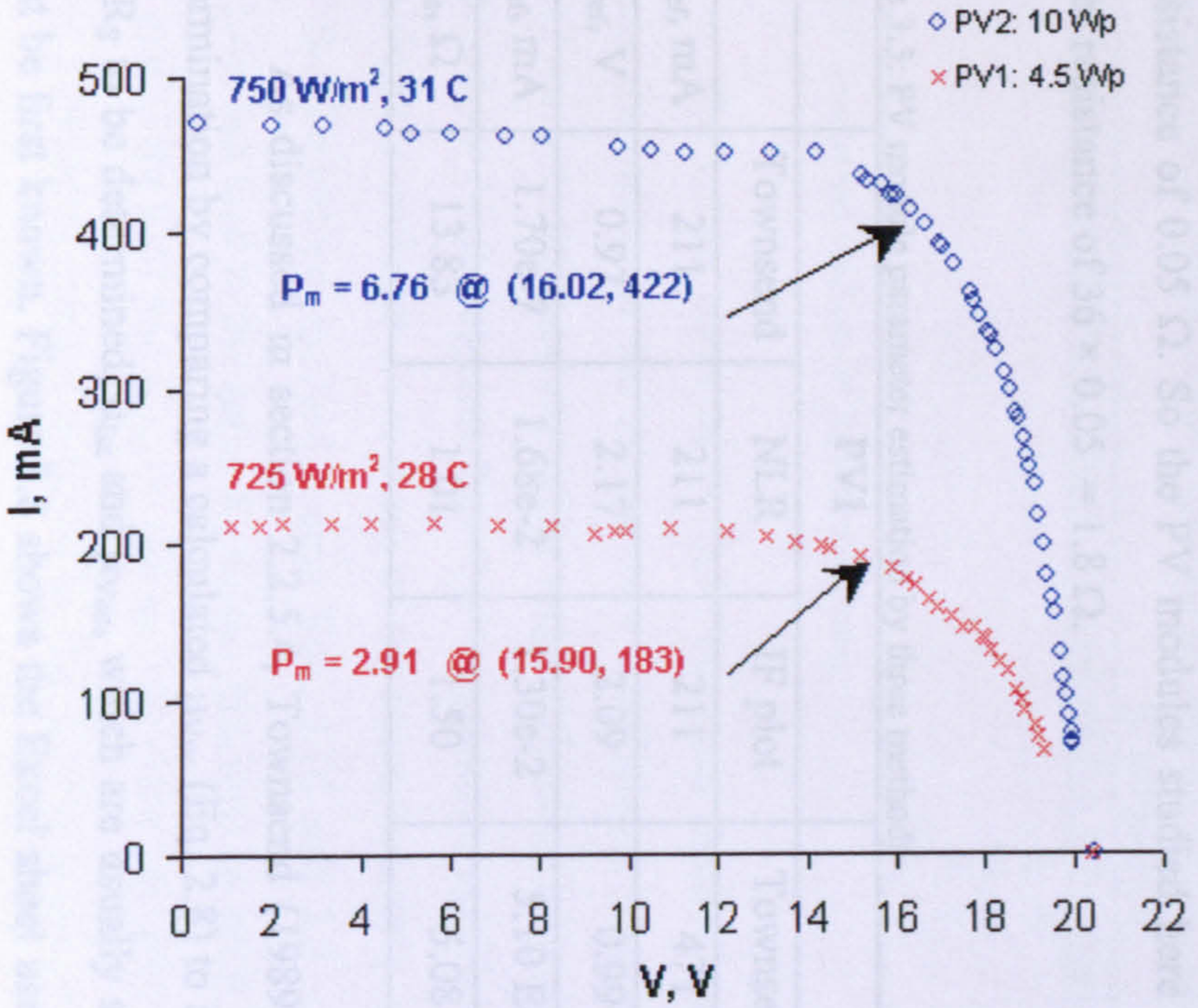

(b)

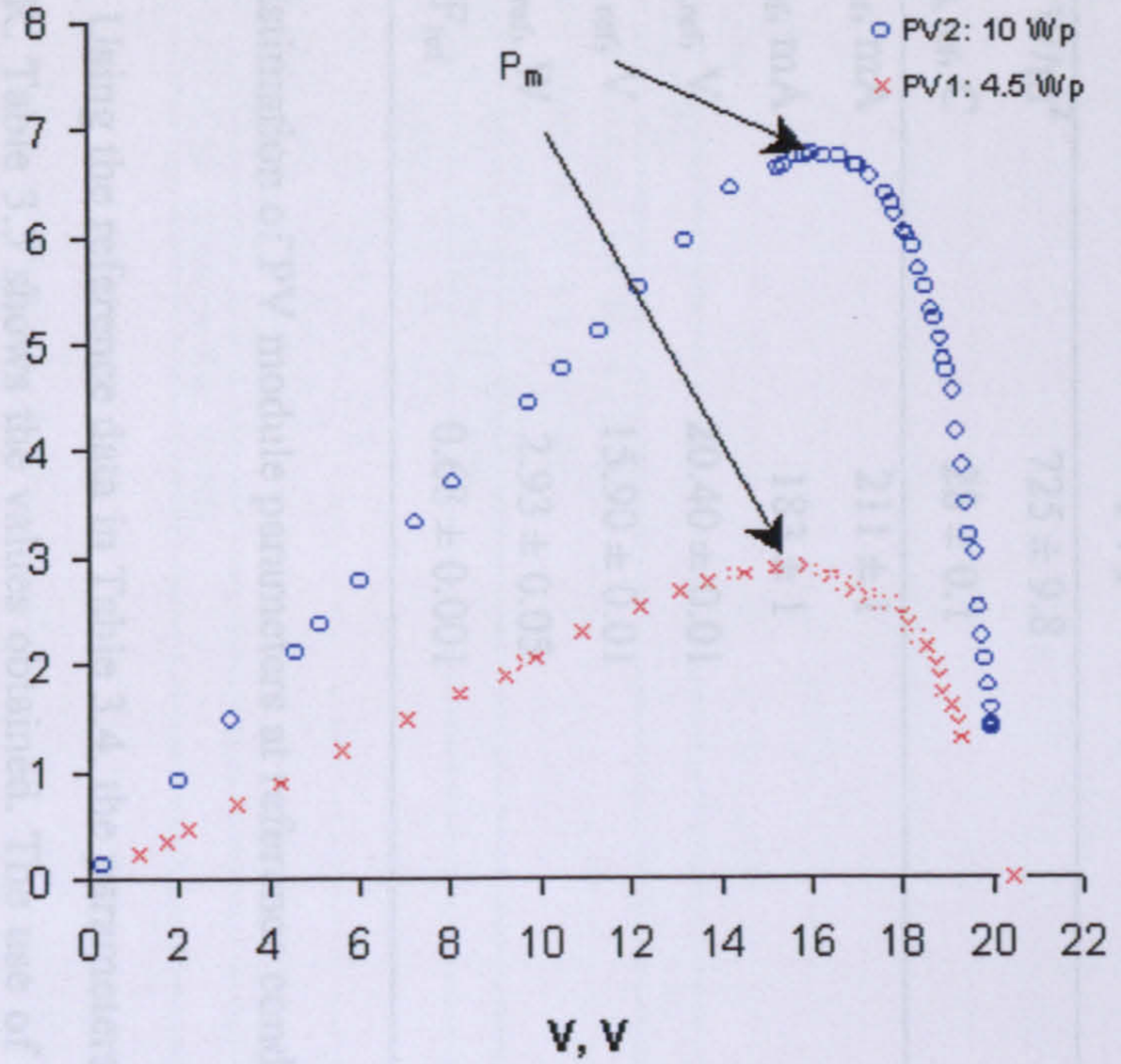

Fig. 3.7: (a) Measured reference IV curves for PV1 and PV2 and (b) corresponding measured power characteristics.

Table 3.4: reference measurements

	PV1	PV2
G_{ref}, W/m^2	725 ± 9.8	750 ± 9.8
$T_{mod, ref}$, C	28 ± 0.1	31 ± 0.1
$I_{sc, ref}$, mA	211 ± 1	471 ± 1
$I_{m, ref}$, mA	183 ± 1	422 ± 1
$V_{oc,ref}$, V	20.40 ± 0.01	20.40 ± 0.01
$V_{m, ref}$, V	15.90 ± 0.01	16.10 ± 0.01
$P_{m, ref}$, W	2.93 ± 0.05	6.76 ± 0.05
FF_{ref}	0.68 ± 0.001	0.70 ± 0.001

3.4.2 Estimation of PV module parameters at reference conditions

Using the reference data in Table 3.4, the parameters in Eq. 3.1 were determined by NLR. Table 3.5 shows the values obtained. The use of Eqs. 3.2-3.4 to evaluate the cell parameters is limited because R_S must be known in advance. The series resistance of the PV module is an immeasurable quantity but it can be determined from measurements. As reported by Green (1982), a rule of thumb is that a single PV cell has a resistance of 0.05 Ω. So the PV modules studied here are expected to both have a series resistance of $36 \times 0.05 = 1.8$ Ω.

Table 3.5: PV module parameter estimation by three methods

	PV1			PV2		
	Townsend	NLR	IF plot	Townsend	NLR	IF plot
$I_{G, ref}$, mA	211	211	211	471	471	470
A_{ref}, V	0.97	2.17	2.09	0.99	1.78	1.70
$I_{o, ref}$, mA	1.70e-7	1.68e-2	1.30e-2	5.10 E-7	4.68e-3	2.80e-3
R_s, Ω	13.83	1.01	1.50	5.08	1.00	1.20

As discussed in section 2.2.5.4, Townsend (1989) proposed a method for R_S determination by comparing a calculated μ_{Voc} (Eq. 2.8) to a measured value. So in order for R_S to be determined, μ_{Isc} and μ_{Voc}, which are usually supplied by the manufacturer, must be first known. Figure 3.8 shows the Excel sheet used for R_S determination using Townsend method and using the manufacturer's value of μ_{Voc}.

MEASUREMENTS	
$T_{mod, ref}$ (^{0}C)	31
G_{ref} (W/m^2)	750
$I_{sc, ref}$, A	0.471
$V_{oc,ref}$, V	20.4
$I_{m, ref}$, A	0.422
$V_{m, ref}$, V	16.02
μ_{Isc}, A/^{0}C	0.00039
μ_{Voc}, V/^{0}C	-0.0800
CONSTANTS	
Band-gap energy for Si, e (eV)	1.12
Electron charge, Q, (coulomb)	1.60E-19
Boltzmann's constant, k (J/K)	1.38E-23
CALCULATED PARAMETERS	
Assume a value for R_s (Ω)	5.08
Calculate I_0 (A) from Eq. 3.2	0.471
Calculate I_0 (A) from Eq. 3.3	5.10E-10
Calculate A (V) from Eq. 3.4	0.99
CORRECTION (Using Eq. 2.10)	
T_{mod}, ^{0}C	25
G, W/m^2	1000
Corrected light generated current, I_L (A)	0.625
Corrected curve fitting parameter, A (V)	0.97
Corrected diode saturation current, I_0 (A)	2.03E-10
Calculate dV_{oc} / dT and compare to measured	
Calculated temp. coefficient of V_{oc} , d V_{oc} / dT (V/^{0}C)	
Calculated μ_{Voc} (Eq. 2.8)	-0.0798
IF difference is unacceptable, change R_s and do all over again	
% Difference	0.19
Acceptable parameters (Those values which minimise difference)	
I_L, A	0.62
I0, A	2.03E-10
A, V	0.97
RS, Ω	5.08

Fig. 3.8: Townsend method for R_S determination.

The values obtained by the Townsend method are shown in Table 3.5. These values are based on the temperature coefficients supplied by the manufacturer (-80 mV/C for both PV modules). The large difference between these values and the values obtained by NLR suggests that the temperature coefficients of the PV modules are significantly different from those of the manufacturer's. By trial and error, it is found that the Townsend method (using Eqs. 2.10 and 3.2 – 3.4 as described in section 2.2.5.4), can lead to the same R_S values obtained by NLR, if a value of μ_{Voc} = -247 to -255 mV/C for PV1 and μ_{Voc} = -189 to -192 mV/C for PV2 are used. While the objective of the Townsend method outlined by Eq. 2.10 is to iteratively determine R_S, it can also serve as a method of estimating the actual temperature coefficients of the PV module if the series resistance is known by a different method such as NLR.

A new approach for determining the series resistance is suggested here. In this section, it is shown that R_S can be estimated from measured (V, I) 'data points without the need for any further measurements. For any given set of (V, I) measurements, the current I is plotted against the exponential term, $F = (e^{\frac{V + I \cdot R_s}{A}} - 1)$. As seen from Eq. 2.4, the plot is expected to be a negative-sloped straight line with a slope of I_0 and intercept of I_{SC}. A value for R_S is assumed, A is calculated from Eq. 3.4, the exponential term, F, is calculated for each point (V, I) and a plot of I vs. F is constructed. The most accurate value of R_S is that which produces a best-fit line with a coefficient of regression closest to unity. "IF" plots for both modules are shown in Fig. 3.9. Using this method, values of $R_s = 1.2\ \Omega$ for the 10 W_p module and $R_s = 1.5\ \Omega$ for the 4.5 W_p module are obtained as shown in Table 3.5. These values are compared with values obtained by NLR in Table 3.5.

This new method for the determination of R_S is useful because, if R_S is known, it can be used as a quality control tool. Data which lies far from the best-fit line can be considered as erroneous data.

The series resistance, R_S, is a weak function of temperature and it can be assumed independent of both temperature and irradiance, (Eckstein, 1990). An estimated value of R_S at reference conditions can be safely applied to describe module IV characteristics at other conditions.

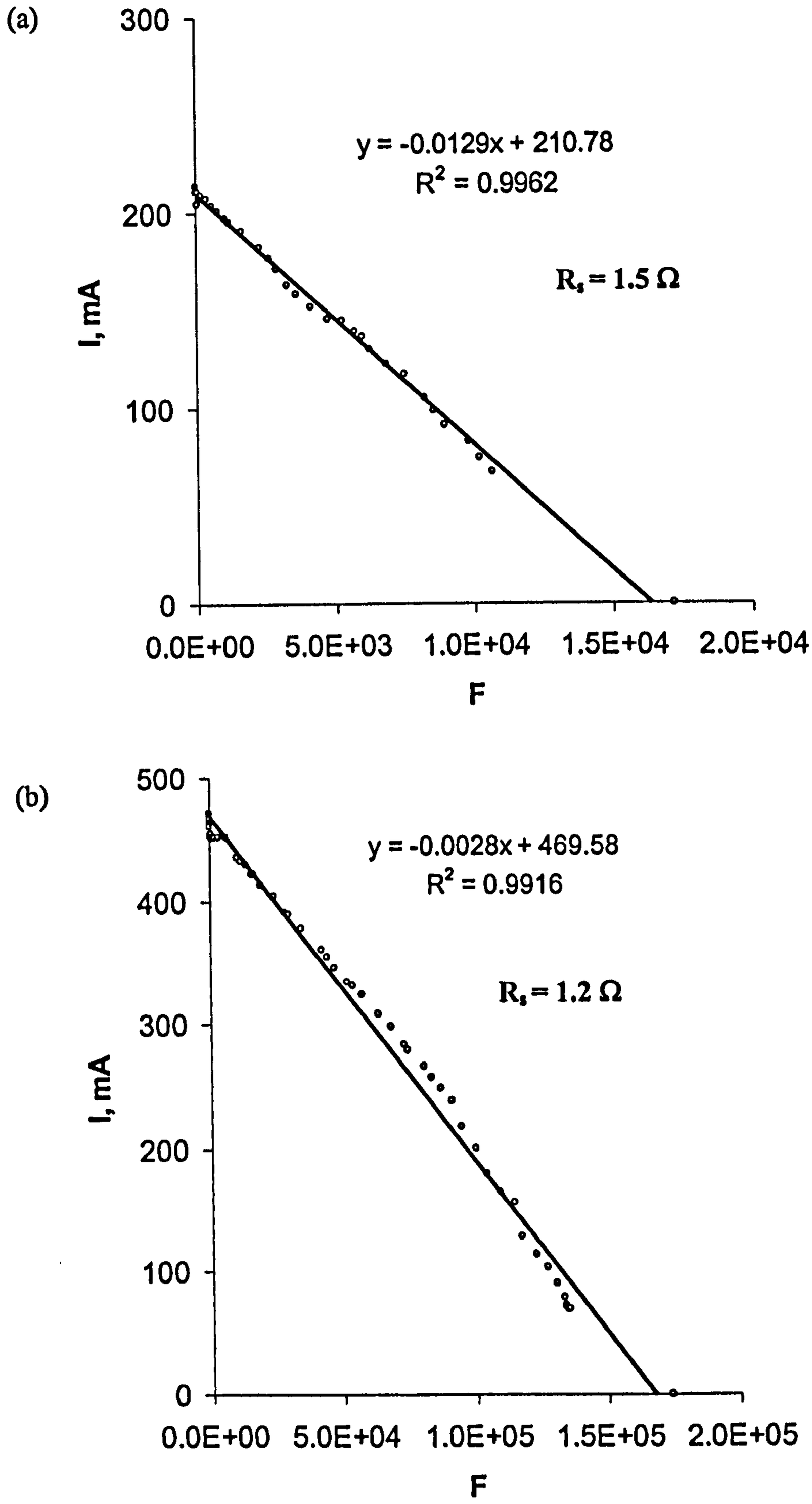

Fig. 3.9: Determination of R_S from IF plots for (a) PV1 and (b) PV2.

3.4.3 Temperature coefficients

Manufacturer's values of temperature coefficients were used for the current work (see Table 3.6). It is assumed that μ_{Vm} is equal to μ_{Voc} (Duffie and Beckman, 1991). A value of μ_{Pm} is calculated using Eq. 3.6 and based on the reference data in Table 3.4. As stated in chapter 2, temperature coefficients can be assumed constant for any conditions of irradiance and module temperature.

Table. 3.6: Temperature coefficients and U values

	PV1	PV2
μ_{Isc}, mA/C	0.19	0.39
μ_{Voc}, mV/C	-80	-80
μ_{Vm}, mV/C	-80	-80
μ_{Pm}, mW/C	-10	-22
U, W/C	1.53 ± 0.04	1.90 ± 0.04

3.4.4 Loss coefficient, U

A load (1.85 Ω resistor) was connected to each of the PV modules and measurements of T_{mod}, T_{amb}, I, V and G were obtained for the configuration described in section 3.4.1. Assuming a $\tau\alpha$ value of 0.9, plots of $\tau\alpha \cdot G' - IV$ vs. $(T_{mod} - T_{amb})$ were constructed for both PV modules as shown in Fig. 3.10. The U values for both modules with their associated errors are summarised at the bottom of Table 3.6.

These coefficients are valid for the specific configuration described here. The measurements must be repeated and U recalculated whenever the PV modules are installed at a different location. However, since in this case the back of the PV modules is covered, the configuration can be a resemblance to BIPV module configurations. In this case, the same U values can be used.

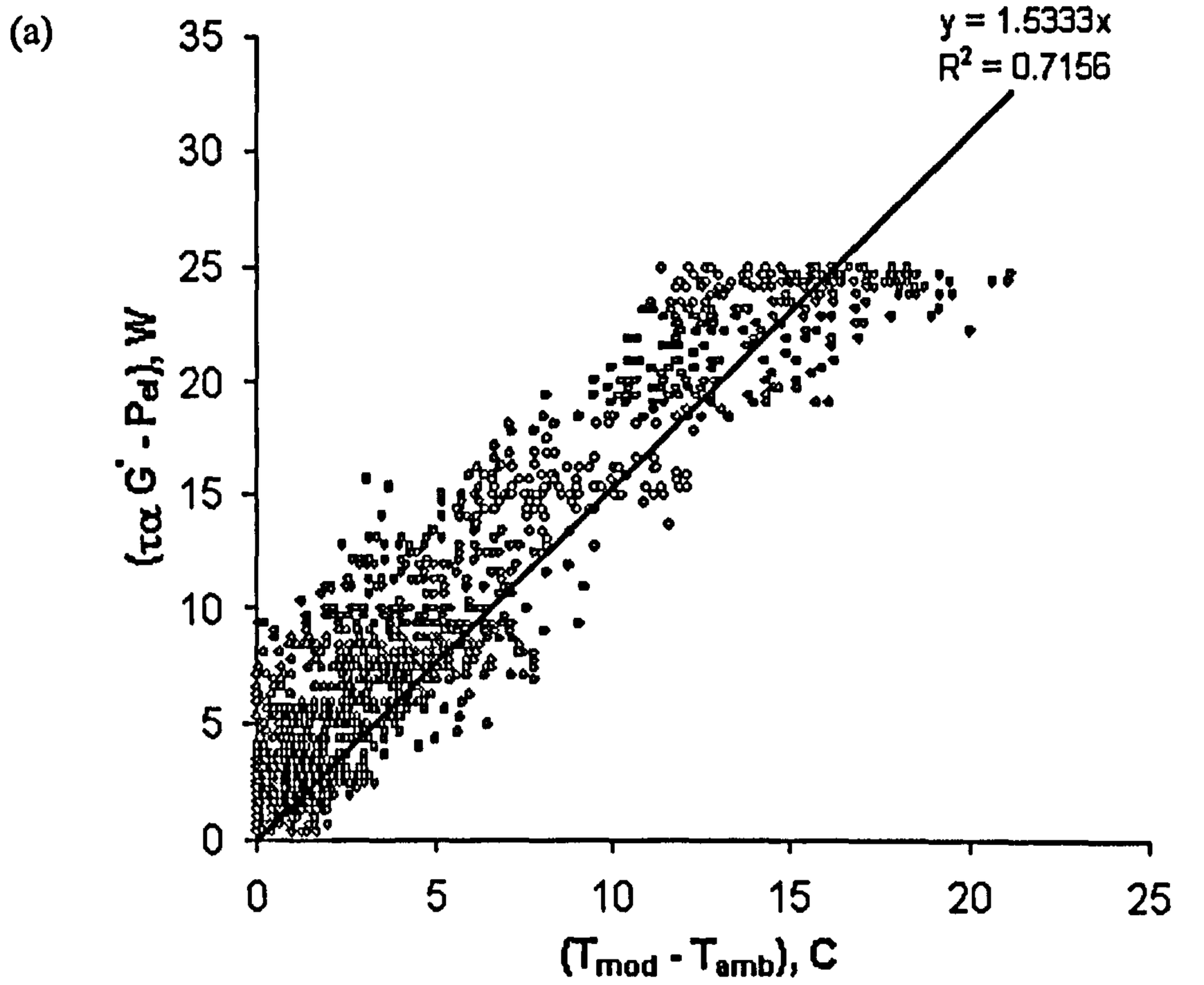

Fig. 3.10: Determination of the loss coefficient, U, for (a) PV1 and (b) PV2

3.4.5 Model validation

Using the predetermined values of R_s, U and temperature coefficients in addition to the reference values of I_{SC}, P_m, V_{OC}, V_m, the IV characteristic at any conditions of irradiance and ambient temperature can be estimated. The PV module temperature is calculated for any given T_{amb} and G values using Eq. 3.8 and the U values given in Table 3.6. This value of T_{mod} is then used with irradiance and the reference values in Table 3.4 in equation 3.5 to determine new corrected values from which a new IV curve can be generated.

In order to check the validity of this method, several IV curves were measured for both PV modules. One full set of (V, I) measurements can be obtained in approximately five minutes. For this reason, measurements were taken on relatively clear sky days so that irradiance and temperature stayed relatively constant over the 5-minute period. The stability of irradiance and temperature was verified by observation of the recorded quantities. Due to the relatively rapid acquisition of data, measurements can also be made on cloudy days with periods of stable irradiance and temperature. Results obtained from measurements on clear-sky days, however, can also be validated for overcast days because the output of the module is a function of how much radiation falls on it rather than the state of the sky (clear or overcast).

Measurements were taken around solar noon and extended to a maximum of two hours so that the beam incidence angles were less than 30^o. This allowed for measurements at several irradiance levels without the need for transmittance correction, which can be considerable for large incidence angles as explained by Duffie and Beckman (1991). During these tests, module temperatures varied from 24 C to 53 C while irradiance varied from 415 W/m^2 to 950 W/m^2. Using the reference data of G and T_{mod}, a program written in Visual Basic for Applications (VBA) was used to determine the PV IV characteristic. Figures 3.11 – 3.13 show comparisons between measured and predicted data. A program was also written in VBA for the SANDSTROM and Townsend methods for predicting the IV characteristic. Figure 3.14 shows a comparison of the curves predicted by each of the three methods at G = 1000 W/m^2 and T_{mod} = 40 C. Furthermore, Table 3.7 shows the predicted values of I_{SC}, I_m, V_{OC}, V_m and P_m for PV2 as calculated by the different methods described in chapter 2.

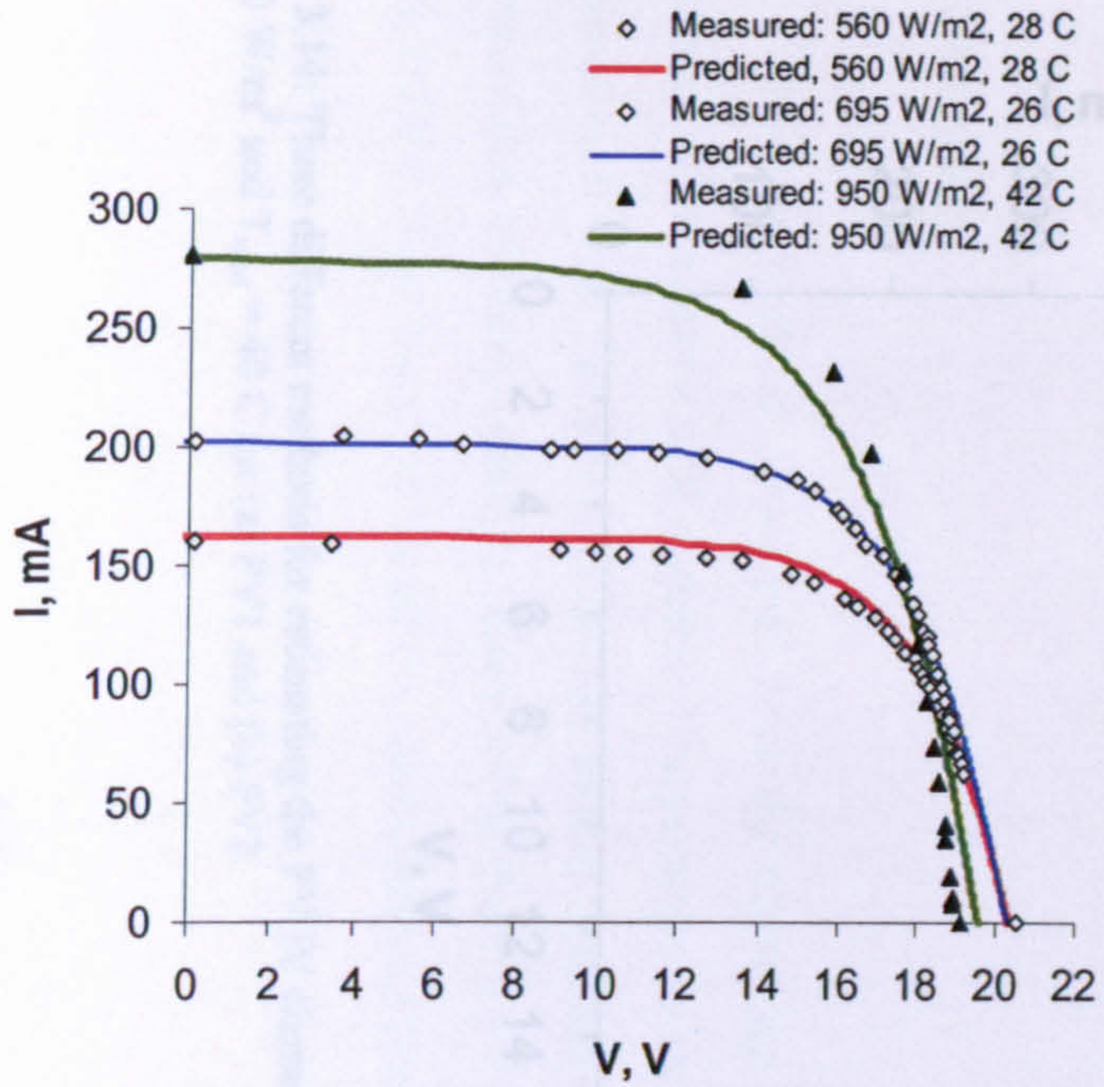

Fig. 3.11: Measurements and predicted IV curves (according to the new method) for PV1 at different conditions of G and T_{mod}.

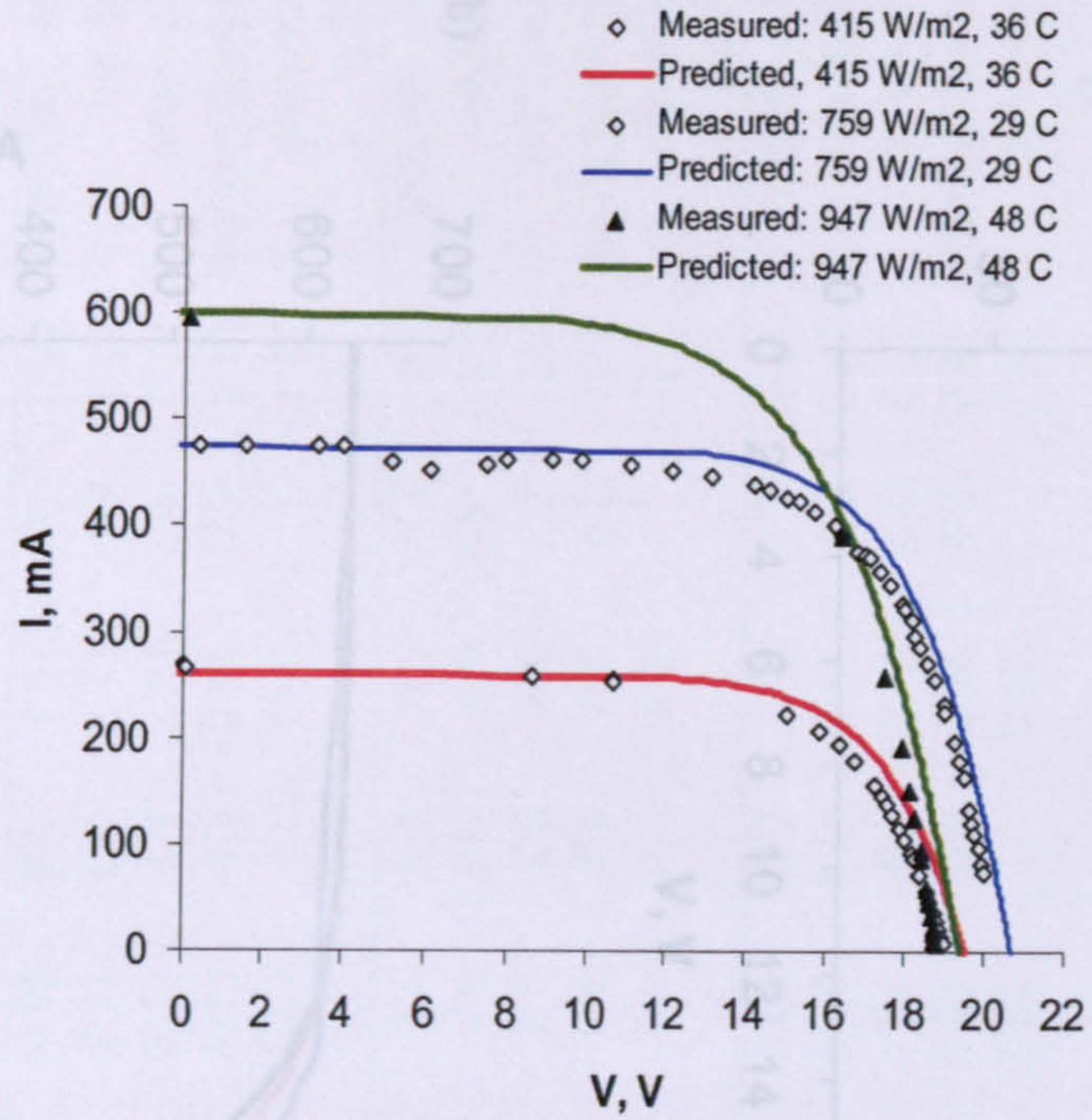

Fig. 3.12: Measurements and predicted IV curves (according to the new method) for PV2 at different conditions of G and T_{mod}.

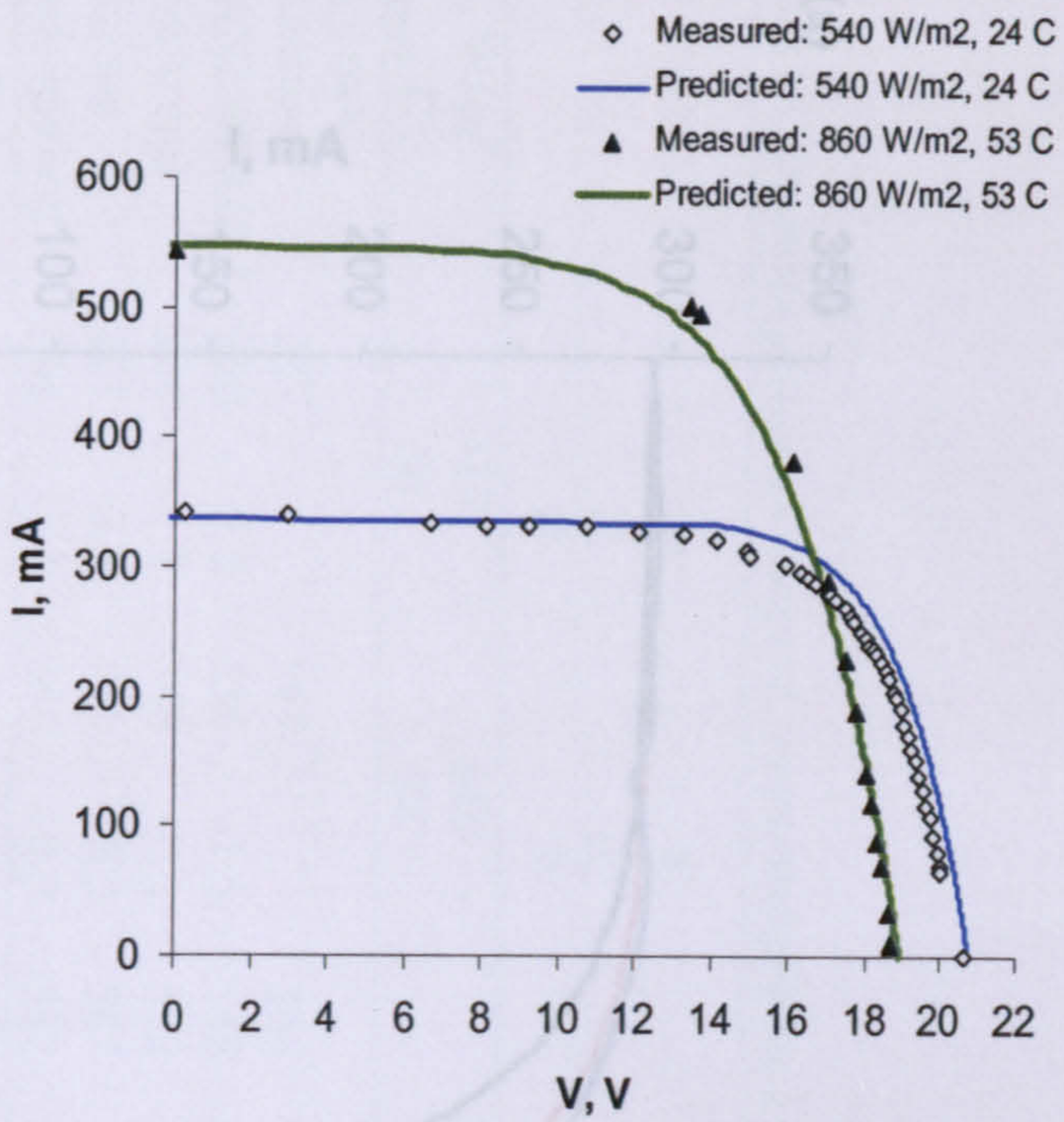

Fig. 3.13: Measurements and predicted IV curves for PV2 (continued) at different conditions of G and T_{mod}.

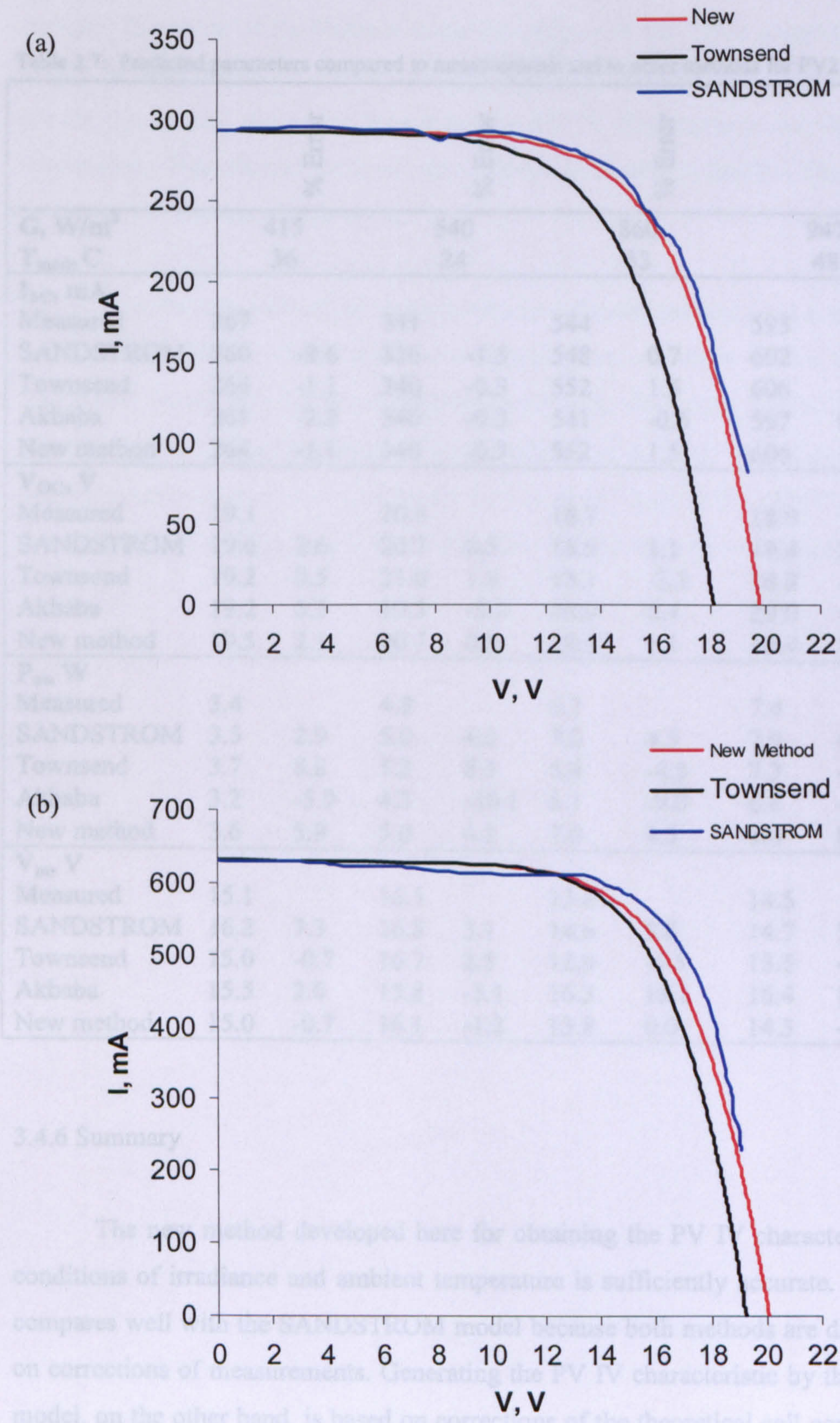

Fig. 3.14: Three different methods for estimating the PV IV characteristic compared at G = 1000 W/m^2 and T_{mod} = 40 C for (a) PV1 and (b) PV2.

Table 3.7: Predicted parameters compared to measurements and to other methods for PV2.

		% Error		% Error		% Error		% Error
G, W/m²	415		540		860		947	
T_{mod}, C	36		24		53		48	
I_{SC}, mA								
Measured	267		341		544		595	
SANDSTROM	260	-2.6	336	-1.5	548	0.7	602	1.2
Townsend	264	-1.1	340	-0.3	552	1.5	606	1.8
Akbaba	261	-2.2	340	-0.3	541	-0.6	597	0.3
New method	264	-1.1	340	-0.3	552	1.5	606	1.8
V_{OC}, V								
Measured	19.1		20.6		18.7		18.9	
SANDSTROM	19.6	2.6	20.7	0.5	18.9	1.1	19.4	2.6
Townsend	19.2	0.5	21.0	1.9	18.1	-3.2	18.8	-0.5
Akbaba	19.2	0.5	19.5	-5.3	19.9	6.4	20.0	5.8
New method	19.5	2.1	20.7	0.5	18.9	1.1	19.4	2.6
P_m, W								
Measured	3.4		4.8		6.7		7.4	
SANDSTROM	3.5	2.9	5.0	4.2	7.0	4.5	7.9	6.8
Townsend	3.7	8.8	5.2	8.3	6.4	-4.5	7.3	-1.4
Akbaba	3.2	-5.9	4.3	-10.1	6.1	-9.0	6.8	-8.1
New method	3.6	5.9	5.0	4.2	7.0	4.5	8.0	8.1
V_m, V								
Measured	15.1		16.3		13.8		14.5	
SANDSTROM	16.2	7.3	16.8	3.1	14.6	5.8	14.7	1.4
Townsend	15.0	-0.7	16.7	2.5	12.9	-6.5	13.5	-6.9
Akbaba	15.5	2.6	15.8	-3.1	16.3	18.1	16.4	13.1
New method	15.0	-0.7	16.1	-1.2	13.8	0.0	14.3	-1.4

3.4.6 Summary

The new method developed here for obtaining the PV IV characteristic at any conditions of irradiance and ambient temperature is sufficiently accurate. The method compares well with the SANDSTROM model because both methods are directly based on corrections of measurements. Generating the PV IV characteristic by the Townsend model, on the other hand, is based on corrections of the theoretical cell parameters (i.e. A, I_0 and I_G).

The method for predicting the series resistance of the PV module is also accurate enough. The value of R_S obtained compares well with the value obtained from NLR. Using the experimentally determined values of the temperature coefficients, the loss coefficient, U, and the series resistance, the PV IV characteristic can be confidently determined. This characteristic is then solved with the motor/fan characteristic to determine the fan operational point.

The errors in each of the experimentally estimated parameters causes an error in the predicted PV IV characteristic which will cause an error in the estimated fan operational point, the fan ΔP_s-Q characteristic and, ultimately, the flow rate in the system. For the G and T_{mod} range of (0 to 1000 W/m^2 and 0 to 60 C), analysis reveals that the maximum error is about 2 % for I_{SC} (up to ±17 mA), 5.3 % for V_{OC} and V_m (up to ± 0.96 V), 7.1 % for I_m (up to ± 34 mA) and 1.4 % for P_m (up to ± 0.14 W).

3.5 MOTOR/FAN CHARACTERISTICS

3.5.1 Determination of motor parameters

Laboratory measurements of current and voltage were obtained for the three fans in Table 3.3. For each of the fans, the voltage was varied using a power pack and the current was recorded. The locked rotor IV curves are shown in Fig. 3.15. The end points of these curves, which are summarised in Table 3.8, are the start-up points of the fans (V_s and I_s). According to Eq. 2.12, the intercept of these lines must be equal to zero but this is not the case here. This suggests that some of the voltage supplied to the motor is dissipated in its electronic components. This dissipated voltage (V_e) is the voltage of the fan when current is zero and so it can be taken as the X-intercept of the graphs in Fig. 3.15. The armature resistance is then the slope of each of these lines. The values of V_e and R_a for each of the motors are also shown in Table 3.8.

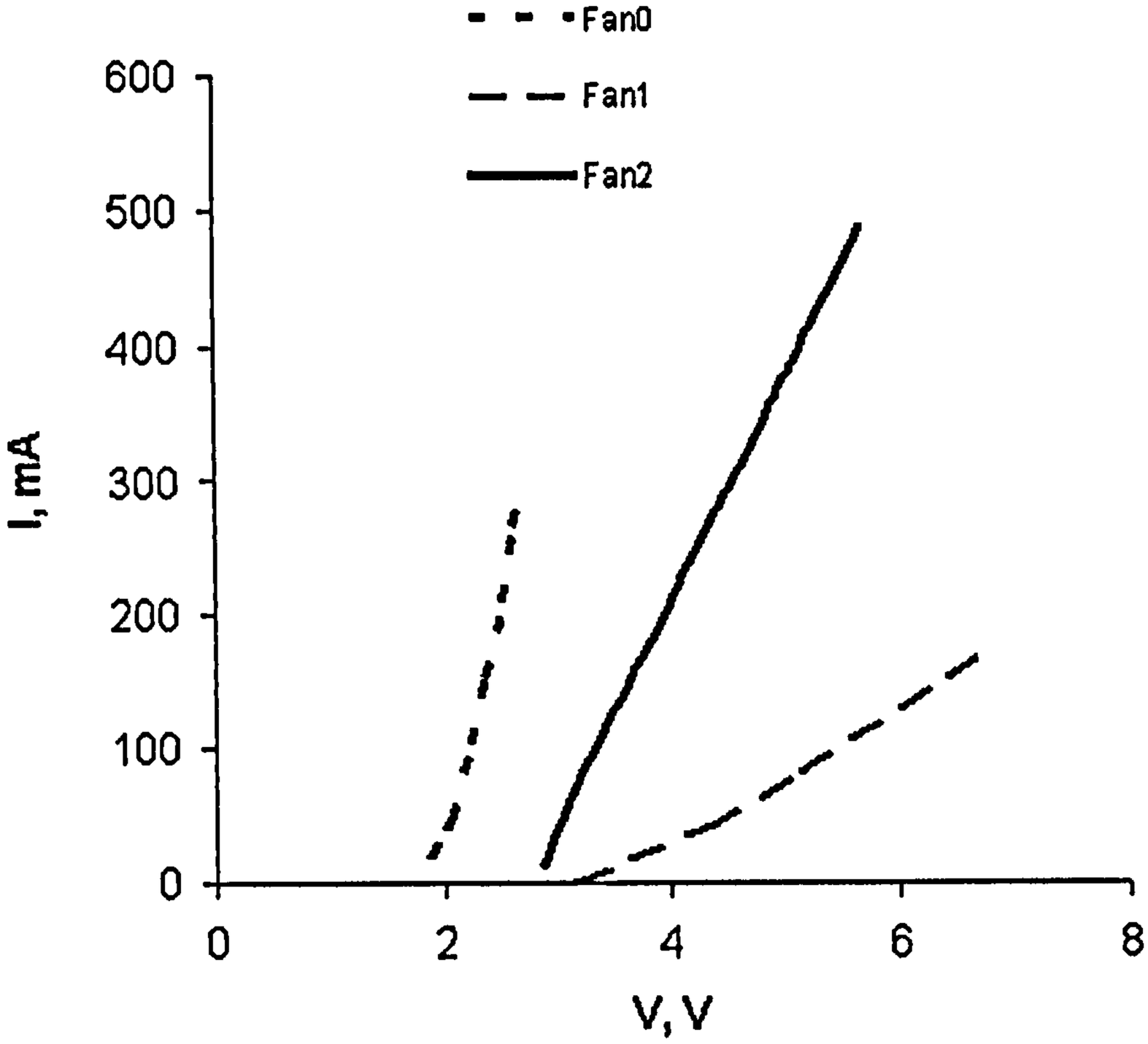

Fig. 3.15: Locked rotor IV characteristics of the fans in Table 3.3.

Table 3.8: Motor parameters as estimated from measurements.

	Fan0	Fan1	Fan2
V_s, V	2.66 ± 0.05	6.78 ± 0.07	5.72 ± 0.05
I_s, mA	311 ± 1	174 ± 1	488 ± 1
V_e, V	1.90 ± 0.05	3.32 ± 0.07	2.79 ± 0.05
V_{max}, V	12*	24*	24*
I_{max}, mA	792*	396*	846*
ω_{max}, rad/s	298 ± 3	298 ± 3	371 ± 4
R_a, Ω	2.8	20.4	6.0
K_m, V.s/rad	0.040 ± 0.06	0.079 ± 0.011	0.064 ± 0.07
K_f, V.s/rad	2.5 e-7	2.4 e-7	4.9 e-7

* Manufacturer's data

Assuming that V_e is independent of current so that it is a fixed value, the voltage term, V, in Textbox 2.2, should be written as $(V-V_e)$. Measurements of speed were obtained at the maximum voltage of each of the fans using the aforementioned handheld optical tachometer. The motor constants, K_m, were then calculated using Eq. 3.11 (after replacing V with $V-V_e$). The motor-fan coupling constant, K_f, can be determined from Eq. 3.12 using measurements of current and speed and the pre-calculated motor constant.

3.5.2 Speed-torque characteristics

Typical ωT characteristics for all three fans at V = 12 V are shown in Fig. 3.16 (See Textbox 2.2 for ωT equation). It is observed that at this voltage, the 12 V fan reaches a maximum speed of 2850 r/min. Figure 3.17 shows these characteristics for Fan1 and Fan2 at three different voltages. Such curves are usually supplied by the manufacturer and they can be used for motor parameter determination. As mentioned above, in the current work, the model is based on motor/fan IV and ωV characteristics.

3.5.3 IV and ωV characteristics

The IV and ωV characteristics can be used to determine the operational voltage and speed of the fan when coupled to the PV module. They are determined from measurements of V, ω and I after start-up of the fan. Figure 3.18 shows these characteristics for each of the fans. Using the running IV characteristics; the parameters A_v and B_v for each of the fans can be determined. These are summarised in Table 3.9.

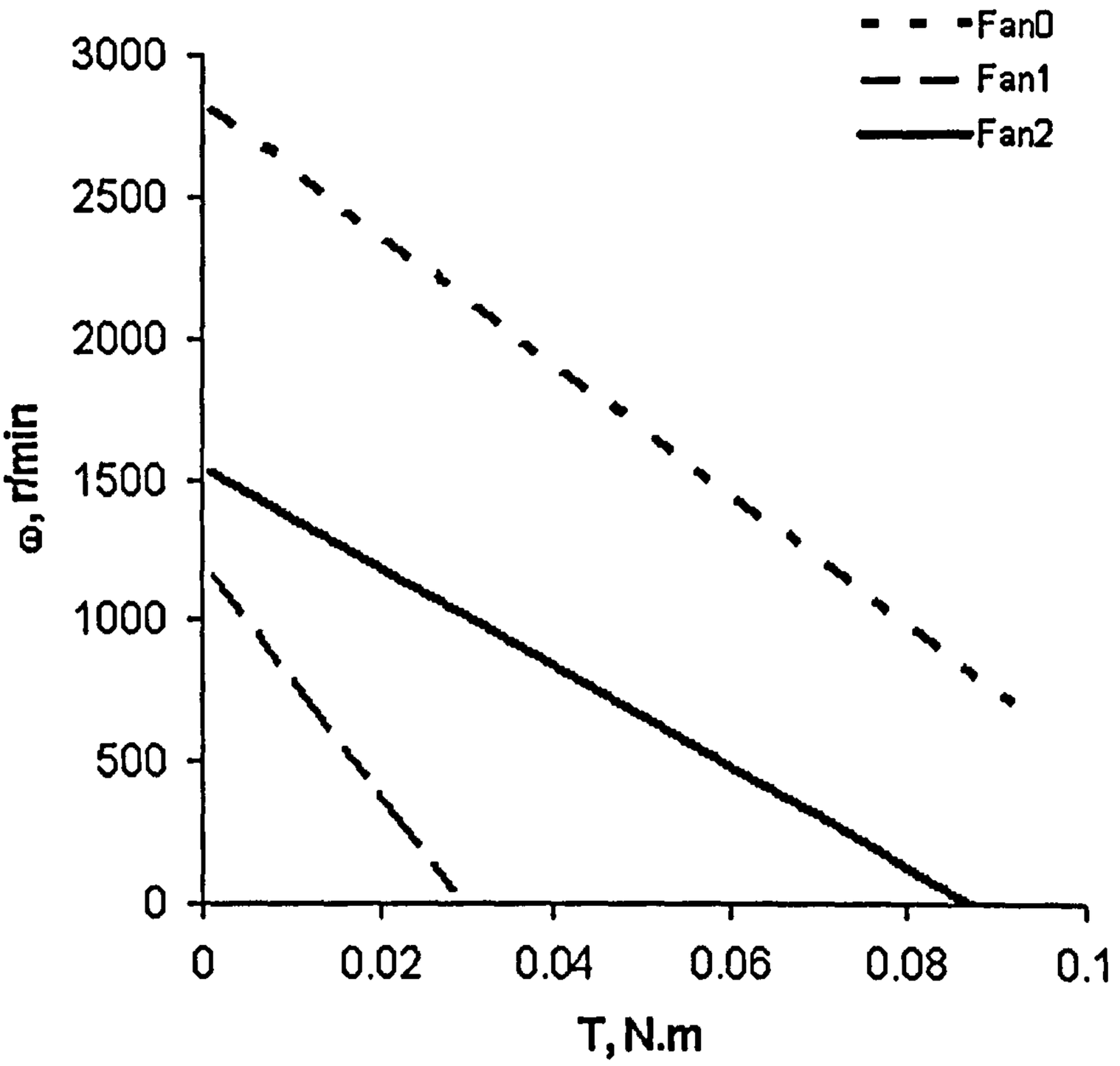

Fig. 3.16: Speed-torque characteristics for all three fans at V = 12 V.

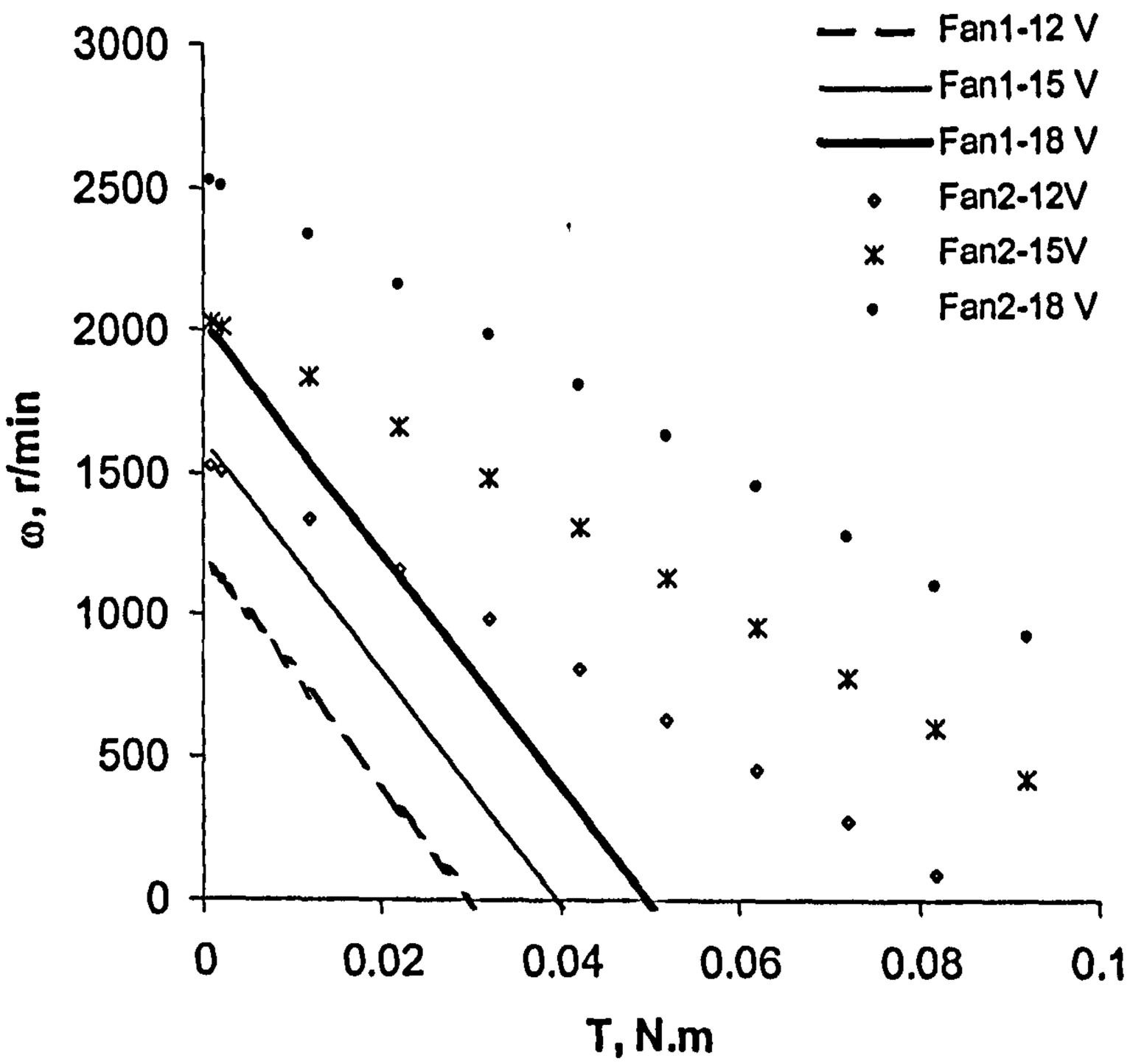

Fig. 3.17: Speed-torque characteristics for Fan1 and Fan2 at three voltages.

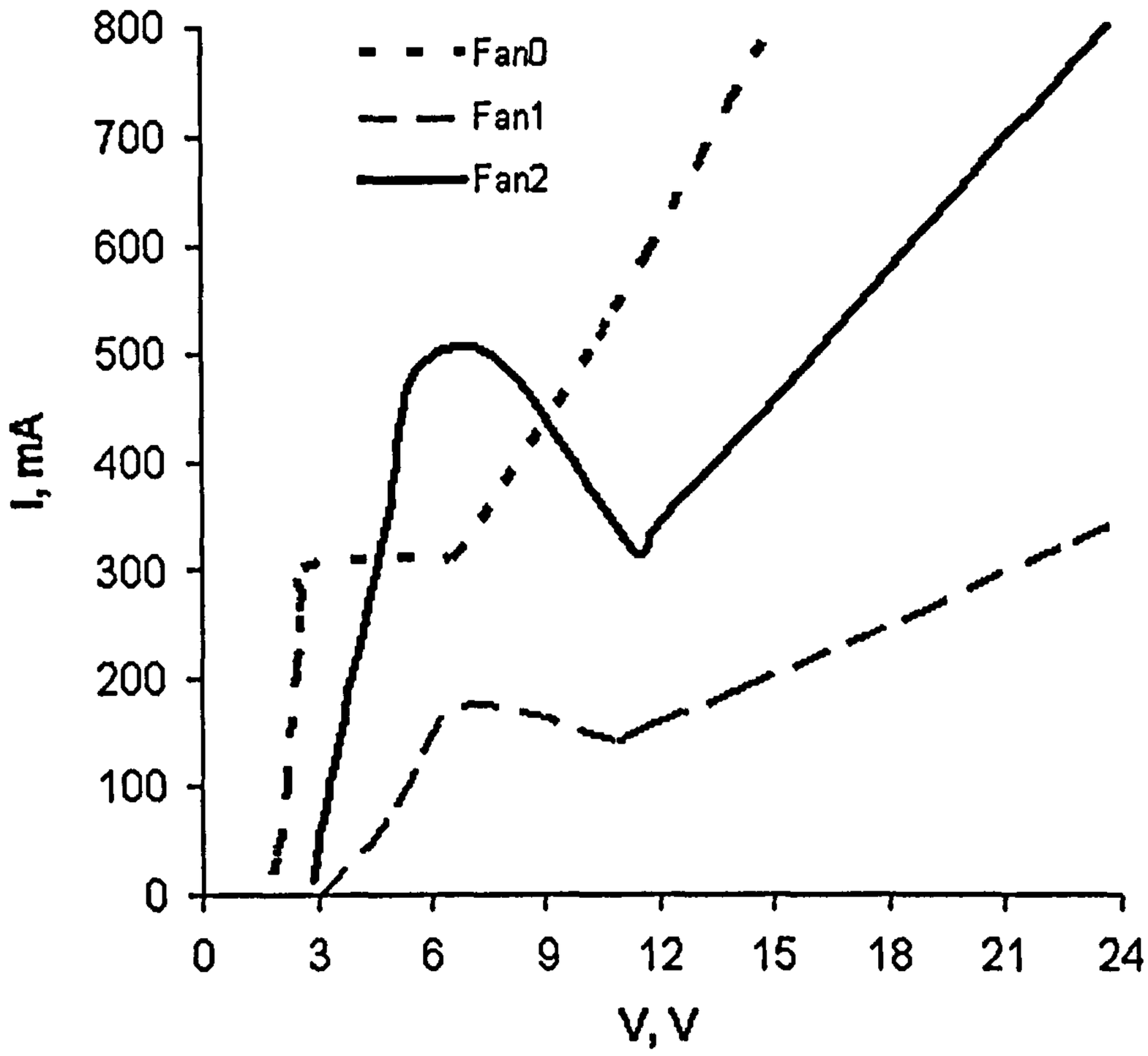

Fig. 3.18: Fan IV characteristics.

Table 3.9: Motor/fan parameters estimated from measurements

	Fan0	Fan1	Fan2
A_v, Ω^{-1}	0.0604 ± 0.0002	0.0144 ± 0.0002	0.0393 ± 0.0002
B_v, A	-0.105 ± 0.002	-0.012 ± 0.002	-0.131 ± 0.06
A_ω, r/min.V	227.66 ± 2.3	131.77 ± 1.3	159.04 ±1.6
B_ω, r/min	-128.53 ± 10.2	-365.58 ± 3.0	-384.23 ± 3.2

3.5.4 Fan ΔP-Q characteristics

The ΔP_f-Q characteristic of the fan changes with fan speed and air temperature as discussed above. By measuring a single fan performance curve at a known speed and air temperature, the characteristic at any other speed and temperature can be derived from this curve using the affinity laws for fans. Measurements were performed on each of the fans. The ΔP_f-Q curve measurement was done according to the procedure described in the ASHRAE Handbook of Equipment (ASHRAE, 1988). A simple instrument was constructed for measuring fan ΔP_f-Q characteristics as shown in Fig. 3.19. The instrument consisted of a 2.5 m long, 141 mm painted steel pipe with a

restriction valve at the end. The fan was fixed at the inlet of the duct and the static pressure across the fan was measured with an error of 0.86 Pa using the aforementioned manometer and a Pitot static tube as shown in the figure. The Pitot static tube was inserted in the pipe at the centre about 30 cm from the fan. The pressure measured was taken as an average value of static pressure even though it was measured at a single point. The flow rate of air was measured using another inclined manometer about 1.4 m away from the fan with the Pitot static tube at the centreline of the pipe. A reference ΔP_f-Q was obtained for the different fans at 2000 r/min (209.4 rad/s) and 18 °C.

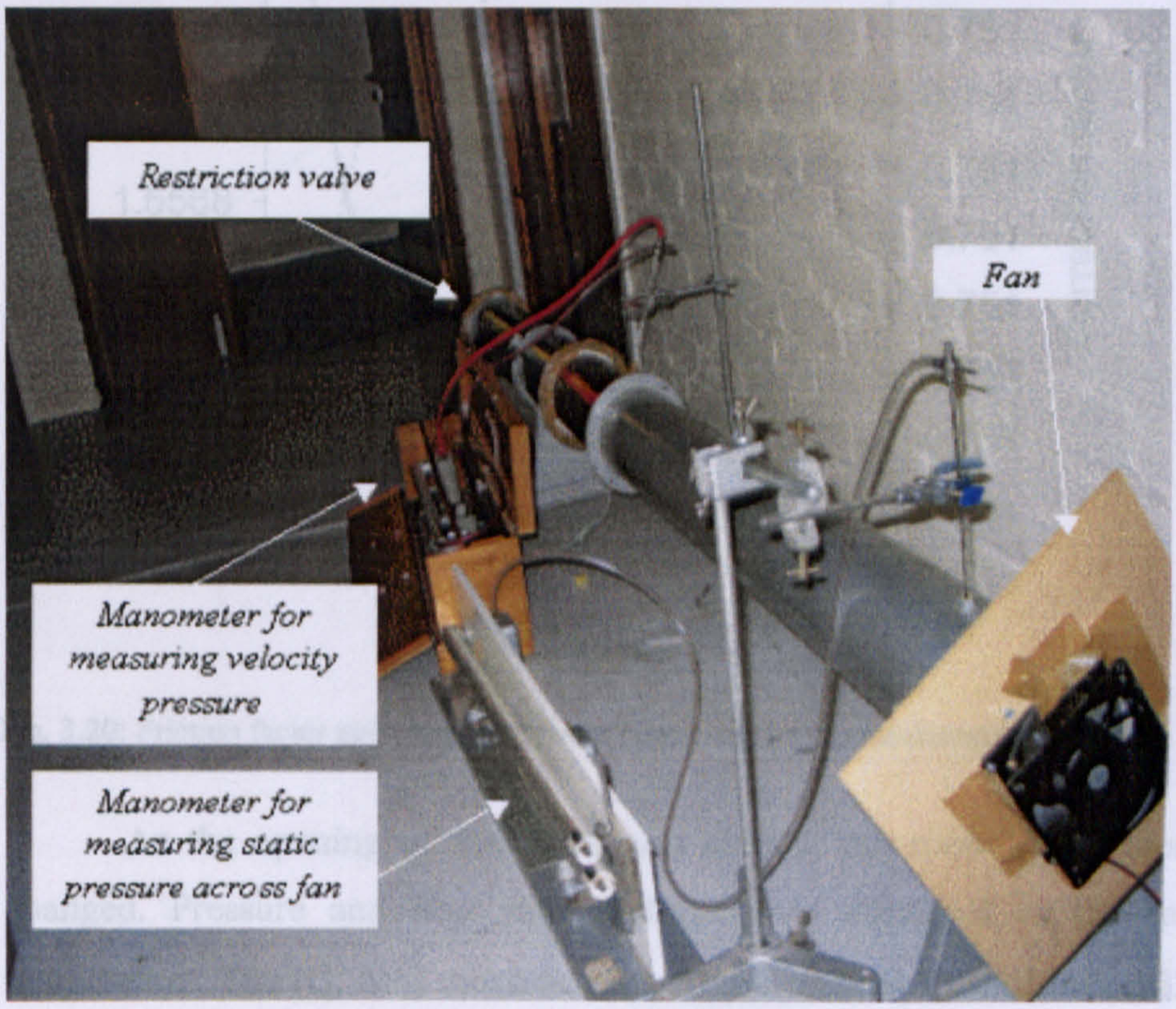

Fig. 3.19: Instrument used for measuring fan ΔP-Q characteristics.

The speed of the fan was kept constant by keeping the voltage constant. The opening of the valve was varied to change the pressure. Starting from a fully open valve, readings of flow rate, pressure, air temperature, and speed were recorded. As the valve was closed, pressure increased while the flow rate decreased.

Since the flow rates were measured only at the center of the pipe and no "traverse" was applied, then as mentioned in section 3.3, a correction was required using Eq. 3.23. The Reynolds numbers for all flow rate measurements in the pipe ranged from 3000 to 40000 ($D = 0.141$ m, $\rho = 1.2$ kg/m^3, $\mu = 1.76 \times 10^{-5}$ kg/m.s). Using

a roughness coefficient for steel pipe of k = 0.046 mm, (McCabe, 1985), the friction factors for this range of Reynolds numbers and the correction factor were calculated as shown in Fig. 3.20. A correction factor of 0.75 was applied to all flow rate measurements in order to obtain an average value of velocity, (McCabe, 1985).

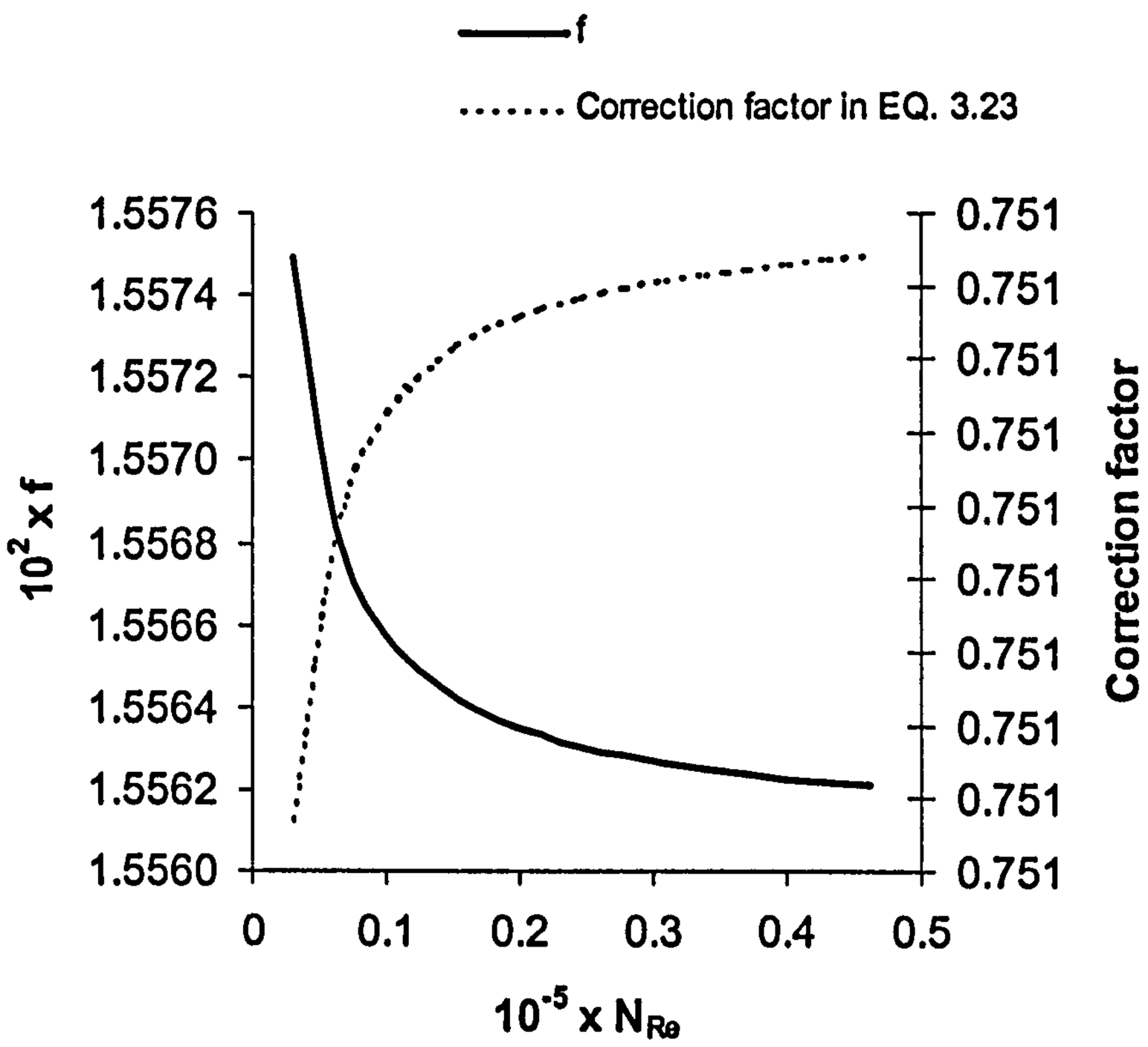

Fig. 3.20: Friction factor and correction factor (Eq. 3.23) for the measured (Q, ΔP_f) data points.

As the opening of the valve was altered, the speed and temperature slightly changed. Pressure and flow rate readings were corrected to the same speed and temperature. The (Q, ΔP_f) measurements at the reference conditions of 2000 r/min and 18 C are shown in Fig. 3.21. It is noticed that, even though their electrical characteristics are different, Fan0 and Fan1 have very similar ΔP_f -Q characteristics.

Using the reference values of speed and temperature, constants C_1 and C_2 are calculated for each of the fans. Furthermore, fitting the data points to a cubic regression as shown in Fig. 3.22, the constants w, x, y and z were obtained for each of the fans. The values are summarised in Table 3.10. The errors in each of the parameters are due to error in the measurement of pressure and flow rate, which will then cause uncertainty in the ΔP_f -Q characteristic.

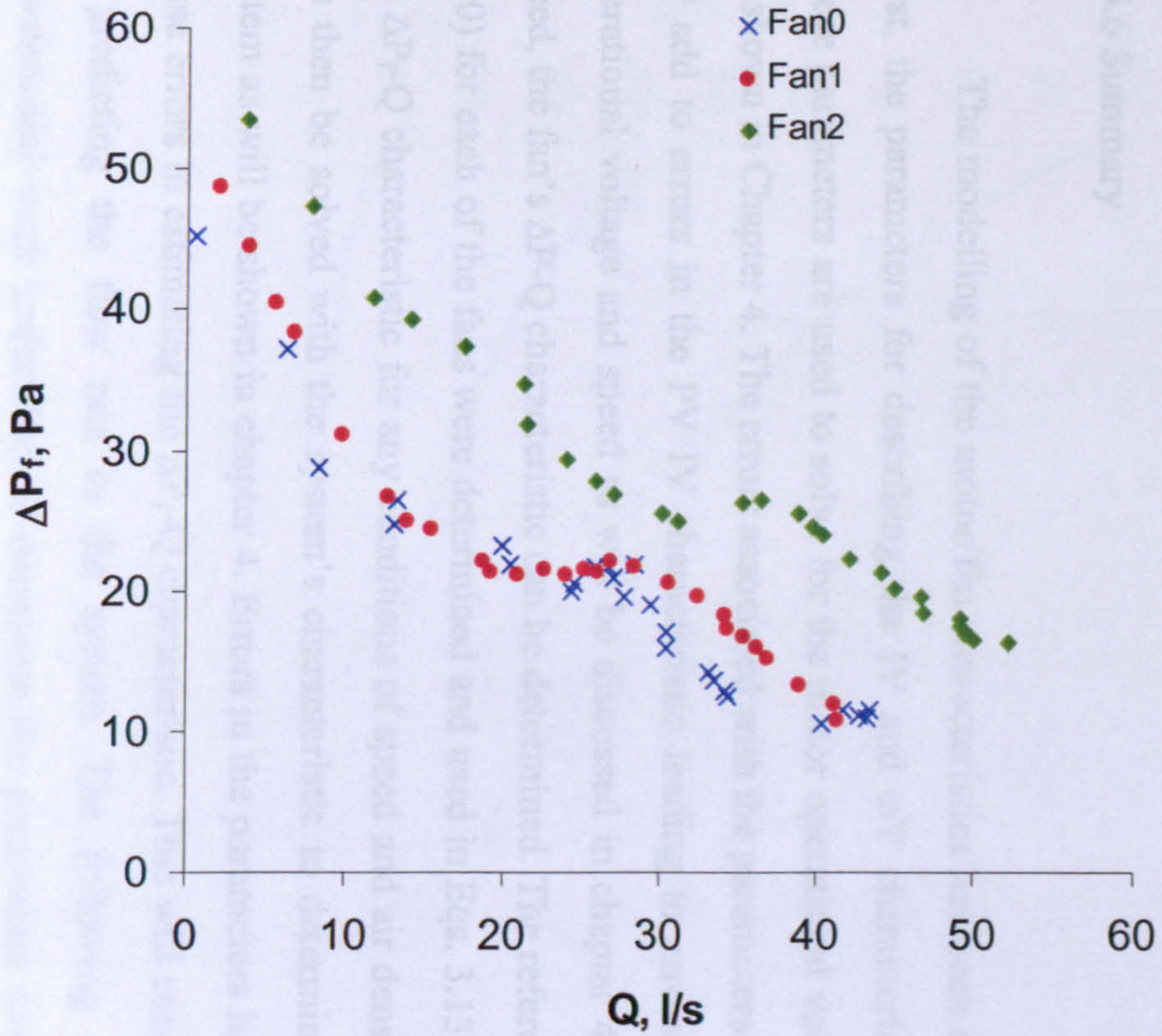

Fig. 3.21: Measured reference (Q, ΔP_f) data at 2000 r/min for all three fans.

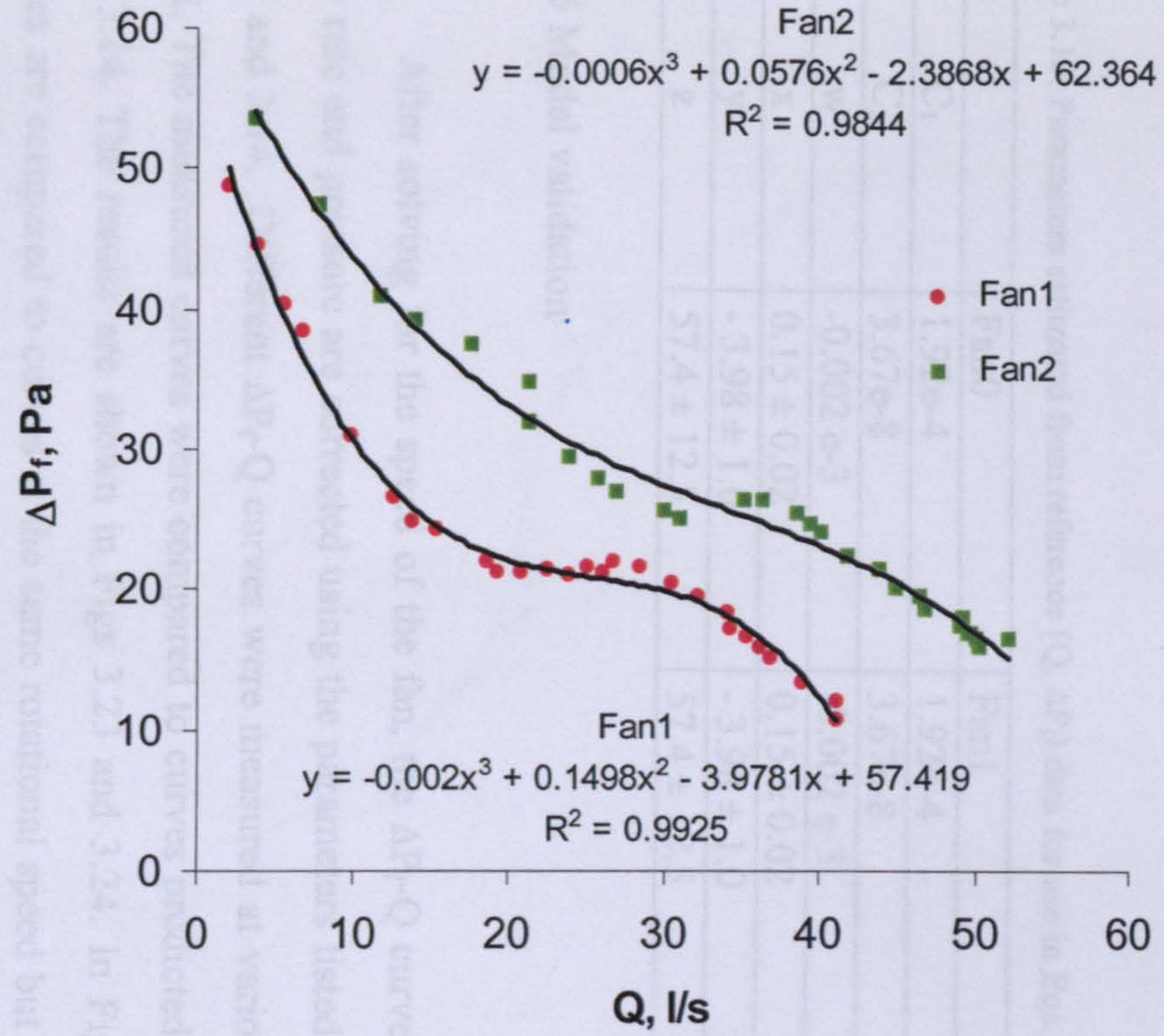

Fig. 3.22: Cubic regression (Fan1 and Fan2) for the measured data.

Table 3.10: Parameters estimated from reference (Q, ΔP_f) data for use in Eqs. 3.13 and 3.14.

	Fan0	Fan1	Fan2
C_1	1.92e-4	1.92e-4	1.92e-4
C_2	3.67e-8	3.67e-8	3.67e-8
w	-0.002 e-3	-0.002 e-3	-0.0006
x	0.15 ± 0.02	0.15 ± 0.02	0.058 ± 0.006
y	- 3.98 ± 1.0	- 3.98 ± 1.0	- 2.39 ± 0.4
z	57.4 ± 12.5	57.4 ± 12.5	62.4 ± 6.6

3.5.5 Model validation

After solving for the speed of the fan, the ΔP_f-Q curve can be generated. The flow rate and pressure are corrected using the parameters listed in Table 3.10 and Eqs. 3.13 and 3.14. Different ΔP_f-Q curves were measured at various speeds for Fan1 and Fan2. The measured curves were compared to curves predicted according to Eqs. 3.13 and 3.14. The results are shown in Figs 3.23 and 3.24. In Fig. 3.25, manufacturer's curves are compared to curves at the same rotational speed but derived from measured data.

3.5.6 Summary

The modelling of the motor/fan characteristics has been achieved in two stages. First, the parameters for describing the IV and ωV characteristics were determined. These parameters are used to solve for the motor operational voltage and speed as will be shown in Chapter 4. The errors associated with the parameters in Table 3.8 and Table 3.9 add to errors in the PV IV characteristic leading to errors in estimating the fan operational voltage and speed as will be discussed in chapter 4. Using the calculated speed, the fan's ΔP-Q characteristic can be determined. The reference parameters (Table 3.10) for each of the fans were determined and used in Eqs. 3.13 and 3.14 to determine the ΔP_f-Q characteristic for any conditions of speed and air density. This characteristic can then be solved with the system's characteristic to determine the flow rate in the system as will be shown in chapter 4. Errors in the parameters listed in Table 3.10 will cause errors in estimating the ΔP_f-Q characteristic. This will consequently lead to error in predicting the flow rate in the system. The following section describes the experimental work undertaken to determine the parameters needed for obtaining the system characteristic (ΔP_S-Q).

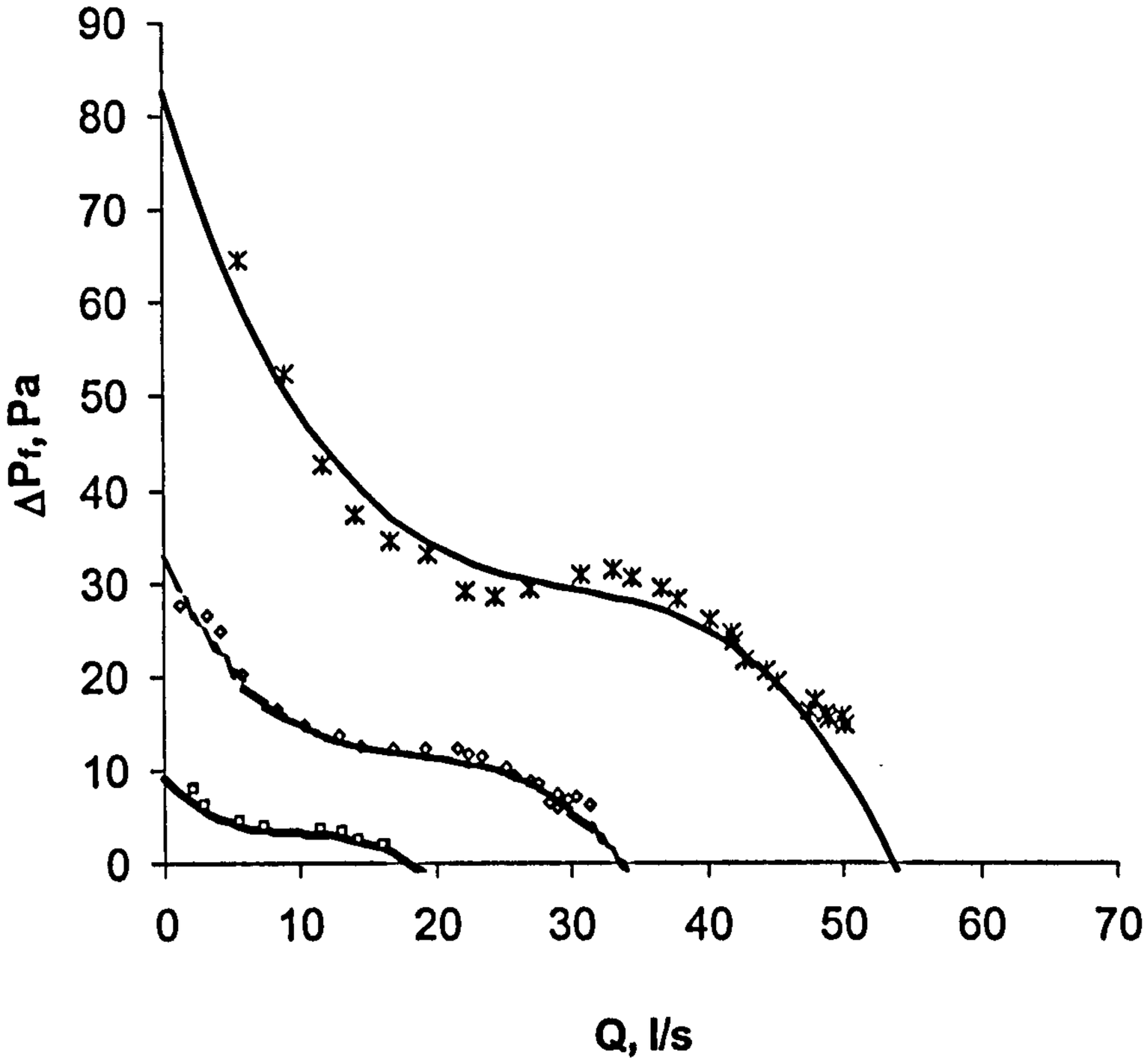

Fig. 3.23: A comparison between measurements and predicted fan ΔP-Q curves for Fan1 at (a) ω = 800 r/min, (b) ω = 1500 r/min, (c) ω = 2400 r/min.

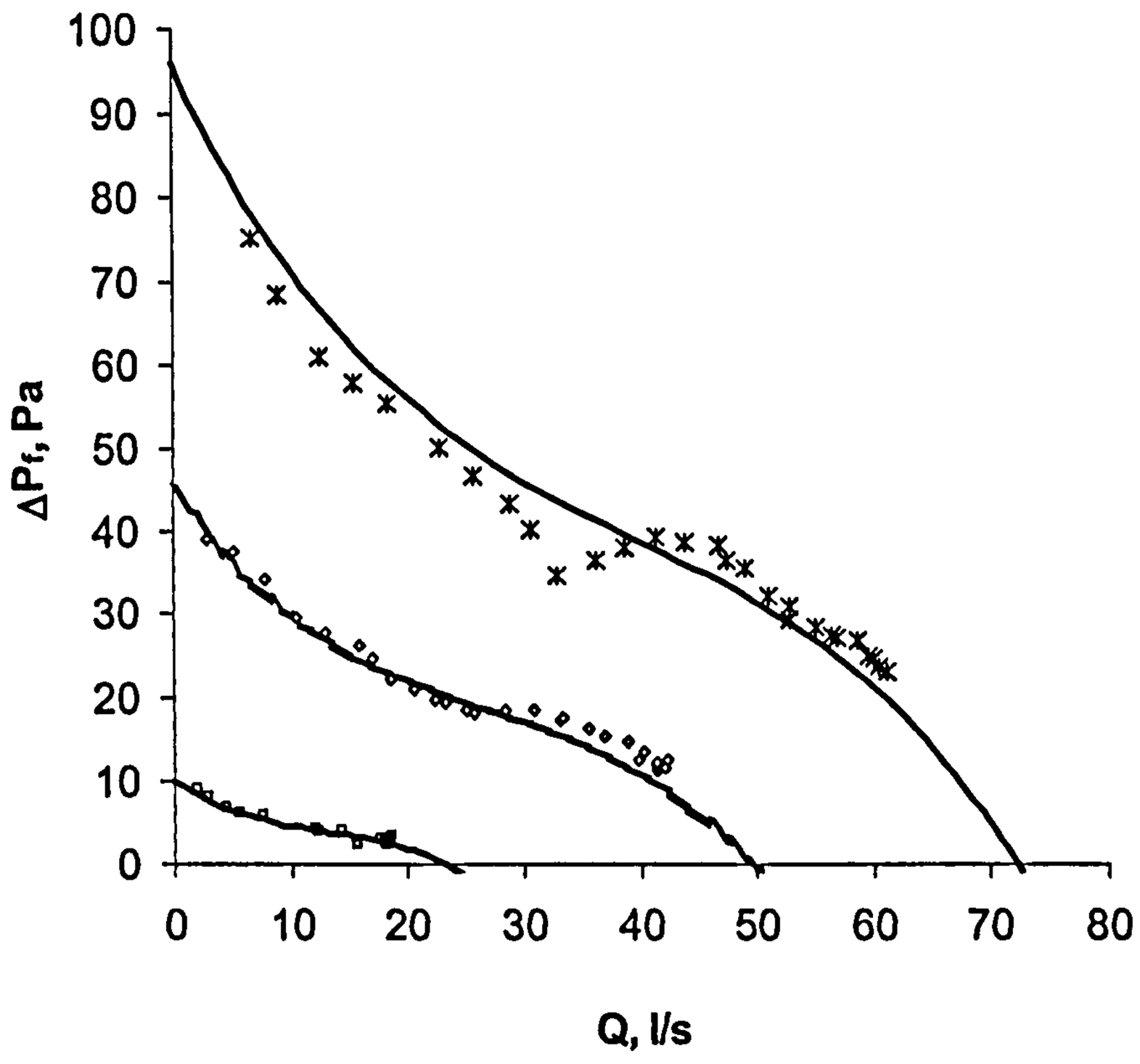

Fig. 3.24: A comparison between measurements and predicted fan ΔP-Q curves for Fan2 at (a) ω = 800 r/min, (b) ω = 1700 r/min, (c) ω = 2400 r/min.

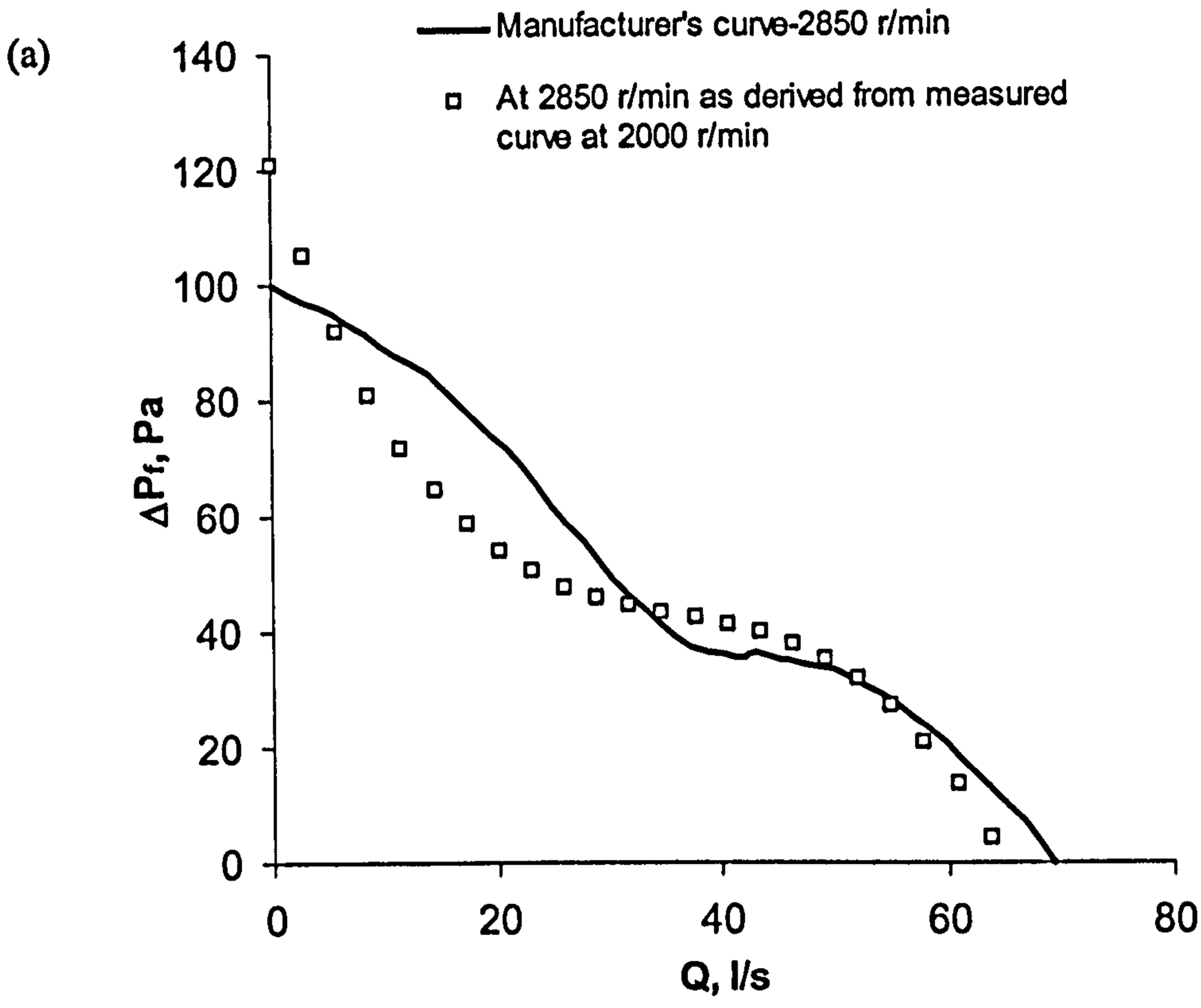

Fig. 3.25: A comparison between manufacturer's curve and curve predicted from measured data at 3500 r/min for (a) Fan1 and (b) Fan2.

3.6 SYSTEM ΔP-Q CHARACTERISTIC

Reference measurements were performed on a 3 m long 152 mm diameter flexible duct for two degrees of extension (100 % and 80 %). The duct was extended horizontally and measurements of static pressure across the fan and flow rate at the outlet of the duct were obtained. The flow rate was measured using an ultrasonic air flow meter (Fig. 3.26) with an accuracy of ± 2.7 l/s. The flow rate reading was obtained by averaging twenty 5-sec measurements. The reference curves for each of the two duct extensions are shown in Fig. 3.27. The curves obtained show a quadratic relationship between pressure and flow rate which gives confidence in the measurement technique used.

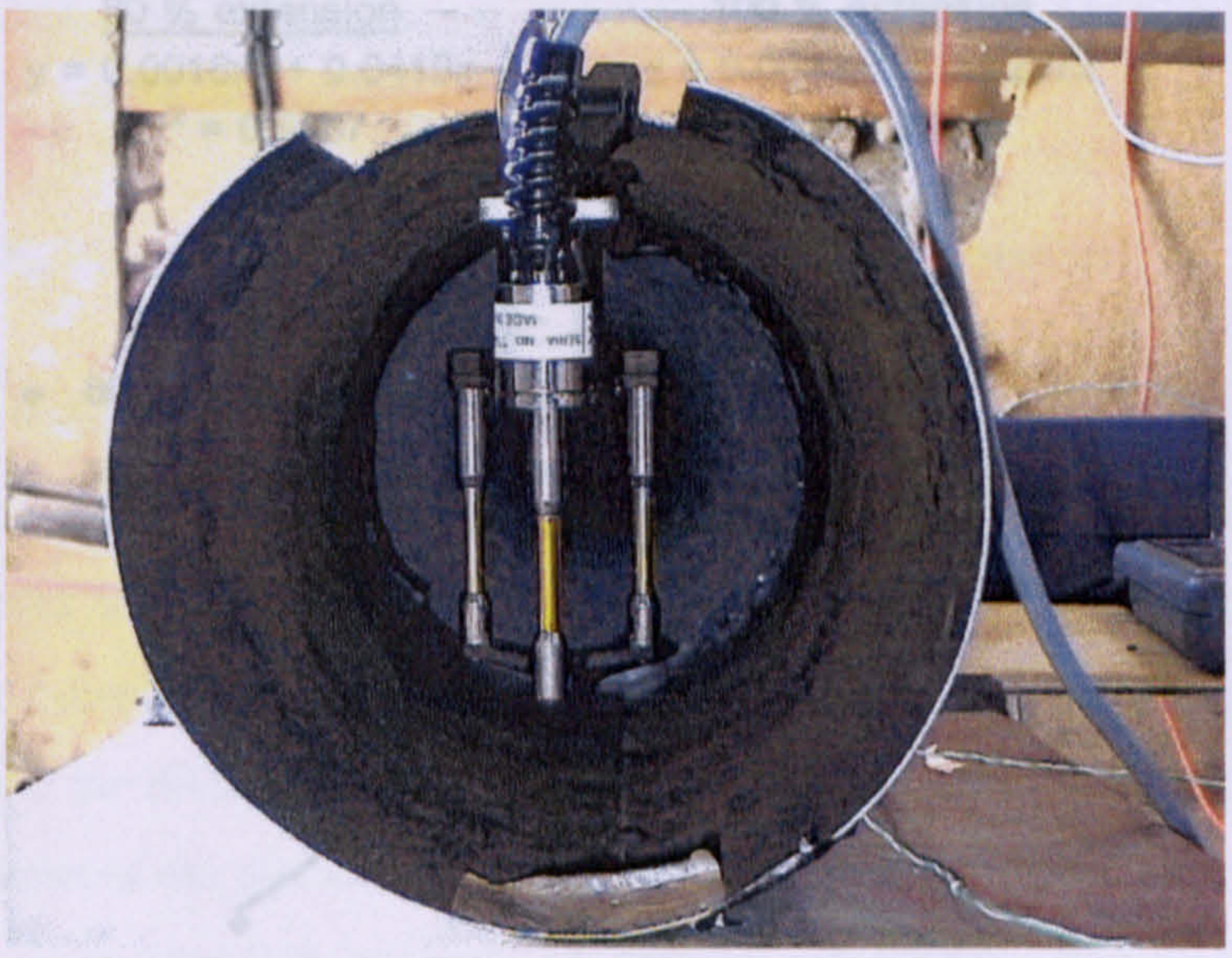

Fig. 3.26: The ultrasonic flow meter used for measuring flow rate.

Using these reference measurements, the parameters V_1, V_2 (method 1A), k (method 1B) and T_1 and T_2 (method 2) were determined as shown in Table 3.11. The parameters T_1 and T_2 are the parameters in the quadratic best-fit equations in Fig. 3.27. Figure 3.28 shows the f-N_{Re} relationships for 80 % and 100 % extension. The parameters in Table 3.11 can now be used to obtain the system's ΔP-Q characteristic for any duct length and diameter at the same extension.

Table 3.11: Parameters estimated from reference data for 80 % and 100 % duct extensions.

	80 % extension	100 % extension
V1	0.1064	0.0606
V2	-1e-5	-6e-6
k, mm	9.6 ± 1.5	2.5 ± 1.2
T_1, Pa.(l/s)$^{-2}$	0.0018	0.0013
T_2, Pa.(l/s)$^{-1}$	0.0419	0.0237

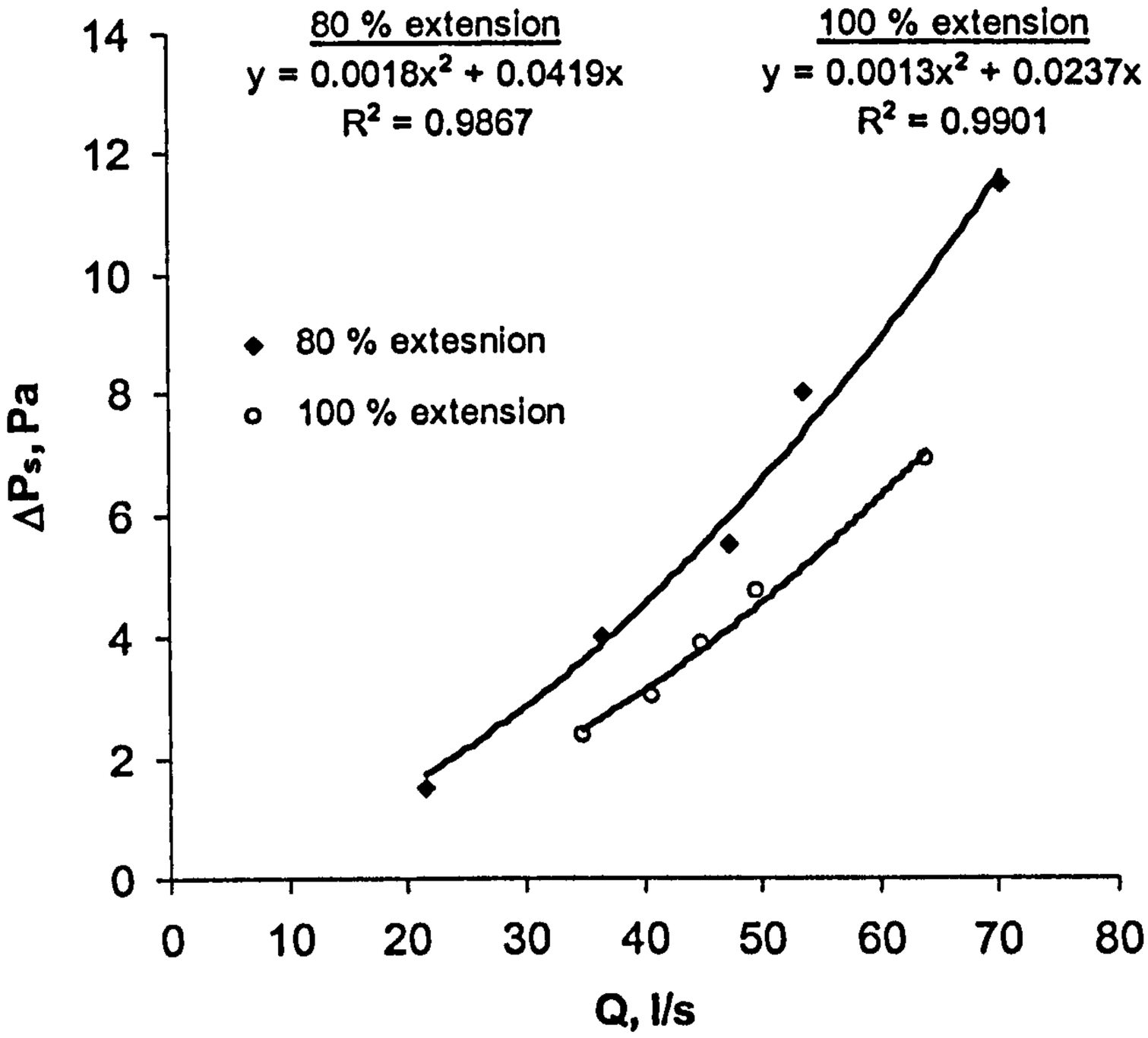

Fig. 3.27: Reference (Q, ΔP_s) data for two duct extensions.

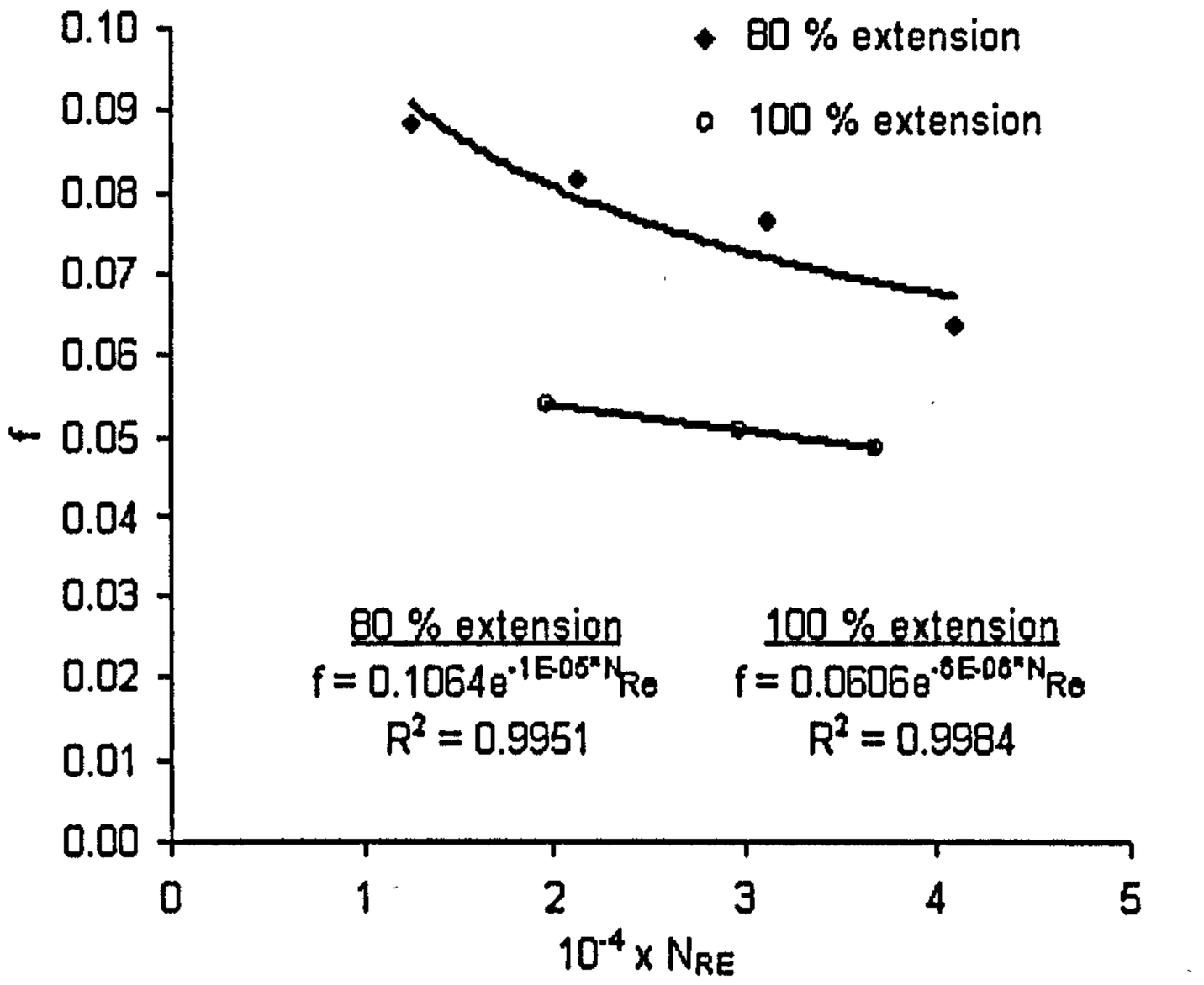

Fig. 3.28: f vs. N_{Re} curves obtained from reference data for two duct extensions.

3.6.1 Model validation

In order to validate the model for predicting the ΔP_s-Q characteristic from the three methods discussed in section 3.2.5 (using Eqs. 3.17, 3.18 and 3.19), measurements were obtained for different duct lengths and diameters at 80 % and 100 % extension. The measurements are checked against predicted values by the three methods as shown in Fig. 3.29. It is seen that methods 1A and 1B give more accurate predictions. These two methods are compared against measurements for a duct with 102 mm diameter and 5 m length at 80 % extension in Fig. 3.30. The values of the parameters V_1, V_2 and k in Table 3.11 can be considered accurate enough to predict the ΔP_s-Q characteristic. For the model in chapter 4, method 1B will be used. More comparisons based on the values of k in Table 3.11 are shown in Fig. 3.31.

For the current work method1B is used because it is the most general of the three methods. The input parameters are length, diameter and degree of extension.

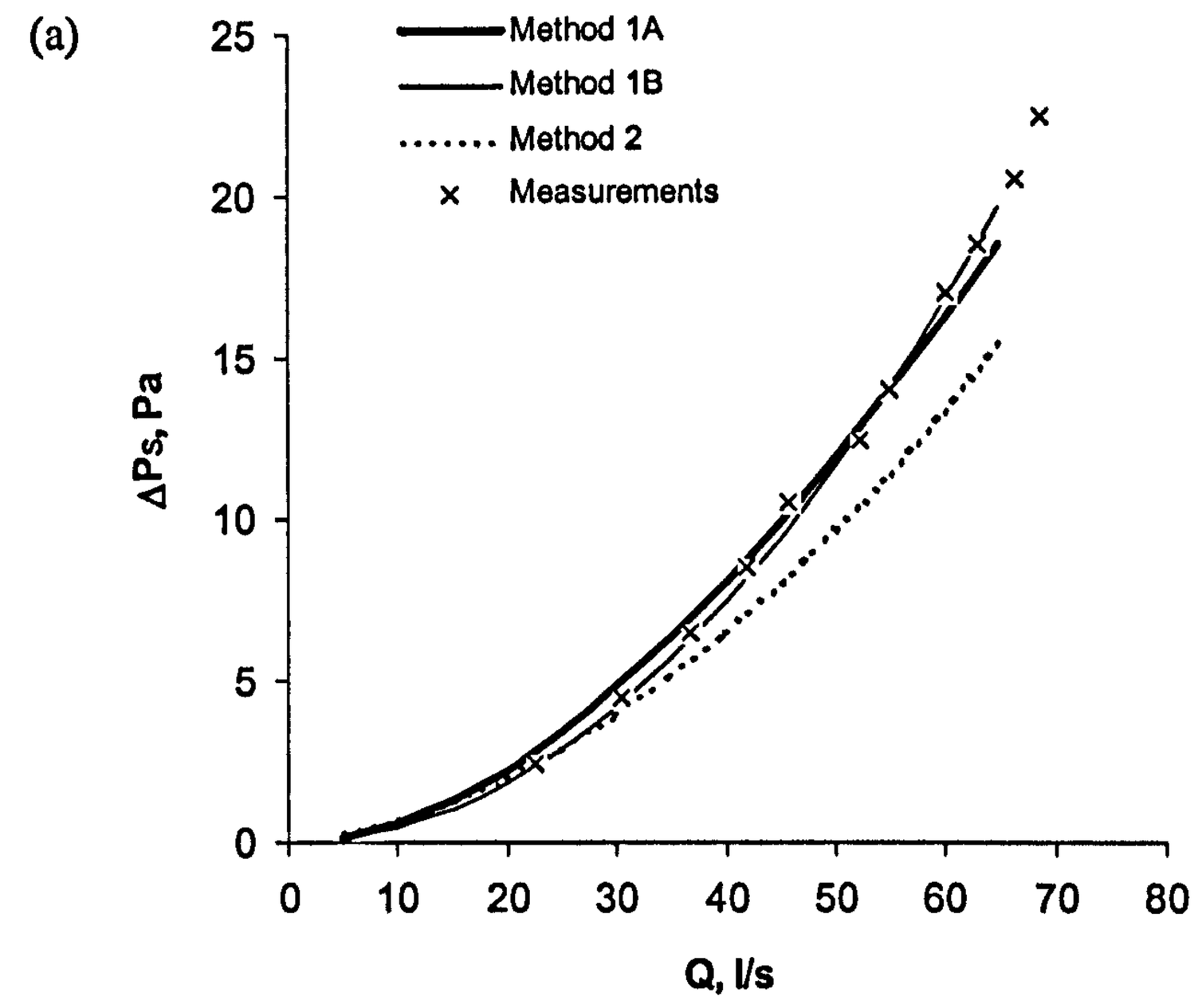

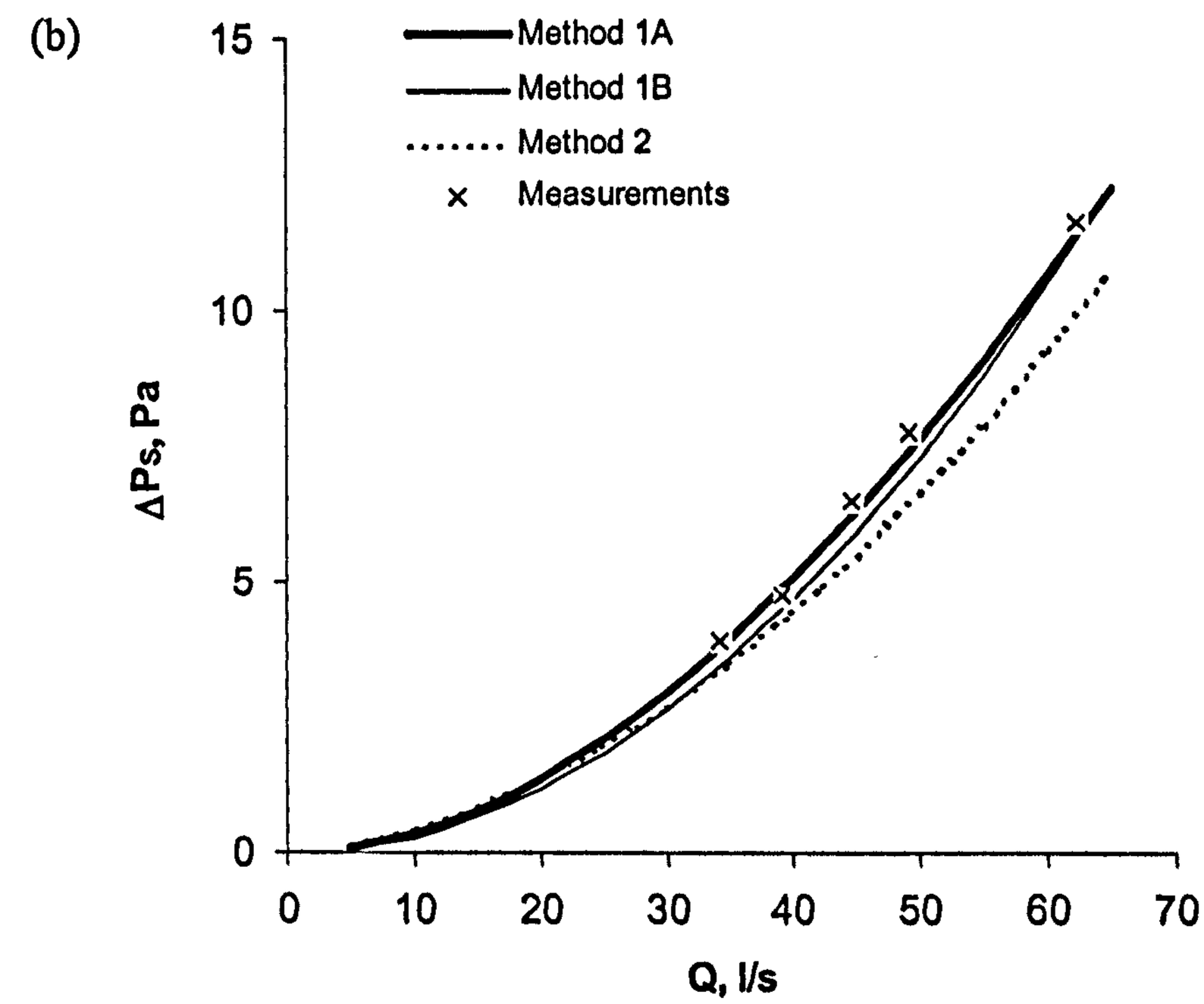

Fig. 3.29: Comparing three methods for generating ΔP_s-Q characteristic (L = 5 m, D = 152 mm) at (a) 80 % extension and (b) 100 % extension.

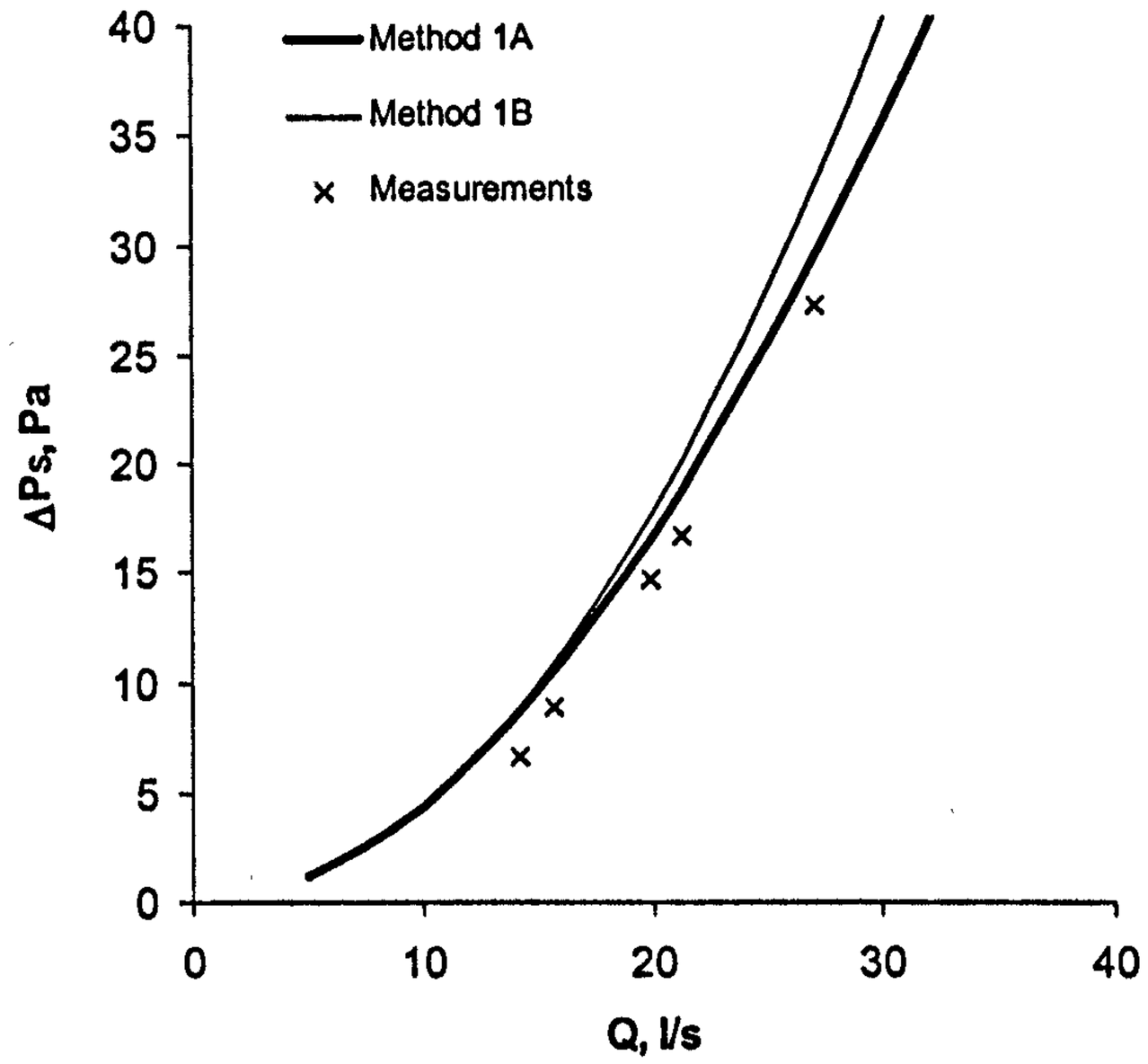

Fig. 3.30: Comparing methods 1A and 1B to measurements for a 5 m long, 102 mm diameter at 80 % extension.

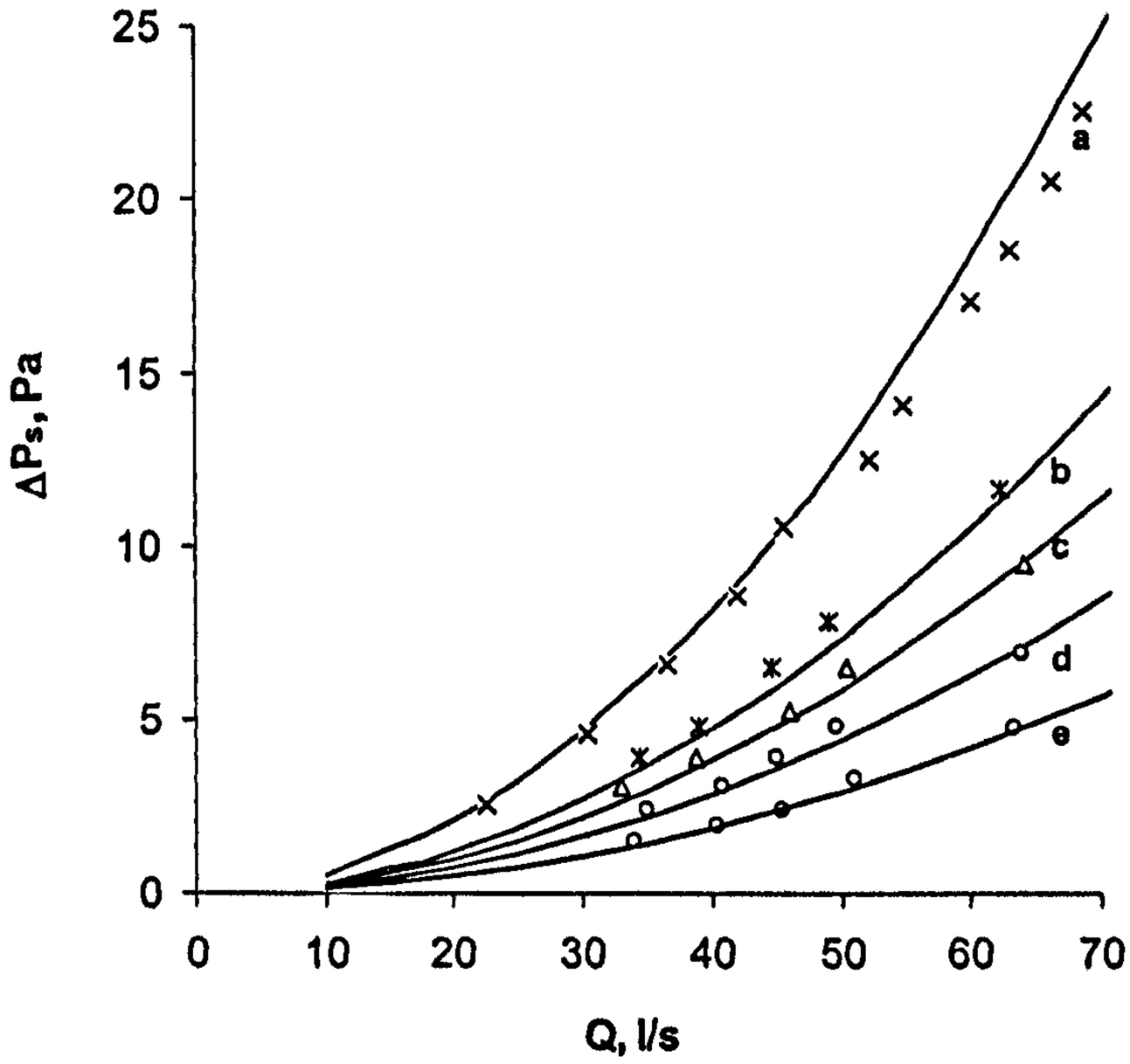

Fig. 3.31: measured and predicted ΔP_s-Q curves at 20 C with (a) L=5 m, Ext. = 80 %, (b) L=5 m, Ext. = 100 %, (c) L=4 m, Ext. = 80 %, (d) L=3 m, Ext. = 80 % and (e) L=2 m, Ext. = 80 %.

3.7 EFFECT OF "SLATE PACKING" ON ΔP_f-Q CHARACTERISTIC

The "slate packing" affects the system $\Delta P - Q$ characteristic. Thus flow rate – irradiance (Q – G) profiles are different for different slate types even if the same PV – fan – duct combination is used. Moreover, It is reported that, for pumping systems, the fan IV and ωV linear relationships change as the pressure across the pump changes (Hadj Arab, 2004). This leads to the conclusion that the speed of the fan and consequently its $\Delta P - Q$ characteristic may also be affected by the "slate packing" thus affecting the flow rate.

The effect of pressure on IV and ωV characteristics of fans was experimentally investigated in the apparatus in Fig. 3.19. Opening and closing the valve alters the pressure across the fan. Fixing the pressure at a desired value and varying the voltage (using a power supply), readings of current and speed for different voltages are obtained. However, as voltage is increased, pressure in the system also increases. By adjusting valve position every time voltage was increased, the pressure across the fan was maintained nearly constant. IV and ωV curves were obtained for different pressures across the fan. Results of ωV curves for Fan2 are shown in Fig. 3.32.

It is seen that, even though pressure is expected to affect speed, voltage and current individually, it has negligible effect on the ωV and IV characteristics of the fan. This effect is more significant in pumping systems because of the associated higher system pressures (meters of water rather than centimetres). The model can thus be simplified by neglecting the pressure dependence of IV and ωV characteristics. The "slate packing" will have an effect on the system's ΔP-Q characteristic and so in order to account for this effect, the system's curve must be experimentally measured in the roof section. This curve can then be incorporated into the model. This will be discussed in chapter 4 and 7.

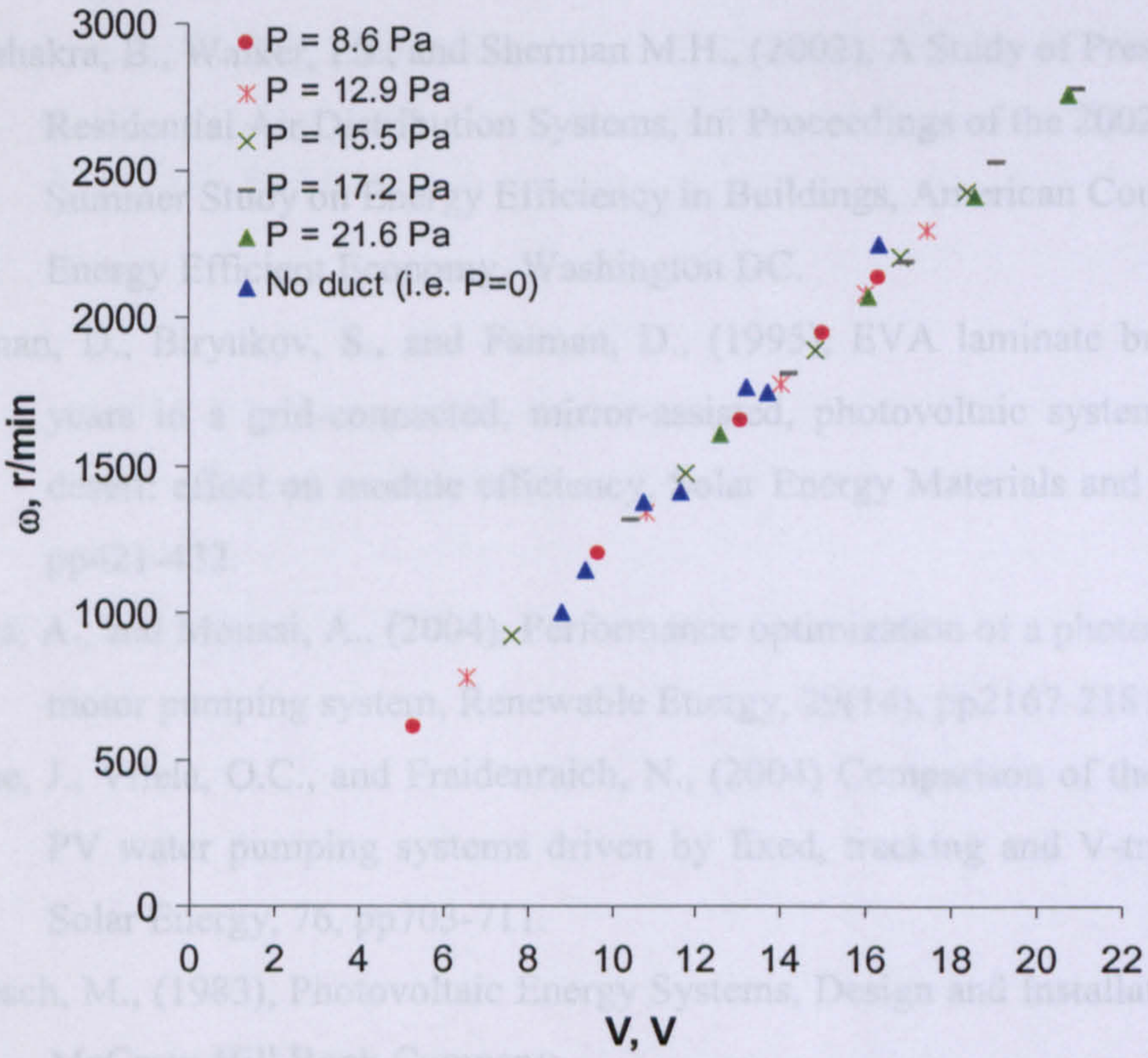

Fig. 3.32: Effect of slate "packing" on fan ΔP-Q Characteristic.

3.8 ERROR ANALYSIS

Since the component-specific constants used in the model are determined experimentally, the predicted flow rate is expected to have some error. Sources of error include the determination of the PV module reference curve, the coefficients in the fan IV, ωV and ΔP_f-Q characteristics and the roughness coefficient of the duct. Considering all sources of error in measurements, the model predicts the PV IV characteristic with an error of (4 to 9 %), the rotational speed of the fan with a maximum error of 8 % and the flow rate with a maximum error of 12 %. This high value of error is basically attributed to the significant error in measuring the flow rate in the system.

REFERENCES

Abushakra, B., Walker, I.S., and Sherman M.H., (2002), A Study of Pressure Losses in Residential Air Distribution Systems, In: Proceedings of the 2002 ACEEE Summer Study on Energy Efficiency in Buildings, American Council for an Energy Efficient Economy, Washington DC.

Berman, D., Biryukov, S., and Faiman, D., (1995), EVA laminate browning after 5 years in a grid-connected, mirror-assisted, photovoltaic system in the Negev desert: effect on module efficiency, Solar Energy Materials and Solar Cells, 36, pp421-432.

Betka, A., and Moussi, A., (2004), Performance optimization of a photovoltaic induction motor pumping system, Renewable Energy, 29(14), pp2167-2181

Bione, J., Vilela, O.C., and Fraidenraich, N., (2004) Comparison of the performance of PV water pumping systems driven by fixed, tracking and V-trough g enerators, Solar Energy, 76, pp703-711.

Buresch, M., (1983), Photovoltaic Energy Systems, Design and Installation, New York, McGraw-Hill Book Company.

Cromer, C., (1983), Sizing and matching a photovoltaic circulation system with a solar domestic hot water system, FSEC-PF-29-83, Florida Solar Energy Center, Cocoa, Florida.

Duffie, J.A., and Beckman, W.A., (1991), Solar Engineering of Thermal Processes, 2nd edn, New York, Wiley Interscience.

Eckstein, J., Townsend, T., Beckman, W.A., and Duffie, J.A., (1990), Photovoltaic powered energy systems, Proceedings of the American Solar Energy Society, Austin, Texas, USA.

Hadj Arab, A., Chenlo, F., and Benghanem, B., (2004), Loss-f-load probability of photovoltaic water pumping systems, Solar Energy, 76, pp713-723.

Jafar, M., (2000), A model for small-scale photovoltaic solar water pumping, Renewable Energy 2000,19:85-90.

Kipp & Zonen Incorporated, (2004), Kipp & Zonen Instruction Manual, CM3 Pyranometer, Delft, Holland.

McCabe, W., Smith, J., and Harriot, P., (1985), Unit Operations of Chemical Engineering, 4th ed., New York, McGraw-Hill.

Meyer, C.J., and Kroger, D.G., (1998), Plenum chamber flow losses in forced draught air-cooled heat exchangers, Applied Thermal Engineering, 18, pp875-93.

Muneer, T, Kubie, J, and Grassie, T., (2003), Heat Transfer-A Problem Solving Approach, London: Taylor & Francis.

Osborne, W.C., (1977), Fans, 2nd ed. Oxford: Pergamon, 1977.

Perry, R.H., and Green D.W., (1997), Perry's Chemical Engineers' Handbook, 7th ed., New York, McGraw-Hill.

4. MODEL VALIDATION AND PERFORMANCE SIMULATIONS

4.1 INTRODUCTION

In Chapter 2 the basic characteristic equations for each of the main components of the present system were given. In chapter 3, these equations were manipulated, and the mathematical model for the system developed. The parameters necessary for predicting the individual performance of each of the components were experimentally determined. In addition, the individual models for each of the components have been tested and validated. Through the consideration of the above models, chapter 4 focuses on developing a computer program necessary for modelling system flow rate.

A flow chart of the model is shown in Fig. 4.1. For any given irradiance and PV module temperature, and starting from the reference conditions of the PV module, the model predicts the PV module's electrical output. This, when solved simultaneously with the fan's electrical characteristic, calculates the operational voltage and rotational speed of the fan. The fan ΔP-Q characteristic is determined at this calculated speed while that of the fan-duct system as a whole is evaluated at the given duct properties (length, diameter and degree of extension). System flow rate is then determined by solving the fan and system ΔP-Q characteristics simultaneously. Using the equations presented in chapter 3, and the experimentally determined reference conditions and parameters, a program was written in Visual Basic for Applications (VBA) to calculate system flow rate. The model was validated through comparison with experimental measurements.

4.2 THE FAN OPERATIONAL POINT

Figure 4.2 shows fan and PV IV characteristics as generated by the program. In this section the program for calculating the fan operational voltage, current and rotational speed is presented and discussed. The values, as predicted from this code for certain PV-fan combinations, are then compared to measurements of voltage and speed obtained at preset conditions of irradiance and ambient temperature.

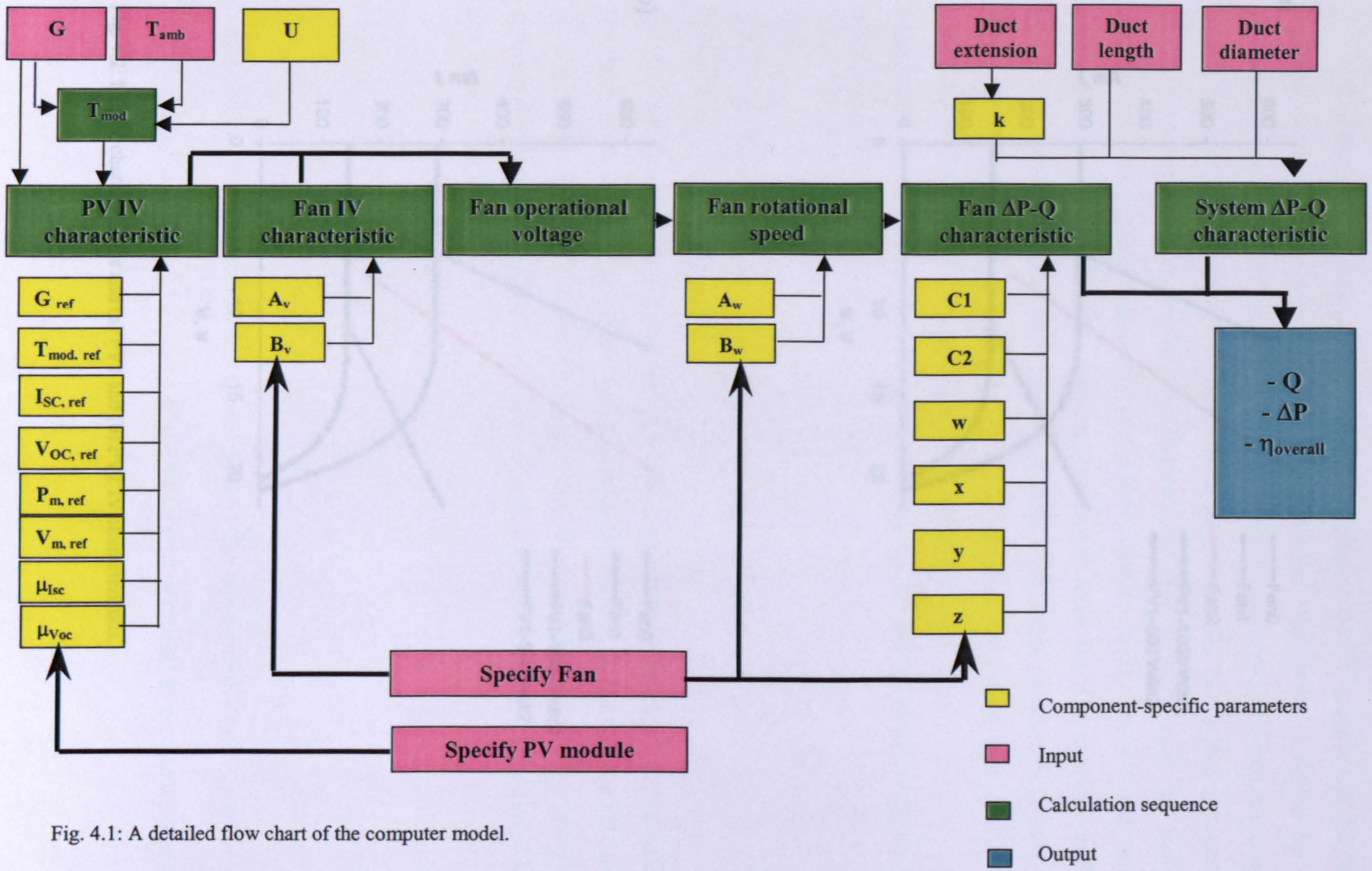

Fig. 4.1: A detailed flow chart of the computer model.

(a)

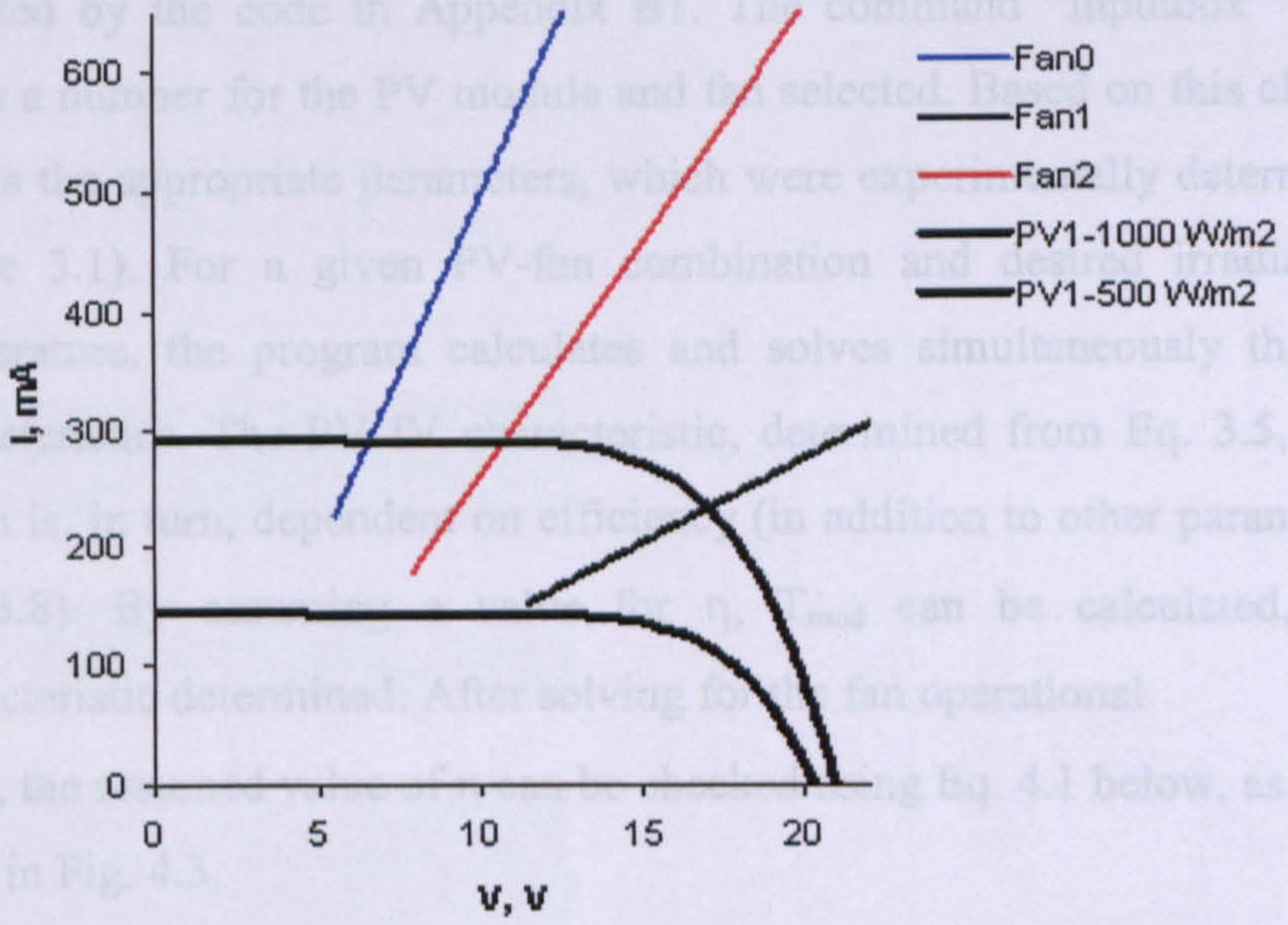

(b)

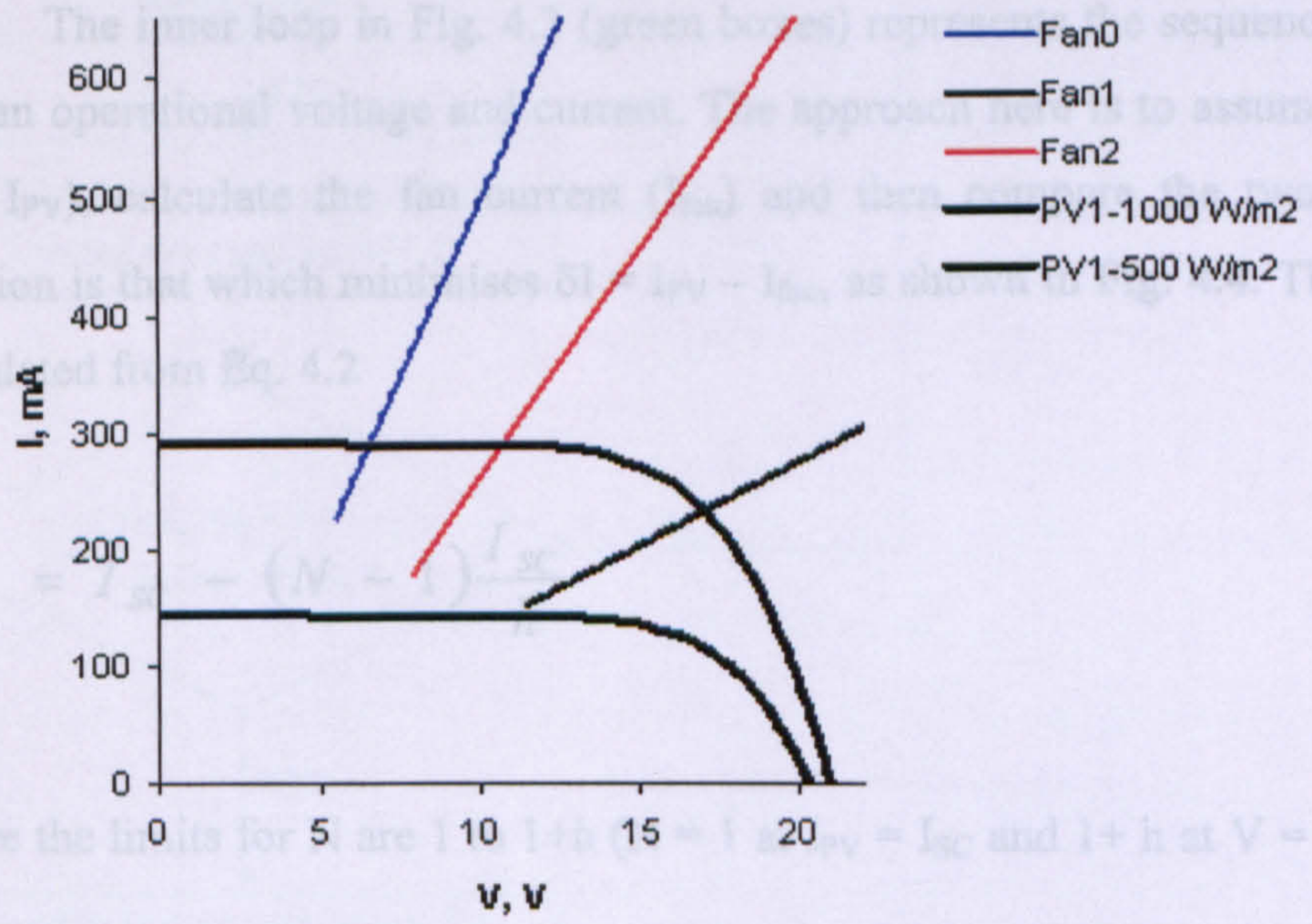

Fig. 4.2: Fan IV characteristics and (a) PV1 and (b) PV2 IV characteristics.

4.2.1 Computer program

The first step in running the program is to choose the PV module and the fan as depicted by the code in Appendix B1. The command "Inputbox" is where the user enters a number for the PV module and fan selected. Based on this choice, the program selects the appropriate parameters, which were experimentally determined in chapter 3 (Table 3.1). For a given PV-fan combination and desired irradiance and ambient temperature, the program calculates and solves simultaneously the PV and fan IV characteristics. The PV IV characteristic, determined from Eq. 3.5, depends on T_{mod}, which is, in turn, dependent on efficiency (in addition to other parameters as shown by Eq. 3.8). By assuming a value for η, T_{mod} can be calculated, and the PV IV characteristic determined. After solving for the fan operational

point, the assumed value of η can be checked using Eq. 4.1 below, as shown by the flow chart in Fig. 4.3.

$$\eta_c = \frac{V \cdot I}{G \cdot a} \tag{4.1}$$

The inner loop in Fig. 4.3 (green boxes) represents the sequence for calculating the fan operational voltage and current. The approach here is to assume the PV current ($I = I_{PV}$), calculate the fan current (I_{fan}) and then compare the two. An acceptable solution is that which minimises $\delta I = I_{PV} - I_{fan}$, as shown in Fig. 4.4. The value of I_{PV} is calculated from Eq. 4.2

$$I_{PV} = I_{SC} - (N - 1)\frac{I_{SC}}{h} \tag{4.2}$$

where the limits for N are 1 to 1+h ($N = 1$ at $I_{PV} = I_{SC}$ and $1+h$ at $V = V_{OC}$) and $\frac{I_{SC}}{h}$ is a fixed step in current. The choice of the value of h is crucial to the iteration process as detailed in Textbox 4.1.

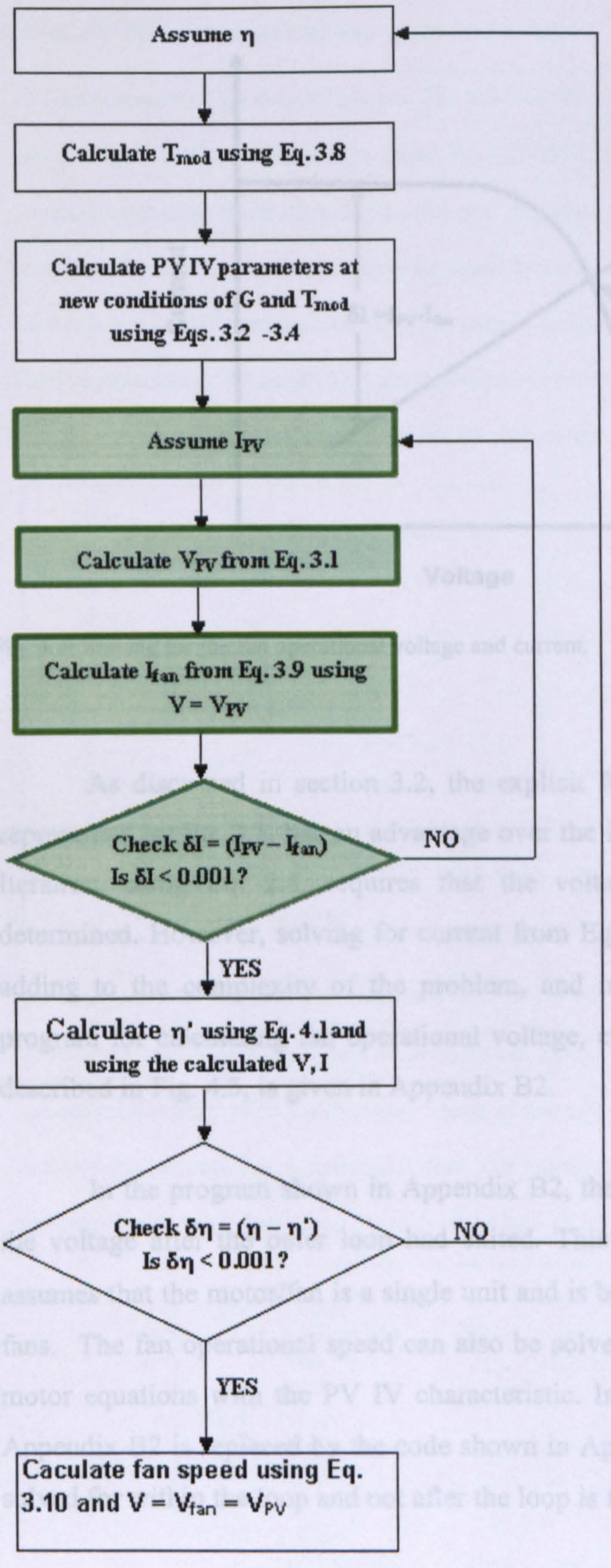

Fig. 4.3: Flow chart for determination of the fan operational voltage.

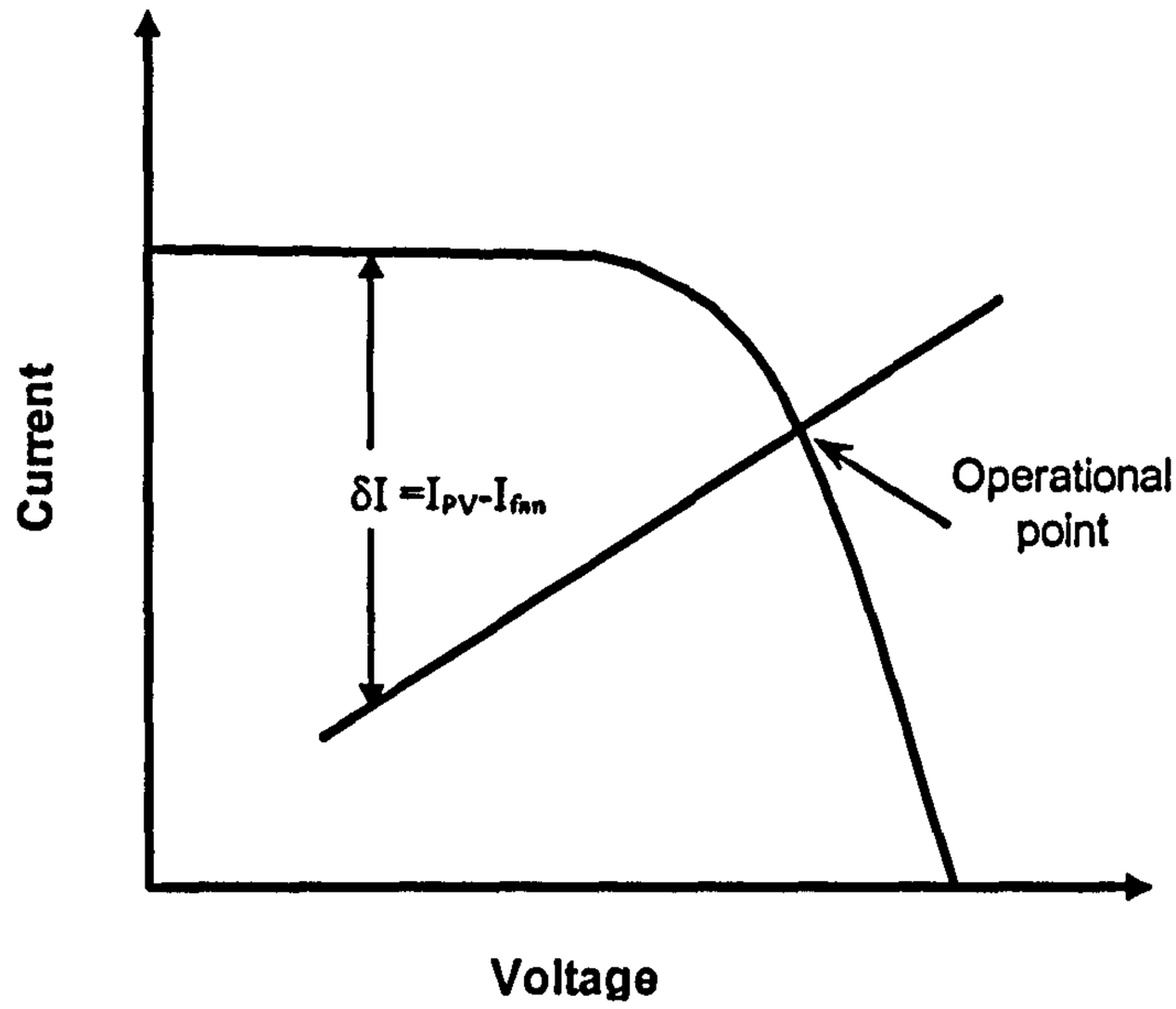

Fig. 4.4: Solving for the fan operational voltage and current.

As discussed in section 3.2, the explicit form of the PV IV characteristic, as represented by Eq. 3.1, has an advantage over the implicit form represented by Eq. 2.4. Iteration, using Eq. 2.4, requires that the voltage is assumed and the current is determined. However, solving for current from Eq. 2.4 requires another iteration loop, adding to the complexity of the problem, and increasing the calculation time. The program for calculating fan operational voltage, current, and speed, using the method described in Fig. 4.3, is given in Appendix B2.

In the program shown in Appendix B2, the fan speed is obtained directly from the voltage after the outer loop had exited. This method, as discussed in chapter 3, assumes that the motor/fan is a single unit and is based on the ωV characteristics of the fans. The fan operational speed can also be solved for within the loop by solving the motor equations with the PV IV characteristic. In this case, the inner loop shown in Appendix B2 is replaced by the code shown in Appendix B3. In this case, fan speed is solved for within the loop and not after the loop is finished.

Textbox 4.1: Selection of iteration step values for Eq. 4.2.

"h" is the inverse of the step of iteration. The value of "h" affects the accuracy of the iteration process significantly. It is desired to reduce the value of h as much as possible in order to reduce computational time. However, a small value of h (say 10000) at low irradiances can sometime lead to misleading results. This is clear from the figure below where it can be seen that if, for example for Fan0, $h = 1 \times 10^6$ then the predicted flow rates at irradiances below 200 W/m^2 are not accurate. Fan0 requires larger values of h (i.e. smaller steps of iteration) because as can be seen from Fig. 4.2, the intersection between the PV and fan IV characteristics is usually at $I = I_{SC}$.

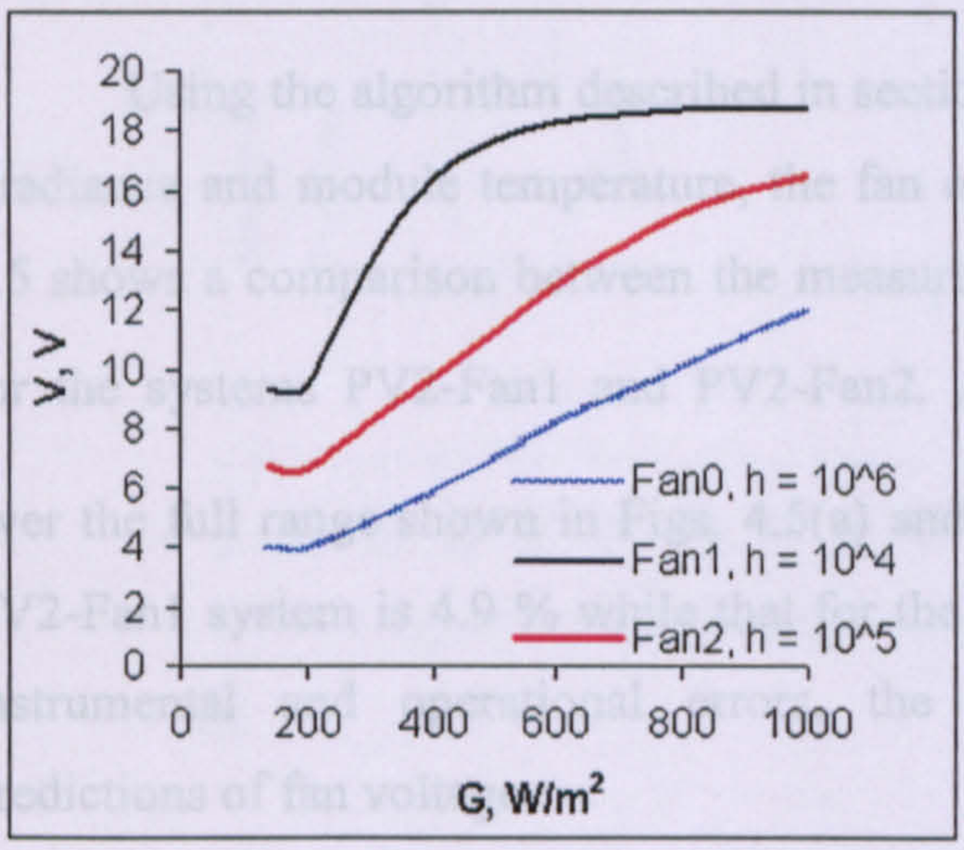

It is determined by trial and error than an h value of 1×10^8 for Fan0, 1×10^5 for Fan1 and 1×10^7 for Fan2 are satisfactory to produce accurate results. However, these values do not have to be maintained throughout the full irradiance range, as this will, especially for a large dataset, considerably increase the computational time. The following conditions, which will lead to accurate results, were determined for each of the fans by trial and error

```
If fan = 0 Then
        If G <= 500     Then    h = 1 × 10^8
        Else                    h = 1 × 10^4

If fan = 1 Then
        If G <= 300     Then    h = 1 × 10^5
        Else                    h = 1 × 10^4

If fan = 2 Then
        If G <= 200     Then    h = 1 × 10^7
        Else                    h = 1 × 10^4
```

4.2.2 Validation

Measurements of irradiance, ambient temperature, and fan voltage were obtained for each of the fans with the10 W_p PV module (PV2). Measurements were recorded with the outlet of the fan open to the atmosphere (i.e. no duct connected). Typical readings are shown for the systems PV2-Fan1 and PV2-Fan2 in Fig. 4.5. It is seen that the operational voltage closely follows the irradiance profile for both days of measurement and that it is, as expected, more affected by irradiance than PV module temperature.

Using the algorithm described in section 4.2.1, and using the measured values of irradiance and module temperature, the fan operational voltage was calculated. Figure 4.5 shows a comparison between the measured and predicted voltage profiles obtained for the systems PV2-Fan1 and PV2-Fan2. Average error ($100 \times \frac{predicted - measured}{measured}$, over the full range shown in Figs. 4.5(a) and 4.5(b)) for predicting the voltage for the PV2-Fan1 system is 4.9 % while that for the PV2- Fan2 system is 7.7 %. Considering instrumental and operational errors, the algorithm provides relatively accurate predictions of fan voltage.

The measured and predicted efficiency profiles for both systems for the days of measurement are shown in Fig. 4.6. Depending on the radiation available, the efficiency of the PV-fan combinations can reach up to 13 %. A lower efficiency is an indication of a lower utilisation of P_m and vice versa. Simulations of efficiency-irradiance profile are discussed in section 4.4.2.

Using the VBA program, voltage profiles are generated for different irradiances at a constant ambient temperature as shown in Fig. 4.7. It is seen that the voltage of Fan1 at high irradiances is more affected by temperature than is Fan2. This can be explained by reference to Fig. 4.2 where is it seen that a slight change in the PV module temperature affects the lower part of the PV IV characteristic where Fan1 is usually operating. It is thus expected that the effect of temperature on the voltage of Fan0 is negligible since the temperature effect on I_{SC} is very small.

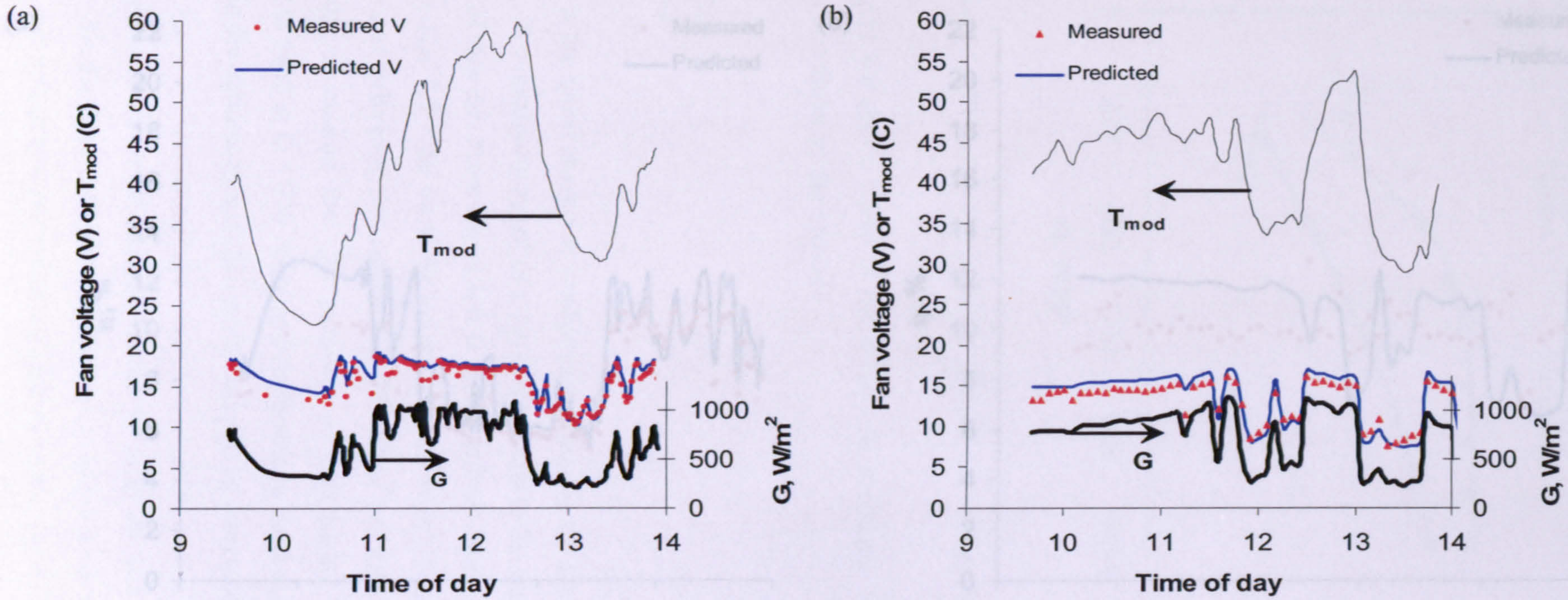

Fig. 4.5: Voltage, T_{mod} and irradiance profiles for (a) PV2-Fan1 and (b) PV2-Fan2 systems.

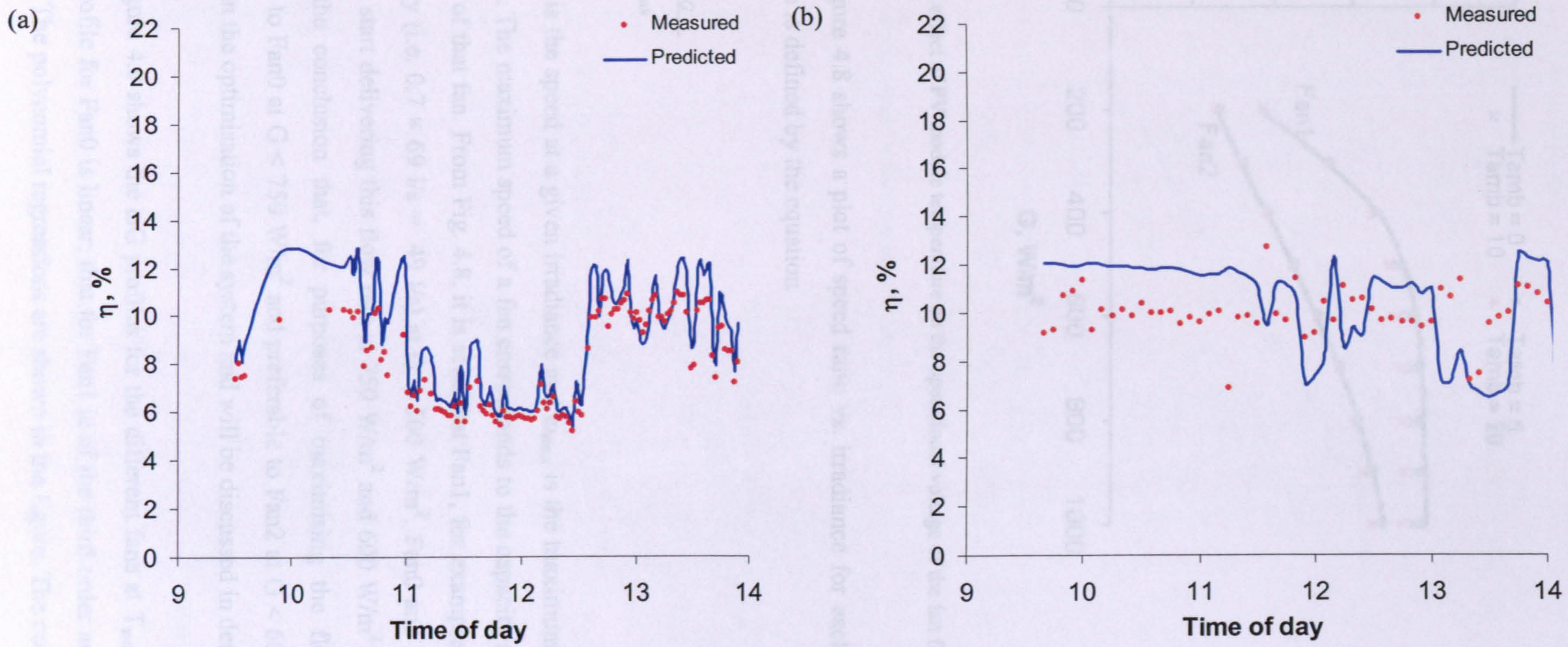

Fig. 4.6: Measured and predicted efficiency profiles for (a) PV2-Fan1 and (b) PV2-Fan2 systems.

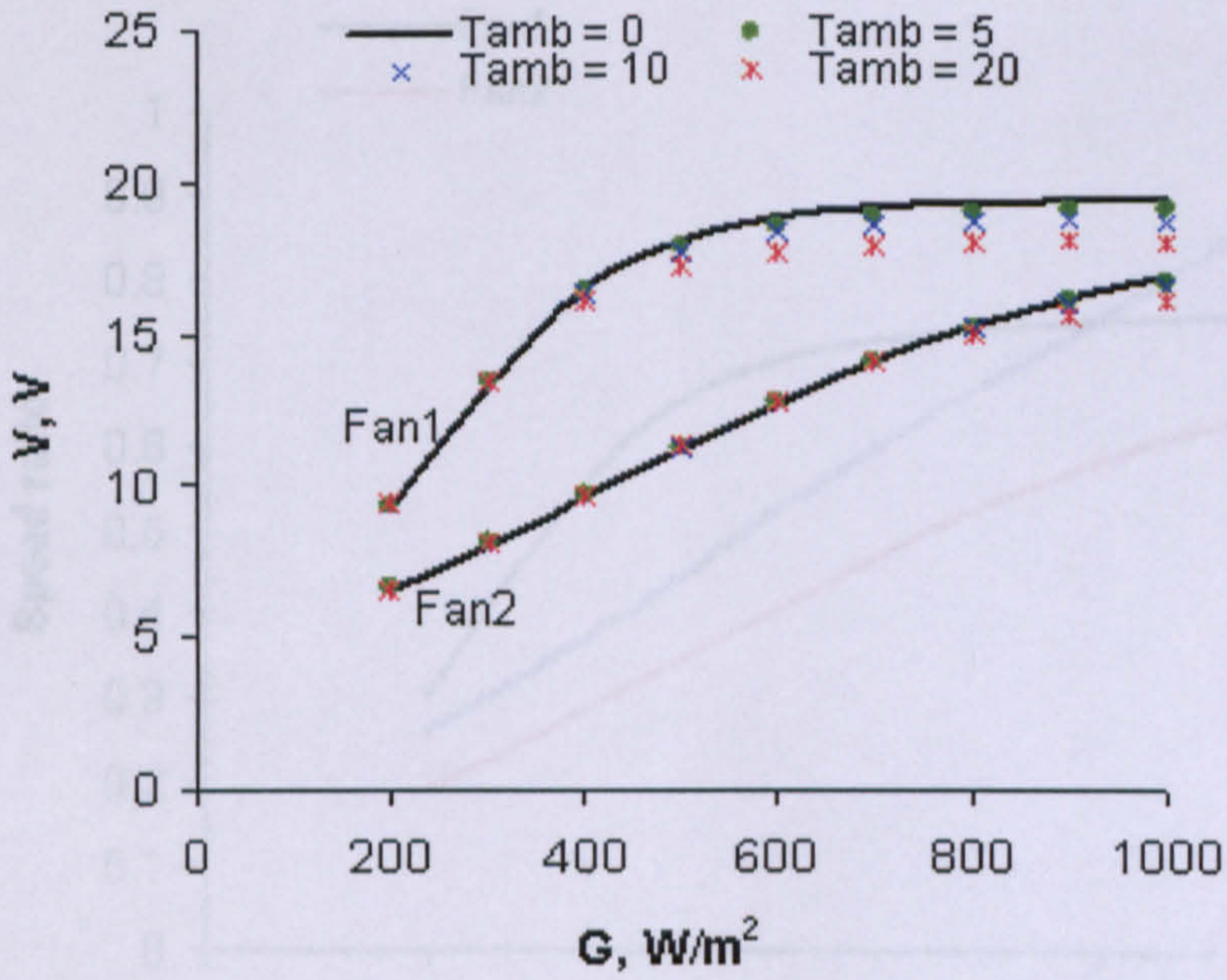

Fig. 4.7: The effect of PV module temperature on the operational voltage of the fan for Fan 1 and Fan2.

Figure 4.8 shows a plot of speed ratio vs. irradiance for each of the fans. The speed ratio is defined by the equation

$$r = \frac{\omega_G}{\omega_{max}} \tag{4.3}$$

where ω_G is the speed at a given irradiance and ω_{max} is the maximum speed achievable by the fan. The maximum speed of a fan corresponds to the capacity (i.e. the maximum flow rate) of that fan. From Fig. 4.8, it is seen that Fan1, for example, delivers 70 % of its capacity (i.e. 0.7 × 69 l/s = 49 l/s) at G = 500 W/m^2. Fan0 and fan2, on the other hand, will start delivering this flow rate at 750 W/m^2 and 600 W/m^2 respectively. This leads to the conclusion that, for purposes of maximising the flow rate, Fan1 is preferable to Fan0 at G < 750 W/m^2 and preferable to Fan2 at G < 600 Wm^2. This will be useful in the optimisation of the system and will be discussed in detail in chapter 6.

Figure 4.9 shows the ωG profiles for the different fans at T_{amb} = 5 C. It is seen that the profile for Fan0 is linear; that for Fan1 is of the third order and that for Fan2 is quadratic. The polynomial regressions are shown in the figure. The coefficients of these

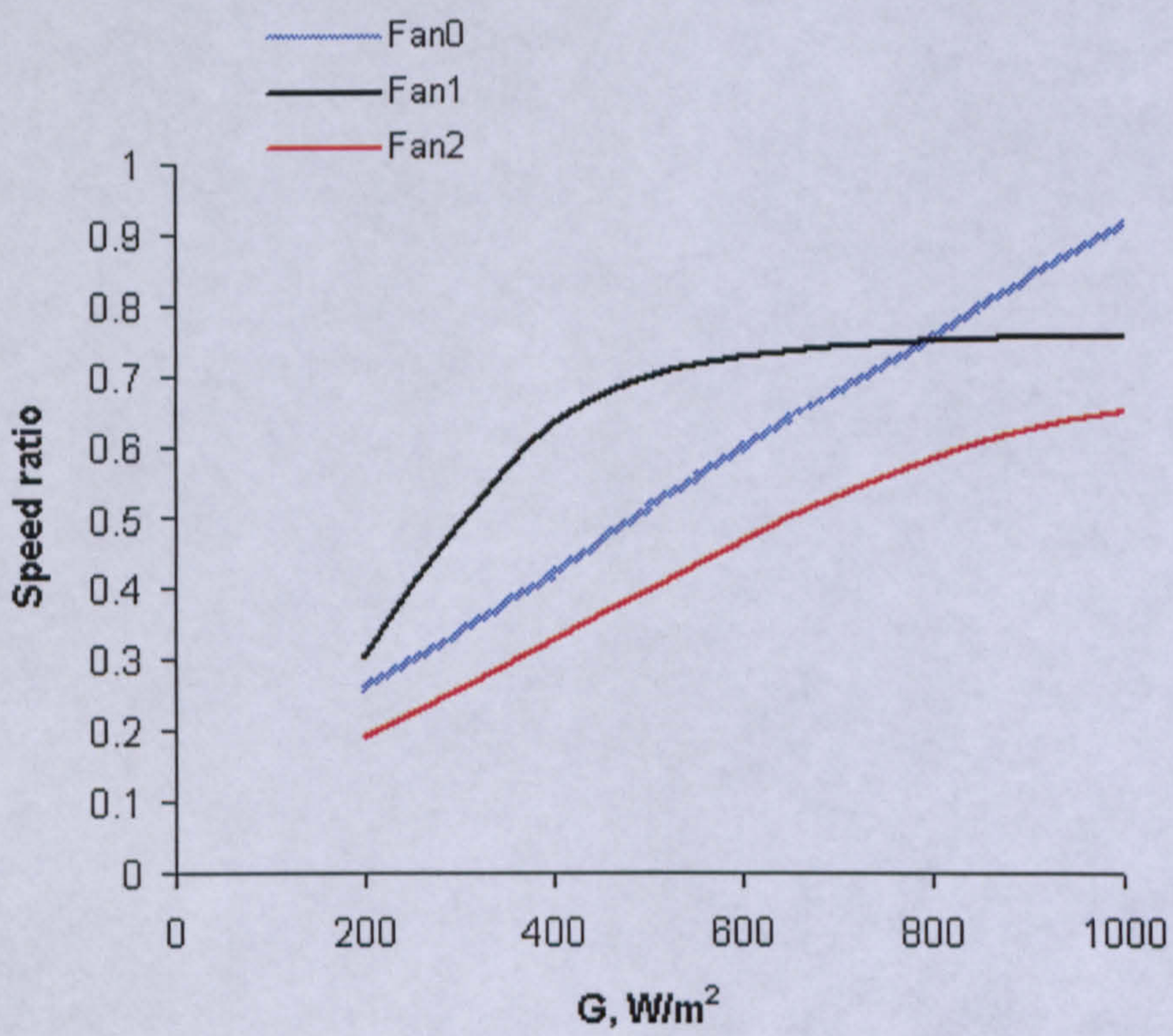

Fig. 4.8: Speed ratio (actual to maximum) vs. irradiance.

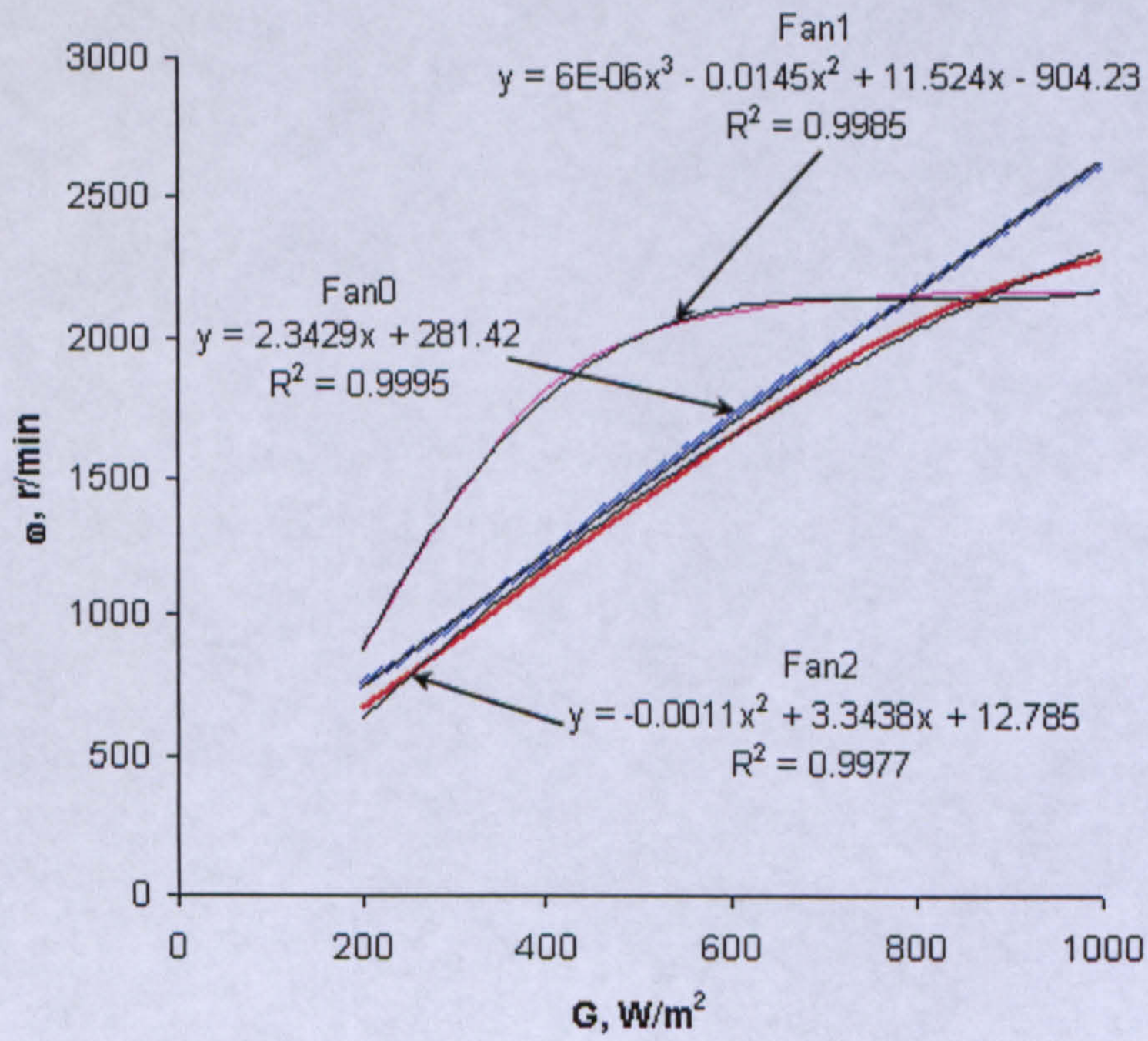

Fig. 4.9: Polynomial fitting of ωG profiles at T_{amb} = 5 C.

polynomials change if temperature changes. Temperature, however, has a pronounced effect in the case of Fan1 only as discussed earlier (Fig. 4.7). As a result, these regressions can be used for predicting speed directly from irradiance without having to iteratively solve for the fan's operational point. Even though, this approach, which has been, as discussed in chapter 2, used by other researchers (Jafar, 2000), will considerably save calculation time, it is specific for a given PV-fan combination. A more general approach is that which solves for the fan operational voltage and speed iteratively.

4.3 FLOW RATE

4.3.1 Computer program

The program thus far described, calculates fan speed. For this speed, the ΔP_f-Q characteristic can be evaluated from the measured reference curve (discussed in sections 3.2.4.2 and 3.5.4). The flow rate in the system is obtained by solving the two non-linear ΔP-Q characteristics shown in Fig. 2.10 simultaneously. The fan characteristic is obtained at the predetermined speed and measured air temperature and atmospheric pressure. The two latter quantities have negligible effect on air properties (At 1 atm, a change of temperature from 5 to 25 C will change density from 1.26 to 1.18 kg/m^3 while a 30 mm Hg decrease in atmospheric pressure at 5 C, changes density from 1.26 to 1.21 kg/m^3) and consequently on the ΔP_f-Q characteristic. Nevertheless, for generality and accuracy purposes, their effect will be accounted for in the current work. As discussed in sections 2.4.4 and 3.2.5, the ΔP_S-Q characteristic can be defined by a simple quadratic equation. The quadratic system characteristic is obtained for the specified duct properties and is also a function of air properties.

Using the reference parameters C_1 and C_2 and the fan specific parameters w, x, y, z, as in section 3.5.4, the fan ΔP-Q curve can be determined. The relevant section of the program for determining the ΔP_f-Q characteristic is shown in Appendix B4. Notice that the program here starts with a request for entering fan speed and air temperature in the duct. In the complete program, however, the speed of the fan is obtained according to the code in section 4.2.

4.3.1.1 Effective duct length

In practical application of the present system, where the duct will generally extend from the fan box downwards (section 1.4), the degree of extension is not fixed. An exact k value is not obtainable. The three methods described in section 3.2.5 and in Fig. 3.2 apply for horizontal situations. Fortunately, any system characteristic can be translated into a corresponding horizontal situation. This is done as follows.

A ΔP_s-Q characteristic ($\Delta P_s = T_1 \cdot Q^2 + T_2 \cdot Q$) is measured in the roof section using a manometer (Fig 3.6). The static pressure is measured across the fan with two Pitot static tubes, one in the fan box and the other in the duct. The flow rate is measured at the duct outlet. A single point of (Q, ΔP_s) or (V, ΔP_s) is sufficient for generating the system curve. This will be discussed in detail in section 7.3.2.

Using the same duct diameter in the roof section and assuming a value for the degree of extension, an effective horizontal length of duct can be determined. Effective duct length (L_{eff}) is defined as the horizontal length of duct (at a given % extension and duct diameter), which has the same ΔP_s-Q curve as the one measured in the roof section. Alternatively, instead of determining an L_{eff}, the measured curve ($\Delta P_s = T_1 \cdot Q^2 + T_2 \cdot Q$) can be used directly (Appendix B5).

4.3.2 Validation of flow rate model

4.3.2.1 Methodology

Validation of the flow rate model was performed by comparing predicted performance with that measured for a roof section constructed at the School of Engineering at Napier University in Edinburgh. Predicted flow rates were based on measured values of irradiance, PV module temperatures and in-duct air temperatures. Since PV module temperature is measured directly, there is no need for efficiency iteration and so the code described in the previous section can be simplified by directly defining the PV module characteristic from G and T_{mod} measurements.

The roof section shown in Fig. 4.10(a) was constructed from interlocking concrete tiles. The interlocking type of the slates causes a minimal suction pressure at the inlet side of the fan and thus imposes negligible resistance to the flow rate of air coming through. 10-cm diameter holes were drilled in the sarking board underneath the slates (Fig. 4.10(b)) and a well-sealed fan box was constructed, (Fig. 4.10(b) and 4.10(c)). The fan-duct system was installed in the box (Fig. 4.10(c)) and connected to the 10 W_p PV module (PV2).

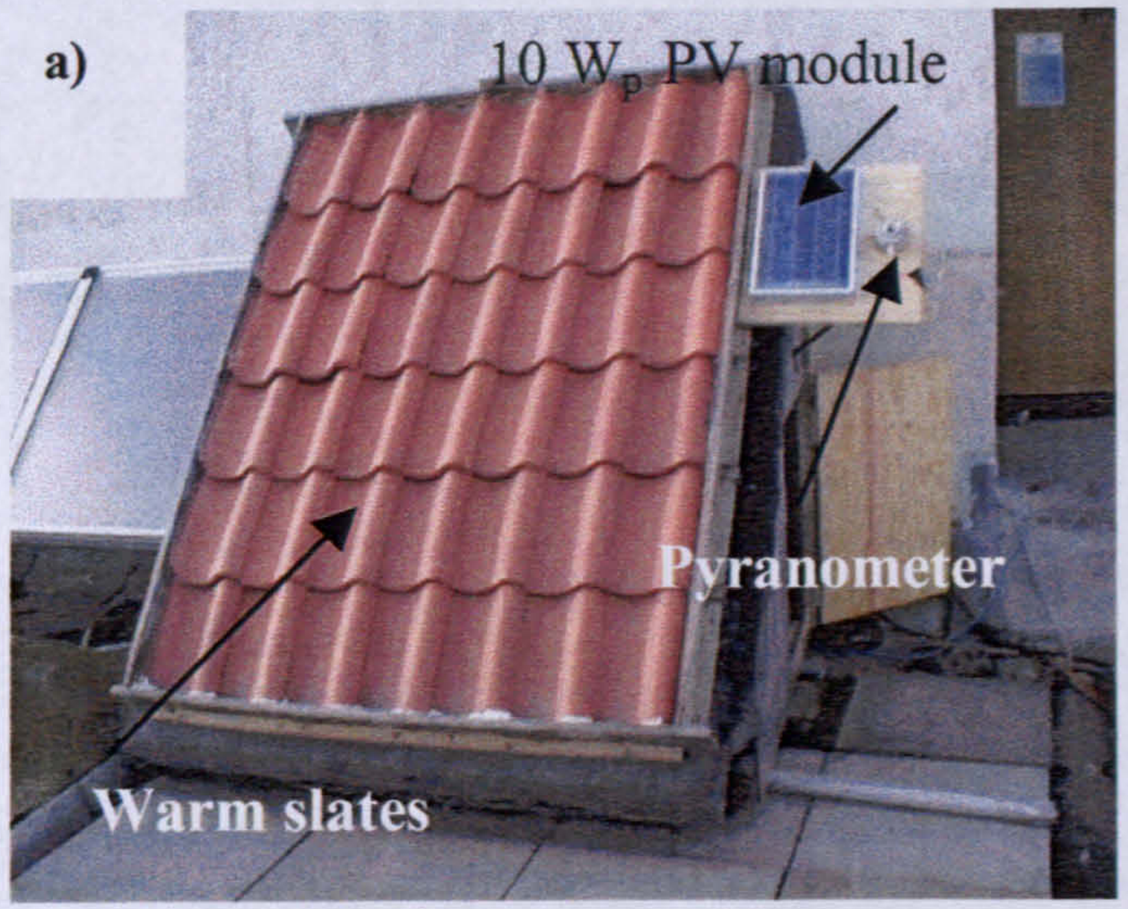

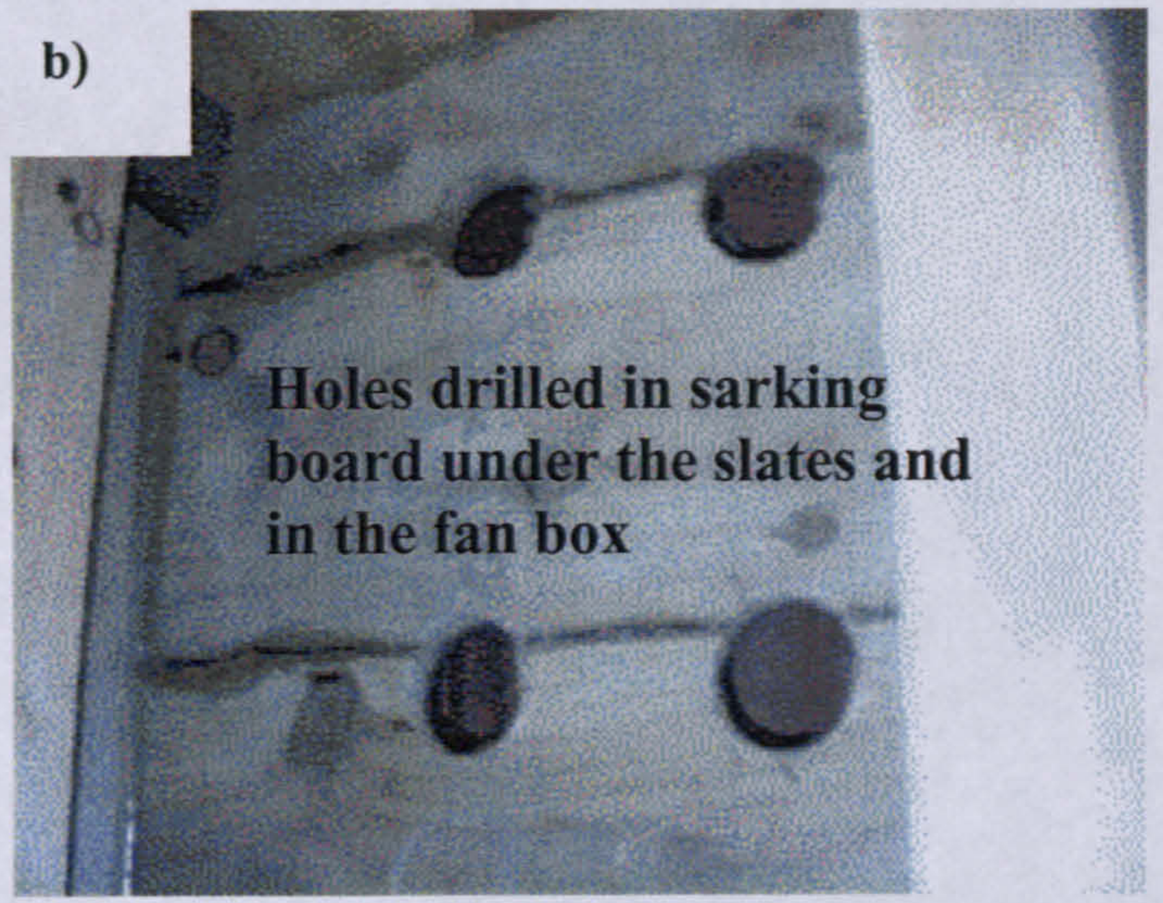

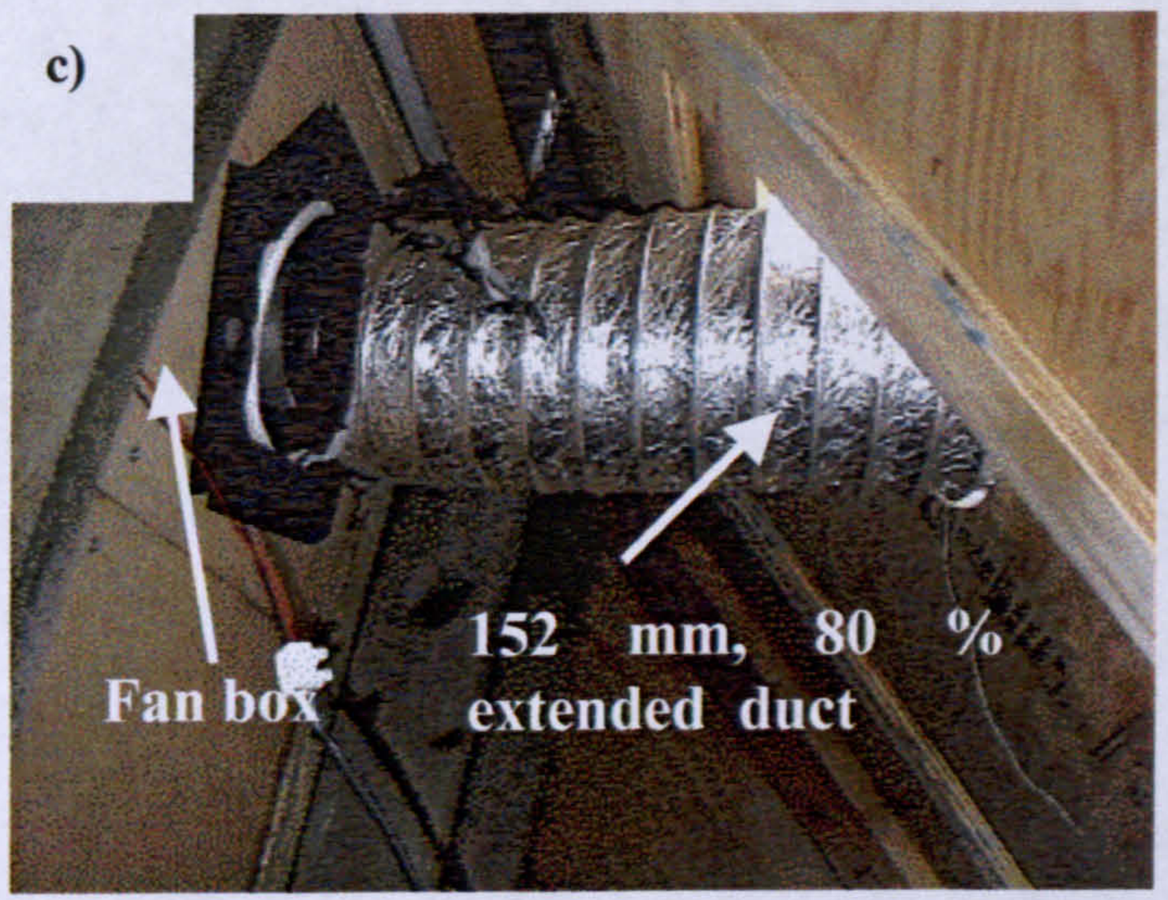

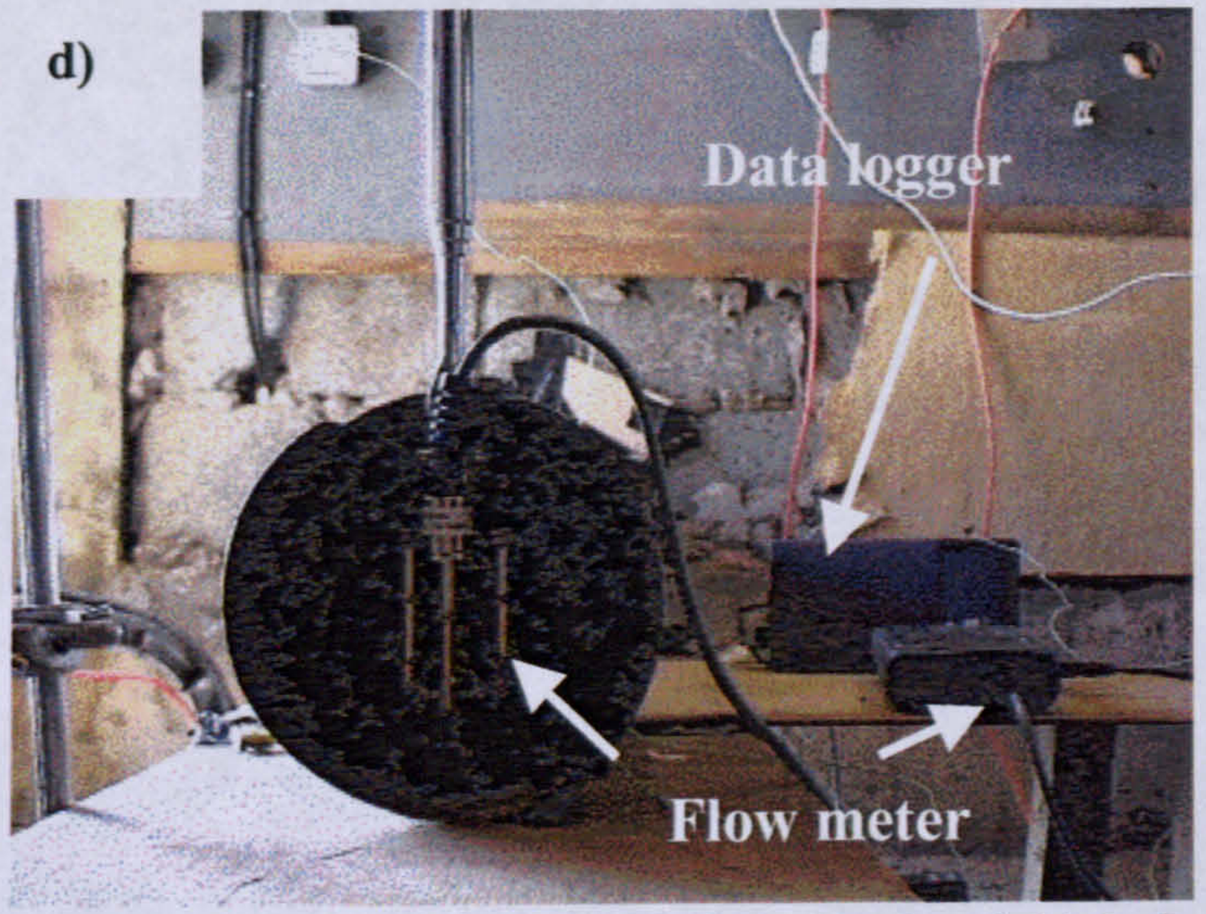

Fig. 4.10: Tested roof section: (a) roof section, PV module, and pyranometer all in the same plane, (b) 10-cm holes drilled in the sarking board, (c) the fan and duct at the outlet of the fan box, (d) flow rate measurement at duct outlet.

Measurements of G, T_{mod}, T_{air}, and Q were taken for periods of constant irradiance to ensure stability of flow rate readings corresponding to that irradiance.

Irradiance was measured with an accuracy of 3 % using a Kipp and Zonen pyranometer (Fig. 3.3) placed in the same plane with the PV module and roof tiles, and directly connected to a data logger. Incidence angles were calculated (Azimuth: -15°, Tilt: 45°, Latitude: 55.95°, Longitude: 3.3°) for the time and date of measurement and, whenever necessary, transmittance correction for irradiance falling on the PV module was applied (Duffie and Beckman, 1991). Two k-type thermocouples, one placed in the middle at the back of the PV module and the other placed at the outlet of the duct, were used for temperature measurements with an accuracy of ± 0.1 °C. The thermocouples were connected to the data logger and irradiance and temperature readings recorded for the duration of each flow rate measurement to ascertain the degree of temperature stability.

Flow rate measurements were carried out at the centre outlet of the duct as shown in Fig. 4.10(d) and were corrected for by the method described in section 3.3.6. The four systems outlined in Table 4.1 were tested. Two duct systems with different $L_{eff,\ 80\ \%\ \&\ 152\ mm}$ (where the subscript means that the effective duct length is evaluated for a duct diameter of 152 mm and extension of 80 %) were tested. The ΔP_s-Q curves were measured in the roof section.

Table 4.1: Systems tested for model validation.

	PV module	Fan	$L_{eff,\ 80\ \%\ \&\ 152\ mm}$, m
System 1	PV2	Fan1	8.5 ± 2
System 2	PV2	Fan2	8.5 ± 2
System 3	PV2	Fan1	11.5 ± 1.5
System 4	PV2	Fan2	11.5 ± 1.5

In order to measure the system curves, the pressure across the fan, the pressure in the fan box and the flow rate were recorded at different fan speeds (i.e. fan voltages). Pressure measurements were carried out with an accuracy of ± 0.5 Pa using the Airflow Developments inclined manometer mentioned above (section 3.3.5) and two Pitot static tubes: one placed in the fan box (through a side hole in the joist) and the other downstream from the fan.

The voltage and speed of the fan were manually altered using a Weir 4000 power supply. The two measured system curves are shown in Fig. 4.11 along with three simulated system curves for different lengths of duct. The effective length of duct was determined in Excel using the method of minimising the sum of residual errors.

(a)

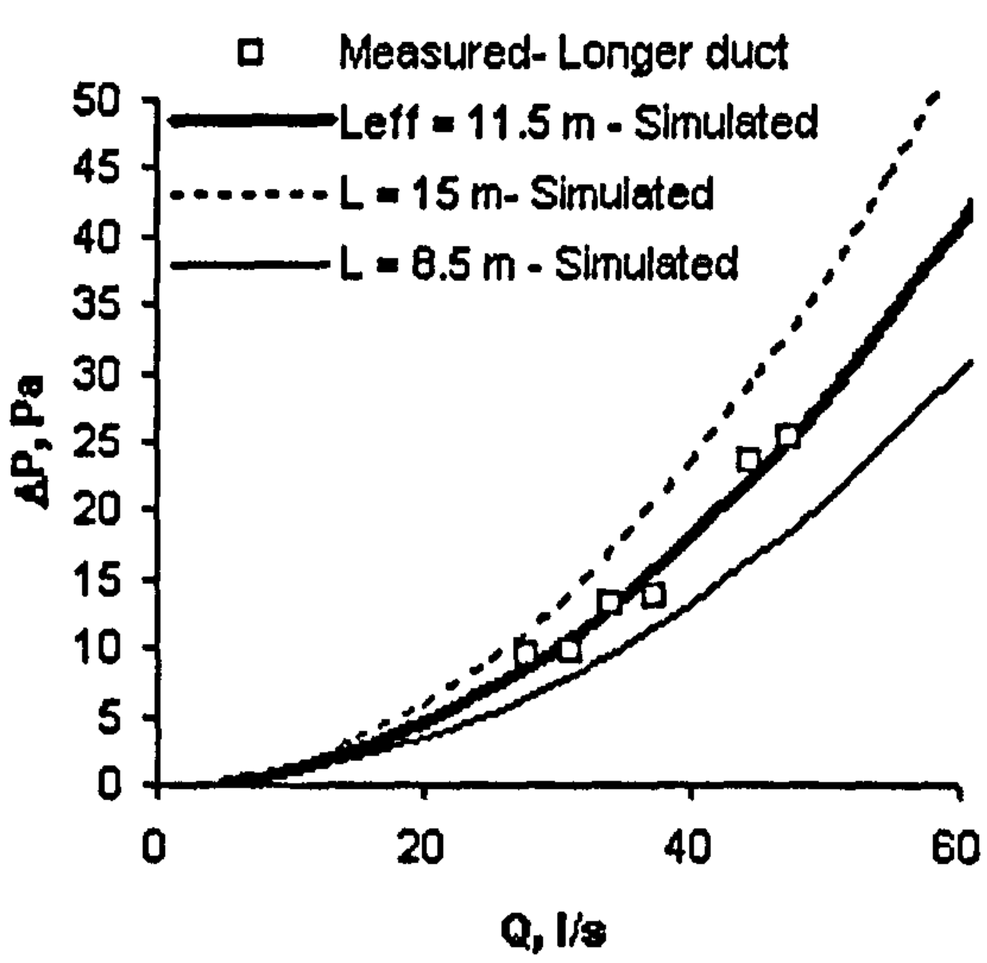

(b)

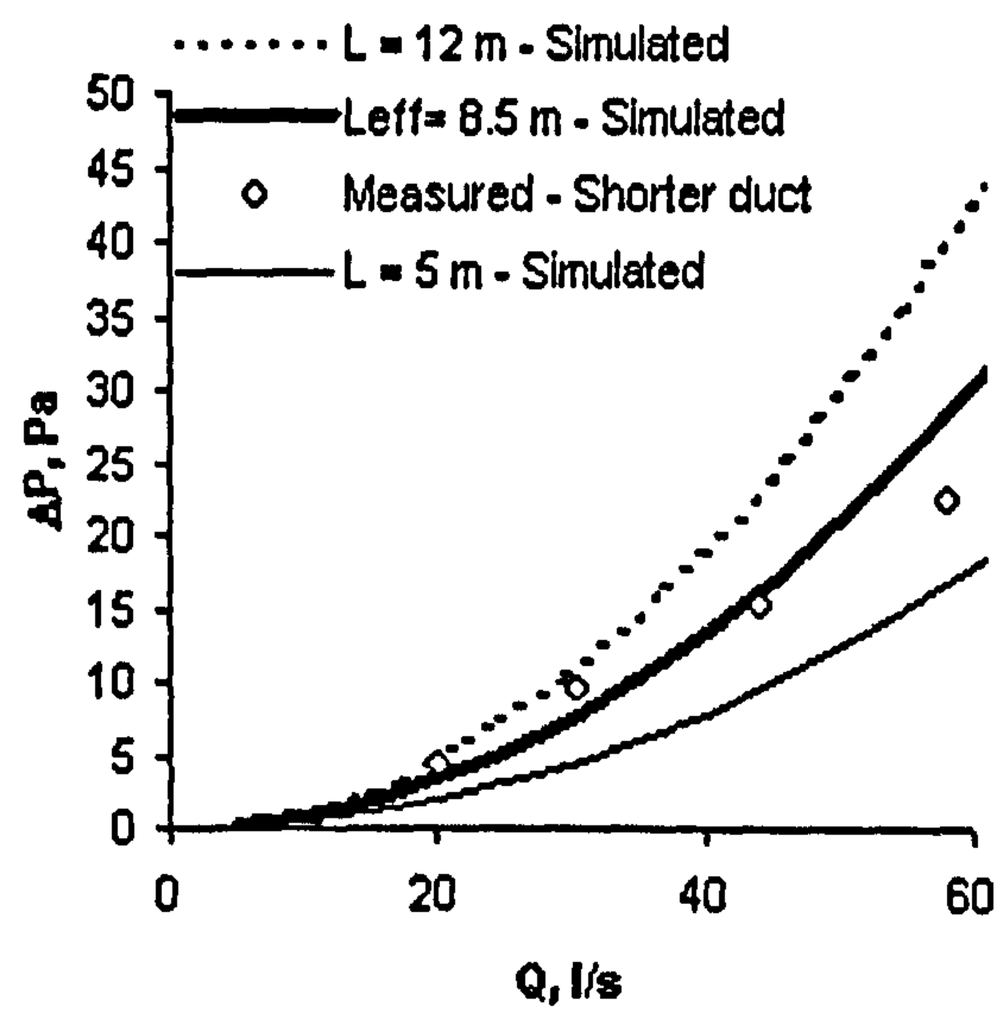

Fig. 4.11: Measured data in the roof section for (a) longer duct (L_{eff} = 11.5 m) and (b) shorter duct (L_{eff} = 8.5 m).

Considering errors in the measured ΔP_s-Q curve (i.e. errors in pressure and flow measurements), the effective duct lengths are also determined with errors as shown by the values in Table 4.1.

As mentioned above, the measured data shown in Fig. 4.11 (the single points) follows a quadratic trend passing through the origin. Thus, this quadratic equation can be solved simultaneously with the fan ΔP_f-Q characteristic for flow rate. The equation is $(\Delta P_s = 0.0036 \cdot Q^2 + 0.1783 \cdot Q)$ for the 8.5 m long duct and $(\Delta P_s = 0.0116 \cdot Q^2 - 0.0163 \cdot Q)$ for the 11.5 m long duct.

A program was written to calculate flow rate for the measurements obtained in the roof section shown in Fig. 4.10. The flow rate is solved for in a similar fashion to that used for solving the fan operational point. A value of (Q_{ref}) is assumed, ΔP_f is calculated as shown by the code in Appendix B4 and ΔP_s is calculated using the code in Appendix B5 either using predetermined L_{eff} values or by directly using the two quadratic equations given above. An acceptable solution is that which minimises the change in $\Delta P = (\Delta P_f - \Delta P_s)$ as shown in Fig. 4.12.

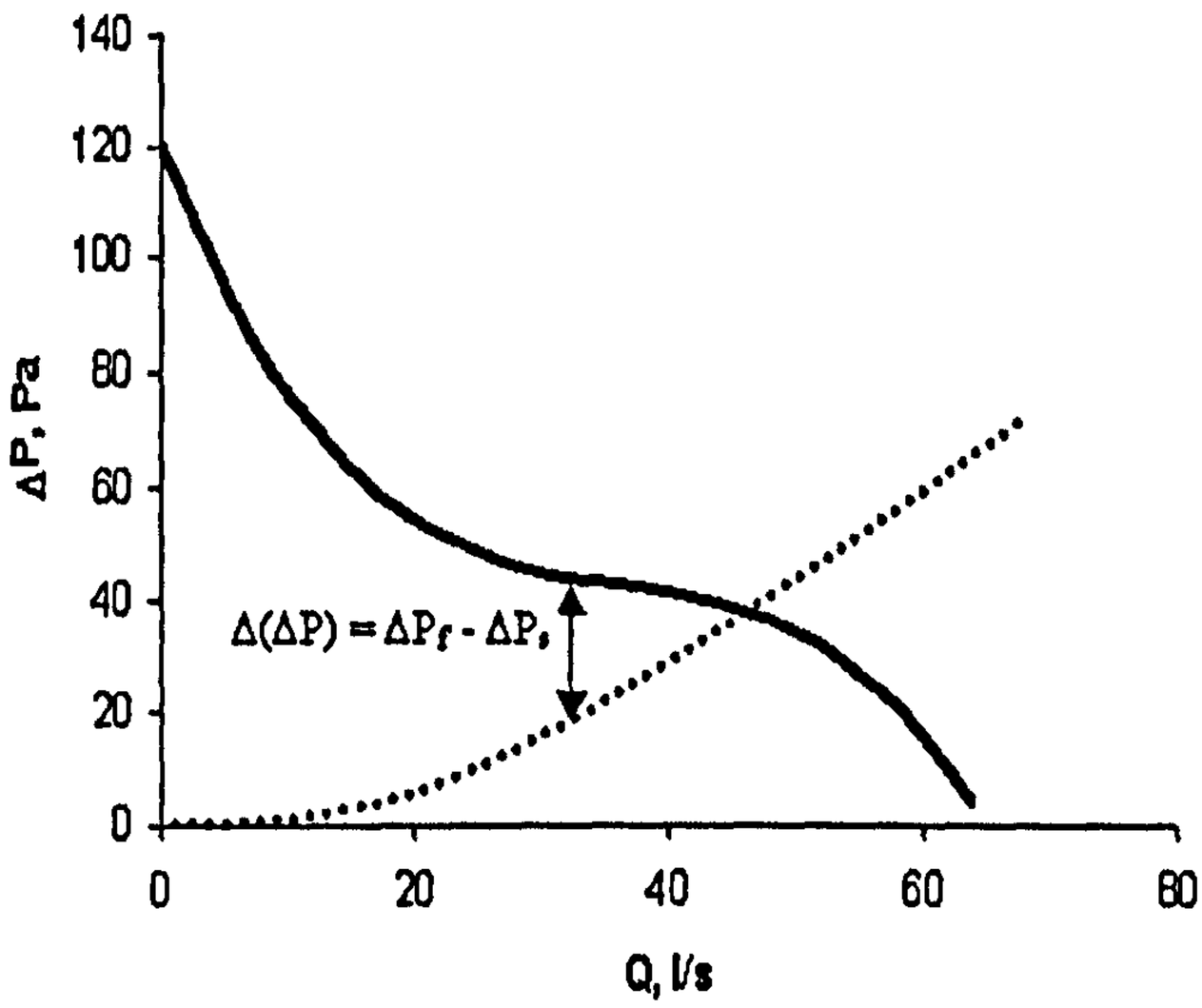

Fig. 4.12: Solving for system flow rate.

4.3.2.2 Results

Appendix B6 outlines the program for determining system flow rate. The program was run for all the measurements described above. The values obtained by the program were then compared to measurements. The results are shown in Fig. 4.13. The solid line with a slope of 0.9873 and a coefficient of determination (R^2) of 0.9417

represents the best-fit line for all data points. The predicted values shown in the figure are within 10 % of measured flow rates.

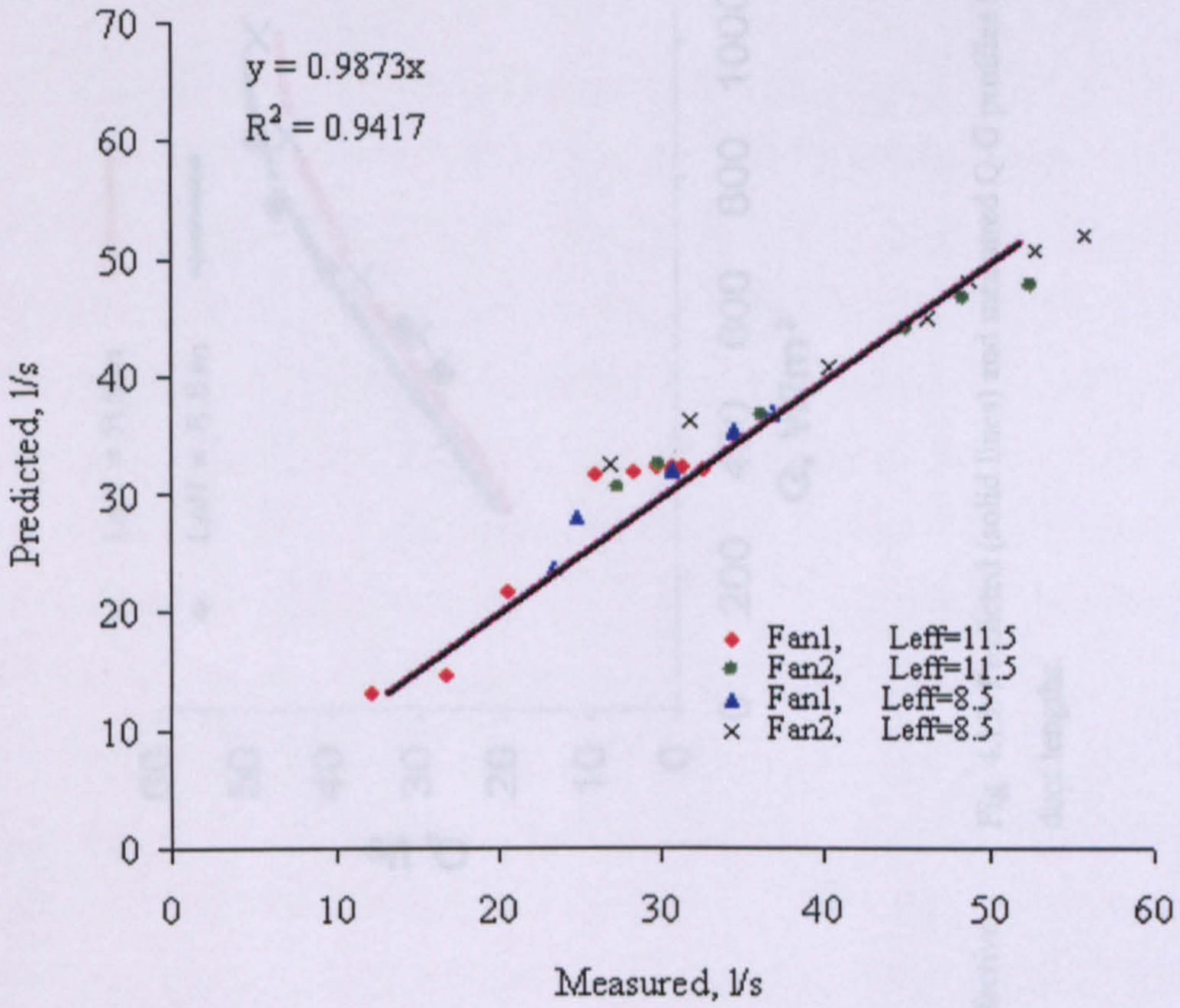

Fig. 4.13: Predicted vs. measured flow rates for the four systems tested.

For comparison purposes, each of Figs. 4.14 to 4.17 shows flow rate vs. irradiance (Q-G) profiles for two of the four systems. Considering experimental sources of error inherited by the model and those attached to the measured flow rate, there is good agreement between measurements and predicted values.

As seen from Figs. 4.14 and 4.15, for a given level of irradiance, a higher flow rate developed with a shorter length of duct. This is expected because for shorter lengths, the system is working against less resistance to flow.

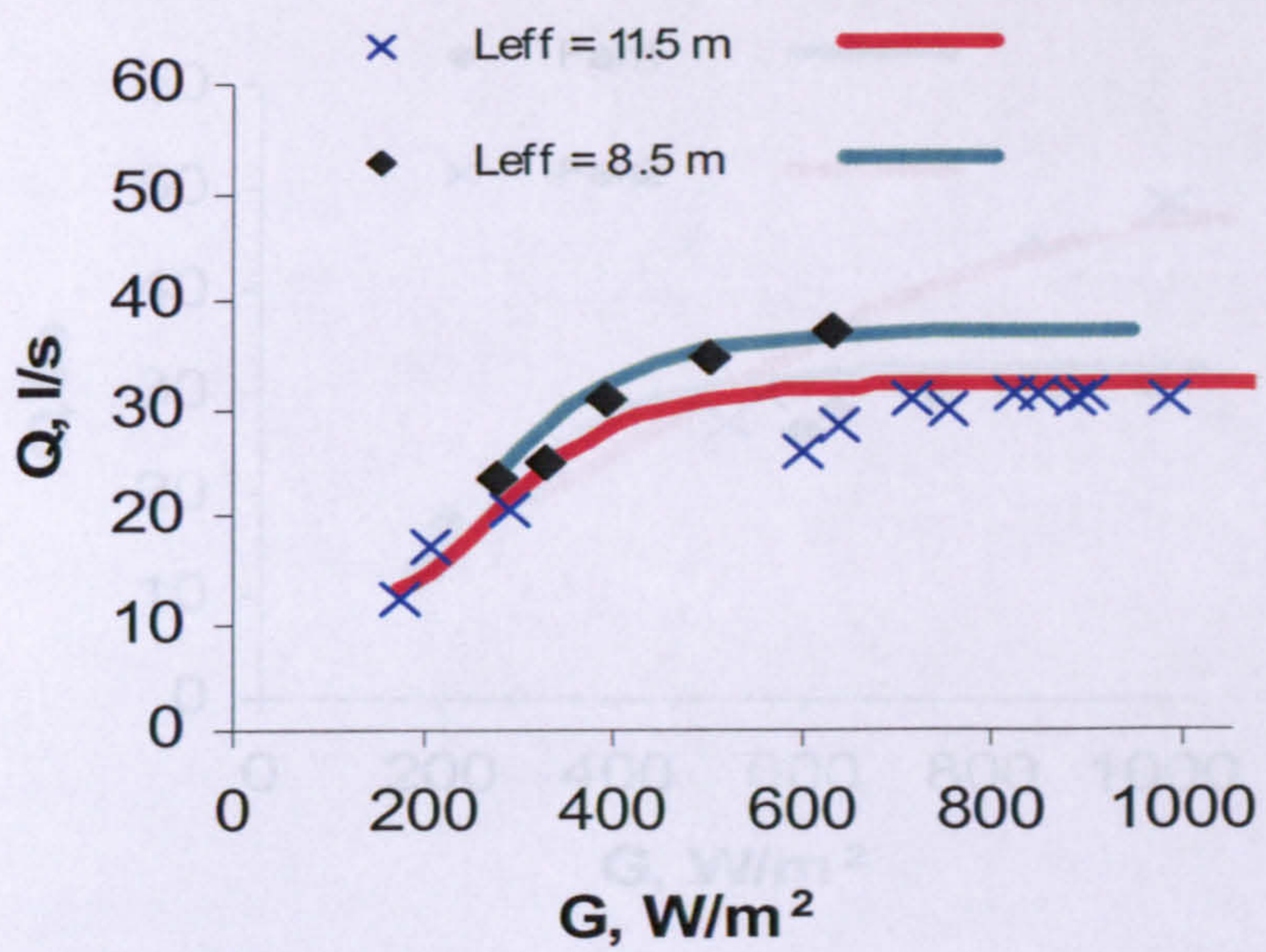

Fig. 4.14: Predicted (solid lines) and measured Q-G profiles for Fan1 at two effective duct lengths.

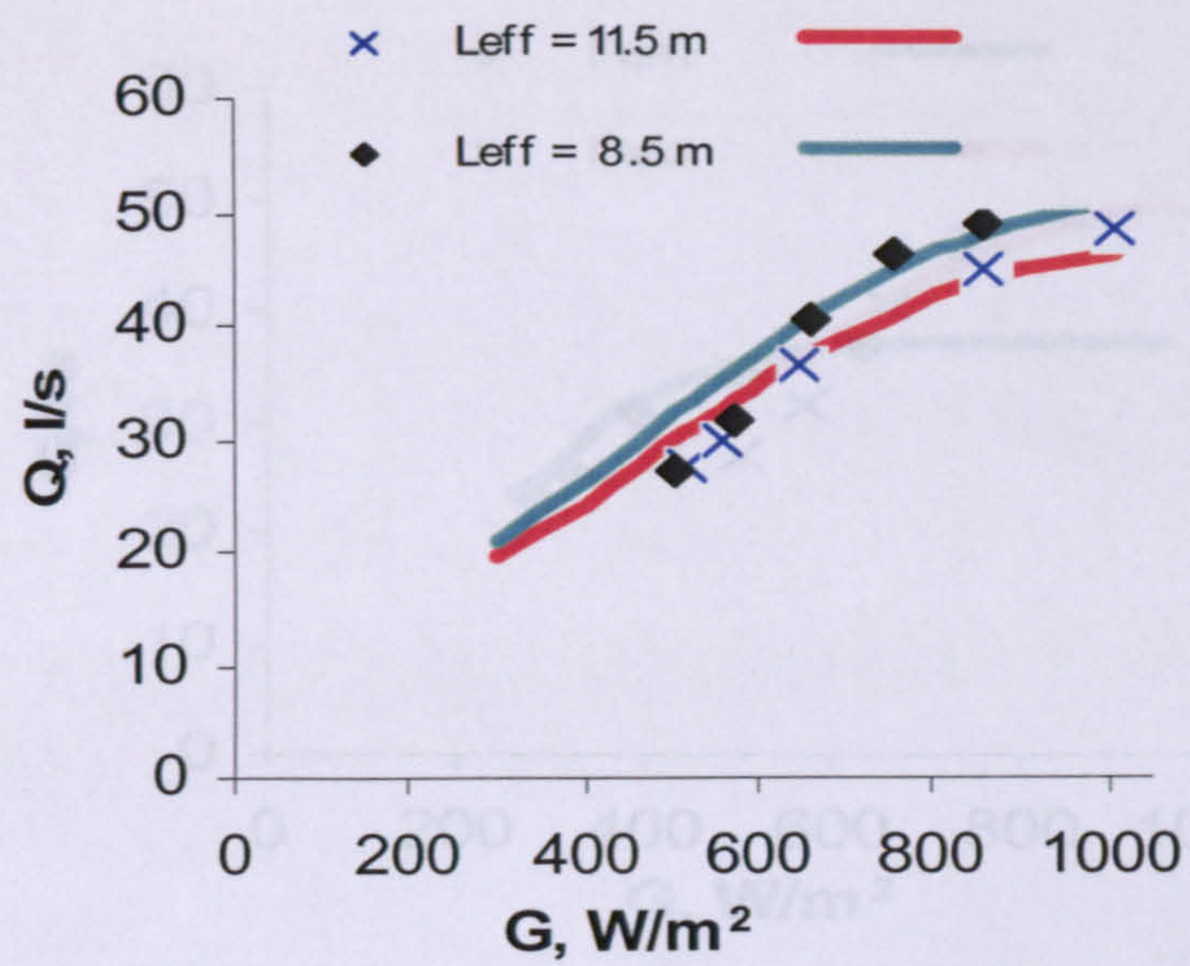

Fig. 4.15: Predicted (solid lines) and measured Q-G profiles for Fan2 at two effective duct lengths.

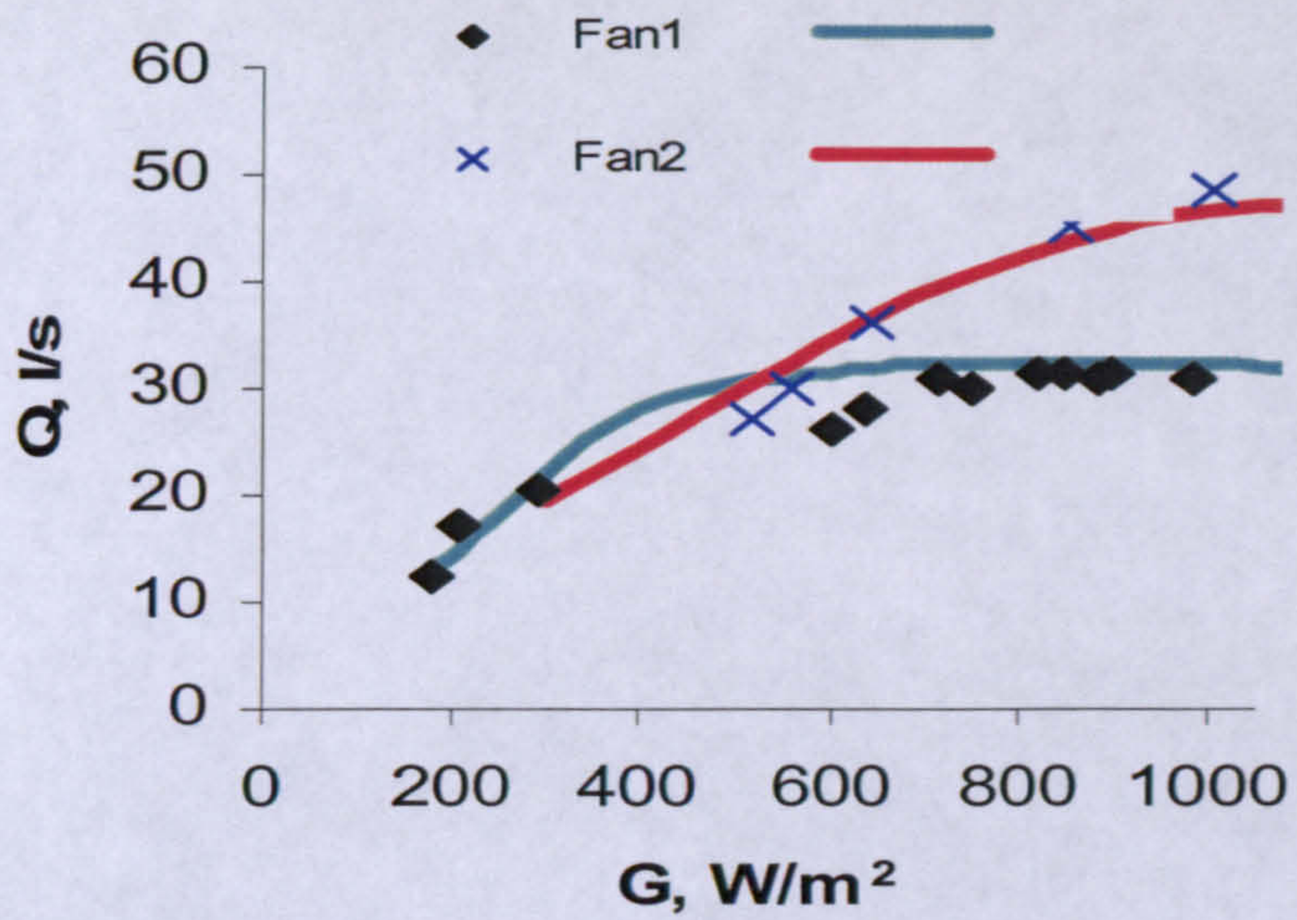

Fig. 4.16: Predicted (solid lines) and Q-G profiles for an effective duct length of 11.5 ± 1.5 m for both fans.

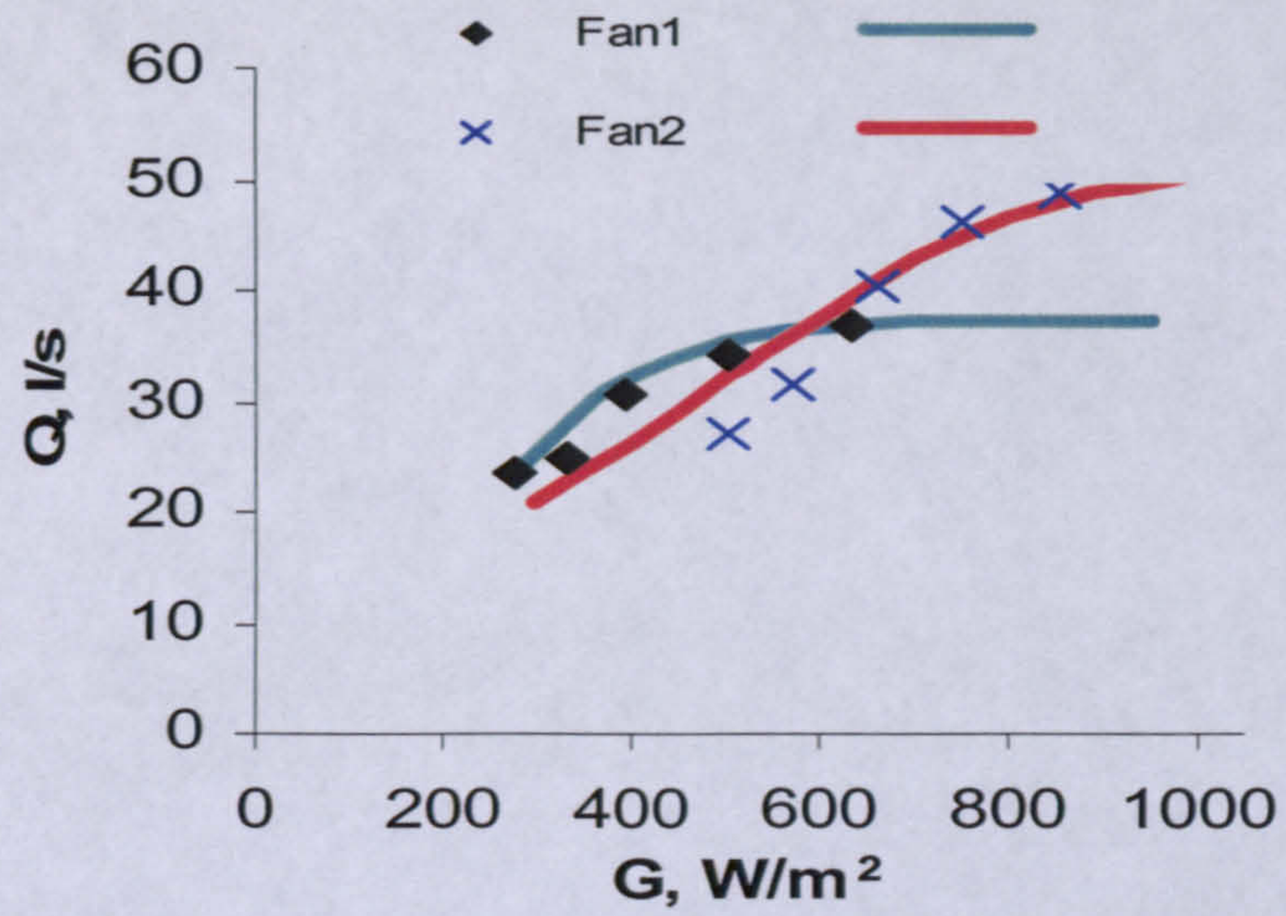

Fig. 4.17: Predicted (solid lines) and measured Q-G profiles for an effective duct length of 8.5 ± 2 m for both fans.

In Figs. 4.16 and 4.17, both predictions and measurements reveal that Fan2 provides a lower flow rate than Fan1 at low irradiances, but starts producing higher flow rates at some inflection irradiance (G = 580 and 520 W/m^2 for the 11.5 and 8.5 m length, respectively).

4.3.2.3 Error analysis

The predicted flow rate profiles in Figs. 4.14 – 4.17 are based on measurements of G and T_{mod}. The errors associated with these readings are as given in Table 3.2. Moreover, PV, fan, and duct parameters were determined experimentally and so they too are associated with error. Furthermore, the system characteristics measured in the roof section and consequently the estimated L_{eff} values have error. As a result, the predicted flow rates are also associated with error inherited from these measurements.

Running the model with the lower and higher limits of the measurements, a flow range can be estimated. It is found that, depending on irradiance, the flow rate is estimated with errors between 4 and 12 %. The predicted values in Figs. 4.14 – 4.17 are within 10 % of measurements.

4. 4 MODEL-BASED SIMULATIONS

Model based simulations of flow rate vs. irradiance (Q-G) and efficiency vs. irradiance (η-G) are essential for understanding the optimisation results in chapter 6. They are also necessary for understanding the performance of the system in general. These simulations are independent of the weather data and they can help in predicting the performance of the system for any location. A flow chart of the simulation algorithm, which is based on the results from chapter 3 and the programs in the previous sections of this chapter, is shown in Fig. 4.18.

For a range of irradiance values, the model calculates flow rate, PV-fan efficiency ($\eta_{PV-Fan} = \frac{I.V}{G.a}$) and fan-duct efficiency ($\eta_{Fan-Duct} = \frac{\Delta P \cdot Q}{I.V}$). For convenience, the subscript (PV-Fan) indicates that the efficiency represents the PV-Fan system (as a whole) as opposed to η_{PV} which indicates the maximum efficiency that can be reached by the system (i.e. $\eta_{PV} = \frac{P_m}{G.a}$). The simulations in sections 4.4.1 and 4.4.2 are carried out for an extension of 80 % and for an ambient temperature of 10 C.

4.4.1 Q-G simulations

Figure 4.19 shows model-based Q-G simulations for three systems. It is clear that systems with the larger duct diameter are expected to produce higher flow rates. At a fixed extension, the friction factor in the duct is only slightly affected by the increase in diameter. Nevertheless, an increase in diameter will decrease pressure loss in the ducting system and thus the flow rate of air will increase. So, if the volume delivered is to be maximised, in this case, it is preferable to use Duct2 rather than Duct1 (refer to Table 3.3 for symbols). In section 6.5.3, it is shown that there exists a critical (or optimum) duct diameter after which the volume of air delivered in a given period of time does not increase any more.

Figure 4.19 also shows that, as expected, the larger PV module (PV2) is preferable to PV1 if higher flow rates are to be achieved. At G = 300 W/m^2, systems with PV2 can deliver 2.5 times as much air as systems with PV1.

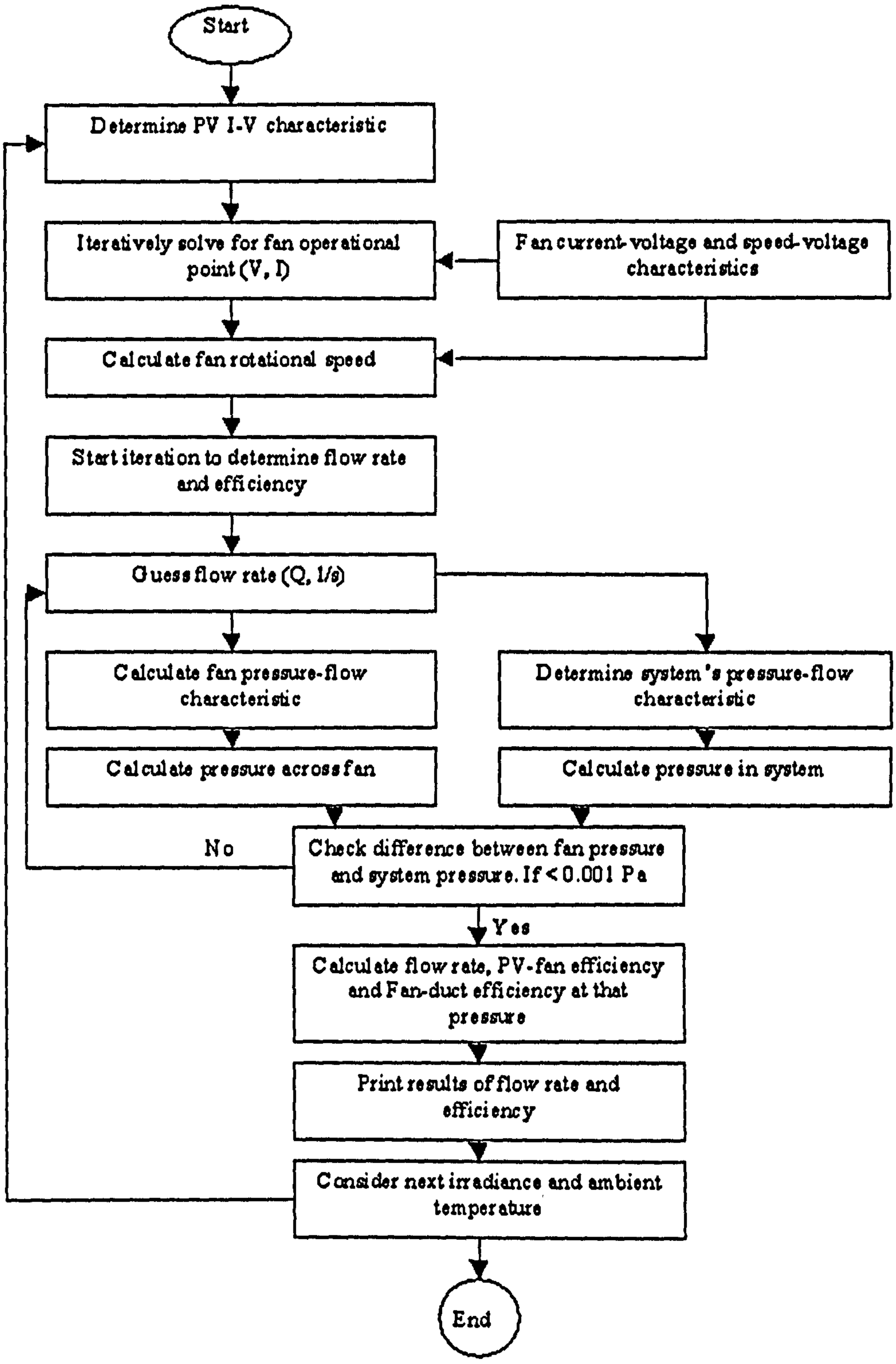

Fig. 4.18: A flowchart of the simulation program.

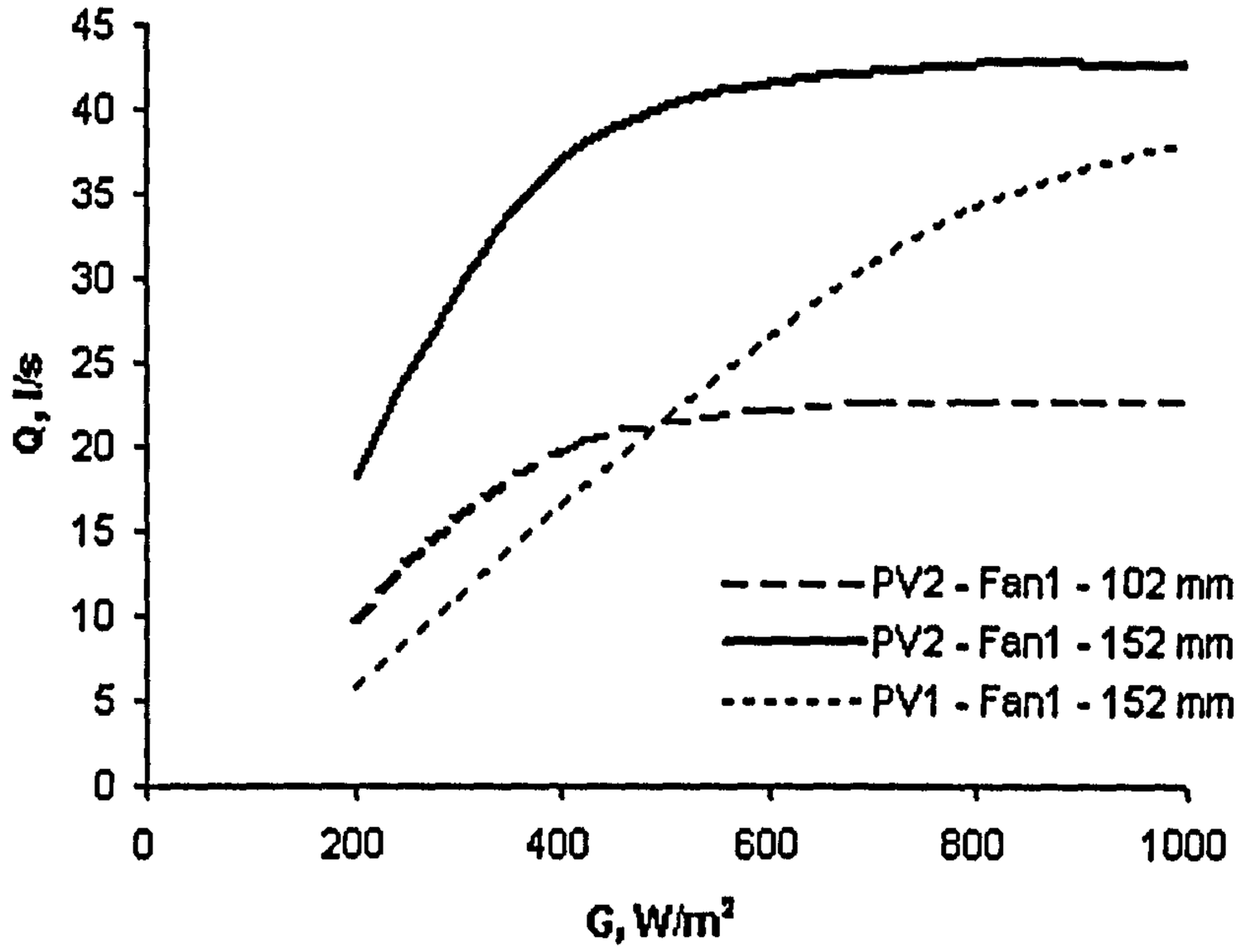

Fig. 4.19. Q – G simulations for three [PV – Fan – Duct diameter] systems for a duct length of 5 m.

Figure 4.20 shows a comparison of simulations for two systems of PV2 with different fans at two different duct lengths. It is seen that a 15 m increase in length can cause a reduction of up to 14 l/s for Fan1 and 20 l/s for Fan2. Also, it is clear that, as discussed above, for irradiances below the inflection point, p (G ~ 580 W/m^2), Fan1 produces higher flow rates than Fan2. At point p, Fan1 utilises 60 % of its free flow capacity (i.e. 69 l/s) while Fan2 utilises only 37 % of its capacity. The inflection irradiance is only slightly affected by the length of the duct as seen in Fig. 4.20 but is significantly influenced by the PV module used as seen from Fig. 4.21 which shows Q-G simulations for systems with PV1. For systems with PV1, Fan1 produces higher flow rates than Fan2 does because it operates at significantly higher voltages and speeds and so utilises a higher percentage of its free flow capacity.

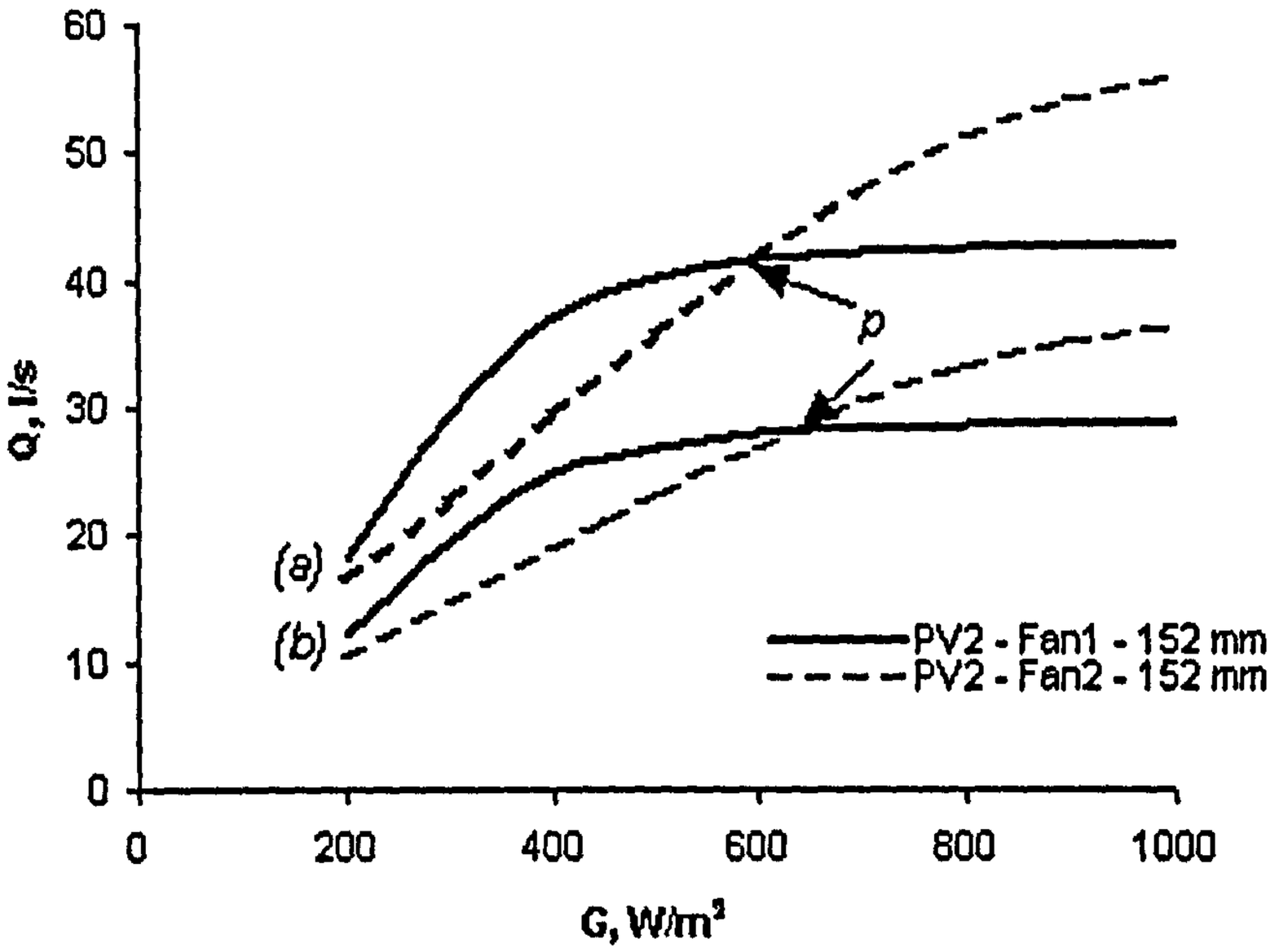

Fig. 4.20: Q - G simulations for (PV2 –Fan -152 mm) systems with a duct length of (a) 5 m (b) 20 m.

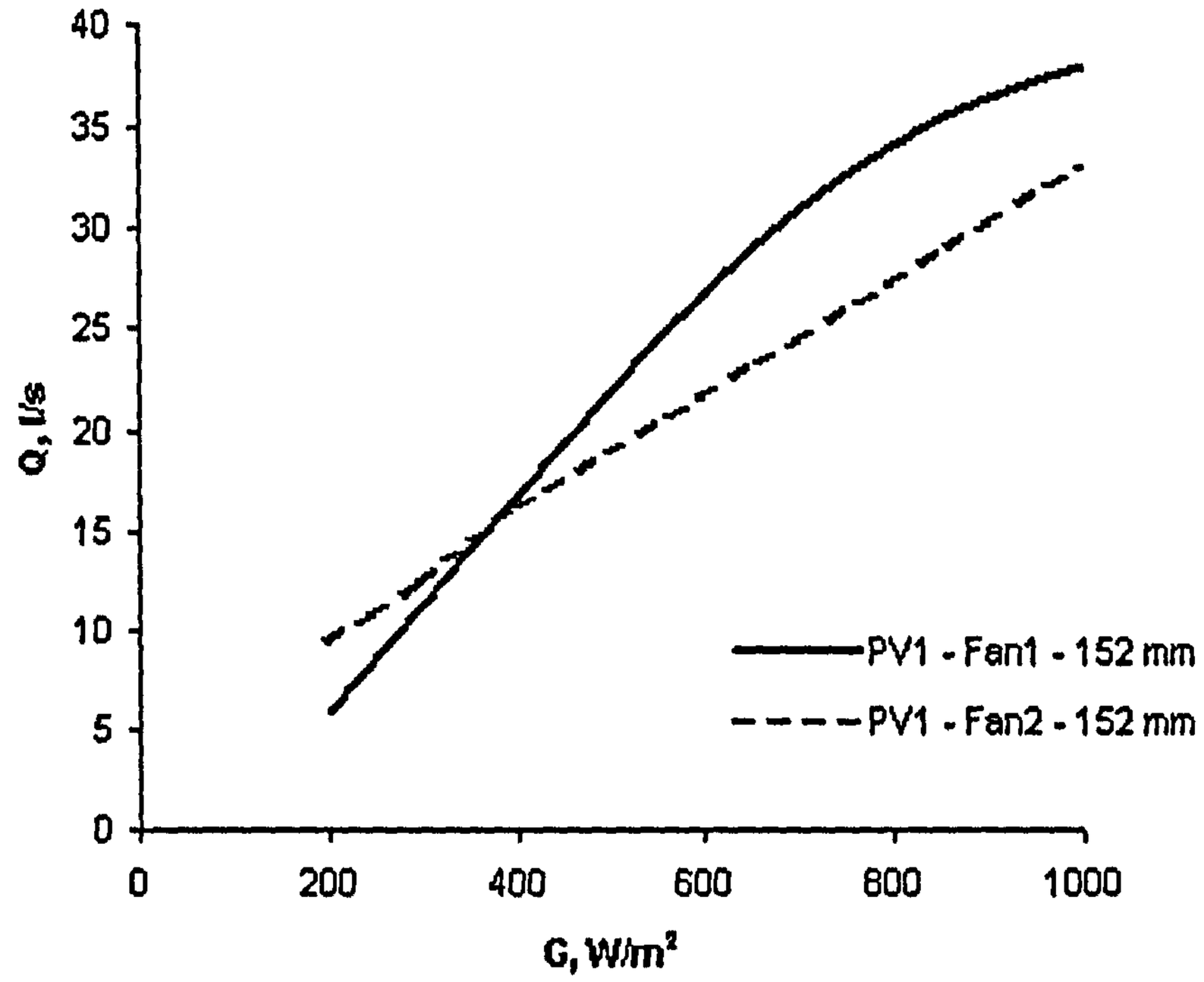

Fig. 4.21: Q - G simulations for (PV1 –Fan -152 mm) systems with a duct length of 5 m.

4.4.2 η - G simulations

For discussion in this section and subsequent chapters, the efficiency defined by Eq. 4.1 will be referred to as $\eta_{PV\text{-}Fan}$. In addition, the efficiency of the fan-duct system is defined as

$$\eta_{Fan-Duct} = \frac{\Delta P \cdot Q}{I \cdot V} \tag{4.4}$$

while ($\eta_{PV-Fan} \cdot \eta_{Fan-Duct}$) is the overall flow efficiency of the system.

4.4.2.1 Flow rate and efficiency

Maximising system flow rate does not necessarily mean that the PV-Fan efficiency and/or Fan-Duct efficiency are maximised. As irradiance increases, the voltage and speed of the fan and consequently the flow rate increase. For Fan1, an increase in flow rate implies lower efficiencies as can be inferred from Fig. 4.22 and Fig .4.23(a). For Fan2, on the other hand, an increase in flow rate results in better utilisation of the PV modules P_m but a decrease in the utilisation of the maximum pneumatic power possible as can be seen from Fig. 4.22 and Fig. 4.23(b).

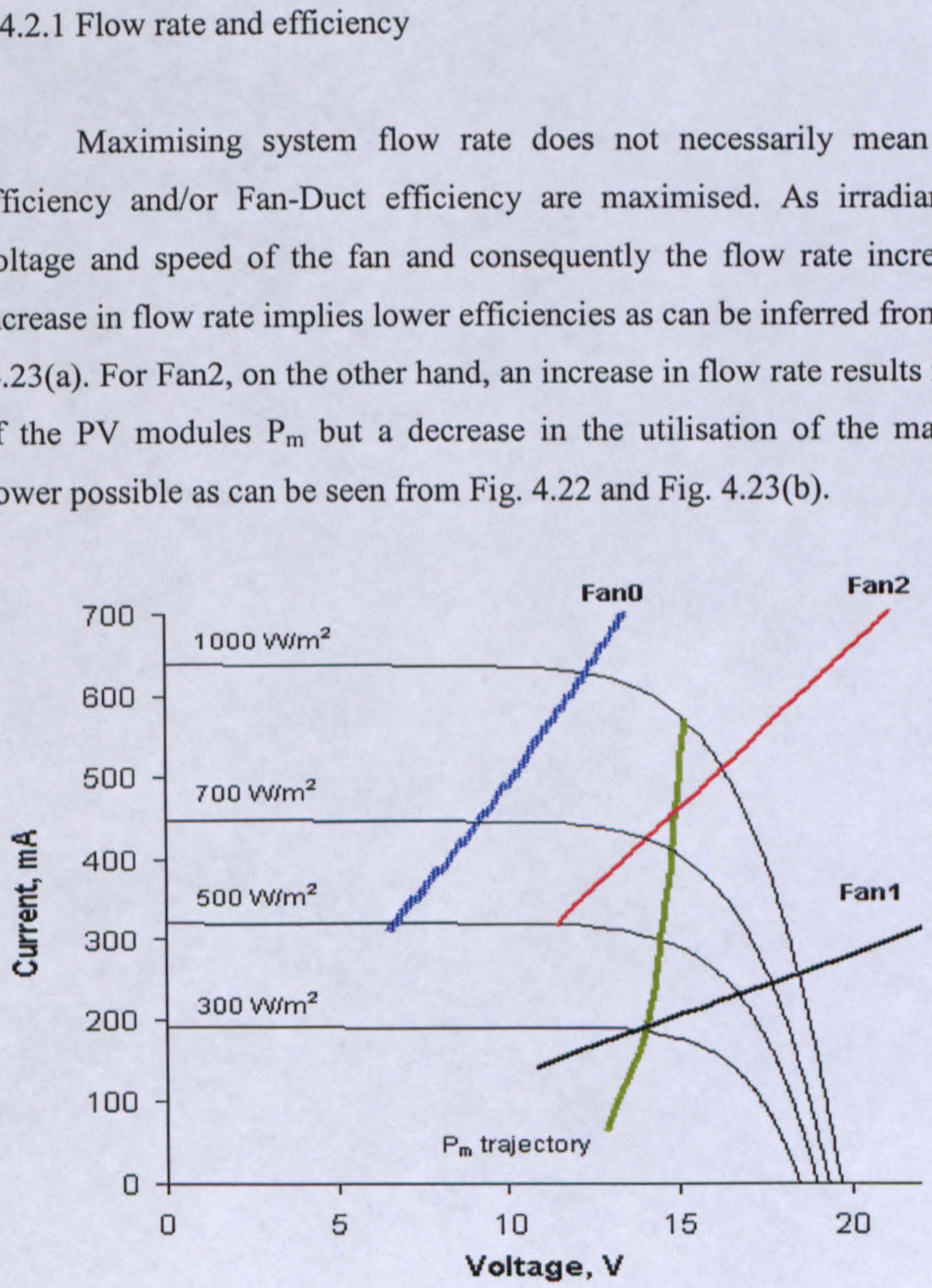

Fig. 4.22: Fan IV characteristics and PV maximum power trajectory for PV2 at T_{amb} = 10 C.

(a)

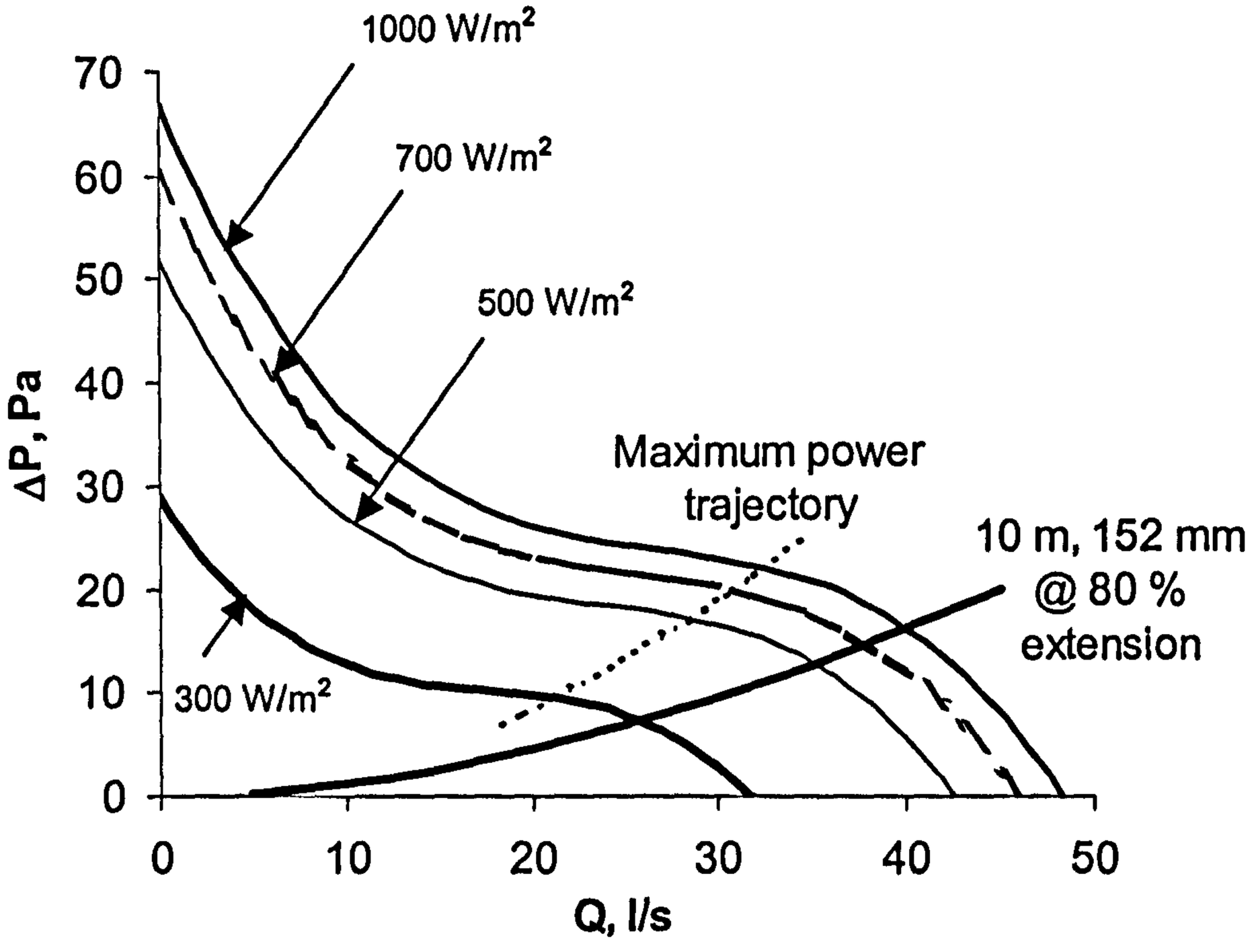

(b)

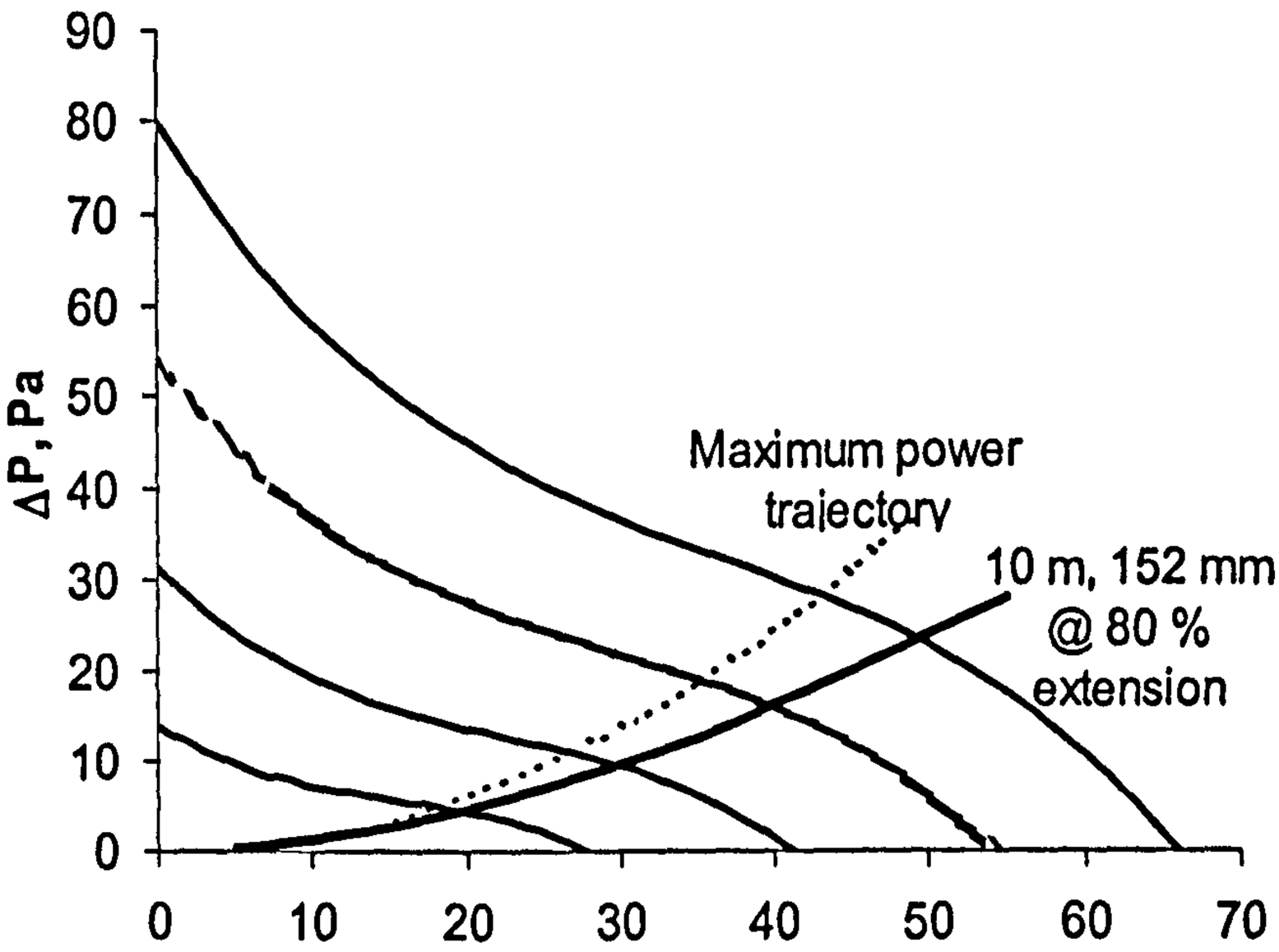

Fig. 4.23: Maximum pneumatic power trajectory for (a) Fan1 and (b) Fan2 at four irradiance levels.

For given system characteristics, as irradiance increases, the overall efficiency for Fan1 decreases while that for Fan2 may either increase or decrease. So, depending on the basis for optimisation, either volume or overall flow efficiency may be maximised. For example, if the optimisation is based on maximising volume delivered over a period of operation, then it may be possible that one fan will maximise the volume but another fan will maximise efficiency. The optimisation strategy in section 6.1.3 explains that the current work considers optimisation based on maximum volume delivered. An optimum motor constant for the fan's motor and an optimal duct length can then be chosen in order to maximise PV and pneumatic output respectively.

4.4.2.2 $\eta_{PV\text{-}Fan}$-G simulations

Simulations of $\eta_{PV\text{-}Fan}$ vs. irradiance for three systems with Duct2 are shown in Fig. 4.24. The peak of the individual efficiency curves is the point when the fan is operating at the maximum power of the PV module. Thus, for the PV2-Fan1 combination, the fan will utilise a 100 % of the electrical power made available by the PV module at 400 W/m^2. These curves show a trend similar to that observed by Q – G curves. There exists an inflection point (in this case 580 W/m^2) below which the PV2-Fan1 combination is always giving the highest efficiencies possible thus utilising more of P_m. For irradiances above this point, the PV2-Fan2 combination becomes favourable. For PV1 systems, Fan1 is always favourable for G > 200 W/m^2.

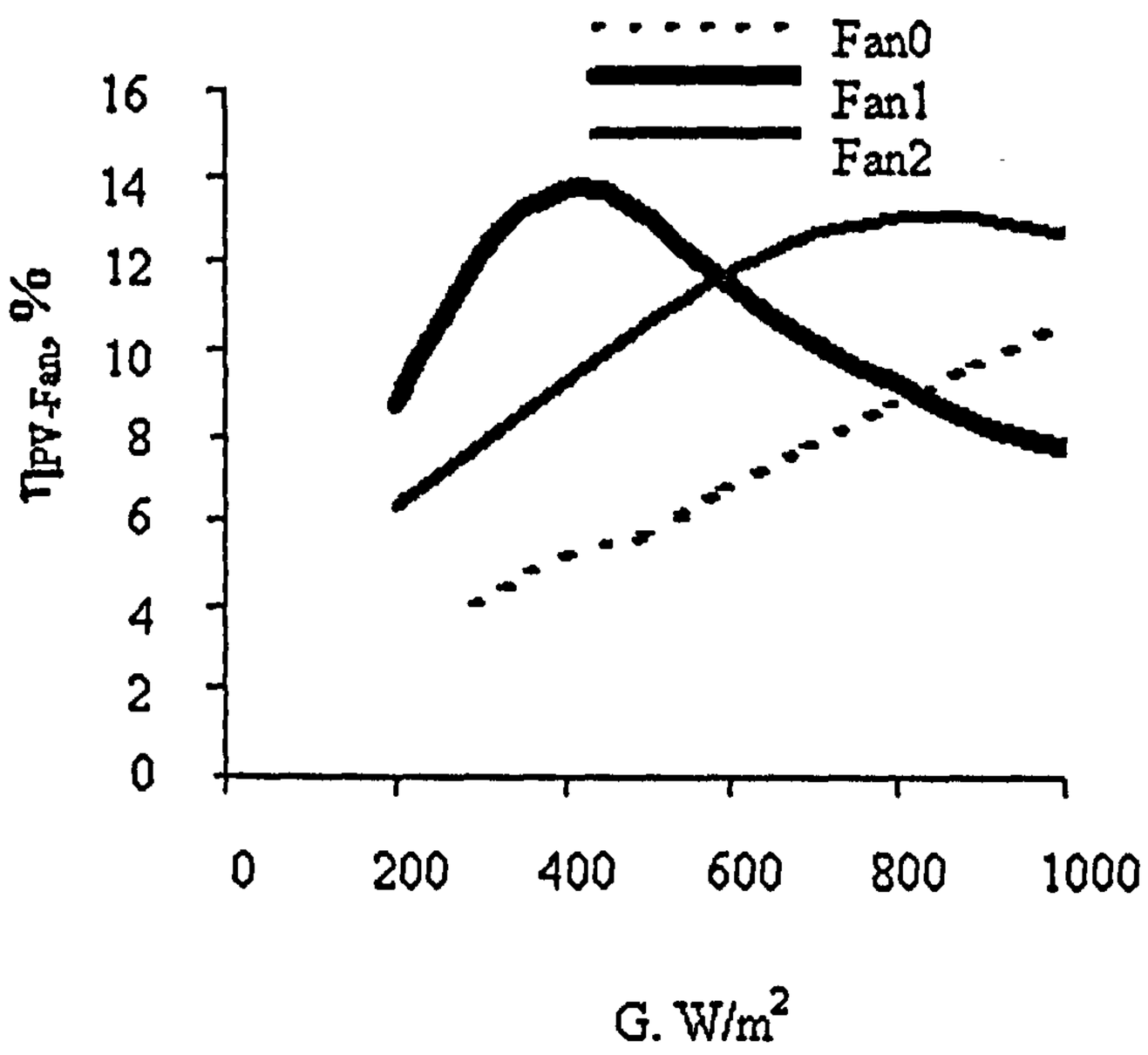

Fig. 4.24: η_{PV-Fan} – G simulations for different PV2 – fan combinations.

4.4.2.3 $\eta_{Fan\text{-}Duct}$-G and $\eta_{Overall}$-G and simulations

Simulations of $\eta_{Fan\text{-}Duct}$-G show that for the full irradiance range, Fan2 produces the highest efficiencies. This can be explained by reference to Fig. 4.23. However, for the range 200 – 580 W/m^2, since Fig. 4.24 shows that Fan1 produces higher PV-fan efficiencies, and Fig. 4.25 shows that the two fans nearly produce equal efficiencies, it can be concluded that for the same range, Fan1 produces higher overall efficiencies as seen from Fig. 4.26.

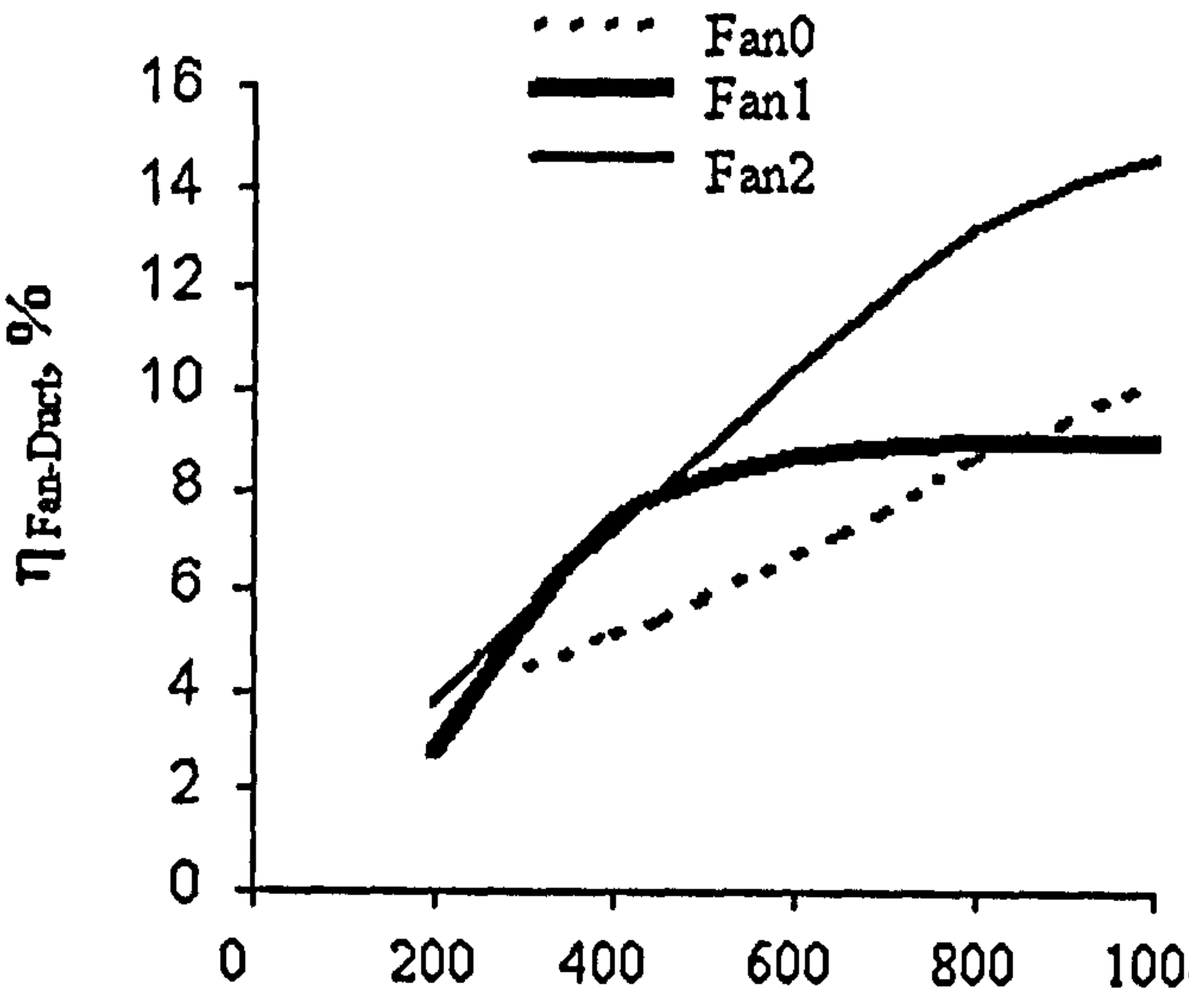

Fig. 4.25: $\eta_{Fan\text{-}Duct}$ – G simulations for different PV – fan combinations.

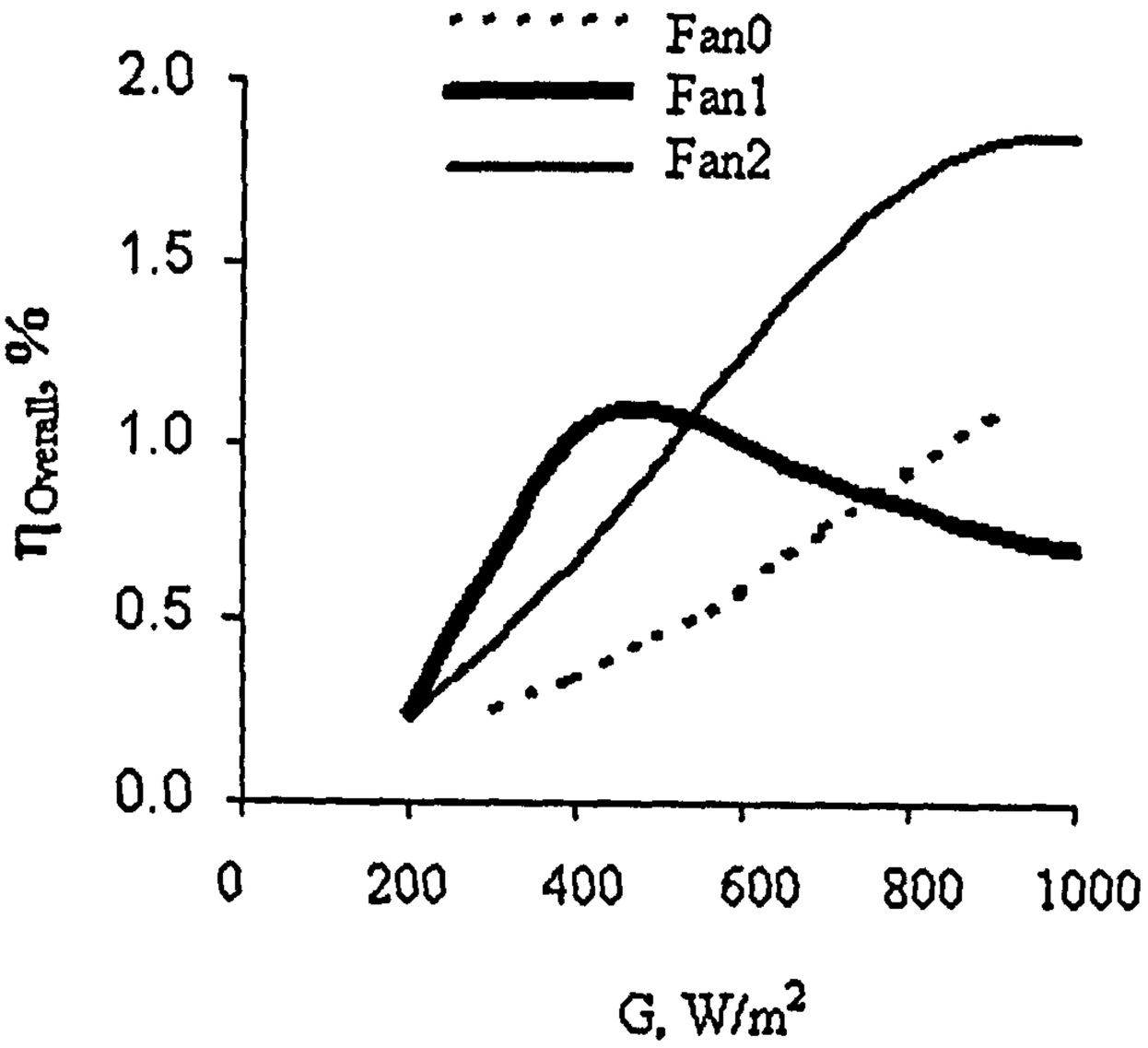

Fig. 4.26: $\eta_{Overall}$ – G simulations for different PV – fan combinations.

4.5 SUMMARY

The mathematical model of the system described in chapter 3 has been modified into a computer program where the equations for the different components are solved simultaneously. Different modules within the computer program are shown in Appendix B. Even though each of these modules stands on its own for a specific purpose, they can be integrated to form a single program as shown in Appendix B6. The iteration step has to be chosen carefully in order to produce accurate results (especially at low irradiances) but without drastically affecting the computational time. VBA programming proves to be very simple and efficient in obtaining solutions for the present system.

The flow rate model developed was validated. A roof section was constructed and measurements of irradiance, temperature, and flow rate were collected for several systems. While chapter 3 (section 3.8) attaches a 12 % error to the predicted flow rate based on cumulative error in the measured performance of each of the components, the validation shows that measurements are within 10 % of the predicted values.

Model simulations show that different PV-fan combinations are associated with optimum intervals of operation. The interval 200 – 580 W/m^2, for instance, is the optimum interval for Fan1. In this range, Fan1 delivers higher flow rates and higher PV-Fan efficiencies. Simulations also reveal that, even though it does not maximise pneumatic output, Fan1 is expected to deliver the highest overall efficiencies.

The Q – G and η – G simulations given in this chapter do not take start-up and "cease" irradiances into account. In section 6.3.4, these limits are considered. Moreover, in chapter 6, systems with PV modules and fans in parallel and series are considered for optimisation and the results are explained in terms of Q-G and η – G simulations. An updated version of the model, which accounts for all these effects in addition to the large files of weather data, is introduced in section 6.3. In chapter 5, the Edinburgh weather data to be used for optimisation is described and a slope irradiance model is introduced.

REFERENCES

Bione, J., Vilela, O.C., and Fraidenraich, N., (2004), Comparison of the performance of PV water pumping systems driven by fixed, tracking and V-trough generators. Solar Energy, 76, pp703-11.

Duffie J.A., and Beckman W.A., (1991), Solar Engineering of Thermal Processes. 2nd ed, New York: Wiley Interscience.

Eckstein, J., Townsend, T., Beckman, W.A., and Duffie J.A., (1990), Photovoltaic powered energy systems. Proceedings of the American Solar Energy Society, Austin, Texas, USA, 1990.

Jafar, M., (2000), A model for small-scale photovoltaic solar water pumping, Renewable Energy, 19, pp85-90.

McCabe, W., Smith, J., and Harriot, P., (1985), Unit Operations of Chemical Engineering, 4th ed., New York, McGraw-Hill.

Perry, R.H., and Green, D.W., (1997), Perry's Chemical Engineers' Handbook, 7th ed., New York, McGraw-Hill, 1997.

5. WEATHER DATA AND SLOPE IRRADIANCE MODELLING

5.1 INTRODUCTION

Accurate long-term weather data is extremely important for appropriate design and, hence, optimised performance of PV-driven systems since power output from the PV array depends on solar radiation and ambient temperature. The current chapter presents the weather data available for Edinburgh. The means for manipulating this data for use in the optimisation process is introduced. As discussed in chapter 2, most widely available irradiance data are in the form of global horizontal irradiance. In order to optimise the PV-driven RSB system under consideration, global irradiance on the roof of the house is needed. The current chapter introduces an anisotropic model for predicting slope irradiance. Measurements on a sloped roof are taken and compared to predictions by both the isotropic (section 2.5.5) and anisotropic models.

For the current research, two datasets, which are equally useful, are available. The first (dataset1) is a 27-year dataset of hourly data for horizontal global and horizontal diffuse radiation in addition to ambient temperature and wind speed. Such a large dataset is very crucial for the optimisation process and for predicting the long-term performance of the system. However, in order to accurately describe the performance of the system, and, account for start-up characteristics of the different systems, a more detailed dataset is required. The second dataset (dataset 2) comprises 1-year, 5-min horizontal global irradiance data. The optimisation procedure discussed in chapter 6 is undertaken with both datasets, and the results compared.

Dataset1 consists of both global and diffuse horizontal irradiance and so it can be directly used for predicting slope irradiance. The available ambient temperature and wind speed data can be input directly into the model discussed in chapters 3 and 4 to define the PV IV characteristic. From dataset1, three-dimensional plots of hourly irradiance, ambient temperature, and wind speed for all days of the year are shown, as an example, in Fig. 5.1, for the year 1976. The model presented in chapter 3 does not account for wind speed (ws, m/s) and assumes that the loss coefficient, U (W/C), is constant. Incorporating the effect of wind speed into the model is a straightforward matter, as will be discussed in section 6.3.1.1.

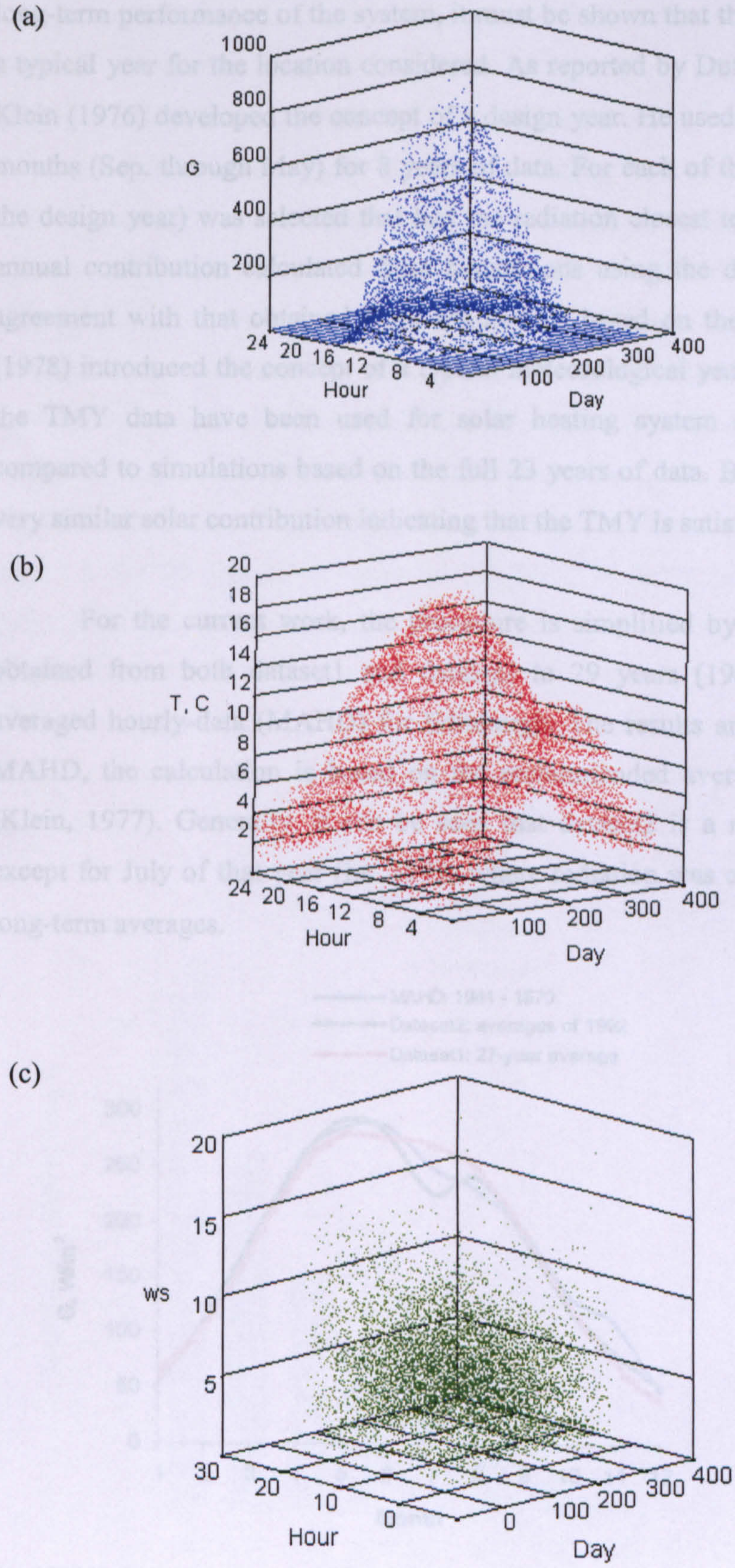

Fig. 5.1: (a) Horizontal global irradiance (W/m^2) (b) ambient temperature (C) and (c) wind speed (m/s) for Edinburgh for 1976.

In order to be able to use dataset2 (a single year of data, 1992) for predicting the long-term performance of the system, it must be shown that this data represents that for a typical year for the location considered. As reported by Duffie and Beckman (1991), Klein (1976) developed the concept of a design year. He used heating season data for 9 months (Sep. through May) for 8 years of data. For each of the months, the month (for the design year) was selected that had the radiation closest to the 8-year average. The annual contribution calculated from simulations using the design year showed good agreement with that obtained from simulations based on the full 8 years. Hall et al. (1978) introduced the concept of a typical meteorological year (TMY). For their work, the TMY data have been used for solar heating system simulations, with results compared to simulations based on the full 23 years of data. Both sets of data indicated very similar solar contribution indicating that the TMY is satisfactory.

For the current work, the procedure is simplified by comparing the averages obtained from both dataset1 and dataset2 to 29 years (1941 to 1970) of monthly averaged hourly-data (MAHD) for Edinburgh. The results are shown in Fig. 5.2. For MAHD, the calculation is based on the recommended average days for the months (Klein, 1977). Generally, it can be seen that dataset2 is a representative set of data except for July of that year (i.e. 1992) where radiation was considerably less than the long-term averages.

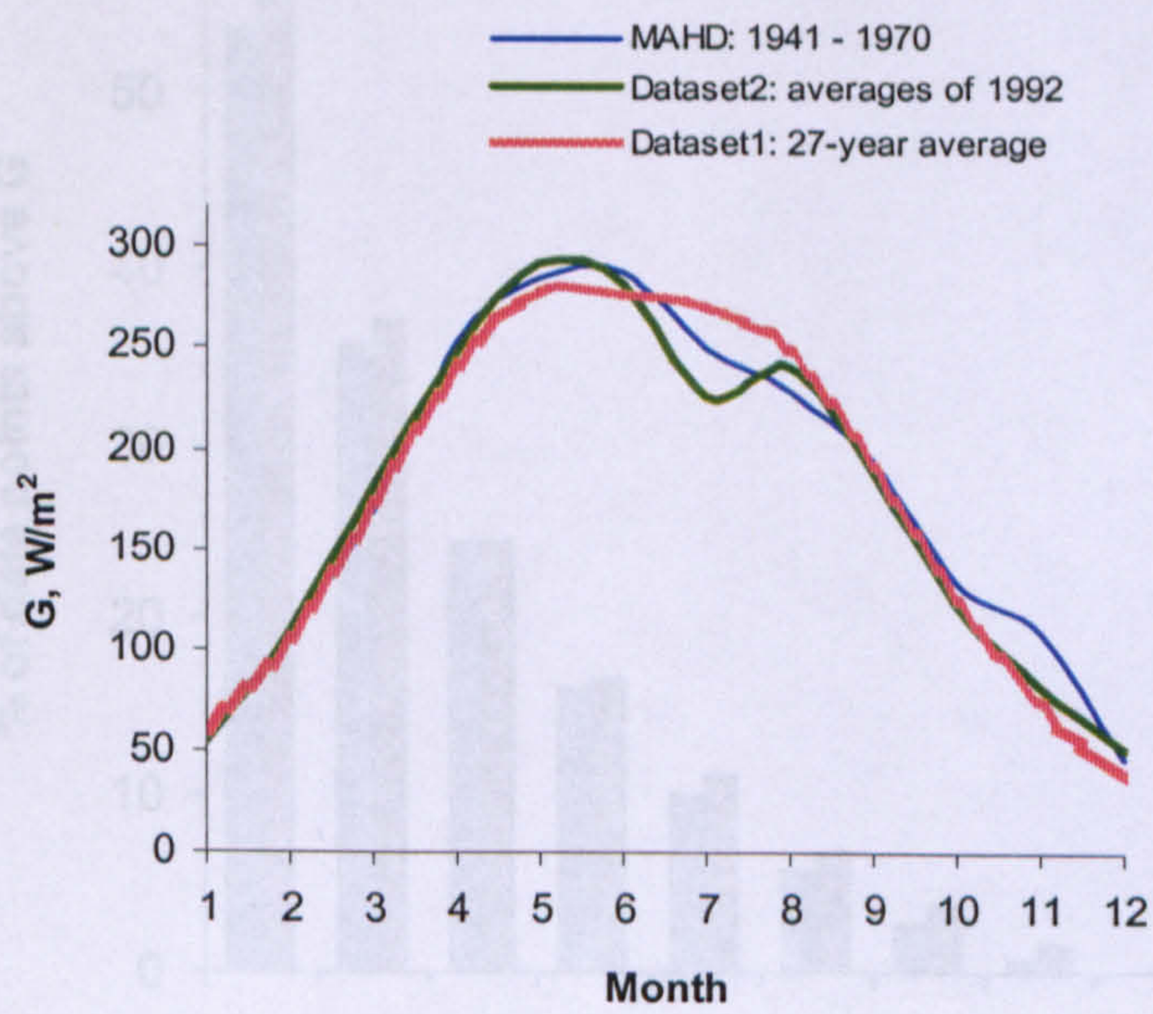

Fig. 5.2: Monthly averaged horizontal irradiance data from three datasets for Edinburgh.

A disadvantage of utilising dataset2, however, is that it lacks diffuse data, which is necessary to obtain an accurate estimate of slope irradiance. Thus, to use this data, the methods discussed in chapter 2 (section 2.5.4) must be applied to predict horizontal diffuse irradiance. Moreover, ambient temperature data is also not available for dataset2. The present chapter introduces already available methods for predicting diffuse irradiance and ambient temperature in order to complete dataset 2. The wind speed is not predicted in this case and so the loss coefficient U is assumed constant. This additional work for predicting diffuse irradiance and ambient temperature is justified since it is desired to optimise system design with detailed 5-min data. This is expected to produce more accurate and representative results than using hourly data. The percentage of data points, which are higher than a given irradiance for both dataset1 and dataset2, is plotted against irradiance in Fig. 5.3. It can be seen that with the 5-min data, 1.6 % (729 data points) are over 800 W/m^2 while for the hourly data; this is only 0.62 % (61 data points for the best year: 1977). As shown in Table 3.8, the start-up current for Fan2 is 488 mA, which corresponds to 800 W/m^2 for the PV2-Fan2 system. If simulations are carried out with dataset1 rather than dataset2, the model would predict that less annual volume would be produced by the PV2-Fan2 systems, which can be misleading.

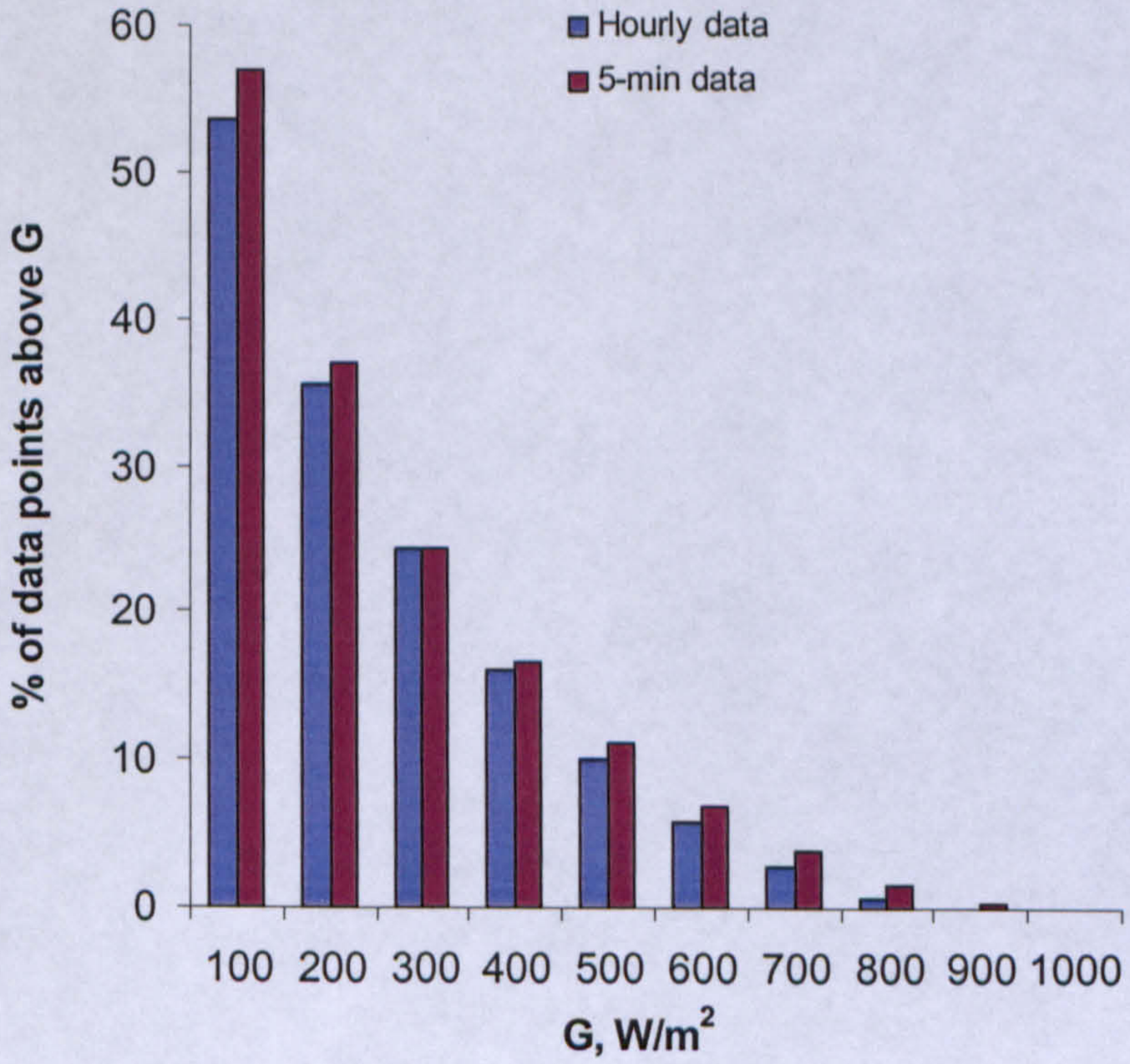

Fig. 5.3: Percentage of data points higher than G for data sets 1 and 2.

5.2 ESTIMATION OF AMBIENT TEMPERATURE

Hourly ambient temperatures throughout a day can be estimated from available daily maximum and minimum values using the ASHRAE hourly temperature model (ASHRAE, 1993). According to this model, the temperature at any hour of the day is estimated from the maximum and minimum temperatures of that day using Eq. 5.1 below

$$T_{amb,hour} = T_{\max,day} - pr \cdot \left(T_{\max,day} - T_{\min,day}\right) \tag{5.1}$$

where "*pr*" is a percentage corresponding to any hour of the day and can be obtained from Fig. 5.4.

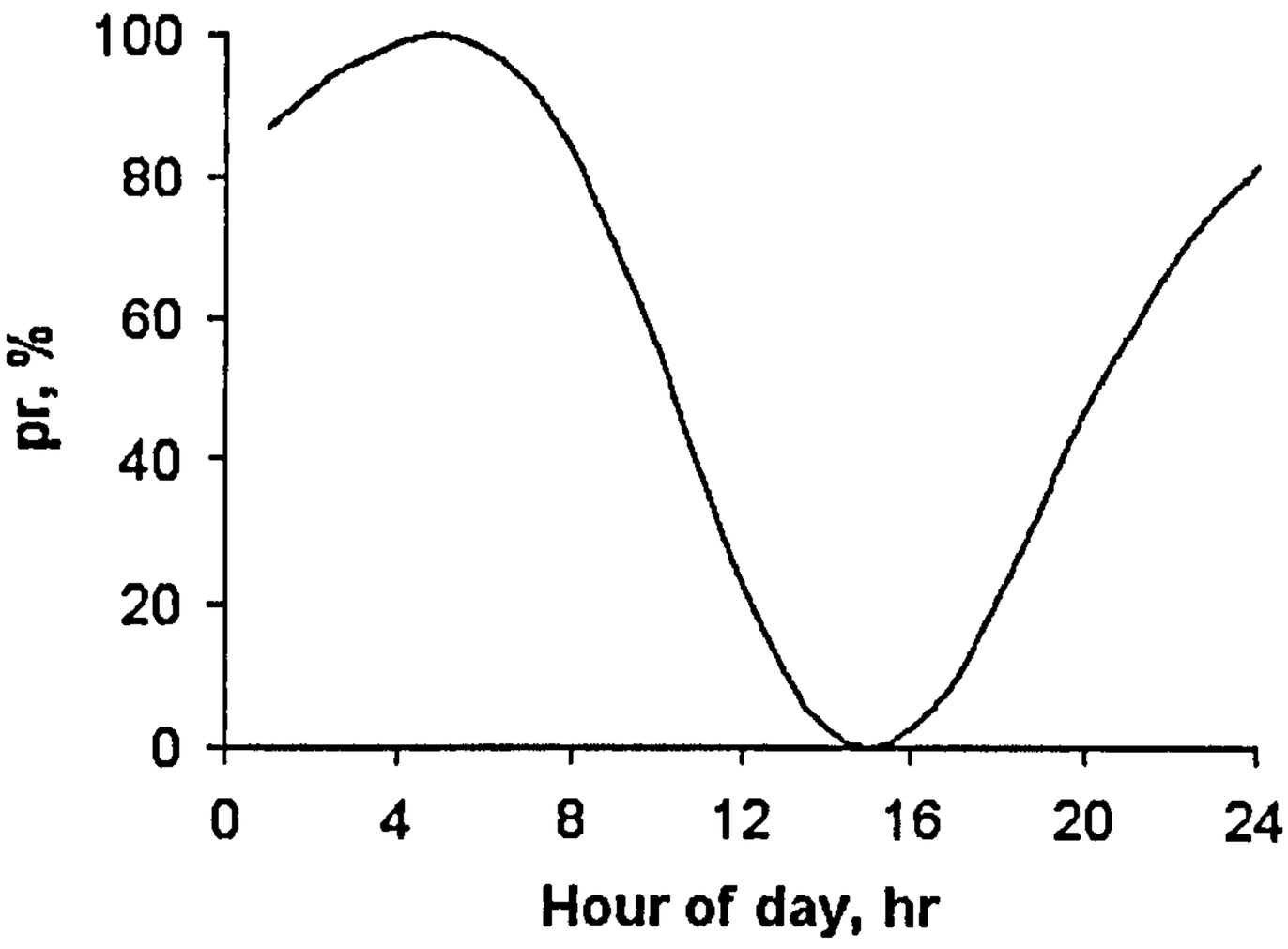

Fig. 5.4: The percentage "pr " in Eq. 5.1 as a function of hour of the day (ASHRAE, 1993).

The ASHRAE model predicts that the lowest ambient temperatures occur around 4 AM and that the highest temperatures occur around 3 PM. The validity of this model is checked for daily data for a warm and a cold day in Edinburgh as shown in Fig. 5.5. As can be seen, there is good agreement between measured and predicted data.

For dataset2, the ambient temperature needs to be calculated every 5 minutes. However, since maximum and minimum temperatures are not available on a 5-min basis, it is assumed that T_{amb} stays constant throughout a given hour. Thus Eq. 5.1 along

with Fig. 5.4 and the extreme temperatures shown by Fig. 5.6 can be used for estimating the ambient temperature for dataset2.

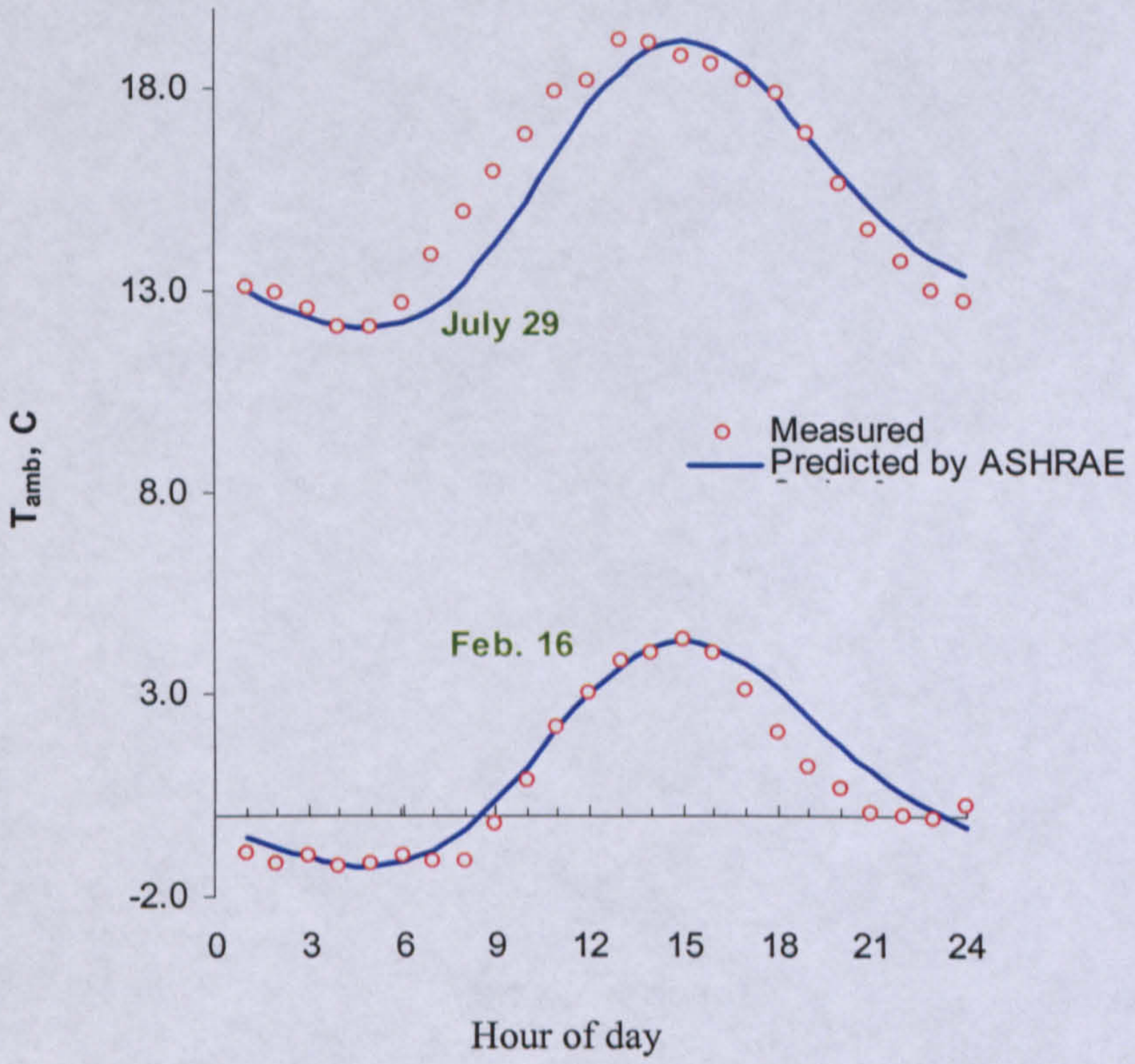

Fig. 5.5: Validation of the ASHRAE model for Feb. 16 and July 29, 2004 in Edinburgh.

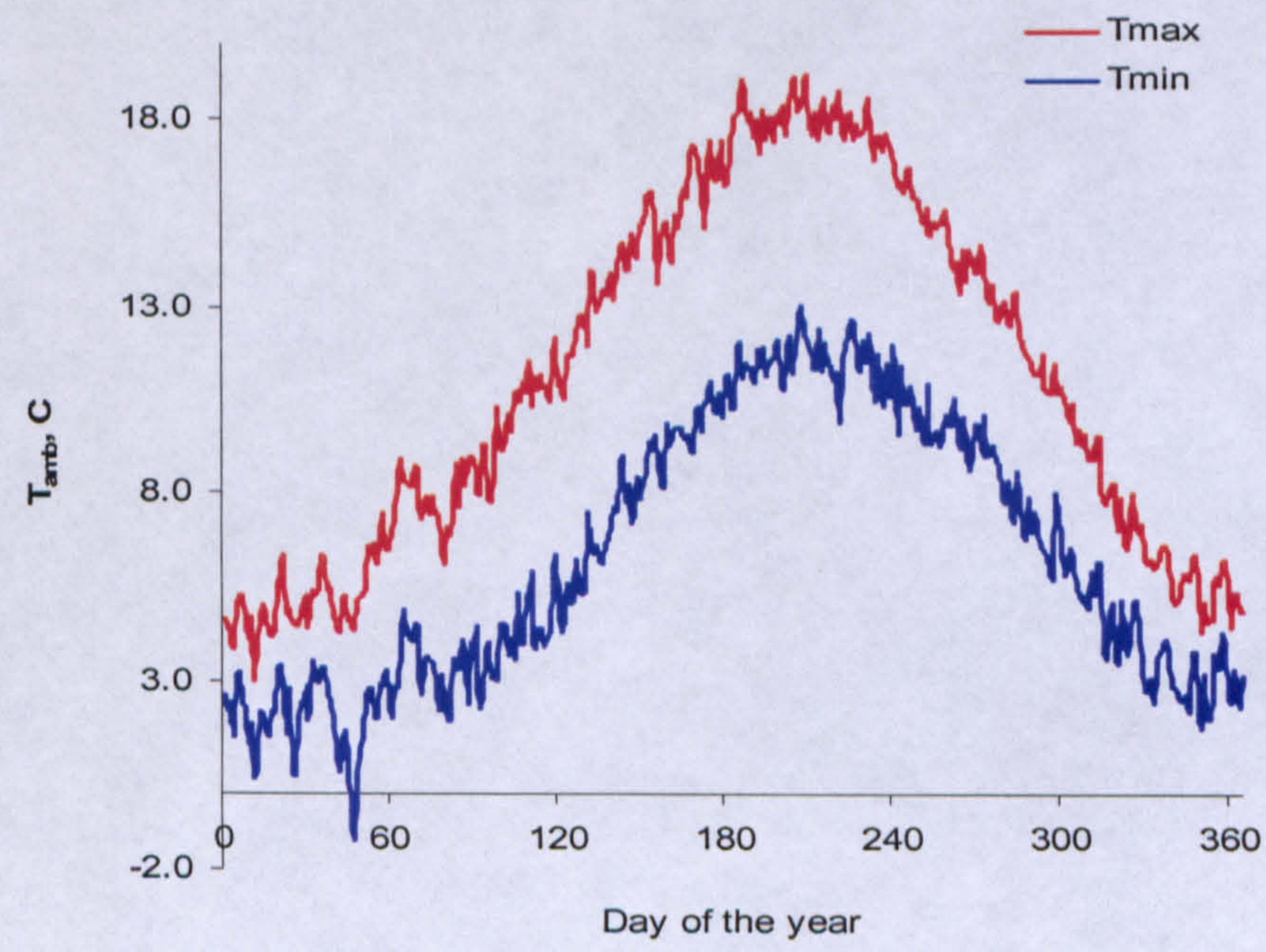

Fig. 5.6: Long-term (16 years) averaged daily maximum and minimum ambient temperatures for Edinburgh.

5.3 ESTIMATION OF SLOPE IRRADIANCE: DATASET1

As mentioned above, for dataset1, the estimation of global slope irradiance is made easier by the availability of horizontal diffuse irradiance. The isotropic model discussed in section 2.5.5 only accounts for diffuse radiation received uniformly from the sky dome. However, diffuse radiation can also be circumsolar diffuse or horizon brightening as can be seen from Fig. 5.7, (Duffie and Beckman, 1991). The former results from forward scattering of solar radiation that is concentrated in the part of the sky around the sun while the latter is concentrated near the horizon.

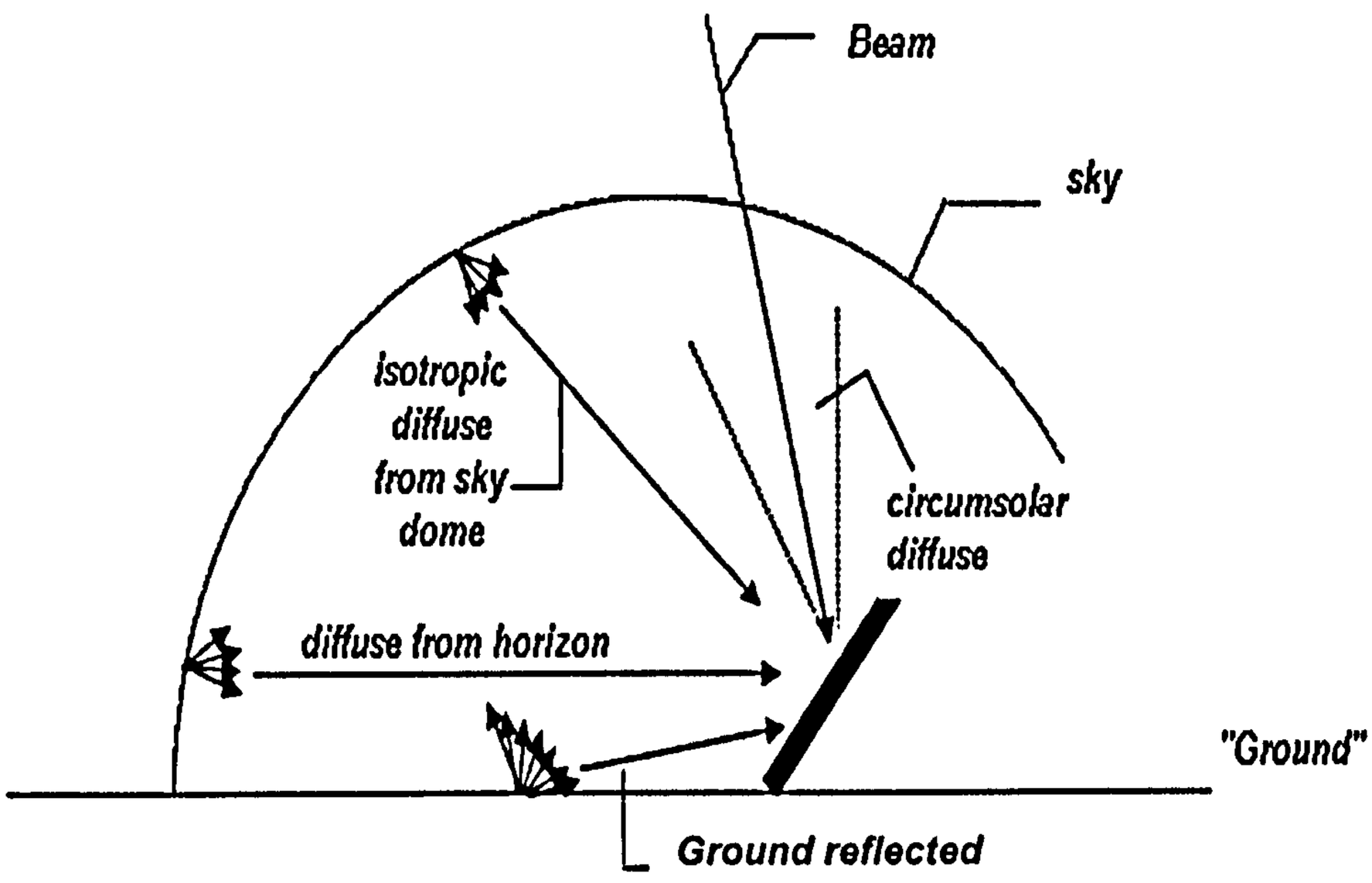

Fig. 5.7: Beam, diffuse and ground-reflected radiation on a tilted surface. Adapted from Duffie and Beckman (1991).

Several models, which account for either two, or all three parts of diffuse radiation, have been developed (Hay and Davis, 1980, Reindl et al, 1990). Reindl et al (1990) indicated that the results obtained by their anisotropic model lead to slightly higher estimates than those produced by the isotropic model. Their model, however, does not account for horizon brightening.

The Northern European anisotropic model developed by Muneer et al. (1987) treats the shaded and sunlit surfaces separately and further distinguishes between

overcast and non-overcast conditions of the sunlit surfaces. Under overcast sky, the diffuse irradiance incident on the sloped surface is calculated from

$$I_{d,tilt} = I_d[TF] \tag{5.2}$$

while for non-overcast conditions, the following equation is used

$$I_{d,tilt} = I_d[TF(1-F_{IR})+F_{IR}\cdot R_B] \tag{5.3}$$

Where TF, the surface tilt factor, is defined as

$$TF = \cos^2(\frac{\alpha}{2})+\frac{2b}{\pi(3+2b)}\left(\sin\alpha-\alpha\cos\alpha-\pi\sin^2(\frac{\alpha}{2})\right) \tag{5.4}$$

The term $\frac{2b}{\pi(3+2b)}$ is location specific and depends on sky and azimuthal conditions.

This term is a function of the clearness function $F_{IR} = \frac{I-I_d}{E_x}$. For Northern Europe, the following Equation is used

$$\frac{2b}{\pi(3+2b)} = 0.00333-0.415\cdot F_{IR}-0.6987\cdot F_{IR}^2 \tag{5.5}$$

Therefore, in order to calculate $I_{d,tilt}$, F_{IR} is first calculated, then used to determine the term $\frac{2b}{\pi(3+2b)}$ for Northern Europe. The tilt factor, TF is then calculated from Eq. 5.4 and substituted with R_b, from Eq. 2.27 (section 2.5.5.1)

$$R_b = \frac{\cos(\phi-\alpha)\cos(\delta)\cos(\omega_s)+\sin(\phi-\alpha)\sin(\delta)}{\cos(\phi)\cos(\delta)\cos(\omega_s)+\sin(\phi)\sin(\delta)}$$

in Eq. 5.3 to determine diffuse on the tilted surface. This calculated diffuse and the beam irradiance (from Eqs. 2.28) are substituted in Eq. 2.26 to calculate global slope irradiance.

Using the 27-year hourly horizontal global and diffuse irradiance data, the slope irradiance was calculated by both the isotropic and anisotropic models for different slopes. Figure 5.8 shows the total yearly slope radiation as calculated by both models. It can be seen that the isotropic model, consistently, predicts, lower values. It is also seen that the optimum slope for Edinburgh, as predicted by the anisotropic model is about 45°.

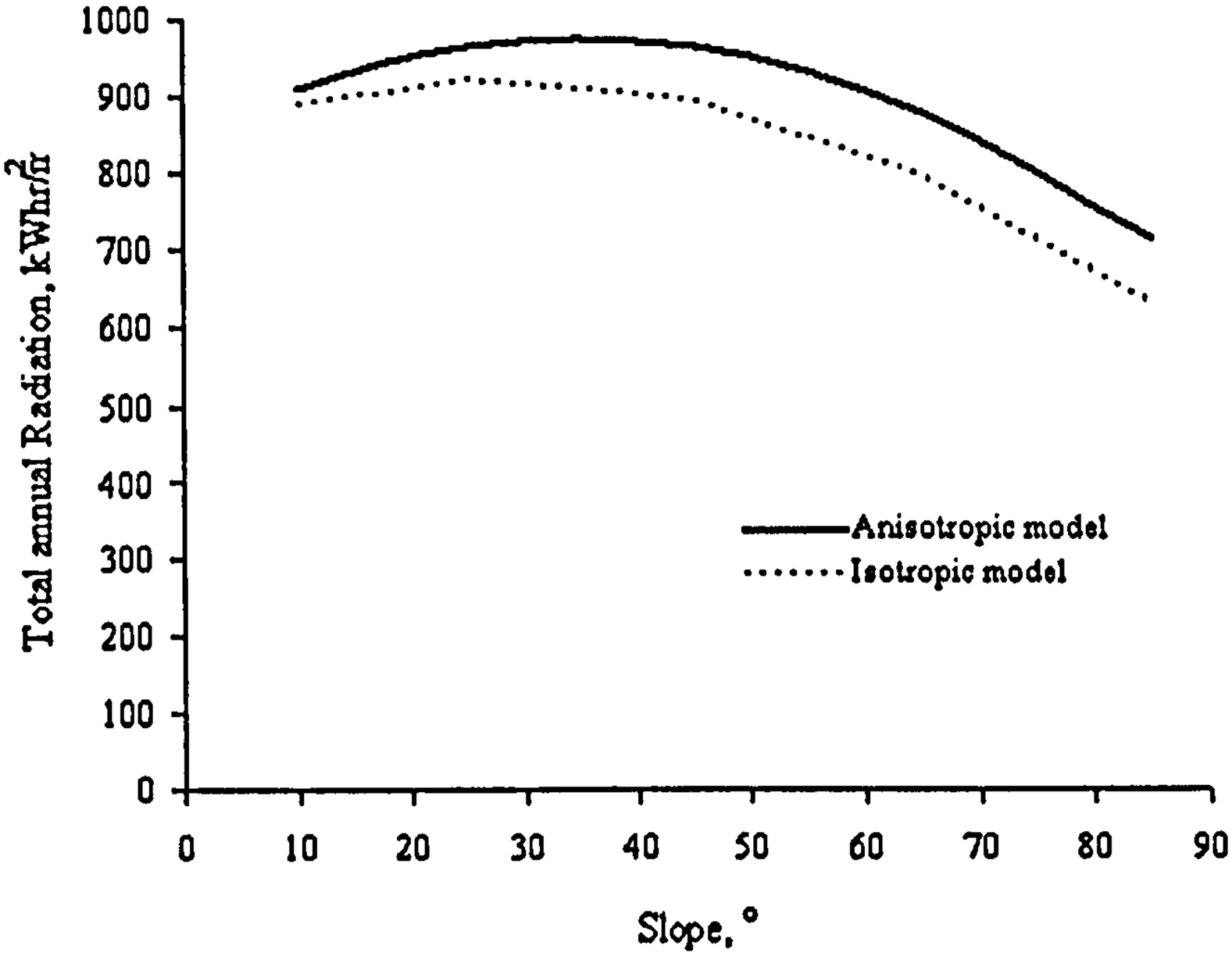

Fig. 5.8: Total yearly radiation in kWhr/m^2 for different collector slopes for Edinburgh at an azimuth of 180° by both the isotropic and anisotropic models based on dataset1.

5.4 ESTIMATION OF SLOPE IRRADIANCE: DATASET2

5.4.1 Estimation of horizontal diffuse irradiance

As discussed above, in order to be able to use the 5-min global horizontal data, a ($dr = \frac{I_d}{I}$ vs. k_T) relationship is to be obtained. In order to obtain such a relationship, measurements of horizontal global and diffuse irradiance are required. Measurements were obtained at Wiston (latitude = 55.62°, longitude = 3.54 °), Scotland about 59.5 km from Edinburgh. The model derived from the experimental data obtained at Wiston is assumed applicable to Edinburgh. In chapter 7, the installation and testing of an RSB solar ventilation air preheating system at a house in Wiston is discussed. A solar measuring station (Fig. 5.9) for measuring horizontal and vertical global irradiance as

well as diffuse irradiance was established at the site about 20 meters from the house. A quintuple pyranometer set (QPS) was used for global solar data collection while two Delta-T sunshine sensors were used for diffuse measurements. The following sections describe the experimental set-up of the measuring station.

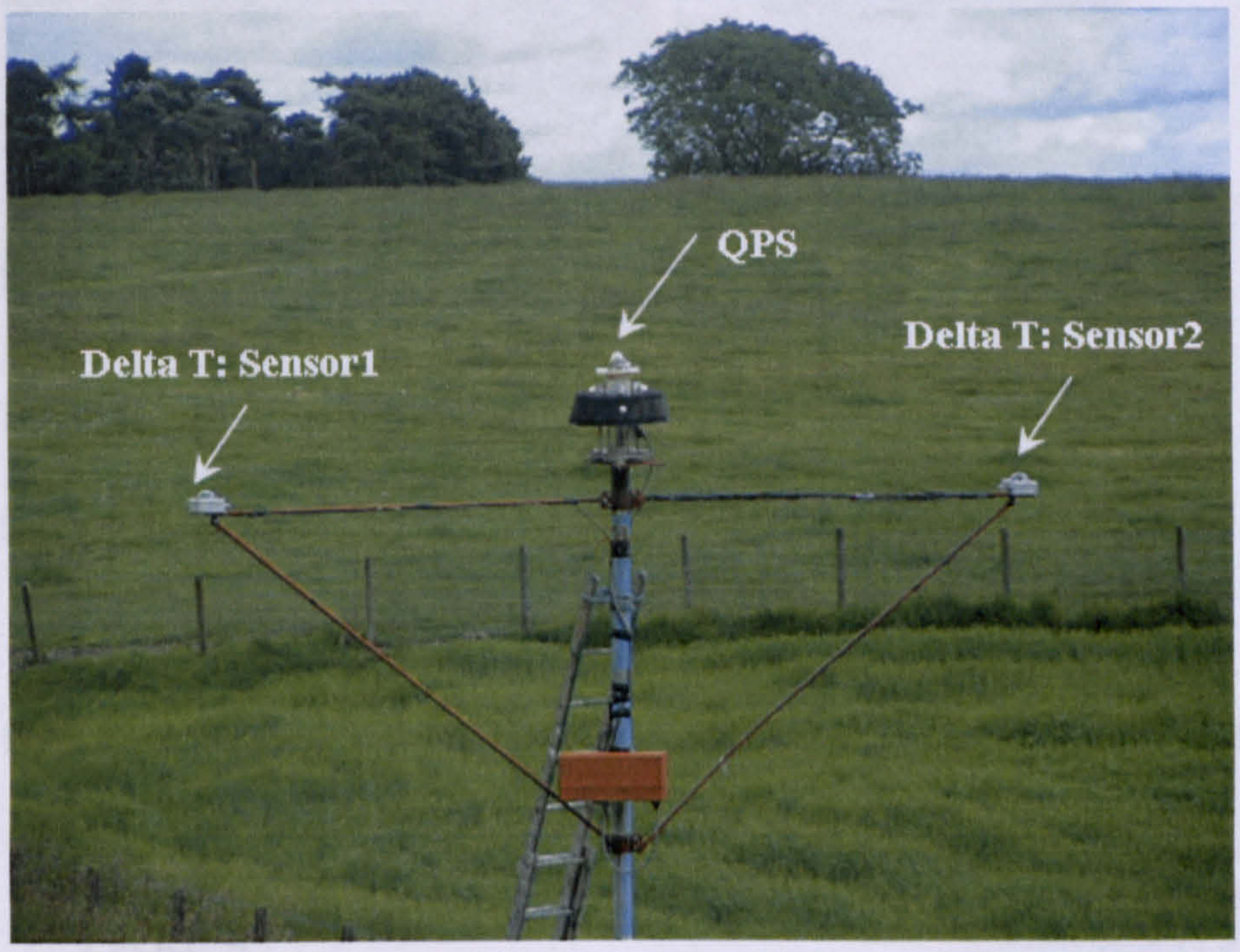

Fig. 5.9: Solar station for measuring horizontal global, vertical global and horizontal diffuse irradiance at Wiston.

5.4.1.1 The quintuple pyranometer set

The QPS is shown in Fig. 5.10. The purpose of measuring vertical data (east, south, west and north) is to verify the slope irradiance model. The five pyranometers and their connections were tested before installation. The calibration factors are shown in Table 5.1. A typical day of measurement of horizontal and vertical (all sides) irradiance is shown in Fig. 5.11 for a clear-sky day at Wiston in September, 2004. The slope irradiance is measured at the roof of the house. The effect of shading on the slope sensor as well as on the west vertical sensor can be seen from the figure.

Fig. 5.10: Quintuple pyranometer set for measuring horizontal and vertical global irradiance.

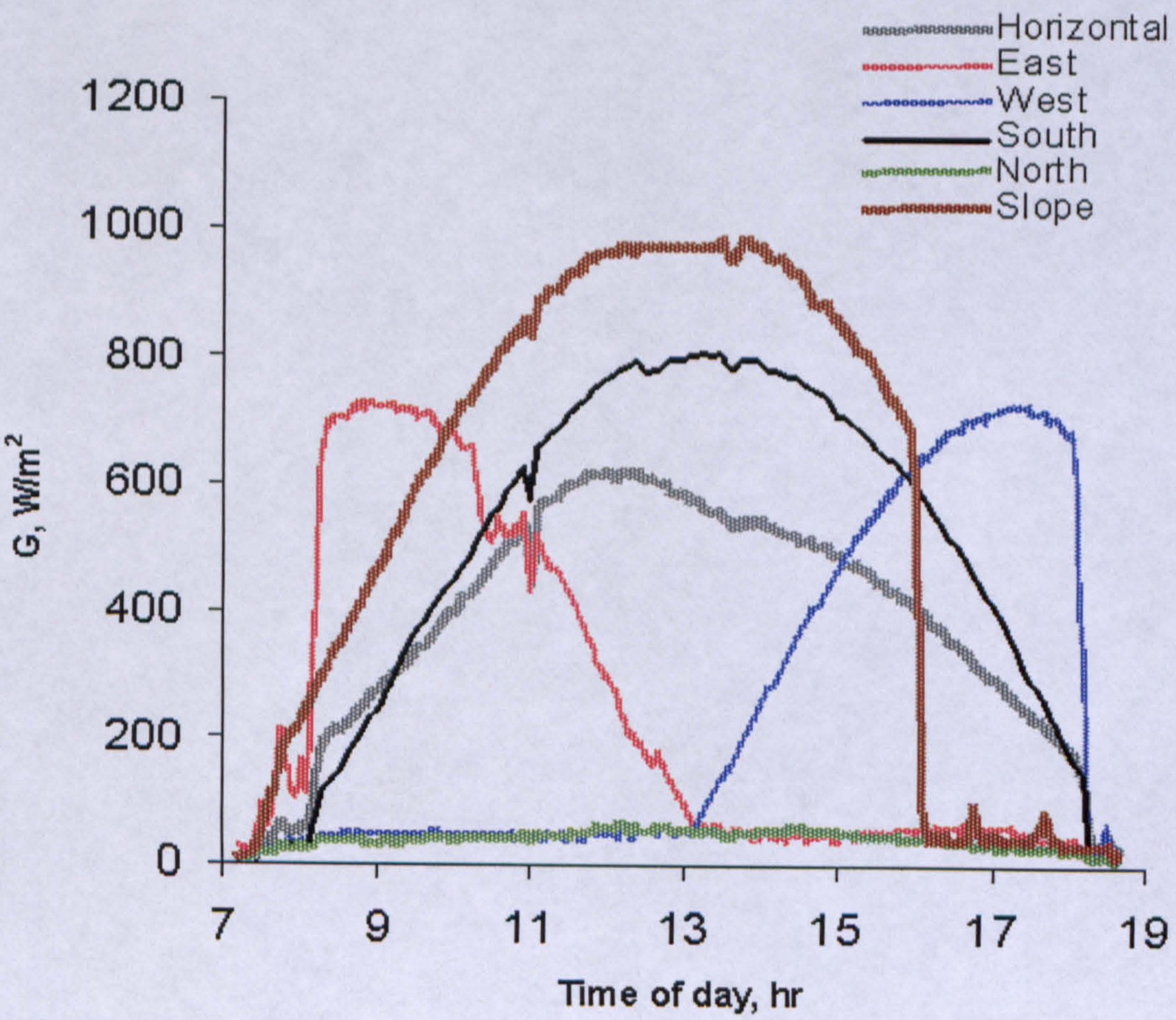

Fig. 5.11: Measurements for Sep. 7, 2004.

5.4.1.2 Calibration of Delta T sunshine sensors

For comparison purposes, two Delta T sunshine sensors were used for diffuse measurements. The Delta T sensors (sensor 1 and sensor 2) were first calibrated for global and diffuse readings against two Kipp and zonen pyranometers. For global reading calibration, readings of voltage from both the two pyranometers and the two Delta Ts were logged at 10-second intervals for 5 minutes. For diffuse reading calibration, a shade ring was held over one of the pyranometers while readings of voltage from all four instruments were recorded for another 5 minutes. The global horizontal readings for the two pyranometers were found to be within 3.6 % of each other. The pyranometer readings were averaged and the Delta Ts were calibrated for global readings against these average values. The diffuse measurements (in Volts) were also plotted against the measured diffuse from the pyranometer and the calibration factors were obtained. The calibration factors are shown in Table 5.1.

Table 5.1: Delta T and QPS calibration factors.

	Calibration factor, V / W.m^{-2}
Sensor 1- Global	2.30 E-3
Sensor 1 - Diffuse	3.40 E-3
Sensor 2- Global	1.20 E-3
Sensor 2 - Diffuse	1.68 E-3
QPS – horizontal	4.72 E-4
QPS – East	4.64 E-6
QPS – South	4.62 E-6
QPS – West	4.65 E-6
QPS – North	4.66 E-6

The diffuse and global measurements from both sunshine sensors were compared to each other for the months of July and November 2003, as shown in Fig. 5.12. Furthermore, the global irradiance as calculated from the calibration coefficients in Table 5.1 for sensor1 was compared to measurements from the Kipp and Zonen pyranometer in Fig. 5.13. The relatively high correlation coefficients give confidence in the calibration factors and in the readings of the Delta T sensors.

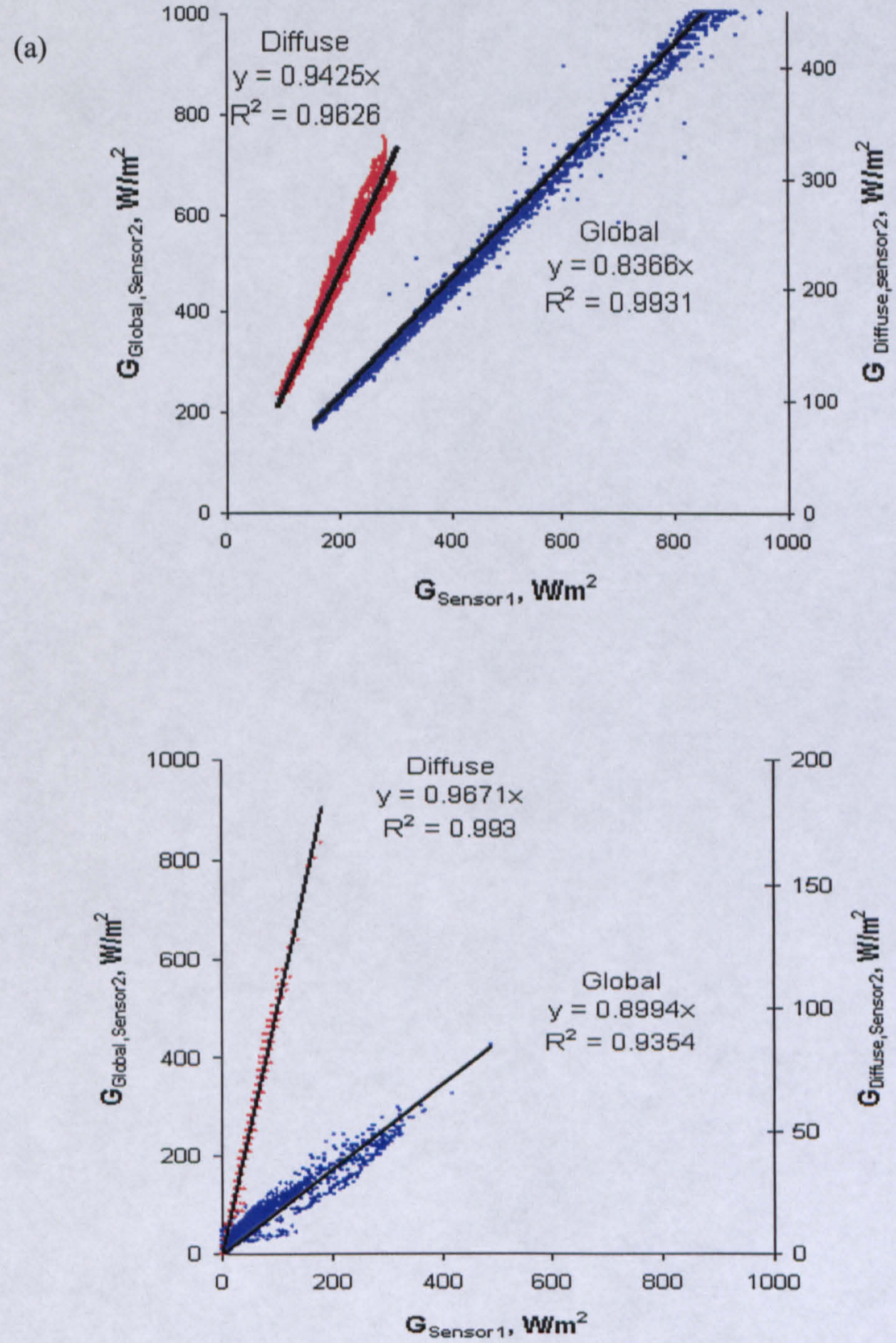

Fig. 5.12: Comparison of global and diffuse irradiance according to the predetermined calibration factors for (a) July, 2004 (1-sec data: July 5 – July 7) and (b) November, 2004 (5-min data: Nov. 1 – Nov.24).

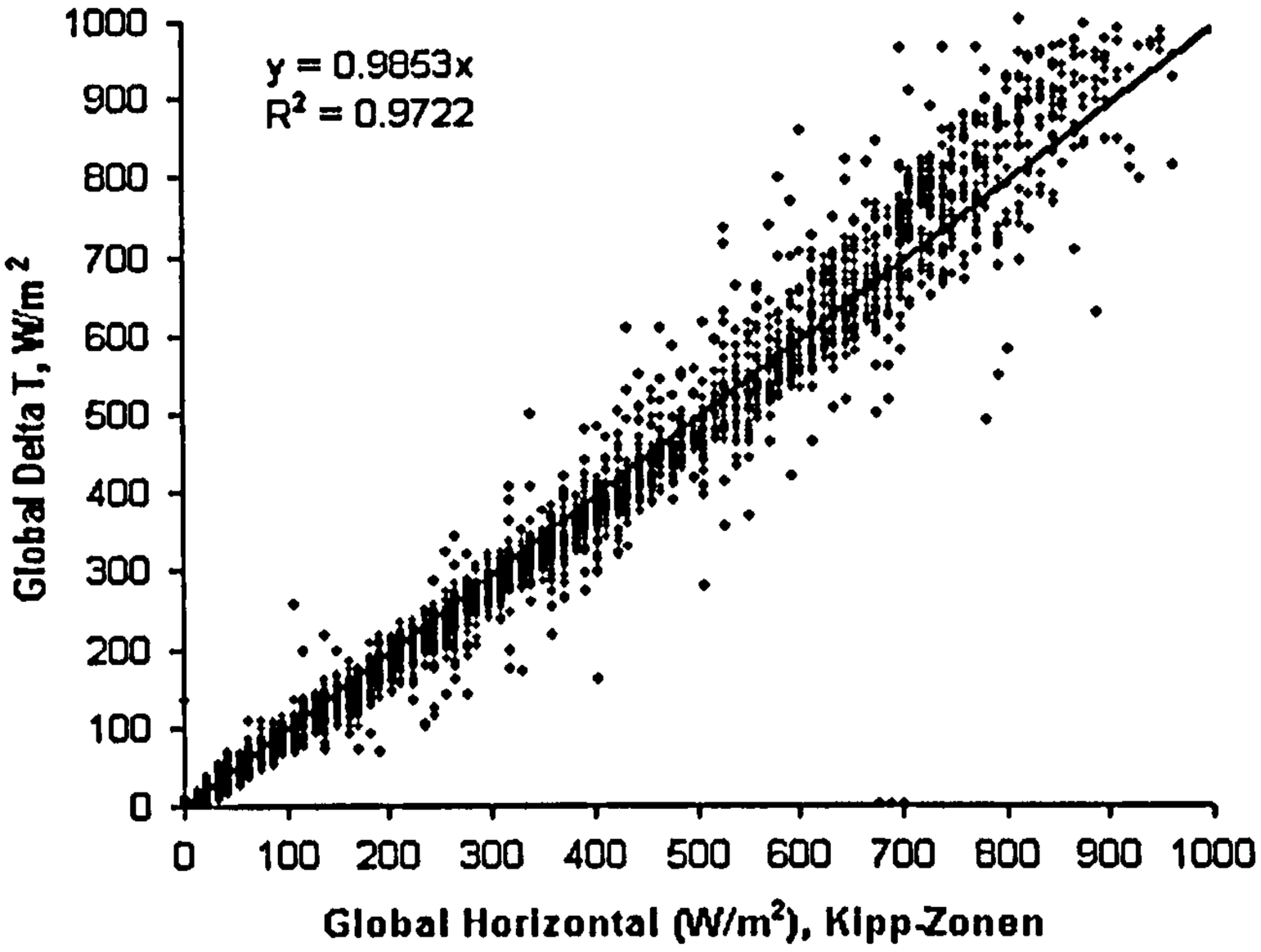

Fig. 5.13: Comparison between global irradiance for sensor 1(based on the predetermined calibration factors) and that for the Kipp and Zonen pyranometer.

5.4.1.3 Diffuse ratio vs. clearness index relationship for Wiston

Data were collected for the month of July 2003 at five-minute intervals. A program (Appendix B7) was written in VBA for calculating extraterrestrial radiation, clearness index and the corresponding diffuse ratio for all measurements. These calculations are straightforward as shown by the flow chart in Fig. 5.14. After performing these calculations, the VBA program applies two levels of filtration (to deal with erroneous measurements) as shown on the right hand side of the flow chart. The program was first tested with dataset1 as shown by the different stages of the filtration process for 1976 in Fig. 5.15.

The program was then applied to the "Wiston" data. The dr-k_T envelope obtained after secondary filtration is shown in Fig. 5.16. The dr-k_T plot for Wiston is compared to that obtained from hourly data in Fig. 5.17. The small difference between the two plots emphasises the fact that the dr-k_T relationship is location specific and so this justifying the need for collecting site-specific data. The shape of the envelope at $k_T > 0.7$ is caused by periods of high beam irradiation from the sun and high diffuse irradiation caused by the clouds. These are periods when the sun shines brightly from behind the cloud

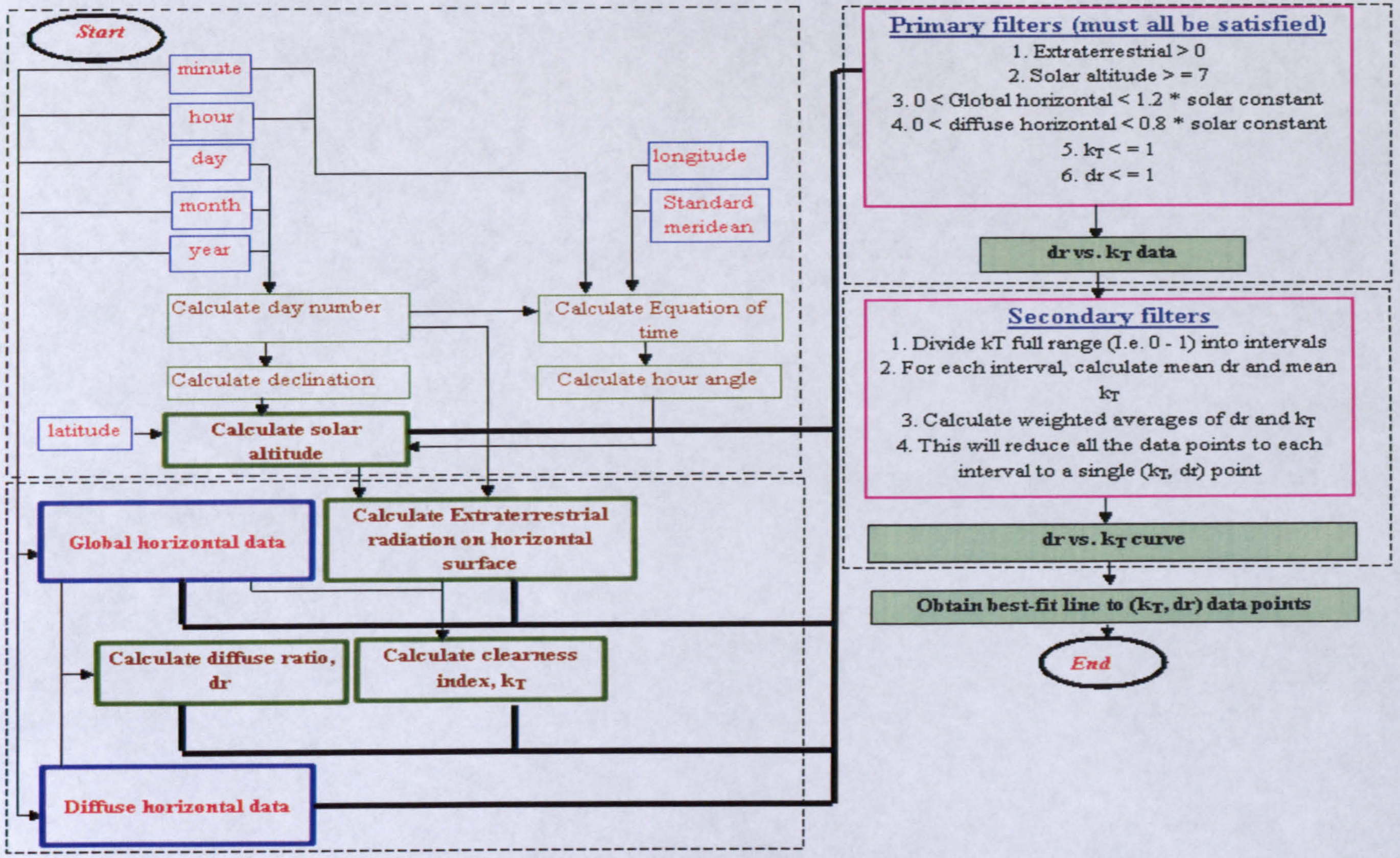

Fig. 5.14: Flow chart for calculating the diffuse ratio and the corresponding clearness index and for filtering the data.

(a)

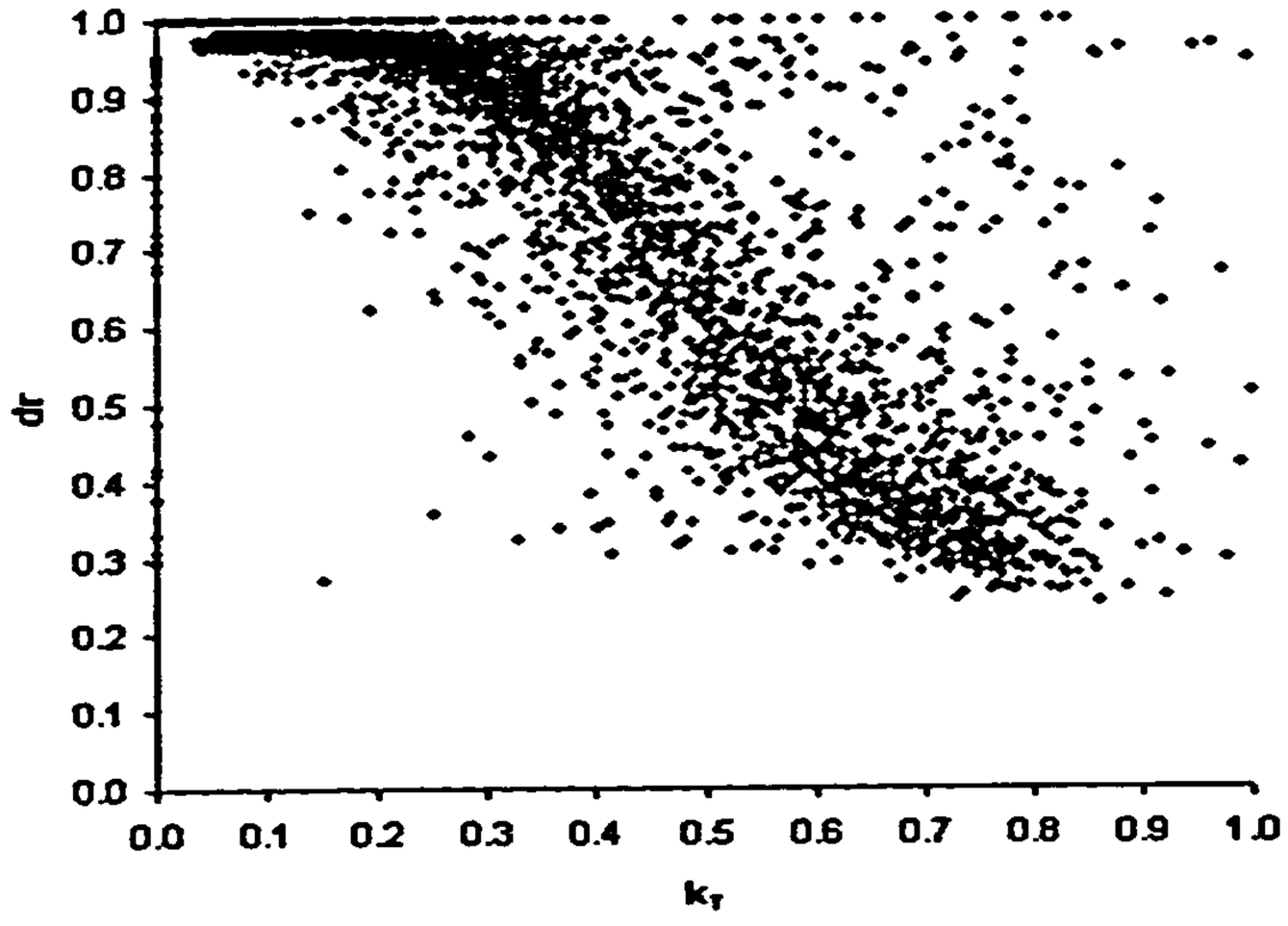

(b)

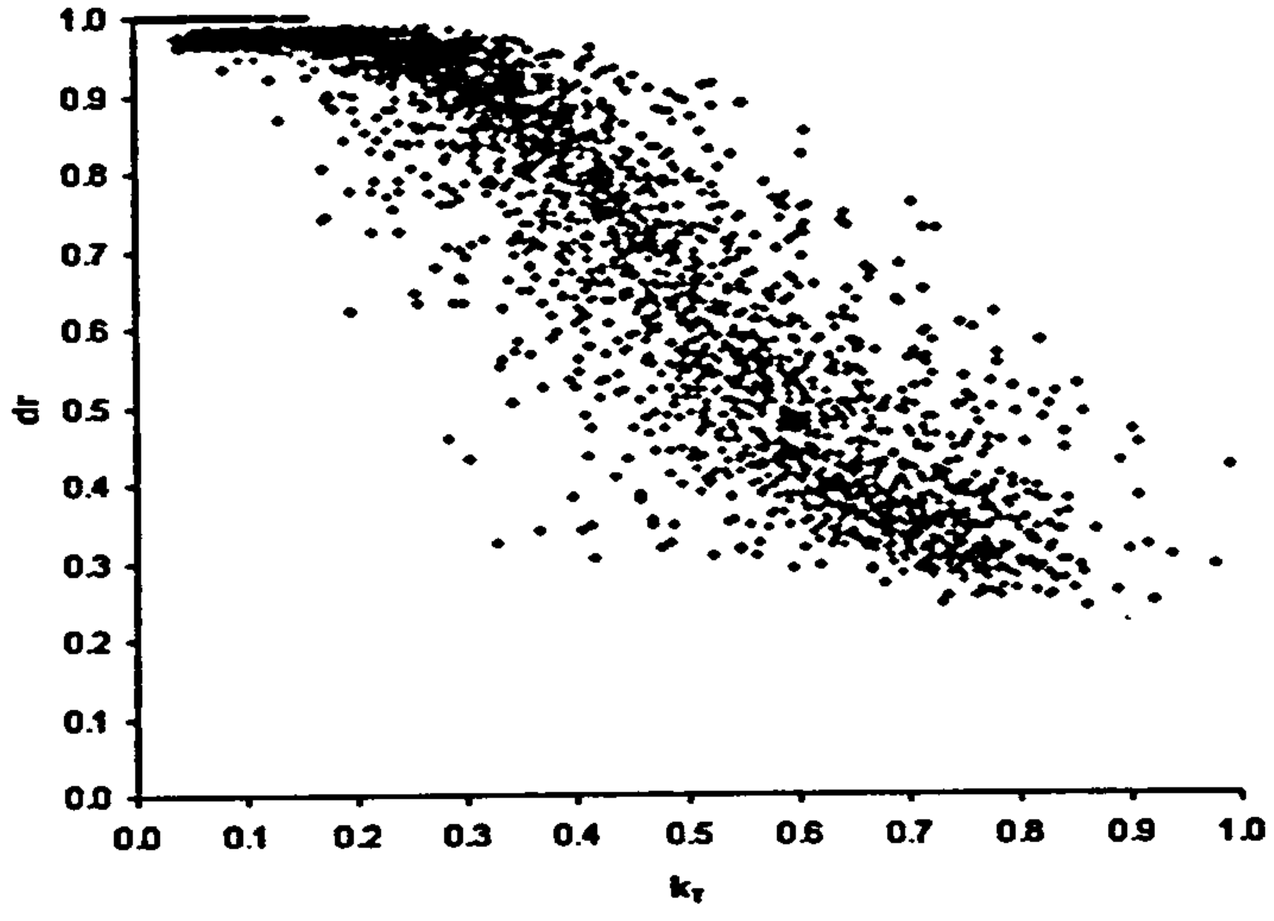

(c)

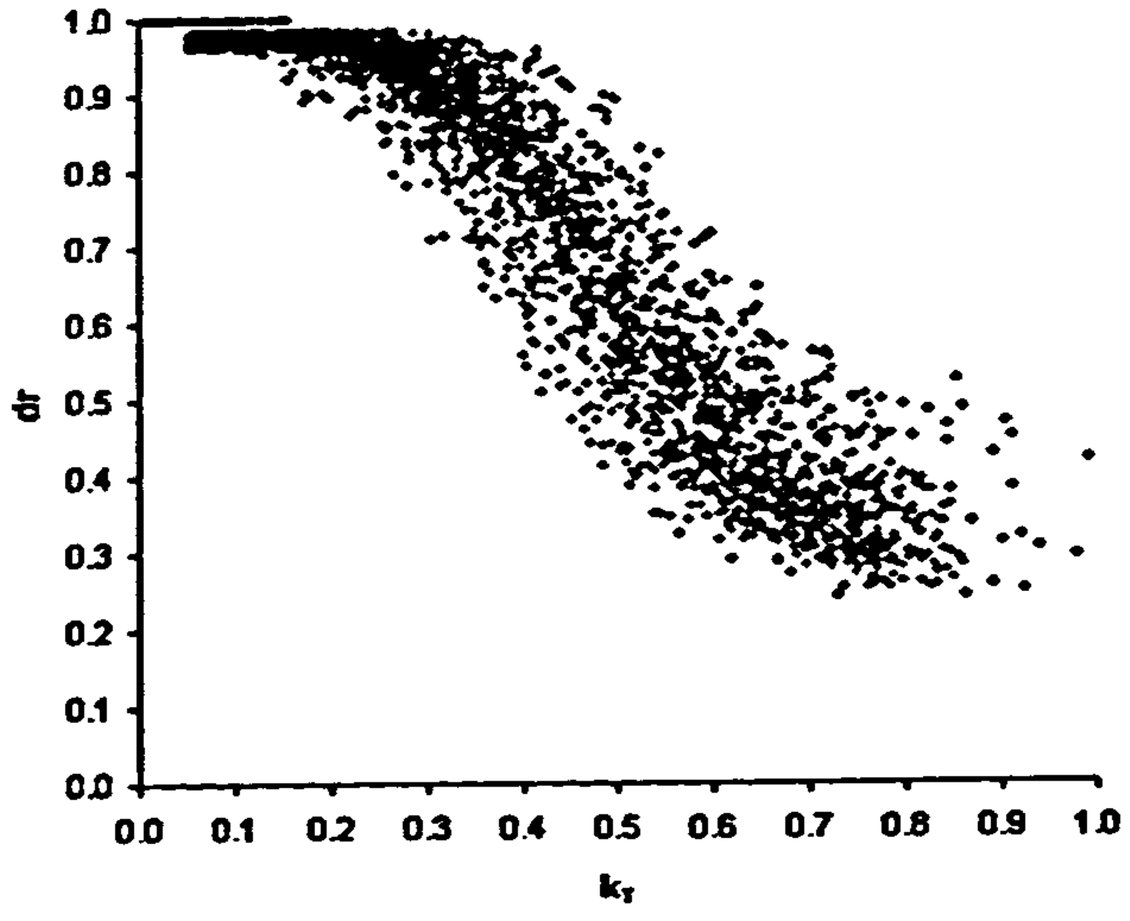

(d)

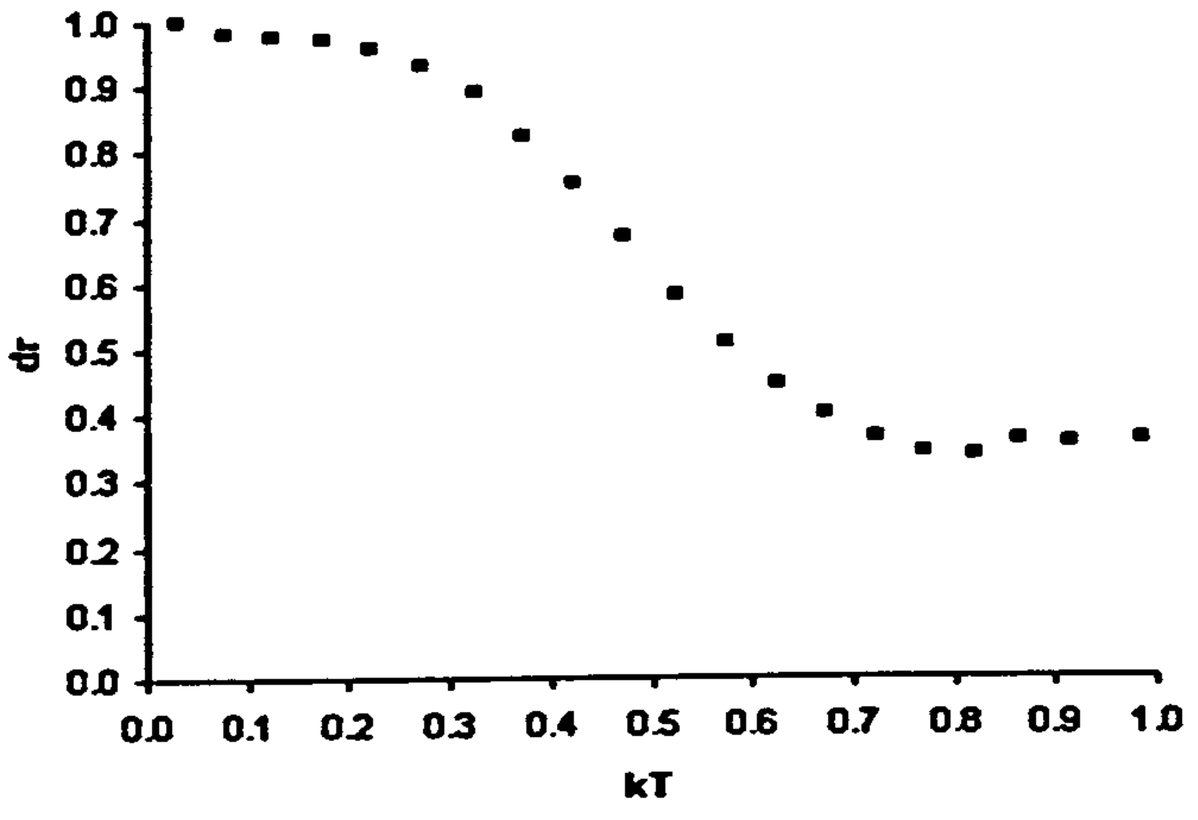

Fig. 5.15: Hourly data for 1976: (a) before filtration, (b) after applying primary filtration, (c) after applying secondary filtration and (d) weighted averages after filtration.

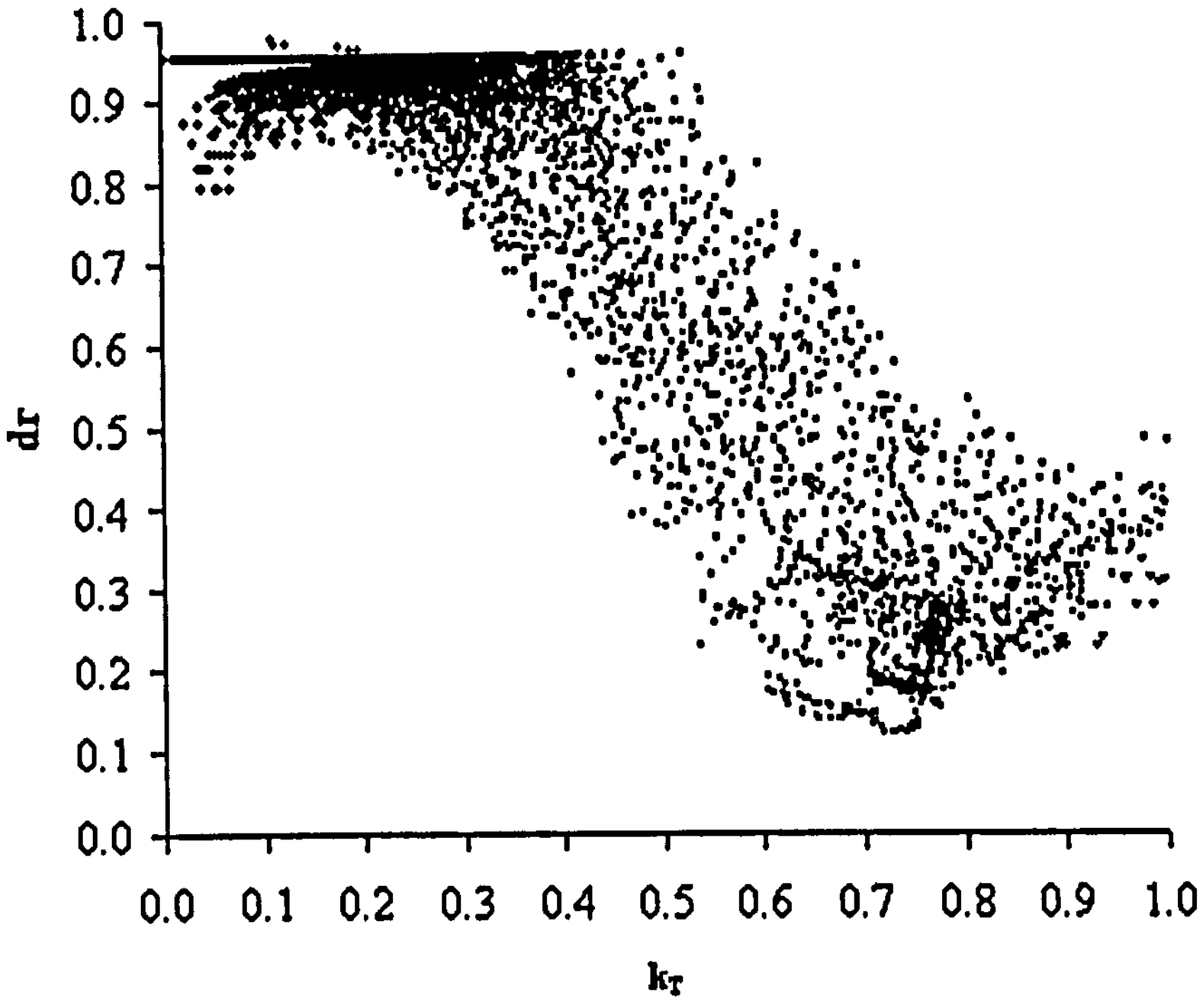

Fig. 5.16: 5-min data for Wiston after secondary filtration.

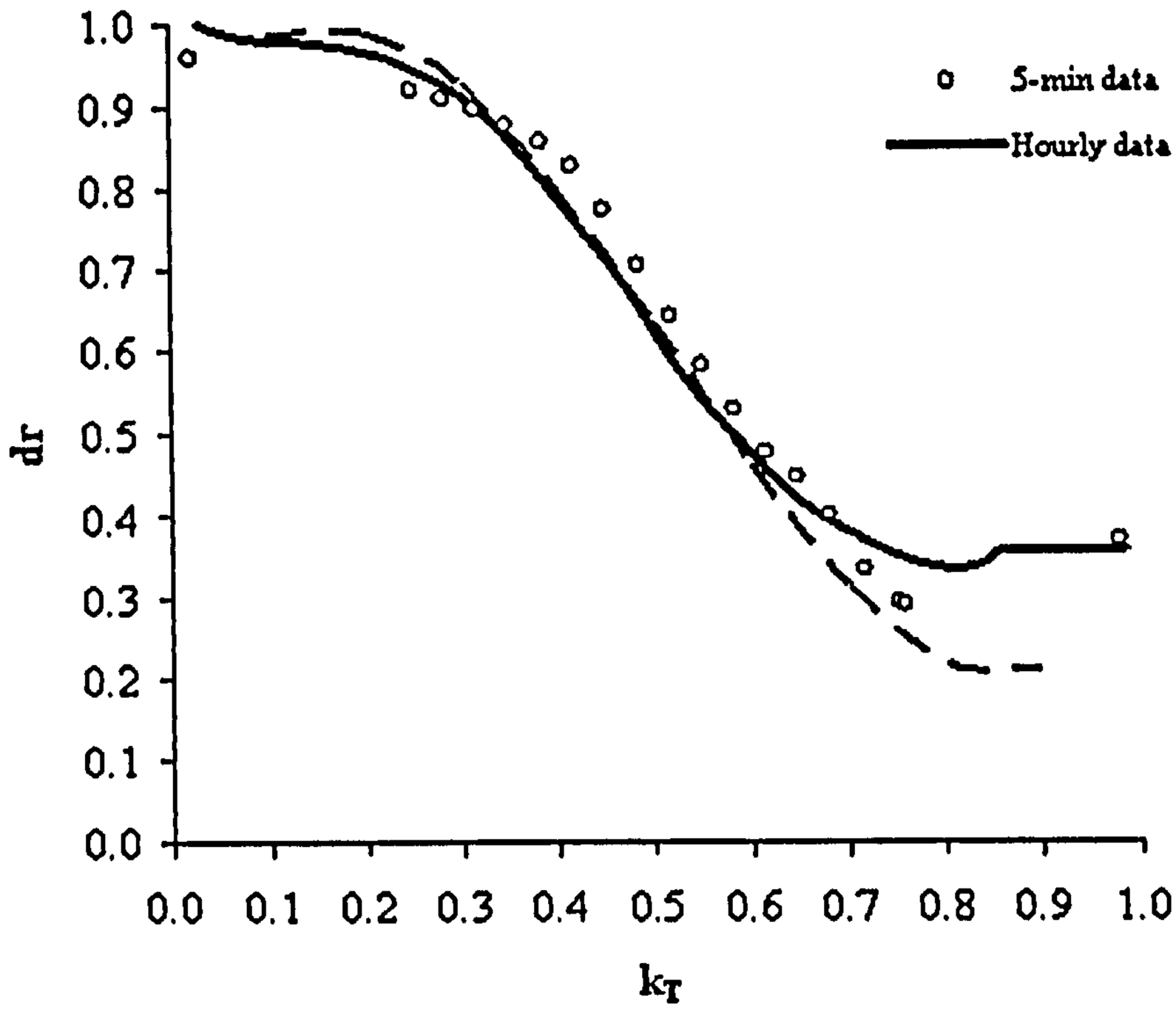

Fig. 5.17: A comparison of (dr vs. k_T) plots as derived from hourly data for Edinburgh and from 5-min data for Wiston.

The curve for the 5-min data in Fig. 5.17 was divided into three segments and best-fit lines were obtained for each of them. This approach for describing the dr-k_T relationship has been adopted by several researchers. While Orgill and Hollands (1977) adopted a linear regression for the middle segment, Erbs et al. (1982) used a 4^{th} degree polynomial to describe the same section. For the current work, a cubic regression with a correlation coefficient of 0.9977 for the middle section is found satisfactory as seen from Fig. 5.18. Thus, for dataset2, the diffuse irradiance can now be predicted from global irradiance using the following Equation

$$\frac{I_d}{I} = 0.9635 - 0.1739\ k_T \quad , \quad k_T < 0.25 \qquad 5.6(a)$$

$$\frac{I_d}{I} = 7.3411k_T^3 - 12.171k_T^2 + 4.985k_T + 0.3139 \quad , 0.25 \le k_T \le 0.78 \qquad 5.6(b)$$

$$\frac{I_d}{I} = 0.0291 + 0.3478\ k_T \quad , \quad k_T > 0.78 \qquad 5.6(c)$$

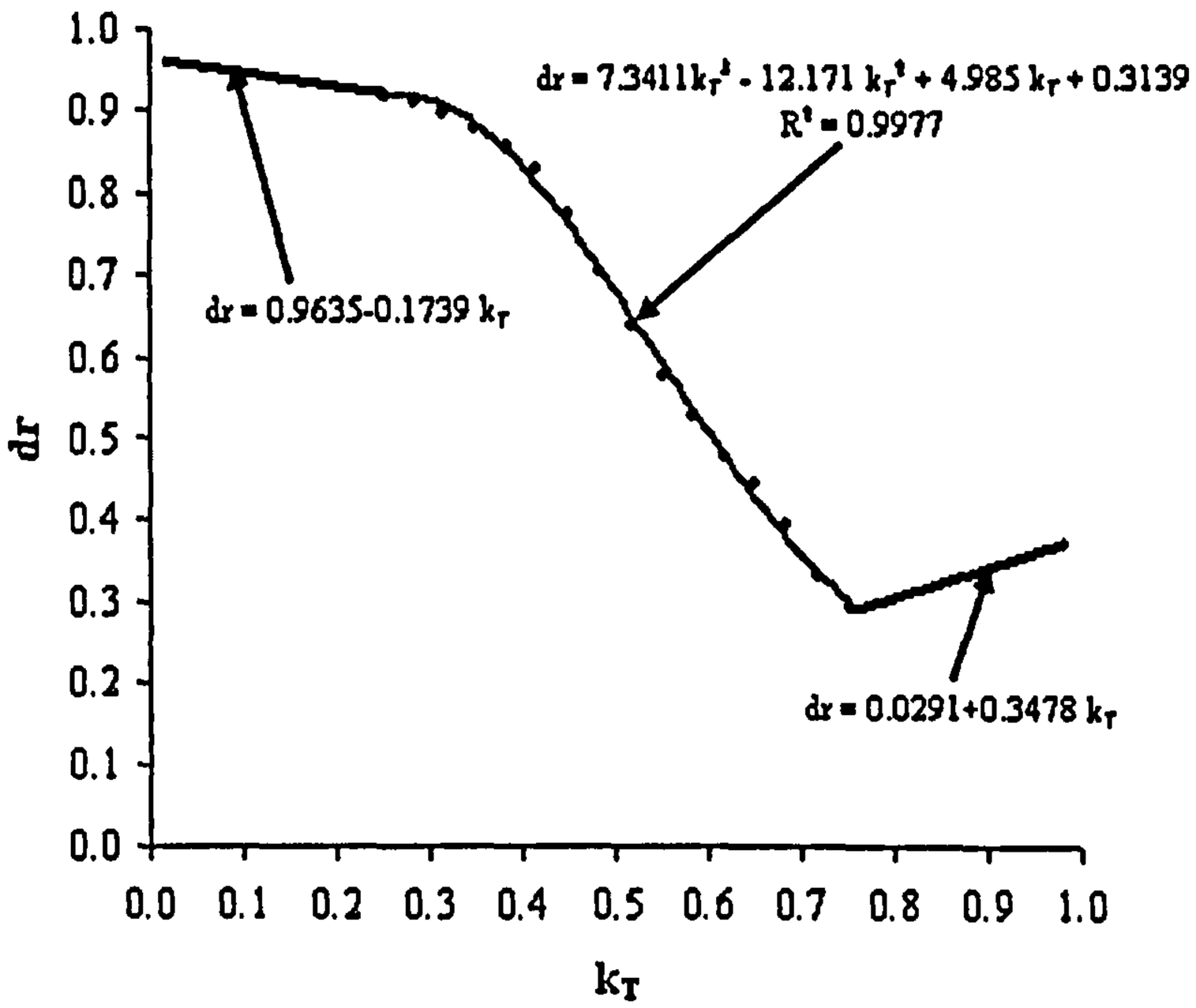

Fig. 5.18: The diffuse ratio vs. clearness index relationship for Wiston.

5.4.1.4 Validation of Northern European anisotropic model for Wiston

Irradiance on the roof (tilt = 40º) of the south facing house at Wiston (i.e. azimuth = 0º) was measured using a calibrated Kipp and Zonen pyranometer (5.17×10^{-6} V / $W.m^{-2}$). The slope measurements were compared to those predicted from the horizontal measurements obtained by the solar station shown in Fig. 5.9. Predictions obtained by both the isotropic model and the anisotropic model for Northern Europe were tested, as shown in Fig. 5.19.

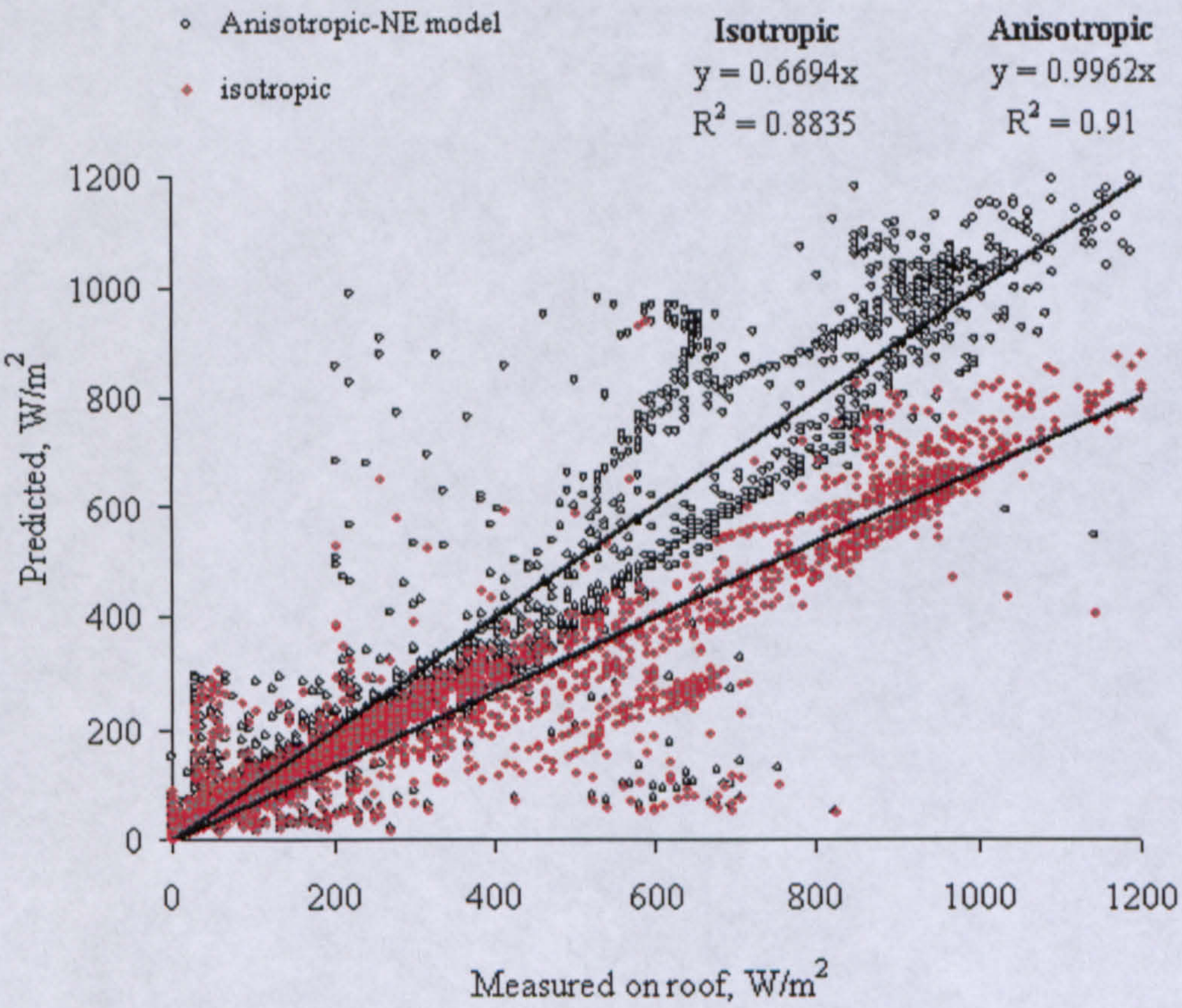

Fig. 5.19: Comparison of slope irradiance measurements and predictions by both the isotropic and anisotropic models for August 2004.

It is clear that the isotropic model under predicts measurements. The anisotropic model, on the other hand, is close enough to measurements so that the NE model can be assumed accurate for Wiston. Shading, caused by the surrounding trees, causes the scattering of the points as shown in the figure. For example, for predictions between 800 and 1000 W/m^2, some measured irradiances are only between 200 and 400 W/m^2 indicating that there is a shading effect. In other cases, the irradiances are significantly under predicted (around 600 W/m^2 on the x-axis) which can be explained by the high reflection and diffuse irradiance caused by the surrounding trees. The shading effect is

also observed from Fig. 5.11 with the curve for slope irradiance. It is seen that at about 4 pm the pyranometer on the roof does not receive any more radiation due to excessive shading to the west of the house.

5.5 SUMMARY

The current chapter introduced two datasets to be used for optimisation. These two datasets are complimentary since the first is a dataset of long-term hourly data while the other is a 1-year dataset of more detailed 5-min data. They are both considered in chapter 6. The first dataset is necessary for predicting the long-term performance of the system while the second is necessary for accurately describing the performance of the system especially when start-up characteristics are to be accounted for. However, even though the first dataset (i.e. hourly data) is complete, the second dataset contains only horizontal global irradiance data and methods for predicting ambient temperature and horizontal diffuse, which is required to predict slope irradiance, are required.

The discussion in this chapter described a method for predicting ambient temperature. A model for predicting 5-min horizontal diffuse data from global data was developed based on measurements (of global and diffuse) at the testing location where the system in chapter 7 is to be installed. This model can now be used along with the slope irradiance model to predict global slope irradiance for the site.

A North European anisotropic model for predicting slope irradiance was experimentally verified and compared to the isotropic model. Results show that the isotropic model under predicts slope irradiance and so the North European model is to be used for optimisation since it is more comprehensive.

REFERENCES

ASHRAE, (1993), Handbook of Fundamentals, American Society of Heating, Refrigeration and Air-conditioning Engineers, Atlanta.

Duffie, J.A., and Beckman, W.A., (1991), Solar Engineering of Thermal Processes, 2nd edn, New York, Wiley Interscience.

Erbs, D.G., Klein, A., and Duffie J.A., (1982), Estimation of the diffuse radiation fraction for hourly, daily and monthly-average global radiation, Solar Energy, 28, p293.

Hall, I.J., Prairie, R.R., Anderson, H.E, and Boes, E.C., (1978), Generation of a typical meteorological year, Proc. Of 1978 Annual Meeting, American sec tion of ISES, Denver, 2(2), p669.

Klein, S.A., (1977), Calculation of Monthly Average Insolation on Tilted Surfaces, Solar Energy, 19, p325.

Muneer, T., Hawas, M.M., and Sahili, K., (1984), Correlation between hourly diffuse and global radiation for New Delhi, Energy Conversion and Management, 24, pp265-267.

Muneer, T., Abodahab, N., Weir, G., and Kubie J., (2000), Windows in Buildings, Architectural Press, Oxford.

Muneer, T., Zhang, X., and Wood, J., (2002), Evaluation of an innovative sensor for measuring global and diffuse irradiance, and sunshine duration, Int. J. of Solar Energy, 22, pp115-122.

Muneer, T., and Fairooz, F., (2002), Quality control of solar radiation and sunshine measurements-lessons learnt from processing worldwide databases, Building Services Engineering Research & Technology, 23, pp151-166.

Muneer, T., Younes, S., and Claywell, R., (2003), Quality control of solar radiation data: Present status and proposed new approaches, Proceedings of the conference Measurement and Modelling of Solar Radiation & Daylight, Edinburgh, UK, 2003.

Muneer, T., (2004), Solar radiation and Daylight models, Elsevier, Oxford

Orgill, J.F., and Hollands, K.G.T., (1977), Correlation equation for hourly diffuse radiation on a horizontal surface, Solar Energy 1977; 19:357.

Reindl, D.T., Beckman W.A., and Duffie, J.A., (1990), Diffuse fraction correlations, Solar Energy, 45, p1.

Wood, J., Muneer, T., and Kubie, J., (2003), Evaluation of a new photodiode sensor for measuring global and diffuse irradiance, and sunshine duration, Journal of Solar Energy Engineering, 125, pp1-6

6. OPTIMISATION OF SYSTEM OUTPUT AND ECONOMIC EVALUATION

In the current chapter, the model developed in chapter 3 and 4 is used with the weather data in chapter 5 to optimise the system based on maximum volume of air delivered. First the literature review in section 2.6 is extended. Next, the basis for selecting maximum volume delivered as the main criterion for optimisation is discussed. Details of the procedure for updating the model to cope with optimisation objectives are then given. The optimisation results are then presented and explained in terms of the model-based simulations given in section 4.4. Finally, the optimum system is discussed and further analysis with respect to efficiency, solar savings, and cost is carried out. Recommendations for duct length in order to maximise efficiency and diameter in order to maximise volume are also given.

6.1 INTRODUCTION

6.1.1 Previous work on optimisation of PV-driven systems

Different optimisation strategies can be considered in order to improve the overall performance of a PV-driven system. Maximum power tracking leads to the more effective utilisation of a PV module's power and thus would increase the PV module-fan efficiency. However, the inclusion of a matching device can be expensive. A simpler and less expensive system is obtained by directly coupling the PV module to the motor and choosing an optimum motor constant so that the annual output of the PV module is maximised (Kolhe et al, 2000). Although most optimum matching studies have, thus far, focused on the ratio between the electrical input to the fan and the available maximum power of the PV module, (Alghuwainem, 1992 and Eskandar and Zaki, 1997), other studies have extended the matching analysis to the motor's mechanical output with respect to the available maximum power of the PV module (Saied, 1988). Furthermore, other authors have considered hydraulic output of a pumping system with respect to maximum power (Koner, 1995). Other optimisation techniques for PV pumping systems are concerned with optimising the configuration of PV modules (Firatoglu, 2004) or maximising the volume of water delivered (Betka et al, 1999).

6.1.2 Maximising volume delivered

In designing solar energy systems in general, it is of interest to find the lowest cost system. Systems utilising solar energy processes are generally characterised by high first installation cost and low operating costs (Duffie and Beckman, 1991). The basic economic problem in solar processes is to compare the initial known investment with estimated future operating costs. Most solar energy processes require an auxiliary energy source so that the annual loads are met by a combination of both conventional and solar sources. In PV-driven systems, while the capital cost is comparatively high, the operating cost is very small.

In economic analysis, it is convenient to express the solar energy contribution to the total load in terms of fractional reduction in the amount of energy that must be purchased. If the purchased energy with a fuel only system is L_0 (kWhr), the auxiliary energy purchased is L_A (kWhr) and the solar energy delivered is L_S (kWhr), then for the i^{th} month, the fractional reduction of purchased energy when a solar energy system is used is

$$sf_i = \frac{L_{o,i} - L_{A,i}}{L_{o,i}} = \frac{L_{S,i}}{L_{o,i}} \tag{6.1}$$

On an annual basis with energy quantities integrated over the year

$$F = \frac{\sum_{year} sf_i . L_{o,i}}{\sum_{year} L_{o,i}} \tag{6.2}$$

The solar fraction for alternative systems can be calculated, and that with the higher solar fraction implemented. In optimising a PV-driven system, the solar fraction should be maximised so that the purchased auxiliary energy is minimised. In considering the present system, the monthly heat delivered to the house, E_{month} (J), for a given period of time is

$$E_{month} = C \cdot \sum_{month} \left(Q \cdot \Delta T \right) \tag{6.3}$$

where C is a constant (assuming the specific heat capacity of air is independent of temperature), and ΔT is the difference between the delivered air temperature and ambient temperature. Maximising the heat delivered to the house requires maximising both the flow rate and air delivery temperature. Delivery temperature is dependent on, among other factors, the amount of heat absorbed by and stored in the slates. Chapter 7 considers the estimation of heat delivered by the system using calculated flow rates (according to the model presented in chapters 3 and 4) and measured temperatures of air delivered. For the present work, the optimisation process is based on two major assumptions:

1. For a given month, the temperature difference ($\Delta T_{month} = \Delta T_{delivered} - T_{amb}$) is taken as a constant (the average (ΔT) for the month).

2. System flow rate has no significant effect on the temperature of the slates.

The two assumptions above necessitate that

$$E_{month} = C \cdot \Delta T_{month} \cdot \sum_{month} Q \qquad (6.4)$$

where the term $\sum_{month} Q$ is proportional to the monthly volume of air delivered. Equation 6.4 reveals that if different systems are compared, the optimum system is the one which delivers the maximum volume of air.

6.1.3 Current optimisation strategy

The main objective of the present chapter is to employ the experimentally validated flow rate model (chapters 3 and 4) along with the slope irradiance model (chapter 5) to optimise the system. The optimum system is defined as that which delivers the maximum monthly (and consequently annual) volume of air. It was mentioned in section 4.4 that maximising the volume delivered does not necessarily imply maximising efficiency. For the current work, the optimum PV-fan system which maximises the volume delivered is first identified. The optimum system is then modified in order to maximise flow efficiency. Even though maximising efficiency will slightly decrease the volume delivered, it is desirable in order to utilise most of the solar

energy available to the PV module and that given by the fan (in terms of pneumatic output). In order to maximise efficiency, parameters such as duct length (section 6.5.2.2), duct diameter (section 6.5.3) and motor constant (6.5.4) are considered.

In designing an RSB ventilation preheating system, the objective can typically be to identify the components, which will deliver at least recommended ventilation rates at the lowest cost. This requires that the designers select from commercially available components. In this case, the input parameters will be different and the model flow chart will also differ from that shown in Fig. 4.1. This will be discussed briefly in Chapter 8 (Future work). In the current work, however, as discussed in section 3.3.7, the system is optimised with respect to a range of previously selected components (Table 3.3).

In PV-driven systems, the equipment is sufficiently expensive that investment costs dominate the life cycle costs and so, over designing the system, is to be avoided. In order to minimise initial cost, the optimisation procedure is applied to systems with single components (i.e. single PV, single fan) only. The optimum system is then compared to systems with PV and fan parallel, and series combinations. The possible combinations of PV modules and fans in series and in parallel are shown in Fig. 6.1.

The optimum system is compared to other systems in several ways including the volume delivered, the overall efficiency, the solar fraction, the potential savings, and the payback period. The results of the optimisation process are presented and explained in terms of the model-based theoretical (Q-G) and (η-G) simulations in chapter 4 (section 4.4).

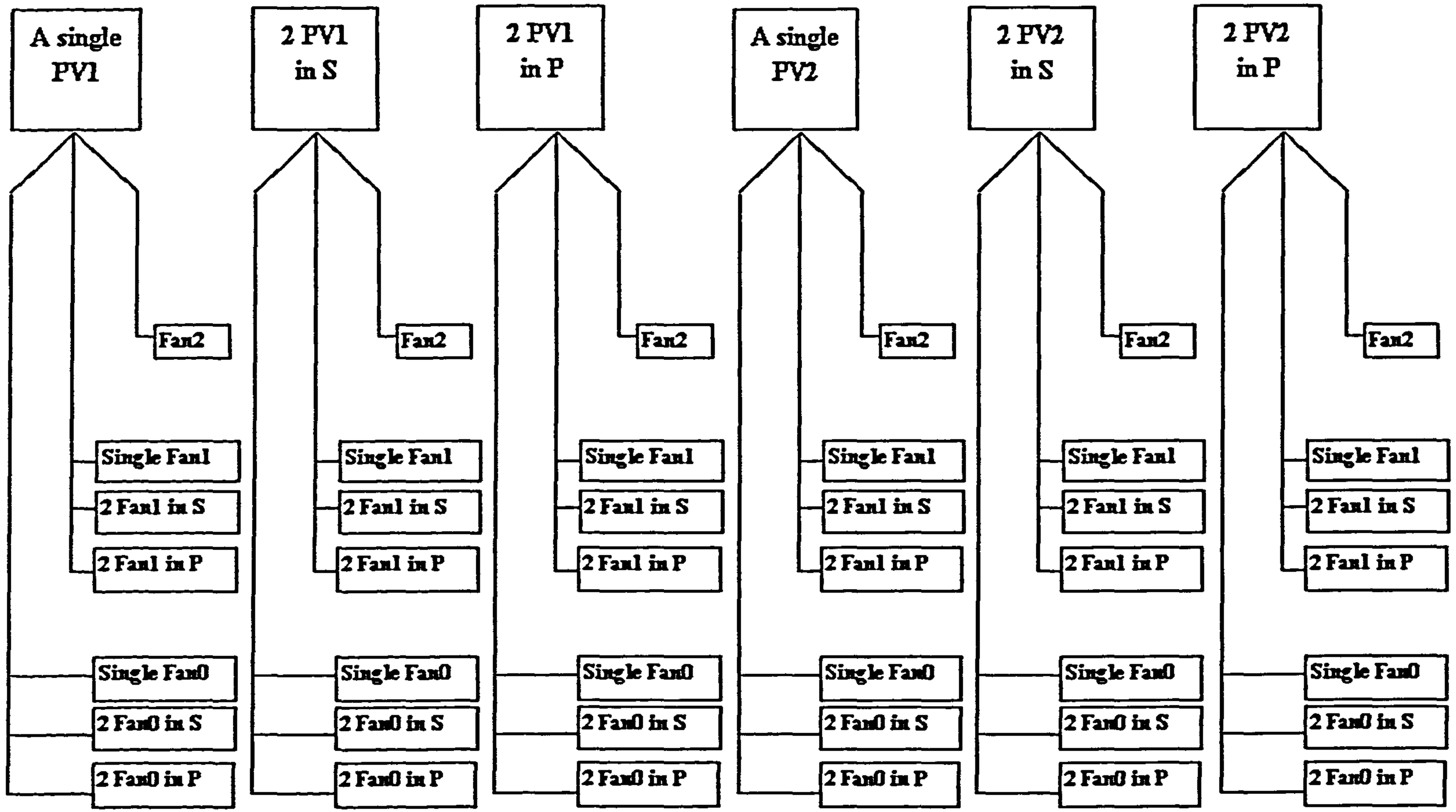

Fig. 6.1: The different PV-Fan combinations considered for optimisation. S stands for series, P strands for parallel.

6.2 ESTIMATING VOLUME DELIVERED

Several PV pumping system studies used the total volume of water delivered as a basis for optimisation since it is desired to maximise the volume of water pumped. The volume delivered in a PV pumping system between times t_1 and t_2 is calculated as

$$V = \int_{t_1}^{t_2} Q \, dt \tag{6.5}$$

Navarre et al (2000) derived the following expression for the daily volume of water delivered

$$V = \int_{t_1}^{t_2} \frac{P_{m,ref} \cdot G \cdot \eta_A \cdot \eta_{MP}}{2.725 \cdot G_{ref} \cdot H_T} \, dt \tag{6.6}$$

where $P_{m,\,ref}$ is the rated power of the PV module at STC, G_{ref} is the irradiance at STC, η_A is the PV array performance factor considering wiring and mismatch losses, η_{MP} is the efficiency of the motor-pump unit and H_T is the total head in the system. As the parameters $P_{m,\,ref}$, η_A, η_{MP} and H_T are all functions of irradiance, ambient temperature and wind speed, the task of integrating Eq. 6.6 is, in practice, clearly complex. Alternatively, since irradiance, ambient temperature and wind speed data are available in tabulated form; the flow rate and efficiency can be calculated for each row and the sum, over a given period of time, determined. The volume delivered over the smallest time interval (i.e. 1 hr for dataset1 and 5-min for dataset2) is calculated from Eq. 6.7, as can be inferred from Fig. 6.2

$$V = (Q_i + Q_{i+1}) \cdot \frac{(t_{i+1} - t_i)}{2} \tag{6.7}$$

where V is in m^3, Q is in m^3/s, and $\Delta t = t_{i+1} - t_i$ is 300 for 5-min data and 3600 for 1-hr data.

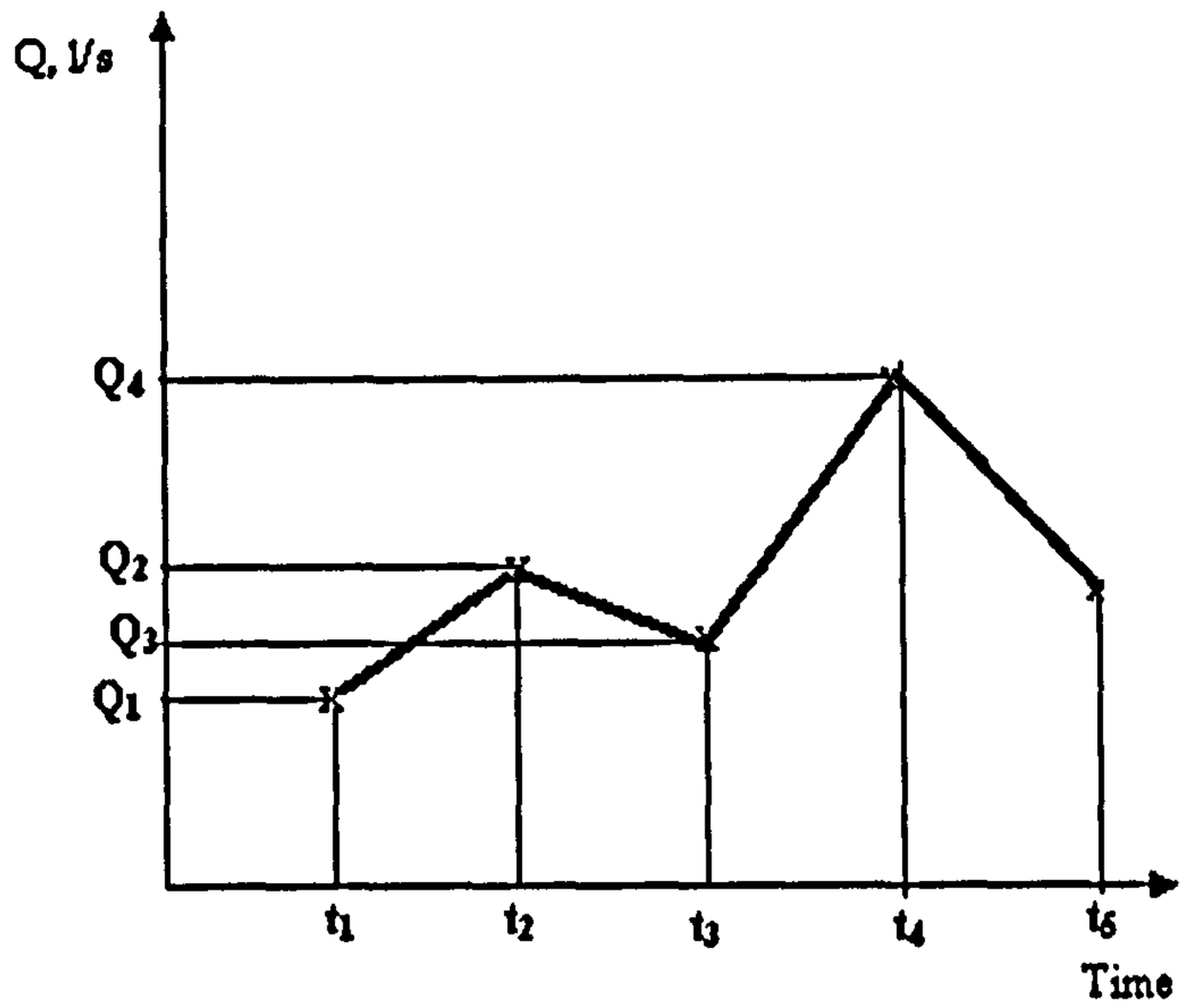

Fig. 6.2: A portion of the flow rate profile for a given day.

So in Fig. 6.2, the total volume delivered (assuming the fan starts at t_1 and stops at t_5) is calculated as

$$V = \frac{\Delta t}{2} \cdot (Q_1 + 2Q_2 + 2Q_3 + 2Q_4 + Q_5).$$

Clearly, the threshold irradiances (start-up and cease) of the PV-fan system significantly affect the volume of air delivered. From Fig. 6.3 it can be seen that, according to irradiance data available, the fan is operating at t_5 but it ceases to operate at some point between t_5 and t_6. If threshold irradiances are not accounted for, the fan will still be operating at t_6 delivering a flow rate of Q_6, as shown. The shaded area in Fig. 6.3 corresponds to the extra volume that would have been predicted if the threshold irradiances were not considered. Considering start-up characteristics, the model will give a zero flow rate at t_6 (or will virtually skip the calculation for that irradiance) since there is not enough irradiance to re-start the fan after it had ceased to operate. Assuming the fan starts at t_1 and ceases to operate at t_8, if start-up characteristics are not accounted for, then the total volume delivered between t_1 and t_8 is calculated as

$$V = \frac{\Delta t}{2} \cdot (Q_1 + 2Q_2 + 2Q_3 + 2Q_4 + 2Q_5 + 2Q_6 + 2Q_7 + Q_8).$$

However, if start-up characteristics are accounted for (i.e. the flow rate at t_6 equals zero), then the volume between t_1 and t_8 is $(V - 2Q_6)$ where the volume delivered between t_5 and t_6 is $V = \frac{\Delta t}{2} \cdot (Q_5)$. This calculation of $V_{5\text{-}6}$ assumes that the fan stops

half way between t_5 and t_6. As a result, it is seen that the smaller the time interval, the better the prediction of the volume delivered.

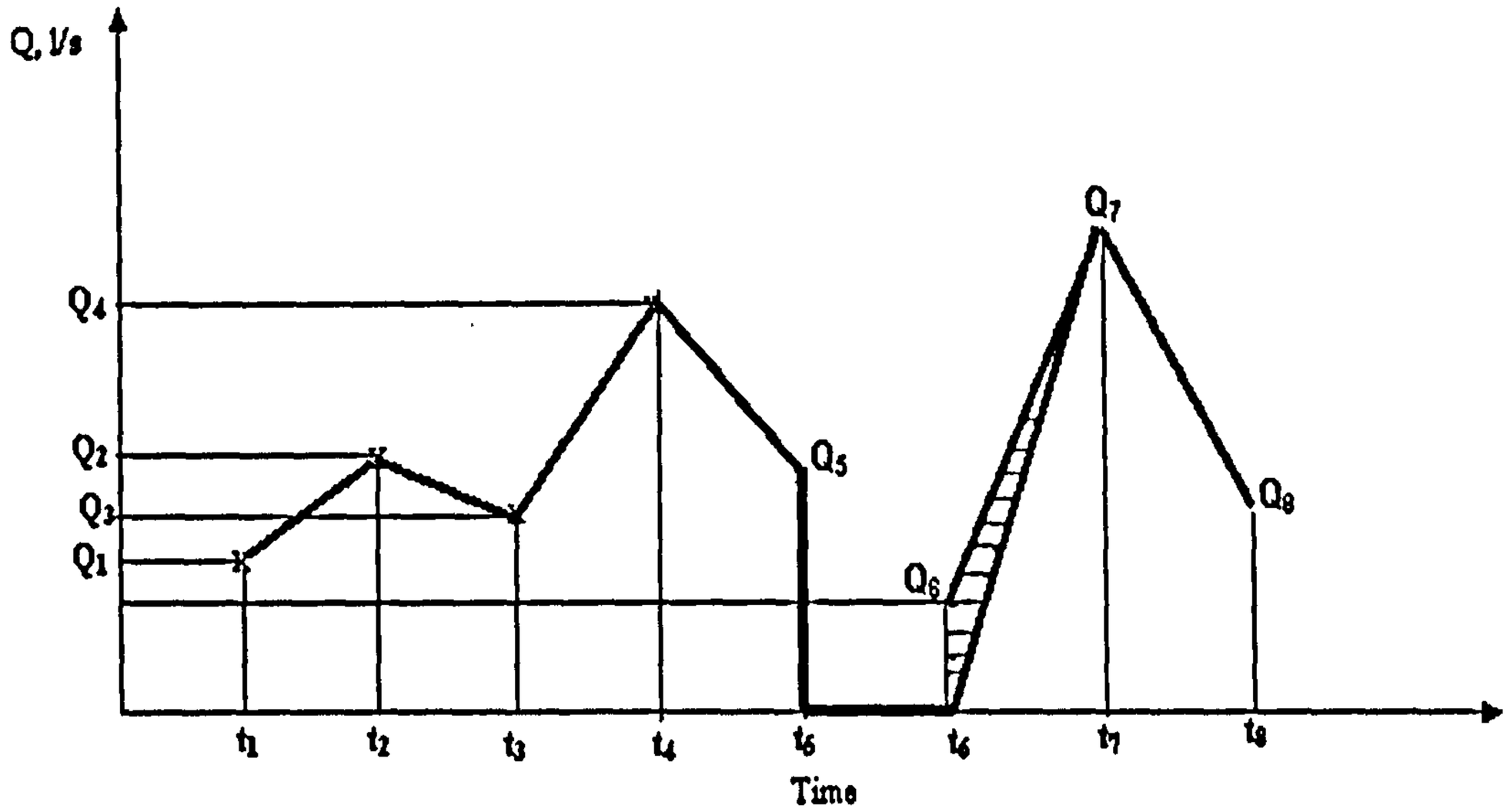

Fig. 6.3: A flow rate profile showing the extra volume that can be predicted if start-up characteristics are not accounted for (the shaded area).

6.2.1 Effect of start-up characteristics on the volume delivered

A start-up characteristic is a determinant factor in the operation of a PV system. Bione et al (2004) stated that the water volume pumped by a PV pumping system depends significantly on the minimum cut in irradiance level to start the operation of the system. The fraction of solar radiation collected above a given threshold irradiance, I_{Tc}, is defined as utilizability (Duffie and Beckman, 1991). That is, useful energy is produced only for solar radiation levels larger than the threshold value. The fraction of an hour's total energy that is above the critical level is the utilizability for that particular hour, as defined by Eq. 6.8

$$\phi_h = \frac{\left(I_T - I_{T,c}\right)^+}{I_T} \tag{6.8}$$

where ϕ_h can have values between 0 and 1. The "+" sign indicates that the utilizable energy can be zero or positive but not negative. The utilizability for a single hour is not useful. However, utilizability for a particular hour for a month of N days (for example 12 pm to 1 pm in January) in which the hour's average radiation is I_T is useful. This can be found from Eq. 6.9

$$\phi_u = \frac{1}{N} \cdot \Sigma^N \frac{\left(I_T - I_{T,c}\right)^+}{I_T} \tag{6.9}$$

The monthly average utilizable energy for the hour is the product $I_T \cdot \phi_u$. The calculation can be done for individual hours and the result can be summed for the whole month to get the month's utilizable energy.

Loxsom and Durongkaverdi (1994) used a superposition methodology to determine utilizability for PV pumping systems. They divided the non-linear curve to two, straight, linear segments to apply the utilizability concept and then added contributions of these two regions. Kiatsiriroat et al (1993) used the concept of utilizability for estimating the long-term performance of direct-coupled PV water pumping systems. A modified utilizability function, based on radiation statistics, was developed, and the monthly average daily amount of water was estimated.

Firatoglu et al (2004) stated that utilizability can be defined in terms of either PV module power output or pumped water rate. They used the former because, as they stated, the volume delivered is linearly related to PV module output. The authors then used this utilizability concept to optimise the system. A three-step optimisation methodology was considered. Firstly, the optimal PV array slope was determined using a linear search method based on 16-year data for Sanliurfa, Turkey. The authors proposed a simple manual tracking system such that the array slope was adjusted, mechanically, only once a month. Secondly, the optimal solar radiation interval was determined by the utilizability method. A utilizability factor was defined as the ratio of monthly peak-power outputs from a single PV module at a selected radiation interval to that at all radiation levels. Thirdly, the optimum number of PV panels and their optimum electrical configuration in the array were determined by a non-linear search method based on a statistical parameter.

For the current work, it is necessary to update the model described in chapter 3 and 4 for start-up characteristics. This will be discussed in detail in section 6.3.4.

6.3 OPTIMISATION PROGRAM

The flow rate model presented in chapters 3 and 4 is valid for a single data point of irradiance and ambient temperature and so it must be updated in order to cope with dataset1 and dataset2, described in chapter 5. A flow chart of the optimisation process is shown in Fig. 6.4. For given duct specifications and air properties, the model calculates the monthly volume, efficiency, and utilisability for each of the combinations shown in Fig. 6.1. The data for a given month is selected from the database and values of instantaneous flow rate are calculated. The slope irradiance and flow rate models are run for each line of data. The volume is then calculated for the whole month and entered into a cell in Excel.

The first update to the model presented in chapter 3 was adapting the program such that the large datasets could be easily handled. Due to the large amount of data in dataset1, it is not possible to handle it in Excel. The data was, therefore, processed in SPSS (the Statistical Package for Social Sciences) software and saved in (.prn) format and a simple code (Appendix B8) for opening the file, extracting and delivering the data (irradiance, ambient temperature and wind speed) corresponding to the required month was developed and presented.

In order to be useful for optimisation, the model presented in chapters 3 and 4 is updated with respect to several parameters. The input parameters necessary for running the updated model are environmental parameters (G, T_{mod}, ws), a number code for each of the PV modules and fans, and start-up characteristics. These are discussed in sections 6.3.1 through 6.3.4. In section 6.3.5, the assumptions used for implementing the optimisation model are outlined.

6.3.1 Environmental parameters

For dataset1, irradiance, ambient temperature and wind speed are available while for dataset2, only irradiance is available. It was shown in chapter 5 that ambient temperature can be predicted for dataset2. The model developed in chapters 3 and 4 does not account for wind speed and assumes that the loss coefficient, U is constant for different wind speeds. A correction term for the effect of wind speed on the loss coefficient can be incorporated as discussed below.

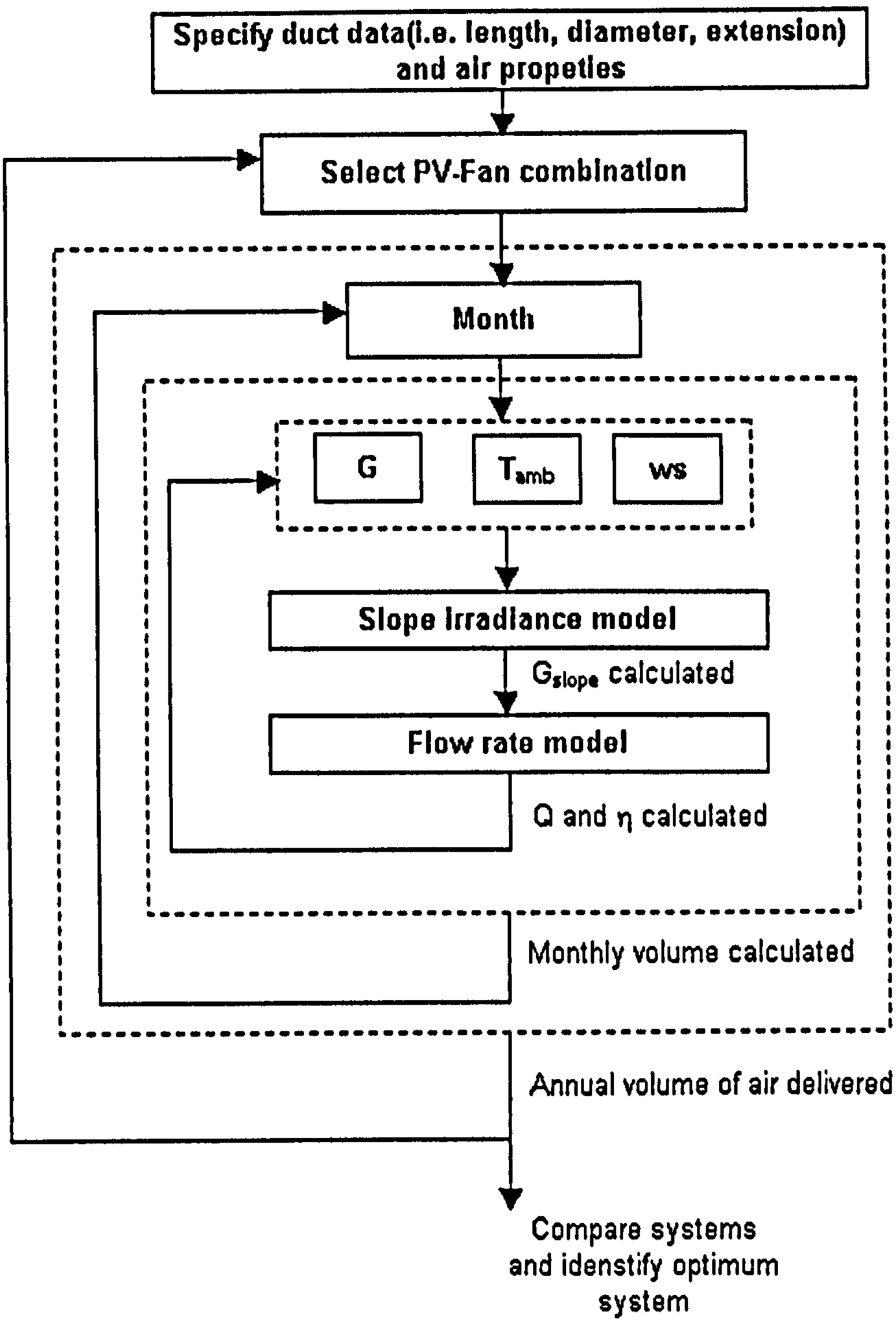

Fig. 6.4: A flow chart of the optimisation process.

6.3.1.1 Effect of wind speed

Both the roof slates and the PV module can be treated as a flat plate collector. The rate of heat loss from flat plates exposed to outside winds affects their temperature, and, consequently their performance. The wind speed over the PV module affects the loss coefficient, U, which is related to PV module temperature. Thus, wind speed indirectly affects the performance of the PV module. McAdams (1954) reported that the loss coefficient from a flat plate is related to wind speed by the equation

$$U' = 5.7 + 3.8 \times ws \qquad (6.10)$$

where ws is in m/s and U' is in W/m^{2}C. The coefficient in Eq. 3.8 is in W/C and so the coefficient obtained from Eq. 6.10 must be multiplied by the area of the PV module before being used in Eq. 3.8. As a result, Eq. 3.8 then accounts for the effect of irradiance, ambient temperature, and wind speed on PV module temperature. The effect of wind speed is considered if dataset1 is used for optimisation. On the other hand, if dataset2 is used, only the effect of irradiance and ambient temperature on PV module temperature are accounted for. In this case, the value of U is assumed constant (Table 3.6).

In order to account for the effect of wind speed, the flow chart in Fig. 4.3 is updated by including Eq. 6.10 after the box "Assume η"and using the value of U' for calculating T_{mod}.

6.3.2 PV module selection

The optimisation process considers different parallel and series combinations of the two PV modules listed in Table 3.3. A code is assigned for each of these combinations as shown Table 6.1 below. A choice of a certain number code directs the model to a database where specifications such as I_{SC}, V_{OC}, P_m, V_m, R_S, U in addition to the temperature coefficients and start-up irradiances are selected. The PV equations presented in chapter 3 are for a single PV module. These equations can be easily adapted for parallel and series combinations. The IV characteristics for PV2 modules in series and in parallel, as generated by the new method (section 3.2.2) are shown in Fig. 6.5.

In cases where two PV modules are connected in series, the operational voltage can be very high and such cases are not considered for optimisation. Furthermore, simulations for Fan0 were carried out only with PV2.

Table 6.1: Codes for PV and fan combinations to be used in the optimisation model.

PV module	Fan
1 A single PV1	0 A single Fan0
2 Two PV1 in parallel	1 A single Fan1
3 Two PV1 in series	2 A single Fan2
4 A single PV2	3 Two Fan0 in parallel
5 Two PV2 in parallel	4 Two Fan0 in series
6 Two PV2 in series	5 Two Fan1 in parallel
	6 Two Fan1 in series

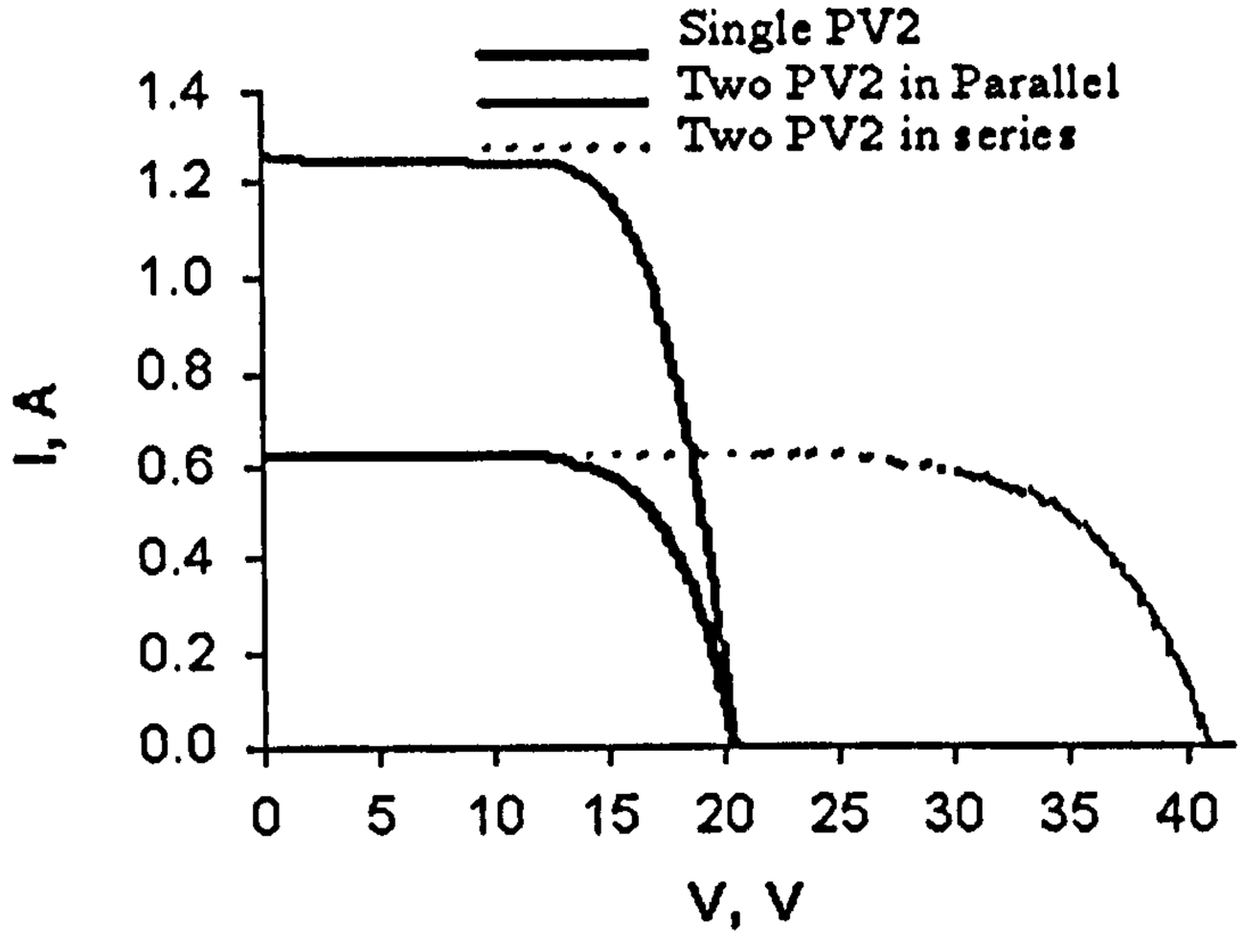

Fig. 6.5: Two PV2 modules in series and in parallel for G = 1000 W/m^2 and T_{mod} = 35 C.

6.3.3 Fan selection

The optimisation process also considers different parallel and series combinations of Fan0 and Fan1. A code is assigned for each of these combinations as shown in Table 6.1. The specifications for single fans include the constants listed in Tables 3.9 and 3.10, while those for fan combinations can be inferred from basic

electrical theory as seen in Fig. 6.6. A brushless DC motor fan can also be expensive and it will add to the cost, so, systems with a single fan are preferable.

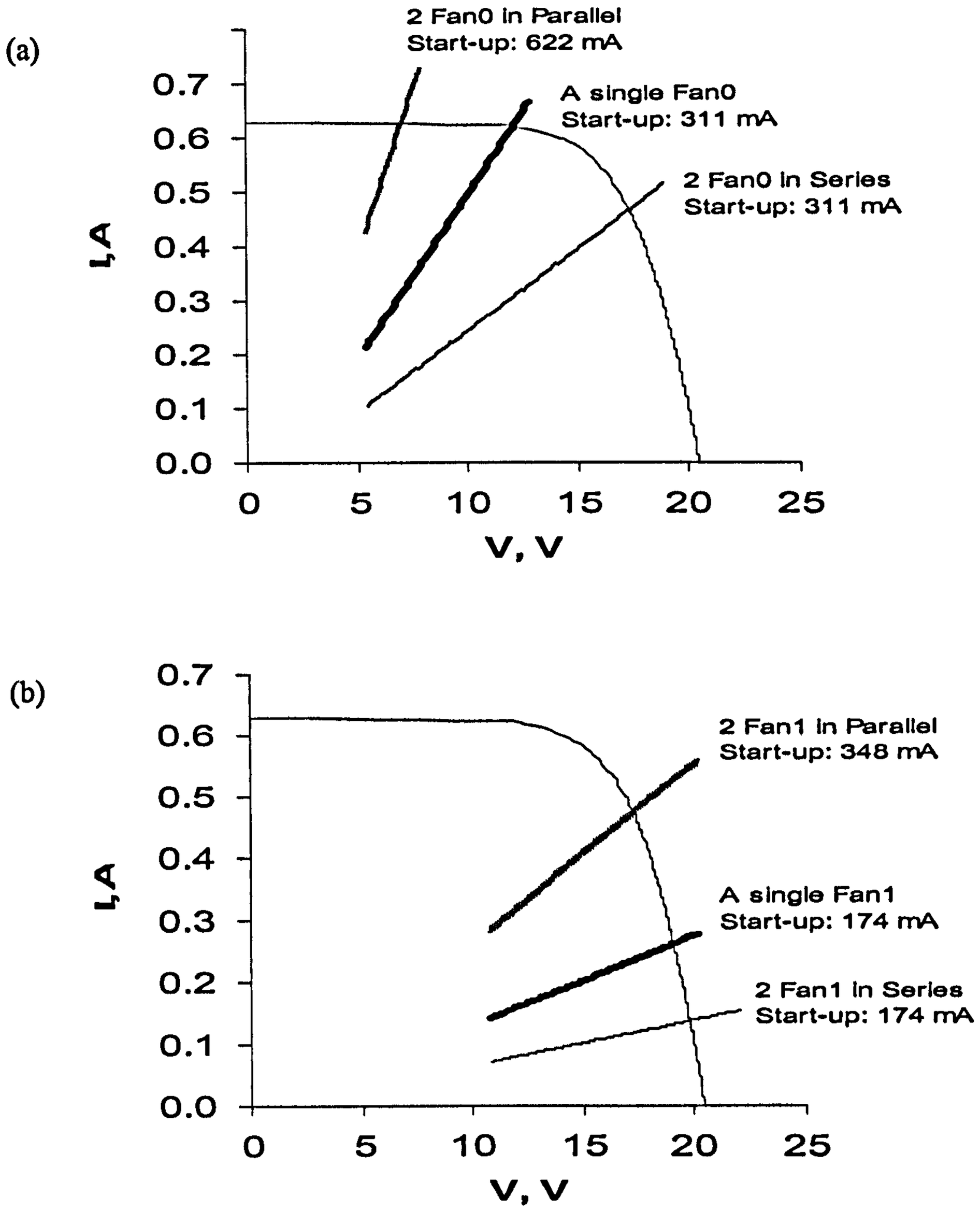

Fig. 6.6: IV characteristics for parallel and series combinations for (a) Fan0 and (b) Fan1.

The optimisation process assumes that the two fans deliver air through separate ducts at the same effective duct length (i.e. same ΔP_s-Q characteristic) and so, the flow rate for one of the branches is doubled (calculations show that for Fan0 and Fan1 with a single duct, the flow is always turbulent). However, when two similar fans are connected in series, the voltage obtained from the iteration process described in section 4.2.1 (Fig. 4.4) is halved. This is based on the assumption that the electrical characteristics of the two fans are identical.

6.3.4 Start-up characteristics

6.3.4.1 Threshold irradiances

The threshold irradiances (start-up and cease) are listed in Table 6.2 for the different PV-fan combinations. In writing the program, start-up and cease irradiances are determined by specifying both the selected PV module and fan. The start-up and cease currents and voltages for systems with single components are measured in the laboratory (V_s and I_s in Table 3.8) and threshold irradiances are calculated. Threshold and cease irradiances for parallel and series combinations are calculated from basic electrical theory.

6.3.4.2 The switch function

After specifying the PV module and fan combination required, the program chooses the corresponding start-up and cease irradiances. The flow rate model will be run only for those data points specified when the fan is operating. However, the fan is not only operating for irradiances above the start-up irradiance. If the fan is already in operation, it will keep operating as long as the irradiances are above the "cease" values as can be seen from the simplified flow chart in Fig. 6.7. A switch function, which assigns a value of "1" to an operating fan and a value of "0" to a non-operating fan, is included in the updated model. This procedure dramatically reduces calculation time as values of "1" and "0" are stored in the program, and only lines with values of "1" are considered for calculation. The switch code is shown in Appendix B9.

6.3.4.3 Kick-starting the fan

The optimisation process also considers cases where systems with high threshold irradiances are kick-started using an electronically controlled capacitor (Faiz et al., 2004). The purpose is to study whether the additional cost of kick starting is justified by the extra benefits, if any, it produces. In this case, the model is run disregarding the "switch" function and all systems are compared for the same start-up and "cease" irradiances.

6.3.5 Assumptions

In order to run the optimisation model, several assumptions are made concerning the input parameters. These assumptions do not affect the optimisation process since they are fixed for all systems considered. These are discussed below.

6.3.5.1 Slope

It was shown in chapter 5 (Fig. 5.8) that the optimum slope for Edinburgh is approximately 45°. There are no statistics about the most prevailing roof tilt in Edinburgh. For the optimisation process considered here, a slope of 45° is assumed.

6.3.5.2 Duct properties

In order to achieve higher flow rates and thus maximise the volume delivered, the resistance to flow must be kept at a minimum. This necessitates that the length of the duct is kept at a minimum. As the grill opening is reduced, the effective duct length increases. Ideally, a system with no grill has the least resistance to flow and thus the least L_{eff}. Practically, however, such a system is not favourable to prevent undesirable sudden draughts of air and also to control the noise from the fan. For the optimisation process, an effective duct length of 10-m is assumed even though through further reducing the grill aperture, it can reach to 20 m. As long as the length is the same for all PV-fan systems to be compared, the optimisation process will not be affected. In the next section it is shown that for a given PV-fan combination, there exists an optimal duct length (for a given diameter and extension) at which the system utilises 100 % of fan pneumatic power, $\Delta P \times Q$ (see Fig. 2.9).

It was shown in chapter 4 that a duct diameter of 152 mm is favourable to the 102 mm diameter. As highlighted in chapter 4, there exists a critical diameter for the system after which the volume delivered does not increase. This diameter is optimum because it maximises the volume delivered. For the current optimisation process and for system testing, in chapter 7, based on the available components, a duct diameter of 152 mm will be used.

Table 6.2: Start-up and cease irradiances (W/m^2) for the different PV-fan combinations.

Fan*		PV1	2 PV1 in P	2 PV1 in S	PV2	2 PV2 in P	2 PV2 in S
0	G_{start}	1072	518	1072	518	259	518
	G_{cease}	303	152	303	152	74	152
1	G_{start}	600	300	600	290	145	290
	G_{cease}	303	152	303	147	74	147
2	G_{start}	1800	900	1800	800	400	800
	G_{cease}	317	159	317	153	77	153
3	G_{start}	2144	1072	2144	1036	518	1036
	G_{cease}	606	303	606	294	147	294
4	G_{start}	1072	518	1072	518	259	518
	G_{cease}	303	152	303	147	74	147
5	G_{start}	1200	600	1200	580	290	580
	G_{cease}	606	303	606	294	147	294
6	G_{start}	600	300	600	290	145	290
	G_{cease}	303	152	303	147	74	147

* refer to Table 6.1 for fan numbers

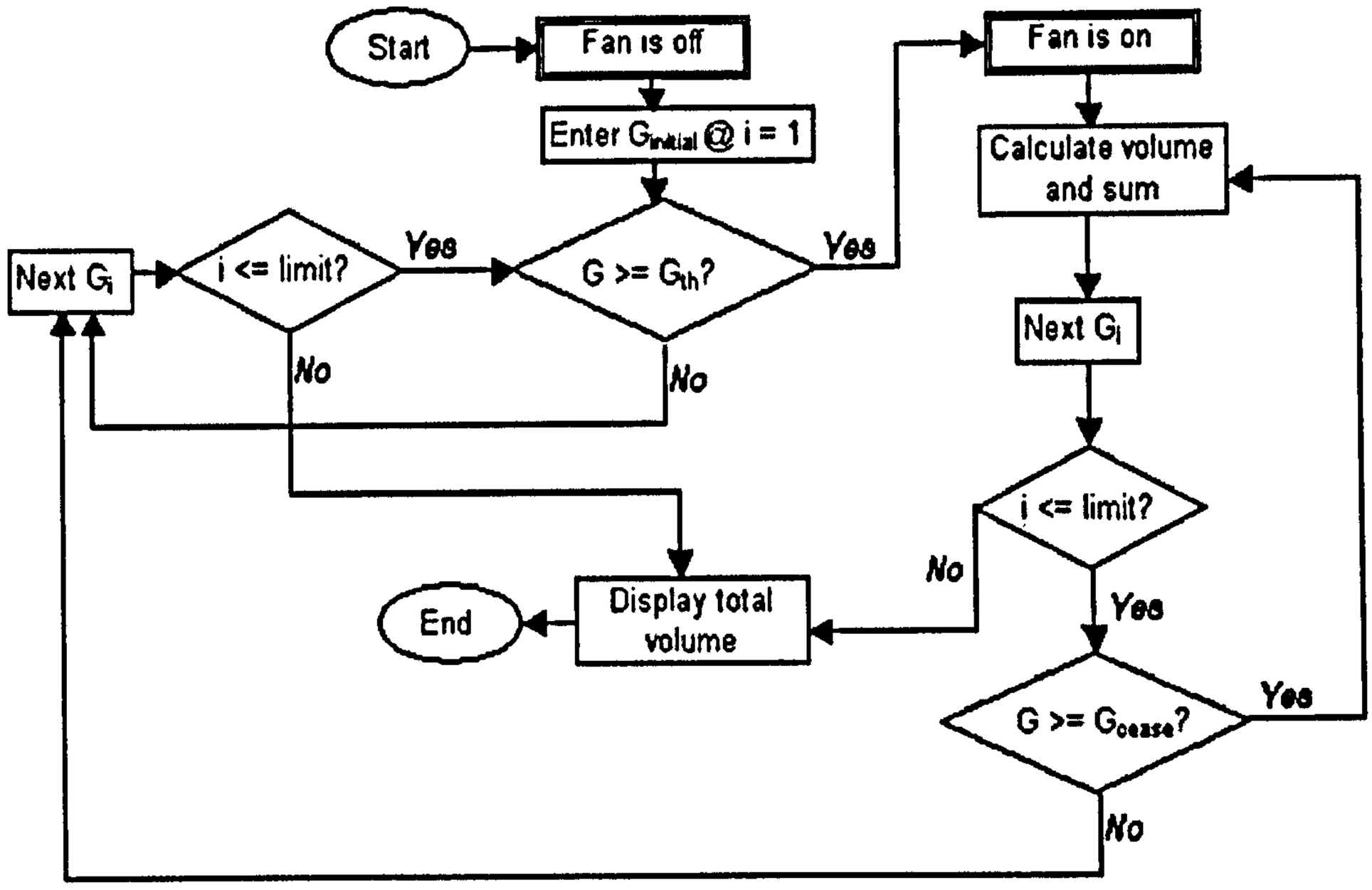

Fig. 6.7. Accounting for start-up characteristics

The degree of extension of the duct is assumed to be 80 %. This allows for entrance and exit losses in addition to twisting and bending of the duct. This assumption does not affect the optimisation of the PV-fan combination (since it is a fixed value for all cases) but clearly affects the volume, and thus the heat, delivered. It can also affect the heat transfer through the walls of the duct to the attic. For a given temperature difference and a given length of duct, a higher degree of extension results in a lower surface area, which implies lower heat transfer rate. In practise, as discussed in chapter 4, it is not possible to measure an exact value for the degree of extension. Alternatively, a measured ΔP_s-Q curve for the system can be translated into an effective duct length for some diameter and some degree of extension. This approach is further discussed in chapter 7.

6.3.5.3 Air properties

The temperature of air and atmospheric pressure are necessary for calculation of density and viscosity. The barometric pressure is fixed at 760 mm Hg. The temperature of air flowing in the duct depends on the temperature of the slates, heat transfer coefficients, heat losses from the duct, ambient temperature and irradiance. For simulation purposes, a temperature of 5 C above ambient is considered for simplification. This assumption does not reflect the real situation since the difference in

temperature depends on the prevailing wind speed, irradiance and other factors. However, an optimum system for a 5 C difference will also be optimum for 10 C. This will be discussed in chapter 7.

6.3.5.4 Effect of suction pressure

As has been shown in section 3.7, the effect of the system pneumatic characteristics on the electrical and speed-voltage characteristics of the fan is negligible.

6.3.6 Economic considerations

The cost for each of the components used for constructing the PV-driven RSB system is shown in Table 6.3. It can be seen that the addition of a PV module in parallel or in series can add more than 50 % to the cost of systems with a single PV module. Table 6.3 will be used for payback period calculation in section 6.6. The payback period depends on both the initial cost of the system and the volume of air delivered (which corresponds to energy savings). Parallel combinations of PV modules incur higher costs but also produce more volumes (as will be seen in the next section).

The use of two fans in parallel or in series can add 25 – 32 % to the cost of single fan systems. The optimisation results will clarify if the additional cost of an extra fan is justified by the extra volume, if any, delivered.

Table 6.3: Component cost

	Cost, £	Description
PV1	104.00	Polycrystalline, 4.5 W_p, PV/SX-ML05, dimensions: 10.8 x 10.5 x 0.6 inches
PV2	135.00	Polycrystalline, 10 W_p, PV/SX-ML10, dimensions 17.5 x 10.5 x 0.6 inches
Fan0	69.29	PAPST, 135 mm standard, 9.5 W, 12 V, 69 l/s Brushless DC motor
Fan1	53.34	PAPST, 135 mm standard, 9.5 W 24 V, 69 l/s Brushless DC motor
Fan2	47.41	Comair Rotron 171 mm, 20.3 W 24 V, 111 l/s Brushless DC motor
Duct 1	12.69	10 m long 102 mm Thermaflex Aliflex Flexible ducting with a multiple layer aluminium/polyester laminate
Duct2	17.57	10 m long 152 mm Thermaflex Aliflex Flexible ducting with a multiple layer aluminium/polyester laminate

6.4. OPTIMISATION RESULTS

6.4.1 Volume delivered by single fan systems

Using dataset1, the program was run month by month for the different fan combinations. Figure 6.8(a) shows the results for the three single fans with a single PV2. It is seen that Fan1, when coupled to PV2, consistently produces higher monthly volumes. This is due to the fact that Fan1 starts at lower irradiances and so operates for longer periods of time. The utilisability for each of the fans, which also corresponds to the percentage of the time the irradiance is above the threshold irradiance, is shown in Fig. 6.9. Figure 6.10 shows utilizability for all three fans for two typical days in January and May, again based on dataset1.

However, even when Fan0 and Fan2 are "kick-started" so that the model is run for these fans for the same period of time as Fan1, the model predicts that they will still deliver lower monthly volumes, as shown by Fig. 6.8(b). This can be explained by reference to Fig. 4.20 where it can be seen that for periods between 200 and 580 W/m^2, Fan1 produces higher flow rates than Fan2. This optimum period of Fan1 is the most prevailing irradiance interval for Edinburgh, and, so, for most of the time, Fan1 will deliver higher flow rates. Figure 6.11 shows ΔP_f-Q characteristics for the three fans at G = 400 W/m^2. It is clear that at this irradiance, Fan1 produces higher flow rates than the two other fans.

This same behaviour is also observed with the smaller PV module. In this case, however, lower volumes are produced. This is also explained by the start-up characteristics. The respective delivered volumes in thousands of m^3 for each of the PV-fan combinations and for the specifications listed in section 6.3.5, are summarised in Table 6.4. It is seen that, considering volume delivered, the PV2-Fan1 system is the most favourable amongst the single PV-single fan systems.

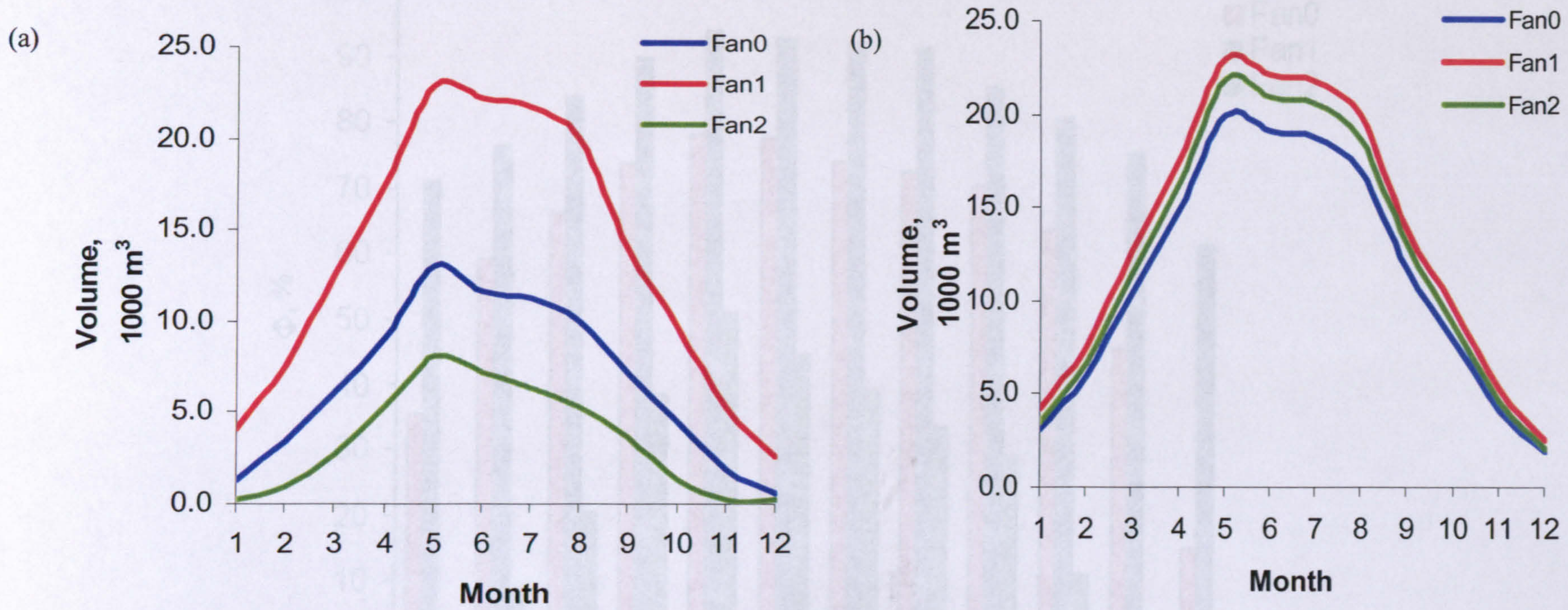

Fig. 6.8: Monthly volume delivered by single fan systems with PV2 (a) without kick-starting Fan0 and Fan2 (b) with kick-starting Fan0 and Fan2

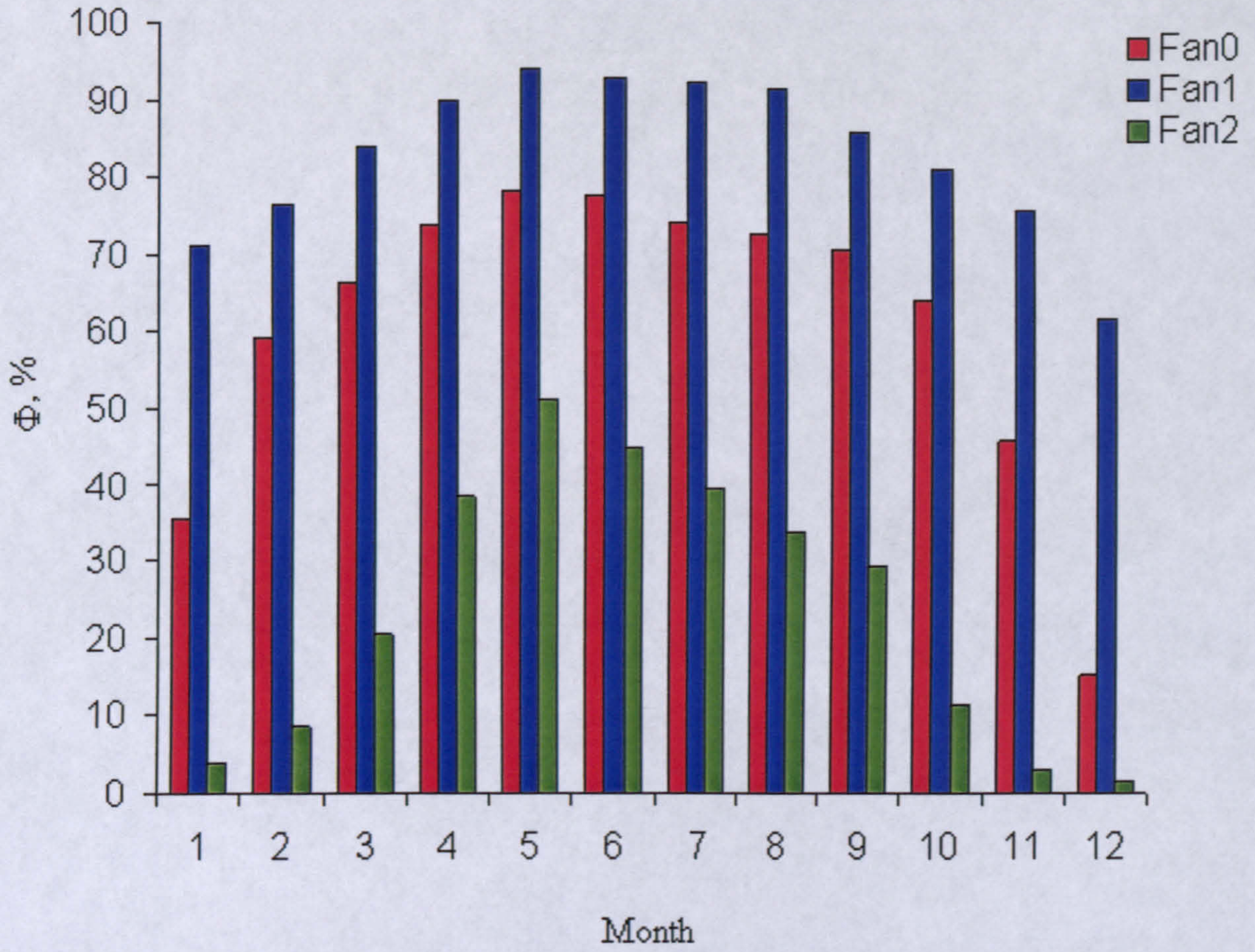

Fig. 6.9: Monthly utilizability of the three PV2-single fan systems.

(a)

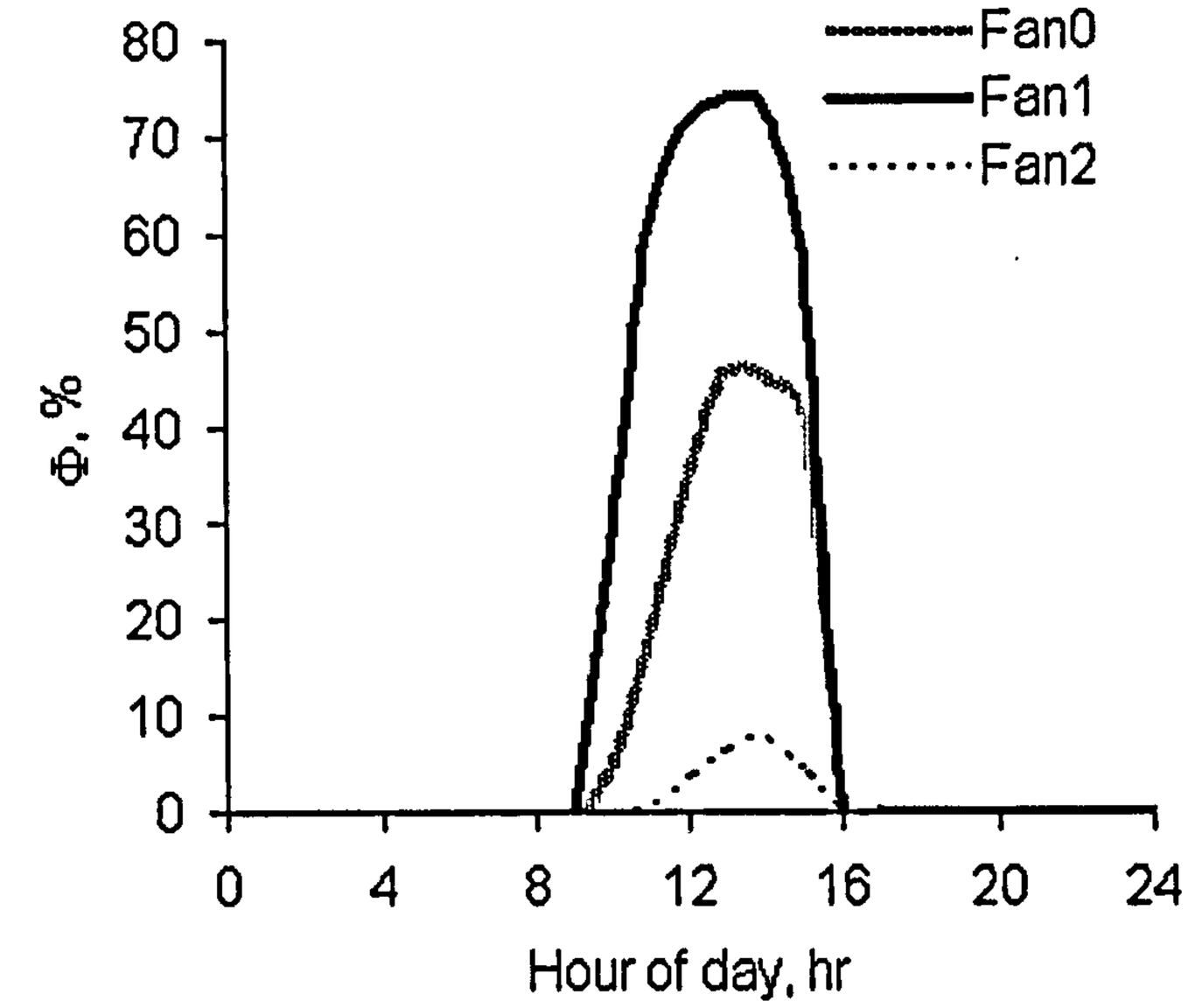

(b)

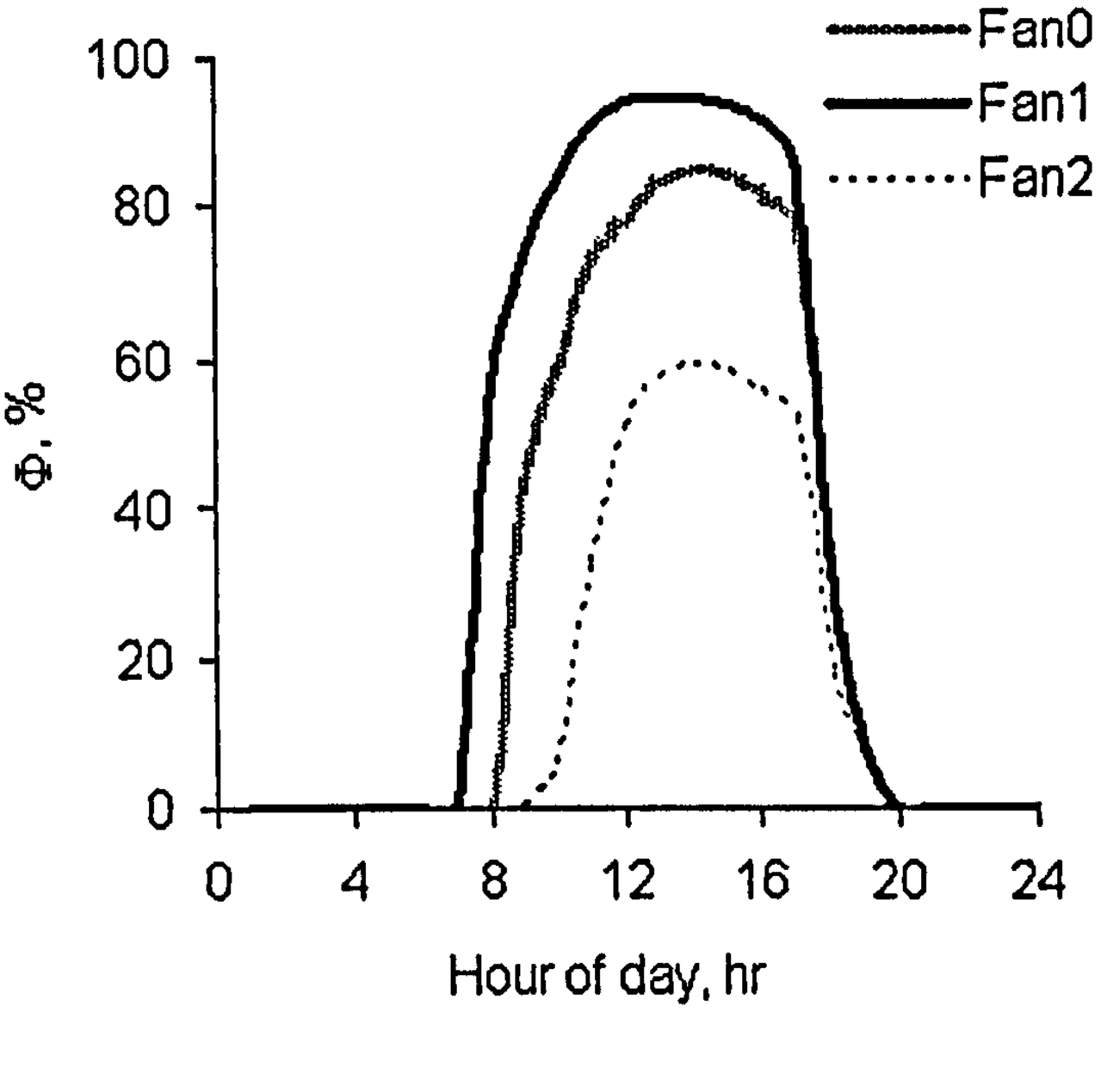

Fig. 6.10: Utilizability for the three fans for a typical day in (a) January and (b) May based on 27 years of data for Edinburgh.

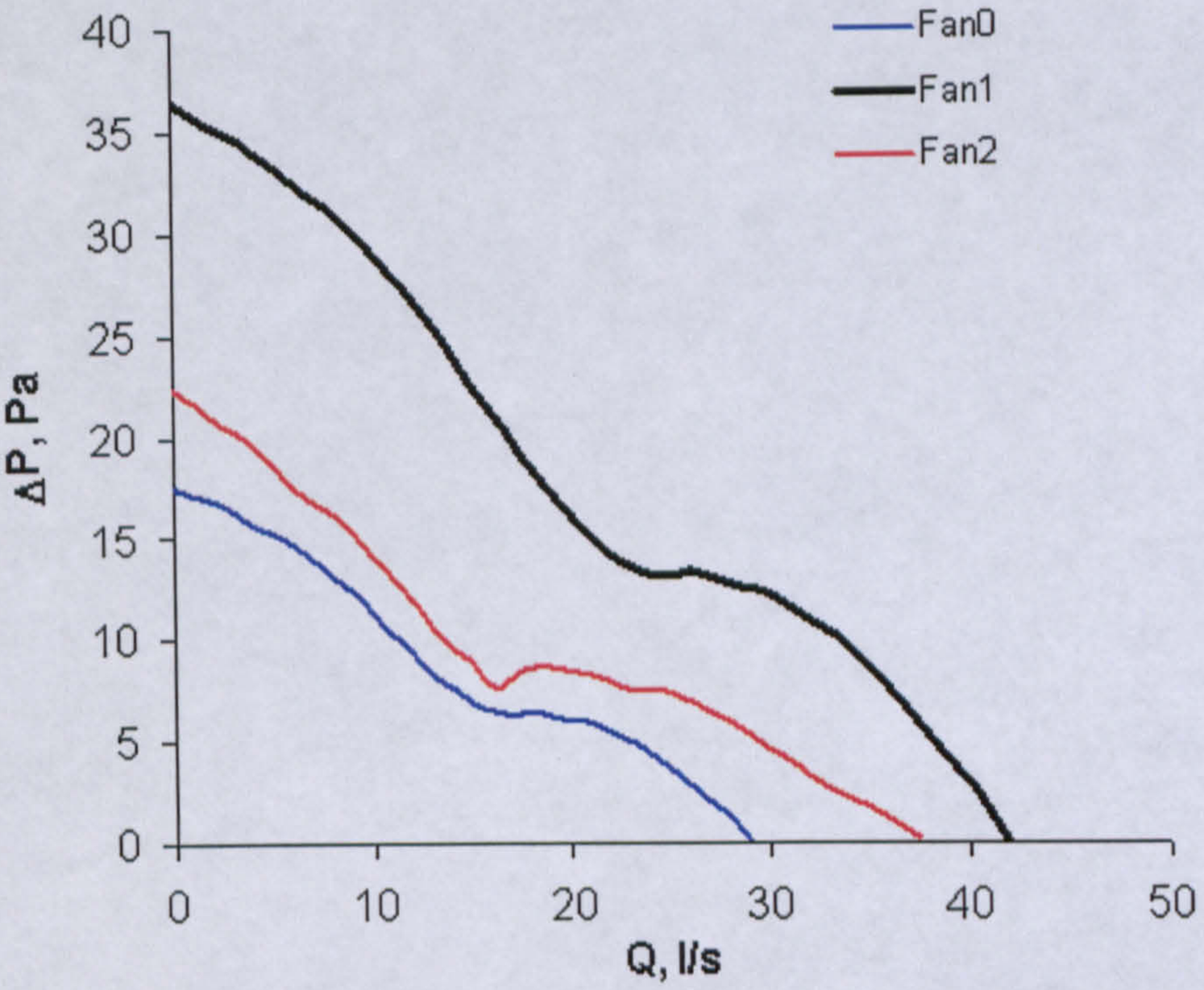

Fig. 6.11: Fan ΔP-Q characteristics at 400 W/m^2.

Table 6.4(a): Annual volume of air delivered (1000 m^3) by different PV-fan systems.

PV	1	2	3	4	5	6
Fan						
0	0	NA	NA	81	NA	NA
1	49	149	-	160	297	-
2	0	21	0	42	175	53
3	0	0	NA	1	NA	NA
4	0	NA	NA	163	NA	NA
5	0	92	0	104	301	119
6	52	140	-	146	252	-

NA: Not available -: Not practical because of high voltages 0: The system does not start due to high start-up irradiances

Table 6.4(b): Volume of air delivered (1000 m^3) during the heating season by different PV-fan systems.

PV	1	2	3	4	5	6
Fan						
0	*0*	*NA*	*NA*	*47*	*NA*	*NA*
1	*24*	*81*	-	*96*	*171*	-
2	*0*	*7*	*0.0*	*23*	*92*	*22*
3	*0*	*NA*	*NA*	*1*	*NA*	*NA*
4	*0*	*NA*	*NA*	*92*	*NA*	*NA*
5	*0*	*46*	*0.0*	*59*	*164*	*59*
6	*26*	*76*	-	*85*	*147*	-

NA: Not available -: Not practical because of high voltages 0: The system does not start due to high start-up irradiances

6.4.2 Volume delivered by different fan combinations

Figure 6.12 shows Q-G simulations for parallel and series combinations of Fan1. The respective modelled monthly volumes delivered by the parallel and series combinations of Fan1 are shown in Fig. 6.13(a). For these combinations, two assumptions are made. First, it is assumed that the two fans deliver air through ducts with the same effective duct length (i.e. the two branches of the system have the same ΔP_s-Q characteristic). Secondly, it is assumed that the electrical characteristics of the two fans and their ωV relationships are identical. Figure 6.13(a) reveals that parallel and series combinations add to the cost but introduce no performance advantage over a single fan system. The parallel combination produces less volume because of the higher start-up irradiances. For the series combination, on the other hand, the start-up irradiances are the same as for the single fan case. However, for the same irradiance, the operational voltage for each of the two series-fans (see Fig. 6.6(b)) is halved. Thus, in this case, each of the two fans in series operates at lower speeds than in the single fan case, and so, in the long run, the volume delivered for the series combination is less.

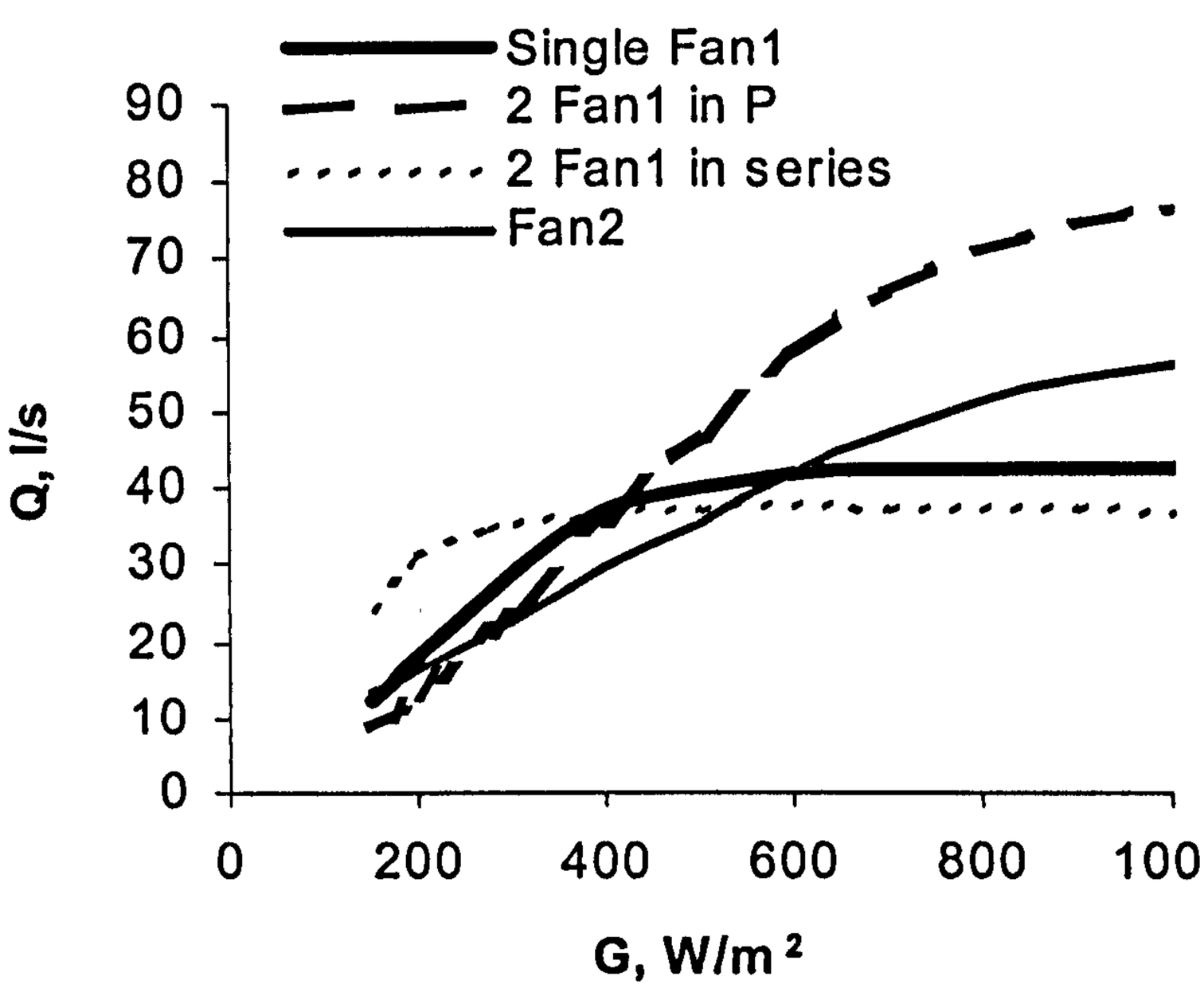

Fig. 6.12: Q-G simulations for parallel and series combinations of Fan1.

For Fan0, the parallel combination has a start-up irradiance of more than 1100 W/m^2 and so the model clearly predicts that the system will remain non operational. Figure 6.13(b) shows that, unlike systems comprising Fan1, operating two Fan0 in series significantly increases the monthly volume of air delivered.

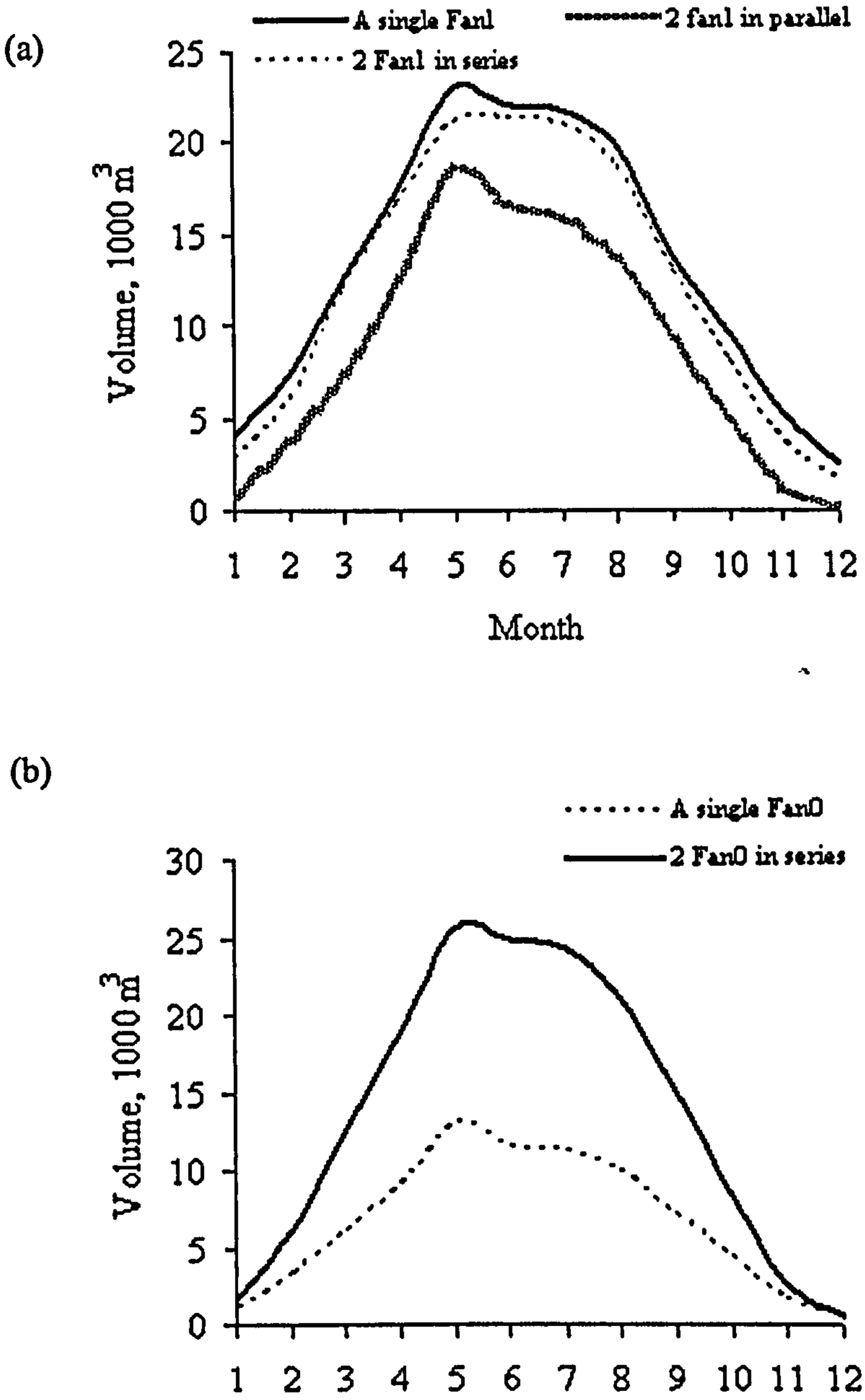

Fig. 6:13: Monthly volume delivered (1000 m^3) by PV2 systems with parallel and series combinations of (a) Fan1 and (b) Fan0.

6.4.3 Optimisation based on dataset2

The model was run with dataset2 (5-min data) for the different PV-fan combinations. The results are shown in Fig. 6.14. Based on 5-min data, the system PV2-Fan1 is still the optimum system. Table 6.5 shows that the total annual volume as calculated by dataset2 is 12 % higher than that calculated by dataset1. This is expected because with detailed data, the periods of operation for each of the systems increase. The effect of using dataset2, however, is more noticeable with Fan0 and Fan2. Table 6.5 also shows that, for all systems, approximately 60 % of the volume is delivered during the heating season. The results reported for the optimum system is the next section are based on dataset1 (long-term hourly data).

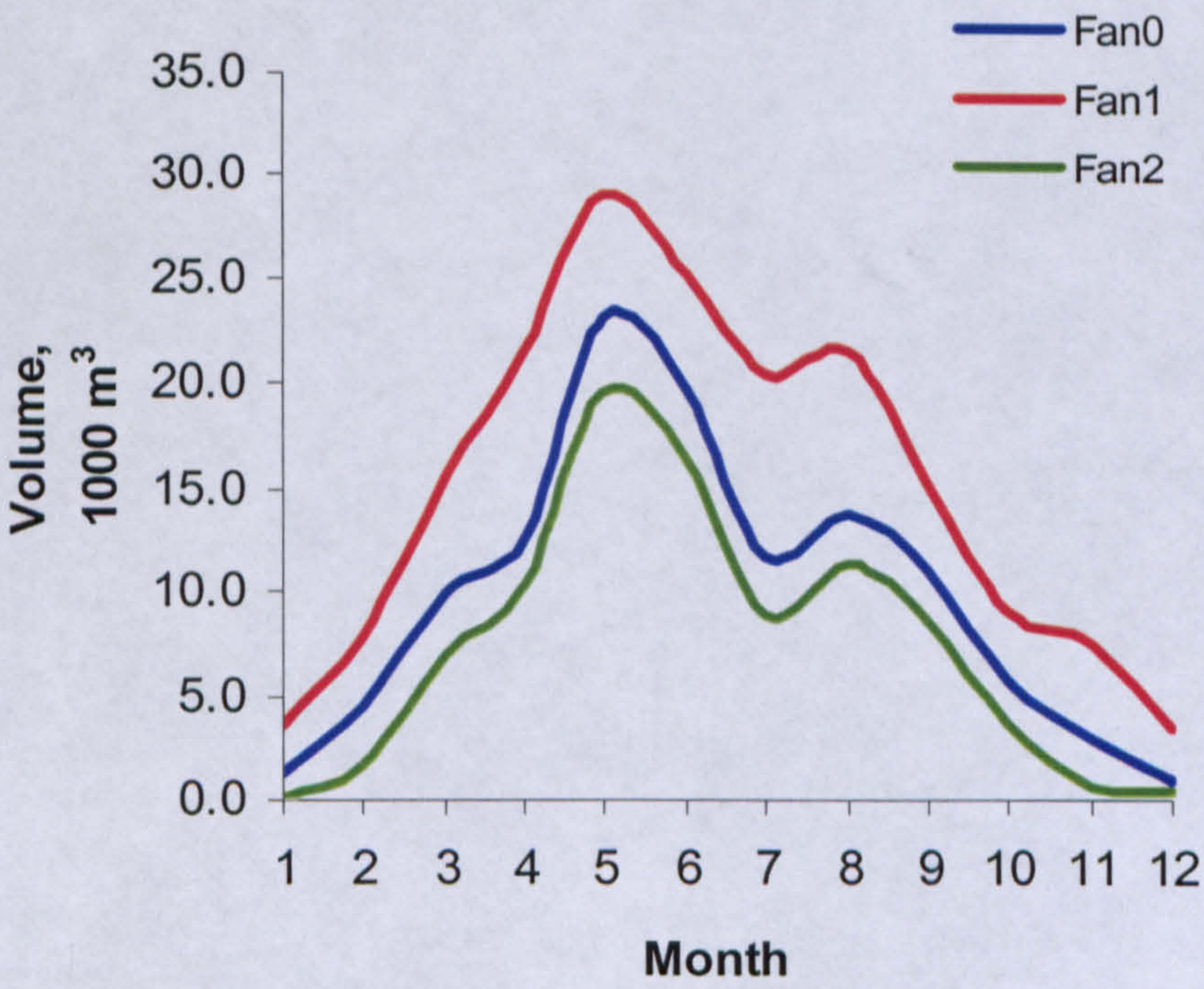

Fig. 6.14: Monthly volume delivered (1000 m^3) for single PV –single fan systems using dataset2.

Table 6.5: Comparison of results as obtained from the two datasets (dataset1 and dataset2).

		Fan0	Fan1	Fan2
Dataset1	Annual volume, 1000 m^3	81	160	42
	During heating season, 1000 m^3	47	96	23
	(Heating season: year), %	59	60	55
Dataset2	Yearly volume, 1000 m^3	116	179	87
	During heating season, 1000 m^3	71	112	51
	(Heating season: year), %	61	63	58
Summary	Increase in predicted volume for whole year (dataset2: dataset1), %	45	12	110
	Increase in predicted volume for heating season (dataset2: dataset1), %	51	16	123

6.5 ANALYSIS OF THE OPTIMUM SYSTEM

6.5.1 Potential of optimum system

Based on dataset1, the optimum system is PV2-Fan1. For the heating season (Sep. through May), this system is expected to deliver approximately 9.6×10^4 m^3 of air (1.1×10^5 m^3 according to dataset2). There are potentially 2890 hours of daytime (sunrise to sunset) in Edinburgh and so the volume delivered by the optimum system corresponds to a constant flow rate of 33.2 m^3/hr (9.2 l/s). This flow rate satisfies the ASHRAE recommendations (ASHRAE, 2001) for a 100-m^3 room with one occupant.

Running the model for a delivery temperature of 1 degree Celsius above ambient temperature and assuming a constant specific heat capacity for air (C_p = 1006 J/Kg.C) and a density of 1.2 Kg/m^3, the heat that can be potentially delivered by the optimum system throughout the heating season is 116.1 MJ (32.2 kWhr). In chapter 7, it will be shown that the delivery temperature for some types of slates can easily reach 5 C above ambient temperature. Using this temperature difference, the amount of heat that can be potentially saved by the optimum system is 161 kWhr. This constitutes more than 15 % of the heat that can potentially fall on a 1m^2 south-facing collector in the UK (Page and Lebens, 1986). A comparison with the two other single-component systems is shown in Table 6.6.

Table 6.6: Average flow rates and total heat delivered for ΔT =1 C during the heating season.

	Optimum system	PV2-Fan0	PV2-Fan2
Volume*, 1000 m^3	96.2	47.1	22.9
ACH for 100-m^3 space	0.32	0.16	0.08
Heat delivered**, kWhr	161	79	39
Solar fraction**, %	0.11	0.05	0.03
CO_2 savings, kg	100	50	25

* During heating season ** For 5 C temperature difference (delivered – ambient)

Assuming that the heating load for a 100-m^3 space is 1500 kWhr during the heating season (an average of 5.5 kWhr/day), a solar fraction of 0.11 is obtained. This means that the optimum system is expected to save 11 % of the heating cost during the

heating season. Furthermore, based on a 630 g CO_2/ kWhr, the potential annual CO_2 savings for this system are 100 kg.

6.5.2 Efficiency

6.5.2.1 PV-fan efficiency

Figure 4.25 shows that for the most prevailing irradiance interval in Edinburgh, Fan1 systems consistently produce higher $\eta_{PV\text{-}Fan}$ values than Fan2 systems. Using dataset1, the model is used to simulate monthly values of $\eta_{PV\text{-}Fan}$. The results are shown in Fig. 6.15. The PV2 - Fan1 combination is preferable because it will produce higher average efficiencies. Efficiencies of 10 %, which correspond to approximately 80 % of the PV maximum power efficiency, can be achieved in May. Choosing a fan with a lower motor constant will provide a better match to the PV module's maximum power as discussed in section 6.5.4. This can increase efficiencies up to 14 %.

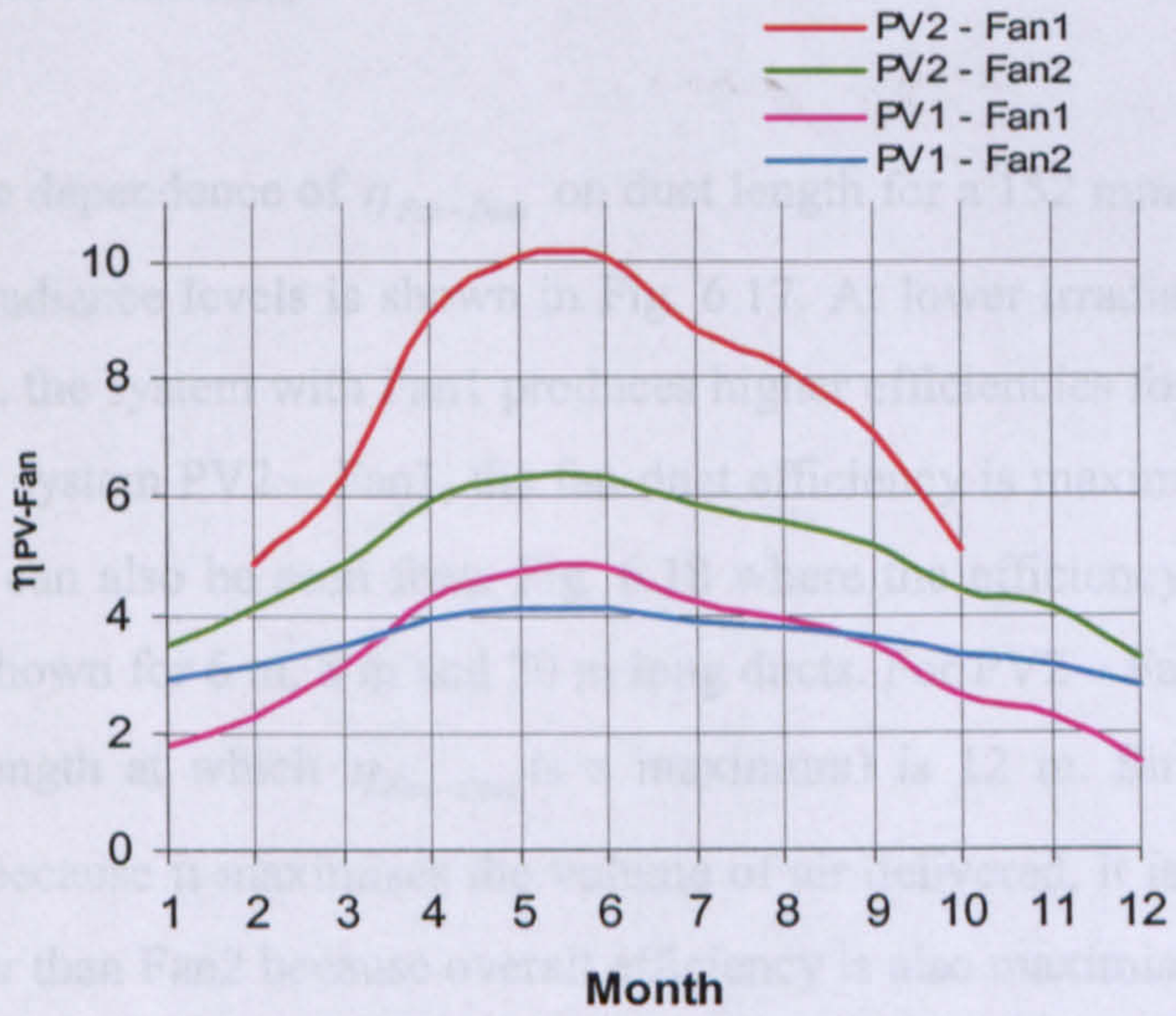

Fig. 6.15: Monthly-averaged PV – Fan efficiencies.

6.5.2.2 Fan-duct efficiency and optimum duct length

Figure 6.16 shows the monthly $\eta_{Fan-Duct}$ for Fan1 and Fan2 with PV2. It is seen from section 4.4.2.3 (Fig. 4.25) that Fan2 produces higher $\eta_{Fan-Duct}$ values for most of the irradiance range. Simulations show that there exists an optimal length of duct for

which the optimum system (i.e. PV2-Fan1) utilises a 100 % of available pneumatic output. This optimal length is a function of the fan ΔP-Q characteristic.

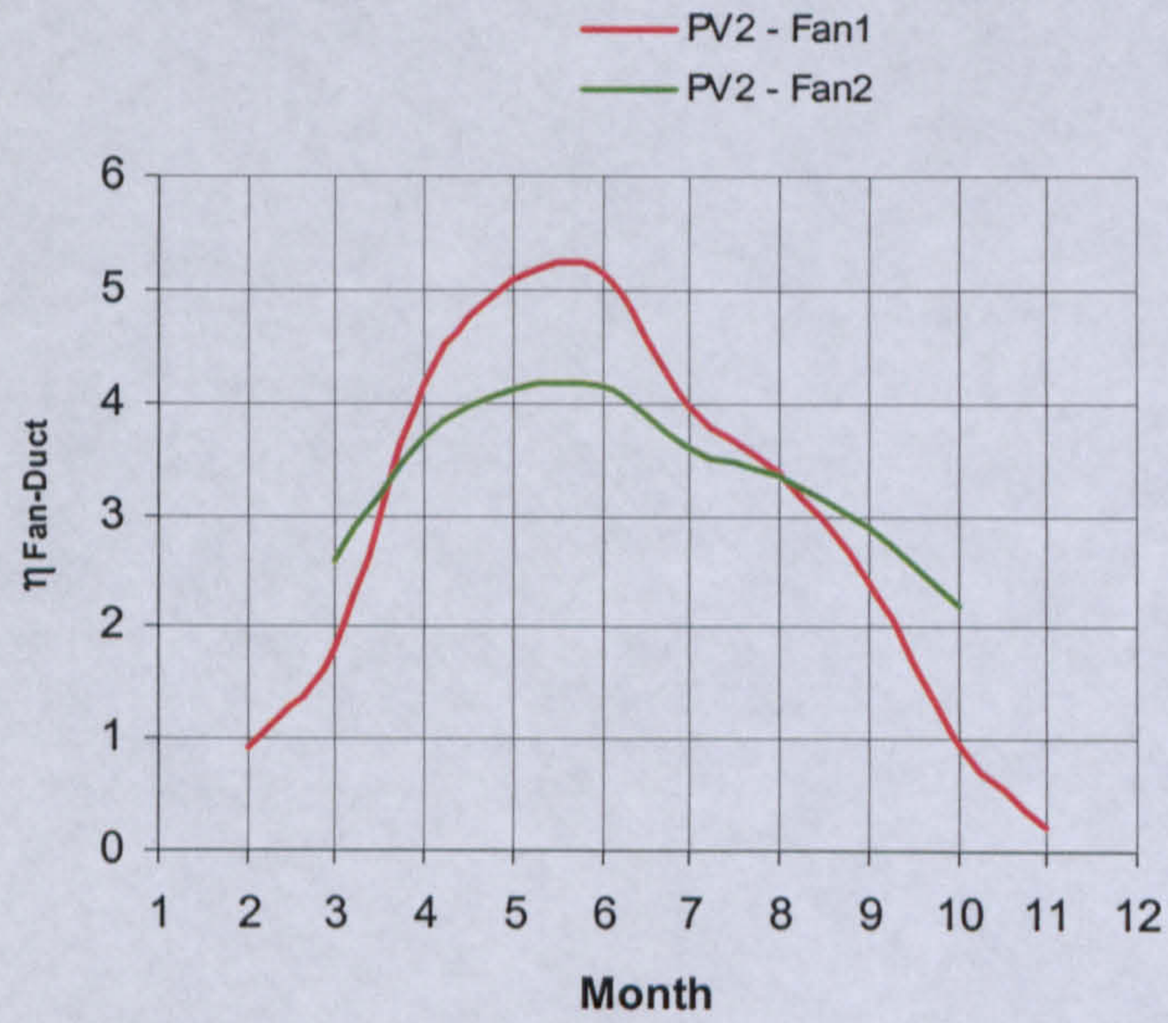

Fig. 6.16: Monthly-averaged Fan-Duct efficiencies for systems with 8 m long duct (152 mm diameter and 80 % extension).

The dependence of $\eta_{Fan-Duct}$ on duct length for a 152 mm duct at 80 % extension for two irradiance levels is shown in Fig. 6.17. At lower irradiances (i.e. 400 W/m^2 in the figure), the system with Fan1 produces higher efficiencies for duct lengths below 12 m. For the system PV2 – Fan1, the fan-duct efficiency is maximised at a duct length of 8 m. This can also be seen from Fig. 6.18 where the efficiency-irradiance profiles for Fan1 are shown for 6 m, 8 m and 20 m long ducts. For PV2 – Fan2, the optimum length (i.e. the length at which $\eta_{Fan-Duct}$ is a maximum) is 12 m. Since, a shorter length is desirable because it maximises the volume of air delivered, it is more beneficial to use Fan1 rather than Fan2 because overall efficiency is also maximised.

With an 8 m long 152 mm diameter duct at 80 % extension, the PV2-Fan1 system produces higher fan-duct efficiencies from April to August as shown in Fig. 6.16. The rest of the year, the system with Fan2 will produce higher $\eta_{Fan-Duct}$ values (but not necessarily higher overall efficiencies since, as shown in Fig. 6.15, PV2 – Fan1 always gives higher η_{PV-Fan} values). Considering cost, the system with Fan1 and the shorter length of duct (i.e. 8 m) is still preferable over that with Fan2 (which requires kick-starting during the period Sep. to Mar.)

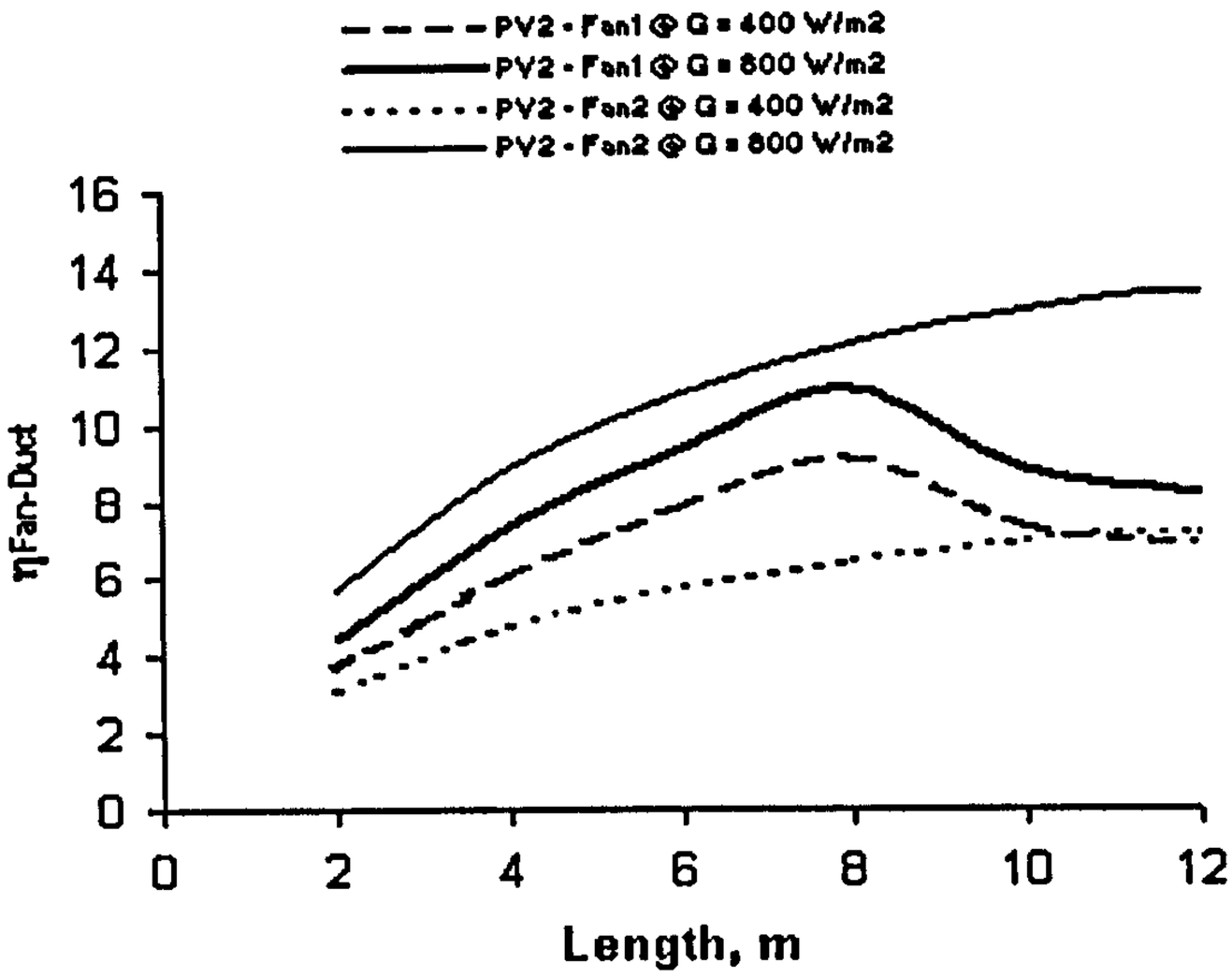

Fig. 6.17: Fan-Duct efficiency as a function of duct length for a 152 mm flexible duct with 80 % extension.

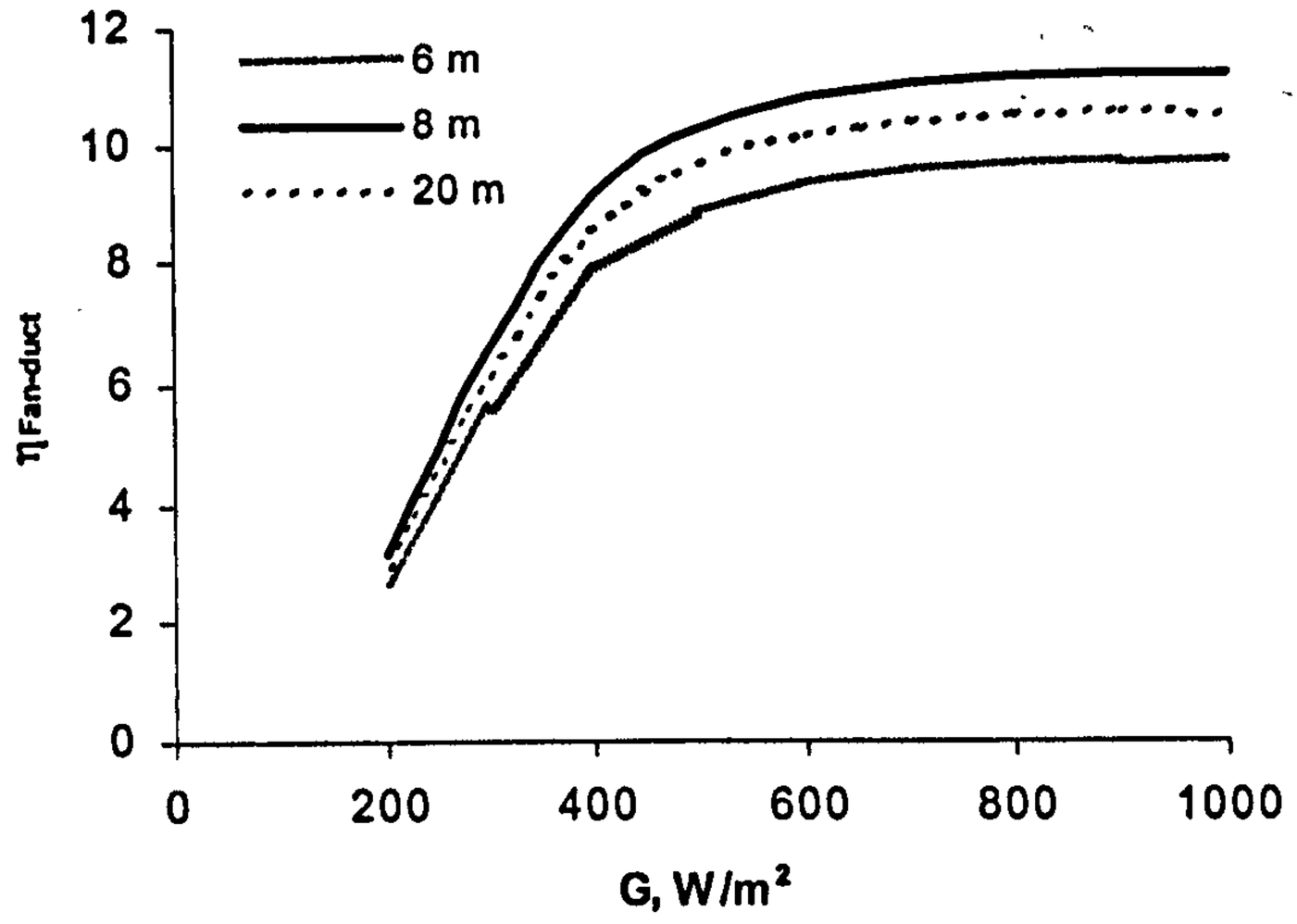

Fig. 6.18: Fan-Duct efficiency for Fan1 as a function of irradiance at different duct lengths (D = 152 mm, ext. = 80 %).

6.5.3 Optimum duct diameter

The diameter of the duct is chosen so that the annual volume of air delivered is maximised for the optimum PV-fan combination. As explained in section 4.4.1, a duct diameter of 152 mm is desirable because it maximises flow rate and consequently, also, the volume of air delivered. The annual volume of air delivered, however, reaches its

maximum value at a critical duct diameter (D_{cr}) as shown in Fig. 6.19. Using the model, and, based on dataset2 (5-min) data, the annual volume of air is calculated for different diameters for a length of 8 m and an extension of 80 %. A critical diameter of approximately 200 mm is obtained. Increasing the diameter from 152 mm to 200 mm will increase the annual volume delivered by the optimum system by 18 %.

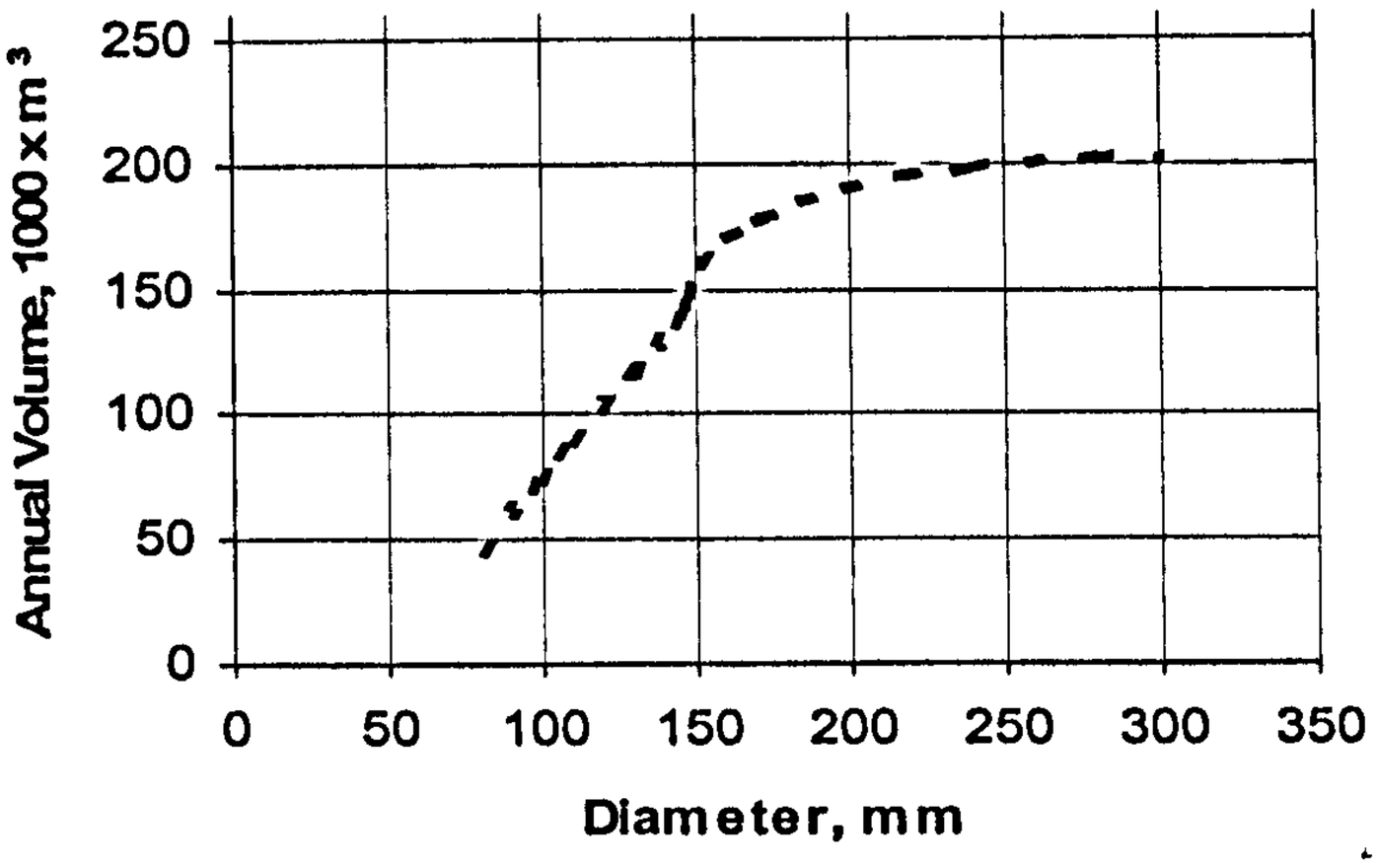

Fig. 6.19: Annual volume of air delivered by the optimum system (i.e. PV2 - Fan1 – 8 m long duct) at 80 % extension as a function of duct diameter.

6.5.4 Optimum motor constant

It was shown in section 6.5.2 that, in addition to maximising volume, the optimum system (PV2-Fan1) also maximises $\eta_{PV\text{-}Fan}$, and according to Fig. 4.26, it also maximises $\eta_{Overall}$. In order to further increase the utilisation of PV maximum power, an optimum motor constant for Fan1 can be determined. The present section, therefore, focuses on the optimum system (PV2-Fan1). While using a duct length of 8m will maximise fan-duct efficiency, selecting an appropriate motor constant for Fan1 can maximise the PV-fan efficiency.

Using a matching device to utilise most of the PV power is undesirable, as explained in section 6.1.1. An alternative approach is to determine a motor constant, which would ensure that the motor/fan operate closer to P_m for most of the year. This optimum motor constant is a function of environmental conditions, in addition to the PV and fan characteristics as described by the Kolhe equation (Kolhe, 2000). In order to apply the Kolhe equation, the PV current at maximum power (I_m) is required. In the

present method, the determination of the optimum motor constant is based on the new method for describing the PV IV characteristic (section 3.2.2).

The determination of the optimum motor constant is based on dataset1. For each data point, I_m is determined and the optimum motor constant for Fan1 calculated. This approach is useful as it produces a K_m value which is representative of the design location since it is based on long-term weather data. However, applying this procedure can be cumbersome since evaluating I_m for each data point is not a straightforward task. Typically, the full PV IV characteristic must be generated and the current at which the power is a maximum is identified. For a large set of data, this increases the computational time significantly.

The new method described in chapter 3 (Eq. 3.5) relates P_m, V_m and I_m directly to irradiance and ambient temperature. This method, which has been validated through the work highlighted in section 3.4.5, can reduce the computational time significantly since it provides the means for estimating I_m directly from weather data. The maximum power current can now be expressed as

$$I_m = \frac{P_m}{V_m} = \frac{\frac{G}{G_{ref}}\left[P_{m,ref} + \mu_m \cdot \Delta T\right]}{V_{m,ref} + \mu_{Vm} \cdot \Delta T + C_{Vm} \ln\left(\frac{G}{G_{ref}}\right)} \tag{6.11}$$

A program written in VBA was run for all data points and an average optimum motor constant was determined for each month. The results are shown in Fig. 6.20. The $K_{m,\,opt}$ value for the whole year was calculated as a radiation energy-weighted average. A value of 0.0745 V.s/rad is obtained (for Fan1, K_m = 0.079 V.s/rad as calculated in section 3.5.1) . This result means that, based on 27-years of data for Edinburgh, a permanent magnet BLDC motor with a motor constant of 0.0745 V.s/rad is expected to utilise most of the yearly available maximum PV output.

For purposes of the RSB system under consideration, if Fan1 is manufactured so that it has the motor constant calculated above, the total yearly PV output will increase from 37.3 MJ to 43.1 MJ (14 % increase) as seen in Fig. 6.21.

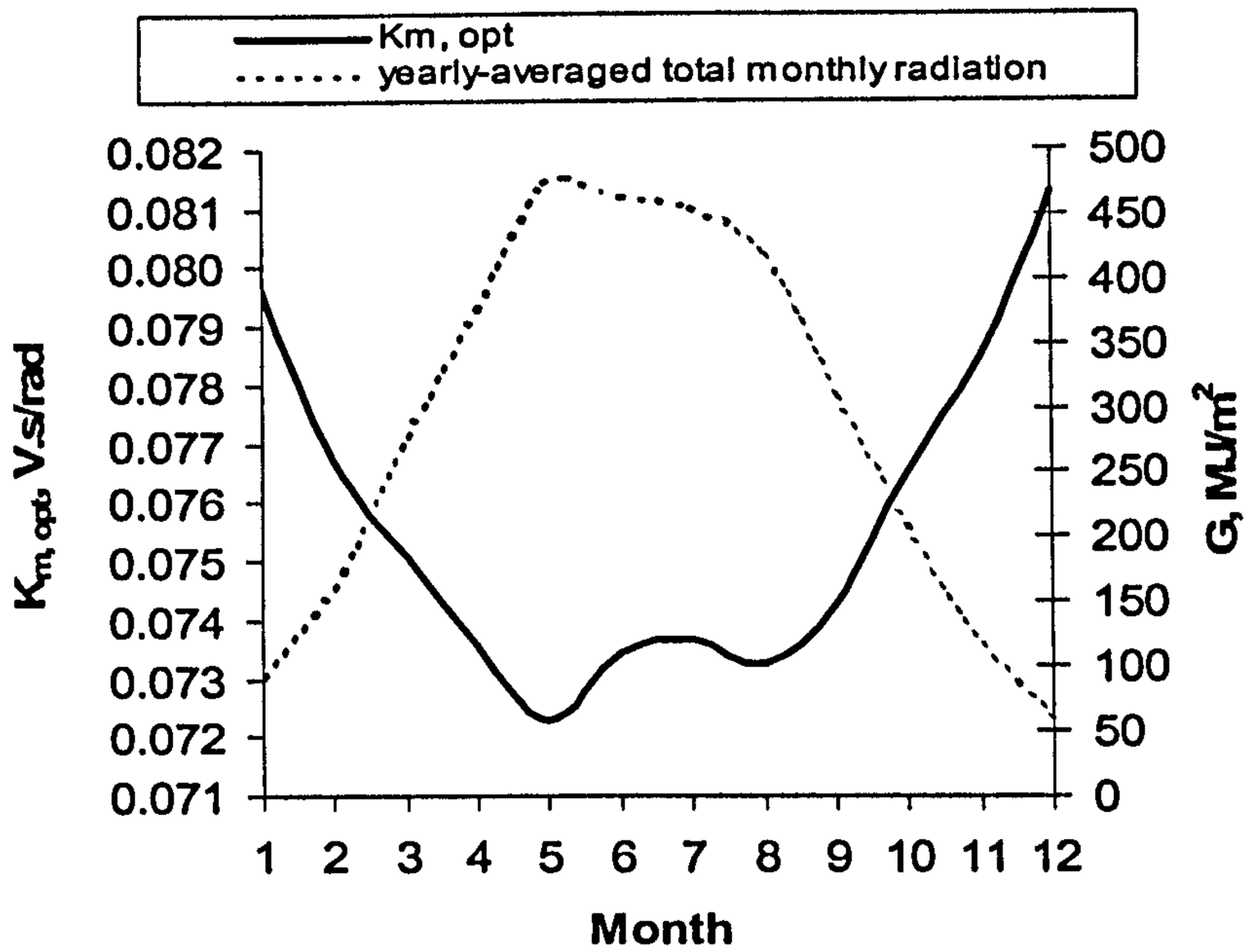

Fig. 6.20: Monthly-average optimum motor constant for the 10 W_p PV module and based on irradiance data for Edinburgh

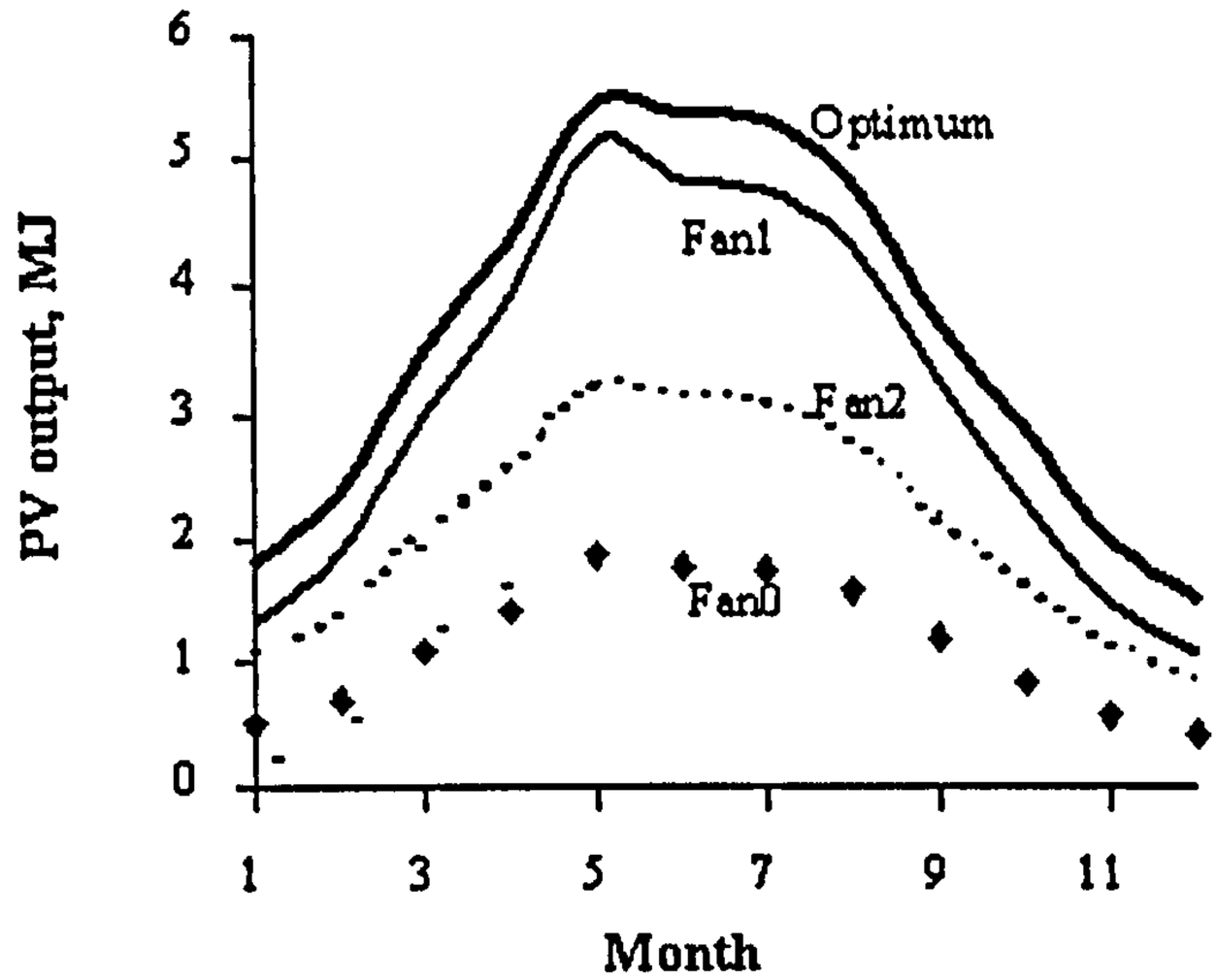

Fig. 6.21: Calculated monthly PV energy output.

Figure 6.22 shows how the output energy for PV-Fan1 changes with the motor constant. It is clear that the $K_{m, opt}$ is around 0.074 V.s/rad and that if the motor constant increases or decreases away from this value, a decrease in the PV output energy occurs.

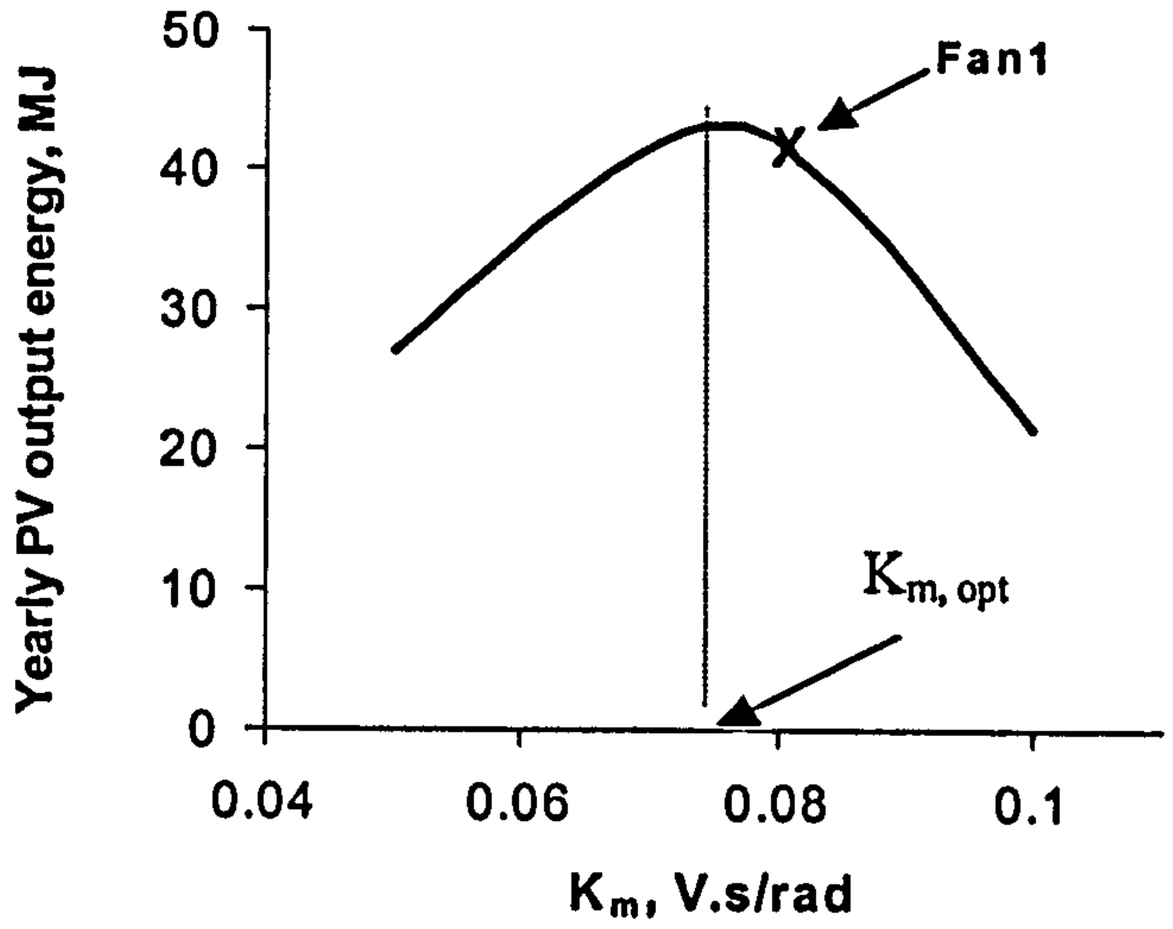

Fig. 6.22: PV energy output at different motor constants for Fan1.

6.6 ECONOMIC EVALUATION OF THE OPTIMUM SYSTEM

Several economic criteria are available for evaluating solar energy systems. The "payback time" method is used here. The payback time is defined as the time needed for the cumulative fuel savings to equal the total initial investment. According to Duffie and Beckman (1991), the common way for calculating the payback time is without discounting the fuel savings. These authors give the following equation for calculating payback

$$N_p = \frac{\ln\left[\frac{C_s i_f}{FLC_{F1}} + 1\right]}{\ln(1+i_f)} \qquad (6.12)$$

where N_p is the payback period (years), C_S is the initial investment (£), i_f is the fuel cost inflation rate, F is the annual solar fraction, L is the annual load (kWhr) and CF1 is the first period's unit energy cost (£/kWhr).

Using the volumes delivered during the heating season in Table 6.4(b) and the information in Table 6.3, the payback time was calculated for the optimum system and compared to other systems as shown in Table 6.7.

The systems with two PV2 modules in parallel are competitive with the optimum system. The system (2 PV2 in parallel with a single Fan1) has a lower payback period than the optimum system due to the high volumes produced. However, the use of two PV modules here is not justified since the fan is operating very far away from P_m and so a very low efficiency will be produced. The option of using two PV2 modules in parallel, however, cannot be entirely discarded and it can be useful for producing higher ventilation rates and delivering more heat.

The use of two 4.5 W_p PV module instead of a single 10 W_p PV module with Fan1 has a lower initial cost but a longer payback period.

Table 6.7: Annual savings, solar fraction and payback period for different PV-fan systems (the optimum system is shown in bold).

PV	Fan	Cost, £	Volume*, m^3	Rate**, m^3/hr	V_{House}***, m^3	heat, kWhr	Annual savings, £	Solar fraction	Payback, years
1	1	174.9	24	8.3	27.7	40.2	2.8	0.03	28.9
1	6	228.3	26	9.0	30.0	43.6	3.1	0.03	31.9
2	1	278.9	81	28.0	93.4	135.8	9.5	0.09	18.5
2	2	272.98	7	2.4	8.1	11.7	0.8	0.01	58.8
2	5	332.3	46	15.9	53.0	77.1	5.4	0.05	28.8
2	6	332.3	76	26.3	87.6	127.4	8.9	0.08	21.6
4	0	221.9	47	16.3	54.3	79.0	5.5	0.05	22.6
4	**1**	**205.9**	**96**	**33.3**	**110.9**	**161.3**	**11.3**	**0.11**	**13.3**
4	2	200.0	23	7.9	26.4	38.4	2.7	0.03	31.8
4	3	291.2	1	0.2	0.8	1.1	0.1	0.00	107.3
4	4	291.2	92	31.8	106.0	154.2	10.8	0.10	17.5
4	5	259.3	59	20.3	67.6	98.3	6.9	0.07	21.7
4	6	259.3	85	29.5	98.4	143.1	10.0	0.10	17.0
5	1	340.9	171	59.1	197.1	286.7	20.1	0.19	12.6
5	2	335.0	92	31.8	106.0	154.3	10.8	0.10	19.2
5	5	394.3	164	56.7	189.0	275.0	19.2	0.18	14.5
5	6	394.3	147	50.8	169.4	246.5	17.3	0.16	15.6
6	2	335.0	22	7.6	25.4	36.9	2.6	0.02	41.3
6	5	394.3	59	20.4	68.0	98.9	6.9	0.07	27.6

* During heating season ** Constant flow rate required by an AC fan throughout the heating season (sunrise to sunset) in order to deliver same volume

*** The volume of a house (with one occupant), which can be ventilated while satisfying the ASHRAE standards (0.35 ACH).

6.7 SUMMARY

In chapter 6, the flow rate model developed in chapters 3 and 4 and the slope irradiance model described in chapter 5 were put together into an updated optimisation model. The model was updated in order to account for different PV and fan combinations in addition to start-up characteristics. A function which assigns and stores a value of "1" for an operating fan and a value of "0" for a non-operating fan has been used. This function simplifies the lengthy calculation procedure since only cases with a value of "1" are considered. The effect of wind speed on the value of the loss coefficient, U, was also accounted for.

The optimisation criteria and methodology were also introduced. The basis for optimisation based on maximum volume delivery was justified. The optimisation process reveals that the optimum system is the PV2-Fan1 system. It was also concluded that kick-starting Fan0 or Fan2 will add to the cost but will not deliver higher monthly volumes than Fan1 does. The optimum system delivers the recommended ASHRAE ventilation rates for a dwelling with a single occupant and it can, for a 1 C temperature difference deliver about 32 kWhr during the heating season.

The optimum system can potentially

1. deliver 96000 m^3 of air during the heating season. This satisfies the ASHRAE recommendations for ventilating a 100 m^3 room with one occupant.
2. deliver 161 kWhr during the heating season (more than 15 % of solar energy falling on a $1m^2$ in the UK). This can save more than 10 % of heating costs (solar fraction = 0.11).
3. save 100 kg of CO_2 annually.

The overall flow efficiency $\frac{H \cdot Q}{G \cdot a}$ can be maximised by maximising both η_{PV-Fan} and $\eta_{Fan-Duct}$. Maximising volume delivered, however, does not necessarily maximise efficiency. It is evident from the model that the system with Fan1 still produces higher efficiencies than other systems.

The following recommendations are given

1. Considering only the components listed in chapter 3, the optimum system is the 10 W_p PV module with the 24 VDC, 9.5 W fan with a free flow capacity of 69 l/s.
2. This fan has a motor constant of 0.079 V.s/rad and on average it can utilise about 86 % of the maximum power of PV2. The same fan but with a motor constant of 0.0745 V.s/rad can increase the yearly output of the PV module by 14 % thus utilising the full of the maximum energy available.
3. An effective duct length of 8 m can maximise the pneumatic power. The system can be set to a given duct length by changing the setting of the grill.
4. The larger the diameter, the more volume delivered. However, no volume increase is achieved for duct diameters larger than 200 mm. So it will be a waste of money to use larger diameters than 200 mm. For the system installed in the next chapter, a 152 mm diameter is used based on availability. A 200 mm diameter is expected to increase the annual volume delivered by 18 %.

REFERENCES

Alghuwainem S.M., (1992), Steady state operation of DC motors supplied from photovoltaic generators with step up converters, IEEE Trans Energy Conv, 7(2), pp267–271.

Anis, W.R., and Metwally H.M.B., (1994), Dynamic performance of a directly coupled PV pumping system, Solar Energy, (1994), 53, pp369-377.

ASHRAE, (2001), ASHRAE Handbook of Fundamentals, American Society of Heating Refrigerating and Air Conditioning Engineers, Atlanta.

Betka, A., and Moussi, A., (2004), Performance optimization of a photovoltaic induction motor pumping system, Renewable Energy, 29(14), pp2167-2181

Bione, J., Vilela, O.C., and Fraidenraich, N., (2004), Comparison of the performance of PV water pumping systems driven by fixed, tracking and V-trough generators, Solar Energy, 76, pp703-711.

Duffie, J.A., and Beckman, W.A., (1991), Solar Engineering of Thermal Processes, 2nd edn., New York, Wiley Interscience.

Eskandar, M.N., and Zaki, A.M., (1997), A maximum efficiency photovoltaic-induction motor pump system, Renewable Energy, 10(1), pp53–60.

Faiz, J., Kasebi, F., Pillay, P., (2004), Design and testing of an integrated electronically controlled capacitor for integral and fractional horsepower single-phase induction motor, Energy Conversion and Management, 45(18-19): pp2989-3000.

Firatoglu, Z.A., and Yesilata, B., (2004), New Approaches on the Optimisation of Directly Coupled PV pumping systems, Solar Energy, 77, pp81-93.

Kiatsiriroat, T., Namprakai, P., and Hiranlabh, J., (1993), Performance estimation of a PV water-pumping system with utilizability function, International Journal of Energy Research, 17, pp305-310.

Kolhe, M., Kolhe, S., and Joshi, J., (2000), Determination of magnetic field constant of DC permanent magnet motor powered by photovoltaic for maximum mechanical energy output, Renewable energy, 21, pp563-571.

Koner, P.K., Joshi, J.C., and Chopra, K.L., (1991), Optimisation study of a pumping load by different configurations of photovoltaic modules, ISES Solar World Congress, Denver, CO.

Loxsom, F., and Durongkaverdi, P., (1994), Estimating the Performance of a Photovoltaic Pumping System, Solar Energy, 52, pp215-219.

McAdams, W.H., (1954), Heat Transmission, 3rd ed., McGraw-Hill, New York.

Narvarte, L., Lorenzo, E., and Caamano, E., (2000), PV pumping analytical design and characteristics of boreholes, Solar Energy, 68(1), pp49-56.

Page, J., and Lebens, R., (1986), Climate in the United Kingdom, Pub HMSO, Department of Energy.

The department of the Environment, (1993), Transport and the Regions Investment Appraisal for Industrial Energy Efficiency: Good Practice Guide 69, Crown Copyright.

7. SYSTEM TESTING AND MODEL APPLICATION

7.1 INTRODUCTION

In chapter 6, the model presented was used to define the combination of system components that maximised the annual volume of air delivered. In the present chapter, this optimum system is installed and the model used with temperature measurements to make conclusions about the amount of heat deliverable by the system. The optimum system described in chapter 6 is installed and tested in two ways. First it is tested at a house in Wiston, Scotland and compared to the system PV2-Fan2. The two systems are installed side by side and measurements are taken for August, September and November (2004). Secondly, the optimum system is installed at three different locations in three different roof sections (with different types of slates) and the effect of the slates on the performance of the system is investigated.

The model developed in chapters 3 and 4 is used to predict the amount of heat delivered during the period of operation of the system. This is to give insight into the potential of RSB systems for preheating ventilation air. The amount of heat delivered per unit time, that stored in the fan box and the maximum available heat absorbed by the slates can be calculated using Eq. 6.3

$$E_{month} = C \cdot \sum_{month} (Q \cdot \Delta T)$$

Running the model for the measured data (i.e. irradiance, ambient temperature and air temperature in the duct), instantaneous values of flow rate are calculated. When integrated over the time period considered, in combination with the measured temperature data, the heat delivered by these different systems can be calculated and the system performance compared.

The current chapter describes the procedure for testing such systems. The system's ΔP-Q characteristic in addition to irradiance and temperature data, require to be measured in order to be able to predict the performance of the system.

7.2 TESTING OF SOLAR AIR HEATING SYSTEMS

7.2.1 Comparative testing of solar systems

A measure of collector performance is the collection efficiency, defined as the ratio of the useful gain, over some specified time period, to the cumulative incident solar energy over the same time period

$$\eta = \frac{E^{'}\, dt}{a_{,} \int G\, dt} \tag{7.1}$$

where a_s is the area of the collector. The basic method of measuring collector performance is to expose the collector to solar radiation and measure the fluid outlet and inlet temperatures and the fluid flow rate. The useful energy delivered, can then be calculated from Eq. 6.3. In addition to inlet and outlet temperatures, irradiance on the collector, ambient temperature, and wind speed are also recorded. Instantaneous efficiency can be calculated as

$$\eta_i = \frac{E_i}{a_s \cdot G_T} \tag{7.2}$$

It is convenient in the economic analysis of solar systems to express the solar energy contribution to the total load in terms of the fractional reduction in the amount of energy that must be purchased. The fractional reduction of purchased energy is calculated from Eq. 6.1 and 6.2, as explained in chapter 6. In the current chapter, the optimum system will be compared to other systems based on solar fraction as an indicator.

Calculating the efficiency of RSB systems, as defined by Eq. 7.1, requires knowledge of the area of the roof through which the fan will draw air. Definition of this area is a complex matter since it depends on irradiance in addition to other environmental factors. For example, as irradiance increases, the speed of the fan increases and so the area from which air is drawn also increases. So it can be difficult to compare different systems based on their thermal efficiency.

Another way of describing the performance of the system is by calculating its effectiveness (ε), which can be defined as the ratio of heat delivered to the maximum heat absorbed by the slates. Assuming constant flow rate, the effectiveness can be calculated as

$$\varepsilon = \frac{E_{outlet}}{E_{maximum}} = \frac{(T_{outlet} - T_{amb})}{(T_{Slate} - T_{amb})} \tag{7.3}$$

where T_{outlet} is the temperature of air delivered.

In the present chapter, three indicators will be used to compare systems:

1. Solar fraction
2. Effectiveness
3. The ratio r defined as the ratio of volume delivered (l) per Joule of irradiance received by the PV module. This indicator is used since the area of the PV module is known while the slate area from which air is drawn is not known.

7.3 COMPARATIVE TESTING OF TWO PV-FAN SYSTEMS

In the current section, the optimum system will be comparatively tested with the system PV2-Fan2. The comparison will be carried out in two ways. First voltage and temperature profiles for selected days are compared for the two systems. This type of comparison will give information on the start-up irradiances and also on the temperatures that can be potentially reached by the slates and delivered by the system. The discussion of the results from these specific days will lead to conclusions about the performance of the systems. Heat quantities are then integrated and the performance of the systems compared for the full period of operation.

The comparison of the two systems was carried out in two different roof sections A (Fig. 7.1) and B (Fig. 4.10(a)). The comparison in roof section A was carried out with the two systems installed side by side. In roof section B, the days of measurement for each of the systems were different (i.e. only one fan box was used at a time and the two fans were exchanged for different periods of operation). In the former case, the results are easier to interpret since the effect of wind speeds and other environmental factors can be neglected. In this case, however, the two side-by-side systems must be adjusted to the same ΔP_s-Q characteristics as discussed in section 7.3.2.

7.3.1 System installation

Two systems were installed side by side on the south-facing roof at a house in Wiston as shown in Fig. 7.1 and according to the procedure outlined in Chapter 1. Measurements of irradiance, fan voltage, ambient temperature, in-box temperature and temperature of the outlet air were recorded.

7.3.2 System characteristic

In order to be able to run the model for the data measured, a system's ΔP-Q characteristic (or alternatively an effective duct length at some diameter and degree of extension) must be entered into the model. This characteristic is different for different systems and must be measured for the specific configuration including the grill opening. The determination of the ΔP_s-Q characteristics requires a single point measurement of pressure and flow rate (and then the affinity laws can be used to generate the rest of the

(a)

(b)

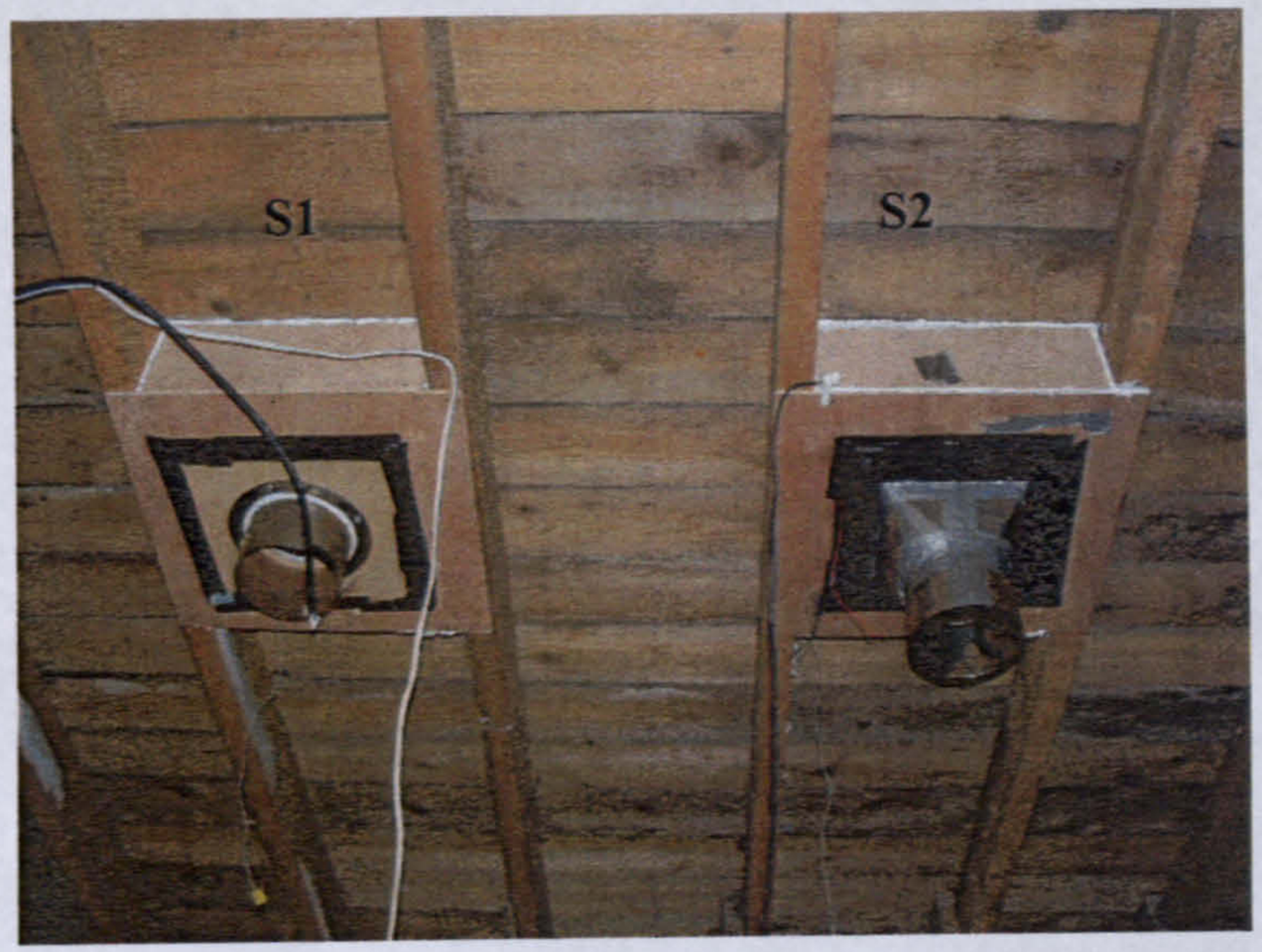

Fig. 7.1: Two systems, S1 (PV2-Fan1) and S2 (PV2-Fan2) installed in a house at Wiston (a) roof section A: two PV modules and a pyranometer, (b) the fan boxes in the attic.

curve) or alternatively, if the ΔP_f-Q characteristic of the fan in use is known, then a single point measurement of fan voltage and pressure across the fan will be satisfactory as shown in Fig. 7.2.

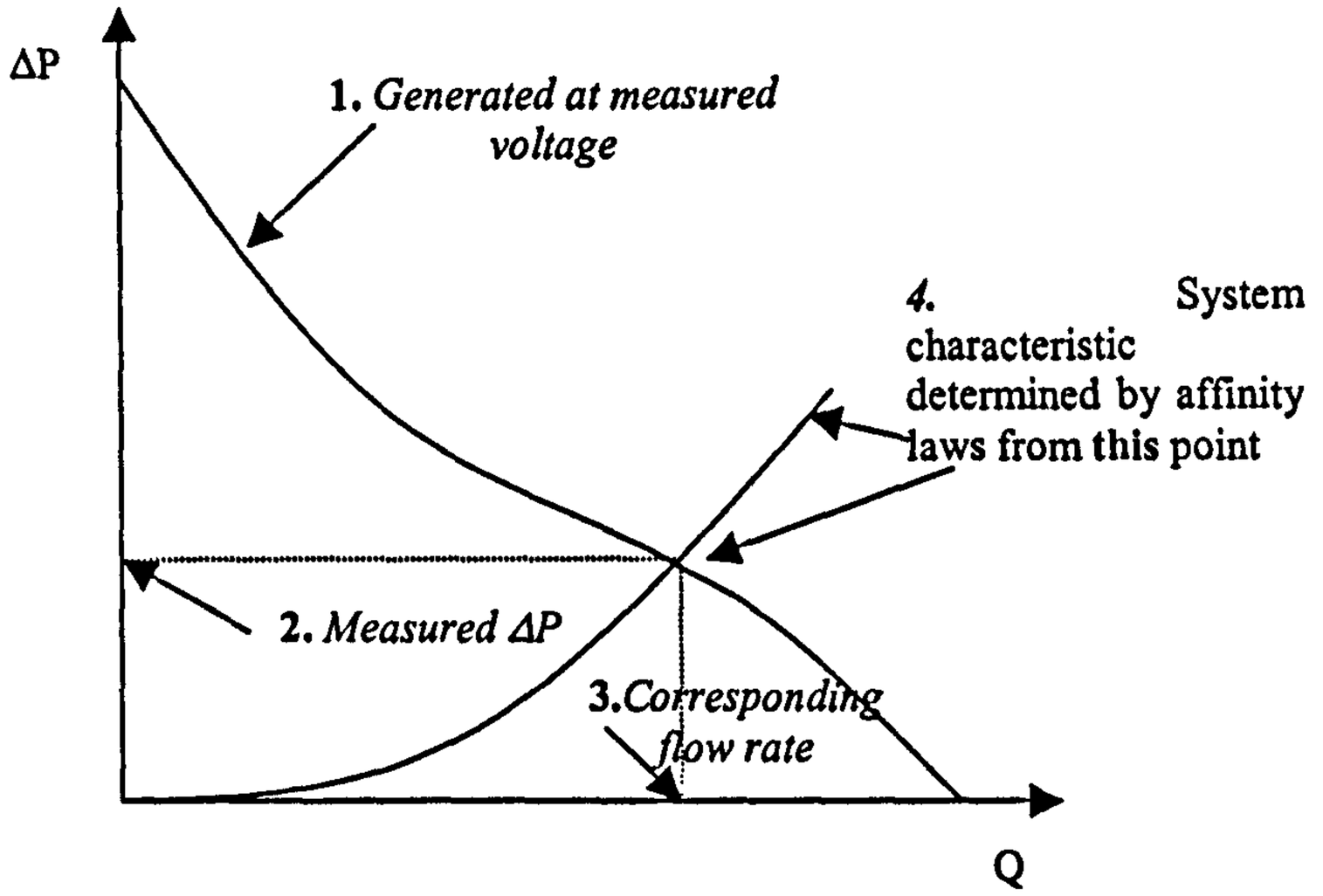

Fig. 7.2: Procedure for determination of the system's ΔP-Q characteristics from a single measurement of fan voltage and pressure across the fan.

In order to compare different PV-fan systems or different slate systems, the grill openings are set so that the different systems have identical ΔP_s-Q characteristics. For systems with the same slates and same PV module but different fans, this requires that a voltage pair (Fan1, Fan2) at which the two fans will give identical ΔP_s-Q characteristics is predetermined. For example, it can be seen from Fig. 7.3 that if Fan1 is operating at 17.5 V and Fan2 at 13 V, they will approximately give the same ΔP_s-Q characteristic. The grill opening for S2 is set so that the pressure at 13 V is the same as that for S1 at 17.5 V. It should be noted that even though this procedure produces small error, it is very simple and provides quick approximations. Figure 7.4 shows the ΔP_f-Q characteristic for the two systems S1 (PV2-Fan1) and S2 (PV2-Fan2) as generated from a single measurement of voltage and pressure across the fan.

The pressure across the fan was measured using the inclined manometer presented in section 3.3.5 with two Pitot static tubes. A program written in VBA is used to convert voltage to speed and then to the ΔP_f-Q characteristic. The pressure is then located on the ΔP_f-Q characteristic and the corresponding flow rate is determined. The system's ΔP-Q curve is then generated by the affinity laws from this determined flow rate and the measured pressure.

(a)

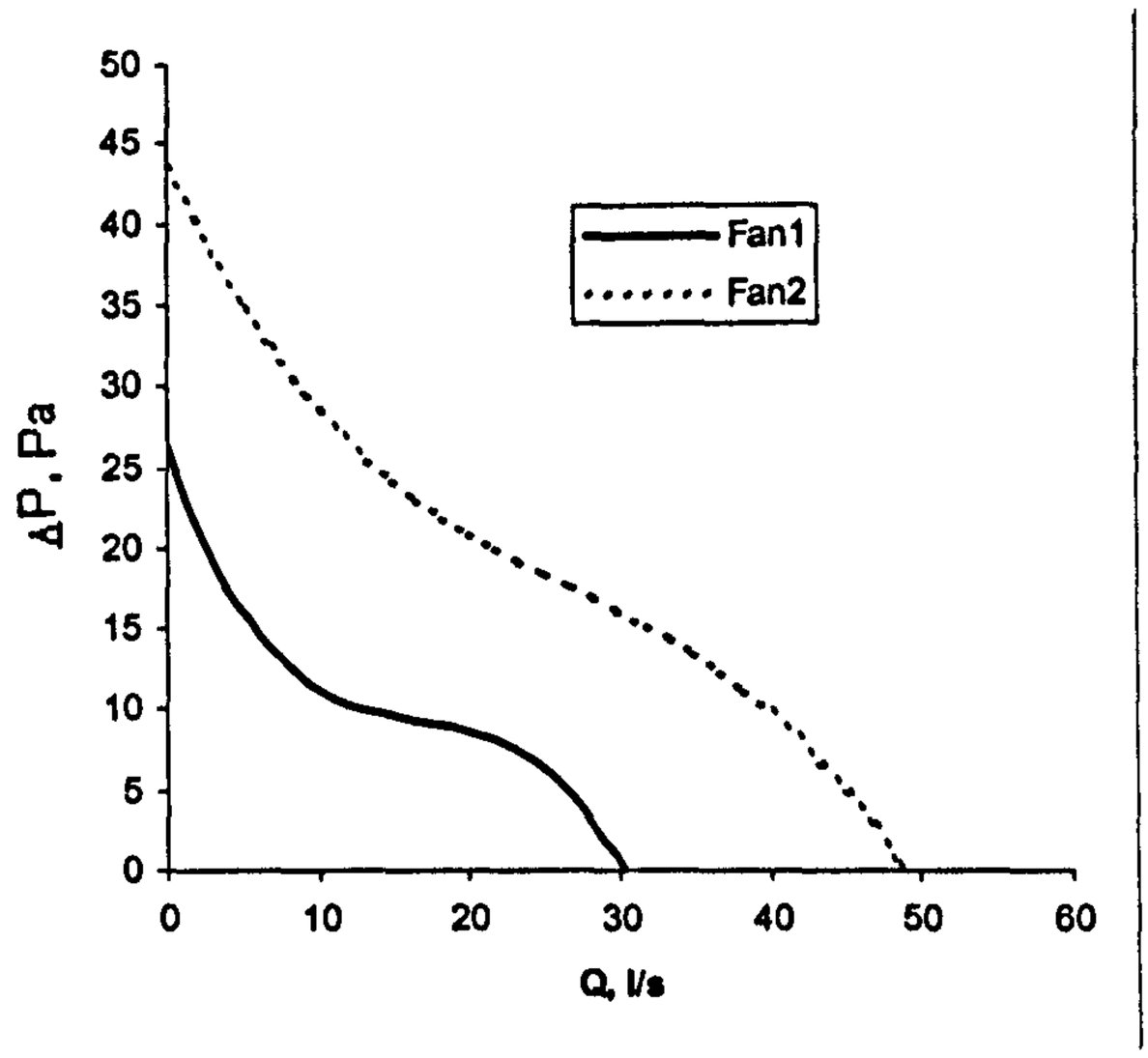

(b)

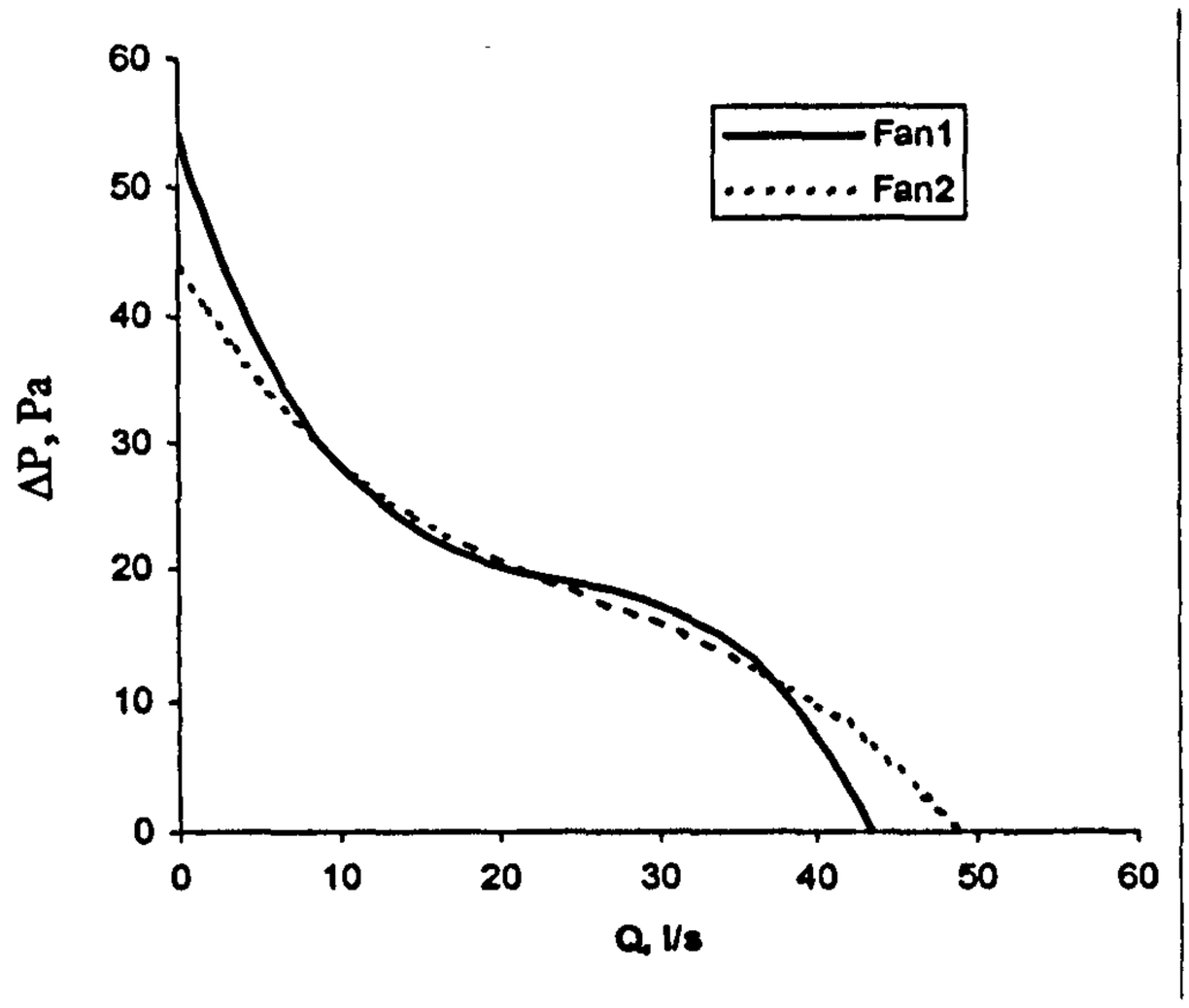

Fig. 7.3: ΔP_f-Q characteristics for Fan1 and Fan2 with (a) both fans at 13 V (Fan1 at 1350 r/min and Fan2 at 1670 r/min) and (b) Fan1at 17.5 V (1940 r/min) and Fan2 at 13 V (1670 r/min).

Using the method outlined in section 4.3.2, an effective duct length of 8 m at 80 % extension and 152 mm diameter was determined for the system curve in Fig. 7.4. This duct length with the corresponding diameter and extension of duct are entered in the model to predict the flow rate as a function of the measured irradiance and ambient temperature. Using the predicted flow rate with temperature measurements, heat can then be calculated.

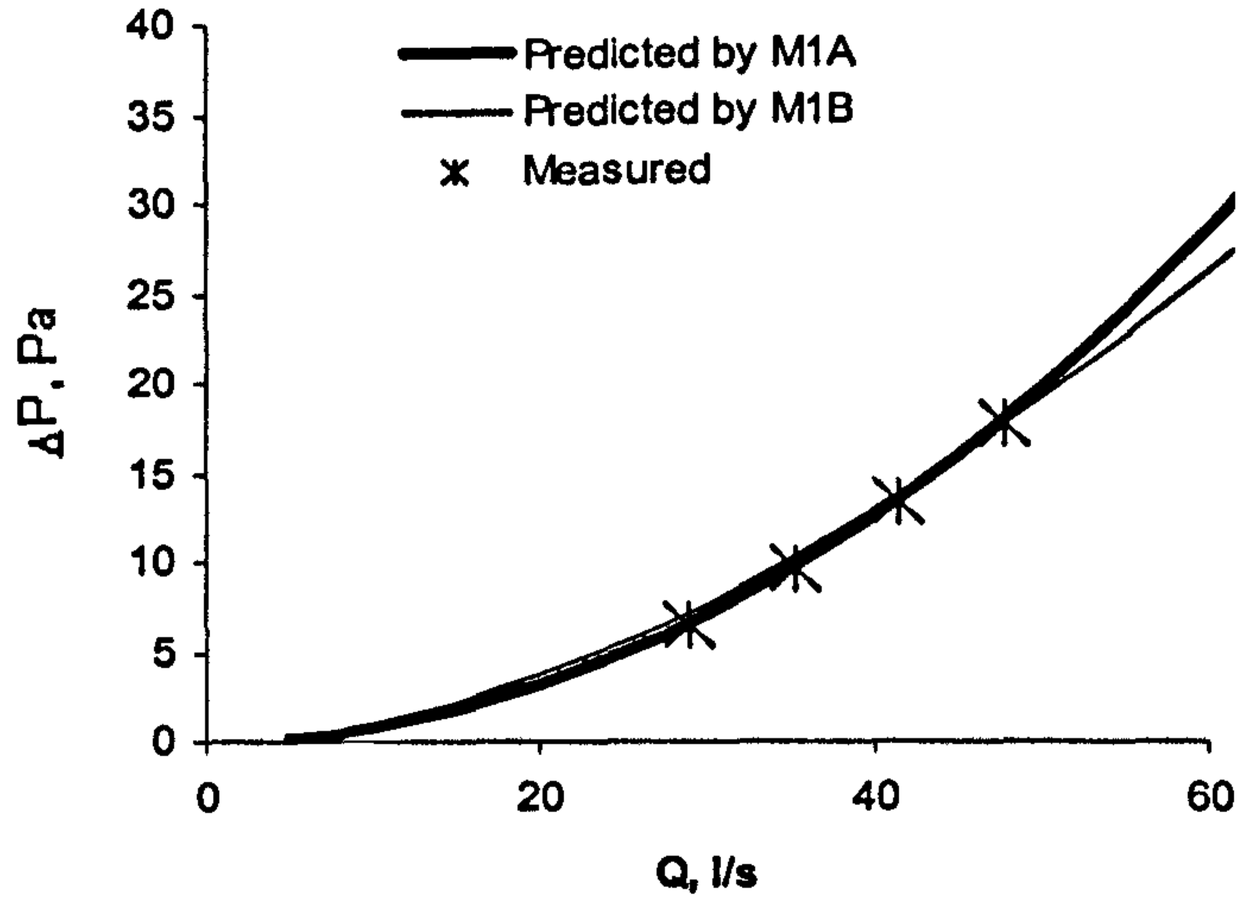

Fig. 7.4: ΔP_s-Q characteristics for S1 and S2.

7.3.3 Voltage and flow rate profiles

The measured voltage profile of the fan gives an indication of when the fan is in operation. Figure 7.5 (a) and Fig. 7.5 (b) show the irradiance and voltage profiles for a single day of measurement for the two systems (S1 and S2). It is noted that Fan1 starts operating at 7:54 AM while Fan2 does not start until 10:00 AM. The start-up irradiances for both fans as read from Fig. 7.5 agree significantly with the laboratory measurements (see section 3.5.1 and Table 6.2). Notice also that the irradiance on the sloped roof can reach up to 1200 W/m^2, which also agrees with predictions by the anisotropic NE model discussed in section 5.3.

Using the irradiance and temperature data, the flow rate profile was calculated for the day shown by Fig. 7.5. The results for both systems are shown in Fig. 7.6. The area underneath the flow rate profile is proportional to the volume of air delivered. This indicates that even though S2 is delivering higher flow rates at midday, S1 produces more volume throughout the day. Based on the method described in section 6.2, calculations reveal that for that day, S1 delivered 735.9 m^3 while S2 delivered 365.7 m^3. The irradiance falling on the roof for the same period of time is 18.3 MJ/m^2 (5.1 kWhr/m^2). Thus it is seen that S1 delivers nearly twice as much volume as S2. This is attributed, as discussed in chapter 6, to the start-up characteristics. Furthermore, for the whole period of operation for that day, Fan2 operates only 26 % of the time while Fan1 operates 62 % of the time.

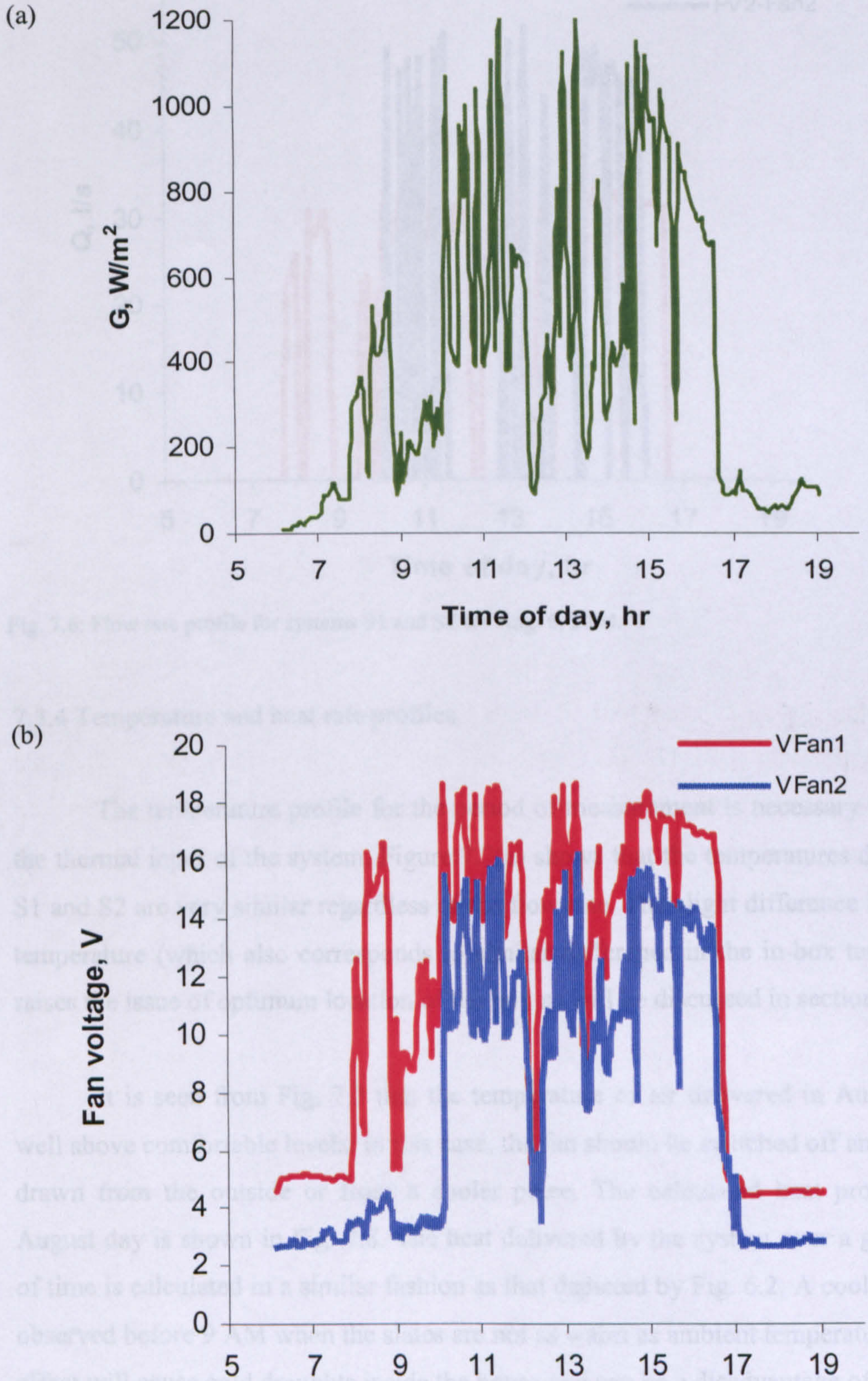

Fig. 7.5: (a) Irradiance profile and (b) voltage profiles for the two fans for Aug. 6, 2004.

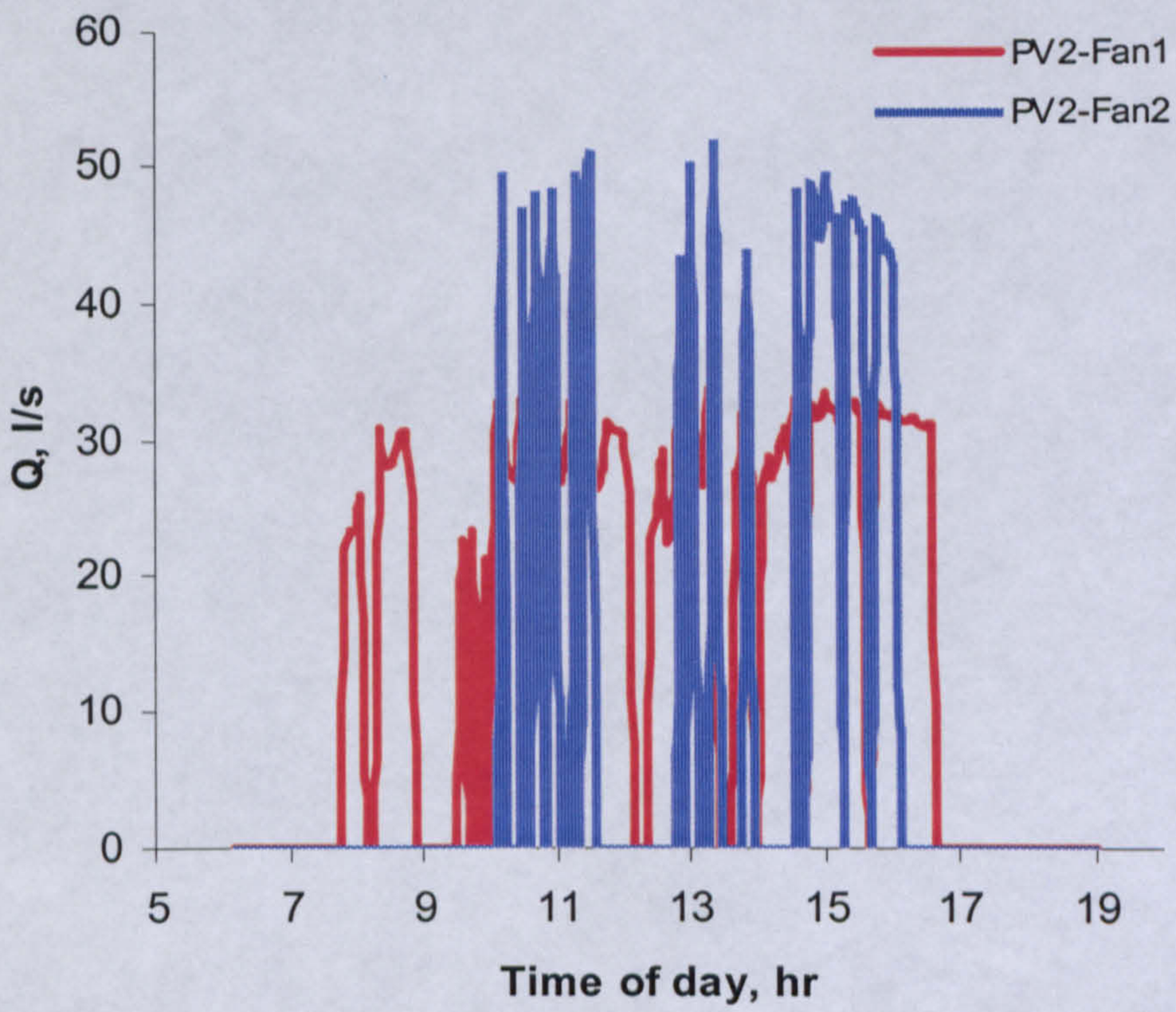

Fig. 7.6: Flow rate profile for systems S1 and S2 for Aug. 6, 2004.

7.3.4 Temperature and heat rate profiles

The temperature profile for the period of measurement is necessary to calculate the thermal input of the system. Figure 7.7(a) shows that the temperatures delivered by S1 and S2 are very similar regardless of the flow rate. The slight difference in delivered temperature (which also corresponds to similar difference in the in-box temperatures) raises the issue of optimum location of the box as will be discussed in section 7.5.

It is seen from Fig. 7.7 that the temperature of air delivered in August can be well above comfortable levels. In this case, the fan should be switched off and air can be drawn from the outside or from a cooler place. The calculated heat profile for the August day is shown in Fig. 7.8. The heat delivered by the system over a given period of time is calculated in a similar fashion as that depicted by Fig. 6.2. A cooling effect is observed before 9 AM when the slates are not as warm as ambient temperature yet. This effect will cause cold draughts inside the house and can be a disadvantage of Fan1.

(a)

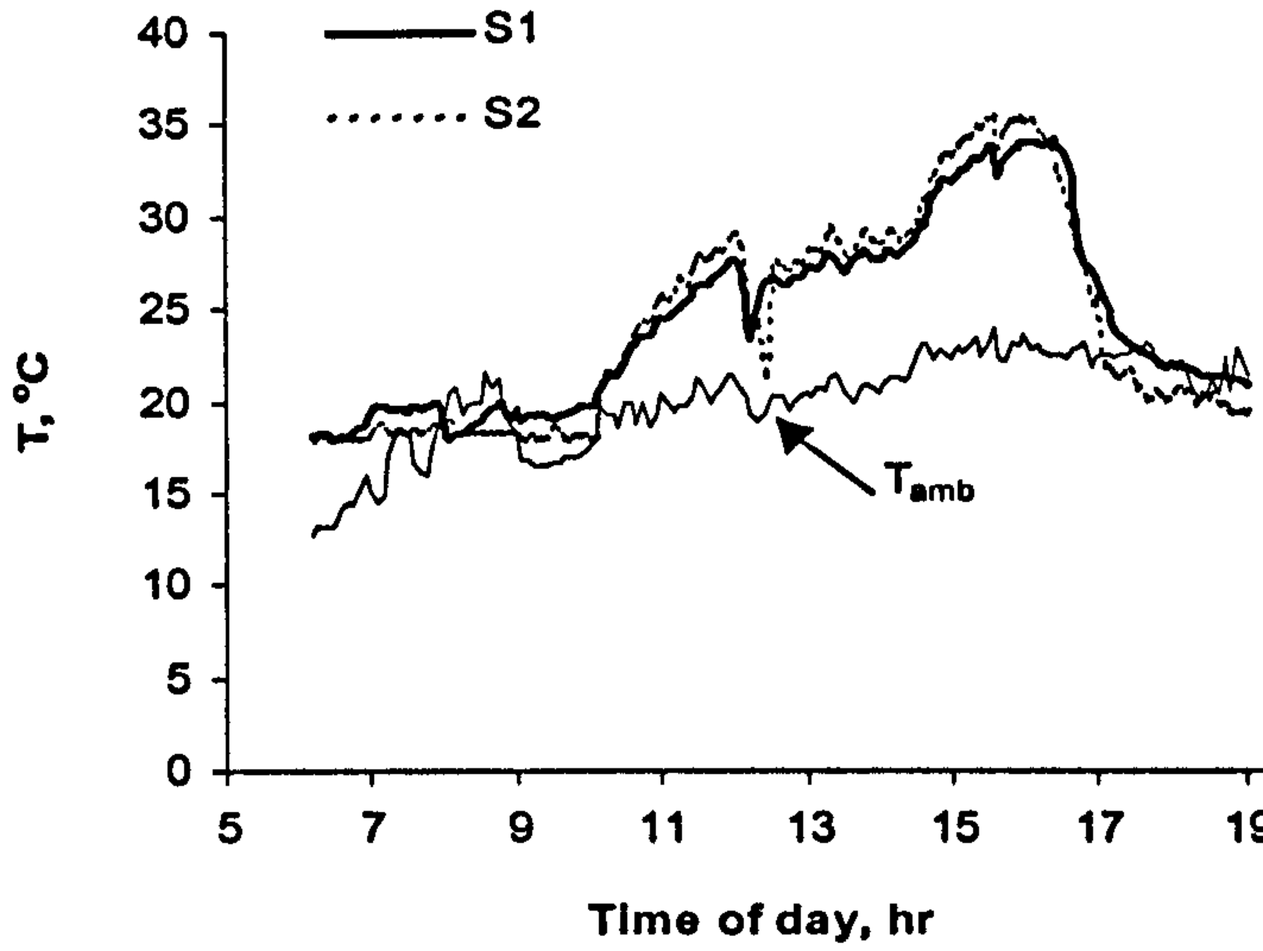

(b)

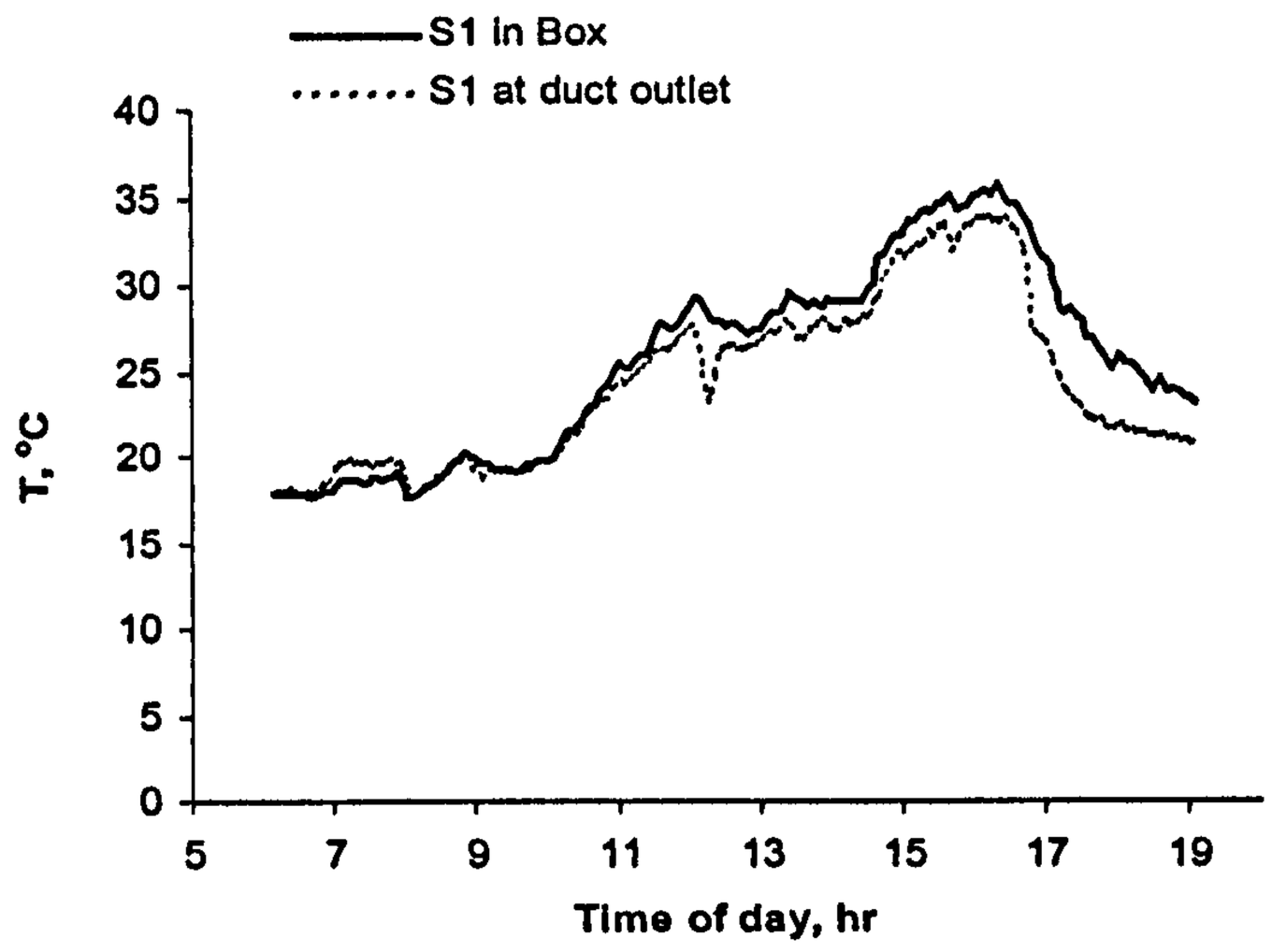

Fig. 7.7: (a) Duct-outlet temperature profiles for systems S1 and S2 and (b) In-box and duct-outlet temperature profiles for S1.

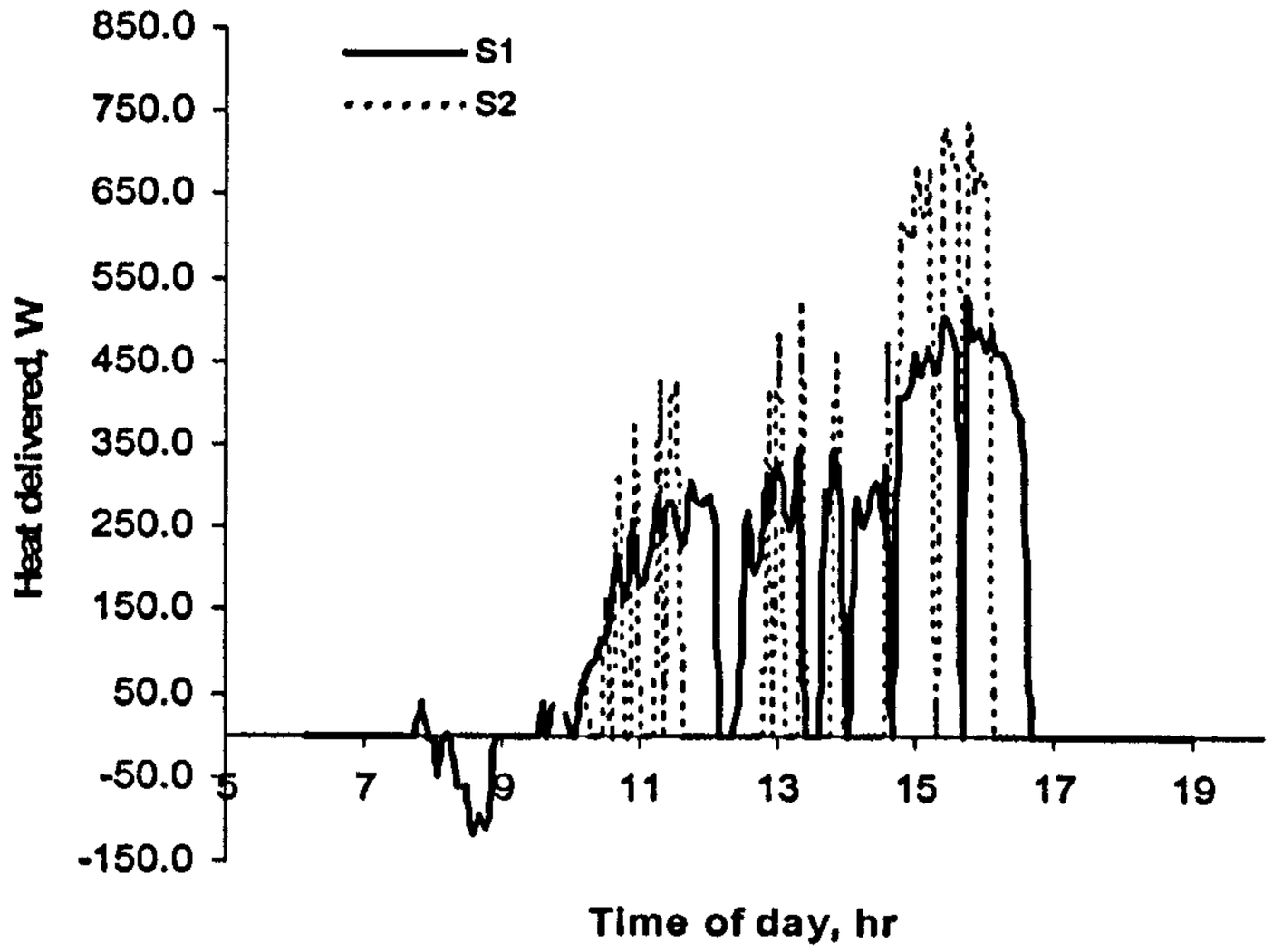

Fig. 7.8: Calculated heating rate for Aug. 6, 2004 for S1 and S2.

This drop in T_{outlet} is observed in Fig. 7.7 and also in Fig. 7.9, which represents a day in November. The profiles for S2 are not shown because Fan2 did not start on that day. As Fan1 starts (at about 9:30 AM), T_{outlet} and T_{Box} drop very close to ambient temperature. This temperature drop from 10 to 6 C causes discomfort. It can be avoided by either delaying the start-up of Fan1 until the slates are warm enough or by enhancing the properties of the slates so that they can warm up quickly. It is calculated that an 18-Ω resistor connected in parallel with Fan1 will delay the start-up from 290 W/m^2 to 800 W/m^2. Alternatively, adding dark paint or antireflective coating to the slates may cause the slates to warm up quickly thus avoiding cold draughts and delivering more heat to the house.

(a)

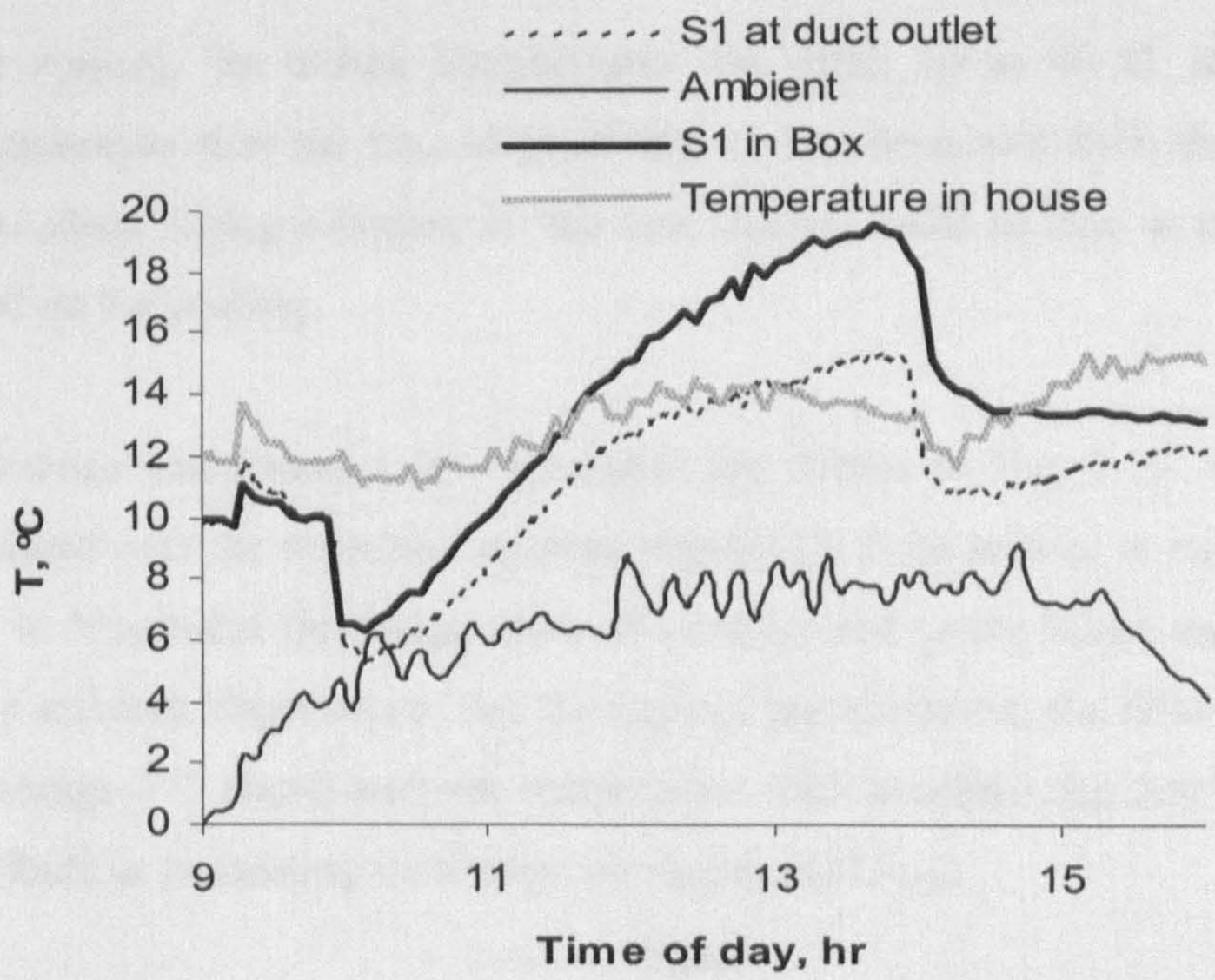

(b)

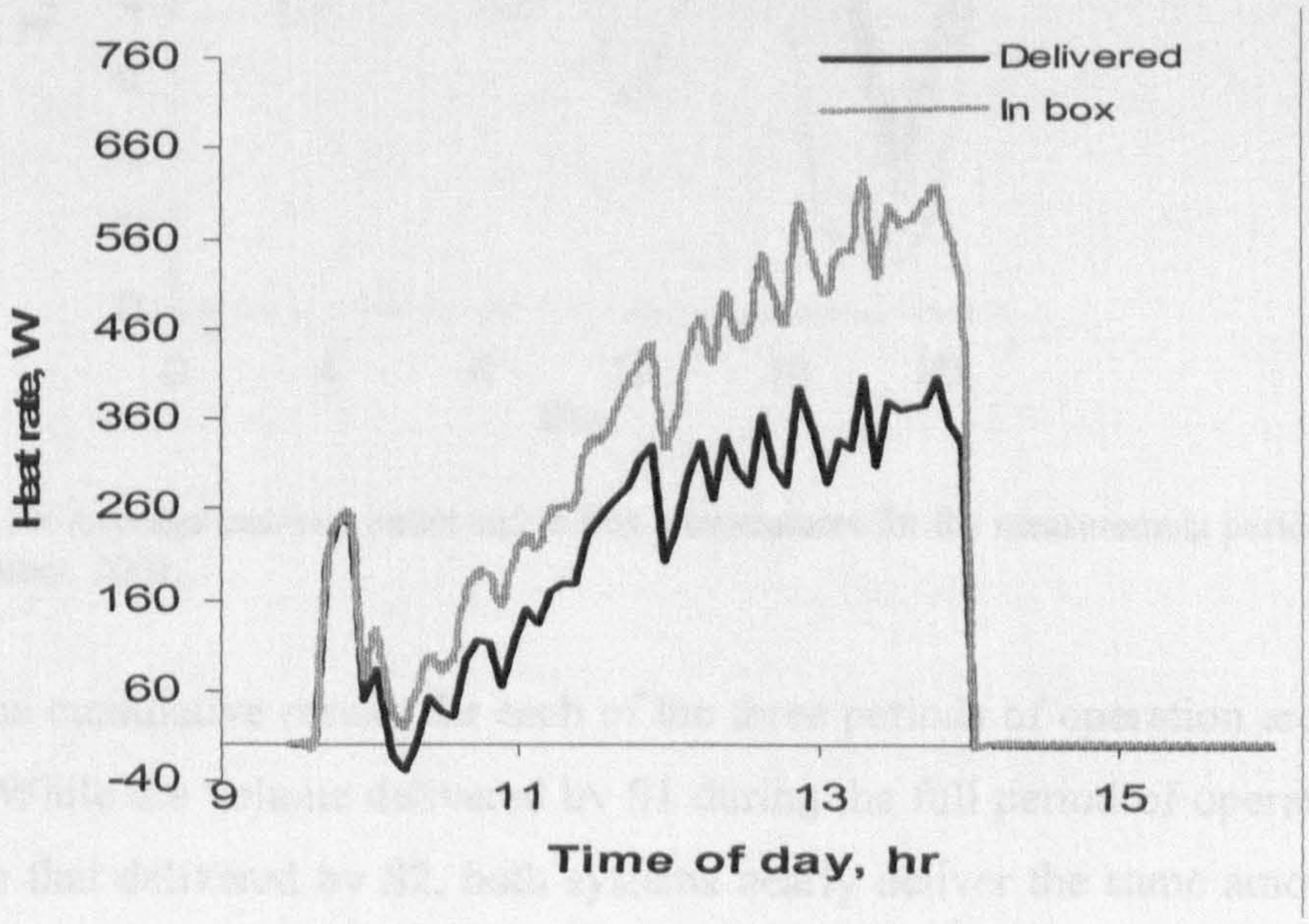

Fig. 7.9: (a) Measured temperature profiles and (b) calculated heat rate profile for a day in November 2004.

7.3.5 General observations and results

7.3.5.1 Roof section A

1. In August, the in-box temperatures can reach up to 40 C. In such cases, it is undesirable to start the fan. Alternatively, air can be drawn from the outside or from a cooler place. Using a battery in this case can be useful so that, at night the fan can be turned on for cooling.

2. Average temperatures for November are shown in Fig. 7.10. These are averages calculated over the potential sunshine period (i.e. from sunrise to sunset). It is seen that even in November the temperature of air delivered to the house can be a few degrees above ambient temperature. For the days of measurement, the delivered temperature is on average 3 C above ambient temperature. This confirms the fact that roof slates can contribute to preheating ventilation air during cold days.

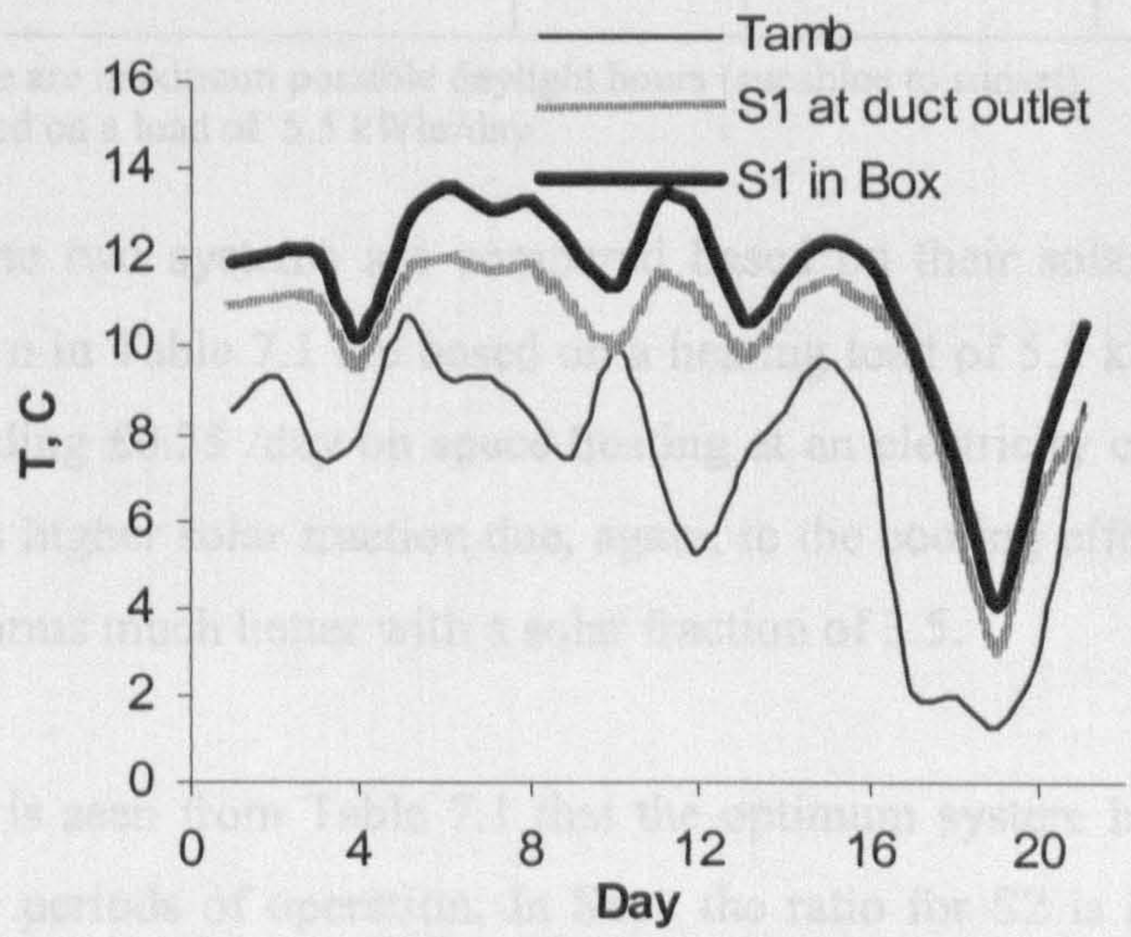

Fig. 7.10: Average ambient, outlet and in-box temperatures for the measurement period during November, 2004.

3. The cumulative results for each of the three periods of operation are shown in Table 7.1. While the volume delivered by S1 during the full period of operation is more than twice that delivered by S2, both systems nearly deliver the same amount of heat. This can be explained by periods when S1 is delivering cold air in the morning as discussed above. Nevertheless, S1 is more advantageous because S2 did not deliver any heat during November, a pattern which may also be repeated during subsequent months. Generally, the start-up characteristic of the system is the most important factor affecting

its performance. Results of the daily volumes and heat delivered by the two systems for the three periods of operation are also shown in Fig. 7.11.

Table 7.1: Results for S1 and S2 for 59 days of operation.

	System	Aug.	Sep.	Nov.
Run days		27	10	22
Total hours*		325.6	124.0	173.8
Total G, MJ/m^2		658.9	250.5	133.0
Total V, m^3	**S1**	12131.5	4812.8	2561.0
	S2	6306.5	3283.0	12.1
r, l/J	**S1**	0.26	0.27	0.27
	S2	0.13	0.18	0.00
Total E, kWhr	**S1**	23.4	11.7	3.8
	S2	22.0	14.8	0.03
Solar fraction**	**S1**	15.6	21.3	3.5
	S2	14.8	26.9	0.0

*These are maximum possible daylight hours (sunshine to sunset)
**Based on a load of 5.5 kWhr/day

4. The two systems are compared based on their solar fractions. The solar fractions shown in Table 7.1 are based on a heating load of 5.5 kWhr/day, which corresponds to spending £0.35 /day on space heating at an electricity cost of £0.07/kWhr. In Sep., S2 gives higher solar fraction due, again, to the cooling effect of S1. In Nov., however, S1 performs much better with a solar fraction of 3.5.

5. It is seen from Table 7.1 that the optimum system has higher values of "r" for the three periods of operation. In Sep., the ratio for S2 is higher because, as can be seen from Fig. 7.11(b), during the last few days of operation in Sep., the received radiation was very high indicating that Fan2 had been delivering higher flow rates during that period. This, in addition to the cooling effect caused by early start-up of Fan1, results in lower thermal energy delivered by S1 during the period of operation in Sep.

6. It is expected that as the flow rate in the system increases, more heat is removed from the slates and so the slate temperature decreases. However, based on the similarity of the temperature profiles (Fig. 7.7 (a)) and the difference in the flow rate profiles for the same day (Fig. 7.6), it can be suggested that the flow rate in the system may not significantly affect the temperature of air in the box or the slate temperature.

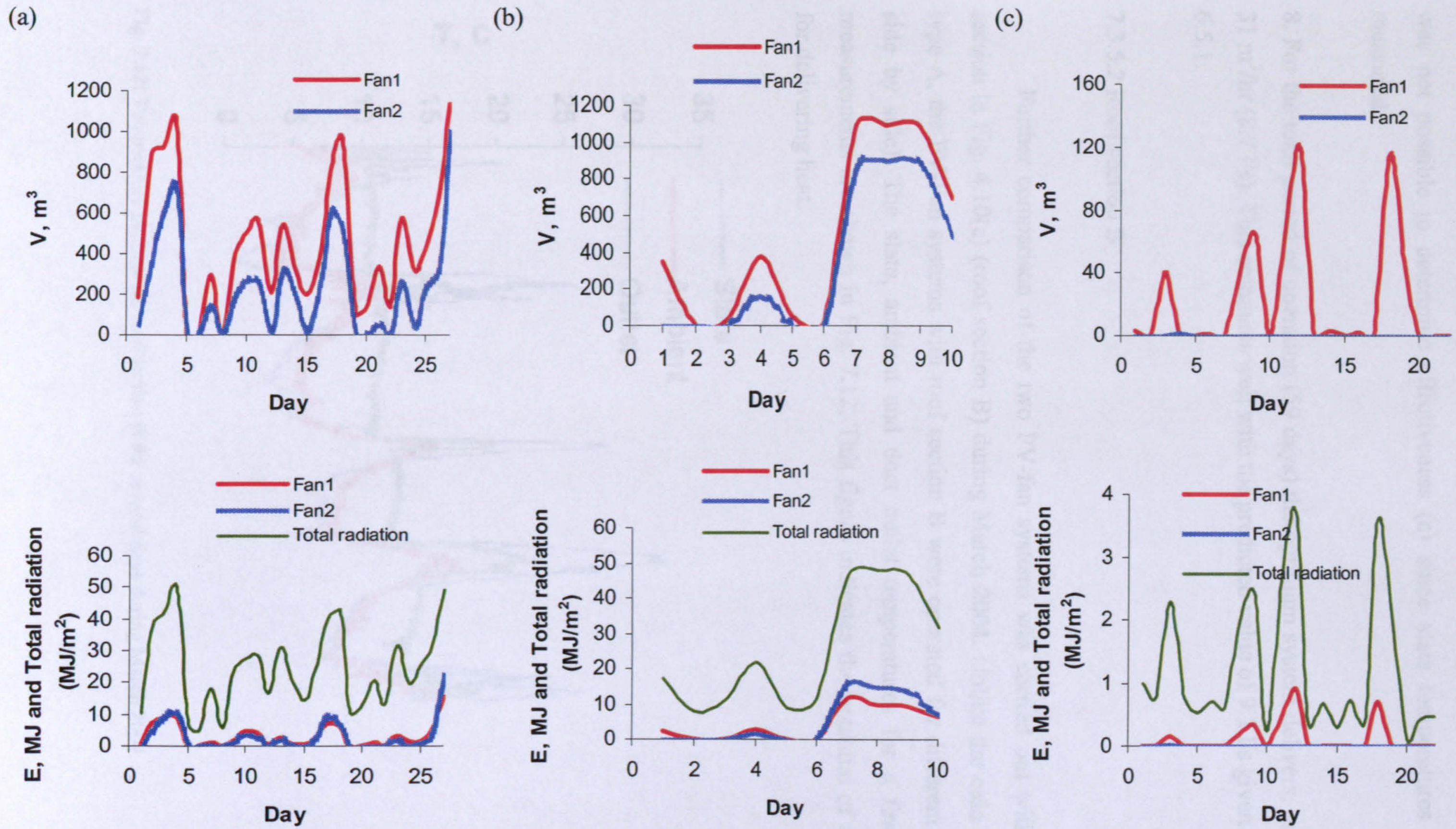

Fig. 7.11: Daily total volume and heat delivered by S1 and S2 for the operation period in (a) August, (b) September and (c) November.

7. The collector area from which air is drawn is variable and depends on irradiance and fan voltage (or speed). Thus it is not possible to calculate an efficiency of the system. It was not possible to determine effectiveness (ε) since slate temperatures were not measured.

8. For the total period of operation (59 days) the optimum system delivers, on average, 31 m^3/hr (8.7 l/s). This compares well with the predicted value of 9.2 l/s given in section 6.5.1.

7.3.5.2 Roof section B

Further comparison of the two PV-fan systems was carried out with the roof section in Fig. 4.10(a) (roof section B) during March 2004. Unlike the case with slate type A, the PV-Fan systems with roof section B were operated for different days (not side by side). The slate, ambient and duct outlet temperatures for a few days of measurements are shown in Fig. 7.12. This figure indicates the potential of roof slates for delivering heat.

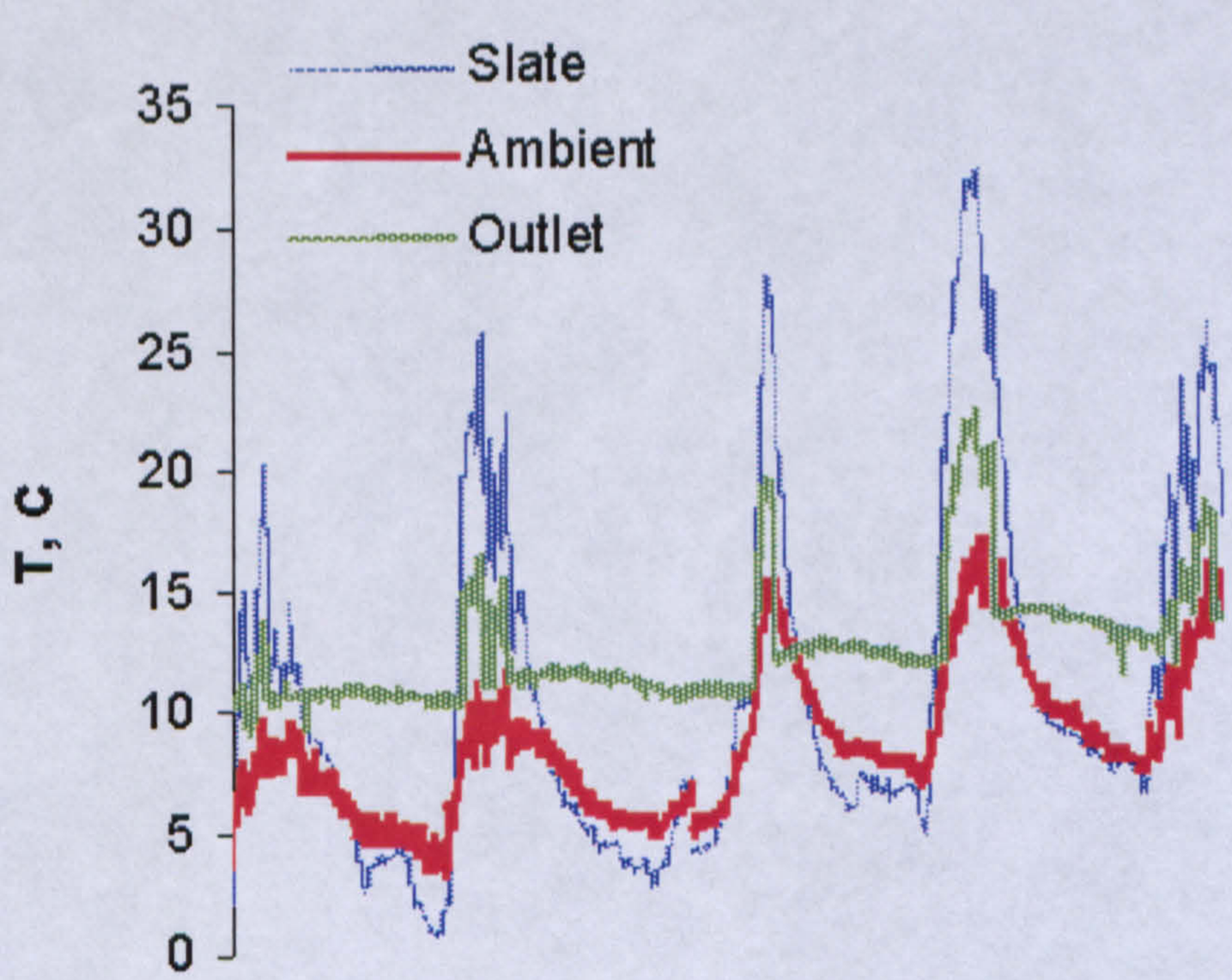

Fig. 7.12: Temperature profiles for roof section B for several days during March 2004.

A comparison for the full period of operation of both systems is shown in Table 7.2. Effectiveness was calculated in two different ways as shown at the bottom of the table. It is seen that the optimum system is expected to have higher effectiveness and solar fractions. It is also seen again that the heat ratio is less than the volume ratio. This is due to the cold draughts produced by Fan1 due to early start-up as can be seen from Fig. 7.13. Moreover, for days with the optimum system, higher wind speeds were measured. Despite the fact that the optimum system was operated with lower slate temperatures (due to high wind speeds) it gave a higher effectiveness due to its longer periods of operation as seen in Table 7.3.

The ratio "r" was calculated for both systems. It can be seen that the optimum system still produces higher volumes for each joule of energy received by the PV module. These values for roof section B are different from the values for roof section A which may be attributed to different system characteristics.

Table 7.2: Results for Fan1 and Fan2 (operated on different days in March, 2004) with roof section B.

	Fan1	Fan2
Run days	11 (Mar. 7-17)	11 (Mar. 18-28)
Max sunshine hours	126.5	126.5
Total G, MJ/m^2	83.8	73.7
Total V, m^3	4893.2	1983.8
r, l/J	0.81	0.37
E_{max}, MJ	41.8	40.2
E_{Box}, MJ	28.4	20.2
$E_{delivered}$, MJ	22.1	16.7
solar fraction*	0.11	0.08
$\varepsilon_{delivered\text{-}max}$	0.53	0.42
$\varepsilon_{box\text{-}max}$	0.68	0.53

* based on 5.5 kWhr/day load.

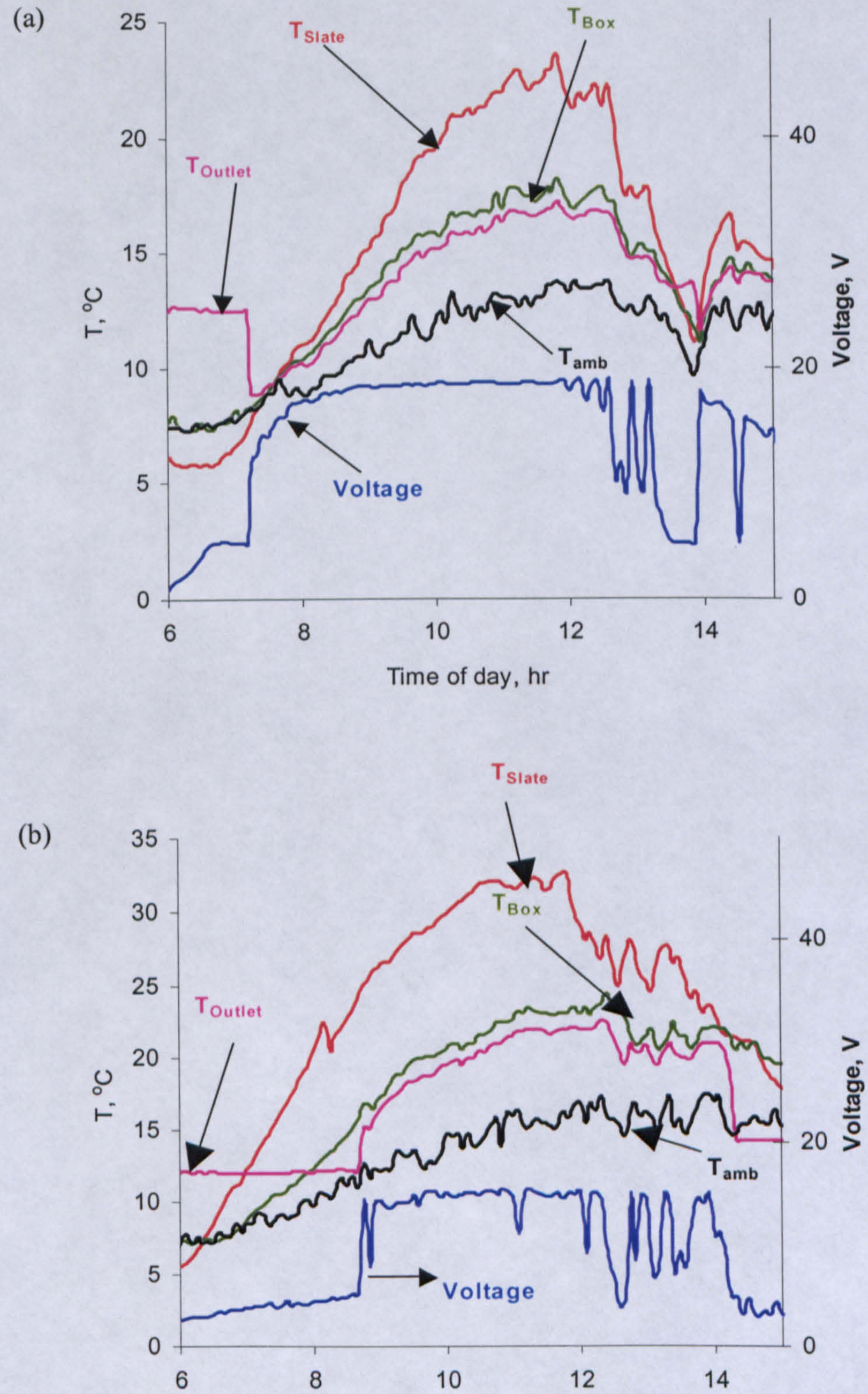

Fig. 7.13. Temperature and voltage measurements (a) for March 17, 2004 with PV– Fan1 and ws = 9.7 m/s) and (b) for March 27, 2004 with PV - Fan2 and ws = 4 m/s).

Table 7.3: Results for PV-Fan1 and PV-Fan2 for two different days of operation with slate type B.

	PV-Fan1	PV-Fan2
day	Mar. 17	Mar. 27
Average ws, m/s	9.7	4
E_{max}, MJ	10.0	11.5
$E_{in\ box}$, MJ	5.1	5.4
$E_{delivered}$, MJ	4.2	4.4
ε	0.42	0.38

7.3.6 Summary

The optimum system is still favourable due to its early start-up characteristics. However, measurements of both systems under identical conditions of wind speed and patterns are necessary for representative comparison to be carried out. Moreover, a matching between slate type and the optimum system is required so that the slates warm up as quickly as the system starts operating. Delaying the start of the system is advisable but in order to make use of the full possible period of operation, the slate properties can be altered in order to enhance their absorption properties.

7.4. TESTING THE OPTIMUM SYSTEM WITH DIFFERENT SLATES

The results with roof sections A and B for the optimum system were further compared to results obtained with a third roof section (C) shown in Fig. 7.14. The new system was installed at a garage in Biggar and measurements were taken during April 2005. In order to compare the system to other roof sections, the grill opening was to be set so that the system characteristic resembles the previous two (8 m effective length of flexible metallic duct at 80 % extension and 152 mm diameter).

Fig. 7.14: The optimum system installed at a house in Biggar (roof section C).

The comparison is a complex matter since the testing was undertaken on different days for different lengths of time and with different prevailing wind speeds. With slate type B and C, the total maximum possible hours of operation (TMPHO) and the irradiance received by the PV module and the slates for both periods were similar. For slate A, the September data is chosen for comparison purposes because it yields the same TMPHO. The total irradiance for that period is also of the same order as the two other systems. However, in order to make sense of the data in Table 7.4, the wind speed for the days of measurement must be known. These were not measured and so they are obtained from the Internet meteorological site "Weather Underground". The wind speed values used here are not specific and they are to be used only to make general impressions about each of the days of operation (i.e. they cannot be used for calculations since they do not represent the location of interest but they represent the general conditions for the city at the time of measurement).

The effect of wind speed can be realized from Fig. 7.15. Generally, for days with high average wind speeds, low temperatures are detected and vice versa. The small amount of heat delivered by slate type B is not caused by lower volumes as can be seen from Table 7.4 but rather by lower slate temperatures. It is reported on the Internet site that for March, 2004 and during the period of measurement for slate type B, wind speeds as high as 12 m/s are measured.

Table 7.4: Results for different slate types.

	Hours	G, MJ/m^2	V, m^3	E, MJ
Slate A	124.0	250.5	4812.8	42.1
Slate B	126.5	205.0	4893.2	20.5
Slate C	125.1	236.6	6633.8	54.8

If equal collector's area for the optimum system is assumed, regardless of the slate type, the overall efficiency (for the full period of operation) for each of the slate systems can be calculated as the ratio of the delivered heat to the available radiation. Based on this assumption, the system with roof section C is more efficient either due to higher temperatures or due to higher flow rates. However, the volume delivered by the optimum system with slate C is much higher than that delivered by the two other systems indicating the system ΔP_s-Q characteristics may not be the same.

If wind speed for the days of measurement for roof A and roof C are the same, the ratio of heat delivered to volume delivered can be an indication of the slate's thermal potential for collecting heat.

Slate C can be advantageous over both slate A and slate B because, as can be seen from Fig. 7.16, the slates were warm enough when the fan started operating. For the day shown in Fig. 7.16 (April 23, 2005), the slate temperature reaches 50 °C and the temperature of air delivered reaches 25 °C. However, the effectiveness of the system shown here ($\varepsilon = 0.3$) is lower when compared with the system in roof section B. This may be due to the higher heat transfer coefficients for slate C resulting more losses by convection and radiation.

Comparing different roof slates requires that they are set up next to each other in the same environment. The model developed in chapter 3 and 4 can then be used to make conclusions about the potential of the optimum system with different slate types.

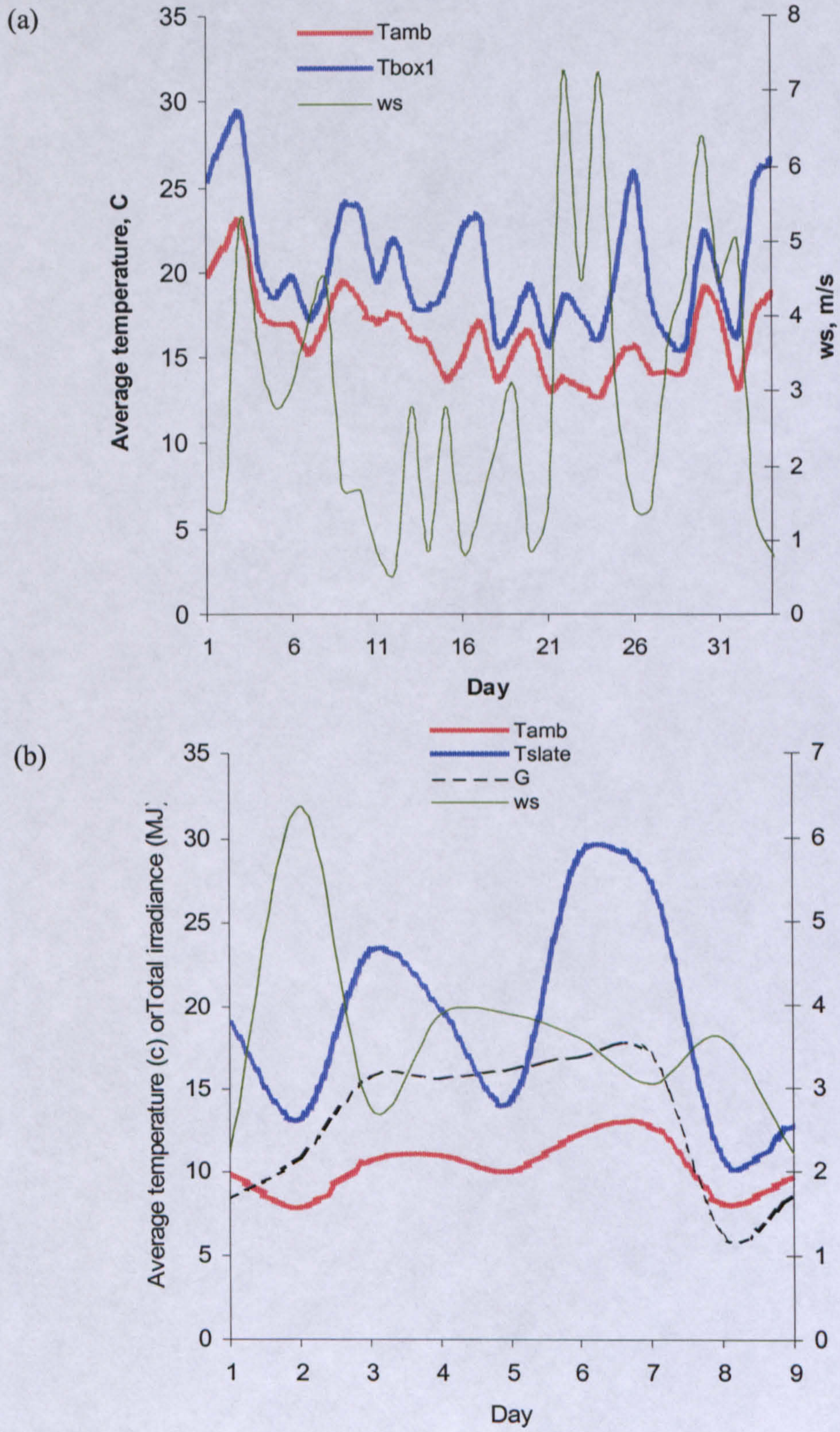

Fig. 7.15: Selected temperature, irradiance and wind speed profiles for several days of operation for the optimum system with (a) roof section A and (b) roof section C.

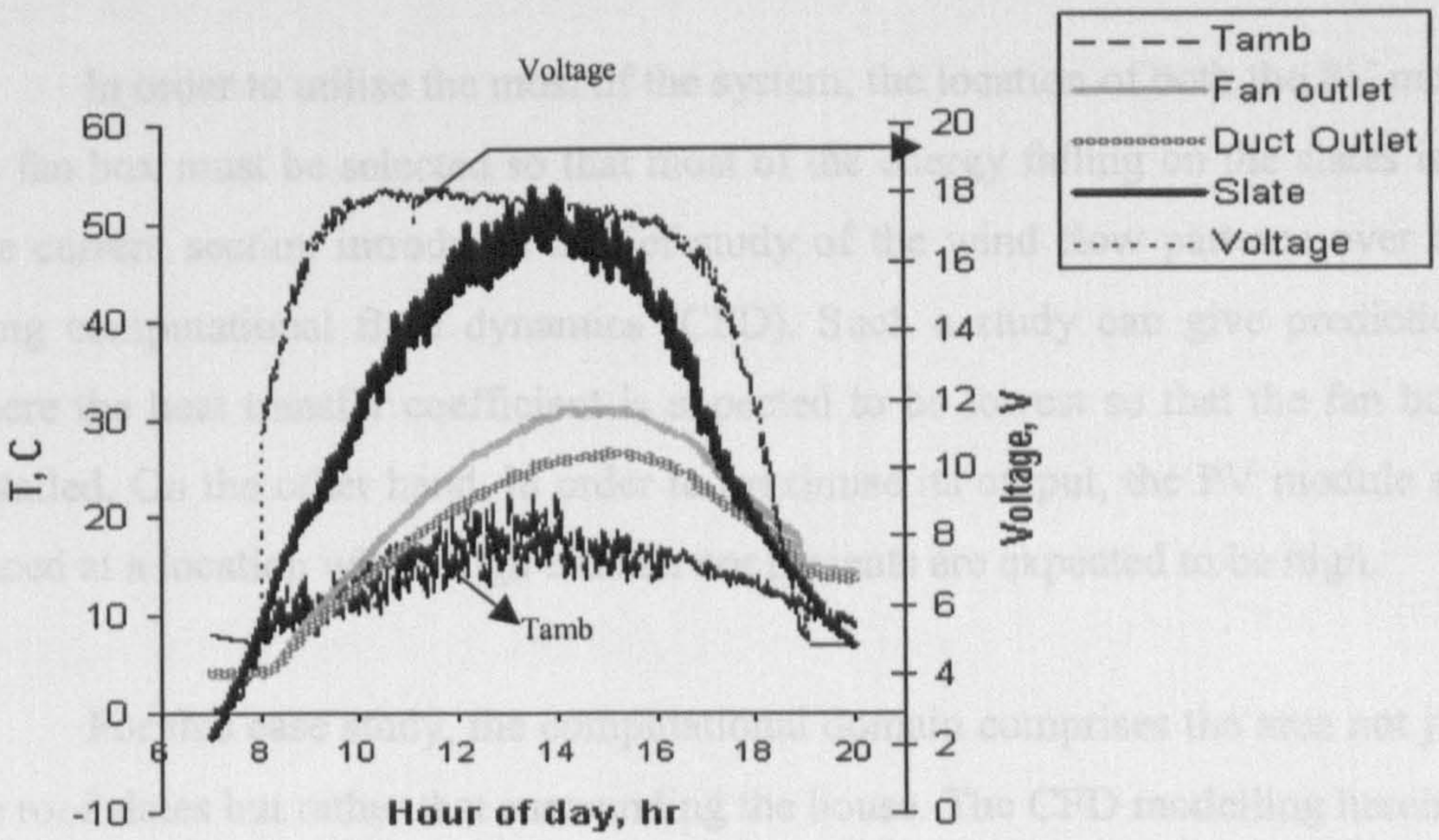

Fig. 7.16: Voltage and temperature profiles for the system: [roof section C-PV-Fan1] for April 23, 2005.

7.5 FLOW PATTERNS OVER ROOF SLATES USING CFD

In order to utilise the most of the system, the location of both the PV module and the fan box must be selected so that most of the energy falling on the slates is utilised. The current section introduces a brief study of the wind flow patterns over the slates using computational fluid dynamics (CFD). Such a study can give predictions as to where the heat transfer coefficient is expected to be lowest so that the fan box can be installed. On the other hand, in order to maximise its output, the PV module should be placed at a location where high transfer coefficients are expected to be high.

For this case study, the computational domain comprises the area not just above the roof slates but rather that surrounding the house. The CFD modelling herein is based on long-term weather data (wind speed, wind direction and ambient temperature) for Edinburgh. Based on 16-year data (1976 to 1992), an average wind speed of 4.56 m/s, an average wind direction of 183° clockwise from North (i.e. 3° west of south) and an average ambient temperature of 8.6 °C are determined. In order to reduce the problem from a 3D problem to 2D one, the wind direction is taken as 180°. The slate temperature can vary depending on irradiance, slate properties and other factors. A uniform slate temperature of 18.6 °C (10 °C above ambient) is assumed. Moreover, a slate length of 20 cm and a thickness of 2 cm are assumed. A small roof section with 8 slates was considered.

The wind speed and direction are not constant but are changing all the time. Here it assumed that the house is located in an open area where the flow over the roof slates is not obstructed by other nearby houses. Even though some of the assumptions may not seem realistic at this point, the purpose here is to try to make general conclusions about the flow over roof slates, which may lead to further work.

CFD simulations show that as air flows over the slates, it increases in velocity due to the convergence effect as shown in Fig. 7.17(a). The convergence of flow in this case is caused by both the restrictions resulting from the inclined surface and the slates themselves. This also explains the sudden increase in the velocity of air as it moves over the tip of the roof. The small velocities at the bottom of the opposite side of the roof (i.e. the side not vulnerable to wind) are caused by the formation of a vortex. It can also

be seen that small velocities are predicted at the end of each of the slates as a result of the restriction caused by the thickness of the slates.

Figure 7.17(b) shows the heat transfer coefficient along the length of the roof section. Each of the colors represents a slate. At the beginning of each of the slates, the heat transfer coefficient is high but then it stays constant along the length of the slate. At the end of each slate, a sharp decrease in the heat transfer coefficient is caused by the restriction to flow resulting from the slate thickness. In general, it can be seen that the heat transfer coefficient stays constant over the length of the roof section but increases rapidly at the end. This behaviour is different from that over a horizontal flat plate where the heat transfer coefficient decreases with length (Fig. 7.18).

It can be concluded from Fig. 7.17(b) that an ideal location for the fan box would be as far away as possible from the top of the roof section. The top of the roof section would, on the other hand, be suitable for the PV module since lower temperatures are expected. In order to verify these CFD simulations, they must be tied with experimental data in the future. Primarily, it can be seen that the flow patterns over inclined surfaces is different from patterns over horizontal surfaces.

(a)

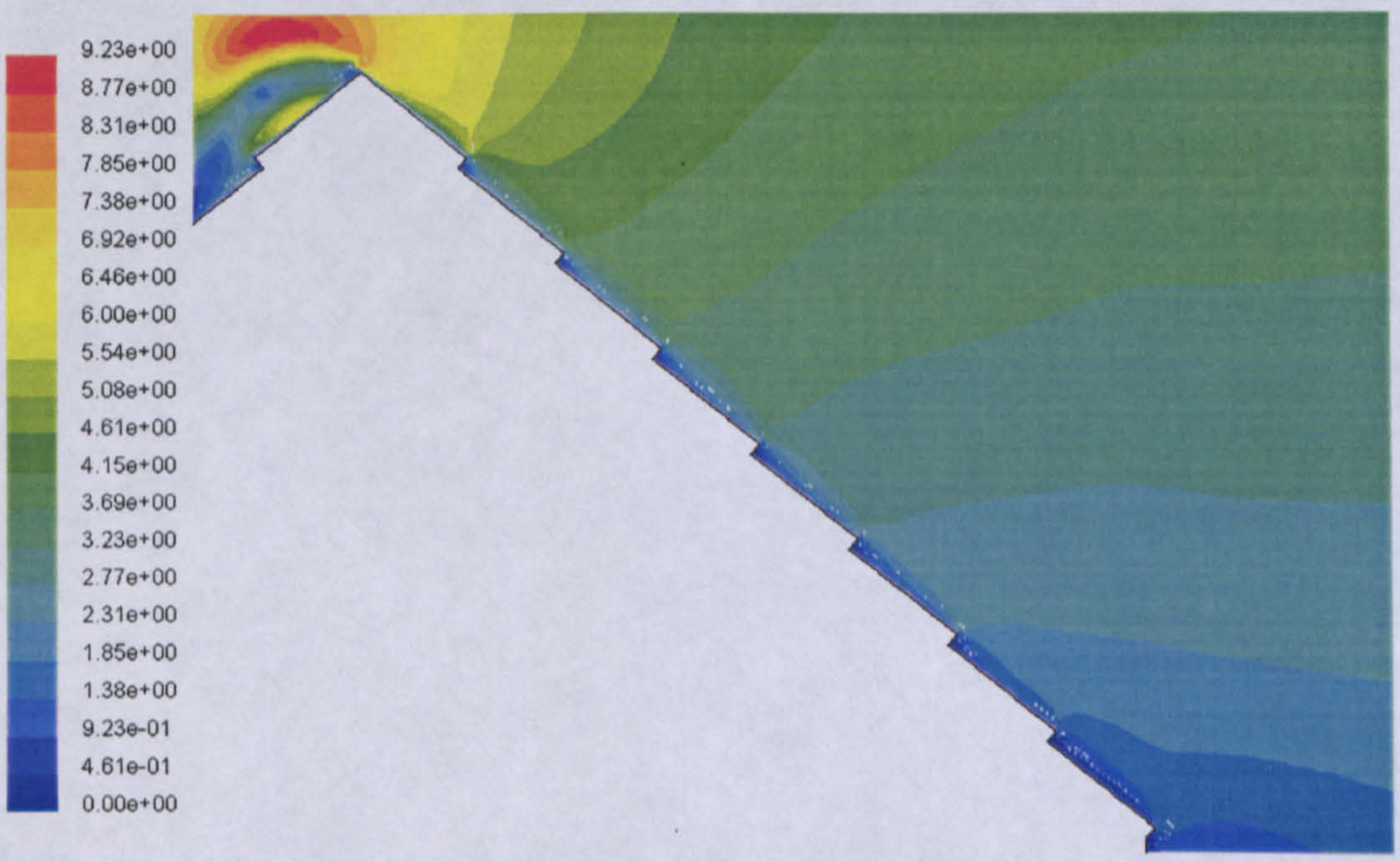

(b)

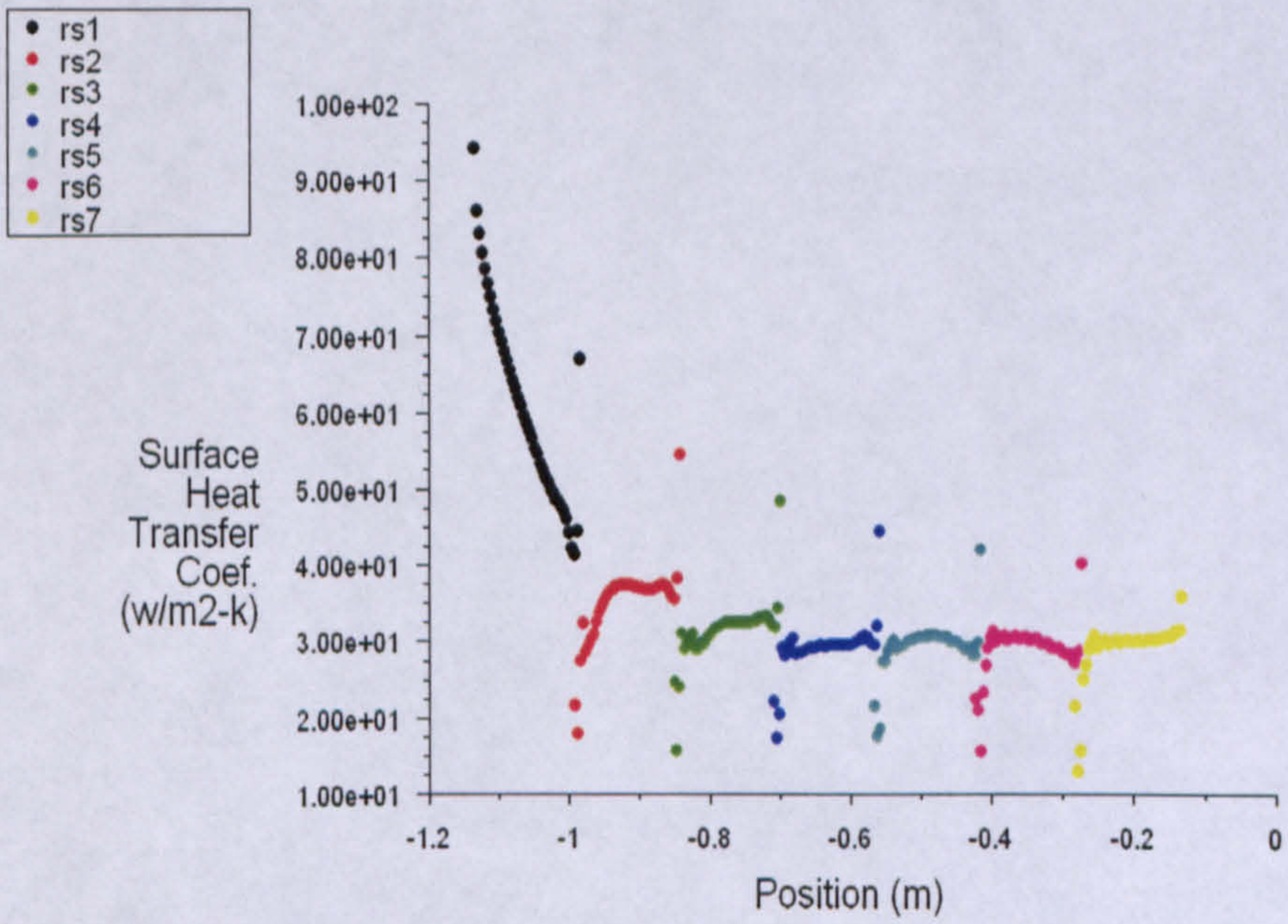

Fig. 7.17: (a) Contours of velocity of air and (b) heat transfer coefficients ($W/m^2.K$) over the length of the slates.

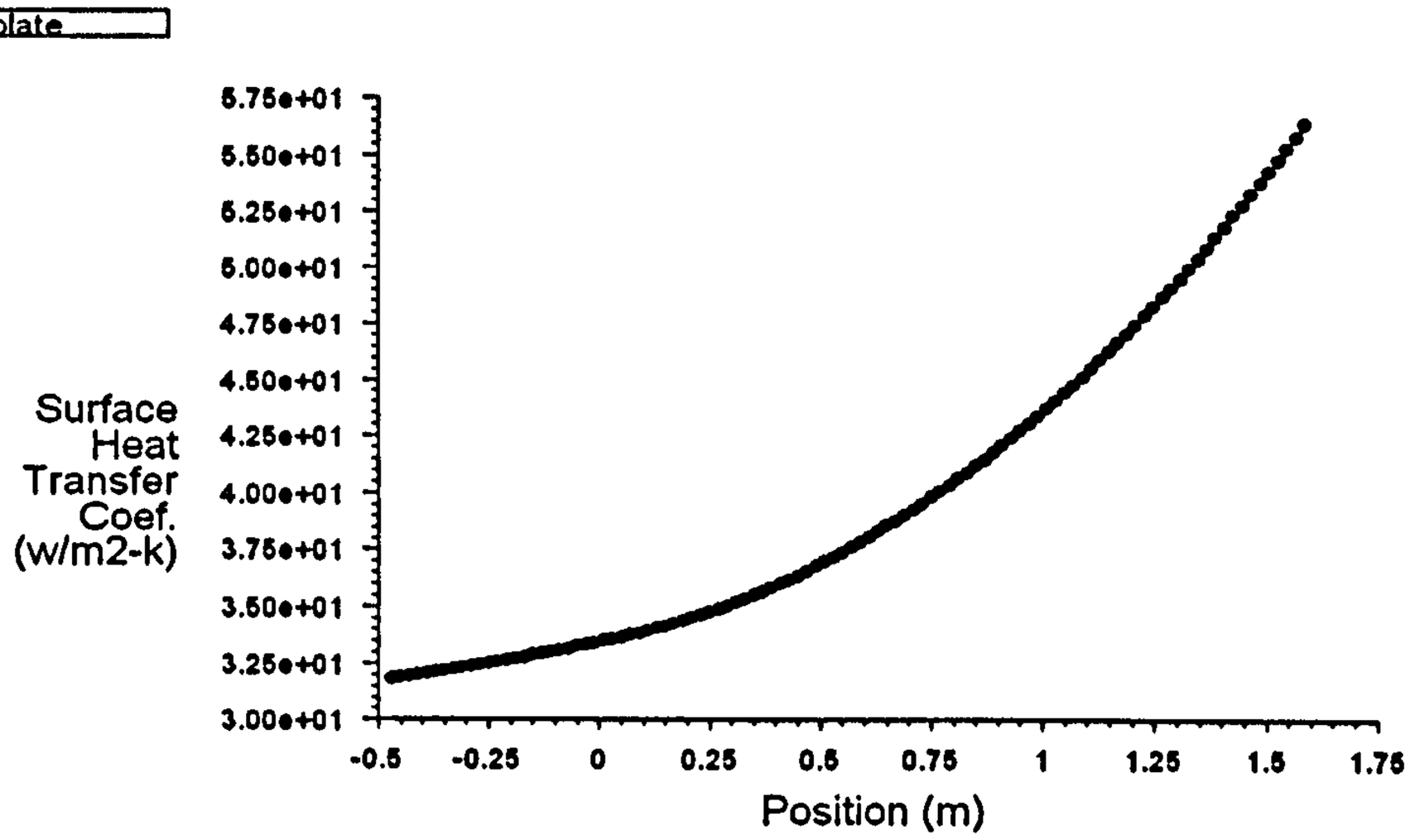

Fig. 7.18: Heat transfer coefficient over the length of a horizontal hot flat plate. Air enteres from the right hand side.

7.6 SUMMARY

1. In order to be able to apply the model, the system characteristics must be measured. A single measurement of the fan voltage and the corresponding pressure across the fan are satisfactory for defining the system characteristic.

2. The testing of the optimum system indicates that early start-up of the fan can be a disadvantage which can result a cooling effect. As explained, this can be overcome by either delaying the start-up of the fan or using dark paint or antireflective coating with the slates so that they warm up quickly. This area is of future work as will be discussed in the next chapter.

3. Because the area from which air is drawn is not defined, other indicators for comparative testing are used. Effectiveness (defined as the ratio of energy delivered to the maximum energy possible) and the volume delivered per joule of energy received by the PV module are two of these indicators. For roof section A, the system delivers 270 l/kJ of energy falling on the PV module while for roof section B, this value rises to 810 l/kJ.

4. For meaningful comparison of systems to be undertaken, measurements must be obtained under identical conditions and wind speed must be accounted for.

5. CFD simulations reveal that the fan box should be located away from the top of the roof section where high heat transfer coefficients exist. This, however, needs to be supported by future experimental studies.

REFERENCES

Duffie J.A., and Beckman W.A., (1991), Solar Engineering of Thermal Processes, 2nd ed., New York: Wiley Interscience.

Weather Underground, http://www.wunderground.com/global/stations/03160.html.

8. CONCLUSIONS AND FURTHER WORK

The current thesis presented a newly developed system for ventilation air preheating using solar energy. This system utilises the existing roof tiles or slates as a solar collector. A PV-driven fan draws air through the spaces between the slates. As air picks up the heat from the slates, it is drawn by the fan through holes drilled in the sarking board and is then delivered via a flexible duct to the house underneath for ventilation. More than a hundred roof slate-based (RSB) solar ventilation preheating systems have been installed in Scotland during the last decade. The current thesis is the first quantitative and optimisation study of such systems.

The primary objective of the current thesis was to develop a model for predicting the flow rate of air in the roof slate-based system described above. The model developed can then serve the double purpose of optimising and studying the heating potential of the system. Conclusions about the volume of air and amount of energy that can be potentially delivered in a given period of time can be made based on long-term data of the design site. This chapter of the thesis presents the most important conclusions regarding the modelling, optimisation and testing of the system. Areas of further work in order to improve the understanding of these systems are then suggested.

CONCLUSIONS

The flow rate model developed was based on the measured performance of each of the components (i.e. the PV module, the fan and the duct). The mathematical model of the system consisted of equations describing the individual performance of each of the components.

A new method for generating the PV IV characteristic by applying corrections for the measurable quantities of short circuit current (I_{SC}), open-circuit voltage (V_{OC}), maximum power (P_m) and the voltage at maximum power (V_m) has been introduced. Empirical relationships were suggested and the method was validated. The IV characteristics generated by this method were in agreement with both measurements and with characteristics generated by other methods. Maximum power was within 8 % of the measured values while the current at maximum power (calculated from P_m and V_m) was within 9 %. This new method is very useful because it allows the determination of

P_m, V_m and I_m without having to generate the IV characteristic and searching for the maximum power as the case before was. Furthermore, this new method provides the means for determining the optimum motor constant directly from irradiance and ambient temperature data.

Using Visual Basic for Applications, the PV module and fan equations were solved simultaneously and iteratively for the voltage and speed of the fan. The model predicts the operational speed of the fan with an accuracy of 92 %. The predicted speed can be used to generate the fan head-flow (ΔP_f-Q) characteristic which can then be solved simultaneously with the system's ΔP-Q characteristics for the flow rate of air in the system. A cubic ΔP_f-Q relationship was found suitable for axial flow fans. A characteristic at reference conditions was measured and used for generating other curves at different air temperatures and rotational speeds. Due to instrumental and operational errors in reference measurements, the model predicts the flow with an accuracy of 88 %.

The model developed is general and useful because it accounts for the effects of irradiance, ambient temperature, and PV module and fan selection in addition to duct length, diameter and extension. Furthermore, it can be used in several input-output scenarios.

The model developed was then updated so that it can be used for optimisation with regard to the maximum monthly and annual volume of air delivered. 27-year hourly weather data for Edinburgh were used for predicting the long-term performance of the system. In order to account for start-up characteristics of the fans, a switch functions, which assigned a value of "1" for an operational fan and a value of "0" for a non-operational fan was used. This procedure considerably saved computational time since data points with a "switch" value of "0" were not considered for calculation.

Considering a range of available components, the optimum system comprises a 10 W_p polycrystalline PV module, a 24 VDC 9.5 W axial flow fan (Fan1) with a free flow capacity of 69 l/s and an 8 m long, 152 mm metallic flexible duct at an extension of 80 %. The optimum effective duct length was obtained at a diameter of 152 mm and an extension of 80 %. While the optimum diameter was determined as 200 mm, a 152 mm duct was used due to availability. The optimum system can deliver flow rates as high as 40 l/s. While other fans could deliver up to 65 l/s, they had high start-up

irradiances and so they delivered less volume over the same period of operation. The start-up characteristics and threshold irradiances play a key role in the optimisation process. It is found that, based on 27-year of hourly data for Edinburgh; the optimum system has a utilisability between 60 and 90 %.

One of the most important findings of this thesis is that, regardless of the start-up characteristic, the optimum system still delivered more volumes even though the fan had a lower free-flow capacity. This was attributed to the optimal interval for Fan1 (200 – 580 W/m^2). Model-based simulations showed that for this interval, Fan1 would produce higher flow rates. Since irradiance data for Edinburgh is within this interval for most of the time, maximising the volume based on long-term data shows that Fan1 is favourable. As a result it is concluded, as expected, that weather data also play a very significant role in the optimisation process.

The optimum system delivers 9.6×10^4 m^3 during the heating season (58 % of the year's total). This volume corresponds to a constant flow rate of 33.2 m^3/hr (9.2 l/s throughout the heating season considering the maximum possible period of operation from sunshine to sunset throughout the heating season). This system can potentially deliver 32.2 kWhr per 1 C difference between delivered and ambient temperatures. For example, depending on the slate type and weather conditions, if the average difference of temperature during the heating season is 5 C, then the system can deliver 161 kWhr. Based on a heating load of 1500 kWhr for the full period of the heating season for a 100-m^3 room, a solar fraction of 11% is obtained (the system can save 11 % of the cost). Furthermore, assuming an inflation rate of 5 % and a fuel cost of £0.07/ kWhr, the system has a payback period of 13 years. The optimum system can also deliver 100 kg of CO_2 savings per year.

The system with two 10 W_p PV modules in parallel with a single Fan1 produced higher volumes and had payback periods similar to the optimum system. However, this system has very low utilisation of the maximum power available and thus low efficiencies. The use of two PV modules in parallel is, thus unreasonable.

When compared to other systems, the optimum system is optimum in different respects. In addition to maximising the volume delivered, it also maximises the utilisation of the PV maximum power (5- 10.5 %) and minimises the payback period. If

the motor constant of Fan1 is reduced from 0.079 to 0.0745 V.s/rad, the annual PV output energy would increase by 14 % from 37.3 MJ to 43.1 MJ.

The optimum system was comparatively tested with another adjacent system consisting of the same PV module, the same ΔP_s-Q characteristic but a different fan. Results show that the optimum system, as desired, consistently delivers more volumes of air than the other system during the period of operation. For the full period of operation and based on the maximum possible hour of sunshine (i.e. from sunshine to sunset for all days of operation), the volume delivered by the optimum system corresponds to a constant flow rate of 8.6 l/s which compares well with predictions (9.2 l/s).

However, it was concluded from testing the optimum system that an undesirable cooling effect can occur early in the morning due to early start-up of the optimum fan. This can be avoided by either delaying the start-up of the fan until the slates are warm enough or by enhancing the absorption properties of the slates. If the first option is to be considered, a resistor connected in parallel with the fan to delay its start is to be used. It is calculated that an 18-Ω resistor delays the start-up from 290 to 800 W/m^2.

Quantitative comparison between the systems was based on several indicators. The average volume of air delivered per Joule of energy falling on the PV module was used in one case where the slate temperatures were not recorded. It was calculated that the optimum system consistently delivered 270 l while the other system (PV2-Fan2) delivered between 130 and 180 l of air per one kilo Joule of energy falling on the PV module. In cases, where the slate temperature was measured, effectiveness, defined as the ratio of delivered energy to the maximum energy that can be possibly delivered (i.e. that absorbed by the slates), was used as an indicator. The optimum system has an effectiveness of 0.53 while the other system has an effectiveness of 0.42. It is concluded, that despite the cooling effect associated with it, the optimum system is still preferable to other systems.

Temperatures of air delivered during March can reach up to 7 C above ambient temperature while in November they can be 3 C above ambient. Even though a value of 5 C was used in chapter 6 for heat estimation purposes, further work needs to be undertaken in this area.

FUTURE WORK

1. In order to be able to make further judgements about the potential of the RSB system, the effective collector area of the slates from which air, for a given situation, is drawn is to be estimated. This area is a function of the fan voltage (or speed), which is in turn a function of irradiance and ambient temperature. On a sunny day, a thermal camera can be used to take photos of the roof and the area from which air is drawn can be calculated. These photos can be taken at different fan voltages (and speeds) in order to estimate the variable area as a function of fan voltage. This relationship can then be entered into the model to determine area after the operational point of the fan is obtained.

2. The optimum system is advantageous due to its lower cost, its higher monthly overall flow efficiencies in addition to the more monthly volumes of air it delivers. The kick starting of a system with high start-up currents (or irradiances) is undesirable because it adds to the cost. Moreover, the delay of the start-up of the optimum system will reduce its potential. An area, which requires further investigation, is matching a slate type to the optimum system so that the slates warm up as quickly as the system starts. Even though the discussion in chapter 7 shows that slate type C warms up quickly and can be potentially a match for the optimum system, further investigation is required. The performance of the different roof sections described in chapter 7 was carried out under different conditions of wind speed. A study with different roof sections and different slate types all with the optimum systems but under the same conditions (i.e. controlled environment) of irradiance, ambient temperature and wind speed is required.

3. The model developed is useful for several reasons. First is can be used for optimisation for any location around the world if weather data is available. Secondly, it can be used in different ways and according to different scenarios. Moreover, the model is not specific to RSB systems but it can be used for any PV-fan system as long as the system's characteristic is measured and included in the model. Furthermore, the VBA language is easy enough to understand and transforming the model can be achieved with minimal effort. The model developed herein, however, is limited because it is specifically intended for optimisation and testing of the RSB system. The real industrial and commercial objective would be to recommend a certain PV-fan combination for a given house or room. Here the input parameters to the model would be the number of

occupants and the volume and floor area of the house in addition to weather data and a database of PV module and fan specifications.

Other suggested areas of future work are as follows:

4. Experimental studies on flow rate patterns over the slates
5. Modelling of slate temperature as a function of irradiance, wind speed and ambient temperature.
6. Studying the potential of RSB systems for drying crops.

APPENDICES

APPENDIX A

EQUIPMENT SPECIFICATIONS

1. PV modules
2. Fans
3. Pyranometer
4. Delta T
5. Thermocouples
6. Multimeters
7. Tachometer
8. Manometer
9. Flow meter
10. Data loggers

1. PV modules

A. 10 W_p modules

- Type: Polycrystalline BP Solarex
- Model: SX10U
- Serial nos.: C1020906 2167374
  C1020906 2167385

B. 4.5 Wp modules

- Type: Polycrystalline BP Solarex
- Model: SX5M
- Serial no.: C1020129 2133644
  C 1020129 2133551

2. Fans

A. 9.5 W / 12 VDC

- Type: PAPST 5112N
- US PAT: 4730136
- Farnell Order code: 635-420

B. 9.5 W / 24 VDC

- Type: PAPST 5114N
- Farnell Order code: 635-431

C. 20.3 W / 24 VDC

- Type: ComairRotron
- Mnufacturer list no.: 013084(PQ24B4)
- Farnell Order code: 202-7008

3. Pyarnometer

- Type: Kipp and Zonen
- CM11
- Serial no.: CM11861376
- Calibration factor: 5.17 × 10-6 $V.m^2 / W$

4. Delta Ts

Type: BF3

5. Thermocouples

- k-type calibrated by technicians at Napier University to within °0.5 C.

6. Multimeters

- Model: GDM-8034
- Appliance #: 1330

7. Tachometer

- Photo contact tachometer
- Solex TA250
- Serial no.: K21765 14-6-93

8. Manometer

- Inclined
- Airflow development Inc.
- Density of Liquid used: 880 kg/m^3.
- US PAT: 2983146

9. Flowmeter

- Anemosonic UA6 Handheld Digital Ultrasonic Anemometer

10. Data loggers

- Several data loggers were used throughout the project
- SQUIRREL by Grant Instruments (Cambridge).
- Model: SQ1023
- Temperature and voltage channels
- Serial nos.: KC0230001, KC0229002

APPENDIX B

SPECIFIC-PURPOSE AND GENERAL COMPUTER PROGRAMS DEVELOPED FOR THE PRESENT PROJECT

1. Input of PV and fan parameters
2. Determination of fan operational point
3. Determination of fan operational point using "motor parameters" (R_a, K_m, K_f) method
4. Determination of fan ΔP-Q curve from speed
5. System ΔP-Q curve
6. Full version of flow arte determination program
7. A program for calculating extraterrestrial radiation, filtering measured data and determining slope irradiance using the anisotropic model for Northern Europe.
8. Opening a large data file
9. The switch function
10. Volume and efficiency calculations

Appendix B1: Input of PV and fan parameters

```
Sub FanOperationalPoint()
' Choose PV module and fan
Module = InputBox("Which PV module?")
Fan = InputBox("Which fan?")
'Define reference parameters of selected PV module
If Module = 1 Then
Gref = 725
Tref = 28
iscref = 0.211
Vocref = 20.4
pmref = 2.93
Vmref = 15.9
Imref = 0.183
disc = 0.00019
dvoc = -0.08
dvm = -0.08
Rs = 4.5
U = 1.53
area = 0.036
ElseIf Module = 2 Then
Gref = 750
Tref = 31
iscref = 0.471
Vocref = 20.5
pmref = 6.76
Vmref = 16
Imref = 0.42
disc = 0.00039
dvoc = -0.08
dvm = -0.08
Rs = 1.2
U = 1.9
area = 0.072
End If
'Define parameters of selected fan
If Fan = 0 Then
Av = 0.0604
Bv = -0.1056
Aw = 227.66
Bw = -128.53
C1 = 0.000192
C2 = 0.0000000367
w = -0.002
x = 0.15
y = -3.98
z = 57.4
ElseIf Fan = 1 Then
Av = 0.0144
Bv = -0.01
Aw = 131.77
Bw = -365.58
C1 = 0.000192
C2 = 0.0000000367
w = -0.002
x = 0.15
y = -3.98
z = 57.4
ElseIf Fan = 2 Then
Av = 0.0393
Bv = -0.1317
Aw = 159.04
Bw = -384.23
```

C1 = 0.000192
C2 = 0.0000000367
w = -0.0006
x = 0.058
y = -2.39
z = 62.4
End If

Appendix B2: Determination of fan operational point

```
' Enter desired irradiance and PV module temperature
G = InputBox("Enter Irradiance")
Tamb = InputBox("Enter ambient temperature")
' Assume efficiency, calculate Tmod then all the other PV module parameters based on G and
Tmod
Eff = 0.2
m = 0
Do
Eff = Eff - m
Tmod = Tamb + ((0.9 / U) * G * area * (1 - (Eff / 0.9)))
' Calculate corrected PV IV parameters
FF = (pmref / (iscref * Vocref))
dpm = FF * ((iscref * dvoc) + (Vocref * disc))
ISC = (G / Gref) * (iscref + disc * (Tmod - Tref))
Pm = (G / Gref) * (pmref + dpm * (Tmod - Tref))
Voc = Vocref + ((dvoc * (Tmod - Tref)) + Application.Ln(G / Gref))
Vm = Vmref + ((dvm * (Tmod - Tref)) + Application.Ln(G / Gref))
Im = Pm / Vm
If (Im / ISC) > 1 Then
   GoTo 1
End If
A = ((Vm - Voc + (Im * Rs)) / (Application.Ln(1 - (Im / ISC))))
I0 = ISC * Exp(-Voc / A)
n = 1
Do
   I = ISC - ((n - 1) * (ISC / 10000))
   V = A * Application.Ln((ISC - I + I0) / I0) - (I * Rs)
   ifan = Av * V + Bv
   n = n + 1
Loop Until (I - ifan) < 0.001
Eff1 = (I * V) / (G * area)
m = m + 0.001
Loop Until (Abs(Eff1 - Eff)) < 0.01
w = Aw * V + Bw
MsgBox V
1 End Sub
```

Appendix B3: Determination of fan operational point using "motor parameters" (R_a, K_m, K_f) method

Replace

```
Do
        I = ISC - ((n - 1) * (ISC / h))
        V = A * Application.Ln((ISC - I + I0) / I0) - (I * Rs)
        ifan = Av * V + Bv
        n = n + 1
Loop Until (I - ifan) < 0.001
```

With

```
Do
        I1 = ISC - ((n - 1) * (ISC / h))
        V1 = A * Application.Ln((ISC - I1 + I0) / I0) - (I1 * RS)
        RPM1 = (V1 - (I1 * RA) - e) / KM
        ifan1 = ((RPM1) ^ 2) * (KF / KM)
        n = n + 1
Loop Until (I - ifan) < 0.001
```

Appendix B4: Determination of fan ΔP-Q curve from speed

```
Sub Method_Based_On_Cubic_Regression()
'
' Method Based On Cubic Regression. The constants here are determined from
' reference (Q, H) data and reference conditions of speed and air temperature
' as discussed in section 3.2.4.3 (Equation 3.16)
'
'Enter speed (r/min), Barometric pressure (mm Hg)and Air temperature (C)
speed = InputBox("Enter speed")
Barometric = InputBox("Enter Barometric pressure")
AirTemp = InputBox("Enter Air Temperature")
density = (Barometric / (AirTemp + 273.15))
' Choose fan
Fan = InputBox("Which Fan?")
' Based on fan choice, determine parameters to be used
If Fan = 0 Or Fan = 1 Then
C1 = 0.000192
C2 = 0.0000000367
w = -0.002
x = 0.15
y = -3.98
z = 57.4
ElseIf Fan = 2 Then
C1 = 0.000192
C2 = 0.0000000367
w = -0.0006
x = 0.058
y = -2.39
z = 62.4
End If
qref = 0
j = 1
Do
   Q = C1 * qref * (speed * density)
   hf = C2 * ((speed * density) ^ 2) * (w * (qref ^ 3) + x * (qref ^ 2) + (y * qref) + z)
   Sheets("HQ").Cells(j, 3).Value = Q
   Sheets("HQ").Cells(j, 4).Value = hf
   qref = qref + 0.1
   j = j + 1
Loop Until hf < 0
End Sub
```

- THE NEXT PAGE SHOWS THE DETERMINATION OF THE FAN DP-Q CURVE BASED ON LINEAR SEGMENTATION

Method based on linear segmentation of ΔP_f-Q curve

```
If fan = "1" Then
   C1 = 1.07
   C2 = 67.9
   C3 = 131.77
   C4 = 365.58
   Qlimit1 = 0.0143 * speed
   Qlimit2 = 0.0183 * speed
   constA1 = -0.00061 * speed - 0.0069
   constB1 = 0.0000125 * (speed ^ 2) - 0.000000536 * speed
   constA2 = -0.000588 * speed - 0.0032
   constB2 = 0.0000144 * speed ^ 2 + 0.00000959 * speed
   Hlimit1 = constA1 * Qlimit1 + constB1
   Hlimit2 = constA2 * Qlimit2 + constB2
   constA3 = (Hlimit1 - Hlimit2) / (Qlimit1 - Qlimit2)
   constB3 = Hlimit1 + (Qlimit1 * ((Hlimit1 - Hlimit2) / (Qlimit1 - Qlimit2)))
ElseIf fan = "2" Then
   C1 = 3.28
   C2 = 25.4
   C3 = 159.04
   C4 = 384.23
   Qlimit1 = 0.0138 * speed
   Qlimit2 = 0.0212 * speed
   constA1 = -0.00079 * speed - 0.00045
   constB1 = 0.0000167 * (speed ^ 2) - 0.00000656 * speed
   constA2 = -0.000492 * speed - 0.000467
   constB2 = 0.0000159 * speed ^ 2 + 0.00000171 * speed
   Hlimit1 = constA1 * Qlimit1 + constB1
   Hlimit2 = constA2 * Qlimit2 + constB2
   constA3 = (Hlimit1 - Hlimit2) / (Qlimit1 - Qlimit2)
   constB3 = Hlimit1 - (Qlimit1 * ((Hlimit1 - Hlimit2) / (Qlimit1 - Qlimit2)))
End If
```

Appendix B5: System ΔP-Q curve

If an effective duct length is available

```
Sub SystemCharacteristic()
'
'Enter diameter (mm), length (m), extension (%), barometric pressure (mm Hg)
'and temperature of air in the duct (C)
Diameter = InputBox("Enter Diameter")
'Calculate area
ductArea = (0.25 * (22 / 7) * ((Diameter / 1000) ^ 2))
'
barometric = InputBox("Enter Barometric pressure")
AirTemp = InputBox("Enter air temperature")
'Calculate density
density = (0.462 * barometric) / (AirTemp + 273.15)
viscosity = 0.0000176
'
Extension = InputBox("Enter degree of extension(%)")
If Extension = 100 Then
   k = 2.5
ElseIf Extension = 80 Then
   k = 9.7
End If
'
roughness = k / Diameter
'
Length = InputBox("Enter Length")
'
Q = 1
j = 1
Do
      Velocity = ((Q / 1000)) / ductArea
      Reynolds = (density * Velocity * (Diameter / 1000)) / viscosity
      F = 1.325 / (((Application.Ln(roughness / 3.3)) + (5.74 / (Reynolds ^ 0.9))) ^ 2)
      HS = ((F * Length * density) / (2 * (Diameter / 1000))) * (Velocity ^ 2)
      Sheets("SystemHQ").Cells(j, 1).Value = Q
      Sheets("SystemHQ").Cells(j, 2).Value = HS
      j = j + 1
      Q = Q + 0.1
Loop Until HS = 60
End Sub
```

Alternatively, enter the best-fit curve for HS (as obtained from measured data). In this case, the Do Loop shown will look like this

```
Q = 1
Do
        HS = T1 * Q^2 + T2 * Q
        Q = Q + 0.1
Loop Until HS = 60
```

Appendix B6: Calculating IV characteristic, fan operational point and fow rate from irradiance and ambient temperature

```
' THE CODE BELOW ASSUMES THAT NOCT IS KNOWN AND SO ITERATION FOR EFFICIENCY IS NOT REQUIRED

G = InputBox("G?")
Tamb = InputBox("Ambient T?")
Tmod = Tamb + ((G / 800) * (NOCT - 20))

' USE REFERENCE DATA IN APPENDIXB1 AND PERFORM CALCULATIONS AT NEW CONDITIONS TO OBTAIN NEW IV CHARACTERISTIC
   dvm = dvoc
   FF = (pmaxref / (Iscref * vocref))
   dpmax = FF * ((Iscref * dvoc) + (VOC * disc))
      '   Calculate Isc, Voc, Pmax, Vm, Im at new conditions
   ISC = (G / gref) * (Iscref + disc * (Tmod - Tref))
   Pmax = (G / gref) * (pmaxref + dpmax * (Tmod - Tref))
   Sheets("Reference Data").Range("H21").Value = Pmax
   VOC = vocref + ((dvoc * (Tmod - Tref)) + Application.Ln(G / gref))
   Vm = Vmref + ((dvm * (Tmod - Tref)) + Application.Ln(G / gref))
   Im = Pmax / Vm
      ' From Rs, Vm, Im, Voc & Isc --- Calculate A
   A = ((Vm - VOC + (Im * Rs)) / (Application.Ln(1 - (Im / ISC))))
      '  From A, Isc & Voc --- Calculate I0
   I0 = ISC * Exp(-VOC / A)
Do
   I = ISC - ((n - 1) * (ISC / 10000))
   V = A * Application.Ln((ISC - I + I0) / I0) - (I * Rs)
   ifan = (V - C1) / C2
   n = n + 1
Loop Until (I - ifan) < 0.001
speed = C3 * V + C4
Length = InputBox("Length of Duct?")
Diameter = 152
EF = 0.80
IF EF = 0.8 THEN
          k = 2.5
ELSEIF EF = 1 THEN
          k = 9.6
END IF
roughness = k / (Diameter)
Barometric = InputBox("What is Barometric pressure? in mm Hg")
AirTemp = InputBox("What is air temperature in Celsius?")
density = ((Barometric / 760) * 101325) / ((AirTemp + 273.15) * 288.297)
viscosity = 0.0000176
Do
        If Q < Qlimit1 Then
           Hf = constA1 * Q + constB1
        ElseIf Q > Qlimit2 Then
           Hf = constA2 * Q + constB2
        ElseIf Qlimit1 <= Q And Q <= Qlimit2 Then
           Hf = constA3 * Q + constB3
        End If
        Velocity = ((Q / 1000)) / DuctArea
        Reynolds = (density * Velocity * Diameter) / viscosity
        f = 1.325 / (((Application.Ln(roughness / 3.3)) + (5.74 / (Reynolds ^ 0.9))) ^ 2)
        HS = ((f * Length * density) / (2 * Diameter)) * (Velocity ^ 2)
        Hdiff = Abs(Hf - HS)
        Q = Q + (Hdiff / 100)
Loop Until Hdiff < 0.01
MsgBox Q
End Sub
```

Appendix B7: A program for calculating extraterrestrial radiation and filtering measured data

A. Calculate Extraterrestrial radiation and apply primary filters

```
Sub Extraterrestrial_and_Primary_Filters()
xlat = 55.62954
YRLNG = 3.53818
yrlong = 0#
DTOR = 3.14159 / 180

''''''''''''''''''''''''''''''''''''''''''''''''''''''''''''''''''''''''''''''''''''''''''''''''''''''''''''''''''''
'  1.   ' FIND THE TOTAL NUMBER OF LINES (OR DATA POINTS)
''''''''''''''''''''''''''''''''''''''''''''''''''''''''''''''''''''''''''''''''''''''''''''''''''''''''''''''''''''

i = 14
1 'start a loop
celvar = Sheets("Original").Cells(i, 1).Value
If (celvar <> "") Then
i = i + 1
GoTo 1
Else
limit = i - 14
End If

''''''''''''''''''''''''''''''''''''''''''''''''''''''''''''''''''''''''''''''''''''''''''''''''''''''''''''''''''''''''''''
'  3.   ' START A LOOP WHICH PERFORMS ALL THE NECESSARY INFORMATION FOR ALL
THE DATA POINTS.
' Read dayno., monthno., yearno.,hourno., and minuteno.
' Calculate equation of time, time correction term and then solar time necessary for calculations.
'
''''''''''''''''''''''''''''''''''''''''''''''''''''''''''''''''''''''''''''''''''''''''''''''''''''''''''''''''''''''''''''

For n = 1 To limit
    dayno = Sheets("Original").Cells(n + 13, 1).Value
    monthno = Sheets("Original").Cells(n + 13, 2).Value
    yearno = Sheets("Original").Cells(n + 13, 3).Value
    hourno = Sheets("Original").Cells(n + 13, 4).Value - 1
    minuteno = Sheets("Original").Cells(n + 13, 5).Value


    xyr = yearno
    xmo = monthno
    xdy = dayno

    imt = xmo
    iyr = xyr
    idy = xdy

      If (imt > 2) Then
      IYR1 = iyr
      IMT1 = imt - 3
      Else
      IYR1 = iyr - 1
      IMT1 = imt + 9
      End If
      INTT1 = Int(30.6 * IMT1 + 0.5)
      INTT2 = Int(365.25 * (IYR1 - 1976))
      DN1 = (idy + INTT1 + INTT2)
      IMT9 = 1
      IYR1 = iyr - 1
      IMT1 = IMT9 + 9
      INTT1 = Int(30.6 * IMT1 + 0.5)
```

```
INTT2 = Int(365.25 * (IYR1 - 1976))
DN2 = (INTT1 + INTT2)
daynum = DN1 - DN2

XLCT = hourno + (minuteno / 60)
UT = XLCT + YRLNG / 15
If xmo > 2 Then
IYR1 = xyr
IMT1 = xmo - 3
Else
IYR1 = xyr - 1
IMT1 = xmo + 9
End If
INTT1 = Int(30.6 * IMT1 + 0.5)
INTT2 = Int(365.25 * (IYR1 - 1976))
SMLT = ((UT / 24) + xdy + INTT1 + INTT2 - 8707.5) / 36525
EPSILN = 23.4393 - 0.013 * SMLT
CAPG = 357.528 + 35999.05 * SMLT
If CAPG > 360 Then
G360 = CAPG - Int(CAPG / 360) * 360
Else
G360 = CAPG
End If
CAPC = 1.915 * Sin(G360 * DTOR) + 0.02 * Sin(2 * G360 * DTOR)
CAPL = 280.46 + 36000.77 * SMLT + CAPC
If CAPL > 360 Then
XL360 = CAPL - Int(CAPL / 360) * 360
Else
XL360 = CAPL
End If
ALPHA = XL360 - 2.466 * Sin(2 * XL360 * DTOR) + 0.053 * Sin(4 * XL360 * DTOR)
eot = (XL360 - CAPC - ALPHA) / 15

XLCT = 12
UT = XLCT + YRLNG / 15
If xmo > 2 Then
IYR1 = xyr
IMT1 = xmo - 3
Else
IYR1 = xyr - 1
IMT1 = xmo + 9
End If
INTT1 = Int(30.6 * IMT1 + 0.5)
INTT2 = Int(365.25 * (IYR1 - 1976))
SMLT = ((UT / 24) + xdy + INTT1 + INTT2 - 8707.5) / 36525
EPSILN = 23.4393 - 0.013 * SMLT
CAPG = 357.528 + 35999.05 * SMLT
If CAPG > 360 Then
G360 = CAPG - Int(CAPG / 360) * 360
Else
G360 = CAPG
End If
CAPC = 1.915 * Sin(G360 * DTOR) + 0.02 * Sin(2 * G360 * DTOR)
CAPL = 280.46 + 36000.77 * SMLT + CAPC
If CAPL > 360 Then
XL360 = CAPL - Int(CAPL / 360) * 360
Else
XL360 = CAPL
End If
ALPHA = XL360 - 2.466 * Sin(2 * XL360 * DTOR) + 0.053 * Sin(4 * XL360 * DTOR)
GHA = 15 * UT - 180 - CAPC + XL360 - ALPHA
If GHA > 360 Then
GHA360 = GHA - Int(GHA / 360) * 360
Else
```

```
    GHA360 = GHA
    End If
    dec = Atn(Tan(EPSILN * DTOR) * Sin(ALPHA * DTOR)) / DTOR

    If (yrlong < 0) Then
    cor = -(Abs(yrlong) - Abs(ylong)) / 15
    ElseIf (yrlong > 0) Then
    cor = (Abs(yrlong) - Abs(ylong)) / 15
    Else
    cor = -ylong / 15
    End If
    cortrm = -cor - eot

   xast = hourno + (minuteno / 60) - cortrm
   horang = 15 * DTOR * Abs(12 - xast)
   xdum1 = Sin(xlat * DTOR) * Sin(dec * DTOR) + Cos(xlat * DTOR) * Cos(dec * DTOR) *
Cos(horang)
   SOLALT = (Application.Asin(xdum1)) / DTOR
   xdum2 = Cos(dec * DTOR) * (Cos(xlat * DTOR) * Tan(dec * DTOR) - Sin(xlat * DTOR) *
Cos(horang)) / Cos(DTOR * SOLALT)
   solazm = (Application.Acos(xdum2)) / DTOR
   If (xast > 12) Then
   solazm = 360 - solazm
   End If
   xdum3 = Cos(SOLALT * DTOR) * Cos((solazm - WAZ) * DTOR) * Sin(TLT * DTOR) +
Sin(SOLALT * DTOR) * Cos(TLT * DTOR)
   SOLINC = (Application.Acos(xdum3)) / DTOR
   ERAD = 0
   If (SOLALT > 0) Then
   ERAD = 1367 * (1 + 0.033 * Cos(0.0172024 * daynum)) * Sin(SOLALT * DTOR)
   End If
   Sheets("Original").Cells(n + 13, 12).Value = ERAD
' Solar altitude is needed so that data below solalt of 7 degrees is filtered.
   GDeltaT = Sheets("Original").Cells(n + 13, 6).Value
   DDeltaT = Sheets("Original").Cells(n + 13, 7).Value
   If GDeltaT = 0 Then
      DR = "No Value"
   Else:
      DR = DDeltaT / GDeltaT
   End If
   Sheets("Original").Cells(n + 13, 14).Value = DR
   If ERAD = 0 Then
      kt = "No Value"
   Else:
      kt = GDeltaT / ERAD
   End If
   Sheets("Original").Cells(n + 13, 13).Value = kt

''''''''''''''''''''''''''''''''''''''''''''''''''''''''''''''''''''''''''''''''''''''''''''''''''''''''''''
' PRIMARY FILTERS
''''''''''''''''''''''''''''''''''''''''''''''''''''''''''''''''''''''''''''''''''''''''''''''''''''''''''''

   If ERAD > 0 Then
      If SOLALT >= 7 Then
         If GDeltaT > 0 And GDeltaT < (1.2 * 1367) Then
            If DDeltaT > 0 And DDeltaT < (0.8 * 1367) Then
               If kt <= 1 Then
                  If DR <= 1 Then
                     Sheets("Original").Cells(n + 13, 15).Value = "PASS"
                  Else: Sheets("Original").Cells(n + 13, 15).Value = "FAIL"
                  End If
               Else: Sheets("Original").Cells(n + 13, 15).Value = "FAIL"
               End If
            Else: Sheets("Original").Cells(n + 13, 15).Value = "FAIL"
            End If
```

```
         Else: Sheets("Original").Cells(n + 13, 15).Value = "FAIL"
         End If
      Else: Sheets("Original").Cells(n + 13, 15).Value = "FAIL"
      End If
   Else: Sheets("Original").Cells(n + 13, 15).Value = "FAIL"
   End If
   If Sheets("Original").Cells(n + 13, 15).Value = "FAIL" Then
      ko = ko + 1
   ElseIf Sheets("Original").Cells(n + 13, 15).Value = "PASS" Then
      Sheets("Filtered1").Cells(n + 13 - ko, 1).Value = Sheets("Original").Cells(n + 13, 1).Value
      Sheets("Filtered1").Cells(n + 13 - ko, 2).Value = Sheets("Original").Cells(n + 13, 2).Value
      Sheets("Filtered1").Cells(n + 13 - ko, 3).Value = Sheets("Original").Cells(n + 13, 3).Value
      Sheets("Filtered1").Cells(n + 13 - ko, 4).Value = Sheets("Original").Cells(n + 13, 4).Value
      Sheets("Filtered1").Cells(n + 13 - ko, 5).Value = Sheets("Original").Cells(n + 13, 5).Value
      Sheets("Filtered1").Cells(n + 13 - ko, 6).Value = GDeltaT
      Sheets("Filtered1").Cells(n + 13 - ko, 7).Value = DDeltaT
      Sheets("Filtered1").Cells(n + 13 - ko, 8).Value = Sheets("Original").Cells(n + 13, 8).Value
      Sheets("Filtered1").Cells(n + 13 - ko, 9).Value = Sheets("Original").Cells(n + 13, 9).Value
      Sheets("Filtered1").Cells(n + 13 - ko, 10).Value = Sheets("Original").Cells(n + 13, 10).Value
      Sheets("Filtered1").Cells(n + 13 - ko, 11).Value = Sheets("Original").Cells(n + 13, 11).Value
      Sheets("Filtered1").Cells(n + 13 - ko, 12).Value = ERAD
      Sheets("Filtered1").Cells(n + 13 - ko, 13).Value = kt
      Sheets("Filtered1").Cells(n + 13 - ko, 14).Value = DR
   End If
Next
End Sub
```

……………………………………………………………………………………………

B. Apply Secondary filters to best-fit equation for data

```
Sub Secondary_Filter()
i = 14
1 'start a loop
celvar = Sheets("Filtered1").Cells(i, 1).Value
If (celvar <> "") Then
i = i + 1
GoTo 1
Else
limit = i - 14
End If

''''''''''''''''''''''''''''''''''''''''''''''''''''''
' Devide filtered data into intervals and Write it
' into a new sheet
' Data for Old Delta T is written to sheet "kt Intervals"
' Data for New Delta T is written to sheet "KtNew Intervals"
''''''''''''''''''''''''''''''''''''''''''''''''''''''
intervals = 30
Sheets("Filtered2Summary").Cells(8, 2).Value = intervals
Sheets("Filtered2Summary").Cells(9, 2).Value = limit
t = 1 / intervals
Dim SumDR(100)
Dim Sumkt(100)
Dim NoPoints(100)
Dim MeanDR(100)
Dim Meankt(100)
Dim wt(15000)
Dim Wtsum1(100)
Dim Wtsum2(100)
Dim Wtsum3(100)
Dim Wtsum4(100)
Dim Wtaverage(100)
Dim Wtstddev(100)
Dim IntervalLowLimit(100)
Dim IntervalHighLimit(100)
```

```
' start is the lowest kt to start with. This is used to wirite data in column B in sheet "Filtered2Summary".
Start = 0
For j = 0 To (intervals - 1)
   Sheets("Filtered2Summary").Cells(j + 14, 2).Value = Start
   Start = Start + t
Next j
For i = 14 To limit
   For j = 0 To (intervals - 1)
      kt = Sheets("Filtered1").Cells(i, 13).Value
      If (t * j) < kt And kt < (t * (j + 1)) Then
         SumDR(j + 1) = SumDR(j + 1) + Sheets("Filtered1").Cells(i, 14).Value
         Sumkt(j + 1) = Sumkt(j + 1) + Sheets("Filtered1").Cells(i, 13).Value
         NoPoints(j + 1) = NoPoints(j + 1) + 1
         Sheets("Filtered2Summary").Cells(j + 14, 3).Value = NoPoints(j + 1)
      End If
   Next j
Next i
For j = 0 To (intervals - 1)
   MeanDR(j + 1) = SumDR(j + 1) / NoPoints(j + 1)
   Meankt(j + 1) = Sumkt(j + 1) / NoPoints(j + 1)
   Sheets("Filtered2Summary").Cells(j + 14, 4).Value = Meankt(j + 1)
   Sheets("Filtered2Summary").Cells(j + 14, 5).Value = MeanDR(j + 1)
Next
For i = 14 To limit
   For j = 0 To (intervals - 1)
      kt = Sheets("Filtered1").Cells(i, 13).Value
      DR = Sheets("Filtered1").Cells(i, 14).Value
      If (t * j) < kt And kt < (t * (j + 1)) Then
         wt(i) = 1 / (Abs(DR - MeanDR(j + 1)))
         Wtsum1(j + 1) = Wtsum1(j + 1) + wt(i) * DR
         Wtsum2(j + 1) = Wtsum2(j + 1) + wt(i)
         Wtaverage(j + 1) = Wtsum1(j + 1) / Wtsum2(j + 1)
         Sheets("Filtered2Summary").Cells(j + 14, 6).Value = Wtaverage(j + 1)
      End If
   Next j
Next i

For i = 14 To limit
   For j = 0 To (intervals - 1)
      kt = Sheets("Filtered1").Cells(i, 13).Value
      DR = Sheets("Filtered1").Cells(i, 14).Value
      If (t * j) < kt And kt < (t * (j + 1)) Then
         dep = (DR - Wtaverage(j + 1)) ^ 2
         Wtsum3(j + 1) = Wtsum3(j + 1) + dep
         Wtsum4(j + 1) = Wtsum4(j + 1) + 1
         Wtstddev(j + 1) = (Wtsum3(j + 1) / Wtsum4(j + 1)) ^ 0.5
         Sheets("Filtered2Summary").Cells(j + 14, 7).Value = Wtstddev(j + 1)
      End If
   Next j
Next i
Stddevfactor = 2
'InputBox ("Enter the standard deviation factor you would like to use")
Sheets("Filtered2Summary").Cells(7, 2).Value = Stddevfactor
For j = 0 To (intervals - 1)
   IntervalLowLimit(j + 1) = Wtaverage(j + 1) - Wtstddev(j + 1) * Stddevfactor
   IntervalHighLimit(j + 1) = Wtaverage(j + 1) + Wtstddev(j + 1) * Stddevfactor
   Sheets("Filtered2Summary").Cells(j + 14, 8).Value = IntervalLowLimit(j + 1)
   Sheets("Filtered2Summary").Cells(j + 14, 9).Value = IntervalHighLimit(j + 1)
Next j
' k is used to delete any empty lines in the sheet which the data is being sent to
k = 0
For i = 14 To limit
   For j = 0 To (intervals - 1)
      kt = Sheets("Filtered1").Cells(i, 13).Value
```

```
DR = Sheets("Filtered1").Cells(i, 14).Value
If (t * j) < kt And kt < (t * (j + 1)) Then
   If DR < IntervalLowLimit(j + 1) Or DR > IntervalHighLimit(j + 1) Then
      k = k + 1
   ElseIf DR >= IntervalLowLimit(j + 1) And DR <= IntervalHighLimit(j + 1) Then
      Sheets("Filtered2").Cells(i - k, 1).Value = Sheets("Filtered1").Cells(i, 1).Value
      Sheets("Filtered2").Cells(i - k, 2).Value = Sheets("Filtered1").Cells(i, 2).Value
      Sheets("Filtered2").Cells(i - k, 3).Value = Sheets("Filtered1").Cells(i, 3).Value
      Sheets("Filtered2").Cells(i - k, 4).Value = Sheets("Filtered1").Cells(i, 4).Value
      Sheets("Filtered2").Cells(i - k, 5).Value = Sheets("Filtered1").Cells(i, 5).Value
      Sheets("Filtered2").Cells(i - k, 6).Value = Sheets("Filtered1").Cells(i, 6).Value
      Sheets("Filtered2").Cells(i - k, 7).Value = Sheets("Filtered1").Cells(i, 7).Value
      Sheets("Filtered2").Cells(i - k, 8).Value = Sheets("Filtered1").Cells(i, 8).Value
      Sheets("Filtered2").Cells(i - k, 9).Value = Sheets("Filtered1").Cells(i, 9).Value
      Sheets("Filtered2").Cells(i - k, 10).Value = Sheets("Filtered1").Cells(i, 10).Value
      Sheets("Filtered2").Cells(i - k, 11).Value = Sheets("Filtered1").Cells(i, 11).Value
      Sheets("Filtered2").Cells(i - k, 12).Value = Sheets("Filtered1").Cells(i, 12).Value
      Sheets("Filtered2").Cells(i - k, 13).Value = kt
      Sheets("Filtered2").Cells(i - k, 14).Value = DR
    End If
  End If
 Next j
Next i
' Find the new number of data points after filtration.
i = 14
2 'start a loop
celvar = Sheets("Filtered2").Cells(i, 2).Value
If (celvar <> "") Then
i = i + 1
GoTo 2
Else
limit1 = i - 14
End If
Sheets("Filtered2Summary").Cells(10, 2).Value = limit1
End Sub
```

Appendix B8: Opening a large data file

```
Open "C:\Mylnefield_StrathAllan.prn" For Input As 100
I = 1
Do Until EOF(100)
Input #100, Yr, mont, dy, Hr, CC, Gsr, Dsr
If (mont = Givemon) Then
Sheets("Main").Cells(I, 1).Value = Yr
Sheets("Main").Cells(I, 2).Value = mont
Sheets("Main").Cells(I, 3).Value = dy
Sheets("Main").Cells(I, 4).Value = Hr
Sheets("Main").Cells(I, 5).Value = Gsr
Sheets("Main").Cells(I, 6).Value = Dsr
I = I + 1
End If
Loop
Close #100
Open "C:\Documents and Settings\sg179\Desktop\allfiles\CIBSEtemp\Tamb.dat" For Input As 200
I = 1
Do Until EOF(200)
Input #200, Tamb, Yr, mont, dy, Hr
If (mont = Givemon) Then
Sheets("Main").Cells(I, 7).Value = Tamb
I = I + 1
End If
```

Appendix B9: The switch function

```
For J = 4 To 50715
G(J) = Sheets("1").Cells(J, 8).Value
If G(J) <= GCEASE Then
   switch(J) = 0
ElseIf G(J) >= GSTART Then
   switch(J) = 1
ElseIf 147 < G(J) < 290 Then
   switch(J) = 2
End If
Next J
For J = 4 To 50715
If switch(J - 1) = 0 Then
   If switch(J) = 2 Then
      switch(J) = 0
   End If
ElseIf switch(J - 1) = 1 Then
   If switch(J) = 2 Then
      switch(J) = 1
   End If
End If
Next J
```

Appendix B10: Monthly volume and efficiency calculations for different fan combinations

```
Sub MONTHLY_VOLUME_AND_EFFICIENCY_DETERMINATION()
'DEFINE DUCT PROPERTIES
Diameter = 152
Length = 10
EF = 0.8
Barometric = 760
viscosity = 0.0000176
ductArea = (3.14 * ((Diameter / 1000) ^ 2)) / 4
If EF = 1 Then
   k = 9.6
ElseIf EF = 0.8 Then
   k = 2.5
End If
roughness = k / (Diameter)
' INITIALISE VOLUME, ELECTRICAL ENERGY, PV ENERGY
Volume(0) = 0
Volume(1) = 0
Volume(2) = 0
Volume(3) = 0
Volume(4) = 0
Volume(5) = 0
Volume(6) = 0
Volume(7) = 0
Volume(8) = 0
ElEnergy(0) = 0
ElEnergy(1) = 0
ElEnergy(2) = 0
ElEnergy(3) = 0
ElEnergy(4) = 0
ElEnergy(5) = 0
ElEnergy(6) = 0
ElEnergy(7) = 0
ElEnergy(8) = 0
ElEnergy(0) = 0
PVEnergy(0) = 0
PVEnergy(1) = 0
PVEnergy(2) = 0
PVEnergy(3) = 0
PVEnergy(4) = 0
PVEnergy(5) = 0
PVEnergy(6) = 0
PVEnergy(7) = 0
PVEnergy(8) = 0
Flow(1) = 0
ElPower(1) = 0
Dim switch(52000)
Dim Volume(8)
Dim ElEnergy(8)
Dim PVEnergy(8)
Dim PneuEnergy(8)
Dim IRR(8)
Dim G(52000)
Dim Flow(52000)
Dim ElPower(52000)
Dim PneuPower(52000)
Dim PVPm(52000)
' DEFINE PARAMETERS FOR ALL PV MODULE CHOICES
For Module = 1 To 6
If Module = 1 Then
Gref = 725
Tref = 28
iscref = 0.211
Vocref = 20.4
pmref = 2.91
Vmref = 15.9
Imref = 0.183
disc = 0.065 * iscref * 0.01
dvoc = -0.08
Rs = 1.5
area = 0.036
U = 1.5
FI = 1
FactV = 1
FP = 1
s = 19 + FAN
```

```
ElseIf Module = 2 Then
Gref = 725
Tref = 28
iscref = 0.211
Vocref = 20.4
pmref = 2.91
Vmref = 15.9
Imref = 0.183
disc = 0.065 * iscref * 0.01
dvoc = -0.08
Rs = 1.5
area = 2 * 0.036
U = 1.5
FI = 2
FactV = 1
FP = 2
s = 23 + FAN
ElseIf Module = 3 Then
Gref = 725
Tref = 28
iscref = 0.211
Vocref = 20.4
pmref = 2.91
Vmref = 15.9
Imref = 0.183
disc = 0.065 * iscref * 0.01
dvoc = -0.08
Rs = 1.5
area = 2 * 0.036
U = 1.5
FI = 1
FactV = 2
FP = 2
s = 27 + FAN
ElseIf Module = 4 Then
Gref = 750
Tref = 31
iscref = 0.471
Vocref = 20.5
pmref = 6.76
Vmref = 16
Imref = 0.42
disc = 0.065 * iscref * 0.01
dvoc = -0.08
Rs = 1.2
area = 0.072
U = 1.9
FI = 1
FactV = 1
FP = 1
s = 7 + FAN
ElseIf Module = 5 Then
Gref = 750
Tref = 31
iscref = 0.471
Vocref = 20.5
pmref = 6.76
Vmref = 16
Imref = 0.42
disc = 0.065 * iscref * 0.01
dvoc = -0.08
Rs = 1.2
area = 2 * 0.072
U = 1.9
FI = 2
FactV = 1
FP = 2
s = 11 + FAN
ElseIf Module = 6 Then
Gref = 750
Tref = 31
iscref = 0.471
Vocref = 20.5
pmref = 6.76
Vmref = 16
Imref = 0.42
disc = 0.065 * iscref * 0.01
dvoc = -0.08
Rs = 1.2
area = 2 * 0.072
```

```
U = 1.9
FI = 1
FactV = 2
FP = 2
s = 15 + FAN
End If
G(3) = Sheets("1").Cells(3, 8).Value
'DEFINE THRESHOLD IRRADIANCES FOR DIFFERENT FAN CHOICES
For FAN = 0 To 6 Step 1
If Module = 4 Or Module = 6 Then
If FAN = 1 Or FAN = 6 Then
GSTART = 290
GCEASE = 147
Elself FAN = 5 Then
GSTART = 580
GCEASE = 293
Elself FAN = 0 Or FAN = 4 Then
GSTART = 518
GCEASE = 147
Elself FAN = 3 Then
GSTART = 1036
GCEASE = 293
Elself FAN = 2 Then
GSTART = 800
GCEASE = 153
End If
Elself Module = 5 Then
If FAN = 1 Or FAN = 6 Then
GSTART = 145
GCEASE = 74
Elself FAN = 5 Then
GSTART = 290
GCEASE = 147
Elself FAN = 0 Or FAN = 4 Then
GSTART = 259
GCEASE = 74
Elself FAN = 3 Then
GSTART = 518
GCEASE = 147
Elself FAN = 2 Then
GSTART = 400
GCEASE = 77
End If
Elself Module = 1 Or Module = 3 Then
If FAN = 1 Or FAN = 6 Then
GSTART = 600
GCEASE = 303
Elself FAN = 5 Then
GSTART = 1200
GCEASE = 606
Elself FAN = 0 Or FAN = 4 Then
GSTART = 1072
GCEASE = 303
Elself FAN = 3 Then
GSTART = 2144
GCEASE = 606
Elself FAN = 2 Then
GSTART = 1800
GCEASE = 317
End If
Elself Module = 2 Then
If FAN = 1 Or FAN = 6 Then
GSTART = 300
GCEASE = 152
Elself FAN = 5 Then
GSTART = 600
GCEASE = 303
Elself FAN = 0 Or FAN = 4 Then
GSTART = 518
GCEASE = 152
Elself FAN = 3 Then
GSTART = 1072
GCEASE = 303
Elself FAN = 2 Then
GSTART = 900
GCEASE = 159
End If
End If
' DEFINE FAN PARAMETERS FOR IV, wV and head-flow chracteristic determination
If FAN = 0 Then
```

```
s = 3
Av = 0.0604
Bv = -0.1056
Aw = 227.66
Bw = -128.53
C1 = 0.000192
C2 = 0.0000000367
w = -0.002
x = 0.15
y = -3.98
Z = 57.4
Fact1 = 1
Fact2 = 1
Elseif FAN = 1 Then
s = 4
Av = 0.0144
Bv = -0.01
Aw = 131.77
Bw = -365.58
C1 = 0.000192
C2 = 0.0000000367
w = -0.002
x = 0.15
y = -3.98
Z = 57.4
Fact1 = 1
Fact2 = 1
Elseif FAN = 2 Then
s = 5
Av = 0.0393
Bv = -0.1317
Aw = 159.04
Bw = -384.23
C1 = 0.000192
C2 = 0.0000000367
w = -0.0006
x = 0.058
y = -2.39
Z = 62.4
Fact1 = 1
Fact2 = 1
' 2 fan0 in Parallel
Elseif FAN = 3 Then
s = 3
Av = 2 * 0.0604
Bv = 2 * -0.1056
Aw = 227.66
Bw = -128.53
C1 = 0.000192
C2 = 0.0000000367
w = -0.002
x = 0.15
y = -3.98
Z = 57.4
Fact1 = 2
Fact2 = 2
' 2 fan0 in Series
Elseif FAN = 4 Then
s = 3
Av = 0.0604 / 2
Bv = -0.1056
Aw = 227.66
Bw = -128.53
C1 = 0.000192
C2 = 0.0000000367
w = -0.002
x = 0.15
y = -3.98
Z = 57.4
Fact1 = 2
Fact2 = 1
' 2 Fan1 in Parallel
Elseif FAN = 5 Then
s = 4
Av = 2 * 0.0144
Bv = 2 * -0.01
Aw = 131.77
Bw = -365.58
w = -0.002
x = 0.15
```

```
y = -3.98
Z = 57.4
Fact1 = 2
Fact2 = 2
' 2 Fan1 in Series
ElseIf FAN = 6 Then
s = 4
Av = 0.0144 / 2
Bv = -0.01
Aw = 131.77
Bw = -365.58
C1 = 0.000192
C2 = 0.0000000367
w = -0.002
x = 0.15
y = -3.98
Z = 57.4
Fact1 = 2
Fact2 = 1
End If
'FOR ALL DATA POINTS, ASSIGN A VALUE OF 1 FOR AN OPERATING SYSTEM AND 0 FOR
A ' NONOPERATING SYSTEM AND STORE THE VALUE
' TO BE RECALLED LATER
For J = 4 To 50715
G(J) = Sheets("1").Cells(J, 8).Value
If G(J) <= GCEASE Then
   switch(J) = 0
ElseIf G(J) >= GSTART Then
   switch(J) = 1
ElseIf 147 < G(J) < 290 Then
   switch(J) = 2
End If
Next J
For J = 4 To 50715
If switch(J - 1) = 0 Then
   If switch(J) = 2 Then
      switch(J) = 0
   End If
ElseIf switch(J - 1) = 1 Then
   If switch(J) = 2 Then
      switch(J) = 1
   End If
End If
Next J
For givenmon = 1 To 12
Volume(FAN) = 0
ElEnergy(FAN) = 0
PVEnergy(FAN) = 0
IRR(FAN) = 0
PneuEnergy(FAN) = 0
'START CALCULATION (FOR SYSTEMS WITH SWITCH = 1 ONLY) BY READING IRRADIANCE AND
'TEMPERATURE FOR EACH LINE OF DATA
For J = 4 To 50715
mont = Sheets("1").Cells(J, 1).Value
If mont = givenmon Then
G(J) = Sheets("1").Cells(J, 8).Value
If G(J) > 1500 Then
   GoTo 1
End If
If G(J) <= 0 Then
   GoTo 1
End If
Tamb = Sheets("1").Cells(J, 7).Value
If FAN = 0 Then
   If G(J) <= 500 Then
      t = 100000000#
   Else
      t = 10000
   End If
ElseIf FAN = 1 Then
   If G(J) <= 300 Then
      t = 100000
   Else
      t = 10000
   End If
ElseIf FAN = 2 Then
   If G(J) <= 200 Then
      t = 10000000
   Else
      t = 10000
```

```
    End If
  End If
  If switch(J) = 1 Then
    GoTo 2
  Else
    GoTo 1
  End If
  2
  Eff = 0.2
  m = 0
  Do
  Eff = Eff - m
  Tmod = Tamb + ((0.9 / U) * G(J) * area * (1 - (Eff / 0.9)))
  FF = (pmref / (iscref * Vocref))
  dpm = FF * ((iscref * dvoc) + (Vocref * disc))
  Isc = FI * (G(J) / Gref) * (iscref + disc * (Tmod - Tref))
  Pm = FP * (G(J) / Gref) * (pmref + dpm * (Tmod - Tref))
  VOC = FactV * (Vocref + ((dvoc * (Tmod - Tref)) + Application.Ln(G(J) / Gref)))
  Vm = FactV * (Vmref + ((dvoc * (Tmod - Tref)) + Application.Ln(G(J) / Gref)))
  Im = Pm / Vm
  If (Im / Isc) > 1 Then
    Im = 0.99 * Isc
  End If
  A = ((Vm - VOC + (Im * Rs)) / (Application.Ln(1 - (Im / Isc))))
  I0 = Isc * Exp(-VOC / A)
  N = 1
  Do
    I = Isc - ((N - 1) * (Isc / t))
    V = A * Application.Ln((Isc - I + I0) / I0) - (I * Rs)
    ifan = Av * V + Bv
    N = N + 1
  Loop Until (I - ifan) < 0.001
  Eff1 = (I * V) / (G(J) * area)
  m = m + 0.001
  Loop Until (Abs(Eff1 - Eff)) < 0.01
  ElPower(J) = V * I
  PVPm(J) = Pm
  ws = Aw * (V / Fact2) + Bw
  speed = ws
  If FAN = 0 Or FAN = 1 Then
  Qlimit1 = 0.0143 * speed
  Qlimit2 = 0.0183 * speed
  constA1 = -0.00061 * speed - 0.0069
  constB1 = 0.0000125 * (speed ^ 2) - 0.000000536 * speed
  constA2 = -0.000588 * speed - 0.0032
  constB2 = 0.0000144 * speed ^ 2 + 0.00000959 * speed
  Hlimit1 = constA1 * Qlimit1 + constB1
  Hlimit2 = constA2 * Qlimit2 + constB2
  constA3 = (Hlimit1 - Hlimit2) / (Qlimit1 - Qlimit2)
  constB3 = Hlimit1 + (Qlimit1 * ((Hlimit1 - Hlimit2) / (Qlimit1 - Qlimit2)))
  ElseIf FAN = 2 Then
  Qlimit1 = 0.0138 * speed
  Qlimit2 = 0.0212 * speed
  constA1 = -0.00079 * speed - 0.00045
  constB1 = 0.0000167 * (speed ^ 2) - 0.00000656 * speed
  constA2 = -0.000492 * speed - 0.000467
  constB2 = 0.0000159 * speed ^ 2 + 0.00000171 * speed
  Hlimit1 = constA1 * Qlimit1 + constB1
  Hlimit2 = constA2 * Qlimit2 + constB2
  constA3 = (Hlimit1 - Hlimit2) / (Qlimit1 - Qlimit2)
  constB3 = Hlimit1 - (Qlimit1 * ((Hlimit1 - Hlimit2) / (Qlimit1 - Qlimit2)))
  End If
  ''''''''''''''''''''''''''''''''''''''''''''''''''''''''''''

  Tair = Tamb + 5
  densityfactor = (Barometric / (AirTemp + 273.15))
  density = ((Barometric / 760) * 101325) / ((Tair + 273.15) * 288.297)
  Qref = 5
  Do
    ' Calculate point on fan curve corresponding to the reference Qref
    '
    Q = C1 * Qref * speed * densityfactor
    hf = C2 * (speed ^ 2) * (densityfactor ^ 2) * (w * (Qref ^ 3) + x * (Qref ^ 2) + y * Qref + Z)
    'If Q < Qlimit1 Then
    '  hf = constA1 * Q + constB1
    'ElseIf Q > Qlimit2 Then
    '  hf = constA2 * Q + constB2
    'ElseIf Qlimit1 <= Q And Q <= Qlimit2 Then
    '  hf = constA3 * Q + constB3
    'End If
    ' Start calculating the corresponding point on the system's curve (Use Q not Qref)
```

```
'
Velocity = ((Q / 1000)) / ductArea
Reynolds = (density * Velocity * (Diameter / 1000)) / viscosity
f = 1.325 / (((Application.Ln(roughness / 3.3)) + (5.74 / (Reynolds ^ 0.9))) ^ 2)
Hs = ((f * Length * density) / (2 * (Diameter / 1000))) * (Velocity ^ 2)
'
'ALTERNATIVELY THE SYSTEM CURVE CAN BE USED IN ONE STEP BY USING THE QUADRATIC
'FIT FOR THE MEASURED DATA POINTS
'HS = 0.0036 * Q ^ 2 + 0.1783 * Q (Statement taken aout of the code to avoid error messages)
'Minimise difference between the two points on the fan curve and system curve
'
Hdiff = Abs(hf - Hs)
'
' Increase the value of Q and continue until the two points come close
'
Qref = Qref + (Hdiff / 100)
Loop Until Hdiff < 0.01
Flow(J) = Q
PneuPower(J) = 0.001 * Q * Hs
If switch(J - 1) = 0 Then
  Volume(FAN) = Volume(FAN)
  ElEnergy(FAN) = ElEnergy(FAN)
  PVEnergy(FAN) = PVEnergy(FAN)
  IRR(FAN) = IRR(FAN)
ElseIf switch(J - 1) = 1 Then
Volume(FAN) = Volume(FAN) + 0.15 * (Flow(J - 1) + Flow(J))
ElEnergy(FAN) = ElEnergy(FAN) + (ElPower(J) + ElPower(J - 1)) * (5 * 30)
PVEnergy(FAN) = PVEnergy(FAN) + (PVPm(J) + PVPm(J - 1)) * (5 * 30)
PneuEnergy(FAN) = PneuEnergy(FAN) + (PneuPower(J) + PneuPower(J - 1)) * (5 * 30)
IRR(FAN) = IRR(FAN) + ((G(J) + G(J - 1)) * (5 * 30) * 0.072)
ElseIf switch(J + 1) = 0 Then
Volume(FAN) = Volume(FAN) + (0.15 * Flow(J - 1))
ElEnergy(FAN) = ElEnergy(FAN) + (ElPower(J - 1)) * (5 * 30)
PVEnergy(FAN) = PVEnergy(FAN) + (PVPm(J - 1)) * (5 * 30)
PneuEnergy(FAN) = PneuEnergy(FAN) + (PneuPower(J - 1)) * (5 * 30)
IRR(FAN) = IRR(FAN) + ((G(J - 1)) * (5 * 30) * 0.072)
End If
End If
Next J
Sheets("Results").Cells(givenmon + 1, (((7 * Module) - 2) + FAN)).Value = Volume(FAN)
Sheets("Results").Cells(givenmon + 14, (((7 * Module) - 2) + FAN)).Value = IRR(FAN)
Sheets("Results").Cells(givenmon + 27, (((7 * Module) - 2) + FAN)).Value = ElEnergy(FAN)
Sheets("Results").Cells(givenmon + 40, (((7 * Module) - 2) + FAN)).Value = PVEnergy(FAN)
Sheets("Results").Cells(givenmon + 53, (((7 * Module) - 2) + FAN)).Value = PneuEnergy(FAN)
Next givenmon
Next FAN
Next Module
End Sub
```